



*materials*

Volume 3

# Environment- Friendly Construction Materials

---

Edited by  
Shaopeng Wu, Inge Hoff, Serji N. Amirkhanian and Yue Xiao  
Printed Edition of the Special Issue Published in *Materials*

# **Environment-Friendly Construction Materials**



# Environment-Friendly Construction Materials

Volume 3

Special Issue Editors

**Shaopeng Wu**

**Inge Hoff**

**Serji N. Amirkhanian**

**Yue Xiao**

MDPI • Basel • Beijing • Wuhan • Barcelona • Belgrade





*Special Issue Editors*

Shaopeng Wu

Wuhan University of Technology

(WUT)

China

Serji N. Amirkhanian

University of Alabama

USA

Inge Hoff

Norwegian University of Science and Technology

(NTNU)

Norway

Yue Xiao

Wuhan University of Technology (WUT)

China

*Editorial Office*

MDPI

St. Alban-Anlage 66

4052 Basel, Switzerland

This is a reprint of articles from the Special Issue published online in the open access journal *Materials* (ISSN 1996-1944) from 2018 to 2019 (available at: [https://www.mdpi.com/journal/materials/special\\_issues/EFCM](https://www.mdpi.com/journal/materials/special_issues/EFCM)).

For citation purposes, cite each article independently as indicated on the article page online and as indicated below:

LastName, A.A.; LastName, B.B.; LastName, C.C. Article Title. *Journal Name* **Year**, Article Number, Page Range.

**Volume 3**

ISBN 978-3-03921-016-9 (Pbk)

ISBN 978-3-03921-017-6 (PDF)

**Volume 1-3**

ISBN 978-3-03897-418-5 (Pbk)

ISBN 978-3-03897-419-2 (PDF)

© 2019 by the authors. Articles in this book are Open Access and distributed under the Creative Commons Attribution (CC BY) license, which allows users to download, copy and build upon published articles, as long as the author and publisher are properly credited, which ensures maximum dissemination and a wider impact of our publications.

The book as a whole is distributed by MDPI under the terms and conditions of the Creative Commons license CC BY-NC-ND.

# Contents

<b>About the Special Issue Editors</b> . . . . .	vii
<b>Wojciech Andrzejuk, Danuta Barnat-Hunek, Rafat Siddique, Bartosz Zegardło and Grzegorz Łagód</b> Application of Recycled Ceramic Aggregates for the Production of Mineral-Asphalt Mixtures Reprinted from: <i>Materials</i> <b>2018</b> , <i>11</i> , 658, doi:10.3390/ma11050658 . . . . .	1
<b>Paweł Ogrodnik, Jacek Szulej and Wojciech Franus</b> The Wastes of Sanitary Ceramics as Recycling Aggregate to Special Concretes Reprinted from: <i>Materials</i> <b>2018</b> , <i>11</i> , 1275, doi:10.3390/ma11081275 . . . . .	21
<b>Kai Wang, Liang Ren and Luqing Yang</b> Excellent Carbonation Behavior of Rankinite Prepared by Calcining the C-S-H: Potential Recycling of Waste Concrete Powders for Prefabricated Building Products Reprinted from: <i>Materials</i> <b>2018</b> , <i>11</i> , 1474, doi:10.3390/ma11081474 . . . . .	36
<b>Xiaoliang Zhang, Ben Zhang, Huaxin Chen and Dongliang Kuang</b> Feasibility Evaluation of Preparing Asphalt Mixture with Low-Grade Aggregate, Rubber Asphalt and Desulphurization Gypsum Residues Reprinted from: <i>Materials</i> <b>2018</b> , <i>11</i> , 1481, doi:10.3390/ma11081481 . . . . .	45
<b>Hongyin Li, Hailong Jiang, Wenwu Zhang, Peng Liu, Shanshan Wang, Fei Wang, Jizhe Zhang and Zhanyong Yao</b> Laboratory and Field Investigation of the Feasibility of Crumb Rubber Waste Application to Improve the Flexibility of Anti-Rutting Performance of Asphalt Pavement Reprinted from: <i>Materials</i> <b>2018</b> , <i>11</i> , 1738, doi:10.3390/ma11091738 . . . . .	65
<b>Yueqin Hou, Xiaoping Ji, Jia Li and Xianghang Li</b> Adhesion between Asphalt and Recycled Concrete Aggregate and Its Impact on the Properties of Asphalt Mixture Reprinted from: <i>Materials</i> <b>2018</b> , <i>11</i> , 2528, doi:10.3390/ma11122528 . . . . .	81
<b>Yanan Li, Yuchao Lyv, Liang Fan and Yuzhen Zhang</b> Effects of Cement and Emulsified Asphalt on Properties of Mastics and 100% Cold Recycled Asphalt Mixtures Reprinted from: <i>Materials</i> <b>2019</b> , <i>12</i> , 754, doi:10.3390/ma12050754 . . . . .	96
<b>Sakdirat Kaewunruen, Dan Li, Yu Chen and Zhechun Xiang</b> Enhancement of Dynamic Damping in Eco-Friendly Railway Concrete Sleepers Using Waste-Tyre Crumb Rubber Reprinted from: <i>Materials</i> <b>2018</b> , <i>11</i> , 1169, doi:10.3390/ma11071169 . . . . .	116
<b>Mian Sun, Youzhi Chen, Jiaoqun Zhu, Tao Sun, Zhonghe Shui, Gang Ling, Haoxuan Zhong and Yourui Zheng</b> Effect of Modified Polyvinyl Alcohol Fibers on the Mechanical Behavior of Engineered Cementitious Composites Reprinted from: <i>Materials</i> <b>2019</b> , <i>12</i> , 37, doi:10.3390/ma12010037 . . . . .	136

<b>Gang Ling, Zhonghe Shui, Tao Sun, Xu Gao, Yunyao Wang, Yu Sun, Guiming Wang and Zhiwei Li</b> Rheological Behavior and Microstructure Characteristics of SCC Incorporating Metakaolin and Silica Fume Reprinted from: <i>Materials</i> <b>2018</b> , <i>11</i> , 2576, doi:10.3390/ma1122576 . . . . .	156
<b>Kaizhi Liu, Rui Yu, Zhonghe Shui, Xiaosheng Li, Xuan Ling, Wenhao He, Shuangqin Yi and Shuo Wu</b> Effects of Pumice-Based Porous Material on Hydration Characteristics and Persistent Shrinkage of Ultra-High Performance Concrete (UHPC) Reprinted from: <i>Materials</i> <b>2019</b> , <i>12</i> , 11, doi:10.3390/ma12010011 . . . . .	172
<b>Baoguo Ma, Yi Peng, Hongbo Tan, Zhenghang Lv and Xiufeng Deng</b> Effect of Polyacrylic Acid on Rheology of Cement Paste Plasticized by Polycarboxylate Superplasticizer Reprinted from: <i>Materials</i> <b>2018</b> , <i>11</i> , 1081, doi:10.3390/ma11071081 . . . . .	194
<b>Weiting Xu, Jiangxiong Wei, Jiajian Chen, Bin Zhang, Peng Xu, Jie Ren and Qijun Yu</b> Comparative Study of Water-Leaching and Acid-Leaching Pretreatment on the Thermal Stability and Reactivity of Biomass Silica for Viability as a Pozzolanic Additive in Cement Reprinted from: <i>Materials</i> <b>2018</b> , <i>11</i> , 1697, doi:10.3390/ma11091697 . . . . .	213
<b>Dong Zhang, Meizhu Chen, Quantao Liu, Jiuming Wan and Jinxuan Hu</b> Preparation and Thermal Properties of Molecular-Bridged Expanded Graphite/Polyethylene Glycol Composite Phase Change Materials for Building Energy Conservation Reprinted from: <i>Materials</i> <b>2018</b> , <i>11</i> , 818, doi:10.3390/ma11050818 . . . . .	231
<b>Gonghan Xia, Wenlai Xu, Qinglin Fang, Zishen Mou and Zhicheng Pan</b> Graphene-Modulated Removal Performance of Nitrogen and Phosphorus Pollutants in a Sequencing Batch <i>Chlorella</i> Reactor Reprinted from: <i>Materials</i> <b>2018</b> , <i>11</i> , 2181, doi:10.3390/ma11112181 . . . . .	247

## About the Special Issue Editors

**Shaopeng Wu** is a chief professor of materials science and engineering at Wuhan University of Technology. Dr. Wu is a prominent researcher in the field of bituminous materials and asphalt pavement. He has completed research projects on subjects including electrically conductive asphalt pavement, rubberized asphalt binder, recycling asphalt materials, self-healing asphalt, and asphalt preventive maintenance technologies. Dr. Wu is an editor of “Journal of Testing and Evaluation” and “International Journal of Pavement Research and Technology”, and a member of the International Society of Asphalt Pavement. He has received 14 provincial awards, including 3 first-prize Science and Technology Progress Awards. He has already supervised more than 30 research projects and published more than 300 SCI peer-reviewed journal papers.

**Inge Hoff** started his research career in the independent research organization SINTEF (Norway) doing contracted research projects for 10 years. Most of the projects were laboratory-based projects financed by the Norwegian Public Roads Administration or producers of different types of materials. Dr. Hoff was appointed to professor in 2009 and has been working at NTNU since then. He was a supervisor of nine completed Ph.D. projects and is currently supervising six Ph.D. students. Dr. Hoff has authored more than 80 scientific and popular scientific papers and is an active reviewer for several international scientific journals. In addition, he has authored several SINTEF reports. Dr. Hoff is the leader of the only research laboratory for materials for transport infrastructure in Norway. The laboratory is used for education of master’s and Ph.D. students, project-based testing for industry, and research purposes.

**Serji N. Amirkhanian** was the Mays Professor of Transportation and the director of the Asphalt Rubber Technology Services (ARTS) in the Department of Civil Engineering at Clemson University until June of 2010, before becoming a professor of civil engineering at the University of Alabama, Tuscaloosa, USA. He is also a professor of civil engineering at Wuhan University of Technology (Wuhan, China), in addition to being an adjunct professor of materials at Norwegian University of Science and Technology (NTNU), Norway.

His research has resulted in over 300 refereed journal papers, conference papers, and research reports. He has also published several book chapters. In addition, he has given over 300 presentations, presenting his research findings in the US and internationally. He has supported over 100 graduate students and over 15 post-doctoral scholars, conducting research for many agencies (e.g., the Federal Highway Administration (FHWA)). He has consulted for many companies or agencies, such as the World Bank, United Nations (UNIDO), BMW, Owens Corning, Michelin, Honeywell International, Ontario Ministry of Transportation, and Honduras Ministry of Transportation, among many others.

**Yue Xiao** has been an associate research professor at State Key Lab of Silicate Materials for Architectures in the Wuhan University of Technology since 2014. He was named the Fok Ying Tung Outstanding Young Teacher by the Ministry of Education of China in 2018. He received the title of CHUTIAN Scholar in material science and engineering from the Hubei provincial department of education in 2014. Dr. Xiao obtained his PhD degree in road and railway engineering from Delft University of Technology, the Netherlands. Subsequently, he joined Wuhan University of Technology. His research interests include eco-efficient pavement materials and construction material recycling.

Dr. Xiao is now conducting three innovative projects founded by the National Natural Science Foundation of China (NSFC), as well as projects supported by provincial departments. Since 2011, Dr. Xiao has published 49 SCI peer-reviewed journal papers.





Article

# Application of Recycled Ceramic Aggregates for the Production of Mineral-Asphalt Mixtures

Wojciech Andrzejuk <sup>1</sup>, Danuta Barnat-Hunek <sup>2</sup>, Rafat Siddique <sup>3</sup>, Bartosz Zegardło <sup>4</sup> and Grzegorz Łagód <sup>5,\*</sup>

<sup>1</sup> Faculty of Economic and Technical Science, Pope John Paul II State School of Higher Education in Biała Podlaska, Sidorska Str. 95/97, 21-500 Biała Podlaska, Poland; w.andrzejuk@dydaktyka.pswbp.pl

<sup>2</sup> Faculty of Civil Engineering and Architecture, Lublin University of Technology, Nadbystrzycka Str. 40, 20-618 Lublin, Poland; d.barnat-hunek@pollub.pl

<sup>3</sup> Department of Civil Engineering, Thapar University, Patiala, Punjab 147004, India; siddique\_66@yahoo.com

<sup>4</sup> Faculty of Natural Sciences, Siedlce University of Natural Sciences and Humanities, 14 B. Prusa Str., 08-100 Siedlce, Poland; bart.z@wp.pl

<sup>5</sup> Faculty of Environmental Engineering, Lublin University of Technology, 40B Nadbystrzycka Str., 20-618 Lublin, Poland

\* Correspondence: g.lagod@pollub.pl; Tel.: +48-81-538-43-22

Received: 30 March 2018; Accepted: 19 April 2018; Published: 24 April 2018

**Abstract:** This paper describes a method of designing and producing innovative mineral–asphalt mixtures, which utilize waste aggregate from the recycling of sanitary ceramics. The work presents the basic properties of the ceramic material, the investigation concerning the microstructure of the aggregate obtained from the grinding of waste, and a comparison with the images obtained for the aggregates usually employed in mineral–asphalt mixtures. The mixtures were designed for the application in the wearing course. Four series of mixtures were prepared. In the first and second, the ceramic aggregate constituted a partial substitute for dolomite, whereas in the third, we substituted granodiorite, and the fourth series contained only dolomite. The mixtures were examined for the content of soluble binder, the bulk density of samples, the presence of voids, the space filled with binder, and the susceptibility to water and frost corrosion. The obtained results were compared with the standard requirements. The microstructure as well as the contact zone in the considered mineral–asphalt mixtures are presented based on research conducted by means of a scanning electron microscope (SEM).

**Keywords:** mineral-asphalt mixtures; aggregate from sanitary ceramic wastes; environmentally friendly construction materials

---

## 1. Introduction

The degradation of the natural environment observed in recent years, resulting from rapid development, has made ecological security one of the top issues for contemporary science to address. The increased production occurring in industry, which consumes a large quantity of energy and yields a huge amount of post-production waste, is especially unfavorable [1,2].

Moreno-Maroto et al. have assessed different wastes for lightweight aggregate (LWA) manufacturing: granite and marble sludge (COR), sepiolite rejections (SEP), and polyethylene–hexene thermoplastics (P) [3]. Some most recent studies on the application of wastes for LWA sintering were presented by Liu et al. [4]—involving sewage sludge and river sediments, Li et al. [5]—sewage sludge and saline clays, as well as Franus et al. [6]—concerning the changes in the microstructure that occurred when spent oil was added to LWA production. Smarzewski and Barnat-Hunek investigated the mechanical and durability-related properties of high-performance concrete made with coal cinder and



waste foundry sand [7]. Apart from the re-use of a waste substance, the advantages include the reduced consumption of aggregates from natural deposits, as presented, e.g., in studies by Suchorab et al. [8]. The results of the research prove that this type of additive, regardless of the form in which it is used in a concrete mixture (powder or aggregate), deteriorates the strength of concrete. Miličević et al. studied the mechanical properties of concrete made with crushed clay bricks and roof tiles aggregate [9].

Ceramic materials are produced in abundance in various parts of the world; they are also exported to other regions owing to their durability and diversification, which makes them suitable for use in numerous designs [10]. Some studies present work conducted on concrete produced with the use of white ceramics [10–12]. Taking into account the properties of ceramics, this has the potential for application as a supplementary cement material or aggregate in conventional concrete [10,12,13]. Ceramic waste constitutes porous materials that act as a wet hardening agent for hydration of cement paste and reduce the autogenous shrinkage, finally increasing the mechanical strength [14]. Ceramic aggregate in concrete improves the layout of pores, reduces the volume of macropores, and increases the number of capillary pores. Zirconium found in ceramic materials does not migrate into cement paste or influence the chemical reaction of hydration [12]. These factors contribute to increasing the mechanical strength and durability to environmental, chemical, and physical factors [10,12].

In terms of ecologically hazardous substances, ceramic products are inert. According to the Regulation of the European Parliament and Council of 2006 on shipments of waste, sanitary ceramic waste is not classified as hazardous waste [15]. Their production process is irreversible. The ceramic products are persistent and non-biodegradable. The increasing demand for ceramic products results in a growing amount of landfilled waste. Due to the abovementioned reasons, many research institutes made an attempt to devise rational methods of recycling ceramic wastes. The main direction involves using the waste for concrete production. The conducted analyses indicate that ceramic is a durable material with good strength parameters, and its application for concrete mixtures does not require special treatment. The authors of studies confirm the usefulness of recycled aggregates for concrete production. This type of material, acquired from waste sanitary or technical ceramics (e.g., electrical insulators), has a beneficial effect on the properties of concrete [16]. The results show that the greater the ceramic aggregate addition is, the better the strength parameters of concrete are. The interesting properties of the concrete produced with broken sanitary ceramics are also presented by Halicka et al. [16]. In order to economically justify the performed works, the authors seek prospective special applications of this type of concrete. The research results indicate that it can be used in cases where concrete is exposed to high temperatures or in places where high abrasion resistance is required. A method of designing highly resistant concrete produced only with ceramic aggregate was presented in [17]. The analysis of results proved that, owing to the porous structure of aggregate granules, the contact point of cement stone with the aggregate is characterized by higher durability than traditional aggregates, and the concretes obtained in this way exhibit higher strength parameters.

Referring to the results of the abovementioned works, the authors of this paper made an attempt to produce mineral–asphalt mixtures that include waste ceramic aggregates. Few publications on this topic exist in the literature. The possibility of using the waste obtained from grinding ceramic roof tiles as a partial substitute for natural aggregates in the binding layers of mineral–asphalt mixtures was presented in [18]. On the basis of the conducted research, it was concluded that ceramic aggregates can be applied in asphalt concrete and their addition up to 30% was appropriate for roads with medium and low traffic intensity. The authors of the paper focused on designing the mixtures for improving the wearing course of roads. The mixtures were examined for: the content of soluble binder, bulk density of samples, content of voids, content of the spaces filled with binder and susceptibility to water and frost corrosion. The results were compared with the ones obtained for the reference samples prepared from traditional aggregates (the analysis of the available mineral–asphalt mixtures (MAM) research results based on the traditional aggregates). The results were also analyzed in terms of standard requirements.

## 2. Materials and Methods

### 2.1. Material Properties

The study materials were selected by sorting the ceramic waste deposited on a dump adjacent to an industrial plant producing sanitary ceramics, mainly washbasins with cracks, enamel damage, or uneven surface. The acquired waste was crushed in a jaw crusher. The crushers operated in a way that enabled us to sort the grains into two sizes, i.e., fine: 0–4 mm and coarse: 4–8 mm. Grains of larger size were crushed again.

It was planned that the obtained aggregate would partially substitute the aggregates traditionally employed in mineral-asphalt mixtures, i.e., dolomite and granodiorite. A series of experiments were conducted for the obtained and reference aggregates, corresponding to the investigations of the natural aggregates commonly used for concrete production, such as: specific density, bulk density, compressive strength, absorptivity and crushing degree [19–22]. The findings were compared with the literature data [23] for the most popular aggregates employed in road industry. The comparison of results was presented in Table 1.

**Table 1.** Properties of ceramic aggregate in relation to aggregates used in concretes [16].

Property	Granite	Granodiorite	Porphyry	Diabase	Basalt	Quartzitic Sandstone	Compact Limestone	Dolomite	Ceramic Aggregate
Specific density (kg/dm <sup>3</sup> )	2.3–2.8	2.67	2.5–2.6	2.8–2.9	2.6–3.2	2.6–2.7	2.6–2.9	2.4–2.8	2.64
Bulk density (kg/dm <sup>3</sup> )	2.1–2.7	2.62–2.64	2.3–2.4	2.6–2.8	2.5–3.1	2.4–2.6	2.5–2.8	2.2–2.6	2.36
Compressive strength (MPa)	160–240	185–215	160–300	180–250	250–400	120–200	80–180	60–180	400–600
Modulus of elasticity (GPa)	13–61	-	36–68	70–90	56–99	4–43	21–53	18–48	40–70
Thermal expansion coefficient ( $\alpha \cdot 10^{-6}$ )	5.0–9.0	6.0–9.0	7.0–9.0	7.0–9.0	8.0–12.0	12.0–18.0	1.0–8.0	3.0–12.0	6.0–7.0
Absorptivity (%)	0.2–0.5	0.34–0.47	0.2–0.7	0.1–0.3	0.1–0.4	0.2–0.5	0.3–1.5	0.3–2	1.53
Crushing degree (%)	18	14.9	13	16	3.8	15	18–20	20	8.9

Using a scanning electron microscope, an analysis of the surface structure of the ceramic and traditional aggregates was conducted, including dolomite, granodiorite, basalt and sand, which were the ingredients of mixtures, including the reference ones. The structure of the grain surface is presented in Figure 1. The microstructure of aggregate grains has a significant impact on the adhesion of the asphalt to the aggregate; the more developed the aggregate grain surface, the greater the contact area of asphalt, as described by Moraes et al. [24]. On the basis of the possible structural similarity of granodiorite (Figure 1c) and ceramics (Figure 1a), it can be supposed that the adhesion of asphalt to ceramic aggregate grains should not differ from the adhesion of asphalt to granodiorite. Detailed analyses are presented in point 5.

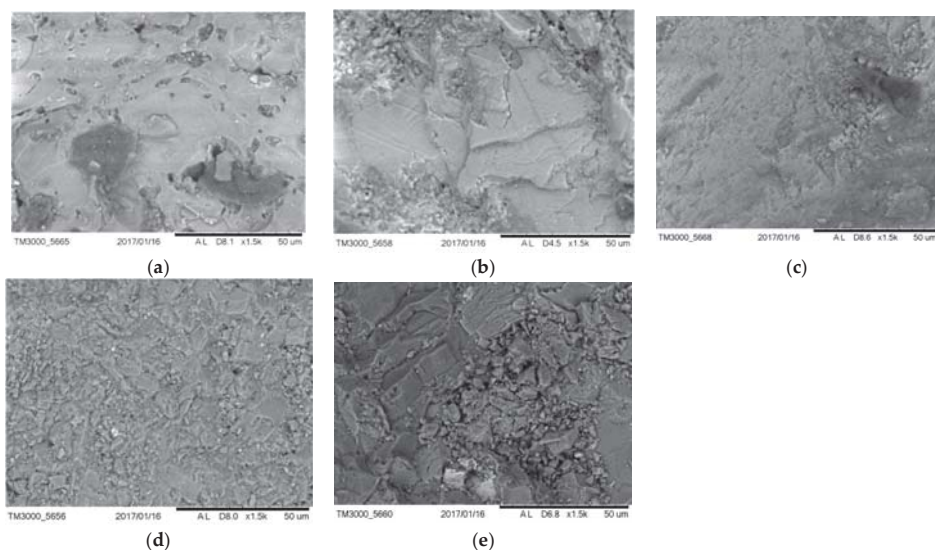


**Figure 1.** Images of aggregate grains structure: (a) obtained from sanitary ceramics, (b) dolomite, (c) granodiorite, (d) basalt, (e) sand ( $\times 1500$ ).

Road asphalt 50/70 with the parameters presented in Table 2 constituted the binder in the mineral-asphalt mixture.

**Table 2.** Parameters of road asphalt 50/70.

Parameter	Unit	Value
Penetration at 25 °C	1/10 mm	50–70
Softening point	°C	46–54
Embrittlement temperature	°C	$\leq -8$
Ignition temperature	°C	$\geq 230$
Solubility	% m/m	$\geq 99.0$
Mass change (absolute value)	% m/m	$\leq 0.5$
Remaining penetration at 25 °C	%	$\geq 50$
Softening point increase	°C	$\leq 9$

Limestone dust was applied as a filling aggregate for bituminous mixtures and surface dressing used on roads, airports and other surfaces intended for traffic, with the grain size of  $2.69 \text{ g/cm}^3$  and properties presented in Table 3.

**Table 3.** Parameters of limestone dust.

Property	Unit	Mean Value	PN-EN 13043:2004 Standard Requirements
passing % through:			
0.150 mm	%	94.5	-
0.125 mm	%	91.7	85–100
0.075 mm	%	81.9	-
0.063 mm	%	76.8	70–100
CaCO <sub>3</sub> content	%	91.6	$\geq 90$
Humidity	%	0.2	$\leq 1.0$

## 2.2. Designing Method of the Mixture

Before the design of the mineral–asphalt mixture could begin, the requirements laid down in WT-2 2014—part I, Mineral–Asphalt Mixtures, Technical Requirements were assumed [25]. The program involved creation of a mixture intended for the wearing course (WC). Preparation of four mixture series was proposed. The series 1 and 2 mixtures (WC-1, WC-2) were prepared on the basis of dolomite and ceramic aggregate, whereas the series 3 mixture (WC-3) was based on granodiorite and ceramic aggregate. The series 4 mixture (WC-4) constituted a reference mixture and is solely comprised of the dolomite aggregate. It was assumed that the laboratory recipe for the WC would be prepared for the asphalt concrete intended for a wearing course, with a grain size of 0–11.2 mm, for the surfaces with traffic load  $1 \div 2$  (TL1  $\div$  2). The preparation of the recipe was based on the standards [26,27]. The first stage of the design involved the choice of appropriate graining. It was planned that the total grain composition of the aggregate would include limestone dust, added as a filler. Table 4 presents the established aggregate compositions for consecutive series. Sieve analyses were conducted for these grain compositions and initial graining curves were prepared.

The aggregates deposited on the premises of bituminous mass production plant are dusty. The presence of dust negatively impacts the production properties of mineral-asphalt mixtures; hence, the production plants employ the dedusting process.

**Table 4.** Composition of mineral mixtures for series 1–4.

No.	Mixture Ingredients	WC-1	WC-2	WC-3	WC-4
1	Filler	limestone	limestone	limestone	limestone
2	Fine-grained aggregate	dolomite 0/2	quartz 0/2 dolomite 0/2	-	quartz 0/2 dolomite 0/2
3	Coarse-grained aggregate	dolomite 2/8 dolomite 8/11	dolomite 2/8 dolomite 8/11 ceramics 4/8	ceramics 4/8 granodiorite 8/11	dolomite 2/8 dolomite 8/11
4	Aggregate with continuous granulation	ceramics 0/4	ceramics 0/4	ceramics 0/4 granodiorite 0/4	-

This process enables us to partially remove dust from aggregates. All aggregates, except for limestone dust, undergo dedusting. This is because limestone dust is supplied directly into the mixer, skipping the dedusting process. The amount of dust removed depends on the type of a production plant as well as the humidity. Dedusting causes a change in the aggregate grain size, which needs to be taken into account during the design stage of a mixture. The dust removal level assumed in the recipe amounted to 50%, being most common in MAM production plants. Hence, it was necessary to recalculate the sieving. While determining the content of particular aggregates in mineral mixture (MM), one should remember to select proportions so that the graining curve is between the borderline curves, in accordance with [25]. The comparison result was positive. The graining of all analyzed series in both batches was between the borderline curves. Because the series were nearly the same, a single exemplary graph is presented (Figure 2).

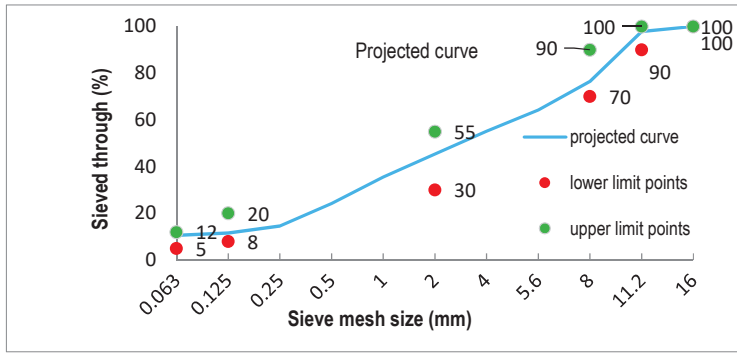


Figure 2. The grading curves for WC-1.

In order to determine the amount of asphalt in a mixture, a calculation method accounting for the specific surface area of mineral mixture of aggregates and the thickness of the asphalt film was selected [28]. As far as the production of mineral-asphalt mixtures is concerned, it is vital that the grains should be covered with a film of asphalt binder of appropriate thickness. If the film is too thin, the mixture will segregate and lose its properties. The thickness of the asphalt film is dependent on the type of binder and the specific surface area of a mineral mixture, which was calculated by means of Equation (1):

$$F = (0.04g + 0.06z + 0.10s + 1.5f) \frac{2.65}{\rho_a} \tag{1}$$

where:

- $F$ —specific surface area of the designer mineral mixture, ( $m^2/kg$ )
- $g$ —content of the fraction  $>4$  mm, (%)
- $z$ —content of the fraction  $>0.25 \leq 4$  mm, (%)
- $s$ —content of the fraction  $>0.063 \leq 0.25$  mm, (%)
- $f$ —content of the fraction  $\leq 0.063$ , (%)
- $\rho_a$ —density of the mineral mixture, ( $g/cm^3$ )

Knowing the specific surface area, the required content of asphalt for a mineral mixture was determined [28]:

$$A_k = \frac{F b \rho_{asf}}{10} \quad [\%] \tag{2}$$

where:

- $A_k$ —content of binder in relation to the mineral mixture, (%)
- $F$ —specific surface area of the mineral mixture, ( $m^2/kg$ )
- $B$ —thickness of bituminous film, ( $\mu m$ )
- $\rho_{asf}$ —binder density, ( $g/cm^3$ )

The thickness of asphalt film, in line with [29] should assume the type of utilized asphalt and the specific surface area of the mineral mixture.

Depending on the type of applied asphalt, the thickness of film for various kinds of asphalt should amount to:

- 35/50 asphalt—3.2–2.7  $\mu\text{m}$
- 50/70 asphalt—2.8–2.4  $\mu\text{m}$
- 70/100 asphalt—2.6–2.2  $\mu\text{m}$
- 100/150 asphalt—2.2–1.7  $\mu\text{m}$ .

The recommended thickness of the asphalt film depending on the specific surface area of the mixture is presented in Table 5.

**Table 5.** Thickness of the asphalt film depending on the specific surface area.

The Specific Surface Area of the Mixture ( $\text{m}^2/\text{kg}$ )	Thickness of the Asphalt Film b ( $\mu\text{m}$ )
0.023–1	40–80
1–3	15–40
3–5	6–15
5–10	4–10
10–25	2–8
25–50	1.5–4

The knowledge on the composition of mineral mixtures and the amount of asphalt in MAM enabled to determine the final composition of mineral-asphalt mixtures for all series. The results were presented in Table 6.

**Table 6.** Composition of mineral and mineral-asphalt mixtures.

Material	WC-1		WC-2		WC-3		WC-4	
	% Share in MM	% Share in MAM	% SHARE in MM	% Share in MAM	% Share in MM	% Share in MAM	% Share in MM	% Share in MAM
limestone	9.0	8.5	9.0	8.3	9.0	8.5	6.0	5.6
quartz 0/2	-	-	16.0	15.0	-	-	22.0	20.7
dolomite 0/2	22.0	20.7	10.0	9.5	-	-	22.0	20.7
dolomite 2/8	24.7	23.3	10.0	9.5	-	-	30.0	28.3
dolomite 8/11	23.7	22.4	25.0	23.6	-	-	20.0	18.9
granodiorite 0/4	-	-	-	-	24.0	22.6	-	-
granodiorite 8/11	-	-	-	-	20.0	18.8	-	-
ceramics 0/4	20.6	19.3	15.0	14.1	25.0	23.6	-	-
ceramics 4/8	-	-	15.0	14.2	22.0	20.7	-	-
asphalt 50/70	-	5.8	-	5.8	-	5.8	-	5.8
TOTAL	100.0	100.0	100.0	100.0	100.0	100.0	100.0	100.0

The preparation of the samples for studies was divided into several stages. Stage 1 constituted the preparation of the aggregate, which involved weighing particular aggregate batches with at least 10% additions, drying them to constant mass, leaving them to cool down, sieving out dust in line with the assumption of the laboratory recipe, weighing the particular aggregate graining in accordance with that calculated for the batch, and thermostating in a dryer at  $155 \pm 5$  °C for 8 h. Stage 2 consisted of the preparation of asphalt in the following way: the asphalt was poured into a container and placed in a dryer so that thermostating of the aggregate and asphalt would finish at the same time.

Afterwards, the ingredients were mixed manually. The mixing process was conducted in the following way: a vessel was placed and heated on a heating plate; weighed aggregate and binder were subsequently poured and mixed with stirring motion. The next stage involved injecting an appropriate amount of asphalt and mixing the batch until the aggregate was entirely covered with asphalt film, for no longer than 5 min.

### 2.3. Methods

The first of the planned investigations involved determining the binder content and grading of particular aggregates, including filler, in the mixture. The investigation included an extraction performed on a sample of a mineral–asphalt mixture, i.e., subjecting the sample to a solvent—tetrachloroethylene. These operations resulted in the separation of the binder from the aggregate and the separation of the filler. The study aims to identify the differences in the amount of asphalts injected to the batch and the amount calculated after extraction. The differences usually stem from the presence of insoluble asphalt absorbed by aggregate grains and insoluble particles in the applied solvent.

The experiment was conducted on the samples collected with the standard [30], where the minimal mass of a sample for a mineral–asphalt mixture with a grain size up to 11.2 mm was determined as 300 g. In order to conduct the experiment, the following devices were prepared: an extractor, a vortex mixer with a set of sieves, a fan dryer enabling to maintain the temperature of  $110 \pm 5$  °C, and laboratory scales.

The investigation for each series was initiated by weighing empty and filled (with the analytic sample) extractor tubes. Afterwards, a paper filter was applied on a dried extraction thimble and everything was weighed again. Subsequently, the extraction thimble and tube were placed in an extractor and the device was turned on. When the extraction was finished, the extraction thimble with the filler was cooled and weighed. The tube with aggregate was put into a dryer at 110 °C and stored until it was totally dry. Then, aggregate was extracted and cooled, weighed, and sieved through the prepared set of sieves with the following mesh sizes: 0; 0.63; 0.125; 0.25; 0.5; 1; 2; 4; 5.6; 8; 11.2 mm. The content of asphalt in percent was calculated from the mass difference by means of Equation (3) [31].

$$S = \frac{M_m - [M_k + (m_2 - m_1)]}{M_m} \times 100\% \quad (3)$$

where:

$M_m$ —mass of the mineral–asphalt mixture, (g)

$M_k$ —mass of aggregate excluding the filler in the extraction thimble, (g)

$m_1$ —mass of the extraction thimble with filter prior to extraction, (g)

$m_2$ —mass of the extraction thimble with filter after extraction, (g).

So-called Marshall samples were prepared for further experiments. The following devices were used for this purpose: a thermostat-equipped fan dryer, a heating plate for manual mixing, laboratory scales, a thermometer capable of measuring temperatures up to 300 °C with the accuracy of at least  $\pm 2$  °C, a compacting mold with an internal diameter of  $101.6 \pm 0.1$  mm, a Marshall compactor, and small support equipment: bowls, pots, spatulas, cleaning cloth, etc.

The samples were prepared in accordance with [32]. The weighed amount of MAM should be adjusted so that the sample (after compacting) has the following dimensions: diameter ( $101.6 \pm 0.1$ ) mm and height ( $63.5 \pm 2.5$ ) mm. Usually, the weighed amount for a single sample ranges between 1150 g and 1250 g. The amount of mineral mixture weighed beforehand should be placed in a suitable vessel in a dryer and heated to the temperature established in the assumptions for the preparation of a mineral–asphalt mixture. The aggregate can be placed in a single or several vessels. In the case of 50/70 asphalt, the mixture temperature ranges from 140 to 180 °C. The aggregate placed into a dryer should be left for at least 8 h. The weighed amount of binder should be dried for an hour in a separate vessel. The asphalt should be placed in a dryer in such a way that the thermostating of the aggregate and asphalt would finish at the same time. The aggregate can undergo thermostating for a longer time, but this is not the case with asphalt. Wetfix adhesive is added to the asphalt, in line with the recipe. The ingredients are mixed manually. A vessel with handles, e.g., a pot with appropriate volume in relation to the batch size, is placed on the heating plate and heated. The aggregate is poured into the pot and stirred. Afterwards, asphalt is added very carefully, because adding too much

would require repeating the entire process. The content is mixed until all MM grains are covered with asphalt and the MAM becomes homogenous. The maximum mixing time, which in this case equals 5 min, should not be exceeded. Prior to forming samples, the molds, along with the equipment, should be placed in a dryer at 120–130 °C. A paper separator is placed in the mold, removed from the dryer, and subsequently filled with the weighed amount of MAM; it is then evened out and another paper separator is added. Prior to compacting, the piston needs to be heated. The prepared mold is placed in a Marshall compactor and compacted. The number of blows depends on the intended MAM application. In this case, it equals 50 blows. After the compaction, a sample is turned 180° and subjected to another 50 blows. The experiment can be initiated 4 h after a sample was removed from the mold, when it cools enough not to be damaged.

The aim of the first experiment, conducted on the samples prepared in such way, was to determine the density of a mineral–asphalt mixture, which is the quotient of the sample mass and its volume, without voids. The experiment was performed on the samples prepared in accordance with the standard [33], which stated that the mass of an analytic sample in grams should be at least 50 times greater than the largest coarse grains of the aggregate in the mineral–asphalt mixture. The samples were crushed into individual grains or lumps so that the diameter did not exceed 6 mm. In the case of the compacted sample, prior to compacting, it was placed in the dryer at 110 °C and heated until compaction was possible. In order to conduct the experiments, the following equipment was prepared: laboratory scales, a fan dryer with a thermostat, a vacuum generator, a pycnometer, a water bath, and a spatula.

The pycnometer was calibrated prior to the experiment. Afterwards, an empty pycnometer was weighed for each series. Then, a crushed mixture sample was poured into the pycnometer to the 2/3 of its capacity, covered with the head and weighed. The head was subsequently removed, distilled water was added to the level of 3 cm below the pycnometer bottle neck, two drops of an active surfactant were added and the pycnometer was placed in a vacuum chamber. The trapped air was removed under vacuum pressure (4 kPa) for 15 min. Afterwards, with the head placed again, the water was topped up to slightly below the line on the bottle neck. The pycnometer was then placed in a water bath at 25 °C for 2 h. When the pycnometer was removed from the bath, the water was topped up again to the line on the neck, surface dried, and weighed. The density  $\rho_{mw}$  of the mineral–asphalt mixture, expressed in  $\text{g}/\text{cm}^3$  was calculated according to Equation (4) [23]:

$$\rho_{mw} = \frac{m_2 - m_1}{V_p - (m_3 - m_2)/\rho_w} \quad (4)$$

where:

$V_p$ —pycnometer volume, ( $\text{cm}^3$ )

$\rho_w$ —density of distilled water assumed for the temperature of the experiment, ( $\text{g}/\text{cm}^3$ )

$m_1$ —mass of the pycnometer with the head, (g)

$m_2$ —mass of the pycnometer with the head and mineral-asphalt sample, (g)

$m_3$ —mass of the pycnometer with the head, sample and distilled water, (g).

The next experiment involved determining the bulk density of the mineral–asphalt mixture, which constitutes the quotient of the sample mass and its volume with voids.

The experiment was conducted on the Marshall samples, prepared as described above. Conducting the experiment required preparation of the following instruments: laboratory scales, thermometer, water bath, and calipers. Prior to the investigation, the samples were cleaned by brushing loose grains off the sample. Afterwards, each sample was weighed and placed in the water bath for 40 min. When the samples were soaked, they were placed in a basket submerged in water and suspended under a hydrostatic balance so the mass of the water-soaked sample could be read. Then, the temperature of water in the water bath was measured in order to determine the density of water. The sample was then removed from water, surface dried, and weighed. The bulk density in



the saturated, surface dry state of the mineral–asphalt mixture expressed in  $\text{g}/\text{cm}^3$  was calculated with Equation (5):

$$\rho_{bssd} = \frac{m_1}{m_3 - m_2} \times \rho_w \quad (5)$$

where:

$\rho_w$ —density of distilled water assumed for the temperature of the experiment, ( $\text{g}/\text{cm}^3$ )

$m_1$ —mass of a dry sample, (g)

$m_2$ —mass of a sample saturated with water, (g)

$m_3$ —mass of a surface dry, saturated sample, (g).

Afterwards, the presence of voids in the mineral–asphalt mixture, which are the free, air-filled spaces between the aggregate grains covered with a binder film in the compressed samples, was determined. This is calculated on the basis of the bulk density of a mineral–asphalt mixture as well as the density of the mineral–asphalt mixture.

Indication of voids was carried out in line with the methodology presented in the standard [34]. Voids  $V_m$ , expressed in %, were calculated by means of Equation (6) [24]:

$$V_m = \frac{\rho_m - \rho_b}{\rho_m} \times 100\% \quad (6)$$

where:

$V_m$ —content of voids in a sample of the mineral-asphalt mixture up to 0.1%,

$\rho_m$ —density of the mineral-asphalt mixture, ( $\text{g}/\text{cm}^3$ )

$\rho_b$ —bulk density ( $\text{g}/\text{cm}^3$ ).

Afterward, the content of voids in the mineral mixture filled with binder was calculated. This compares the asphalt volume in the mineral–asphalt mixture to the content of voids in the compacted mineral mixture, which is calculated on the basis of the binder and void content in MM as well as the bulk density of a given sample along with the binder density.

The content of voids in MM filled with asphalt is provided with an accuracy of 0.1% and calculated on the basis of Equation (7), in line with the standard [34]:

$$VFB = \frac{B \times \frac{\rho_b}{\rho_B}}{VMA} \times 100\% \quad (7)$$

where:

$VMA$ —corresponds to the content of voids in the mineral mixture, expressed in %, which can be calculated by means of the Equation (8) [24],

$$VMA = V_m + B \cdot \frac{\rho_b}{\rho_B} \quad (8)$$

where:

$B$ —content of binder in the mineral-asphalt mixture, (%)

$\rho_b$ —bulk density of a mineral-asphalt mixture sample, ( $\text{g}/\text{cm}^3$ )

$\rho_B$ —binder density, ( $\text{g}/\text{cm}^3$ )

$V_m$ —content of voids in the mineral-asphalt mixture, (%).

The aim of the final experiment was to determine the resistance of the mineral-asphalt mixture samples to the effect of water and frost, expressed by means of ITSR (indirect tensile strength ratio) index. This index involves the ratio of the indirect tensile strength obtained on conditioned (wet) samples to the indirect tensile strength of the dry samples.

The experiment was conducted on Marshall samples, in accordance with the standard [35]. The following instruments were prepared: Marshall compactor characterized with the parameters stated in the standard [36], test head conforming to the standard [35], vacuum pump, vacuum tank, water bath, thermostatic chamber, freezer, scales, thermostat-equipped dryer, calipers, plastic bags, and a syringe.

In order to determine the susceptibility to the water and frost effect, 10 samples were prepared for each series. The samples for research were compacted according to the guidelines found in [26]. Each side of a sample was hit with 35 blows. The dimensions of each sample were measured and the bulk density was calculated. A set of 10 samples was divided into two equal parts with similar dimensions and bulk density. The first group of similar samples constitute the “wet” samples, whereas the other—the “dry” ones. The samples from the “dry” set were subjected to conditioning by storage on a level surface at room temperature ( $20 \pm 5^\circ\text{C}$ ). The set of “wet” samples was placed in a vacuum apparatus filled with distilled water. The set pressure was maintained for ( $30 \pm 5$ ) min. Afterwards, the samples were placed in the water bath at ( $40 \pm 1^\circ\text{C}$ ) for 68 to 72 h. The samples were subsequently removed from the water bath and their surface was gently dried. The next step involved placing the samples in plastic containers, so that the surface fitted closely to the bag. The samples were then placed in a freezer at  $-18 \pm 3^\circ\text{C}$  for approximately 16–18 h. After their removal from the freezer, the samples were once again put in the water bath at the temperature of  $60 \pm 1^\circ\text{C}$ . Following the thawing process, the samples were removed from the bags as quickly as possible. The samples taken from the water bath were stored at room temperature for at least two hours. The research procedure itself begins with achieving a temperature of  $25 \pm 2^\circ\text{C}$  for both the wet and dry sample sets. The experiment on a sample should be carried out 1 min following the removal from water.

The ITSR expressed in % was calculated by means of the Equation (9), in line with the standard [35].

$$ITSR = \frac{ITS_w}{ITS_d} \times 100\% \quad (9)$$

where:

$ITS_w$ —stands for the average strength of the wet samples, rounded up to an integer, which can be calculated from Equation (10) [35],

$$ITS_w = \frac{2 \times P_w}{\pi \times D \times H} \quad (10)$$

$ITS_d$ —corresponds to the average strength of the dry samples, rounded up to an integer, which can be calculated from Equation (11) [35],

$$ITS_d = \frac{2 \times P_d}{\pi \times D \times H} \quad (11)$$

where:

$P_w$ —maximum value of the compressive strength for the wet samples (kN)

$P_d$ —maximum value of the compressive strength for the dry samples (kN)

$D$ —sample diameter rounded up to 0.1 (mm),

$H$ —sample height rounded up to 0.1 (mm).

#### 2.4. Scanning Electron Microscopy with EDS Analysis

SEM (Quanta FEG 250 microscope by FEI, Hillsboro, OR, USA), equipped with a system for the chemical composition analysis based on the energy-dispersive X-ray spectroscopy (EDS) manufactured by EDAX (Mahwah, NJ, USA), was used for determining the morphology and porous structure of MAM, and the interfacial transition zone between aggregates and asphalt.

### 3. Results

The results obtained from the research on the asphalt content following extraction are presented in Table 7.

**Table 7.** Results pertaining to the soluble binder content.

	WC-1	WC-2	WC-3	WC-4
Binder content determined on the basis of research (%)	5.6	5.6	5.7	5.6
Binder content according to the recipe (%)	5.8	5.8	5.8	5.8
Difference between the measured value and the recipe (%)	0.2	0.2	0.1	0.2
Acceptable difference (%)	±0.5	±0.5	±0.5	±0.5

Following the extraction, it was observed that there are differences in the amount of asphalt added to the batch and the amount of asphalt calculated after extraction. These differences resulted from the presence of undissolved asphalt absorbed by aggregate grains and particles undissolved in the solvent. In the first and second series, this difference amounted to 0.2% and was twice as high as the one in the third series, which equaled 0.1%. According to the standard [37], these differences should not exceed ±0.5%. Therefore, the designed mixtures conform to the abovementioned requirements. The graining of the aggregate produced after extraction is presented in Tables 8–10.

The experiment showed that the graining of the aggregate differs between the ones introduced to the batch and the ones obtained after extraction. According to the standard [37], the differences should be within range of acceptable deviations, which amount to:

- −8 ± +5 for the aggregates stopped on the 11.2 mm sieve,
- ±7 for the aggregates stopped on the 5.6 mm sieve,
- ±6 for the aggregates stopped on the 2.0 mm sieve,
- ±4 for the aggregates stopped on the 0.125 mm sieve,
- ±2 for the aggregates stopped on the 0.063 mm sieve.

**Table 8.** Aggregate graining following extraction for WC-1.

Sieve #, mm	WC-1				Acceptable Difference in the Composition of a Single Sample According to [37], %	Acceptable Difference in the Composition of a Single Sample According to WT-2 2008 [26], %
	Stopped on Sieve, %	Passed Through Sieve, %		Difference in the Composition, %		
		According to Extraction	According to the Assumed Composition			
16.0	0.0	100.0	100.0	0.0		
11.2	1.3	98.7	98.7	0.0	−8 ± +5	-
8.0	20.4	78.3	79.5	−1.2		
5.6	10.0	68.3	69.5	−1.2	±7	-
4.0	6.7	61.6	62.3	−0.7		
2.0	16.0	45.6	47.5	−1.9	±6	-
0.125	33.7	11.9	12.4	−0.5	±4	-
0.063	2.2	9.7	9.8	−0.1	±2	-
	<0.063 mm	9.7	9.8	−0.1	-	±3
	<0.125 mm	11.9	12.4	−0.5	-	±4
	0.063–2.0 mm	35.9	37.7	−1.8	-	±8
	≥2.0 mm	54.4	52.5	1.9	-	±8
	≥11.2 mm	1.3	1.3	0.0	-	−8 ± +5

Table 9. Aggregate grading following extraction for WC-2.

Sieve #, mm	WC-2				Acceptable Difference in the Composition of a Single Sample According to [37], %	Acceptable Difference in the Composition of a Single Sample According to WT-2 2008 [26], %
	Stopped on Sieve, %	Passed Through Sieve, %		Difference in the Composition, %		
		According to Extraction	According to the Assumed Composition			
16.0	0.0	100.0	100.0	0.0		
11.2	3.3	96.7	97.9	-1.2	-8 ± +5	-
8.0	22.8	73.9	76.5	-2.6		
5.6	11.4	62.5	64.3	-1.8	± 7	-
4.0	8.4	54.1	55.2	-1.1		
2.0	9.5	44.6	45.4	-0.8	± 6	-
0.125	33.7	10.9	11.6	-0.7	± 4	-
0.063	1.2	9.7	10.6	-0.9	± 2	-
	<0.063 mm	9.7	10.6	-0.9	-	±3
	<0.125 mm	10.9	11.6	-0.7	-	±4
	0.063–2.0 mm	34.9	34.8	0.1	-	±8
	≥2.0 mm	55.4	54.6	0.8	-	±8
	≥11.2 mm	3.3	2.1	1.2	-	-8 ± +5

Table 10. Aggregate grading following extraction for WC-3.

Sieve #, mm	WC-3				Acceptable Difference in the Composition of a Single Sample according to [37], %	Acceptable Difference in the Composition of a Single Sample According to WT-2 2008 [26], %
	Stopped on Sieve, %	Passed Through Sieve, %		Difference in the Composition, %		
		According to Extraction	According to the Assumed Composition			
16.0	0.0	100.0	100.0	0.0		
11.2	0.4	99.6	99.7	-0.1	-8 ± +5	-
8.0	11.8	87.8	89.2	-1.4		
5.6	20.0	67.8	71.3	-3.5	±7	-
4.0	13.0	54.8	57.0	-2.2		
2.0	12.4	42.4	43.7	-1.3	± 6	-
0.125	29.5	12.9	12.8	0.1	± 4	-
0.063	3.0	9.9	10.1	-0.2	± 2	-
	<0.063 mm	9.9	10.1	-0.2	-	±3
	<0.125 mm	12.9	12.8	0.1	-	±4
	0.063–2.0 mm	32.5	33.6	-1.1	-	±8
	≥2.0 mm	57.6	56.3	1.3	-	±8
	≥11.2 mm	0.4	0.3	0.1	-	-8 ± +5

The density values obtained for particular series were presented in Figure 3. The WC-3 sample was characterized by lower density—equal to 2.321 g/cm<sup>3</sup>—than the samples prepared with dolomite. A similar situation concerned the density of the aggregates used for the preparation of mixtures. The granodiorite aggregate was characterized by a lower density than the dolomite aggregate. The bulk density values for particular series are presented in Figure 4.

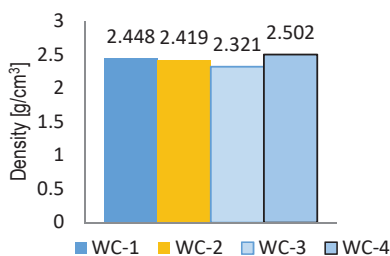


Figure 3. Density of mineral-asphalt mixtures.

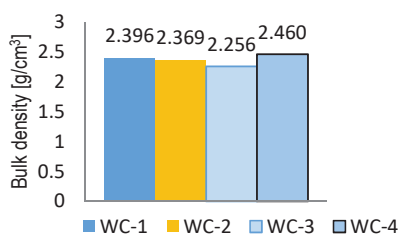


Figure 4. Bulk density of mineral-asphalt mixtures.

A sample of mineral-asphalt mixture prepared with granodiorite was characterized by a lower bulk density, amounting to 2.256 g/cm<sup>3</sup>, than the samples prepared with dolomite.

The void content calculations results in a mineral-asphalt mixture for particular series are presented in Table 11.

Table 11. Content of voids in MAM for particular series, %.

	WC-1	WC-2	WC-3	WC-4
Content of voids in MAM, (%)	2.1	2.0	2.8	1.7

The mineral-asphalt mixtures prepared with granodiorite (WC-3) reached the highest content of voids, amounting to 2.8%. In the case of the mixtures prepared solely with dolomite (WC-4), voids reached the lowest values and were 39% lower than WC-3 MAM. Therefore, it may be supposed that due to the higher absorptivity of the ceramic aggregate presented in Table 1, a partial absorption of asphalt by the waste aggregate occurred. A similar situation was described by Silvestre et al. [18] and Pérez et al. [38]. This caused an increase of voids in MAM.

According to [27], the voids in a mineral-asphalt mixture should not be lower than 1% and greater than 3%. The designed mixtures meet the presented technical requirements.

The results of void content calculations in a mineral mixture filled with binder for particular series are depicted in Table 12.

Table 12. Content of voids in MM and in the MM filled with binder for particular series.

	WC-1	WC-2	WC-3	WC-4
content of voids in MM (%)	15.9	15.1	15.8	15.7
content of voids in MM filled with binder, VFB (%)	86.6	86.3	82.2	89.3

According to [27], the voids in the mineral mixture should reach at least 14%. On the other hand, the voids in the mineral mixture filled with binder should not be lower than 75% and greater than 93%. Therefore, the designed mixtures fulfil the technical requirements.

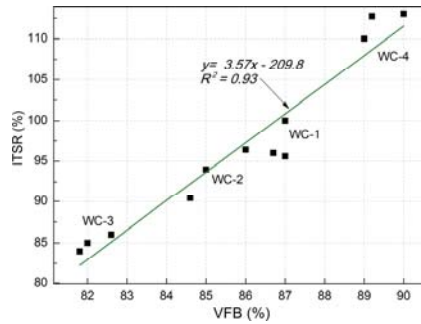
The results of indirect tensile strength ratio (ITSR) calculation were presented in Table 13.

Table 13. Value of indirect tensile strength ratio for particular series.

	WC-1	WC-2	WC-3	WC-4
ITSR (%)	97.5	95	85	112

In accordance with [27], the indirect tensile strength ratio for the mineral-asphalt mixture for the wearing course should be at least 90%. The WC-3 mixture does not meet this criterion, but the remaining three mixtures do. The highest ITSR was obtained with WC-4 MAM and it was 24% higher

than the value achieved with WC-3. The best results were obtained with the mixtures containing dolomite alone and the mixture comprising dolomite and ceramic aggregate with the graining of 0/4. A significant influence of voids in MM filled with binder (VFB) on the ITSR was observed (Figure 5).



**Figure 5.** Correlation between voids in the mineral mixture filled with VFB binder and indirect tensile strength ratio (ITSR).

The correlations can be described using the equation:  $y = 3.57x - 209.8$ , which is characterized by a good coefficient of determination  $R^2 = 0.93$ . The higher the void content in MM, the higher the ITSR value. The type of utilized aggregate also influences ITSR, with dolomite aggregate yielding the best results. The resistance to the effect of water and frost characterizing MAM also depends on the content of voids (Table 11). An inverse dependency was observed in this case (Figure 6). The higher the void content in MAM, the lower the tensile strength—which is the parameter corresponding to frost resistance. The linear trend exhibited the coefficient of correlation  $R^2 = 0.75$  and relatively low errors in the intercept.

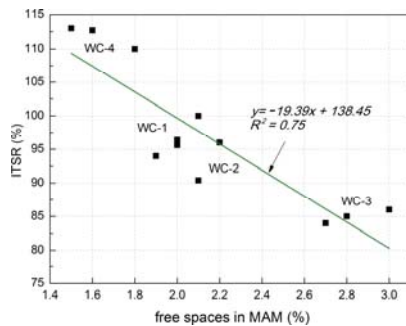


**Figure 6.** Correlation between the voids in MAM and ITSR.

It was observed that a mixture comprising granodiorite and waste ceramics is least resistant to the water and frost effect among the analyzed mixtures intended for use in the wearing course.

#### Scanning Electron Microscopy with EDS Analysis

The MAM microstructure examination, coupled with the EDS analysis, was conducted to determine the morphology and texture of the created forms as well as identify the basic chemical components of MAM (Figure 7).

The lack of cracks or air gaps, further supplemented by good adhesive properties between the ceramic aggregate (Figure 8a,b), dolomite aggregate (Figure 7d) and asphalt, resulted in the high

durability and frost resistance of WC-1, WC-2 and especially WC-4. The cracks and poor adhesion between the granodiorite (Figure 7c) and asphalt could have influenced the increase of voids in MAM, as well as a drop in durability and frost resistance of this MAM, which was confirmed by earlier studies. There are 75–102.6  $\mu\text{m}$  cracks in the mixture, which results in lower tensile strength and the lowest density among the analyzed MAMs, equal to 2.256  $\text{g}/\text{cm}^3$ .

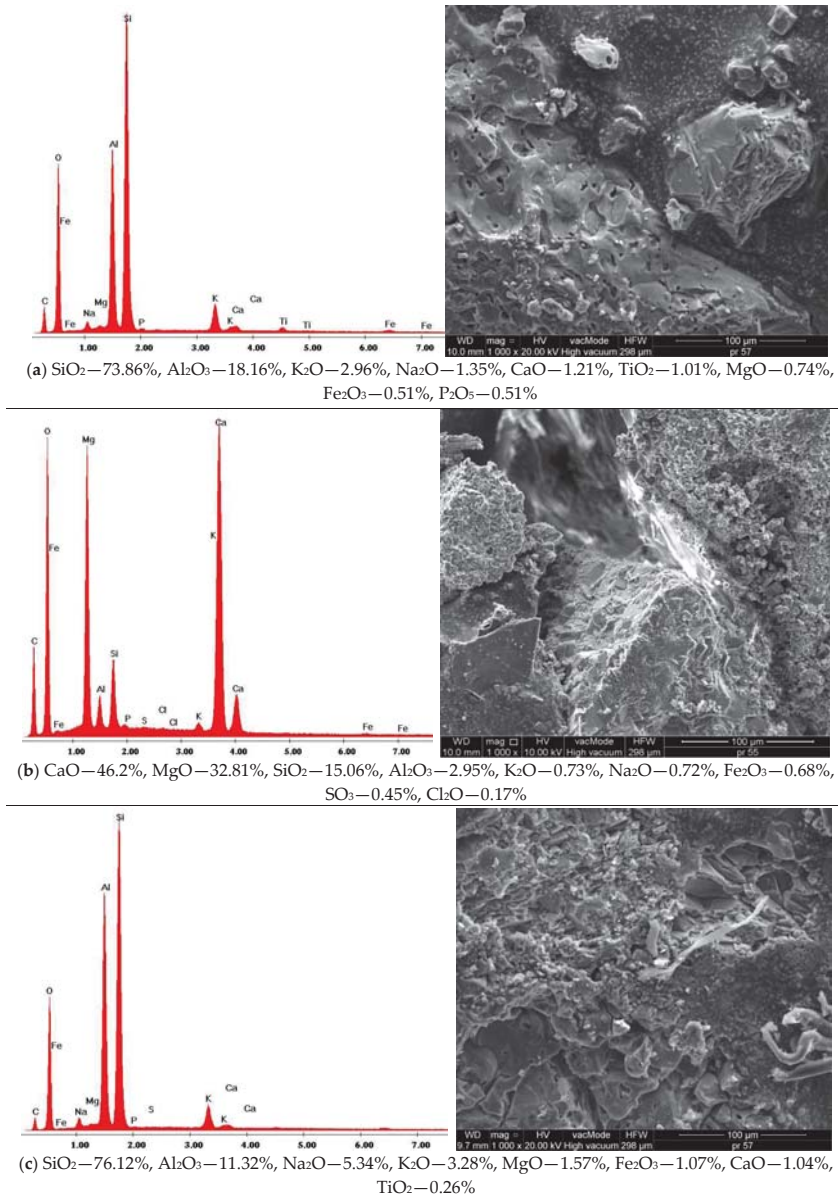


**Figure 7.** SEM Microstructure of MAM, results of the elemental analysis in EDS microarea: (a) WC-1, (b) WC-4, (c) WC-3.



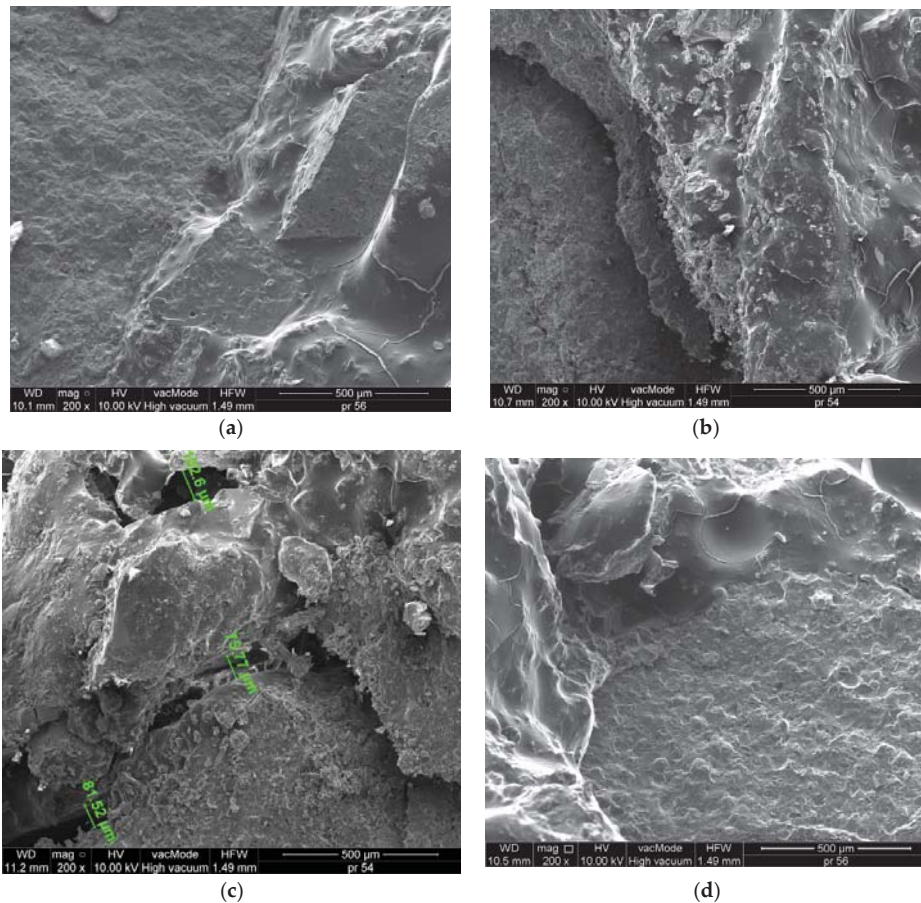


**Figure 8.** Micro-structure of MAM: (a) WC-1 dolomite + ceramics 0/4, (b) WC-2 dolomite + ceramics, (c) WC-3 granodiorite + ceramics, (d) WC-4 dolomite ( $\times 200$ ).

In Figure 8, the chemical composition of the MAM is presented on the basis of energy dispersive spectrometry (EDS). A similar chemical composition of WC-1 and WC-3, with the dominant content of  $\text{SiO}_2$  and  $\text{Al}_2\text{O}_3$ , was observed. The chemical composition of the mixture with dolomite (WC-4) is different, because  $\text{CaO}$  and  $\text{MgO}$  are the prevailing compounds. The content of silica in this mixture is approximately 5 times lower (15.06%).

#### 4. Conclusions

The presented research results prove that the ceramic aggregate is not suitable for all types of mineral-asphalt mixtures. The performed studies, conducted on the basis of the required technical specification [27] indicated that:

- a. The obtained results of soluble binder content and aggregate produced after the extraction, conducted for the mixtures in each series, are comparable for typical mineral-asphalt mixtures and do not exceed the standard values.
- b. The study on the density and bulk density of the mineral-asphalt mixture, on the basis of which the content of voids in the mineral-asphalt mixture and the mineral mixture filled with



binder were calculated, indicates that these parameters are within the ranges of the standard requirements. The ceramic aggregate addition increased the void content in MAM by 15% through increased asphalt absorption and porous structure of the material.

- c. The microstructure investigation indicated a very good adhesion of asphalt to the carbonate and ceramic aggregate. On the other hand, wide cracks appeared in the mixture with granodiorite, increasing the void content in MAM and reducing the bulk density of the mixture.
- d. The highest resistance to water and frost was obtained in the mixture with dolomite WC-4 as well as dolomite and waste sanitary ceramics aggregate WC-1 and WC-2. The highest ITSR was obtained for WC-4 MAM and it was 24% higher than ITSR for WC-3 mixture.
- e. A very good correlation between the content of voids in the MM filled with binder, as well as void content in MAM and the ITSR—corresponding to the resistance to water and frost—was obtained.
- f. The conducted research indicates that ceramics may be successfully applied in the asphalt mixtures intended for use in the wearing course based on carbonate aggregates, i.e., dolomite. The mixture with 20 and 30% addition of recycled ceramic aggregate, used as a partial substitution of the natural dolomite aggregate, meets the majority of requirements related to mechanical properties stated in the technical specification.

**Author Contributions:** Wojciech Andrzejuk, Bartosz Zagardło and Danuta Barnat-Hunek conceived the idea of the experiment, conducted the experimental part, and analyzed the results. All authors analyzed and discussed the experimental results. Grzegorz Łagód translated the article. Wojciech Andrzejuk provided manuscript formatting. All authors of the article provided substantive comments.

**Acknowledgments:** This work was financially supported by the Ministry of Science and Higher Education, within the statutory research number S/14/2018, S-70/WIŚ/2018 and 2017-WNET/KNT/ZB/1.

**Conflicts of Interest:** The authors declare no conflict of interest.

## References

1. Dondi, M.; Cappelletti, P.; D'Amore, M.; de Gennaro, R.; Graziano, S.F.; Langella, A.; Raimondo, M.; Zanelli, C. Lightweight aggregates from waste materials: Reappraisal of expansion behavior and prediction schemes for bloating. *Constr. Build. Mater.* **2016**, *127*, 394–409. [[CrossRef](#)]
2. Siddique, R.; Cachim, P. *Waste and Supplementary Cementitious Materials in Concrete: Characterisation, Properties and Applications*; Woodhead Publishing: Cambridge, UK, 2018; p. 570. ISBN 9780081021569.
3. Moreno-Maroto, J.M.; Gonzalez-Corrochano, B.; Alonso-Azcarate, J.; Rodríguez, L.; Acosta, A. Development of lightweight aggregates from stone cutting sludge, plastic wastes and sepiolite rejections for agricultural and environmental purposes. *J. Environ. Manag.* **2017**, *200*, 229–242. [[CrossRef](#)] [[PubMed](#)]
4. Liu, M.; Xu, G.; Li, G. Effect of the ratio of components on the characteristics of lightweight aggregate made from sewage sludge and river sediment. *Process Saf. Environ. Prot.* **2017**, *105*, 109–116. [[CrossRef](#)]
5. Li, B.; Ling, T.C.; Qu, L.; Wang, Y. Effects of a two-step heating process on the properties of lightweight aggregate prepared with sewage sludge and saline clay. *Constr. Build. Mater.* **2016**, *114*, 119–126. [[CrossRef](#)]
6. Franus, M.; Jozefaciuk, G.; Bandura, L.; Lamorski, K.; Hajnos, M.; Franus, W. Modification of lightweight aggregates' microstructure by used motor oil addition. *Materials* **2016**, *9*, 845. [[CrossRef](#)] [[PubMed](#)]
7. Smarzewski, P.; Barnat-Hunek, D. Mechanical and durability related properties of high performance concrete made with coal cinder and waste foundry sand. *Constr. Build. Mater.* **2016**, *121*, 9–17. [[CrossRef](#)]
8. Suchorab, Z.; Barnat-Hunek, D.; Franus, M.; Łagód, G. Mechanical and physical properties of hydrophobized lightweight aggregate concrete with sewage sludge. *Materials* **2016**, *9*, 317. [[CrossRef](#)] [[PubMed](#)]
9. Miličević, I.; Štirmer, N.; Pečur, I.B. Residual Mechanical Properties of Concrete Made with Crushed Clay Bricks and Roof Tiles Aggregate after Exposure to High Temperatures. *Materials* **2016**, *9*, 295. [[CrossRef](#)] [[PubMed](#)]
10. Rashid, K.; Razaq, A.; Ahmad, M.; Rashid, T.; Tariq, S. Experimental and analytical selection of sustainable recycled concrete with ceramic waste aggregate. *Constr. Build. Mater.* **2017**, *154*, 829–840. [[CrossRef](#)]

11. Guerra, I.; Vivar, I.; Liamas, B.; Juan, A.; Moran, J. Eco-efficient concretes: the effects of using recycled ceramic material from sanitary installations on the mechanical properties of concrete. *Waste Manag.* **2009**, *29*, 643–646. [CrossRef] [PubMed]
12. Medina, C.; Frías, M.; Sánchez de Rojas, M.I. Microstructure and properties of recycled concretes using sanitary ware industry waste as coarse aggregate. *Constr. Build. Mater.* **2012**, *31*, 112–118. [CrossRef]
13. Senthamarai, R.M.; Manoharan, P.D.; Gobinath, D. Concrete made from ceramic industry waste: durability properties. *Constr. Build. Mater.* **2011**, *25*, 2413–2419. [CrossRef]
14. Suzuki, M.; Seddik Meddah, M.; Sato, R. Use of porous ceramic waste aggregates for internal curing of high-performance concrete. *Cem. Concr. Res.* **2009**, *39*, 373–381. [CrossRef]
15. Regulation (EC) No 1013/2006 of the European Parliament and of the Council of 14 June 2006 on Shipments of Waste. Available online: <http://extwprlegs1.fao.org/docs/pdf/eur65175.pdf> (accessed on 12 July 2006).
16. Halicka, A.; Ogrodnik, P.; Zegardło, B. Using ceramic sanitary ware waste as concrete aggregate. *Constr. Build. Mater.* **2013**, *48*, 295–305. [CrossRef]
17. Zegardło, B.; Szeląg, M.; Ogrodnik, P. Ultra-high strength concrete made with recycled aggregate from sanitary ceramic wastes—The method of production and the interfacial transition zone. *Constr. Build. Mater.* **2016**, *122*, 736–742. [CrossRef]
18. Silvestre, R.; Medel, E.; García, A.; Navas, J. Using ceramic wastes from tile industry as a partial substitute of natural aggregates in hot mix asphalt binder courses. *Constr. Build. Mater.* **2013**, *45*, 115–122. [CrossRef]
19. *BS EN 933-1:2012, Test of Geometrical Properties of Aggregates. Part 1: Determination of Particle Size Distribution—Sieving Method*; British Standard, BSI: London, UK, 2012.
20. *BS EN 12620:2002, Aggregate for Concrete*; British Standard, BSI: London, UK, 2002.
21. *BS EN 1097-6:2000, Tests for Mechanical and Physical Properties of Aggregate. Part 6: Determination of Particle Density and Water Absorption*; British Standard, BSI: London, UK, 2000.
22. *BS EN 1097-7:1999, Tests for Mechanical and Physical Properties of Aggregate. Part 7: Determination of Particle Density of Filler—Pycnometer Method*; British Standard, BSI: London, UK, 1999.
23. Jamróży, Z. *Concrete and Its Technologies*; Oficyna Wydawnicza PWN: Warszawa, Poland, 2006. (In Polish)
24. Moraes, R.; Velasquez, R.; Bahia, H. Using bond strength and surface energy to estimate moisture resistance of asphalt-aggregate systems. *Constr. Build. Mater.* **2017**, *130*, 156–170. [CrossRef]
25. *WT-1 2014 Aggregates, Technical Requirements*; General Directorate for National Roads and Motorways: Warszawa, Poland, 2014. (In Polish)
26. *WT-2 2014 Asphalt Mixtures, Technical Requirements*; General Directorate for National Roads and Motorways: Warszawa, Poland, 2014. (In Polish)
27. *EN 13108-1:2016 [IDT], Bituminous Mixtures—Material Specifications—Part 1: Asphalt Concrete*; Swedish standard, Swedish Standards Institute: Stockholm, Sweden, 2016.
28. Piłat, J.; Radziszewski, P. *Road Asphalt Surfaces*; Wydawnictwo Komunikacji i Łączności: Warszawa, Poland, 2010. (In Polish)
29. Kalabińska, M.; Piłat, J.; Radziszewski, P. *Technology of Materials and Road Surfaces*; Oficyna Wydawnicza PWN: Warszawa, Poland, 2008. (In Polish)
30. *BS EN 12697-28:2001, Bituminous Mixtures—Test Methods for Hot Mix Asphalt—Part 28: Preparation of Samples for Determining Binder Content, Water Content and Grading*; British Standard, BSI: London, UK, 2001.
31. *BS EN 12697-1:2012 [IDT], Bituminous Mixtures—Test Methods for Hot Mix Asphalt—Part 1: Soluble Binder Content*; British Standard, BSI: London, UK, 2012.
32. *BS EN 12697-30:2012 [IDT], Bituminous Mixtures—Test Methods for Hot Mix Asphalt—Part 30: Specimen Preparation by Impact Compactor*; British Standard, BSI: London, UK, 2012.
33. *BS EN 12697-5:2009 [IDT], Bituminous Mixtures—Test Methods for Hot Mix Asphalt—Part 5: Determination of the Maximum Density*; British Standard, BSI: London, UK, 2009.
34. *BS EN 12697-8:2003 [IDT], Bituminous Mixtures—Test Methods for Hot Mix Asphalt—Part 8: Determination of Void Characteristics of Bituminous Specimens*; British Standard, BSI: London, UK, 2003.
35. *BS EN 12697-23:2003 [IDT], Bituminous Mixtures—Test Methods for Hot Mix Asphalt—Part 23: Determination of the Indirect Tensile Strength of Bituminous Specimens*; British Standard, BSI: London, UK, 2003.

36. BS EN 12697-34:2012 [IDT], *Bituminous Mixtures—Test Methods for Hot Mix Asphalt—Part 34: Marshall Test*; British Standard, BSI: London, UK, 2012.
37. BS EN 13108-21:2006 [IDT], *Bituminous Mixtures—Material Specifications—Part 21: Factory Production Control*; British Standard, BSI: London, UK, 2006.
38. Pérez, I.; Pasadín, A.R.; Medina, L. Hot mix asphalt C&D waste as coarse aggregates. *Mater. Des.* **2012**, *36*, 840–846. [[CrossRef](#)]



© 2018 by the authors. Licensee MDPI, Basel, Switzerland. This article is an open access article distributed under the terms and conditions of the Creative Commons Attribution (CC BY) license (<http://creativecommons.org/licenses/by/4.0/>).

Article

# The Wastes of Sanitary Ceramics as Recycling Aggregate to Special Concretes

Paweł Ogrodnik <sup>1</sup>, Jacek Szulej <sup>2,\*</sup> and Wojciech Franus <sup>2</sup>

<sup>1</sup> The Main School of Fire Service, Faculty of Fire Safety Engineering, 52/54 Słowackiego Str., 01-629 Warszawa, Poland; pogrodnik@sgsp.edu.pl

<sup>2</sup> Lublin University of Technology, Faculty of Civil Engineering and Architecture, 40 Nadbystrzycka Str., 20-618 Lublin, Poland; w.franus@pollub.pl

\* Correspondence: j.szulej@pollub.pl; Tel.: +48-502-552-808; Fax: +48-22-833-07-24

Received: 22 May 2018; Accepted: 16 July 2018; Published: 24 July 2018

**Abstract:** This article presents the results of research on the wastes of sanitary ceramics as an aggregate to concretes. The case of high temperature load was taken into account. Six concrete mixes were designed on Portland and calcium aluminate cement with various content of aerating admixture. Only the ground waste ceramics were used as an aggregate from one of the Polish sanitary ceramics plants. The abrasion test by Boehme blade of the designed concrete was conducted within the frame of study and compression strength tests on the cylindrical samples were performed as well. Some samples were initially annealed at 400 or 800 °C prior to strength tests. In order to determine the impact of annealing on the phase content and the concrete sample structure, the analyses on phase content (XRD—X-ray diffraction) and scanning electron microscopy (SEM) were conducted. The tests on compression strength demonstrated that there is considerable resistance of concrete containing ceramic aggregate and calcium aluminate cement to high temperatures. Abrasion tests confirmed that selected mixes have a high resistance to abrasion and they can be applied as a concrete coating. The possibility of ceramic cullet use as an aggregate to special concretes has been confirmed by the conducted research on specific features. Taking into consideration the available literature, the article presents widely conducted research in the area of the internal structure of concrete designed on the basis of recycled ceramic aggregate, the phase content of individual components, and basic mechanical tests both in normal temperatures and under thermal stress.

**Keywords:** recycling; sanitary ceramics; concrete; recycling aggregate

## 1. Introduction

The growth of concrete use in the world simultaneously generates increased demand on resources that are essential for its production. At the same time, the growth of social awareness as well as concerns related to environmental protection reflected in the new legislation incline the concrete industry to decrease the emission of greenhouse gases and the use of natural resources as well [1,2]. This action falls within the concept of sustainable development for which it is extremely important to cut down on the energy consumption and the use of natural resources according to the rule 4R (Reduce-Reuse-Recover-Recycle) [3]. Due to the decrease of natural resources in specific areas, many resources must be transported over long distances. As a result, their prices are raised, simultaneously causing greater interest in aggregates to concrete obtained from recycling and by-products of production in the form of admixtures [4–6]. Currently, brick, glass, tire and recycled concrete aggregates (RCA) are frequently applied as a recycled aggregate. According to data presented by [7], the most common recycled aggregate in the USA is a concrete aggregate (RCA) whose share in the market constitutes 54%. Its cost is relatively low, and the likelihood of obtaining it is substantially due to the fact that there is a necessity to demolish buildings and engineering facilities. The use of fly

dust constitutes 20% of the recycled aggregate market. The consumption of remaining waste materials as aggregates is as following: slag 11%, microsilica 9%, and rubber tires 4%. The issue of optimal use of concrete rubble obtained from concrete structure demolition has lately been the subject of research and decisive actions in highly industrialized countries.

The key parameter of recycled concrete aggregates is their density which as a rule is lower in comparison to the density of natural aggregate. It also has an impact on considerable water absorption, lower strength, and on cyclic freezing and defrosting. The properties of recycled concrete aggregate significantly influence the quality of concrete. The quality of concrete from RCA is dependent on the initial strength of the construction wastes as well as on the content of mortar that is left on the aggregate and graining [8,9]. The use of concrete aggregate is also reflected in standards and procedures such as [10,11]. The standard [12] makes it possible to use a recycled aggregate in concrete on the condition that it satisfies the criteria concerning the content of possible pollution, which can have an impact on concrete quality and, at the same time, the standard recommends conducting research on the aggregates within the scope of requirements relating to further concrete application. Despite the fact that a series of studies has been performed confirming that recycled concrete aggregates can be an alternative to natural ones, it is still used with great caution. Concretes of average strength are obtained from these aggregates. It requires also applying greater amount of cement in reference to concrete of the same class, obtained from natural aggregates. In order to improve its quality, all the pollutants shall be removed, introducing selective demolition of construction facilities [13]. These aggregates are characterized by great water absorption, which is caused by the mortar adhering to the initial aggregates [9,14]. It should be emphasized that while fulfilling several conditions, it is possible to obtain the concrete from RCA aggregate, which is not different from concrete of similar content on the basis of natural aggregates.

A commonly known research direction, constantly being developed, is the use of ceramic materials as recycled aggregates to concretes. Both red ceramics in the form of bricks, hollow bricks, or tiles as well as white ones (table, sanitary, electric insulators) belong to the materials not subjected to biodegradation, and their utilization is a severe issue [15]. The results of studies on red ceramics as a recycled aggregate are ambiguous. The studies conducted by [16] demonstrated that fragmented bricks can be applied as coarse aggregates to concrete and it does not cause the subsequent deterioration of its strength. However, this type of aggregate is not recommended in reinforced concrete constructions. In the research conducted by [17], two concrete mixes were prepared in the proportion of 1:2:4 (cement:sand:coarse aggregate). One of them on the basis of gravel, the other on crushed bricks. The use of brick aggregates decreased concrete strength up to 80% in relation to samples made from gravel. Moreover, in the research carried out by [18–20], it is demonstrated that the total replacement of natural aggregate by red ceramics is virtually impossible due to the significant drop in strength of such a concrete. The attempts have been also made to use white and red ceramics in the form of ground powder with a 0–3 mm grain, as an additive replacing cement to prepare mortars. The research results show that the wastes from usable ceramics from the production of pots and covers can be used in the manufacture of cement mortar. The replacement of both cement and natural aggregate in 15% by wastes from the production of usable ceramics in the cement mortar does not negatively influence its compression strength after 28 days. Nevertheless, the compression strength of examined cement mortars with the addition of ceramics wastes after 150 cycles of freezing and defrosting was subjected to decrease [21,22]. More beneficial results were definitely obtained by the researchers using white ceramics. The studies conducted by [23,24] demonstrated that the concrete made completely from the aggregate of white sanitary ceramics does not differ from natural aggregates in terms of physical and mechanical properties. In the research conducted by [25,26] coarse aggregates were replaced by fragmented ceramic cullets in the amount of 15–20%. Prepared concretes were characterized by similar properties to the ones on the basis of natural coarse aggregates. It was also stated that along with the increase of ceramic matter, the compression strength of concrete also increases. The research conducted by [27–29] showed the positive impact of aggregates from ceramic

cullets as an additive to concrete, which benefited from its strength and durability and other features as well. Performing their own studies [30–33] enabled the researchers to demonstrate that the concrete, on the basis of the ceramic cullet aggregates, is resistant to fire temperature and is characterized by great resistance to an aggressive chemical environment. It is possible to obtain mixes of strength parameters that exceed natural aggregate concretes.

## 2. Materials and Methods

### 2.1. The Description of Concrete Samples Content and Research

#### 2.1.1. Ceramic Cullet

Sanitary ceramic wastes were used in this study and were obtained from used goods produced by one of the Polish sanitary fittings plants (Reybud, Rejowiec Fabryczny, Poland). Ceramics were fragmented into two fractions 0–4 mm and 4–8 mm and subjected to sieve analysis according to [34]. It allowed obtaining the following results of particular fractions (related to aggregate occurring in the designed concrete mix content): (0–0.125 mm) 1.14%, (0.125–0.25mm) 2.79%, (0.25–0.5 mm) 6.29%, (0.5–1.0 mm) 11.21%, (1.0–2.0 mm) 21.79%, (2.0–4.0 mm) 28.07% and (4.0–8.0 mm) 28.57%. Within the frame of conducted research on the aggregate, its crushing strength was measured on the basis of [35].

To determine the mineral content of the ceramic aggregates we used calcium aluminate cement and observed the phase changes taking place during the annealing process of the designed concrete. X-ray diffraction (XRD, Panalytical, Almelo, The Netherlands) was applied. The analysis was conducted by the powder method using X-ray diffractometer Panalytical X'pertPRO MPD (Panalytical, Almelo, The Netherlands) with goniometer PW 3050/60 (Panalytical, Almelo, The Netherlands). As the source of X-radiation, a copper lamp Cu ( $\text{CuK}_{\alpha} = 0.154178 \text{ nm}$ ) was used. Software X'Pert (Panalytical, Almelo, The Netherlands) Highscore was used for diffraction data processing. The identification of mineral phases was based on data basis PDF-2 release 2010 formalized by JCPDS/ICDD (Panalytical, Almelo, The Netherlands). The microstructure of the examined materials was determined by the Scanning Electron Microscope (SEM) Quanta 250 FEG by FEI (Hillsboro, OR, USA), equipped with the system of chemical content analysis based on the energy dispersion of the X-ray using Energy Dispersive X-ray Spectroscopy (EDS, Panalytical, Almelo, The Netherlands) by EDAX.

#### 2.1.2. Characteristics of Concrete Mix and Samples

Two sample series, which differed solely by the binder, were prepared with the use of an iterative designing method, limiting the substrates of mix commonly used in cements and the appropriate amount of aerating additive. The first series was based on calcium aluminate cement 'Górkal 70', and the other comparative one on Portland cement 32.5 R. Only the aggregates from sanitary ceramic wastes were used in each series, fragmented to the two above mentioned fractions. Both series of samples were divided into three series: basic ones and the ones with aerating additive. 0, 5, and 10% degrees of aeration of the concrete mix on the basis of the calcium aluminate and Portland cement were assumed in the research according to [36]. The amounts of aerating mix and the content of particular groups of samples are listed in Table 1. The additive is based on abietic salt, which generates small air bubbles of a diameter from 10 to 300  $\mu\text{m}$  in a concrete mix. It is characterized by a density of  $1015 \pm 20 \text{ kg/m}^3$ , pH within the range of 10–12, chloride content  $\leq 0.1\%$ , and alkalis  $\leq 7\%$ . Thus far, the aerating mix was used in concretes in order to increase its resilience to low temperatures. The research assumed that the active pores created as a result of aerating would limit the propagation of ruptures, thus increasing the durability of the concrete. Samples were made in the cylindrical shape of diameter 100 mm and the height of 200 mm. In total, there were 90 items, 15 of every described type. Moreover, in order to perform abrasion tests, three tests from each designing group were conducted in the form of cubes  $100 \times 100 \times 100 \text{ mm}$ . In compliance with the requirements

of the norm, the created samples were demolded after 2 days of cementing, and then they matured for 14 days in a water-bath. The samples then matured in laboratory conditions at a temperature of  $20\text{ }^{\circ}\text{C} \pm 2\text{ }^{\circ}\text{C}$ , and in air conditions with a mean relative humidity of 50% for a further 28 days. Next, in accordance to the PN-EN 1363-1:2012 [37], Fire resistance tests, Part 1: General requirements standard; the samples were kept in the described conditions for 3 months, before thermal stress tests were conducted.

**Table 1.** The comparison of prepared concrete mixes in  $1\text{ m}^3$  of concrete mix.

Group	Group I			Group II		
Marked samples	P0	P5	P10	C0	C5	C10
Calcium aluminate cement “Gorkal 70” (kg)	488	488	488	-	-	-
Portland cement 32.5 R (kg)	-	-	-	488	488	488
Aggregate 0–4 mm (kg)	997.14	997.14	997.14	997.14	997.14	997.14
Aggregate 4–8 mm (kg)	398.86	398.86	398.86	398.86	398.86	398.86
Water (L)	199	199	199	199	199	199
Aerating additive (kg)	-	0.244	0.488	-	0.488	0.976

### 2.1.3. Thermal Processing of Samples

Before compression tests, five samples of each group were annealed to 400 and 800 °C. The remaining samples from each group were not subjected to thermal processing. Samples were annealed in the electric chamber furnace (Thermolab, Warszawa, Poland) PK 1100/5 type. The furnace enables random determining that increase temperature during the course of testing, monitoring, and registration of temperature in real time from 16 measuring thermoelements. The furnace structure is made from square tubes and a stainless steel plate. Heating elements of furnace are made from a resistance wire Kanthal A1 in the spiral shape.

The furnace for annealing samples is shown in Figure 1a. In the ceiling there are two chimneys to channel the vapor or to introduce additional measuring sensors. During the research, the temperature in the furnace chamber and the temperature reached on the external surface of selected samples was measured. In order to avoid the damage of furnace chamber, concrete samples were placed in steel covers Figure 1b.



**Figure 1.** (a) Furnace for samples annealing, (b) Samples in the furnace chamber secured by steel covers.

In the course of thermal action, the distribution of temperature was as close as possible to the conditions of a real fire occurring in closed facilities. For this reason, standard distribution



temperature-time was assumed as the basis according to [37]. A standard curve temperature-time is described by the formula (1).

$$T = 20 + 345 \log(8t + 1), \tag{1}$$

T—temperature (°C)

t—time (min)

The increase of thermal loading was implemented in line with the standard curve ‘temperature-time’. After reaching the assumed temperature, according to the research plan amounting to 400 or 800 °C, samples were still annealed for 60 min, which aimed at equalizing the temperature in the whole density of samples. The curve which describes thermal loading of concrete samples is shown in Figure 2. The cooling of the samples was conducted naturally in the chamber of the furnace until they reached room temperature. In the case of samples heated to 800 °C, they were kept in the furnace for the next 36 h after annealing.

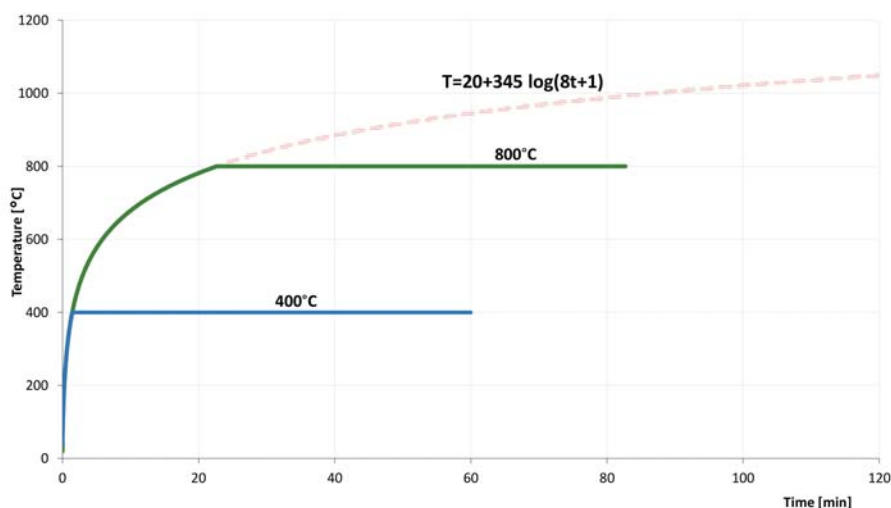


Figure 2. The diagram of temperature distribution while annealing concrete samples.

Marking of particular samples used to research is presented in Table 2.

Table 2. Marking of samples used to research.

Group	Portland Cement			Calcium Aluminate Cement		
	0%	5%	10%	0%	5%	10%
Basic samples not subjected to annealing 20 °C	P0_20	P5_20	P10_20	C0_20	C5_20	C10_20
Samples annealed in 400 °C	P0_400	P5_400	P10_400	C0_400	C5_400	C10_400
Samples annealed in 800 °C	P0_800	P5_800	P10_800	C0_800	C5_800	C10_800

#### 2.1.4. The Research on Abrasion and Compression Strength

The research on concrete abrasion on the basis of sanitary ceramic wastes was performed according to the standard [38]. A test stand was equipped with a Boehme shield along with the equipment. The corundum powder was used as an abrasive according to standard recommendations. Cubic samples had the side length (71.0 ± 1.5) mm. For this purpose, cubes of the side length 100 mm were cut by a stationary saw with a blade directed to cut concrete. The samples were weighed and measured before testing. The sample was mounted in a handle and axially loaded by the strength



( $294 \pm 3$ ) N. The sample was subjected to abrasion in the cycles by the blade rotation in line with standard requirements. In the course of studies, it was monitored whether the corundum powder was evenly distributed on the whole abrasion surface. The blade and sample surface were cleaned, it was rotated by  $90^\circ$  and new abrasive powder was spread after every cycle. In total, 18 samples, 3 per each prepared mix, were subjected to research. They were then measured and weighed in the same way as it was performed during the preparation phase. The research on compression strength of all cylindrical samples was conducted according to [39,40] using the system to examine concrete and mortars: Advantest 9 by Controls (250 kN, Milan, Italy). The system cooperates with a strain gauge bridge with the possibility of distortion readings in four measuring points. The machine is equipped with three frames. The compression frame was used during strength tests within the range of 3000 kN.

### 3. Results

#### 3.1. Characteristics of Ceramic Aggregates

The research was conducted on aggregates of 4–8 mm fraction. The average rate of crushing is 6.75%, which means that the aggregates from sanitary ceramic wastes are resistant to crushing. For comparison, the crushing rate of limestone aggregate is 18–20%, granite about 18%, quartzitic sandstone about 15%; whereas gravel is 12–16%. More importantly, ceramic aggregates were submitted to elementary analysis by means of EDS (Energy Dispersive Spectroscopy) during SEM observations. In order to compare, the analysis of several other aggregates that are frequently used have been also performed. The obtained results are listed in Table 3.

**Table 3.** The comparison of chemical content of selected concrete aggregates.

Type of Aggregate	Compounds Content (%)								
	SiO <sub>2</sub>	Al <sub>2</sub> O <sub>3</sub>	Fe <sub>2</sub> O <sub>3</sub>	CaO	MgO	Na <sub>2</sub> O	K <sub>2</sub> O	TiO <sub>2</sub>	Other
Gravel	16.7	8.0	1.0	31.8	40.8	0.9	0.8	-	-
Granite	74.8	14.2	-	1.6	0.6	5.6	2.8	-	0.4
Red clay ceramics	51.7	18.2	6.1	6.1	2.4	0.2	4.6	0.8	10.0
Sanitary ceramics	67.6	24.1	0.6	-	0.4	1.3	3.0	-	3.0

Example photographs made with the SEM scanning microscope depicting the microstructure of the aggregate used in research are presented in Figure 3.

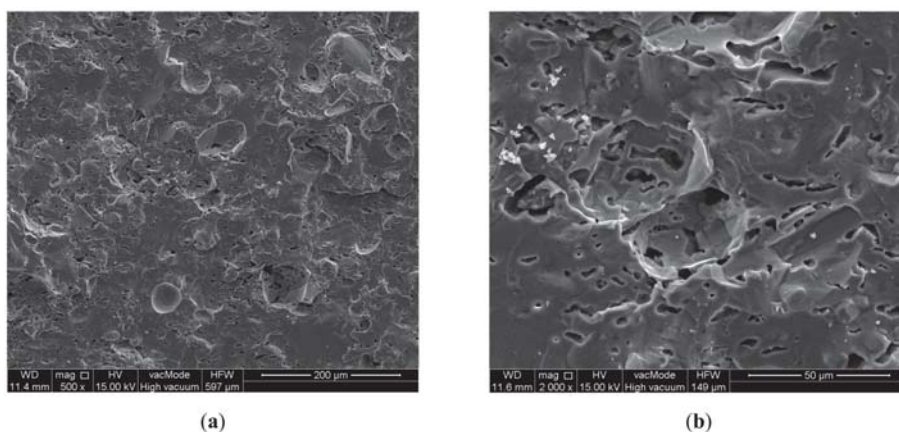


**Figure 3.** Micrographs of the aggregate ((a) magnification 500 $\times$ , (b) magnification 2000 $\times$ ) used in research scanning electron microscope (SEM).

The minerals of ceramic aggregates used in the designed concrete mixes were also studied. The diffractogram of the aggregates is shown in Figure 4. The main mineral content of the ceramic aggregate constitutes multi-recognized characteristic interplanar distances:  $d_{hkl} = 0.5376; 0.3425; 0.3390; 0.2882; 0.2427; 0.2294; \text{ and } 0.2208 \text{ nm}$ . In addition, quartz occurs collaterally, recognized by  $d_{hkl} = 0.4255; 0.3344, 0.2456; 0.2283; 0.2237; 0.2128; \text{ and } 0.1981 \text{ nm}$ ; and cristobalite  $d_{hkl} = 0.4055; 0.3140; 0.2847; \text{ and } 0.2486 \text{ nm}$ ; and calcite  $d_{hkl} = 0.3861; 0.3040; 0.2283; \text{ and } 0.2096 \text{ nm}$ . Together with the crystal phases in the used aggregates, there was also an amorphous substance (aluminosilicate glaze) whose occurrence on diffractograms is visible by the increase of its background in the range of angles from 15 to 35 ( $2\theta$ ).

### 3.2. Calcium Aluminate Cement

Calcium aluminate cement ‘Górkal 70’ and Portland cement CEM II/B-V 32.5 R were used in this research. The minerals of both cements are presented in Figure 4. In the case of calcium aluminate cement, the predominating crystal phase is calcium monoaluminate (CA), which is accompanied by calcium dialuminate  $CA_2$ . The first was recognized by characteristic interplanar distances  $d_{hkl} = 0.5956; 0.5529; 0.4687; 0.4052; 0.3718; 0.3309; 0.3199; 0.2974; \text{ and } 0.2911 \text{ nm}$ ; and the latter  $d_{hkl} = 0.6185; 0.4448; 0.3506; 0.2850; \text{ and } 0.2601 \text{ nm}$ . The main mineral phases of used Portland cement are as follows: alite ( $C_3S$ ), belite ( $C_2S$ , tricalcium aluminate ( $C_3A$ ), and brownmillerite ( $C_4AF$ ), which is collaterally accompanied by gypsum and quartz. Alite was recognized by the strongest reflections  $d_{hkl} = 0.2618; 0.2611; 0.2179; \text{ and } 0.2174 \text{ nm}$ ; belite  $d_{hkl} = 0.2793; 0.2786; 0.2747; \text{ and } 0.2611 \text{ nm}$ ; and brownmillerite  $d_{hkl} = 0.7246; 0.3650; 0.2786; 0.2674; \text{ and } 0.2646 \text{ nm}$ . The occurrence of gypsum is confirmed by reflections  $d_{hkl} = 0.7634; 0.4292; 0.3067; \text{ and } 0.2874 \text{ nm}$ .

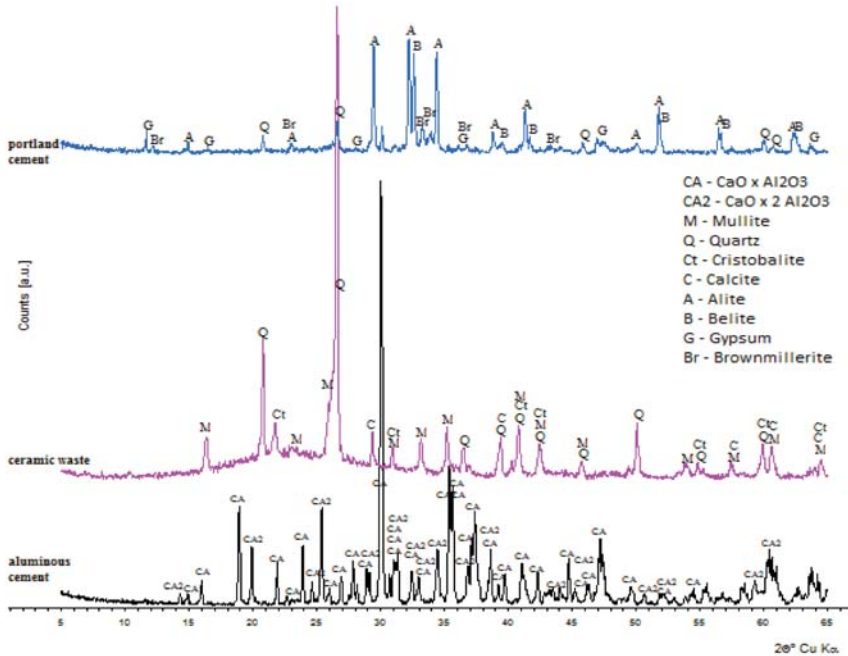
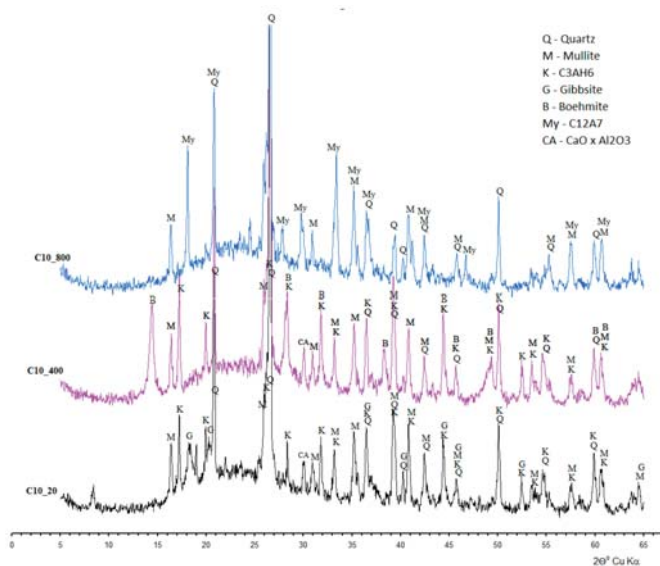


Figure 4. Diffractograms of mineral content of ceramic aggregate.

### 3.3. Phase Content and Microstructure of Concretes Containing Calcium Aluminate Cement and 10% of Aeration

To study the differences in the phases and microstructure, only the samples containing calcium aluminate cement were selected with 10% of aeration (the group of samples marked by C10\_20, C10\_400, C10\_800). The choice of these groups depended on the positive results of research referring to the compression strength of the concrete subjected to temperature load as well as the will to learn about the mechanisms that generate such positive impacts. The studies on mineral identification were conducted as the first regarding the ceramic aggregate itself and unheated calcium aluminate cement; subsequently, the research on concrete samples was performed taking into account basic samples and the ones subjected to temperature loads of 400 and 800 °C.

The phases of concretes, dependent on the used cement, are shown in Figure 5. In the minerals of concretes based on calcium aluminate cement, apart from contents from the aggregate and relics of the cement phases (CA and CA<sub>2</sub>), there are new crystalline phases visible on the diffractograms, which are the result of the hydration process and the action of ‘annealing-fire’ temperatures. In the samples of concrete cured at 20 °C (C10\_20), as a result of the hydration process, hydrates appear whose chemical content is similar to C<sub>3</sub>AH<sub>6</sub> (katoite) and AH<sub>3</sub> (gibbsite) appear. Katoite was recognized by the strongest reflections  $d_{hkl} = 0.5139; 0.3347; 0.3145; 0.2810; 0.2462; 0.2296; \text{ and } 0.2040 \text{ nm}$ ; whereas gibbsite resulted in  $d_{hkl} = 0.3185; 0.3106; 0.2453; 0.2451; 0.2165; \text{ and } 0.2049 \text{ nm}$ .



**Figure 5.** Diffractograms of mineral content of examined concretes containing calcium aluminate cement.

The annealing process at the temperature of 400 °C (C10\_400) causes the increase of phase content, C<sub>3</sub>AH<sub>6</sub> type, whereas gibbsite turns into boehmite recognized by the most intensive reflections  $d_{hkl} = 0.6098; 0.3165; \text{ and } 0.2347 \text{ nm}$ .

In the diffractograms of the sample subjected to temperature action of 800 °C (C10\_800), katoite, occurring at lower temperatures, turns into C<sub>12</sub>A<sub>7</sub> (mayenite) recognized by  $d_{hkl} = 0.4899; 0.4266; 0.3202; 0.2998; \text{ and } 0.2681 \text{ nm}$ . Concretes, on the basis of Portland cement, demonstrate definitely lower variability in the phase content (Figure 6). Apart from amorphous or poorly ordered hydrated calcium silicate (C-S-H), portlandite predominates and is recognized by characteristic interplanar distances  $d_{hkl} = 0.4901; 0.2628; \text{ and } 0.1927 \text{ nm}$ , and whose quantity decreases along with the increase of annealing temperature.

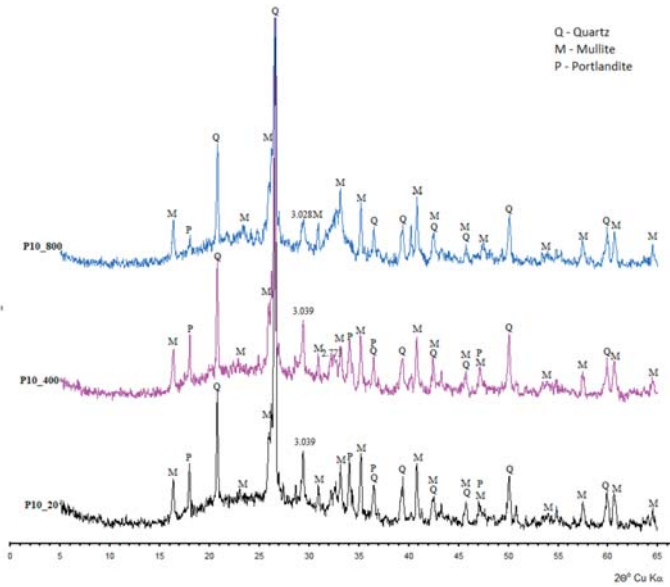


Figure 6. Diffractogram of mineral content of studied concretes containing Portland cement.

The microstructural observations of the designed concretes are shown in Figure 7. The observations with the use of SEM demonstrated that the ceramic aggregate and calcium aluminate cement have an impact on the change in concrete microstructure in the condition of high temperature. In the SEM micrographs of concretes C10\_20 there are a distinct share of irregularly occurring pores, in which there are relics of monocalcium aluminate (CA). Mineral phases predominating in this concrete are as follows; katoite formulates very fine crystalline toppings, and gibbsite, shaped in the form of bars and posts, with accumulations that form dripstone concentrations (Figure 7a). The microstructure of the concrete samples C10\_400 is basically shaped by morphological relations between boehmite, which was formed as a result of the thermal processing of gibbsite, and irregularly shaped katoite panels (Figure 7b). In relation to concrete C10\_20. There is the almost complete lack of pores of large dimensions >10 μm. Porosity is solely related to the presence of empty spaces between dripstone boehmite forms. The impact of the annealing temperature on the concrete structure is distinctly visible in the sample C10\_800 (Figure 7c). Along with phase changes related to the transformation of katoite into mayenite, there are some fractures and microcracks in the contact zone: aggregate-cement paste.

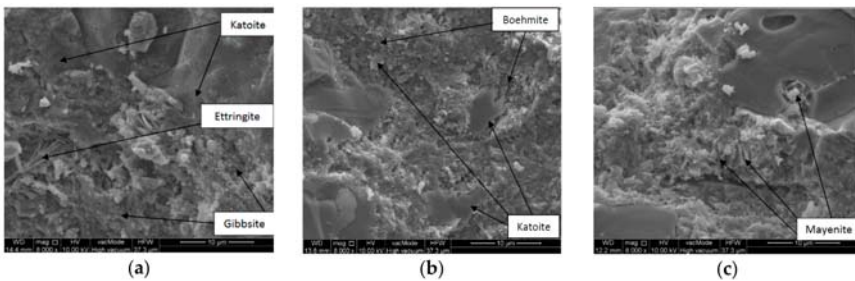


Figure 7. SEM micrograph of sample: (a) C10\_20, (b) C10\_400, (c) C10\_800.

In the concretes based on Portland cement, the SEM micrograph shows that there is a fine-grained and locally fine-fibrous ettringite phase whose crystal concentration reaches the dimension about 10  $\mu\text{m}$ . There is a distinct presence of portlandite occurring in the form of relatively large bars of hexagonal outline and layered structure. In the SEM microphotographs of the concretes, needle forms of ettringite can be observed whose length amounts to 0.5  $\mu\text{m}$  (Figure 8a). The impact of the annealing process of concretes with the use of Portland cement as a binder on the microstructure is visible by the concentrations blur of the dehydrated calcium aluminate C-S-H type, and the portlandite crystals as well as the disappearance of ettringite (Figure 8b). The SEM observations also demonstrate the increase of porosity and the presence of numerous fractures (Figure 8c).

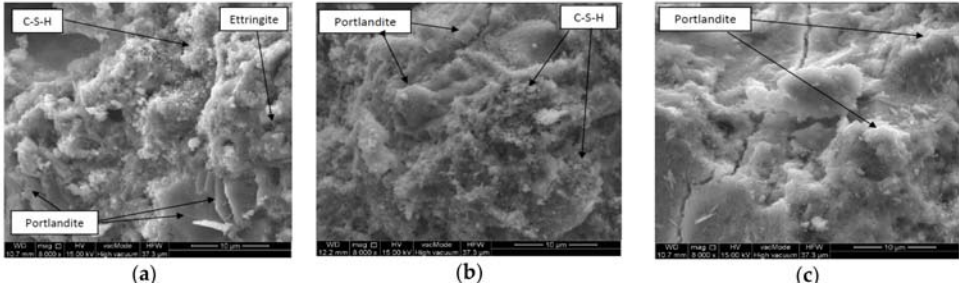


Figure 8. SEM micrograph of sample: (a) P10\_20, (b) P10\_400, (c) P10\_800.

3.4. The Values of Compression Strength and Abrasion Level of Concrete Samples

The diagrams presented below show the average values together with standard deviations of the compression strength of cubic samples (Figures 9 and 10) and abrasion determined on the basis of height loss (Figure 11). Figure 10 shows the results referring to the series of samples containing Portland cement, whereas Figure 9 illustrates the results of samples containing calcium aluminate cement. Particular series were marked in the graphs according to Table 2. Basic samples, which were not subjected to annealing, are marked in the graphs by a white color. Samples annealed at the temperature of 400 °C are marked in grey and samples annealed at 800 °C are marked in black.

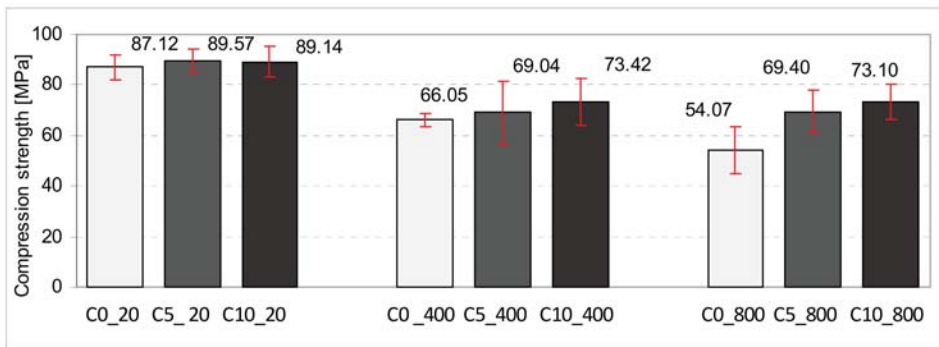


Figure 9. The average values with standard deviations of compression strength of cubic samples containing calcium aluminate cement.

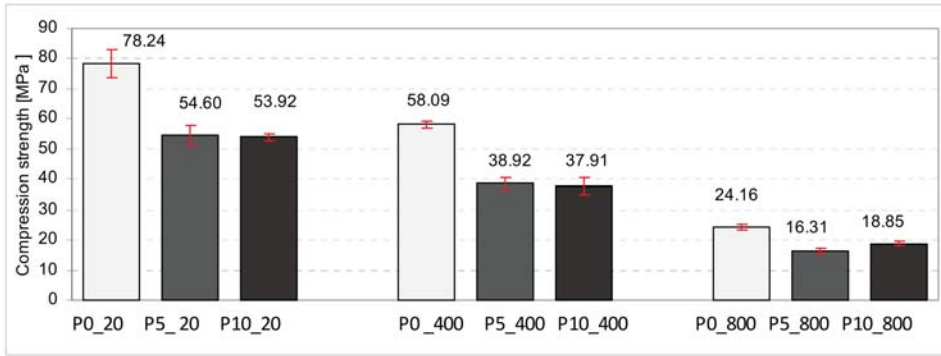


Figure 10. The average values with standard deviations of compression strength of cubic samples containing Portland cement.

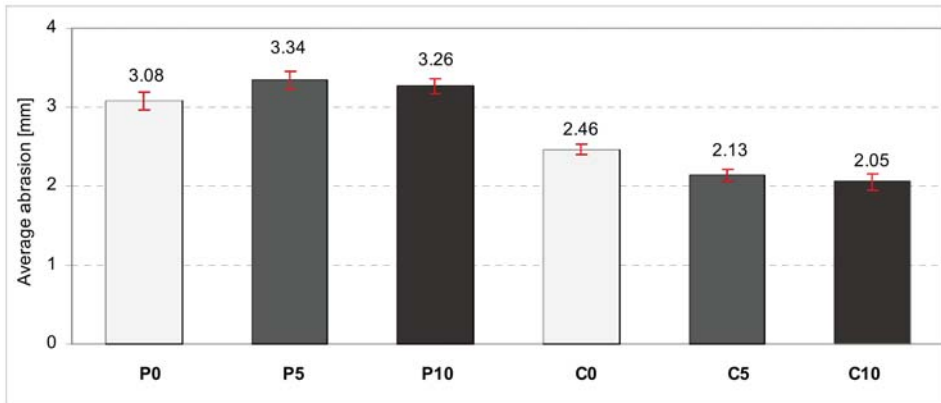


Figure 11. The average values with standard deviations referring to the abrasion of concrete samples.

The series of examined samples with Portland cement contained 45 items. It shall be emphasized that while annealing at high temperatures, none of the samples were damaged. In the group of basic samples, the greatest compression strength was demonstrated by the samples without the aerating additive. Their average compression strength was greater by about 32% in comparison to the samples that contained aeration of 5 and 10%. Annealing had an adverse effect on samples' strength on the basis of the Portland cement. The higher the annealing temperature, the lower the compression strength of the samples. In the group of samples subjected to annealing at 400 °C, the average compression strength of the base samples (without the aerating additive) dropped by about 27% in comparison to samples that were not subjected to annealing. Moreover, in reference to samples containing 5 and 10% degrees of aeration, their compression strength decreased within the range of 28–10% in relation to samples that were not subjected to thermal processing. After the analysis of samples subjected to initial thermal processing at 800 °C, it shall be stated that their compression strength is the lowest for every tested group of samples. The average strength of base samples without the aerating additive is lower by about 71% in reference to samples that were not subjected to thermal processing. Nevertheless, their compression strength is the greatest in comparison to aerated samples by 5 and 10%. The lowest average strength was obtained by samples containing a 5% degree of aeration, which were simultaneously subjected to thermal processing at 800 °C.



In the case of samples made from calcium aluminate cement, 45 samples were examined in total. In this case, however, the average compression strength of the base samples containing 0, 5, and 10% degrees of aeration was nearly identical. The difference in the average strength was only about 2 MPa. The higher the annealing temperature, the lower the average compression strength of particular groups of samples. In the case of samples annealed at 400 °C, the lowest average strength was observed for samples that were not subjected to aeration. Their strength dropped by about 26% in comparison to samples that were not subjected to thermal processing. In the case of samples subjected to aeration, the drop was considerably lower. In relation to samples with 5% aeration it was 22%, whereas for samples containing 10%, the degree of aeration was 18%, comparing the same groups of samples that were not annealed.

In the case of samples that were initially annealed at 800 °C, the greatest drop in the average strength was demonstrated by the samples without an aerating additive. It was 38% in comparison to samples that were not subjected to thermal processing. In the case of samples with the aerating additive of 5% and 10%, the decrease in strength was nearly identical as in the case of samples annealed to the temperature of 400 °C.

It must be highlighted that in the case of concrete made from calcium aluminate cement, the drop in concrete strength after initial annealing at 400 and 800 °C is considerably lower than in the case of samples made from Portland cement.

Our study conducted on abrasion with the use of a Boehm blade was aimed at determining the height loss susceptibility of particular samples. The research was performed on base samples that were not subjected to annealing. The samples made from all designed concrete mixes were tested. The greatest level of abrasion was observed in the groups of samples C0\_20 and P0\_20. The aeration led to the decrease of abrasion level by about 10% in the case of samples containing calcium aluminate cement. The lowest level of abrasion was observed in the samples with Portland cement and 5% of aeration, however, these differences were not substantial in comparison to samples containing Portland cement. When comparing the obtained results with those of [31], it should be noted that the results of the durability tests in normal temperature were similar. However, the results of tests conducted after thermal load differed significantly. It is caused by the fact that in the research paper [31], thermal load was applied in a different method, which was modeled after tests for heat resistant cement, contrasting to those described in this article, where the temperature-time norm curve was used.

#### 4. Conclusions

The obtained results showed that there is the likelihood of waste matter use in the form of sanitary ceramic cullet as the aggregate to concrete of high resistance to fire conditions. The type of cement applied to their preparation has a significant impact on the microstructure of concretes subjected to annealing. Concretes that contained calcium aluminate cement are characterized by the variability of mineral content, which is the effect of progressing the hydroxylation process of the cement phase surfaces accompanied by the release of calcium and aluminum ions. After exceeding the solubility equilibrium of these compounds, new phases start to crystalize such as, katoite and mayenite, whereas aluminum hydroxides are transformed from gel forms into more and more ordered forms such as gibbsite and boehmite. The formation of new phases decreases considerably the amount of pores in the slurry. Nevertheless, in the case of concretes with Portland cement, the annealing process causes dehydration and dehydroxylation of hydrated phases that liberate water vapor in the pores and generate pressure, leading to matrix cracking, which directly decreases the mechanical properties of these concretes.

It was demonstrated that by using the binder in the form of calcium aluminate cement, the obtained concrete demonstrates high resistance to compression. The impact of the aerating additive showed a slight increase of strength in the group of base samples containing calcium aluminate cement. The application of the aerating additive for the group of samples subjected to annealing in the temperature of 400 and 800 °C reduced the decrease of strength. The results at the temperature of

800 °C are particularly significant since in the case of fire developed in closed rooms, it corresponds to the temperature value occurring in the fire developed under the ceiling. It shall be stated that the use of additive led to the almost identical decrease of strength at 400 and 800 °C. The situation is completely different in the case of concrete made from Portland cement. The greatest average compression strength was demonstrated by the base samples (without aerating additive), which were not subjected to annealing. The application of the aerating additive both at 5% and 10% to this concrete resulted in a greater drop in strength than for the concrete without the additive both at room temperature and after annealing. It shall be noticed that in the case of concrete on the basis of calcium aluminate cement and Portland cement, there were no thermal phenomena and explosive chipping of concrete while annealing, as it took place in the case of samples in the shape of cubes. Moreover, it shall be stated that samples used in this research were stored in a dry room at the temperature of 20 °C through the period of 12 months, which is most likely the reason why the described phenomena did not appear. Furthermore, the research on abrasion demonstrated that the use of aerating additive causes the decrease of abrasion with calcium aluminate and Portland cement. The application of additive to concrete based on Portland cement resulted in the decrease of the abrasion level of samples. Demonstrated studies confirmed the possibility of a ceramic cullet application as the aggregate to concrete. Such an approach contributes to the reduction of natural resource extraction and use, and enables the utilization of wastes of this type.

**Author Contributions:** Conceptualization: P.O., J.S. and W.F.; methodology: P.O., J.S. and W.F. validation: J.S.; P.O., and formal analysis: P.O., J.S. and W.F.; investigation: J.S. and W.F.; resources: P.O. and J.S.; writing—original draft preparation: J.S, P.O. and W.F; writing—review & editing: J.S.; visualization: P.O.; and W.F.; funding acquisition: J.S. and W.F.

**Funding:** This research was funded by Ministerstwo Nauki i Szkolnictwa Wyższego, Poland.

**Acknowledgments:** This work was financially supported by Polish Ministry of Science and Higher Education within the statutory research of cooperating universities: The Main School of Fire Service in Warsaw, Lublin University of Technology (S-16/B/2018 and S-12/II/B/2018).

**Conflicts of Interest:** The authors declare no conflicts of interest.

## References

1. Motz, H.; Geiseler, J. Products of steel slags an opportunity to save natural resources. *Waste Manag.* **2001**, *21*, 285–293. [[CrossRef](#)]
2. Mroueh, U.; Eskola, P.; Laine-Ylijoki, J. Life-cycle impacts of the use of industrial by-products in road and earth construction. *Waste Manag.* **2001**, *21*, 285–293. [[CrossRef](#)]
3. Bromberek, Z. Energy efficiency and urban development. *Izolacje* **2014**, *1*, 14–18. (In Polish)
4. Evangelista, L.; De Brito, J. Durability performance of concrete made with fine recycled concrete aggregates. *Cem. Concr. Compos.* **2010**, *32*, 9–14. [[CrossRef](#)]
5. Kou, S.-C.; Poon, C.-S.; Wan, H.-W. Properties of concrete prepared with low-grade recycled aggregates. *Constr. Build. Mater.* **2012**, *36*, 881–889. [[CrossRef](#)]
6. Gomez-Soberon, J.M.V. Porosity of recycled concrete with substitution of recycled concrete aggregate: An experimental study. *Cem. Concr. Res.* **2002**, *32*, 1301–1311. [[CrossRef](#)]
7. Bolden, J.; Abu-Lebdeh, T.; Fini, E. Utilization of recycled and waste materials in various construction applications. *Am. J. Environ. Sci.* **2013**, *9*, 14–24. [[CrossRef](#)]
8. Ahn, T.-H.; Kishi, T. Crack self-healing behavior of cementitious composites incorporating various mineral admixtures. *J. Adv. Concr. Technol.* **2010**, *8*, 180. [[CrossRef](#)]
9. Abbas, A. Durability of Green Concrete as a Structural Material. Ph.D. Thesis, Department of Civil and Environmental Engineering, Carleton University, Ottawa, ON, Canada, 2007.
10. DIN 4226-100:2002-02: Aggregates for Concrete and Mortar—Part 100: Recycled Aggregates; DIN Standards: Germany. Available online: <https://www.beuth.de/de/norm/din-4226-100/44711226> (accessed on February 2002).



11. BS 8500-2:2006+A1:2012. *Concrete. Complementary British Standard to BS EN 206-1. Specification for Constituent Materials and Concrete*; British Standards Institution (BSI): London, UK, 2006; Available online: <https://shop.bsigroup.com/ProductDetail/?pid=00000000030274450> (accessed on 30 November 2006).
12. PN-EN 12620+A1:2010. *Kruszywa do Betonu. Aggregates for Concrete*. Available online: <http://sklep.pkn.pl/pn-en-12620-a1-2010p.html> (accessed on 7 December 2010). (In Polish)
13. Weil, M.; Jeske, U.; Schebek, L. Closed-loop recycling of construction and demolition waste in Germany in view of stricter environmental threshold values. *Waste Manag. Res.* **2006**, *24*, 197–206. [[CrossRef](#)] [[PubMed](#)]
14. Anastasiou, E.; Filikas, K.G.; Stefanidou, M. Utilization of fine recycled aggregates in concrete with fly ash and steel slag. *Constr. Build. Mater.* **2014**, *50*, 154–161. [[CrossRef](#)]
15. Pytel, Z. Characteristic features of ceramic materials containing waste moulding sand. *Ceram. Mater.* **2011**, *63*, 64–73.
16. Adamson, M.; Razmjoo, A.; Poursae, A. Durability of concrete incorporating crushed brick as coarse aggregate. *Constr. Build. Mater.* **2015**, *94*, 423–426. [[CrossRef](#)]
17. Fadia, S.K. Use of crushed bricks as coarse aggregate in concrete. *Tikrit J. Eng. Sci.* **2009**, *16*, 64–69.
18. Debieb, F.; Kenai, S. The use of coarse and fine crushed bricks as aggregate in concrete. *Constr. Build. Mater.* **2008**, *22*, 886–893. [[CrossRef](#)]
19. Mansur, M.A.; Wee, T.H.; Charan, L.S. Crushed bricks as coarse aggregate for concrete. *ACI Mater. J.* **1999**, *96*, 478–484.
20. Poon, C.S.; Kou, S.C.; Lam, L. Use of recycled aggregates in molded concrete bricks and blocks. *Constr. Build. Mater.* **2002**, *16*, 281–289. [[CrossRef](#)]
21. Halbinika, J.; Ulewicz, M. Application of utilitarian and sanitary ceramics in cement mortars. *Ceram. Mater.* **2015**, *67*, 438–442.
22. Binici, H. Effect of crushed ceramic and basaltic pumice as fine aggregates on concrete mortars properties. *Constr. Build. Mater.* **2007**, *21*, 1191–1197. [[CrossRef](#)]
23. Guerra, I.; Vivar, I.; Llamas, B.; Juan, A.; Moran, J. Eco-efficient concretes: The effect of using recycled ceramic material from sanitary installations on the mechanical properties of concrete. *Waste Manag.* **2009**, *29*, 643–646. [[CrossRef](#)] [[PubMed](#)]
24. García-González, J.; Rodríguez-Robles, D.; Juan-Valdés, A.; Morán-Del Pozo, J.M.; Guerra-Romero, M.I. Ceramic ware waste as coarse aggregate for structural concrete production. *Environ. Technol.* **2015**, *36*, 3050–3059. [[CrossRef](#)] [[PubMed](#)]
25. Medina, C.; Sánchez De Rojas, M.I.; Thomas, C.; Polanco, J.A.; Frías, M. Durability of recycled concrete made with recycled ceramic sanitary ware aggregate. Inter-indicator relationship. *Constr. Build. Mater.* **2016**, *105*, 480–486. [[CrossRef](#)]
26. Medina, C.; Frías, M.; Sánchez De Rojas, M.I. Microstructure and properties of recycled concretes using sanitary ware industry waste as coarse aggregate. *Constr. Build. Mater.* **2012**, *31*, 112–118. [[CrossRef](#)]
27. Bakri, M.M.; Hussin, K.; Mohd, C.; Baharin, S.; Ramly, R.; Khairiatun, N. Concrete Ceramic Waste Slab (CCWS). *J. Eng. Res. Educ.* **2006**, *3*, 139–145.
28. Senthamarai, R.M.; Manoharan, P.D.; Gobinath, D. Concrete made from ceramic industry waste: Durability properties. *Constr. Build. Mater.* **2011**, *25*, 2413–2419. [[CrossRef](#)]
29. De Brito, J.; Pereira, A.S.; Correia, J.R. Mechanical behavior of non-structural concrete made with recycled ceramic aggregates. *Cem. Concr. Compos.* **2005**, *27*, 429–433. [[CrossRef](#)]
30. Ogrodnik, P.; Zegardło, B.; Halicka, A. Preliminary assessment of utilization of sanitary ceramics wastes as an aggregate in concrete working at the high temperature. *Saf. Fire Tech.* **2012**, *1*, 49–56.
31. Halicka, A.; Ogrodnik, P.; Zegardło, B. Using ceramic sanitary ware waste as concrete aggregate. *Constr. Build. Mater.* **2013**, *48*, 295–305. [[CrossRef](#)]
32. Zegardło, B.; Ogrodnik, P. Analysis of destructive influence of water saturation on the strength of concrete subjected to fire. *Saf. Fire Tech.* **2016**, *1*, 27–35. [[CrossRef](#)]
33. Ogrodnik, P.; Zegardło, B.; Radzikowska, M. The use of post-production sanitary ceramic waste as a filler for cement composites with high chemical resistance. *Przemysł Chemiczny* **2017**, *96*, 5. [[CrossRef](#)]
34. PN-EN 933-1:2012. *Badania Geometrycznych Właściwości Kruszyw—Część 1: Oznaczanie Składu Ziarnowego—Metoda Przesiewania*. Polski Komitet Normalizacyjny: Poland. Available online: <http://sklep.pkn.pl/pn-en-933-1-2012e.html> (accessed on 19 July 2018). (In Polish)

35. PN-B-06714-40:1978. *Kruszywa Mineralne. Badania. Oznaczenie Wytrzymałości na Miażdżenie*. Polski Komitet Normalizacyjny: Poland. Available online: <http://sklep.pkn.pl/pn-b-06714-40-1978p.html> (accessed on 19 July 2018).
36. PN-EN 12350-7:2011. *Badania Mieszanki Betonowej. Część 7. Badanie Zawartości Powietrza—Metody Ciśnieniowe*. Polski Komitet Normalizacyjny: Poland. Available online: <http://sklep.pkn.pl/pn-en-12350-3-2011p.html> (accessed on 07 December 2009). (In Polish)
37. PN-EN 1363-1:2012. *Badania Odporności Ogniowej. Część 1. Wymagania Ogólne*. Polski Komitet Normalizacyjny: Poland. Available online: <http://sklep.pkn.pl/pn-en-1363-1-2012p.html> (accessed on 17 February 2014). (In Polish)
38. PN-EN 14157:2005. *Kamień Naturalny—Oznaczenie Odporności na Ścieranie*. Polski Komitet Normalizacyjny: Poland. Available online: <http://sklep.pkn.pl/pn-en-14157-2005p.html> (accessed on 12 December 2005). (In Polish)
39. PN-EN 12390-3:2011. *Badania Betonu. Część 3. Wytrzymałość na Ściskanie Próbek do Badania*. Polski Komitet Normalizacyjny: Poland. Available online: <http://sklep.pkn.pl/pn-en-12390-3-2011p.html> (accessed on 19 July 2018). (In Polish)
40. PN-EN 12390-4:2001. *Badania Betonu Część 4. Wytrzymałość na Ściskanie. Wymagania dla Maszyn Wytrzymałościowych*. Polski Komitet Normalizacyjny: Poland. Available online: <http://sklep.pkn.pl/pn-en-12390-4-2001p.html> (accessed on 19 July 2018). (In Polish)



© 2018 by the authors. Licensee MDPI, Basel, Switzerland. This article is an open access article distributed under the terms and conditions of the Creative Commons Attribution (CC BY) license (<http://creativecommons.org/licenses/by/4.0/>).

Article

# Excellent Carbonation Behavior of Rankinite Prepared by Calcining the C-S-H: Potential Recycling of Waste Concrete Powders for Prefabricated Building Products

Kai Wang \*, Liang Ren and Luqing Yang

School of Civil and Architecture Engineering, East China Jiaotong University, Nanchang, 330013, China; renliang@163.com (L.R.); 2017018085213020@ecjtu.jx.cn (L.Y.)

\* Correspondence: 1506@ecjtu.jx.cn; Tel.: +86-791-8704-6084

Received: 23 July 2018; Accepted: 16 August 2018; Published: 19 August 2018

**Abstract:** Pure rankinite ( $C_3S_2$ ) was prepared by calcining a C-S-H gel precursor at a temperature of 1300 °C. The carbonation hardening behavior of the resulting rankinite was revealed by X-ray diffraction (XRD), Fourier transform-infrared (FT-IR) spectroscopy, thermogravimetry and differential thermal analysis (TG/DTA), and scanning electron microscope (SEM) coupled with energy dispersive spectrum (EDS). The results indicate that the pure rankinite can be easily prepared at a lower temperature. The cubic compressive strengths of the resulting rankinite samples reach a value of 62.5 MPa after 24 h of carbonation curing. The main carbonation products formed during the carbonation process are crystalline calcite, vaterite and highly polymerized amorphous silica gels. The formed carbonation products fill the pores and bind to each other, creating a dense microstructure, which contributes to the excellent mechanical strength. These results provide a novel insight into potential recycling of waste concrete powders for prefabricated building products with lower  $CO_2$  emissions.

**Keywords:** rankinite; carbonation; waste concrete;  $CO_2$

## 1. Introduction

At present, China is at the peak of infrastructure construction. The number of new concrete buildings being constructed and old buildings being demolished is enormous. It has been conservatively estimated that China produces nearly 100 million tons of waste concrete each year [1]. Disposal of waste concrete not only requires a large amount of land resources, but also poses serious environmental issues. In this age of greater environmental awareness, an increased number of environmental laws and the desire to reduce construction costs, the recycling of waste concrete into recycled aggregate concrete has many benefits, thus, making it an attractive option [2–7]. In this way, waste concrete is crushed and the aggregate is separated and recovered. However, the crushing process also produces 25–40% waste concrete powder (WCP). These powders are mainly C-S-H gels, with large specific surface areas, high water demands and have not been well reused in the past [8–11].

On the other hand, the use of some low-lime calcium silicate phases such as dicalcium silicate ( $C_2S$ ), rankinite ( $C_3S_2$ ) and wollastonite (CS) to produce prefabricated buildings by carbonation, with significantly lower carbon dioxide emissions, is creating concern worldwide [12–16]. Rankinite ( $C_3S_2$ ) is a low-lime calcium silicate phase. However, the traditional preparation method requires a higher calcination temperature (1460 °C) and cannot be synthesized easily [17].

In this paper, pure  $C_3S_2$  minerals were prepared by calcining the prepared C-S-H gel precursor. The carbonation hardening behavior of the prepared  $C_3S_2$  was revealed by X-ray diffraction (XRD),

Fourier transform-infrared (FT-IR) spectroscopy, thermogravimetry and differential thermal analysis (TG/DTA), and scanning electron microscope (SEM) coupled with energy dispersive spectrum (EDS). The results provide a novel insight into the potential recycling of waste concrete powders for prefabricated building products, with lower CO<sub>2</sub> emissions.

## 2. Materials and Methods

### 2.1. Preparation of C<sub>3</sub>S<sub>2</sub>

The C-S-H gel precursor was firstly prepared by exposing the mixtures of CaO and amorphous SiO<sub>2</sub> (at 3:2 molar ratios) to a hydrothermal process. The water to solid ratio was 10 and the mixtures were sealed at 60 °C for 6 h to allow the complete reaction at ambient pressure. Then, the prepared C-S-H gel precursor was dried in a vacuum oven at 100 °C for 24 h. The dried C-S-H gel precursor was later calcined at 1300 °C for 2 h. Subsequently, the prepared C<sub>3</sub>S<sub>2</sub> was cooled down to room temperature at a rapid cooling rate (approximately 500 °C/min) and ground for 20 min to achieve a Blaine fineness of 3970 cm<sup>2</sup>/g.

### 2.2. Carbonation of C<sub>3</sub>S<sub>2</sub>

C<sub>3</sub>S<sub>2</sub> is a non-hydraulic mineral that does not set and harden when mixed with water. Thus, the resulting C<sub>3</sub>S<sub>2</sub> powder was mixed with water at a water to solid ratio of 0.1 which is conducive to the carbonation reaction. Then, the wet mixtures were cast into a stainless steel mold (20 mm × 20 mm × 20 mm) and compacted at 5 MPa for 1 min. Thereafter, the compacted C<sub>3</sub>S<sub>2</sub> samples were placed in a sealed stainless chamber at a temperature of 25 ± 2 °C, relative humidity of 70%, CO<sub>2</sub> concentration of 99.9% and CO<sub>2</sub> pressure of 0.3 MPa for 2, 5, 8 and 24 h, respectively.

### 2.3. Test Methods

#### 2.3.1. The Cubic Compressive Strength

The cubic compressive strength was measured using a universal testing machine with a deformation speed of 0.5 mm/min. Six cubic samples with a dimension of 20 mm × 20 mm × 20 mm were tested.

#### 2.3.2. X-ray Diffraction Analysis

The phase structure of the C<sub>3</sub>S<sub>2</sub> phase before and after carbonation were characterized by powder X-ray diffraction on a Rigaku SmartLab X-ray diffractometer (Rigaku Corporation, Tokyo Akishima, Japan) with Cu K<sub>α</sub> radiation (λ = 1.5406 Å). The X-ray tube was operated at 40 kV and 15 mA. The XRD patterns were recorded in the range of 10–55°.

#### 2.3.3. Fourier Transform-Infrared Spectroscopy

The FT-IR spectroscopy data of the C<sub>3</sub>S<sub>2</sub> phase before and after carbonation was collected using a Bruker V70 Fourier transform infrared spectrometer (Bruker Corporation, Karlsruhe, Germany) with the KBr pellet technique, and the ranges of spectrograms were 1800–800 cm<sup>-1</sup> at a resolution of 4 cm<sup>-1</sup>. Each spectrum presented in this paper is an average of six scans.

#### 2.3.4. Thermogravimetry and Differential Thermal Analysis

The TG/DTA tests were performed using a simultaneous thermal analyzer (BJ-HCT-3, Nanjing sangli electronic equipment factory, Nanjing, China). The sample weighing 20 mg was placed into a ceramic crucible, and then heated with a rate of 10 °C/min from 20 °C to 950 °C using an alumina reference material. N<sub>2</sub> was used as purge gas during the TG/DTA tests.

### 2.3.5. Scanning Electron Microscope

A small cut portion of the compacted  $C_3S_2$  sample before and after carbonation was dried and epoxy impregnated, respectively. After impregnation, one of the surfaces was polished to a 0.5 micrometer finish. The polished surface was sputter coated with a thin layer of gold (Au) and examined under a SEM in backscattered mode. A Merlin Compact ultra-high-resolution field emission scanning electron microscope (FEI Corporation, Hillsboro, OR, USA) coupled with Oxford energy dispersive spectrum at 20 kV was used to acquire the images.

## 3. Results

### 3.1. The Cubic Compressive Strength

The cubic compressive strengths of the compacted  $C_3S_2$  samples carbonated for 0, 2, 5, 8 and 24 h, respectively, are provided in Figure 1. The results show that compacted  $C_3S_2$  samples can be rapidly hardened under carbonation conditions and reach a compressive strength of 62.5 MPa within 24 h. In addition, the strength development was mainly focused in the initial eight hours. These results indicate that  $C_3S_2$  prepared from C-S-H gel precursors can achieve excellent strength after rapid carbonation curing, providing a novel insight into potential recycling of waste concrete powders for prefabricated building products with lower  $CO_2$  emissions.

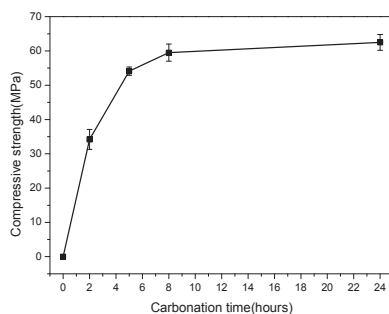


**Figure 1.** The compressive strength of compacted  $C_3S_2$  samples with different carbonation times.

### 3.2. Carbonation Products

#### 3.2.1. XRD Analysis

Figure 2 illustrates the XRD patterns of the  $C_3S_2$  phase before carbonation and carbonated for 24 h. For the  $C_3S_2$  phase before carbonation, the pattern matches well with the published XRD pattern for  $C_3S_2$  [17,18]. It is indicated that the pure  $C_3S_2$  phase can be easily prepared by calcining the C-S-H gel precursor at 1300 °C for two hours. After carbonation, the main crystalline carbonation products are calcite and vaterite and there are no diffraction peaks of silica, revealing that the silica formed during the carbonation is amorphous ( $SiO_2$  gels). These results are distinct from the results achieved by Qian [17] who believes that crystalline quartz and cristobalite are the main silica products formed after 24 h of carbonation. Moreover, some unreacted  $C_3S_2$  phase still exists. The mass fractions of calcite, vaterite and unreacted  $C_3S_2$  measured from the XRD pattern of the  $C_3S_2$  phase after carbonation for 24 h by the Rietveld method are 44.7, 20.1 and 35.2%, respectively.

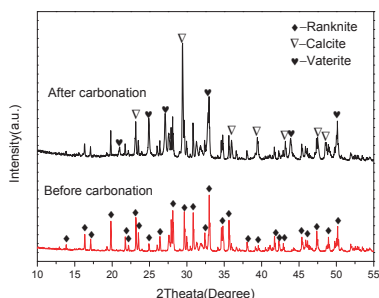


**Figure 2.** X-Ray Diffraction (XRD) patterns of the  $C_3S_2$  phase before carbonation and carbonated for 24 h.

### 3.2.2. FT-IR Analysis

To reveal the structure of the  $SiO_2$  gels formed during carbonation, the FT-IR spectrums of the  $C_3S_2$  phase before carbonation and carbonated for 24 h are shown in Figure 3. It is well established that the FT-IR spectrum for silicate compounds exhibit a large absorption between 800 and 1200  $cm^{-1}$ , which correspond to the asymmetrical stretching vibration ( $V_3$ ) of the Si-O bond. With the increasing polymerization degree of the silicate compound, the bonding strength of the Si-O increases and the  $V_3$  band shifts to a higher wavenumber. For the  $C_3S_2$  phase before carbonation, there were three major absorptions bands located at approximately 847, 945 and 998  $cm^{-1}$ . These are higher than the pure  $C_2S$  phase (orthosilicate group), indicating that the  $C_3S_2$  phase is composed of dimer silicate tetrahedrons (sorosilicates group), that is, one oxygen atom is shared between two neighboring tetrahedrals. For the  $C_3S_2$  phase after carbonation, new bands were observed to appear at approximately 867, 1440 and 1085  $cm^{-1}$ . The band located at around 1440  $cm^{-1}$  is due to the asymmetric stretching ( $V_3$ ) of the C-O bond present in  $CaCO_3$ , and the band located at around 867  $cm^{-1}$  corresponds to the out of plane bending vibration ( $V_2$ ) of the same C-O bond. Moreover, the position of the  $V_3$  vibration of Si-O bonds were much higher (1085  $cm^{-1}$ ) than the  $V_3$  band position present in  $C_3S_2$  phase before carbonation, indicating that highly polymerized  $SiO_2$  gels were formed after carbonation.

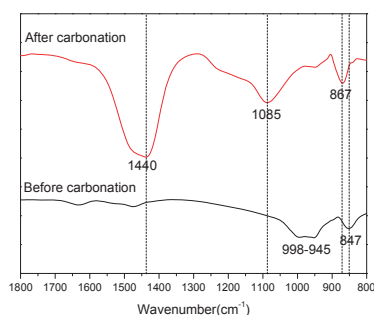


**Figure 3.** Fourier Transform-Infrared (FT-IR) spectrums of the  $C_3S_2$  phase before carbonation and carbonated for 24 h.

### 3.2.3. TG/DTA Analysis

The TG/DTA curves for the  $C_3S_2$  phase carbonated for 24 h are presented in Figure 4. The mass losses in the range of 20–400  $^{\circ}C$  were attributed to the dehydration of the gel water from the formed  $SiO_2$  gels. The mass losses in the range of 400–700  $^{\circ}C$  and 700–950  $^{\circ}C$  were used, respectively,

to calculate the mass fraction of vaterite and calcite present in the carbonated  $C_3S_2$  phase [19]. The mass losses from the decomposition of vaterite and calcite were 4.64 and 11.62%, respectively, indicating that the  $CaCO_3$  of  $C_3S_2$  phase after carbonation was primarily formed from calcite and some vaterite. These results are consistent with the FT-IR and XRD results.

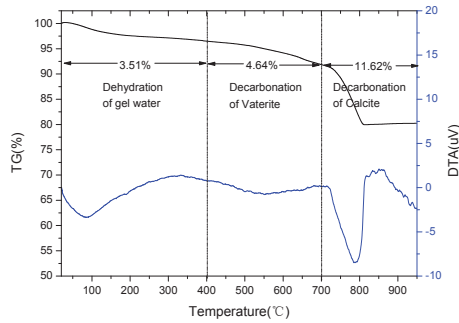


**Figure 4.** Thermogravimetry and Differential Thermal Analysis (TG/DTA) curves of the  $C_3S_2$  phase carbonated for 24 h.

3.3. Microstructure

Figures 5 and 6 show the SEM-EDS images of the compacted  $C_3S_2$  samples before and after carbonation, respectively. Before carbonation, the  $C_3S_2$  particles (approximately 5–25  $\mu m$ ) were loosely packed. After carbonation, a dense microstructure was observed. According to the elemental maps and EDS results, the distribution of the carbonation products was illustrated as follows. The unreacted  $C_3S_2$  core was enveloped by a  $SiO_2$  gel rim and the initial pores of the sample were filled with  $CaCO_3$ .

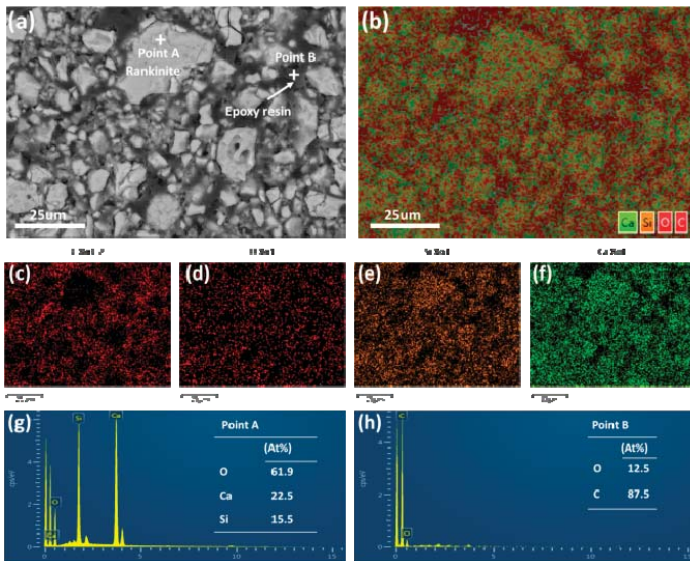


**Figure 5.** SEM and EDS images of the compacted  $C_3S_2$  samples before carbonation: (a) Backscattered Electron (BSE) image, (b–f) elemental maps for composite elements and C, O, Si, Ca, respectively, (g,h) EDS analysis of point A and B.



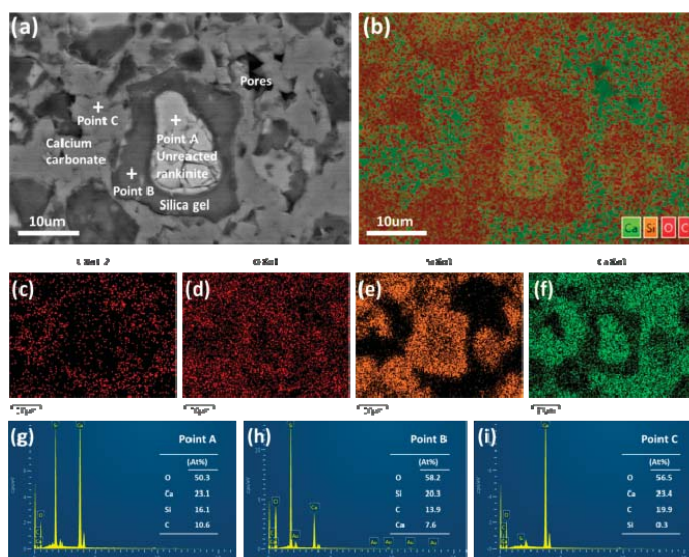


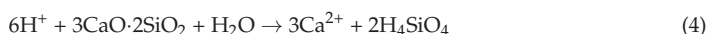
**Figure 6.** SEM and EDS images of the compacted  $C_3S_2$  samples carbonated for 24 h: (a) BSE image, (b–f) elemental maps for composite elements and C, O, Si, Ca, respectively, (g–i) EDS analysis of point A, B and C.

### 3.4. Reaction Mechanism

Based on the results achieved above, the reaction mechanism that occurred during the carbonation of  $C_3S_2$  can be illustrated in Figure 7. When the compacted  $C_3S_2$  samples that were partially filled with water come in contact with  $CO_2$ , the  $CO_2$  will dissolve in the pore water and ionize to produce  $H^+$ ,  $HCO_3^-$  and  $CO_3^{2-}$ .



The ionization process of  $H_2CO_3$  will generate a lot of  $H^+$ , making the pH value of the pore water fall by approximately 3 units at 20 °C, typically from 7 to 4. Compared with neutral water, the significantly increased  $H^+$  concentration will induce the solvation of  $Ca^{2+}$  from the  $C_3S_2$  phase and drive the polymerization of the resulting silicon tetrahedral monomers ( $H_4SiO_4$ ) to form highly polymerized  $SiO_2$  gels.



With the progress of dissolution and polymerization, the  $H^+$  is gradually consumed and the pH of the pore solution is recovered, making it possible to precipitate calcium carbonate. At the beginning, vaterite and aragonite can be formed, but these  $CaCO_3$  polymorphs eventually revert to calcite. However, in some special circumstances, such as a suitable pH value or specific impurity ions for example, the metastable  $CaCO_3$  morphology can be stabilized [16]. However, the mechanism by which different polymorphs of  $CaCO_3$  form during the carbonation process is unclear.





In general, the carbonation reaction of  $\text{C}_3\text{S}_2$  can be simplified by combining the above equations. It is important to note that there is no  $\text{H}_2\text{O}$  in Equation (7). If the silicon tetrahedral monomers are completely polymerized, it is believed that the water plays only a catalytic role in the carbonation reaction process and is not consumed. These results are distinct from the results obtained by Ashraf [18] who believes that water will participate in the carbonation reaction to form C-S-H gels. A possible explanation is that the sample is not completely carbonated. If the C-S-H gels are carbonated completely, the chemically bound water in C-S-H will be released.



As the carbonation reaction proceeds, the pores of the samples are gradually filled with crystalline  $\text{CaCO}_3$  and highly polymerized  $\text{SiO}_2$  gels and the reaction rate is greatly reduced, leaving the unreacted  $\text{C}_3\text{S}_2$  cores. Moreover, it is believed that  $\text{Ca}^{2+}$  is more mobile than silicon tetrahedral monomers during the carbonation process. Therefore, the highly polymerized  $\text{SiO}_2$  gels remain around the unreacted  $\text{C}_3\text{S}_2$  cores and the  $\text{CaCO}_3$  precipitates in the initial pores. Eventually, a dense microstructure will be formed, which contributes to the excellent mechanical strength.

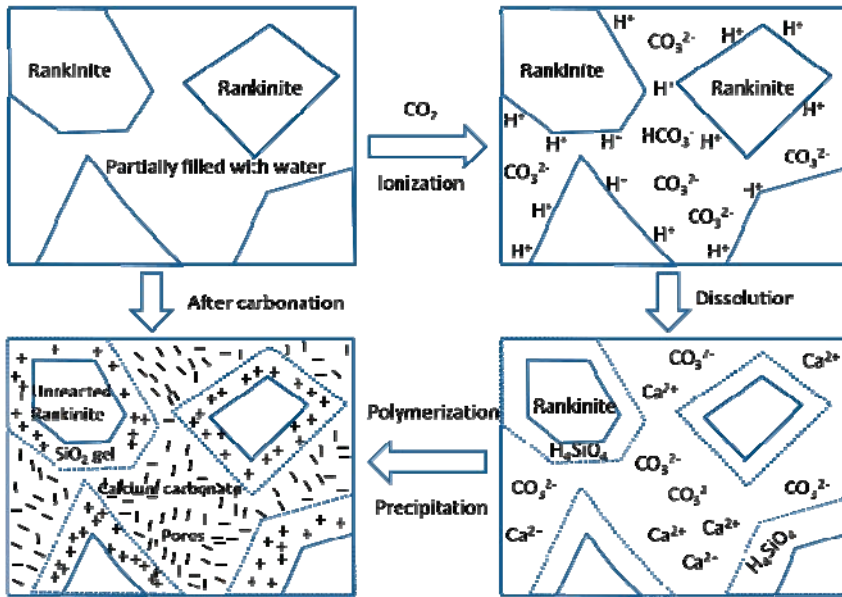


Figure 7. The reaction mechanism that occurred during the carbonation of  $\text{C}_3\text{S}_2$ .

#### 4. Conclusions

Based on the aforementioned results and discussion, the primary conclusions drawn from this work are:

- (1) The pure rankinite phase can be easily prepared by calcining the C-S-H gel precursor at a lower temperature.
- (2) The cubic compressive strength of the resulting rankinite reaches a value of 62.5 MPa after 24 h of carbonation curing.

(3) The main carbonation products formed during the carbonation process are crystalline calcite, vaterite and highly polymerized amorphous silica gels.

(4) The formed carbonation products fill the pores and bind to each other, creating a dense microstructure which contributes to the excellent mechanical strength.

(5) The results provide a novel insight into potential recycling of waste concrete powders for prefabricated building products with lower CO<sub>2</sub> emissions.

**Author Contributions:** K.W. conceived and designed the experiments; L.R. and L.Y. performed the experiments; K.W. analyzed the data and wrote the paper.

**Funding:** This research was funded by the National Natural Science Foundation of China (51478183), the Jiangxi Province Specialized Research Fund for Science and Technology Project of Higher Education, China (KJLD13039), and the Jiangxi Province Fund for Distinguished Young Scientists, China (20142BCB23012).

**Acknowledgments:** We would like to thank the funds from the National Natural Science Foundation of China (51478183), the Jiangxi Province Specialized Research Fund for Science and Technology Project of Higher Education, China (KJLD13039), and the Jiangxi Province Fund for Distinguished Young Scientists, China (20142BCB23012).

**Conflicts of Interest:** The authors declare no conflict of interest.

## References

1. Li, X. Recycling and reuse of waste concrete in China. *Resour. Conserv. Recy.* **2008**, *53*, 36–44. [[CrossRef](#)]
2. Günçan, N.F. Using waste concrete as aggregate. *Cement Concrete Res.* **1995**, *25*, 1385–1390.
3. Silva, R.V.; de Brito, J.; Dhir, R.K. Properties and composition of recycled aggregates from construction and demolition waste suitable for concrete production. *Constr. Build. Mater.* **2014**, *65*, 201–217. [[CrossRef](#)]
4. Behera, M.; Bhattacharyya, S.K.; Minocha, A.K.; Deoliya, R.; Maiti, S. Recycled aggregate from C&D waste & its use in concrete -A breakthrough towards sustainability in construction sector: A review. *Constr. Build. Mater.* **2014**, *68*, 501–516.
5. Fan, C.C.; Huang, R.; Hwang, H.; Chao, S.J. Properties of concrete incorporating fine recycled aggregates from crushed concrete wastes. *Constr. Build. Mater.* **2016**, *112*, 708–715. [[CrossRef](#)]
6. Paris, J.M.; Roessler, J.G.; Ferraro, C.C.; Deford, H.D.; Townsend, T.G. A review of waste products utilized as supplements to Portland cement in concrete. *J. Clean. Prod.* **2016**, *121*, 1–18. [[CrossRef](#)]
7. Bru, K.; Touzé, S.; Bourgeois, F.; Lippiatt, N.; Ménard, Y. Assessment of a microwave-assisted recycling process for the recovery of high-quality aggregates from concrete waste. *Int. J. Miner. Process.* **2014**, *126*, 90–98. [[CrossRef](#)]
8. Ahmari, S.; Ren, X.; Toufigh, V.; Zhang, L. Production of geopolymeric binder from blended waste concrete powder and fly ash. *Constr. Build. Mater.* **2012**, *35*, 718–729. [[CrossRef](#)]
9. Kim, Y.J.; Choi, Y.W. Utilization of waste concrete powder as a substitution material for cement. *Constr. Build. Mater.* **2012**, *30*, 500–504. [[CrossRef](#)]
10. Moon, D.J.; Kim, Y.B.; Ryou, J.S. An approach for the recycling of waste concrete powder as cementitious materials. *J. Ceram. Process. Res.* **2008**, *9*, 278–281.
11. Ma, X.; Wang, Z. Effect of Ground Waste Concrete Powder on Cement Properties. *Adv. Mater. Sci. Eng.* **2013**, *2013*, 1–5. [[CrossRef](#)]
12. Ashraf, W.; Olek, J. Elucidating the accelerated carbonation products of calcium silicates using multi-technique approach. *J. CO<sub>2</sub> Util.* **2018**, *23*, 61–74. [[CrossRef](#)]
13. Ashraf, W.; Olek, J.; Jain, J. Microscopic features of non-hydraulic calcium silicate cement paste and mortar. *Cement Concrete Res.* **2017**, *100*, 361–372. [[CrossRef](#)]
14. Ashraf, W. Carbonation of cement-based materials: Challenges and opportunities. *Constr. Build. Mater.* **2016**, *120*, 558–570. [[CrossRef](#)]
15. Chang, J.; Fang, Y.; Shang, X. The role of  $\beta$ -C<sub>2</sub>S and  $\gamma$ -C<sub>2</sub>S in carbon capture and strength development. *Mater. Struct.* **2016**, *49*, 4417–4424. [[CrossRef](#)]
16. Liu, S.; Dou, Z.; Zhang, S.; Zhang, H.; Guan, X. Effect of sodium hydroxide on the carbonation behavior of  $\beta$ -dicalcium silicate. *Constr. Build. Mater.* **2017**, *150*, 591–594. [[CrossRef](#)]
17. Qian, B.; Li, X.; Shen, X. Preparation and accelerated carbonation of low temperature sintered clinker with low Ca/Si ratio. *J. Clean. Prod.* **2016**, *120*, 249–259. [[CrossRef](#)]

18. Ashraf, W.; Olek, J. Carbonation behavior of hydraulic and non-hydraulic calcium silicates: potential of utilizing low-lime calcium silicates in cement-based materials. *J. Mater. Sci.* **2016**, *51*, 6173–6191. [[CrossRef](#)]
19. Fang, Y.; Chang, J. Microstructure changes of waste hydrated cement paste induced by accelerated carbonation. *Constr. Build. Mater.* **2015**, *76*, 360–365. [[CrossRef](#)]



© 2018 by the authors. Licensee MDPI, Basel, Switzerland. This article is an open access article distributed under the terms and conditions of the Creative Commons Attribution (CC BY) license (<http://creativecommons.org/licenses/by/4.0/>).

Article

# Feasibility Evaluation of Preparing Asphalt Mixture with Low-Grade Aggregate, Rubber Asphalt and Desulphurization Gypsum Residues

Xiaoliang Zhang, Ben Zhang, Huaxin Chen \* and Dongliang Kuang \*

School of Materials Science and Engineering, Chang'an University, Xi'an 710061, China; fibergroup@126.com (X.Z.); emailforpaper@sina.com (B.Z.)

\* Correspondence: chenhx\_paper@163.com (H.C.); kuangdl@chd.edu.cn (D.K.); Tel.: +86-029-82337246 (H.C. & D.K.)

Received: 30 July 2018; Accepted: 15 August 2018; Published: 20 August 2018

**Abstract:** Road construction consumes great amounts of high-grade natural resources. Using low-grade natural rocks or some solid wastes as substitute materials is a hot topic. Considering this, the feasibility of using low-grade granite aggregate, solid waste-based filler (desulphurization gypsum residues, DGR) and binder (waste tire rubber modified asphalt, RMA) simultaneously in asphalt mixtures has been fully investigated in this research. The commonly used base asphalt and limestone powder (LP) filler were control groups. Material characteristics of raw materials mainly including micro-morphology, functional group, mineral phase, chemical composition and thermal stability were first evaluated in order to recognize them. Four asphalt mixtures (two asphalt binder and two filler) were then designed by standard Superpave method. Finally, a detailed investigation into the pavement performance of asphalt mixtures was carried out. The moisture damage resistance and low-temperature crack resistance were detected by the changing rules of stability, strength and fracture energy, and the high-temperature stability and fatigue performance were determined by wheel tracking test and indirect tensile (IDT) fatigue test, respectively. Results suggested that RMA and DGR both showed positive effects on the low-temperature crack resistance and fatigue property of the granite asphalt mixture. DGR also strengthened moisture stability. The contribution of RMA on high-temperature deformation resistance of the granite asphalt mixture was compelling. It can offset the insufficiency in high-temperature stability made by DGR. A conclusion can be made that asphalt mixture prepared with granite, DGR and RMA possesses satisfactory pavement performances.

**Keywords:** granite aggregate; desulphurization gypsum residues; rubber modified asphalt; asphalt mixture; pavement performance

---

## 1. Introduction

In many countries, asphalt mixture is widely used in the construction of grade roads, and more than 90% of high-grade roads are paved with asphalt mixture in UK and China [1,2]. The reason why asphalt mixture is so popular is its good pavement and service performance [3,4]. In China, the road network has well developed over the past decades due to the rapid growth of the national economy. The total mileage of asphalt mixture paved expressway reached 136,500 km by the end of 2017 according to official statistics. While the road construction task is still of concern in the future because of the vast territory and national development demand.

Asphalt mixture is composed of aggregate, filler and asphalt binder [5]. The aggregate is mainly involved in the formation of the asphalt mixture skeleton. Filler and asphalt are the main components of asphalt mastic, which fills and cements the asphalt mixture skeleton [6,7]. The aggregate accounts for more than 90% of the asphalt mixture by weight. Therefore, the construction of asphalt pavement

consumes great amounts of natural rocks. Many strategies have been proposed in order to reduce the supply pressure of high-quality natural aggregate. The typical method is using low-quality aggregate or some solid wastes as substitute materials [8–14].

The reason why some kinds of rock are known as low-quality aggregates when considering the use in asphalt mixture is that they are acidic. Gneiss, granite and quartzite are typical acidic rocks. Acidic aggregates show poor bonding performance with asphalt mastic [15]. The bonding behavior obviously affects pavement performance of asphalt mixture, especially the moisture-induced damage resistance. Many work has been done in order to improve the bonding performance of acidic aggregate-based mixture, and mainly focus on two aspects: adjusting the combination of aggregate types and modifying the asphalt mastic [8,9,16].

In terms of adjusting aggregate types, using some high-quality fine aggregate to replace the fine part of acidic aggregate-based mixture is the common technical measure. Wu et al. evaluated the performance of acidic gneiss mixture with high-quality limestone fine aggregate, which was proved to be an effective method. Chen et al. also indicated that the alkaline solid waste, steel slag, worked pretty well when used as fine aggregate in gneiss mixture [15]. The fine aggregate commonly accounts for more than 30% of asphalt mixture by volume. Using high-quality fine aggregate to replace the fine part of acidic mineral mixture is not conducive to the full use of inferior resource. Therefore, asphalt mixture with 10% of acidic aggregate is desirable.

Modifying asphalt mastic with different modifiers is a popular way to save natural resource and improve some specific performances of the asphalt mixture [9,16–21]. Previous research suggested that the use of alkaline modifiers such as cement and hydrated lime in asphalt mastic can raise the bonding performance of asphalt mixture [9,16]. While the contribution made by common alkaline filler was not as effective as high-quality fine aggregates [9]. Therefore, the key question is to prepare asphalt mastic with suitable types of filler and asphalt in order to realize the 100% use of low-grade acidic aggregate.

The desulphurization gypsum residues (DGR) are mainly generated in the power plants, which produce electricity power by burning coal. The flue gas generated during coal combustion should be purified before releasing into the air. This is because it contains some harmful ingredients such as SO<sub>2</sub>. Using slurry of CaCO<sub>3</sub>/CaO to absorb SO<sub>2</sub> is a common method [22]. Finally, the generated products and excess absorbent form DGR. DGR is a strong alkali due to the excess absorbent. The alkaline feature gives it a potential to improve the bonding behavior between aggregate and asphalt mastic when used as a filler. In addition, modifying the asphalt mastic by solid waste-based modifiers is rarely reported.

Modified asphalt is considered to perform better in enhancing the performance of asphalt mixture than base asphalt binder. The amount of abandoned rubber products is increasing year by year all over the world, and waste tires form a great part of this [23]. The efficient disposal of waste rubber products is very urgent for the purpose of environmental protection and comprehensive utilization of resources. The utilization of crumb rubber for asphalt modification is proposed as a promising solution [24]. According to previous research, the rubber modified asphalt (RMA) can improve many performances of asphalt mixture such as the fatigue performance and high-temperature deformation resistance [25,26]. Considering this, the utilization of RMA in low-quality aggregate mixture may also bring benefits for the performance of asphalt mixture.

Based on the above, in order to fully use the low-quality aggregate, the feasibility of preparing asphalt mixture with granite acidic aggregate, DGR and RMA were fully investigated in this research. Three studies have been conducted: (1) The basic technical indexes and main material characteristics of raw materials including micro-morphology, functional group, mineral phase, chemical composition and thermal stability were detected and compared in order to fully recognize them. (2) Designing four asphalt mixtures (two asphalt binder and two fillers) by means of the standard Superpave procedure. (3) Determining the feasibility of preparing asphalt mixture with granite aggregate, DGR and RMA by comprehensive pavement performance evaluation, including moisture damage

resistance, low-temperature crack resistance, high-temperature stability and fatigue performance. The research flow chart is shown in Figure 1.

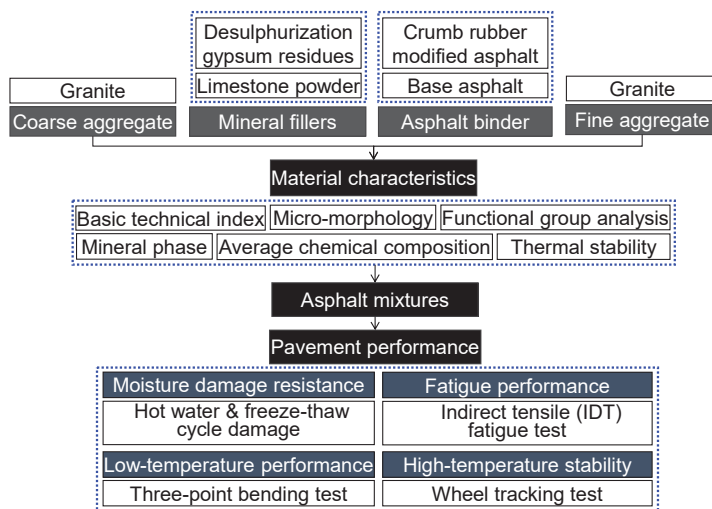


Figure 1. Research flow chart of this research.

## 2. Materials and Research Methodologies

### 2.1. Materials

In this research, the coarse aggregates and fine aggregates were both granite. Limestone powder (LP) and desulphurization gypsum residues (DGR) were used as fillers. Granite aggregate and LP were provided by the Xiangyu Mining Co., Ltd., Anhui, China. DGR was from the Datang Shaanxi Power Generation Co., Ltd., Shaanxi, China. In addition, two types of asphalt binder namely base asphalt and tire rubber modified asphalt (RMA) were adopted. The base asphalt grade 80/100 was produced by the Jiangsu Baoli Asphalt Co., Ltd., Jiangsu, China. RMA was prepared in the laboratory. Crumb rubber was obtained by grinding waste tire and the maximum size of rubber particle was 60 mesh. The dosage of rubber powder was set to 20% of base asphalt grade 60/80 by weight according to the suggestion given in previous research [27,28]. The wet process was used to prepare RMA. Crumb rubber mixed with base asphalt at 185 °C, and the mixture was sheared for 90 min with a shearing rate of 4000 r/min.

### 2.2. Research Methodologies

#### 2.2.1. Technical Indexes and Material Characteristics of Raw Materials

Almost every country will establish corresponding technical specifications for road construction. There are strict requirements for the basic technical indexes of raw materials in technical specifications. Therefore, checking the basic technical indexes is the first step to determine the feasibility of raw materials. In this research, basic technical indexes of aggregate, filler and asphalt binder (density, water absorption, penetration, ductility, etc.) were tested according to Chinese standard methods [29,30].

Except for the basic technical indexes, the material characteristics of raw materials also directly affect the performance of asphalt mixture. Hence, the main material characteristics of raw materials were further detected in order to fully understand them, especially for the uncommonly used DGR and RMA. The micro-morphology of aggregate, filler and tire rubber powder was observed by the Scanning Electron Microscope (SEM, Hitachi, Japan). The functional groups of base asphalt and RMA were

determined by the Fourier Transform Infra-red Spectrometer (FT-IR, Thermo Fisher, Waltham, MA, USA). The X-ray Diffraction (XRD, Bruker, Karlsruhe, Germany), and Polarizing Optical Microscopy (POM, Olympus Corporation, Tokyo, Japan), X-ray Fluorescence (XRF, Panalytical Axios, Almelo, The Netherlands), Thermal Gravimetric (TG, Netzsch, Selb, Germany) analysis system were used to characterize the mineral phase, average chemical composition, thermal stability of aggregate and filler, respectively.

2.2.2. Design of Asphalt Mixtures

Four asphalt mixtures with a nominal maximum size of 12.5 mm were designed by Superpave method. The combination of raw material types for each mixture is shown in Table 1. The only difference for these four mineral mixtures is the types of filler. So the four mixtures can be divided into two categories when designing the hybrid gradation of mineral materials (aggregate and filler), namely mixture of granite and LP ( $M_{GL}$ ) and mixture of granite and DGR ( $M_{GD}$ ).

In order to keep volume compositions of all mineral mixtures simultaneous, the same blending proportion of raw materials for each mixture was used. Coarse aggregate, fine aggregate and filler accounted for 63%, 32% and 5% by total volume of hybrid mineral mixture, respectively. The hybrid gradations used in this research are shown in Figure 2. The optimum asphalt content (OAC) and volumetric property indexes for each asphalt mixture were determined and checked according to the Superpave design procedure.

Table 1. Combination of raw materials types for each mixture.

Mixtures	Coarse Aggregate	Fine Aggregate	Filler	Asphalt
$M_{GLB}$	Granite	Granite	LP	Base asphalt
$M_{GDB}$	Granite	Granite	DGR	Base asphalt
$M_{GLR}$	Granite	Granite	LP	RMA
$M_{GDR}$	Granite	Granite	DGR	RMA

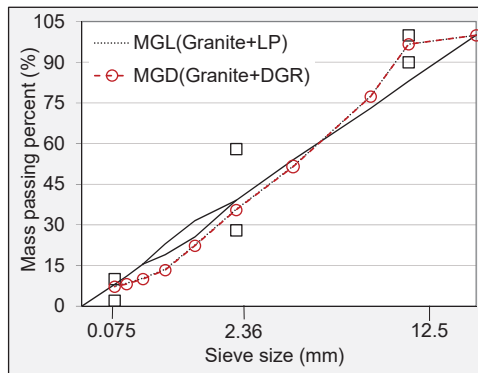


Figure 2. Hybrid gradations used in this research.

2.2.3. Performance Evaluation of Asphalt Mixtures

Moisture-Induced Damage Resistance

The moisture stability of asphalt mixtures was first investigated by the hot water damage test and freeze–thaw damage test, and then further analyzed by means of the energy method. The tested samples were prepared by coring and cutting the cylindrical specimens compacted in Superpave gyratory compactor, and the final dimension of prepared samples was 50 mm thickness, 100 mm in

diameter. The air voids of samples for hot water damage test and freeze–thaw damage test were 4–6% and 6–8%, respectively. A total of 12 samples for each asphalt mixture were prepared. They were equally divided into four groups; one was the control group, the others were conditioned groups.

Hot water damage test and freeze–thaw damage test were conducted according to the Chinese standard methods [29]. For hot water damage test, the control group and three conditioned groups were first immersed in water bath of 60 °C for 0.5, 24, 48 and 72 h, respectively. The Marshall stabilities of all samples were then determined by the Marshall stability tester. The parameter of retained Marshall stability (RMS), reflecting hot water damage resistance of asphalt mixture, was computed according to Equation (1).

$$\text{RMS} = \frac{\text{MS}_n}{\text{MS}_0} \times 100\% \quad (1)$$

where  $\text{MS}_0$  is the average Marshall stability of control group, and  $\text{MS}_n$  is the average stability of conditioned group ( $n = 24, 48$  and  $72$  h).

For freeze–thaw damage test, three conditioned groups were subjected to freeze–thaw damage for 1, 2 and 3 cycles, respectively. A single freeze–thaw damage process was composed of freezing at  $-18$  °C for 16 h and thawing at 60 °C for 24 h. All samples of control and conditioned groups were moved to water bath of 25 °C for 2 h to keep the temperature same before being tested. The splitting failure of all samples was conducted by the splitting test instrument with real-time data collection module. The parameter of tensile strength ratio (TSR), reflecting freeze–thaw damage resistance of asphalt mixture, was computed according to Equation (2).

$$\text{TSR} = \frac{\text{SS}_i}{\text{SS}_0} \times 100\% \quad (2)$$

where  $\text{SS}_0$  is the average splitting strength of control group, and  $\text{SS}_i$  is the average splitting strength of conditioned group ( $i = 1, 2$  and  $3$  cycles).

Except for the traditional parameters (RMS and TSR), the change rule of energy parameter was also commonly adopted in moisture stability evaluation [8]. Fracture energy ( $E_f$ ) can be determined based on the stress–strain curve drawn according to the splitting test raw data as shown in Figure 3, and computed according to Equation (3). The energy parameter of retained energy ratio (RER) under different freeze–thaw damage cycles for each asphalt mixture was determined by Equation (4). The winner of four asphalt mixtures in freeze–thaw damage resistance can be decided by comparing their RER values. The energy method involved the strain and stress of sample simultaneously. It has been reported to be more scientific than traditional RMS and TSR methods, which only consider the change of single stability and strength (stress).

$$E_f = \int_0^{\varepsilon_f} S(\varepsilon) d\varepsilon \quad (3)$$

where  $\varepsilon_f$  is the failure strain of sample, at which the splitting strength is also largest ( $S_f$ ), and  $S(\varepsilon)$  is the real-time splitting strength of sample when strain is  $\varepsilon$ .

$$\text{RER} = \frac{E_{fi}}{E_{f0}} \times 100\% \quad (4)$$

where  $E_{fi}$  is the average fracture energy of samples in conditioned group with freeze–thaw damage for  $i$  cycles, and  $E_{f0}$  is the average fracture energy of samples in control group.



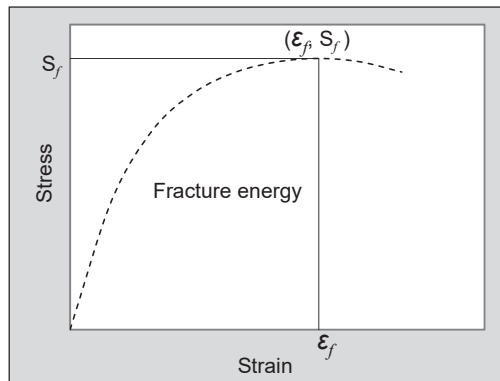


Figure 3. Determination mechanism of fracture energy.

#### Low-Temperature Crack Resistance

The three-point bending test, conducted according to the Chinese standard method [29], was adopted to evaluate the low-temperature performance of asphalt mixtures. The used beam samples with a dimension of 250 mm length, 30 mm width and 35 mm height were processed by cutting roller compacted large-size concrete slabs. Three beam samples for each mixture were prepared. The test was conducted by a universal test machine (UTM) at  $-10\text{ }^{\circ}\text{C}$ , forcing the beam sample into bending and fracture with a deformation rate of 50 mm/min. Samples were placed in a temperature-controlled chamber for 4–5 h in advance to maintain the surface and internal of sample at the same test temperature. The real-time strain and stress (flexural strength) of the tested sample were obtained based on previously obtained test data. Fracture energy was also determined according to Equation (3). The low-temperature crack resistance ability of asphalt mixture was assessed by the failure strain and fracture energy.

#### High-Temperature Deformation Resistance

The wheel tracking test, also conducted according to the Chinese standard method [29], was adopted to reveal the high-temperature stability of asphalt mixture. The used slab samples, prepared by a roller compaction, were 300 mm length, 300 mm width and 50 mm height. Three replicates for each mixture were considered. Samples were placed in a wheel tracking device to raise the temperature to  $60\text{ }^{\circ}\text{C}$  beforehand. The test was conducted under repeated wheel loading. For the standard wheel tracking test, the wheel pressure was 0.7 MPa. In order to reveal the high-temperature behavior of asphalt mixture under overloading, 1.0 MPa was also selected. The test process was simple; the wheel rolled back and forth on the surface of samples along the axis of symmetry with a wheel speed of 42 pass/min for 1 h, and the real-time rutting depth was recorded. The dynamic stability (DS), reflecting the high-temperature stability of asphalt mixture, was computed according to Equation (5).

$$DS = \frac{15 \times 42}{d_{60} - d_{45}} \quad (5)$$

where  $d_{45}$  and  $d_{60}$  are rutting depths of slab samples when testing time reaches 45 min and 60 min respectively, mm.

#### Fatigue Crack Resistance

The fatigue crack resistance of asphalt mixture was evaluated by means of indirect tensile (IDT) fatigue test according to AASHTO-TP31 standard [31]. The samples were the same as those used in hot water damage test. IDT fatigue test was also conducted by UTM. The test temperature was

15 °C, and samples were moved to a temperature control chamber of UTM to keep the surface and internal parts at the same test temperature. Stress-controlled mode with three stress levels of 400, 500 and 600 kPa was adopted, and loading signal was haversine waveform as shown in Figure 4. Three replicates for every asphalt mixture at each stress level were considered. The loading number, at which the main radial crack propagated completely through the specimen, was defined as fatigue life ( $N_f$ ).

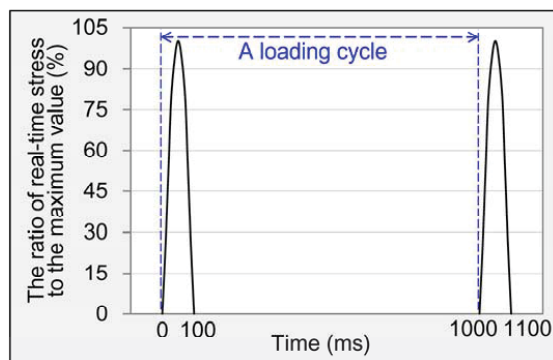


Figure 4. Loading signal used in this research.

### 3. Results and Discussions

#### 3.1. Technical Properties and Material Characteristics of Raw Materials

##### 3.1.1. Technical Properties

The basic technical properties of raw materials should first meet the requirement of relevant technical specification in terms of their use in asphalt mixture. The test results of basic technical property indexes of aggregate, filler and asphalt binder were listed in Tables 2–4, respectively. It can be seen from the results that all basic technical property indexes of raw materials meet the requirements of Chinese specification [32,33]. In detail, DGR was lighter than LP, and the density of the former was 6% lower than that of the latter. The gradation of DGR was slightly finer according to the particles size distribution shown in Table 3. The introduction of waste tire rubber powder has significantly lowered the penetration, ductility and raised the softening point of base asphalt binder. Table 4 also suggested that rubber powder gave asphalt binder excellent elasticity.

Table 2. Basic technical properties of granite aggregates.

Measured Index	Coarse Aggregate			Fine Aggregate	Requirements in China
	19–9.5	9.5–4.75	4.75–2.36	2.36–0	
Apparent specific gravity	2.719	2.722	2.717	2.701	≥2.5
Water absorption (%)	0.4	0.6	0.6	1.1	≤2
Flakiness and elongation (%)	7.9	10.8	NA	NA	≤18
Los Angeles abrasion (%)	23.8	23.8	21.4	NA	≤30
Crush value (%)	19.9	NA	NA	NA	≤28
Fine aggregate angularity (%)	NA	NA	NA	51	≥30
Sand equivalent (%)	NA	NA	NA	66	≥60

Note. “NA” stands for the index is not applicable at that situation, and the same in latter tables.

**Table 3.** Basic technical properties of fillers.

Measured Index	LP	DGR	Requirements in China
Specific gravity ( $\text{g}/\text{cm}^3$ )	2.728	2.557	$\geq 2.5$
Percent passing (%)	0.6 mm	100	100
	0.15 mm	95.2	90–100
	0.075 mm	87.1	75–100

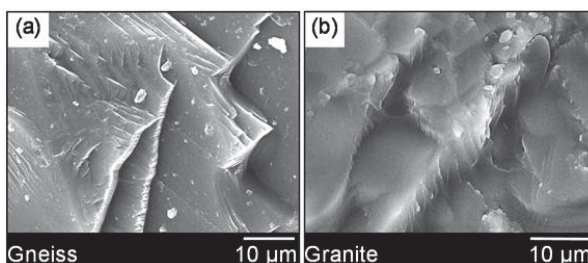
**Table 4.** Basic technical properties of base asphalt and RMA.

Measured Index	Base Asphalt	RMA	Requirements in China	
			Base Asphalt	RMA
Penetration (25 °C; 0.1 mm)	68	46	60–80	30–60
Ductility (base asphalt, 15 °C; RMA, 5 °C; cm)	155	8.9	$\geq 100$	$\geq 5$
Softening point (°C)	47.2	70.1	$\geq 46$	$\geq 60$
Elasticity resume (25 °C; %)	NA	79	NA	$\geq 60$

### 3.1.2. Material Characteristics

#### Granite Aggregate

Micro-morphology and chemical composition of aggregates are very important features in terms of the use in asphalt mixture. The former affects the physical bonding behavior between aggregate and asphalt mastic, and the latter influences the chemical bonding behavior. Unlike the common acid gneiss aggregate with flat and layered surface texture (see picture a in Figure 5), the surface of granite was very coarse and spur-and-gully, as shown in Figure 5b. The rich surface feature was beneficial for the physical bonding behavior. Therefore, the poor chemical bonding behavior of aggregate and asphalt mastic should be responsible for the less-than-ideal performance of granite based asphalt mixture.

**Figure 5.** Micro-morphology images of aggregate particles: (a) Gneiss [15]; (b) Granite.

The main chemical compositions of granite are shown in Figure 6. It can be seen that the  $\text{SiO}_2$  almost accounts for 70% by weight of granite. The acid–alkaline feature of rocks can be easily decided according to the content of  $\text{SiO}_2$  suggested by previous researchers, and the rock can be defined as acid aggregate when the content of  $\text{SiO}_2$  is beyond 65% [34]. Granite was actually a kind of typical acid aggregate according to this rule. High content of  $\text{SiO}_2$  resulted in poor chemical bonding of aggregate and asphalt mastic. Therefore, improving the bonding behavior of the granite mixture system by modifying other raw materials (filler and asphalt) was very important. Figure 6 also showed that granite contains more  $\text{Al}_2\text{O}_3$  and some percent of  $\text{Na}_2\text{O}$ ,  $\text{K}_2\text{O}$ ,  $\text{CaO}$ ,  $\text{MgO}$  and  $\text{Fe}_2\text{O}_3$ . This was related to the mineral phases of granite.

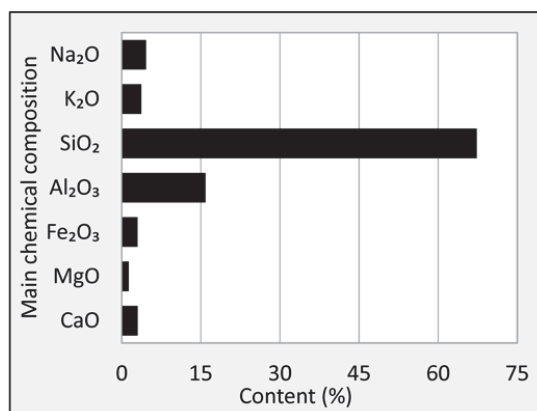


Figure 6. Main chemical compositions of granite.

The mineral phases of granite are shown in Figure 7. It suggested that quartz, plagioclase and potassium feldspar were the main mineral phases of granite, and small amount of biotite can be also observed. All these phases contain SiO<sub>2</sub>, as a result, the content of SiO<sub>2</sub> in granite was very high. Quartz made the greatest contribution to the content of SiO<sub>2</sub>. All other phases also contain Al<sub>2</sub>O<sub>3</sub> besides quartz, naturally, a large amount of Al<sub>2</sub>O<sub>3</sub> was detected in granite as shown in Figure 6. The rest of Na<sub>2</sub>O, K<sub>2</sub>O, CaO, MgO and Fe<sub>2</sub>O<sub>3</sub> mainly participated in the generation of plagioclase (Na(AlSi<sub>3</sub>O<sub>8</sub>), Ca(Al<sub>2</sub>Si<sub>2</sub>O<sub>8</sub>)), potassium feldspar (K<sub>2</sub>O·Al<sub>2</sub>O<sub>3</sub>·6SiO<sub>2</sub>) and biotite (K(Mg, Fe<sup>2+</sup>)<sub>3</sub>(Al,Fe<sup>3+</sup>)Si<sub>3</sub>O<sub>10</sub>(OH,F)<sub>2</sub>).

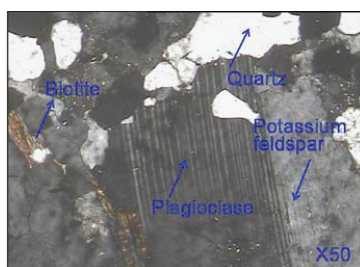


Figure 7. Mineral phases of granite.

## Fillers

It is well known that the main phase of LP is calcium carbonate (CaCO<sub>3</sub>). The mineral phases of DGR are analyzed in this section. Figure 8 suggested that calcium carbonate, dihydrate gypsum (CaSO<sub>4</sub>·2H<sub>2</sub>O) and calcium hydroxide (Ca(OH)<sub>2</sub>) were the main phases of DGR. The phase types were directly related to the generation process of DGR. The absorbent for SO<sub>2</sub> was a slurry of CaCO<sub>3</sub>/CaO, and CaO transformed into Ca(OH)<sub>2</sub> under wet condition, which was the active ingredient for SO<sub>2</sub> absorption. Ca(OH)<sub>2</sub> turned into CaSO<sub>3</sub>·0.5H<sub>2</sub>O by absorbing SO<sub>2</sub> in wet condition, which can be further oxidized into CaSO<sub>4</sub>·2H<sub>2</sub>O. It was the source of CaSO<sub>4</sub>·2H<sub>2</sub>O. This process was accompanied by the decomposition of CaCO<sub>3</sub>, which can provide sufficient CaO. It can be seen from Figure 8 that almost all strong diffraction peaks were possessed by Ca(OH)<sub>2</sub>. It meant that the dosage of CaCO<sub>3</sub>/CaO was excessive. A great amount of the remaining Ca(OH)<sub>2</sub> gave DGR with high alkalinity, which was good for the bonding behavior of the asphalt mixture system.

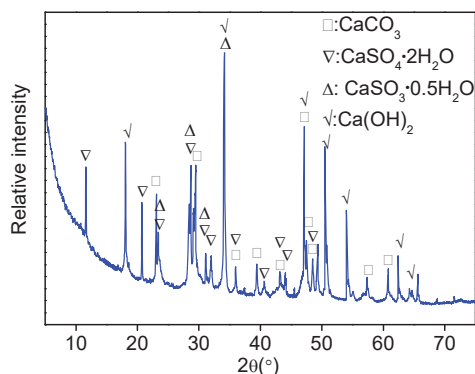


Figure 8. Mineral phases of DGR.

The average chemical compositions of LP and DGR corresponded to the mineral phase results. The decomposition of  $\text{CaCO}_3$  in LP resulted in large amounts of CaO and loss on ignition (LoI). The mass ratio of CaO to LoI was 1.28, which was very close to the molecular weight ratio of CaO to  $\text{CO}_2$ . It proved that the release of  $\text{CO}_2$  should be responsible for the large LoI in LP. For DGR, the contents of CaO,  $\text{SO}_3$  and LoI were much larger than that of other chemical compositions. The CaO was related to  $\text{CaCO}_3$ ,  $\text{Ca(OH)}_2$ ,  $\text{CaSO}_3 \cdot 0.5\text{H}_2\text{O}$  and  $\text{CaSO}_4 \cdot 2\text{H}_2\text{O}$  phase. Supposing the large LoI was completely caused by the decomposition of  $\text{CaCO}_3$  (in fact, the dehydration process of mineral phases also made contribution to it), the amount of CaO generated during the release of  $\text{CO}_2$  was 18.98%. The content of CaO corresponding to  $\text{CaSO}_3 \cdot 0.5\text{H}_2\text{O}$  and  $\text{CaSO}_4 \cdot 2\text{H}_2\text{O}$  was 14.15%, computed according to the total content of  $\text{SO}_3$  shown in Table 5. The total content of CaO for DGR was 59.88%, therefore, there were about 26.75% of CaO was from  $\text{Ca(OH)}_2$ . It also indicated that the amount of retaining  $\text{Ca(OH)}_2$  was large, which contributed to the alkaline of DGR.

Table 5. Average chemical compositions of DGR and LP.

Filler	Content (%)								
	$\text{SiO}_2$	$\text{Al}_2\text{O}_3$	CaO	$\text{Fe}_2\text{O}_3$	MgO	$\text{K}_2\text{O}$	$\text{SO}_3$	LoI	Others
DGR	0.41	0.22	59.88	0.61	1.12	0.67	20.21	14.91	1.97
LP	3.01	1.01	53.02	0.54	0.28	0.22	0.06	41.35	0.51

The micro-morphology images of DGR and LP are shown in Figure 9. The figures suggested that the surface texture of commonly used LP filler particles was coarser than that of DGR particles. Furthermore, the outline of DGR particles was much sleeker and more ellipsoid than that of common used LP filler. Ellipsoid particles could make the asphalt mastic easy to flow at high temperature because of poor friction action between particles. This disadvantage may harm the pavement performance of asphalt mixture, especially the high-temperature stability. The specific situation will be revealed in the section of pavement performance evaluation.

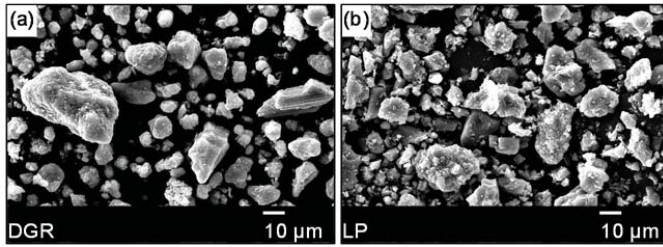


Figure 9. Micro-morphology images of fillers: (a) DGR, (b) LP.

Asphalt mixture was prepared at a high temperature of 165 °C for base asphalt and 185 °C for modified asphalt. Therefore, evaluating the thermal stability of DGR as a type of new filler was very important. Figure 10 shows the thermal analysis result of DGR. It shows that there are two stages. In the first stage, a strong endothermic peak appeared at 88.5 °C due to the volatilization of free water contained in DGR. It accordingly resulted in 0.8% of mass loss in this stage. In the second stage, another endothermic peak appeared at 150 °C; it belonged to the crystal water release of  $\text{CaSO}_4 \cdot 2\text{H}_2\text{O}$ , and dihydrate gypsum transformed into half-water gypsum during this stage. About 1.5% of mass loss was seen. The total mass reduction was quite small, hence, the thermal stability of DGR was good in terms of mass change, while the phase types changed at the mixing temperature of asphalt mixture.

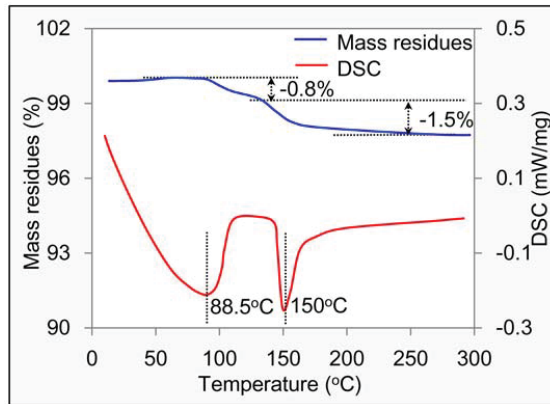
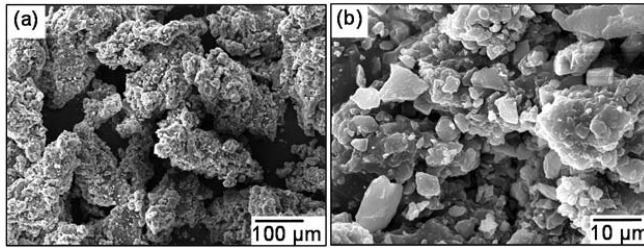


Figure 10. TG-DSC analysis result of DGR.

### Asphalt Binders

The micro-morphology images of used rubber particles are displayed in Figure 11. Picture a showed that the edges and corners of the rubber particles were quite clear, and their appearance was blistered. The large amount of free fine particles and rich channel structures contributed to the blistered surface. The coarse and blistered surface could result in the adsorption and absorption of asphalt, which was a benefit for the compatibility and integrity of base asphalt and crumb rubber particles. Using crumb rubber to modify asphalt was advantageous in terms of its micro-morphology feature.



**Figure 11.** Micro-morphology images of crumb rubber particles: (a) under low magnification times; (b) under high magnification times.

Figure 12 gave the functional group analysis results of base asphalt and RMA. It can be seen that the infrared spectrum curves of these two asphalts were similar. The main characteristic peaks were displayed at wavenumbers of 2924, 2853, 1600, 1461, 1377, 1031 and 722  $\text{cm}^{-1}$ . The peaks at 2924 and 2853  $\text{cm}^{-1}$  attributed to the stretching vibration of  $-\text{CH}_2-$  bond and C–H bond. And the peaks at 1600, 1461 and 1377  $\text{cm}^{-1}$  attributed to the stretching vibration of C=C bond, in-plane bending vibration of  $-\text{CH}_2-$  and bending vibration of C–H. The infrared spectrum curves and peak strengths of base asphalt and RMA at wavenumbers of 500–1400  $\text{cm}^{-1}$  was a little different. The characteristic peak strengths of RMA such as at 1377, 1031 and 722  $\text{cm}^{-1}$  were smaller than that of base asphalt. It suggested that the introduction of crumb rubber may change the structural network of asphalt binder slightly. While the effect was limited. Conclusions can be made that mainly have physical changes during the mixing of crumb rubber and base asphalt.

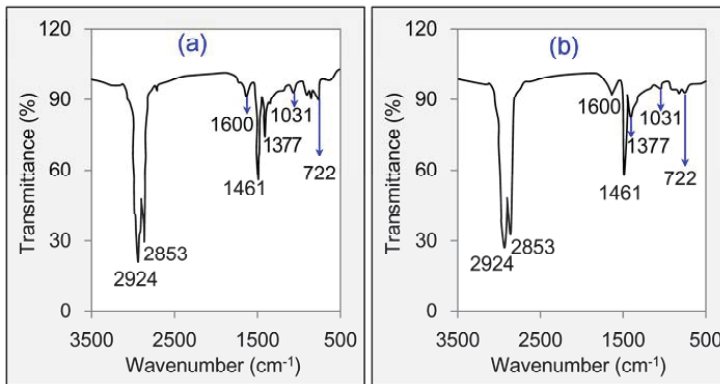


**Figure 12.** FT-IR analysis results: (a) Base asphalt, (b) RMA.

### 3.2. Asphalt Mixture and Its Pavement Performances

#### 3.2.1. Design Results of Asphalt Mixtures

The volumetric properties of four asphalt mixtures used in this research are shown in Table 6. It can be seen from the results that all volumetric indexes met the design requirements. The optimum asphalt content (OAC) of asphalt mixture containing RMA was higher than that of asphalt mixture with base asphalt. The increment of asphalt content caused by RMA was 0.4%. This was mainly due to the reduction of base asphalt content in RMA. More RMA was needed in order to fully wet the mineral mixture. The OAC values of asphalt mixtures containing different fillers were the same when the same type of asphalt binder was used. It indicated that the effect of filler types on the asphalt content was

weak. Table 6 also shows that the air void and void in mineral aggregate (VMA) of asphalt mixture containing DGR were slightly lower than that of asphalt mixture with LP. It suggested that DGR made the asphalt mixture a little densely compacted. The VMAs of asphalt mixtures prepared with RMA were obviously higher than that of asphalt mixture with base asphalt. It meant the RMA lowered the compatibility of asphalt mixture.

Table 6. Volumetric properties of designed asphalt mixtures.

Volumetric Property	Mixture Type				Design Requirement
	M <sub>GLB</sub>	M <sub>GDB</sub>	M <sub>GLR</sub>	M <sub>GDR</sub>	
Optimum asphalt content (%)	5.0	5.0	5.4	5.4	NA
Air voids (%)	4.5	4.3	4.7	4.5	4–6
Voids in mineral aggregate (%)	14.1	13.8	15.4	15.1	≥13
Voids filled with asphalt (%)	69.5	68.8	69.5	70.2	65–75

### 3.2.2. Moisture-Induced Damage Resistance

The original Marshall stabilities of M<sub>GLB</sub>, M<sub>GDB</sub>, M<sub>GLR</sub> and M<sub>GDR</sub> were 8.4, 8.9, 11.5 and 10.9 kN, respectively. This suggested that the contribution of RMA on increasing Marshall stability was big, and the increments for LP and DGR asphalt mixtures were 3.1 and 2.0 kN, respectively, while the effect of DGR on Marshall stability was weak and inconsistent for asphalt mixtures with different asphalt. The RMS values for each mixture after suffering different times of hot water damage are listed in Figure 13. The downward trend for all asphalt mixtures is displayed with the rise of damage time. Hence, the damage caused by hot water was serious. DGR showed a very positive role in maintaining the stability of asphalt mixture according to the results. For base asphalt, the RMS of asphalt mixture prepared with DGR was still up to 79% even after hot water damage for 72 h, and the value for LP asphalt mixture was only 62% under the same condition. For RMA, RMS of DGR asphalt mixture was as high as 81% after damage for 72 h, which was 16% numerically larger than that of LP asphalt mixture. Figure 13 also revealed that the type of asphalt weakly effected hot-water stability. The RMS of asphalt mixture containing LP and DGR simultaneously was largest among these four asphalt mixtures after a longtime hot water damage. Hence, it is preferable to prepare asphalt mixture with LP and DGR considering the hot water damage resistance.

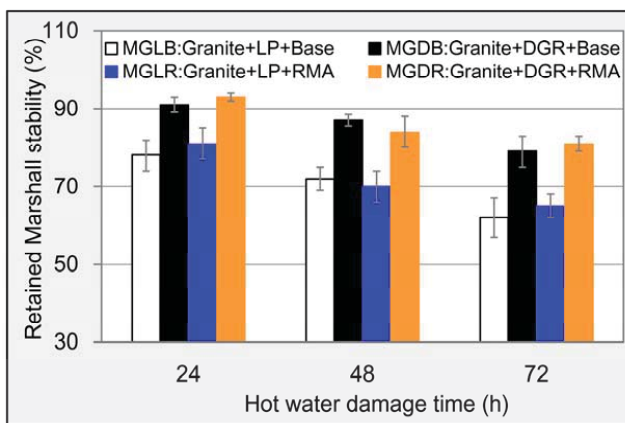


Figure 13. RMS results of different asphalt mixtures.



The original splitting strengths of  $M_{GLB}$ ,  $M_{GDB}$ ,  $M_{GLR}$  and  $M_{GDR}$  were 0.94, 0.97, 1.05 and 1.10 MPa, respectively. Hence, DGR and RMA both can enhance the strength of asphalt mixture. Compared to LP, DGR improved the strength of base asphalt mixture and RMA mixture by 3.2% and 4.8%, respectively. For RMA, the improved percentages were 11.7% and 13.4% for LP asphalt mixture and DGR asphalt mixture, respectively, compared to base asphalt. So the contribution made by RMA was much more obvious. Similar to the change rule of RMS, TSR for each mixture decreased gradually with the rise of freeze-thaw damage cycles (see Figure 14). DGR also performed better than RMA in maintaining the strength of asphalt mixture. Furthermore, compared to LP, DGR raised TSR value of base asphalt mixture and RMA mixture by 5.4% and 9.3%, respectively, even after three cycle's freeze-thaw damage. For RMA, the situation was a little complex. RMA did better than base asphalt in maintain the strength of LP asphalt mixture at early stage of freeze-thaw damage. The rule gradually turned to the opposite with the strengthening of the damage degree. It meant that the durability of bonding feature between aggregate and RMA was insufficient. The strength loss of asphalt mixture containing RMA and DGR was smallest among these asphalt mixtures even serious freeze-thaw damage for three cycles was applied. It meant that the combination of RMA and DGR was also a good method to improve the freeze-thaw damage resistance ability.

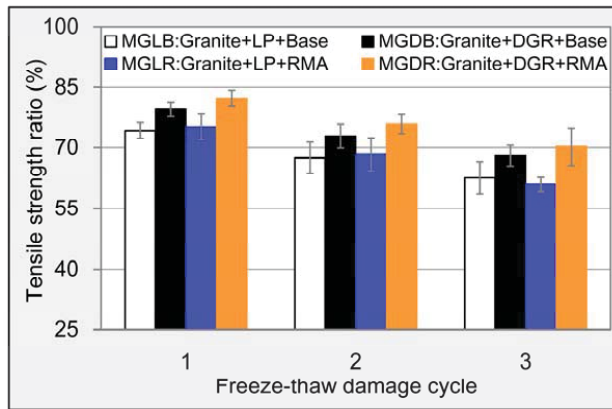


Figure 14. TSR results of different asphalt mixtures.

Figure 15 gave the computed results of RER. It can be seen that the change rule of RER was a little different from that of TSR. RMA also displayed an obvious effect on RER. Compared to base asphalt, the increment of RER caused by RMA were 5.5% and 10.1% for LP asphalt mixture and DGR asphalt mixture, respectively, even after three cycle's freeze-thaw damage. For DGR, its contribution were 5.3% and 9.9% for base asphalt mixture and RMA mixture, respectively. And the RER of asphalt mixture containing DGR and RMA was still up to 75.9% after serious freeze-thaw damage. The loss ratio of RER was less than that of spitting strength; this was because of the crumb rubber contained in RMA which enhanced the flexibility and the ability of bearing big deformation. Large deformation will result in big fracture energy according to Equation (3). Concluding this section, the combined use of DGR and RMA played a much more positive role in improving the water damage resistance of asphalt mixture than when they were used alone.

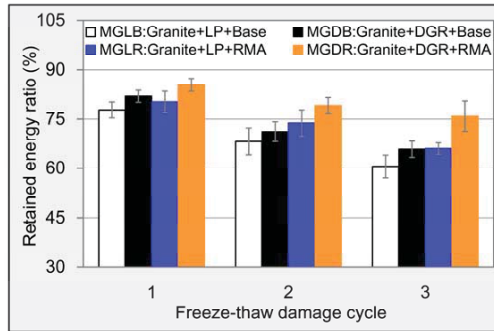


Figure 15. RER results of different asphalt mixtures.

### 3.2.3. Low-Temperature Crack Resistance

The computed strain and fracture energy of these four asphalt mixtures are shown in Figure 16. In terms of strain, LP and DGR almost performed the same either in base asphalt mixture or RMA mixture. While the effect of RMA on the low-temperature strain was significant. Compared to base asphalt, RMA increased the strain of LP asphalt mixture and RMA mixture by 41.3% and 50.0%, respectively. It indicated that the introduction of crumb rubber enhanced the deformability of asphalt mixture at low temperature. In terms of fracture energy, the energy values were gradually rising by changing filler types and asphalt types in turn. It suggested that the DGR and RMA both can improve the fracture energy of asphalt mixture. Asphalt mixture prepared with DGR and RMA possessed the largest fracture energy, about 10 kJ/m<sup>3</sup>. Therefore, similar to moisture stability, the combination of DGR and RMA did better in improving the low-temperature performance of asphalt mixture.

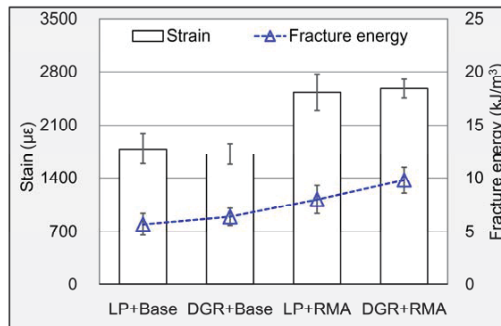


Figure 16. Strain and fracture energy of different asphalt mixtures.

### 3.2.4. High-Temperature Deformation Resistance

The high-temperature stability is very important to the durability of asphalt pavement especially at some regions of higher temperature. The computed dynamic stabilities of the four asphalt mixtures are displayed in Figure 17. It clearly shows that the DGR worsened the high-temperature deformation resistance of asphalt mixture. Specifically, at wheel pressure of 0.7 MPa, the reduction percent of dynamic stabilities for base asphalt mixture and RMA mixture caused by DGR were 20.5% and 5.7%, respectively, and which were 13.4% and 4.3% at wheel pressure of 1.0 MPa. This may be due to the sleek and ellipsoid appearance of DGR particles, which made asphalt mastic easy to flow. The improvement made by the rubber was compelling. At wheel pressure of 0.7 MPa, 31.8% and 56.2% higher dynamic stability were shown for LP asphalt mixture and DGR asphalt mixture, respectively, compared to base

asphalt. The values were 49.4% and 65.0%, respectively, at wheel pressure of 1.0 MPa. This was mainly due to the contribution of rubber's excellent elasticity. The results suggested that RMA obviously made up the weakness of DGR in terms of high-temperature performance of asphalt mixture. Figure 17 also indicated that the change of dynamic stability for RMA mixture was quite small when applied wheel pressure increasing from 0.7 MPa to 1.0 MPa. Hence, the RMA was suitable for the road located in the high-temperature region.

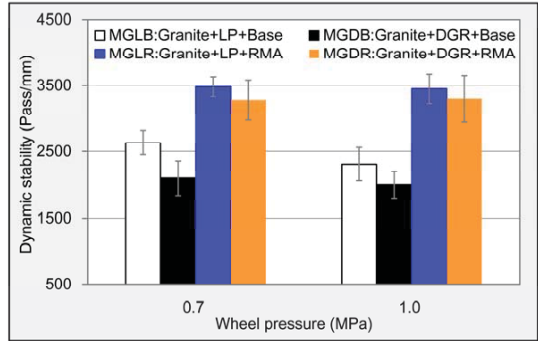


Figure 17. Dynamic stability results of different asphalt mixtures.

### 3.2.5. Fatigue Crack Resistance

Figure 18 gave the fatigue life results of every asphalt mixture at each stress level. It displayed that the fatigue lives of all asphalt mixtures rapidly decreased with the rising of stress levels. A more significant fluctuation can be observed at the low stress level. DGR and RMA both showed good potential to raise fatigue life of asphalt mixture. Furthermore, DGR raised the fatigue lives of base asphalt mixtures tested at 400, 500 and 600 kPa by 7.6%, 32.4% and 25.0%, respectively. The values were 1.7%, 6.0% and 7.1% for RMA mixture. In terms of RMA, it increased the fatigue lives of LP asphalt mixtures tested at 400, 500 and 600 kPa by 26.1%, 98.6% and 73.5%, respectively, and the percentage increases in fatigue lives were 19.2%, 58.9%, and 48.6%, respectively, for DGR asphalt mixtures. It indicated that the improvement of fatigue life made by RMA was much more obvious. Figure 18 also showed that asphalt mixture containing DGR and RMA simultaneously always possessed the highest fatigue lives among the four asphalt mixtures at all stress levels. So the combination of DGR and RMA also did better in improving fatigue life of asphalt mixture than when they were used alone.

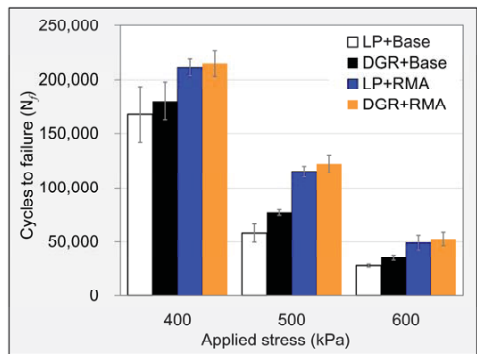


Figure 18. Fatigue life test results of different asphalt mixtures.

The relationship between fatigue life, applied stress and initial strain is commonly expressed as Equations (6) and (7), respectively. The parameters ( $L, m, K, n$ ) contained in the fatigue equations were determined by regression analysis of obtained test raw data. Three replicates for every asphalt mixture at each stress level were applied in this research. The data points would be highly overlapped in a coordinate system with the stress level as abscissa if the fatigue performance was analyzed by means of Equation (6). Considering this, Equation (7) was used in this research. The fatigue life and initial strain should meet a linear relationship at a double logarithmic coordinate system according to Equation (7).

$$N_f = L \left( \frac{1}{\sigma_0} \right)^m \tag{6}$$

$$N_f = K(\epsilon_0)^n \tag{7}$$

where  $N_f$  is the fatigue life (loading cycles to failure),  $\sigma_0$  is applied stress level,  $\epsilon_0$  is the initial strain of sample (the strain caused by applied stress level), and  $L, K, m, n$  are material constants of the tested asphalt mixture.

The relationship between fatigue life and initial strain caused by applied stress was displayed in a double logarithmic coordinate system as shown in Figure 19. The fatigue life and initial strain should meet linear relationship at double logarithmic coordinate system according to Equation (7). The parameter  $n$  in Equation (7) corresponded to the slope of the fitting line shown in Figure 19. So the absolute value of parameter  $n$  can reflect the falling speed of fatigue life for certain asphalt mixture with the increase of stress level. It can be seen from the figure that the absolute values of parameter  $n$  for  $M_{GLB}, M_{GDB}, M_{GLR}$  and  $M_{GDR}$  were gradually reduced. It meant that the fatigue durability of asphalt mixture prepared with DGR and RMA was the best among these asphalt mixtures, and the fatigue equations determined by regression analysis (see Table 7) also supported this conclusion, although the absolute value of parameter  $n$  (1.34) was just a little smaller than that of asphalt mixture containing LP and RMA (1.36).

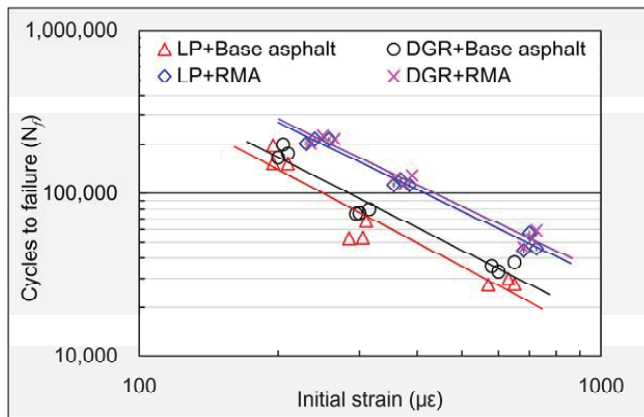


Figure 19. Regression analysis of obtained data points of fatigue life.

Table 7. Fatigue equations of different asphalt mixtures.

Mixture	Parameters		Fatigue Equation	Correlation Coefficient
	K	n		R <sup>2</sup>
M <sub>GLB</sub>	$3.7 \times 10^8$	-1.49	$N_f = 3.7 \times 10^8 (\epsilon_0)^{-1.49}$	0.95
M <sub>GDB</sub>	$3.3 \times 10^8$	-1.44	$N_f = 3.7 \times 10^8 (\epsilon_0)^{-1.44}$	0.90
M <sub>GLR</sub>	$3.7 \times 10^8$	-1.36	$N_f = 3.7 \times 10^8 (\epsilon_0)^{-1.36}$	0.97
M <sub>GDR</sub>	$3.4 \times 10^8$	-1.34	$N_f = 3.7 \times 10^8 (\epsilon_0)^{-1.34}$	0.98

#### 4. Conclusions

In terms of raw material characteristics and main pavement performances of asphalt mixture, the feasibility of preparing asphalt mixture by means of low-grade granite aggregate, rubber modified asphalt (RMA) and desulphurization gypsum residues (DGR) simultaneously was investigated in this research. The basic technical properties and main material characteristics of raw materials were first detected in order to fully recognize them. Then the pavement performances of asphalt mixture prepared with granite aggregate, DGR and RMA were fully evaluated to reveal the feasibility. Based on the research results, the following conclusions can be drawn.

- (1) Unlike the common acid gneiss aggregate with flat and layered surface texture, the surface of granite was very coarse and spur-and-gully. The quartz, plagioclase and potassium feldspar were the main mineral phases of granite, and they were responsible for the high content of SiO<sub>2</sub> in granite;
- (2) The large amount of Ca(OH)<sub>2</sub> from the excess absorbent of SO<sub>2</sub> increased the percent of alkaline ingredients in DGR, which made DGR an potential modifier to enhance the bonding property of asphalt mixture system. The ellipsoid outline of DGR particles would increase the liquidity of mastic theoretically, which was not good for the high-temperature stability of asphalt mixture;
- (3) DGR made asphalt mixture easier to be compacted. RMA was just the opposite, it lowered the compatibility of asphalt mixture. The used content of RMA was larger than that of base asphalt binder, and this was due to the reduction of base asphalt percentage in RMA. Much more RMA was needed in order to fully wet the surface of mineral particles;
- (4) DGR showed a very positive role in strengthening the moisture-induced damage resistance, and the combination of DGR and RMA even did better although the effect of RMA on the moisture stability of granite asphalt mixture was slight and erratic;
- (5) DGR significantly worsened the high-temperature deformation resistance of granite asphalt mixture, and the improvement of the high-temperature stability made by RMA was compelling. The combination of RMA and DGR can make up the weakness of DGR in terms of the high-temperature performance of granite asphalt mixture;
- (6) DGR and RMA both showed an excellent ability to increase low-temperature crack resistance, fatigue life and the fatigue durability of granite asphalt mixture. The combined use of DGR and RMA in the granite asphalt mixture also performed much better than when they were used alone.

**Author Contributions:** X.Z. and D.K. conceived and designed the experiments, X.Z. and B.Z. performed the experiments, B.Z. analyzed the data, X.Z. and H.C. wrote the paper.

**Funding:** This research was funded by the project of Science and Technology of Qinghai Province (Nos. 2018-ZJ-760, 2018-SF-111 and 2018-SF-139), the project of Transportation Department of Inner Mongolia Autonomous Region (Nos. NJ-2016-7 and NJ-2017-15), and the Fund for Basic Scientific Research of Central Colleges of Chang'an University (Nos. 310831171015, 300102318401 and 300102318501).

**Conflicts of Interest:** The authors declare no conflicts of interest.

## References

- Huang, Y.; Bird, R.N.; Heidrich, O. A review of the use of recycled solid waste materials in asphalt pavements. *Resour. Conserv. Recycl.* **2007**, *52*, 58–73. [[CrossRef](#)]
- Chen, Z.; Wu, S.; Xiao, Y.; Zeng, W.; Yi, M.; Wan, J. Effect of hydration and silicone resin on Basic Oxygen Furnace slag and its asphalt mixture. *J. Clean. Prod.* **2016**, *112*, 392–400. [[CrossRef](#)]
- Liu, P.; Hu, J.; Wang, D.; Oeser, M.; Alber, S.; Ressel, W.; Falla, G.C. Modelling and evaluation of aggregate morphology on asphalt compression behavior. *Constr. Build. Mater.* **2017**, *133*, 196–208. [[CrossRef](#)]
- Uzun, İ.; Terzi, S. Evaluation of andesite waste as mineral filler in asphaltic concrete mixture. *Constr. Build. Mater.* **2012**, *31*, 284–288. [[CrossRef](#)]
- Li, P.; Ding, Z.; Rao, W. Evaluation of deformation properties of asphalt mixture using aggregate slip test. *Int. J. Pavement Eng.* **2016**, *17*, 542–549. [[CrossRef](#)]
- Ahmedzade, P.; Sengoz, B. Evaluation of steel slag coarse aggregate in hot mix asphalt concrete. *J. Hazard. Mater.* **2009**, *165*, 300–305. [[CrossRef](#)] [[PubMed](#)]
- Pasetto, M.; Baldo, N. Influence of the aggregate skeleton design method on the permanent deformation resistance of stone mastic asphalt. *Mater. Res. Innov.* **2014**. [[CrossRef](#)]
- Chen, Z.; Wu, S.; Wen, J.; Zhao, M.; Yi, M.; Wan, J. Utilization of gneiss coarse aggregate and steel slag fine aggregate in asphalt mixture. *Constr. Build. Mater.* **2015**, *93*, 911–918. [[CrossRef](#)]
- Wu, S.P.; Hu, D.M.; Pang, L.; Wang, H. Utilization of Gneiss in Asphalt Concrete Mixtures. *Mater. Sci. Forum* **2009**, *620–622*, 1–4. [[CrossRef](#)]
- Andrzejuk, W.; Barnathunek, D.; Siddique, R.; Zegardło, B.; Łagód, G. Application of Recycled Ceramic Aggregates for the Production of Mineral-Asphalt Mixtures. *Materials* **2018**, *11*, 658. [[CrossRef](#)] [[PubMed](#)]
- Wu, S.; Zhong, J.; Zhu, J.; Wang, D. Influence of demolition waste used as recycled aggregate on performance of asphalt mixture. *Road Mater. Pavement* **2013**, *14*, 679–688. [[CrossRef](#)]
- Gómez-Mejide, B.; Pérez, I. Effects of the use of construction and demolition waste aggregates in cold asphalt mixtures. *Constr. Build. Mater.* **2014**, *51*, 267–277. [[CrossRef](#)]
- Wu, S.; Xue, Y.; Ye, Q.; Chen, Y. Utilization of steel slag as aggregates for stone mastic asphalt (SMA) mixtures. *Build. Environ.* **2007**, *42*, 2580–2585. [[CrossRef](#)]
- Pasetto, M.; Baldo, N. Performance comparative analysis of stone mastic asphalts with electric arc furnace steel slag: A laboratory evaluation. *Mater. Struct.* **2012**, *45*, 411–424. [[CrossRef](#)]
- Chen, Z.; Jiao, Y.; Wu, S.; Tu, F. Moisture-induced damage resistance of asphalt mixture entirely composed of gneiss and steel slag. *Constr. Build. Mater.* **2018**, *177*, 332–341. [[CrossRef](#)]
- Chen, Z.W.; Wang, P.; Zhou, X.X.; Wu, S.P. Effect of Portland Cement on Moisture Resistance of Gneiss Based HMA. *Key Eng. Mater.* **2014**, *599*, 120–124. [[CrossRef](#)]
- Qu, X.; Liu, Q.; Wang, C.; Wang, D.; Oeser, M. Effect of Co-Production of Renewable Biomaterials on the Performance of Asphalt Binder in Macro and Micro Perspectives. *Materials* **2018**, *11*, 244. [[CrossRef](#)] [[PubMed](#)]
- Zeng, W.; Wu, S.; Pang, L.; Sun, Y.; Chen, Z. The Utilization of Graphene Oxide in Traditional Construction Materials: Asphalt. *Materials* **2017**, *10*, 48. [[CrossRef](#)] [[PubMed](#)]
- Cui, P.; Wu, S.; Li, F.; Xiao, Y.; Zhang, H. Investigation on Using SBS and Active Carbon Filler to Reduce the VOC Emission from Bituminous Materials. *Materials* **2014**, *7*, 6130–6143. [[CrossRef](#)] [[PubMed](#)]
- Cui, P.; Wu, S.; Xiao, Y.; Wan, M.; Cui, P. Inhibiting effect of Layered Double Hydroxides on the emissions of volatile organic compounds from bituminous materials. *J. Clean. Prod.* **2015**, *108*, 987–991. [[CrossRef](#)]
- Yao, H.; You, Z. Effectiveness of Micro- and Nanomaterials in Asphalt Mixtures through Dynamic Modulus and Rutting Tests. *J. Nanomater.* **2016**. [[CrossRef](#)]
- Srivastava, R.K.; Jozewicz, W.; Singer, C. SO<sub>2</sub> scrubbing technologies: A review. *Environ. Prog. Sustain. Energy* **2010**, *20*, 219–228. [[CrossRef](#)]
- Sienkiewicz, M.; Borzędowska-Labuda, K.; Zalewski, S.; Janik, H. The effect of tyre rubber grinding method on the rubber-asphalt binder properties. *Constr. Build. Mater.* **2017**, *154*, 144–154. [[CrossRef](#)]
- Sheng, Y.; Li, H.; Geng, J.; Tian, Y.; Li, Z.; Xiong, R. Production and Performance of Desulfurized Rubber Asphalt Binder. *Int. J. Pavement Res. Technol.* **2017**, *10*, 262–273. [[CrossRef](#)]
- Liu, S.; Cao, W.; Fang, J.; Shang, S. Variance analysis and performance evaluation of different crumb rubber modified (CRM) asphalt. *Constr. Build. Mater.* **2009**, *23*, 2701–2708. [[CrossRef](#)]

26. Wang, H.; Dang, Z.; Li, L.; You, Z. Analysis on fatigue crack growth laws for crumb rubber modified (CRM) asphalt mixture. *Constr. Build. Mater.* **2013**, *47*, 1342–1349. [[CrossRef](#)]
27. Zhang, L.; Xing, C.; Gao, F.; Li, T.S.; Tan, Y.Q. Using DSR and MSCR tests to characterize high temperature performance of different rubber modified asphalt. *Constr. Build. Mater.* **2016**, *127*, 466–474. [[CrossRef](#)]
28. Ding, X.; Ma, T.; Zhang, W.; Zhang, D. Experimental study of stable crumb rubber asphalt and asphalt mixture. *Constr. Build. Mater.* **2017**, *157*, 975–981. [[CrossRef](#)]
29. *Standard Test Methods of Bitumen and Bituminous Mixtures for Highway Engineering*; Ministry of Transport of the People's Republic of China: Beijing, China, 2011; JTG E20. (In Chinese)
30. Cantarino, M.V.; de Carvalho Filho, C.; Mansur, M.B. Selective removal of zinc from basic oxygen furnace sludges. *Hydrometallurgy* **2012**, *111*, 124–128. [[CrossRef](#)]
31. AASHTO. *Standard Test Method for Determining the Resilient Modulus of Bituminous Mixtures by Indirect Tension*; AASHTO Designation: TP 31; American Association of State Highway and Transportation Officials: Washington, DC, USA, 1996.
32. *Technical Specifications for Construction Highway Asphalt Pavements*; Ministry of Transport of the People's Republic of China: Beijing, China, 2004; JTG F40. (In Chinese)
33. *Technical Code for Asphalt Rubber Pavement*; Shanghai Construction and Traffic Committee: Shanghai, China, 2012; DG/TJ08-2109. (In Chinese)
34. Groome, D.R. The Geochemistry of the Devonian Lavas of the Northern Lorne Plateau, Scotland. *Mineral. Mag.* **1974**, *39*, 621–640. [[CrossRef](#)]



© 2018 by the authors. Licensee MDPI, Basel, Switzerland. This article is an open access article distributed under the terms and conditions of the Creative Commons Attribution (CC BY) license (<http://creativecommons.org/licenses/by/4.0/>).

Article

# Laboratory and Field Investigation of the Feasibility of Crumb Rubber Waste Application to Improve the Flexibility of Anti-Rutting Performance of Asphalt Pavement

Hongyin Li <sup>1</sup>, Hailong Jiang <sup>1</sup>, Wenwu Zhang <sup>1</sup>, Peng Liu <sup>1</sup>, Shanshan Wang <sup>1</sup>, Fei Wang <sup>1</sup>, Jizhe Zhang <sup>2,\*</sup> and Zhanyong Yao <sup>2</sup>

<sup>1</sup> Department of Maintenance, Qilu Transportation Development Group, Yinfeng Fortune Plaza D Block, Jinan 250014, China; qypgj@126.com (H.L.); sddxzjz@sina.com (H.J.); sdjzdxscj@sina.com (W.Z.); sddxlsj@sina.com (P.L.); 15969677683@139.com (S.W.); vdvvfv@163.com (F.W.)

<sup>2</sup> School of Qilu Transportation, Shandong University, Jinan 250061, China; zhanyong-y@sdu.edu.cn

\* Correspondence: jizhe.zhang@sdu.edu.cn; Tel.: +86-139-640-32980

Received: 20 August 2018; Accepted: 13 September 2018; Published: 15 September 2018

**Abstract:** Resistance of asphalt mix to low-temperature cracking and rutting at high temperature is very important to ensure the service performance of asphalt pavement under seasonal changes in temperature and loading. However, it is challenging to balance the improvement of such resistance by using additives, e.g., anti-rutting agent (ARA). This study focuses on improving the flexibility of anti-rutting asphalt mix by incorporating crumb rubber (CR) and ARA. The properties of the prepared modified asphalt mix were evaluated in the laboratory by performing wheel tracking, three-point bending, indirect tensile, and uniaxial compression tests. The experimental results showed that the dynamic stability of modified asphalt mix was significantly increased due to the addition of ARA and further improved by incorporating CR. The maximum bending strain at  $-10\text{ }^{\circ}\text{C}$  was increased due to the contribution of CR. The results of indirect tensile strength and resilient modulus further indicated that the CR-modified anti-rutting mixture was more flexible. Moreover, the field observation and evaluation indicated that the CR-modified anti-rutting asphalt pavement met the standard requirements, better than normal asphalt mixture in many parameters. A conclusion can be made that incorporating CR in asphalt mixture prepared with ARA can improve pavement performance at both high and low in-service temperatures.

**Keywords:** crumb rubber; anti-rutting agent; flexibility; field evaluation

## 1. Introduction

Owing to economic growth and the high demand of transport, especially in developing countries, traffic volume is experiencing a dramatic increase and the number of overloaded vehicles is increasing as well. Consequently, road pavement suffers severe loading conditions, under which severe distress occurs much earlier than its designed service life [1,2]. For instance, the mass of an overloaded lorry in China can be  $>150$  tons, with contact pressure  $>1$  MPa. Rutting, which is defined as permanent deformation along the wheel path caused by traffic loading, is one of the principal distress modes in Chinese asphalt pavement [3]. The presence of rutting not only accelerates already existing distress, but also increases the potential for driving crashes and reduces driving comfort [4].

For asphalt pavement, the hot-mixed asphalt mixture is commonly obtained at high temperatures by mixing predetermined rations of aggregates (coarse and fine), bitumen, and filler, which, after paving and compaction processes, form a flexible pavement [5,6]. As it is a composite material, its aggregate type, aggregate gradation, air void, binder type, and binder content are the primary factors



that control rutting resistance [7]. It has been found that aggregate gradation influences the internal structure and stress distribution of asphalt mixture, which in turn affects the intergranular friction of particles inside [8,9]. Furthermore, intergranular friction influences the movement (rotation or repositioning) of aggregate particles, which finally contributes to the rutting resistance of asphalt pavement [10]. During aggregate movement, the slide action of well-bounded particles shear the binder film [3]. For the same aggregate skeleton, asphalt mix produced with a high-modulus bitumen binder results in better rutting resistance [5]. Therefore, enhancing the bitumen properties seems to be a feasible method to provide good resistance to rutting.

Traditionally, the use of polymer-based materials in bitumen incorporated by mechanical mixing or chemical reactions can significantly improve the properties of conventional bitumen binder in asphalt mix [11]. Two types of polymers are widely used for bitumen modification: plastomers and thermoplastic elastomers [12]. Using plastomers and elastomers usually results in improved rutting resistance at elevated temperatures. The common plastomers used for bitumen modification include polyethylene (PE), polypropylene (PP), ethylene-vinyl acetate (EVA), and ethylene-butyl acrylate (EBA) [13]. The addition of plastomers brings high rigidity to the bitumen and substantially reduces its deformation under traffic load [14]. As the dosage of plastomers increases to a certain extent, two interlocked continuous phases are formed and result in substantially improved bitumen modulus [15]. Based on this behavior, plastomers are usually employed as anti-rutting agents, with the view of improving the high-temperature performance of asphalt mix. However, it was found that plastomers can weaken asphalt's ability to disperse accumulated stress at low temperatures [16]. These plastomers materials thus failed to improve the fatigue and fracture resistance of asphalt mix at low temperatures [17].

With the rapid growth of car ownership, a huge amount of vehicle tire waste is generated. According to some statistics, around 10 billion tires are discarded every year, and their inadequate disposal results in some adverse effects such as fire risk, rodents, soil pollution, and water pollution, which eventually threaten the environment and human health [18]. Crumb rubber (CR), a thermoplastic elastomer that can be produced from end-of-life tires, has been successfully used as an additive for bitumen modification due to its excellent properties and low cost. Previous researchers have reported that CR plays an important role in improving the resistance of permanent deformation of bitumen, fatigue cracking, and crack reflection at both high and low in-service temperatures [19,20]. CR also improved the elastic recovery of bitumen and showed good performance both in the lab and in field tests [21]. However, it seems difficult for CR-modified bitumen to substantially improve the high-temperature performance of asphalt pavement [22].

To overcome the drawbacks of common polymer modified techniques and improve the performance of asphalt mixture, an integrated modification method was employed in this study to produce modified asphalt mix by using both anti-rutting agent (ARA) and crumb rubber (CR). The main objective of this paper was to investigate the possibility of using CR to improve the flexibility of anti-rutting asphalt pavement. CR-modified bitumen was prepared by mixing base bitumen with a specific dosage of CR. Then, an asphalt mixture prepared with the modified bitumen was developed and produced with the anti-rutting agent added directly during mixing. The properties of asphalt mix were tested by wheel tracking, three-point bending, indirect tensile strength, and resilient modulus tests in order to evaluate the mechanical performance. Moreover, field tests were carried out on constructed test roads, followed by numerous field measurements, to investigate the properties of the field asphalt pavement.

## 2. Materials and Experimental Methods

### 2.1. Materials

Grade 70 base bitumen with a penetration grade of around 70 dmm produced by Chinese Qilu Transportation Development Group (Jinan, China) was used to produce asphalt mix and test roads.

Properties of this bitumen, which were evaluated in accordance with the Chinese JTG E20-2011 standard [23], are presented in Table 1.

**Table 1.** Physical and chemical properties of bitumen.

Bitumen Test	Result	Technical Requirements	Test Standard
Softening point (°C)	49.0	≥46	T0606
Penetration (25 °C, 0.1 mm)	68	60–80	T0604
Ductility (15 °C, cm)	>100	≥100	T0605
Viscosity at 60 °C (Pa·s)	198	≥180	T0625
Flash point (°C)	295	≥260	T0611
Solubility in C <sub>2</sub> HCl <sub>3</sub>	99.73	≥99.5	T0607
Relative density at 15 °C	1.004	–	T0603

The aggregates used in the mix were produced from the Daolang limestone quarry in Taian City, Shandong Province. The physical properties of fine and coarse aggregate were characterized according to the Chinese JTG E20-2011 standard [23], and the results are presented in Table 2.

**Table 2.** Physical properties of coarse and fine aggregates.

Aggregate Test	Results		Technical Requirements	Test Standards
	Coarse Aggregate	Fine Aggregate		
Specific gravity (g/cm <sup>3</sup> )	2.738	2.725	≥2.5	T0304/T0328
Water absorption (%)	0.44	0.73	≤3.0	T0304/T0328
Los Angeles abrasion loss (%)	15.4	–	≤30	T0317
Crushing value (%)	19.3	–	≤28	T0316

The CR used in this research was reclaimed from end-of-life vehicle tires. Tires were first shredded and chipped using large machinery to obtain rubber shreds. Furthermore, the ambient grinding process was implemented to reduce the particle size to 40 mesh, and the physical properties are listed in Table 3. The ARA used in the mixture was supplied by Chinese Shandong Qilufa Transportation Technology Co. Ltd (Dezhou, China). The ARA was derived from reclaimed PE, and its properties are shown in Table 4.

**Table 3.** Properties of crumb rubber (CR) used in this research.

CR Test	Result	Technical Requirements
Relative density	1.21	1.10–1.30
Moisture content (%)	0.08	0.5
Metal content (%)	0.005	0.05
Fiber content (%)	0.12	0.5

**Table 4.** Properties of anti-rutting agent (ARA) used in this research.

ARA Test	Result	Technical Requirements	Test Standards
Particle mass (g)	0.023	≤0.03	JT/T860.1
Gravity (g/cm <sup>3</sup> )	0.946	≤1.0	GB/T 1033
Melt index (g/10 min)	1.3	≥1.0	GB/T 3682
Ash content (%)	3.3	≤5	JTG E20

## 2.2. Mix Design

Before preparing the asphalt mix, the CR-modified bitumen was produced by the following procedure. The base bitumen was heated up to 160 °C until it melted. Then, CR in a dosage of 15% by mass was added to the bitumen, followed by a swelling process at 160 °C for 1 h. The CR-modified bitumen experienced a high-speed shearing process at a speed of 5000 r/min for 1 h in order to obtain the essentially homogeneous CR-modified bitumen.

The asphalt mixture designed in this research was used for the middle layer of asphalt pavement with a maximum particle size of 19 mm. The mixture was designed based on Chinese JTG E20-2011 [23], JTG E42-2005 [24], and JTG F40-2004 [25] standards. Three aggregate gradations were designed, as shown in Figure 1. The ARA content used was 0.3% of the total weight of the mixture and first blended with aggregates before bitumen. This ARA content is the supplier’s recommended optimum dosage. The Marshall specimens were prepared by using 5 different binder contents (3.1%, 3.6%, 4.1%, 4.6% and 5.1%). The best aggregate gradation and optimum binder content were determined by considering targeting air voids of 4.0–4.5% and the highest Marshall stability. Finally, gradation B was selected as the best, and the optimum binder content was found to be 4.3% for base bitumen and 4.4% for CR-modified bitumen. The results of Marshall stability and flow of 3 selected mixes are shown in Table 5.

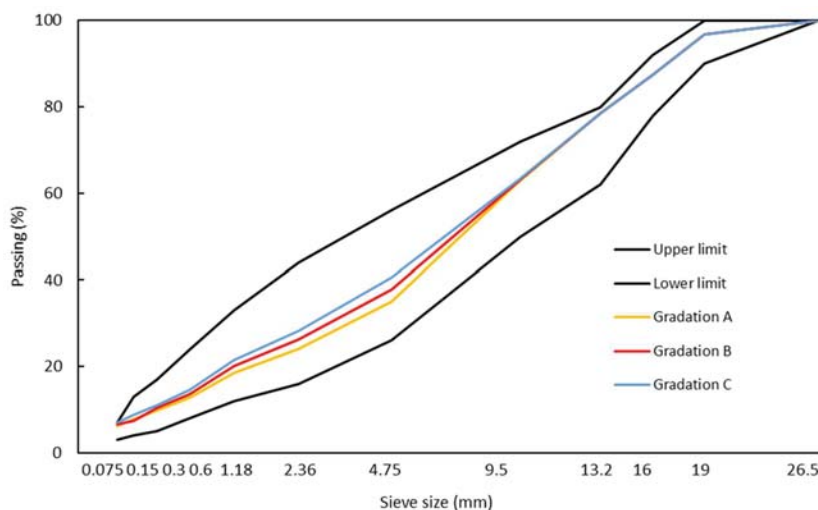


Figure 1. Gradation curves of aggregates used compared with standard requirements.

Table 5. Results of Marshall stability test for selected mix.

Mixture Type	Stability (kN)	Flow (mm)
Base	10.2	2.44
Base-ARA	16.4	1.81
CR-ARA	15.2	2.19

### 2.3. Laboratory Testing Methods

#### 2.3.1. Wheel Tracking Test

The wheel tracking test (WTT), in accordance with the JTG E20-2011 standard [23], was used to evaluate the rutting resistance of asphalt mix at high loading and high temperature. Owing to its ability to induce a stress state in asphalt slabs similar to that in actual pavement, the WTT was considered to be a suitable method for rutting investigation [26]. Asphalt specimens with dimensions of 300 × 300 × 50 mm<sup>3</sup> were compacted by a roller compactor (Shandong Luda Test Instruments Co. LTD, Taian, China) to obtain slabs with air voids in the range of 4.0–4.5%. Before testing, these slab specimens were conditioned in an environmental chamber at 60 °C for 6 h. During testing, the contact pressure between rubber wheel and specimen surface was 0.7 MPa, with a loading speed of 42 passes per minute. Two replicated tests were performed on each asphalt mixture. The development of rutting

depth was measured and recorded with a linear variable differential transformer (Shandong Luda Test Instruments Co. LTD, Taian, China). The dynamic stability value was calculated by Equation (1):

$$DS = \frac{15N}{d_2 - d_1} \quad (1)$$

where  $DS$  is the dynamic stability (cycles/mm),  $N$  is the loading speed (42 cycles/min),  $d_1$  is the rutting depth (mm) at 45 min, and  $d_2$  is the rutting depth (mm) at 60 min.

### 2.3.2. Three-Point Bending Test

The three-point bending (3PB) test is a uniaxial loading system used to evaluate the low-temperature cracking resistance of asphalt mix [27]. The 3PB was performed according to the JTG T0715-2011 standard [23]. Before testing, asphalt mixture slabs were compacted, followed by a cutting process to obtain prismatic beams with dimensions of  $250 \times 30 \times 35 \text{ mm}^3$ , as shown in Figure 2a. The air voids of asphalt mixture beams were measured, and these 3 types of mixture obtained similar average air voids, with values in the range of 4.1–4.5%. Before testing, these mixture beams were placed in an environmental chamber at  $-10 \text{ }^\circ\text{C}$  for at least 1.5 h to ensure homogeneous temperature distribution. During testing, the specimen was supported by 2 rollers with a span length of 200 mm, and a concentrated loading rate of 50 mm/min was applied, as shown in Figure 2b. The maximum bending strain was calculated by Equation (2):

$$\varepsilon_B = \frac{6 \times h \times d}{L^2} \quad (2)$$

where  $\varepsilon_B$  is the maximum bending strain ( $\mu\varepsilon$ ),  $h$  is the height of the specimen (mm),  $d$  is the deflection of specimens in mid-cross-section (mm), and  $L$  is the span of the support roller (mm).



**Figure 2.** Specimen and setup used for three-point bending test: (a) prismatic beam; (b) test setup.

### 2.3.3. Indirect Tensile Strength Test

The indirect tensile strength (*ITS*) test is commonly used to test the rutting and cracking properties of asphalt pavement [28]. This test was carried out at a loading rate of 50 mm/min and  $25 \text{ }^\circ\text{C}$  with testing procedures according to the JTG T0716-2011 standard [23]. Cylindrical specimens with a thickness of  $63.5 \pm 1.3 \text{ mm}$  and diameter of 101.6 mm were prepared using the Marshall compacter

(Shandong luda test instruments co. LTD, Taian, China). During testing, the vertical compressive load was converted into uniform horizontal tensile stress [1,7]. *ITS* was calculated by Equation (3):

$$ITS = \frac{2P_{\max}}{\pi td} \quad (3)$$

where *ITS* is the indirect tensile strength (MPa),  $P_{\max}$  is the maximum applied load (N), *t* is the specimen thickness (mm), and *d* is the specimen diameter (mm).

The moisture resistance of asphalt mixture was also characterized by using the *ITS* test in accordance with the JTG T0729-2000 standard. The moisture-saturated Marshall specimens were conditioned in a refrigerator at  $-18\text{ }^{\circ}\text{C}$  for 16 h, followed by water soaking at  $60\text{ }^{\circ}\text{C}$  for 24 h. Before testing, these specimens were immersed in water at  $25\text{ }^{\circ}\text{C}$  for 2 h. Moisture sensitivity of different mixes can be compared using the tensile strength ratio (TSR) value as follows:

$$TSR = TS_1/TS_0 \quad (4)$$

where  $TS_0$  and  $TS_1$  are the indirect tensile strength before and after the freeze-thaw cycle, respectively.

### 2.3.4. Resilient Modulus Test

Resilient modulus (RM) of asphalt mix was evaluated using a uniaxial compression test according to the JTG T0713-2000 standard [23]. It is a commonly used stress-strain measurement to measure the elastic properties of asphalt mix [29]. The compressive strength (*P*) of asphalt specimen was first measured at  $15\text{ }^{\circ}\text{C}$  with a loading rate of 2 mm/min before the RM test. Then, uniaxial loading with 7 steps (0.1 *P*, 0.2 *P*, 0.3 *P*, . . . , 0.7 *P*) was applied to the specimen and the resilient deformation of each loading stage ( $\Delta L_i$ ) was recorded after 30 s of unloading. The compressive strength of asphalt mix was calculated by:

$$R_c = \frac{4P}{\pi d^2} \quad (5)$$

where  $R_c$  is the compressive strength (MPa), *P* is the peak loading (N), and *d* is the specimen diameter (mm).

The resilient deformation at loading of 0.5 *P* was selected to calculate the RM value according to Equation (6):

$$E = \frac{q_5 \times h}{\Delta L_5} \quad (6)$$

where *E* is the compressive resilient modulus (MPa),  $q_5$  is the compressive strength at 0.5 *P* loading (MPa), *h* is the height of the specimen (mm), and  $\Delta L_5$  is the resilient deformation (mm).

## 3. Field Test Road and Evaluation

Based on the CR-modified anti-rutting asphalt mixture designed in the laboratory, a test road was constructed in September 2017. This test road was based on a maintenance project on the S31 expressway with a length of 2.2 km (K6+400~K8+600) in Taian, Shandong Province, China. The maintenance project was designed to remove the top and middle layers of the asphalt pavement, followed by paving with new asphalt mix. The CR-modified anti-rutting asphalt mixture was used in the middle layer with a thickness of 60 mm, as shown in Figure 3. The original designed AC-20 intermediate layer was used as a benchmark to compare with the anti-rutting middle layer.

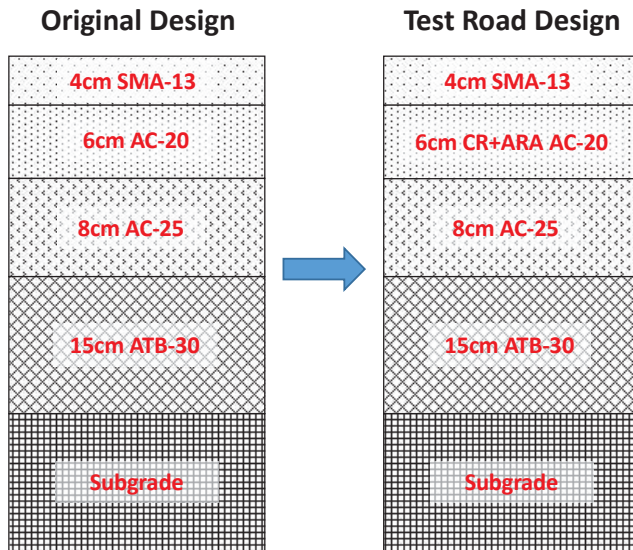


**Figure 3.** Cross-sections of the road structure: the original designed AC-20 in the middle layer was replaced by CR-modified anti-rutting AC-20.

### 3.1. Production of Asphalt Mix in the Plant

The CR-modified bitumen was prepared by using a reaction kettle (Kaifeng Road construction equipment co. LTD, Dezhou, China) with a capacity of 7 tons, then it was transferred to the bitumen tank and ready for the mixture production. An Ammann-4000 asphalt mixing plant (Ammann Group, Germany), which can produce 3.5 tons of mixture at a time, was used for this project. During the asphalt mixing, the temperature of aggregates and bitumen was controlled in the range of 180–200 °C and 165–175 °C, respectively, to make sure the temperature of the asphalt mixture was not less than 175 °C. The asphalt mixture was dropped onto the lorry immediately after mixing and transferred to the test road for paving. To evaluate the quality of the asphalt mixture, about 30 kg was taken from the lorry for the Marshall stability test and wheel tracking test.

### 3.2. On-site Paving and Compaction

Before paving the middle layer, the substrate layer surface was cleaned to remove dust and covered with a layer of emulsified bitumen (Chinese Qilu Transportation Development Group, Jinan, China) to obtain good interface adhesion, as shown in Figure 4. The construction range included a travel lane and an overtaking lane with a width of 7.5 m. Hot mix was first dropped into the pitch paving, with the temperature not less than 165 °C. During the paving process, the coefficient of compaction was 1.34 and the speed was controlled at 3 m/min. Two Sany STR130C-6 (Sany Heavy Industry, Changsha, China) road rollers followed closely behind the pitch paver to finish the first compaction immediately after paving, as shown in Figure 5. At least four cycles of compaction were applied to obtain the required degree of compaction.





**Figure 4.** Treatment of underlayer surface with emulsified bitumen to ensure good bonding with the middle layer.



**Figure 5.** Mechanical equipment used for asphalt paving and compaction: pitch paver and road roller.

### 3.3. Core Samples from Test Roads

Eight cored samples with a diameter of 100 mm were collected in four locations after the middle layer construction was completed. Four cores were used to determine the *ITS*, and another four cores were used to evaluate the compressive strength and resilient modulus. Another eight cored samples were collected from the original designed AC-20 layer and the same tests were performed as with the anti-rutting mixture. The cored samples were then cut and trimmed to obtain cylindrical specimens, as shown in Figure 6. The anti-rutting mixture and the normal AC-20 layer were placed on top of the existing AC-25 underlayer. Because of the matching aggregate gradation, the anti-rutting mixture and the normal AC-20 mixture showed almost equivalent skeletal structure.

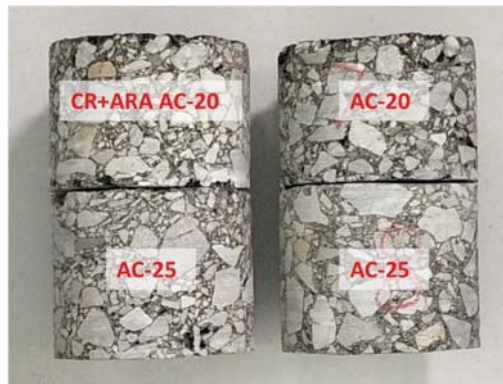


**Figure 6.** Core samples from the field pavement: (left) CR-modified anti-rutting mixture, and (right) normal AC-20 mixture.

## 4. Results and Discussion

### 4.1. Laboratory Results

#### 4.1.1. Rutting Resistance and Dynamic Stability of Asphalt Mix

Rutting curves of the three designed asphalt mixes are presented in Figure 7. These three mixes obtained similar air voids.

It can be seen that the rutting depth of asphalt mix increased gradually when the repeated loading time was prolonged, and the base asphalt mixture obtained the greatest rutting depth. The addition of ARA significantly decreased the rutting depth of the asphalt mixture, while the incorporation of CR helped to slightly reduce the rutting depth.

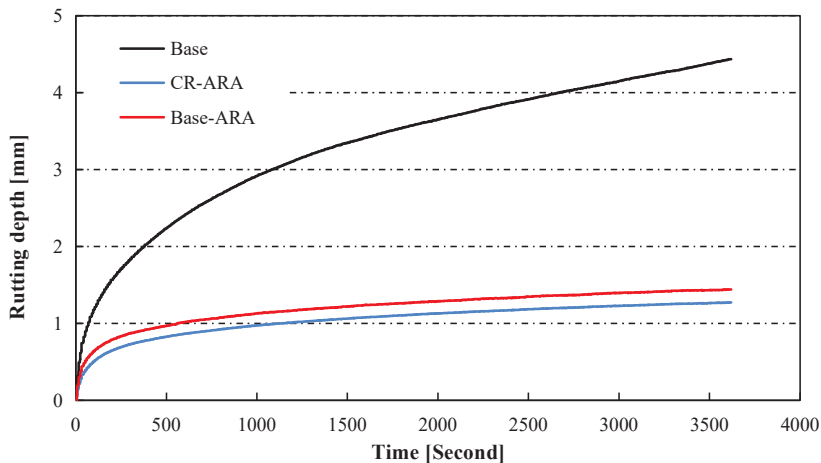


**Figure 7.** Rutting depth development in asphalt mixture slabs under repeated wheel tracking.

Dynamic stability (DS), one of the most widely used indicators for evaluating the rutting behavior of asphalt pavement, was calculated based on Equation (1), and the results and standard deviations are presented in Table 6. The dynamic stability of the asphalt mixture prepared with the base bitumen was 1526 cycles/mm, which was the lowest value among the tested specimens. It was found that the



dynamic stability of the ARA-modified asphalt mixture was about six times higher than that of the base asphalt mixture, with the value reaching 9324 cycles/mm. However, adding CR did not further enhance the dynamic stability of the ARA-modified asphalt mixture. This indicates that ARA is the main factor in improving the rutting resistance of asphalt mixture. The increased dynamic stability implies that the integrated modification of asphalt mixture using ARA and CR obviously improved the rutting resistance, which in turn contributed to enhanced pavement performance at high temperature.

**Table 6.** Dynamic stability of asphalt mix after wheel tracking test.

Property	Base	Base-ARA	CR-ARA
Dynamic stability (cycles/mm)	1526 ± 119	9324 ± 291	9631 ± 317

#### 4.1.2. Maximum Bending Strain of Asphalt Mix

The stress-strain curves of asphalt mix tested by the three-point bending test are plotted in Figure 8. Maximum bending strain is an indicator of pavement flexibility, and a higher value indicates better resistance to thermal cracking. The results of maximum bending strain are shown in Table 7. In comparison with the base asphalt mixture, the addition of ARA decreased the bending strain from 2067  $\mu\text{m}$  to 1831  $\mu\text{m}$ . However, when CR was added to the mixture, the bending strain showed an obvious increase to 2439  $\mu\text{m}$ . This shows that ARA reduced the deformation capacity of the asphalt mix, which indicates potential resistance to thermal cracking at low temperatures. In contrast, CR improved the flexibility of bitumen and resulted in better low-temperature performance. It can be concluded that the integrated modification of adding ARA and CR improved the low-temperature flexibility of the anti-rutting asphalt mixture.

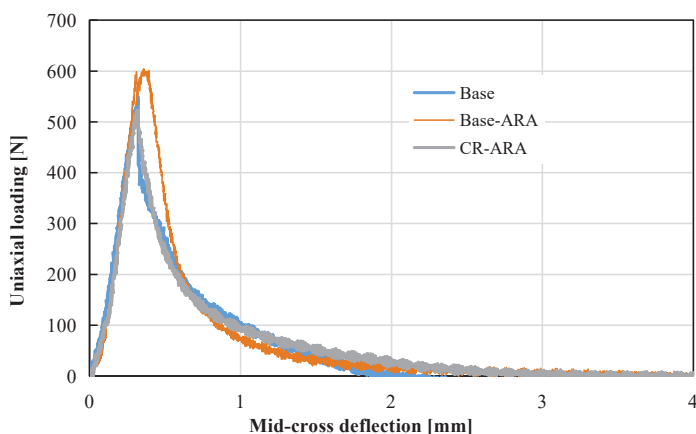


**Figure 8.** Plots of mid-cross deflection versus uniaxial loading of all specimens.

**Table 7.** Maximum bending strain ( $\epsilon_B$ ) of asphalt mix at  $-10\text{ }^\circ\text{C}$ .

Property	Base	Base-ARA	CR-ARA
Maximum bending strain ( $\mu\text{m}$ )	2067 ± 77.9	1831 ± 92.6	2439 ± 124.5

#### 4.1.3. Indirect Tensile Strength (ITS) Test and Moisture Sensitivity

The indirect tensile strength of asphalt mix before and after the freeze-thaw cycle was measured and the retained tensile strength ratios were calculated, with the results presented in Figure 9. In dry conditions, the asphalt mixture prepared with the base bitumen showed the lowest ITS of 0.524 MPa.

With the addition of ARA, *ITS* increased to nearly twice that of the base asphalt mixture. This can be attributed to the formation of two interlocked continuous phases in the bitumen, resulting in improved strength of the asphalt mixture. ARA significantly improved the tensile strength of the asphalt mixture, which may contribute to rutting and cracking resistance of asphalt pavement. However, CR-ARA obtained nearly the same *ITS* value as Base-ARA. It is suggested that CR has no further contribution to the *ITS* value of anti-rutting asphalt mixture.

After the freeze-thaw cycle, the *ITS* of all specimens had an obvious reduction due to moisture damage, as shown in Figure 9. Based on the JTG D50-2017 standard [30], the minimum requirement of tensile strength ratio (TSR) for asphalt mix is 75%. As shown in Figure 9, the TSR of the anti-rutting asphalt mixture was greater than that of the asphalt mix prepared with base bitumen, which indicates better resistance to moisture damage. In addition, the CR-modified bitumen resulted in further improvement in TSR. Therefore, the addition of both CR and ARA enhanced the adhesion of aggregate-bitumen interface, which in turn improved the durability of asphalt mixture against moisture.

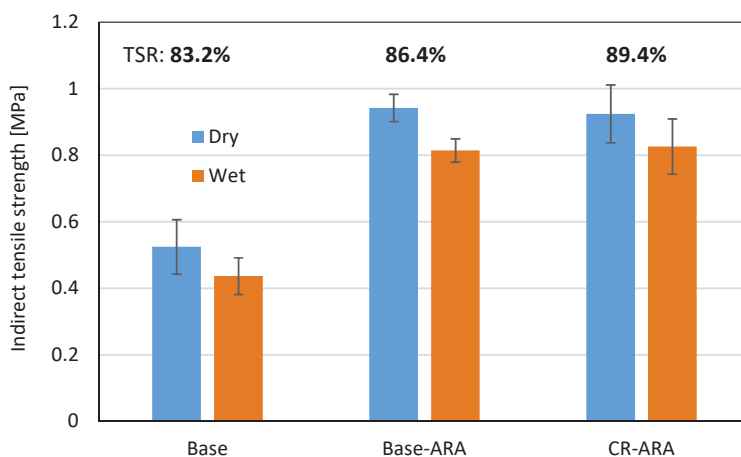


Figure 9. Indirect tensile strength (*ITS*) and tensile strength ratio before and after freeze-thaw cycle.

#### 4.1.4. Compressive Strength and Resilient Modulus of Asphalt Mix

The relationship between uniaxial loading and resilient modulus of related specimens is shown in Figure 10. It can be observed that the seven points selected in this test are all located on one trend line. The compressive strength and resilient modulus were calculated based on Equations (5) and (6), as shown in Figures 11 and 12, respectively. In terms of compressive strength, the asphalt mixture prepared with the base bitumen obtained the lowest result (5.83 MPa), and the mixture prepared with ARA had the highest (8.49 MPa). Such results indicate that the addition of ARA improved the resistance of asphalt mixture to vertical loading. The addition of CR in the anti-rutting asphalt mixture slightly decreased the compressive strength. Considering the standard deviation, Base-ARA and CR-ARA obtained similar compressive strength. This phenomenon reveals that ARA is the main factor in improving compressive strength and CR does not contribute to this parameter.

As shown in Figure 12, the anti-rutting asphalt mixture obtained the highest resilient modulus value, which means ARA increases the stiffness of asphalt mixture and results in less deformation under loading. However, using CR in the anti-rutting mixture can reduce the resilient modulus, and this can be attributed to the increased recoverable deformation. This demonstrates that adding CR can improve the elasticity of the anti-rutting asphalt mixture.

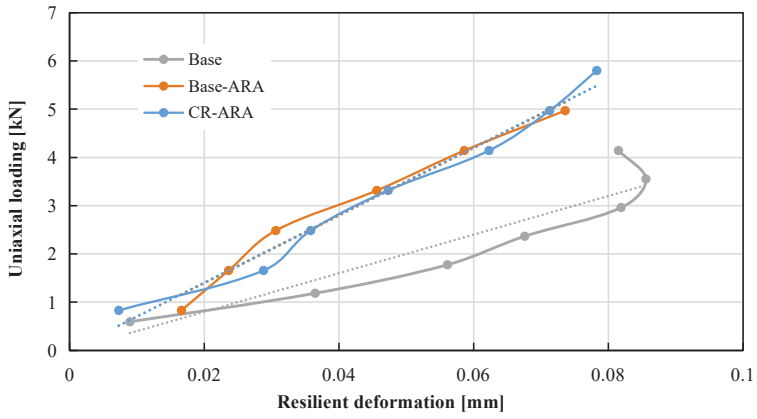


Figure 10. Relationship between uniaxial loading and resilient modulus of all specimens.

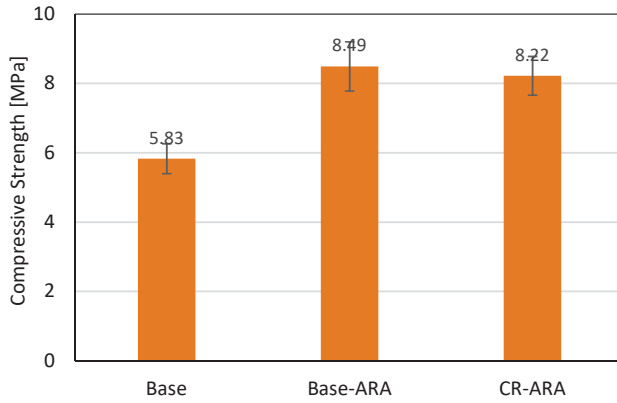


Figure 11. Compressive strength of asphalt mix at 15 °C.

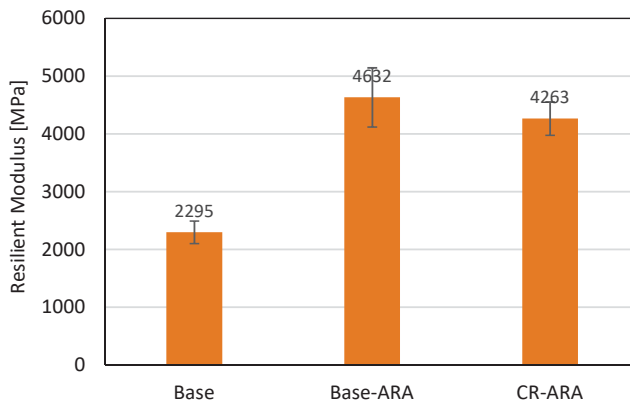


Figure 12. Resilient modulus of asphalt mix at 15 °C.

## 4.2. Results of Test Road Evaluation

### 4.2.1. Properties of Asphalt Mix Used in the Test Road

The asphalt mix taken from the mixing plant was tested, and the evaluated properties included Marshall stability and rutting resistance by the wheel tracking test. The properties of the asphalt mix used in the test road are listed in Table 8. As presented in this table, the Marshall stability value of CR-modified anti-rutting mixture was over 30% higher compared with the base asphalt mixture. The flow of the CR-modified anti-rutting mixture was slightly lower than that of the base asphalt mixture. This phenomenon indicates that the integrated modification led to the increased strength of the asphalt mixture and contributed to the high-temperature performance of asphalt pavement. In terms of the wheel tracking results, the dynamic stability of the CR-modified anti-rutting mixture was about six times higher than that of the base asphalt mixture. This result shows the enhancement of the rutting resistance of the CR-ARA mixture. The results obtained from the plant-mixed asphalt mixture had good correlation with the experimental results, as shown in Tables 5 and 6. This indicates that the integrated modification of using ARA and CR improved the pavement performance in the test road.

**Table 8.** Marshall stability and wheel tracking results of mix obtained from mixing station.

Experimental Test	Result		Technical Requirement
	Base	CR-ARA	
Stability (kN)	10.7 ± 0.43	14.1 ± 0.84	≥8
Flow (mm)	2.87 ± 0.32	2.19 ± 0.19	1.5–4
Dynamic stability (cycles/mm)	1732 ± 112	10216 ± 568	≥1000/≥2800

### 4.2.2. Properties of Cored Specimens from Test Road

After test road compaction, the cored specimens were collected by using a core-drilling machine, as shown in Figure 13a. The core locations and thicknesses of cored specimens were recorded, as shown in Figure 13b. The properties of the cored specimens were evaluated, and the results are presented in Table 9. The degree of compaction was the proportion of bulk specific gravity of the cored specimen divided by bulk specific gravity of the Marshall specimen. As presented in this table, the degree of compaction and thickness of these two test roads met the design requirements. The *ITS* results were similar to the laboratory study, which indicates that the CR-ARA asphalt mixture had a higher value. The addition of ARA improved the stiffness of bitumen, which resulted in enhanced strength of the asphalt mixture. However, in terms of the same asphalt mixture, the cored specimen obtained relatively lower *ITS* value compared with the laboratory specimen. One reason could be the specimen dimensions, with the height and diameter of cored specimens differing from those of the Marshall specimen. Another reason could be that the cored specimen destroyed the continuous structure of the compacted road, and the aggregates on the side walls were not restricted by binders. Regarding the compressive strength and resilient modulus, higher values were also related to the CR-ARA asphalt mixture. The improvement of compressive strength and resilient modulus can be attributed to two major factors. First, the addition of ARA (plastomers) creates two interlocked continuous phases and results in increased stiffness. Second, owing to the contribution of CR, a rubbery support network is formed and results in improved elastic response [12]. As a consequence, it can be anticipated that the CR-modified anti-rutting asphalt pavement would be more durable than the base asphalt pavement.

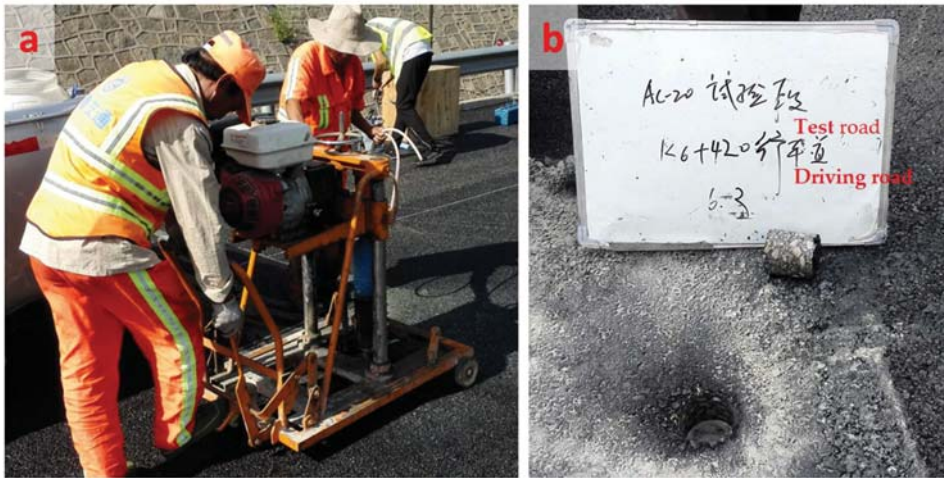


Figure 13. Equipment used for on-site coring and measurement: (a) core-drilling machine; (b) information of cored specimen.

Table 9. Related properties of cored specimens from the test road.

On-Site Test	Results		Technical Requirements
	Base	CR-ARA	
Compaction degree (%)	98.6 ± 0.5	98.4 ± 0.6	≥98
Thickness (mm)	63 ± 0.2	65 ± 0.2	≥60
ITS (MPa)	0.457 ± 0.042	0.839 ± 0.034	–
Compressive strength (MPa)	3.15 ± 0.40	4.40 ± 0.51	–
Resilient modulus (MPa)	1209 ± 97	2923 ± 304	–

### 5. Conclusions

Recent efforts to develop anti-rutting asphalt pavement show that the addition of ARA failed to maintain good low-temperature pavement performance. This paper investigated the feasibility of using CR and ARA to improve the rutting resistance and flexibility of asphalt pavement, which were evaluated by laboratory tests and field evaluation. The first phase of this study was to clearly evaluate the mixture properties before and after incorporating CR at both low and high service temperatures. The second phase was to construct test roads and detect the related pavement performance. The major findings can be summarized as follows:

- 1) The addition of ARA significantly reduced the rutting depth and improved the dynamic stability of asphalt mix. This indicates improvement of asphalt mix under high-temperature conditions. Moreover, the dynamic stability of asphalt mixture can be further improved by incorporating CR.
- 2) ARA can decrease the maximum bending strain, and incorporating CR can obviously increase the maximum bending strain of asphalt mix prepared with ARA. This implies that adding CR can improve the flexibility of anti-rutting asphalt mixture at low temperature.
- 3) Using ARA in asphalt mix can obviously improve the ITS value, resilient modulus, and moisture resistance. The addition of CR into the anti-rutting asphalt mixture can slightly reduce the ITS and resilient modulus.
- 4) The properties of asphalt mix produced by the asphalt mixing plant for field tests had good correlation with the mix prepared in the laboratory. The quality of asphalt mix used for test roads met the standard requirements.

- 5) The results of *ITS* and resilient modulus of the specimens cored from test roads showed a similar trend to the results obtained in the laboratory, which indicates that the CR-modified anti-rutting asphalt pavement showed the best pavement performance.

It should be noted that the test roads were just constructed, service performance cannot be evaluated over the short term, and more tests should be carried out in the future. Therefore, long-term tracking observation will be performed to characterize the properties of test roads, which in turn can provide guidelines for further research.

**Author Contributions:** Data curation: H.L.; Formal analysis: H.J., W.Z.; Project administration: P.L., S.W.; Writing—original draft: J.Z.; Writing—review & editing: F.W., Z.Y.

**Funding:** The authors acknowledge the financial support of the Transportation Technology Project in Shandong Province (Project No. YHKY-7), China Postdoctoral Science Foundation (Project No. 2017M622207) and Special Funding for Postdoctoral Innovation Project in Shandong Province (Project No. 201702011). Special thanks are to the State Key Laboratory of Silicate Materials for Architectures (Wuhan University of Technology) (Project No. SYSJJ2018-07).

**Conflicts of Interest:** The authors declared that they have no conflicts of interest to this work. We declare that we do not have any commercial or associative interest that represents a conflict of interest in connection with the work submitted.

## References

1. Moghaddam, T.B.; Soltani, M.; Karim, M.R. Experimental characterization of rutting performance of Polyethylene Terephthalate modified asphalt mix under static and dynamic loads. *Constr. Build. Mater.* **2014**, *65*, 487–494. [[CrossRef](#)]
2. Zhang, J.Z.; Airey, G.D.; Grenfell, J.R.A. Experimental evaluation of cohesive and adhesive bond strength and fracture energy of bitumen-aggregate systems. *Mater. Struct.* **2016**, *49*, 2653–2667. [[CrossRef](#)]
3. Young, K.C. Visco-Elastic Analysis of the Elastomeric Binder Shear Resistance in Relation to Asphalt Rutting. *Road Mater. Pavement* **2011**, *12*, 767–794.
4. Liao, G.Y.; Wang, S.Y.; Shi, Q. Enhancing anti-rutting performance of asphalt pavement by dispersing shear stresses within asphalt layers. *Road Mater. Pavement* **2016**, *19*, 453–469.
5. Zhang, J.; Apeagyei, A.K.; Airey, G.D.; Grenfell, J.R.A. Influence of aggregate mineralogical composition on water resistance of aggregate-bitumen adhesion. *Int. J. Adhes. Adhes.* **2015**, *62*, 45–54. [[CrossRef](#)]
6. Chen, Z.W.; Wu, S.P.; Xiao, Y.; Zeng, W.; Yi, M.; Wan, J. Effect of hydration and silicone resin on Basic Oxygen Furnace slag and its asphalt mixture. *J. Clean. Prod.* **2016**, *112*, 392–400. [[CrossRef](#)]
7. Moghaddam, T.B.; Soltani, M.; Karim, M.R. Evaluation of permanent deformation characteristics of unmodified and Polyethylene Terephthalate modified asphalt mix using dynamic creep test. *Mater. Des.* **2014**, *53*, 317–324. [[CrossRef](#)]
8. Masad, E.; Muhunthan, B.; Shashidhar, N.; Harman, T. Internal structure characterization of asphalt concrete using image analysis. *ASCE J. Comput. Civ. Eng.* **1999**, *13*, 88–95. [[CrossRef](#)]
9. Cui, P.Q.; Wu, S.P.; Xiao, Y.; Wan, M.; Cui, P. Inhibiting Effect of Layered Double Hydroxides on the Emissions of Volatile Organic Compounds from Bituminous Materials. *J. Clean. Prod.* **2015**, *108*, 987–991. [[CrossRef](#)]
10. Sefidmazgi, N.R.; Tashman, L.; Bahia, H. Internal structure characterization of asphalt mix for rutting performance using imaging analysis. *Road Mater. Pavement* **2012**, *13*, 21–37. [[CrossRef](#)]
11. Jafari, M.; Nasrekani, A.A.; Nakhaei, M.; Babazadeh, A. Evaluation of rutting resistance of asphalt binders and asphalt mix modified with polyphosphoric acid. *Pet. Sci. Technol.* **2017**, *35*, 141–147. [[CrossRef](#)]
12. Zhu, J.Q.; Birgisson, B.; Kringos, N. Polymer modification of bitumen: Advances and challenges. *Eur. Polym. J.* **2014**, *54*, 18–38. [[CrossRef](#)]
13. Yeh, P.-H.; Nien, Y.-H.; Chen, J.-H.; Chen, W.-C.; Chen, J.-S. Thermal and rheological properties of maleated polypropylene modified asphalt. *Polym. Eng. Sci.* **2005**, *45*, 1152–1158.
14. Domingos, M.D.I.; Faxina, A.L. Rheological behaviour of bitumens modified with PE and PPA at different MSCR creep–recovery times. *Int. J. Pavement Eng.* **2015**, *16*, 771–783. [[CrossRef](#)]
15. Polacco, G.; Berlincioni, S.; Biondi, D.; Stastna, J.; Zanzotto, L. Asphalt modification with different polyethylene-based polymers. *Eur. Polym. J.* **2005**, *41*, 2831–2844. [[CrossRef](#)]

16. Yan, K.Z.; Xu, H.B.; You, L.Y. Rheological properties of asphalts modified by waste tire rubber and reclaimed low density polyethylene. *Constr. Build. Mater.* **2015**, *83*, 143–149. [[CrossRef](#)]
17. Isacson, U.; Lu, X. Testing and appraisal of polymer modified road bitumens-state of the art. *Mater. Struct.* **1995**, *28*, 139–159. [[CrossRef](#)]
18. Presti, D.L. Recycled tyre rubber modified bitumens for road asphalt mix: A literature review. *Constr. Build. Mater.* **2013**, *49*, 863–881. [[CrossRef](#)]
19. Georges, A.J.; Mturi, G.A.J.; O’Connell, J.; Zoorob, S.E.; Beer, M.D. A study of crumb rubber modified bitumen used in South Africa. *Road Mater. Pavement* **2014**, *15*, 774–790.
20. Szerba, E.I.; Nicoterab, I.; Teltayevc, B.; Vaiana, R.; Rossi, C.O. Highly stable surfactant-crumb rubber-modified bitumen: NMR and rheological investigation. *Road Mater. Pavement* **2017**, *19*, 1192–1202. [[CrossRef](#)]
21. Shatanawia, K.M.; Birob, S.; Nasera, M.; Amirkhanian, S.N. Improving the rheological properties of crumb rubber modified binder using hydrogen peroxide. *Road Mater. Pavement* **2013**, *14*, 723–734. [[CrossRef](#)]
22. Yuan, J.; Wang, J.; Xiao, F.; Amirkhanian, S.; Wang, J.; Xu, Z. Impacts of multiple-polymer components on high temperature performance characteristics of airfield modified binders. *Constr. Build. Mater.* **2017**, *134*, 694–702. [[CrossRef](#)]
23. China Standards Publication. *Standard Test Methods of Bitumen and Bituminous Mixtures for Highway Engineering*; JTG E20-2011; China Communication Press: Beijing, China, 2011.
24. China Standards Publication. *Test Methods of Aggregate for Highway Engineering*; JTG E42-2005; China Communication Press: Beijing, China, 2005.
25. China Standards Publication. *Technical Specification for Construction of Highway Asphalt Pavements*; JTG F40-2004; China Communication Press: Beijing, China, 2004.
26. Javilla, B.; Mo, L.; Hao, F.; Wu, S.; Shu, B. Multi-stress loading effect on rutting performance of asphalt mix based on wheel tracking testing. *Constr. Build. Mater.* **2017**, *148*, 1–9. [[CrossRef](#)]
27. Chen, L.L.; Qian, Z.D.; Qing, L.Q. Crack initiation and propagation in epoxy asphalt concrete in the three-point bending test. *Road Mater. Pavement* **2014**, *15*, 507–520. [[CrossRef](#)]
28. Islam, M.R.; Hossain, M.I.; Tarefder, R.A. A study of asphalt aging using Indirect Tensile Strength test. *Constr. Build. Mater.* **2015**, *95*, 218–223. [[CrossRef](#)]
29. Xiao, F.P.; Amirkhanian, S.N. Resilient Modulus Behavior of Rubberized Asphalt Concrete Mix Containing Reclaimed Asphalt Pavement. *Road Mater. Pavement* **2008**, *9*, 633–649.
30. China Standards Publication. *Specification for Design of Highway Asphalt Pavement*; JTG D50-2017; China Communication Press: Beijing, China, 2017.



© 2018 by the authors. Licensee MDPI, Basel, Switzerland. This article is an open access article distributed under the terms and conditions of the Creative Commons Attribution (CC BY) license (<http://creativecommons.org/licenses/by/4.0/>).



Article

# Adhesion between Asphalt and Recycled Concrete Aggregate and Its Impact on the Properties of Asphalt Mixture

Yueqin Hou <sup>1</sup>, Xiaoping Ji <sup>2,\*</sup>, Jia Li <sup>2</sup> and Xianghang Li <sup>2</sup>

<sup>1</sup> School of Human Settlements and Civil Engineering, Xi'an Jiaotong University, Xi'an 710049, China; houyueqin527@xjtu.edu.cn

<sup>2</sup> Key Laboratory for Special Area Highway Engineering of Ministry of Education, Chang'an University, Xi'an 710064, China; chdli1996@163.com (J.L.); hanglx.gd@foxmail.com (X.L.)

\* Correspondence: jixp82@163.com; Tel.: +86-029-62630078

Received: 15 November 2018; Accepted: 10 December 2018; Published: 12 December 2018

**Abstract:** To study and evaluate the adhesion between recycled concrete aggregate and asphalt, the contact angles (CAs) between droplet (water and ethanol) and recycled concrete aggregate (RCA), natural aggregates, and solid bitumen (matrix asphalt, SBS modified asphalt) were tested via the sessile drop method with an optical microscope. The surface free energy was then calculated. The CAs between hot asphalt and RCA and natural aggregates were tested via the hanging slice method. The adhesive energy between asphalt and RCA and natural aggregates were calculated based on the test results of the surface free energy and CAs. Then, the influence of RCA on the water stability and fatigue performance of the asphalt mixture was analyzed by testing the water stability and fatigue properties of hot mix asphalts containing RCA (HMA-RCA) with different aggregates and RCA dosages. The surface energy of the various aggregates and the CAs between aggregates and asphalts were sorted as follows: Granite > RCA > serpentinite > limestone. The surface energy and CA of RCA were very close to that of serpentinite. The adhesive energy between various aggregates and asphalt were sorted as follows: Limestone > serpentinite > RCA > granite. The adhesive energy between RCA and asphalt was also very close to that of serpentinite. The residual Marshall stability, tensile strength ratio, and fatigue performance of the HMA-RCAs were gradually reduced along with the increasing RCA dosage. This effect may be attributed to the fact that the adhesive energy between the RCA and the asphalt was less than that of water and that the asphalt was easily stripped from the RCA surface. Excessive RCA content in the aggregate can lead to excessive porosity of the HMA-RCA. The CAs and adhesive energy between RCA and asphalt showed significant effects on the water stability and fatigue performance of HMA-RCA.

**Keywords:** hot mix asphalt containing recycled concrete aggregate; contact angle; adhesion energy; water stability; fatigue performance

## 1. Introduction

### 1.1. Research Background

Given the constant development of human production activities, the contradiction between the supply and demand of high-quality gravels that are used in pavements becomes increasingly prominent, and the price of such products continues to increase. In addition, the construction and demolition of buildings, as well as the construction and renovation of cement concrete or asphalt concrete pavement, produce up to 600 million tons of solid wastes each year, thereby leading to a series of environmental and social problems. Therefore, recycling solid waste not only alleviates



the shortage of natural aggregates, but also solves the problem of processing construction waste [1]. Recycled concrete aggregates (RCA) are less than 40 mm in particle size and are produced from waste concrete after sorting, carving, crushing, and grading. RCA can be widely used in non-load-bearing structural concrete, such as foundation cushions, gutters, drainage troughs, coastal protection dikes, and so on. The construction of asphalt concrete pavement requires a large amount of aggregates, and because high-quality aggregates are non-renewable resources, researchers hope to replace some of the natural aggregates with recycled aggregates, so RCA application in asphalt mixture has attracted the attention of researchers. At present, in asphalt pavement, RCA can be used to build the asphalt concrete surface layer, cushion layer, base layer, and so on [2–4].

The properties of asphalt mixture are closely related to the performance and adhesion between aggregate and asphalt. Loss of adhesion is caused by the breaking of adhesive bonds between the aggregate surface and the asphalt binder primarily because of the coupled action of water and load. Therefore, loss of adhesion leads to several distresses in the asphalt pavement, such as water damage and fatigue damage. Previous studies [5,6] have shown that RCA is composed of natural sandstone material and cement mortar with a special surface microscopic structure and chemical composition. The adhesion between RCA and asphalt is closely related not only to the chemical properties of materials, but also to their surface structure. RCA is used in cement hydration products, including C–S–H ( $x\text{CaO}\cdot\text{SiO}_2\cdot y\text{H}_2\text{O}$ ), ettringite ( $3\text{CaO}\cdot\text{Al}_2\text{O}_3\cdot\text{CaSO}_4\cdot 32\text{H}_2\text{O}$ ), single-sulfur type of calcium sulfoaluminate ( $3\text{CaO}\cdot\text{Al}_2\text{O}_3\cdot\text{CaSO}_4\cdot 12\text{H}_2\text{O}$ ), and  $\text{Ca}(\text{OH})_2$ . These components have a certain activity that can lead to feeble chemical reactions with acid asphalt. The adhesion between RCA and asphalt is affected by chemical reactions. Moreover, the surface of RCA is rougher than that of natural gravels because of many micro cracks and voids. Therefore, the adhesion between RCA and asphalt demonstrates a unique behavior that complicates the relationship between the road performance of hot mix asphalt containing RCA (HMA-RCA) and the dosage of RCA. Moreover, the road performance of HMA-RCA cannot satisfy the required technical specifications. Therefore, revealing the micro-mechanism and influencing factors of the adhesion between RCA and asphalt serves as a theoretical basis for optimizing the design of HMA-RCA.

## 1.2. Literature Review

The recycling of recycled aggregates in asphalt mixtures has attracted research attention in recent years. Existing studies mainly focus on the road performance of HMA-RCA, including their Marshall and volume indices, water stability, permanent deformation, and fatigue performance. At the same time, some studies have evaluated the performance of HMA-RCA from a microscopic perspective [7,8]. Numerous studies show that RCA contains a certain amount of cement mortar with low density, large pores, rough surface, and many micro cracks.

Many studies have shown that the asphalt content of HMA-RCA is higher than that of natural gravels due to a large amount of asphalt absorbed by the pores and micro cracks of RCAs, and it increases along with the increasing of RCA dosage [9–12]. The asphalt in the mixture can be divided into effective asphalt and asphalt absorbed by the aggregate. Although HMA-RCA contains a large amount of asphalt, its effective asphalt content is lower than that of HMA with natural gravels [12–14]. RCA can be divided into recycled coarse aggregate ( $\geq 4.75$  mm) and recycled fine aggregate ( $< 4.75$  mm). Some studies suggest that the dosage of recycled fine aggregate must be limited to decrease the asphalt content [15] because recycled fine aggregate contains a large amount of cement mortar [16] with a large specific surface area [17] and high oil adsorption [18].

Water stability is caused by the stripping of asphalt from the aggregate surface because of the coupled actions of water and load. The water stability of HMA-RCA varies with RCA content, and the law behind such variation is very complicated. Some studies show that RCA can improve the water stability of HMA-RCA and that the water stability of HMA-RCA increases along with increasing RCA dosage [12,13,19–22]. However, other studies find that the water stability of HMA-RCA decreases with

increasing RCA content [23,24]. Some studies find that the water stability of HMA-RCA does not meet the specification requirements [13], but others show opposite results [19,21,22,25].

In terms of resistance to permanent deformation and modulus, some studies suggest that HMA-RCA is more capable of resisting permanent deformation, meeting specification requirements [10,12,13,21,26–28], and demonstrating high rebound, dynamic, and bending moduli compared with traditional mixtures [13,24,26,29]. However, other studies claim that the stiffness modulus and resistance of HMA-RCA to permanent deformation decrease [30] along with increasing RCA content, and that HMA-RCA does not meet specification requirements [13,15] because its asphalt content is greater than that of traditional HMA.

The fatigue properties of HMA-RCA are identical to those of traditional HMA [12,20,25], and recycled fine aggregate can improve fatigue performance [18]. Numerous studies show that the low temperature cracking performance of HMA-RCA is reduced along with increasing RCA content [23,24,30] because the effective asphalt content of HMA-RCA decreases with increasing RCA dosage.

Few studies have investigated the micro structure of RCA and the adhesion properties between RCA and asphalt. Hou et al. [9] studied the microscopic properties of RCA by means of SEM. The crushed value, water absorption, density, and adhesion with asphalt of RCA were tested. However, the adhesion between the aggregate and the asphalt and the macroscopic asphalt mixture water stability and fatigue performance are not closely related.

In other words, the adhesive mechanism and its influencing factors must be determined to improve the road performance of HMA-RCA. In this study, the contact angles (CAs) among droplets (water and ethanol), RCA, several natural aggregates, and solid bitumen (matrix asphalt, styrene-butadiene-styrene (SBS)-modified asphalt) were tested using the sessile drop method. The surface free energy was then calculated. The CAs among hot asphalt, RCA, and natural aggregates were tested using the hanging slice method. The adhesive energy among the asphalt, RCA, and natural aggregates were calculated based on the test results of the surface free energy and CAs. HMA-RCA with RCA dosages of 0%, 30%, 60%, and 100% were designed, and the water stability and fatigue performance of these HMA-RCA were tested. The effects of the adhesive on the water stability and fatigue performance were then analyzed.

## 2. Raw Materials and Mixtures

### 2.1. Raw Materials

The 70# matrix asphalt and SBS modified asphalt were used in experiments, and the technique performances were tested and shown in Table 1 according to the Chinese Specification of JTJ 052-2000 (RIOH, 2000) [31].

**Table 1.** Technique performance of asphalts.

Asphalts Type	Penetration/0.1 mm	Ductility/cm	Brookfield Viscosity/(Pa·s)	Softening Point/ <sup>o</sup> C	Density at 15 °C/(g/cm <sup>3</sup> )
Matrix asphalt	66.0	>150	0.486	47.5	1.018
SBS modified	72.3	42.3	1.345	71.0	1.033

Note: The testing temperatures of the ductility of the unmodified and SBS modified bituminous binder were 15 °C and 5 °C, respectively. The Brookfield viscosity at 135 °C was tested for the 70# matrix asphalt and SBS modified asphalt.

Waste cement concrete was directly collected from a bridge demolishing spot and then crushed and sorted to obtain RCA. The performance of RCAs was tested and shown in Table 2 according to the Chinese Specification of JTG E42-2005 (RIOH, 2005) [32]. Three different natural gravels were utilized in the experiments for the comparative analysis, namely limestone, granite, and serpentine.

**Table 2.** Technique performance of aggregates.

Aggregate Type	Crushed Value/%	Apparent Relative Density				Water Absorption/%		
		0–5 mm	5–10 mm	10–20 mm	20–30 mm	5–10 mm	10–20 mm	20–30 mm
RCA	26.7	2.483	2.657	2.684	2.838	6.2	5.3	4.8
Activated RCA	21.8	2.523	2.707	2.731	2.845	1.9	1.8	1.1
Limestone	20.9	2.652	2.698	2.705	2.713	1.7	0.9	0.1
Granite	13.4	2.602	2.668	2.675	2.660	1.3	1.2	0.7
Serpentine	4.8	2.639	2.728	2.690	2.714	0.9	0.4	0.5

Note: The crush value refers to the performance index of the aggregate against crushing. It is used to measure the ability of the stone to resist crushing under the increasing load. The ratio of the weight of the crushed aggregate to the total weight of the sample is measured by a prescribed test method, expressed as a percentage.

Water and ethyl alcohol were used in the CAs tests with aggregates and solid asphalts, and the parameters are shown in Table 3.

**Table 3.** Parameters of the surface energy of water and ethyl alcohol.

Liquid Types	Surface ENERGY $\gamma_l/(10^{-3} \text{ J/m}^2)$	Dispersion Component of Surface Energy $\gamma_l^d/(10^{-3} \text{ J/m}^2)$	Polar Component of Surface Energy $\gamma_l^p/(10^{-3} \text{ J/m}^2)$
Water	72.8	21.8	51
Ethyl alcohol	48.3	29.3	19

## 2.2. Mixtures

Four HMAs were designed to investigate the water stability of the mixture. The aggregate used in the asphalt mixture was RCA and limestone, and the content of RCA in the aggregate was 0%, 30%, 60%, and 100%, respectively, which were marked as M1, M2, M3, and M4. To determine the optimal asphalt content of the above HMAs, the bulk relative density, Marshall stability and flow value, air voids, voids in mineral aggregate, and voids filled with asphalt were measured according to the Chinese Specification of JTG F40-2004 (RIOH, 2004) [33]. The results are listed in Table 4.

**Table 4.** Marshall indices of mixtures.

Mixture	Asphalt Content/%	Bulk Relative Density	VV/%	VMA/%	VFA/%	Effective Asphalt Content/%	Oil Absorbing Content/%	Stability/KN	Flow Value/0.1 mm
M1	3.57	2.462	4.4	12.21	63.97	3.45	0.12	11.2	23.5
M2	4.12	2.409	4.3	12.14	64.53	3.53	0.59	10.5	31.9
M3	5.12	2.335	4.3	12.99	66.76	4.04	1.08	9.8	30.1
M4	6.98	2.315	4.8	12.03	59.80	3.38	3.60	8.5	37.8
Limit value			3–6	$\geq 12.0$ (when VV = 4.0%)	55–70	-	-	$\geq 7.5$	15–40

Note: VV: air voids content; VMA: voids in mineral aggregate; VFA: voids filled with asphalt. According to the Chinese Specification of JTG F40-2004 (RIOH, 2004.) [33], the oil absorbing content can be calculated according to the density parameters of the aggregate, asphalt, and asphalt mixture.

## 3. Experimental Methods

### 3.1. CA between Aggregate and Solid Asphalt Tested with a CA Measurement Device

The CA is an important index that indicates the wetting ability of a liquid to solid. On the junction of the three phases of gas, liquid, and solid, the tangent lines of the interface between gas and liquid and those of the interface between solid and liquid can be obtained. The CA refers to the angle between two tangent lines through the liquid internal part. The smaller the CA is, the greater the wetting ability of the liquid to solid is. The CA between the asphalt and aggregate indirectly reflects the adhesion in the asphalt mixture, which is a basic parameter for calculating the adhesive energy.

This study used an optical CA measuring device that included a host computer, dosage controlling unit, an injecting unit, and a specific analysis software. The device is shown in Figure 1.

Several pictures can be captured per second with a measurement accuracy of  $\pm 0.1^\circ$ . Sessile drop method was selected instead of the hanging drop method or inclined plate method. In the chosen method, the droplets were dropped on the solid surface, two tangent lines were obtained, and the angle between these lines was measured. Six parallel experiments were performed for each test. The CAs among the droplets, several aggregates, and solid asphalts were surveyed using the abovementioned methods. Water and ethanol droplets were used in the experiment. The solids used in the experiment included limestone, granite, serpentine, RCA, and two solid asphalts (matrix and SBS-modified asphalts). The testing temperature was  $15^\circ\text{C}$ .

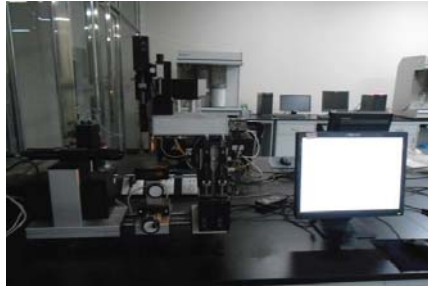


Figure 1. Optical CA measuring device.

An aggregate is usually a particulate and lacks a flat surface, which greatly influences the measurement of surface energy parameters. To improve the accuracy, stones with the same materials as those of the aggregates were polished using a metallographic polishing machine. Different types of the aggregate test pieces are shown in Figure 2. Asphalt is a solid with a viscous state below  $60^\circ\text{C}$  or at a normal temperature. Therefore, the test method for liquid materials cannot be used to survey the surface free energy of asphalt. First, a 1 mm-thick glass slide was used as a base plate, washed, and placed in an oven for drying at  $60^\circ\text{C}$  for 15 min. Second, the asphalt was heated to  $160^\circ\text{C}$  and sufficiently liquefied. Third, the prepared glass slide was immersed into the liquid asphalt, slowly removed, and completely adhered. The thicker portion of the asphalt was scraped off on the slide edge. Fourth, the glass slide was cooled at room temperature and stored in dry condition for more than 8 h.



Figure 2. Aggregate test piece.

### 3.2. CA between HMA and Aggregate Tested using the Hanging Slice Method

To calculate the adhesive energy between asphalt and aggregates, the CA between asphalt and aggregates must be determined. However, given the high viscosity properties, asphalt cannot be dropped to a solid surface even in a hot-melt state. Moreover, that the hot-melt asphalt will form a smooth surface on the solid surface cannot be ensured because of the favorable ductility of asphalt

and the easy formation of long tar silk. Therefore, the CA cannot be easily measured using the CA measurement device.

The hanging slice method was selected to measure the CA between hot-melt asphalt and aggregate. The testing principle is described as follows. Before the stone or aggregate touches the surface of hot-melt asphalt, the asphalt surface can be regarded as a horizontal plane. When the stone touches the asphalt surface, the hot-melt asphalt rises along with the stone to a certain distance because of the effect of surface energy and then forms a new asphalt surface, as shown in Figure 3. The testing temperature was 160 °C. The new asphalt surface tends to contract automatically, thereby leading to surface tension, which can be detected by using the dynamometer. The angle,  $\theta$ , between the direction of surface tension and the stone surface denotes the CA between the hot-melt asphalt and stone. The relationship of the surface energy of hot-melt asphalt ( $\gamma_a$ ), with the CA between the hot-melt asphalt and stone ( $\theta$ ) and the force value ( $N$ ), satisfies Equation (1) as follows:

$$\gamma_a \cos \theta = \frac{N - mg}{2(b + c)}, \tag{1}$$

where:

$\gamma_a$  is the surface energy of the hot-melt asphalt,  $10^{-3} \text{ J/m}^2$ .

$\theta$  is the CA between the hot-melt asphalt and aggregate, °;

$N$  is the force value, N;

$m$  is the weight of the stone plate, g; and

$b$  and  $c$  are the length and width of aggregate, respectively, cm.

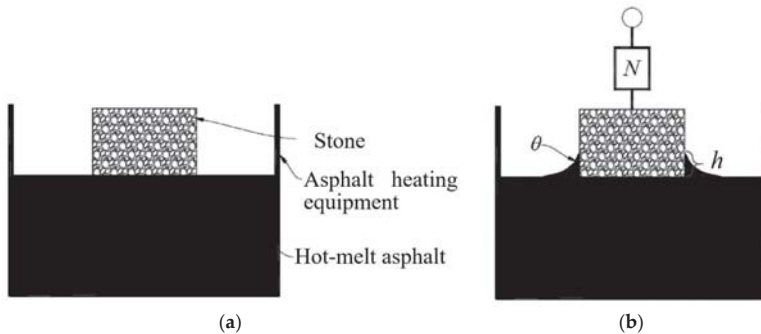


**Figure 3.** The hanging slice method: (a) Before the stone touches the liquid asphalt; (b) After the stone touches the liquid asphalt.

### 3.3. The Calculation Method of Surface Free Energy and CA

Young equation [34] can be used to describe the relationship between the CA and surface free energy between the solid-liquid interface:

$$\gamma_s - \gamma_{sl} = \gamma_l \cos \theta, \tag{2}$$

where  $\gamma_s$ ,  $\gamma_{sl}$ , and  $\gamma_l$  are the surface free energies of the solid, solid-liquid interface, and liquid, respectively, N; and  $\theta$  is the CA between the solid-liquid interface, °.

The adhesive energy in the adhesion process is equal to the variation of the Gibbs free energy per unit surface area, which can be calculated as follows. We can use the variation of the Gibbs free energy

per unit surface area to describe the adhesive energy between the aggregate and the asphalt during the adhesion process. The formula is as follows:

$$W_a = -\Delta G = \gamma_l - \gamma_{sl} + \gamma_s, \quad (3)$$

The adhesive energy can be calculated as follows according to Equations (2) and (3):

$$W_a = -\Delta G = \gamma_l(\cos \theta + 1), \quad (4)$$

The adhesive energy between asphalt and aggregate can be thought to be composed of two parts, namely, the dispersion component and polar component when combining van der Waals force theory and Lewis theory on acid and alkali, as well as by ignoring the small force between the molecules:

$$W_a = 2\sqrt{\gamma_s^d \gamma_l^d} + 2\sqrt{\gamma_s^p \gamma_l^p}, \quad (5)$$

where  $\gamma_l^d$  and  $\gamma_l^p$  are the dispersion and polarity components (acid-alkali effect) of the surface free energy of liquid, respectively;  $\gamma_s^d$  and  $\gamma_s^p$  are the dispersion and polarity components (acid-alkali effect) of the surface free energy of solid, respectively.

According to Equations (4) and (5), the adhesive energy can be calculated as follows:

$$W_a = \gamma_l(\cos \theta + 1) = 2\sqrt{\gamma_s^d \gamma_l^d} + 2\sqrt{\gamma_s^p \gamma_l^p}, \quad (6)$$

### 3.4. Water Stability Test

Residual Marshall stability (RMS) is among the indices used to evaluate the water stability of an asphalt mixture. A large RMS value indicates the favorable water stability of asphalt mixtures. For each mixture type, eight specimens measuring  $\Phi 101.6 \text{ mm} \times 63.5 \text{ mm}$  were fabricated with 75 times of two-face compaction. These specimens were divided into two groups. The stability of the first group,  $MS_0$ , was tested after being immersed in a  $60^\circ \text{C}$  water bath for 30 min to 40 min, whereas the stability of the second group,  $MS_1$ , was tested after being immersed in a  $60^\circ \text{C}$  water bath for 48 h. The immersion RMS was then calculated using Equation (7). The evaluation method is similar to that specified in ASTM D 1559 (Determining the Marshall Stability of Bituminous Mixture):

$$\text{RMS} = \frac{MS_1}{MS_0} \times 100, \quad (7)$$

where:

RMS is the residual Marshall stability, %;

$MS_1$  is the stability after 48 h immersion, kN; and

$MS_0$  is the stability after 30 min immersion, kN.

TSR is another index for evaluating the water stability of asphalt mixture. A large TSR value indicates the favorable water stability of asphalt mixtures. For each mixture type, eight specimens measuring  $\Phi 101.6 \text{ mm} \times 63.5 \text{ mm}$  were fabricated with 50 times of two-face compaction. The specimens of group 1 were saturated under a 730 mm Hg vacuum condition for 15 min, placed in sealed plastic bags containing 10 mL water, placed in a refrigerator with a constant temperature of  $-18^\circ \text{C}$  for 16 h, taken out of the plastic bags, and immersed in a  $60^\circ \text{C}$  water bath for 24 h. The specimens of both groups 1 and 2 were then tested to obtain their tensile strength after being immersed in a  $25^\circ \text{C}$  water bath for 2 h. TSR was calculated with Equation (8). Although this testing method is similar to that specified in AASHTO T 283-03 (Standard Method of Test for Resistance

of Compacted Asphalt Mixtures to Moisture-Induced Damage), the experiment parameters were slightly different:

$$TSR = \frac{ITS_1}{ITS_0} \times 100, \tag{8}$$

where:

TSR is the tensile strength ratio, %;

ITS<sub>0</sub> is the tensile strength without freeze-thaw circles, MPa; and

ITS<sub>1</sub> is the tensile strength under freeze-thaw circles, MPa.

### 3.5. Fatigue Test

According to the Chinese Specification of JTG E20-2011 (RIOH, 2011) [35], granite, serpentinite, limestone, and RCA were used as aggregates, 300 mm long, 300 mm wide, and 50 mm thick and were prepared by a wheel roller forming instrument. When the temperature of the test piece dropped to room temperature, it was cut into standard trabecular test pieces with a length of 250 mm, a width of 30 mm, and a thickness of 35 mm. In order to calculate the corresponding load at each stress level in the fatigue test, the trabecular bending test was carried out. The loading speed was 10 mm/min, and the maximum load of the standard trabecular test piece was obtained. The aggregate types and numbers of different asphalt mixtures are shown in Table 5. Mechanical testing and simulation (MTS) was adopted to test the fatigue performance of the HMA-RCA specimens under the stress-control mode. Three stress levels were used, which were 80%, 75%, and 70% of the maximum load, respectively. The loading frequency was 15 Hz, and the testing temperature was 15 °C. The MTS and standard trabecular test pieces are shown in Figures 4 and 5.

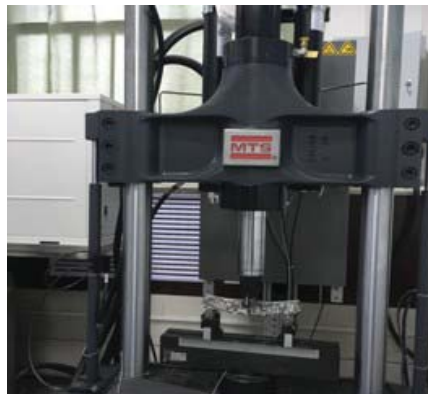


Figure 4. MTS Landmark (MTS 810).

Table 5. Aggregate types and numbers of different asphalt mixtures.

Aggregate Type	Granite			Serpentinite			Limestone			RCA
RCA content/%	60	30	0	60	30	0	60	30	0	100
Number	F1	F2	F3	F4	F5	F6	F7	F8	F9	F10



Figure 5. Standard trabecular test pieces.

#### 4. Results and Discussion

##### 4.1. CA and Surface Energy Parameters of Aggregates and Solid Asphalt

###### 4.1.1. CA

The CAs among the aggregates, solid asphalts, water, and ethanol were tested using a CA measurement device. Table 6 presents the results, from which the following can be deduced. The CAs among various aggregates and water are sorted as follows: Limestone > serpentinite > RCA > granite. The CA between the RCA with water is very close to that of serpentinite. The CA between asphalt and water is close to 90°, which indicates that water and asphalt are two different materials with poor compatibility and the water shows a stronger polarity than asphalt. Considering the opposite polarity of water and asphalt, those materials with favorable wettability to water show a poor wettability to asphalt. The experiment results indicate that water has the best wettability to granite and the worst wettability to limestone. From this, it can be inferred that limestone has the best wettability to asphalt. Serpentinite and RCA have a moderate level of wettability to asphalt.

Table 6. CA results of Aggregates and solid asphalts.

Types of Aggregates and Solid Asphalts	Testing Liquid	
	Water	Ethyl Alcohol
Limestone	39.719	43.002
Granite	16.791	35.903
Serpentine	30.167	40.076
RCA	27.273	39.543
Matrix asphalt	93.649	74.269
SBS modified asphalt	84.163	71.924

###### 4.1.2. Surface Free Energy

According to the parameters of the surface energy of water and ethanol (Table 3) and the CAs between aggregates and asphalts (Table 6), the surface energy parameters between various solid bitumens and aggregates can be solved with Equation (8), as shown in Table 7. The results indicate the following:

- (1) The polar components comprise the main part of the surface energy of various aggregates and are much greater than the dispersion components. The surface energy of aggregates is sorted as follows: Granite > RCA > serpentinite > limestone.



- (2) The surface energy of the modified asphalt is greater than that of the matrix asphalt.

**Table 7.** Surface energy of aggregates and solid asphalts.

Types of Aggregates and Solid Asphalts	$\gamma_s^d/(10^{-3} \text{ J/m}^2)$	$\gamma_s^p/(10^{-3} \text{ J/m}^2)$	$\gamma_s = \gamma_s^p + \gamma_s^d/(10^{-3} \text{ J/m}^2)$
Limestone	0.955	70.202	71.16
Granite	0.008	98.397	98.40
Serpentine	0.221	84.579	84.80
RCA	0.099	88.760	88.86
Matrix asphalt	14.901	5.057	19.96
SBS modified asphalt	7.817	14.344	22.16

#### 4.2. CA between Liquid Asphalt and Aggregate

Table 8 present the test results of CAs between hot-melt asphalt and aggregate. The results indicate the following:

- (1) A small CA indicates the good wettability of asphalt to aggregate. The CA between various aggregates and the same melt-asphalt is sorted as follows: Granite > RCA > serpentine > limestone. The surface energy and CA of RCA and serpentine are very similar to each other.
- (2) The CA between the SBS-modified asphalt and the aggregate is greater than that of the matrix asphalt because decreasing the light oil content in modified asphalt decreases its infiltration property, thereby increasing the CA of modified asphalt.

**Table 8.** CA between liquid asphalt and aggregate.

Aggregates	Matrix Asphalt	SBS Modified Asphalt
Limestone	25.182	28.925
Granite	32.515	40.810
Serpentine	26.916	30.094
RCA	29.192	32.948

It can be seen from the CA test that the CAs between different aggregates and water or asphalt were different. This may be due to the different chemical composition of the different aggregates. Related studies have shown that the CA between asphalt and aggregate has a close relationship with the content of elements, such as Si, Al, Ca, and Mg, on the aggregate surface, and the composition of the chemical composition determines the acidity and basicity of the aggregate to a certain extent, thereby affecting the chemical reaction with the asphalt.

Limestone has a high content of Ca and Mg, a low SiO<sub>2</sub> content, an alkaline aggregate, the surface is easily infiltrated by asphalt, and its CA is lower with asphalt, while granite is the opposite, the SiO<sub>2</sub> is high and an acidic aggregate, so the same acidic asphalt is difficult to infiltrate. Although RCA has a complex chemical composition, the RCA surface contains a small amount of cement hydration products, including CSH, ettringite, monosulfide-type sulphoaluminate, and Ca(OH)<sub>2</sub>. These components have a certain activity and can cause weak chemical reactions with acidic asphalt. Therefore the CA between RCA and asphalt is between limestone and granite.

#### 4.3. Adhesive Energy between Asphalt and Aggregate

According to the parameters of the surface energy of asphalt (Table 7) and the CAs between aggregates and liquid asphalts (Table 8), the adhesive energy of liquid asphalts and aggregates can be calculated with Equation (8), as shown in Table 9. The results indicate the following:

- (1) A great adhesive energy indicates the excellent adhesion between aggregate and asphalt. When the same asphalt is used, the adhesive energy of different aggregates is sorted as follows:

Limestone > serpentine > RCA > granite. The adhesion between RCA and asphalt is similar to that of serpentine.

- (2) The adhesive energy between modified asphalt and aggregate is greater than that of matrix asphalt because the SBS-modified asphalt has a high surface free energy.

**Table 9.** Adhesion energy between asphalt and aggregate.

Aggregates	Matrix Asphalt	SBS Modified Asphalt
Limestone	38.020	41.559
Granite	36.789	38.935
Serpentine	37.755	41.336
RCA	37.382	40.759

#### 4.4. Water Stability and Fatigue Performance

##### 4.4.1. Water Stability

The adhesive energy between RCA and asphalt is less than that of serpentine according to the results of CA and adhesive energy. Therefore, the water stability of HMA-RCAs are worse than those of the traditional mixture. Figure 6 shows the RMS results of the four HMA-RCAs. The RMS values of M1, M2, M3, and M4 are 89.4%, 86.2%, 84.3%, and 81.3%, respectively. The RMS of HMA-RCAs decreases gradually as the RCA content increases because the adhesive energy between asphalt and RCA is less than that of limestone, and the CA between RCA and asphalt is greater than that of water. So, the asphalt spalls more easily from the RCA surface under water, resulting in a decrease in water stability of the asphalt mixture.

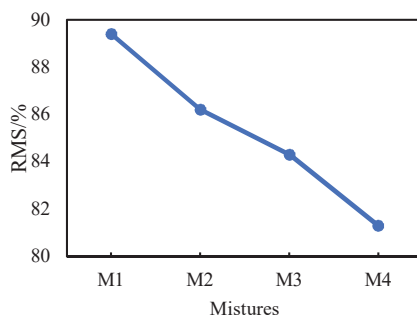


**Figure 6.** RMS Results.

Figure 7 shows the TSR results. The TSR values of M1, M2, M3, and M4 are 80.2%, 80.6%, 78.6%, and 77.0%, respectively. The TSR of HMA-RCAs gradually decreases as the RCA content increases, which varies with the same law as that of RMS. When the RCA content is increased, the water stability of the asphalt concrete is generally weakened. However, it can be found from the TSR test results that when the RCA content was increased from 0% to 30%, the water stability of asphalt concrete was slightly increased by 0.4%, which may be due to experimental errors.

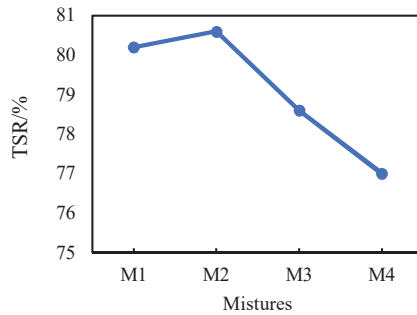


Figure 7. TSR Results.

4.4.2. Fatigue Performance

Table 10 shows the fatigue test result of HMA-RCA. It can be seen from Table 10 that as the stress level increases, the fatigue life of all standard trabecular specimens decreases rapidly. Moreover, as the RCA dosage increases, the fatigue life of the test piece also decreases significantly. When the content of RCA (F10) is 100%, the fatigue life of the test piece is only 30% of that of the ordinary aggregate test piece (F3; 6; 9). The fatigue life of standard trabecular specimens with different granite, serpentinite, limestone, and RCA contents under different stress levels is shown in Figure 8.

Table 10. Results of the fatigue life.

Stress Level	Fatigue Life/(cycle)									
	F1	F2	F3	F4	F5	F6	F7	F8	F9	F10
0.8	6124	8012	13254	5698	10320	12124	6917	9987	12798	3587
0.75	8945	9648	13715	6796	11230	14561	7523	11245	15243	4532
0.7	12345	17269	20147	11026	17865	21453	16248	17742	22178	5901

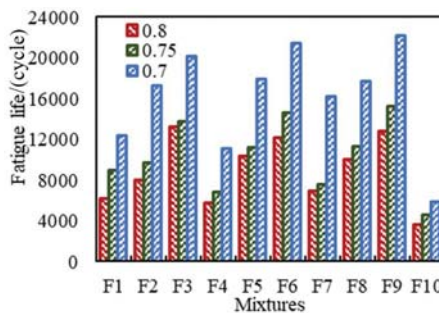


Figure 8. Curves of the fatigue life.

The adhesion of aggregate and asphalt, and the aggregate strength characteristics and the porosity of asphalt mixture are the main factors affecting the fatigue performance of asphalt mixture. It can be concluded from Figure 8 that the fatigue life of the test pieces with the aggregate as limestone (F7–9) is higher, the serpentinite (F4–6) is the second highest, and the fatigue life of the specimen with granite (F1–3) is the lowest, regardless of the load level. This phenomenon is mutually confirmed by the results of the CA test and adhesion energy calculation between different aggregates and asphalt. From the above test results, limestone has the best adhesion to asphalt, followed by serpentine and granite. This is because when the adhesion between the aggregate and the asphalt decreases, the intermolecular van der Waals force on the surface of the asphalt and stone decreases, and the

asphalt mixture loosens, resulting in a decrease in the shear strength and bond strength of the asphalt mixture, ultimately leading to a decrease in fatigue performance.

It can be seen from the test results that although the CA and adhesion energy of RCA are very similar to the CA and adhesion energy of serpentine, when the RCA content in the aggregate increased, the fatigue life of the test pieces were significantly reduced, and when the RCA content was 100%, the fatigue life of the test pieces were the lowest. This is because, in addition to adhesion, the strength characteristics of the aggregate and the void ratio of the asphalt mixture also affect the fatigue performance. From the test results of the aggregate crushing values in Table 2, it can be known that the fatigue performance of the test pieces was poor due to the insufficient compressive strength of the RCA, which was easily destroyed during the fatigue performance test process. Referring to Table 4, as the RCA content increases, the porosity of the asphalt mixture also increases. The high air voids' content causes this to reduce the fatigue life of the test piece.

## 5. Conclusions

The polar component was the major part of the surface energy of aggregates and was much greater than the dispersion component. The surface energy of aggregates was sorted as follows: Granite > RCA > serpentine > limestone.

The CA between various aggregates and the same melt-asphalt was sorted as follows: Granite > RCA > serpentine > limestone. The CA of RCA and serpentinite were very close, and activation can reduce the CA and improve wettability. When the same asphalt was used, the adhesive energy of different aggregates was sorted as follows: Limestone > serpentine > RCA > granite. The adhesion between RCA and asphalt was the same as that of serpentinite.

The RMS and TSR of HMA-RCAs decrease gradually as the RCA content increases because the adhesive energy between RCA and asphalt was less than that of water. The water stability of HMA-RCAs was closely related to the CA and adhesive energy between RCA and asphalt. A small CA and great adhesive energy indicated good water stability.

The variation law of the fatigue performance of HMA-RCAs along with RCA content was determined by the interaction of the adhesion and porosity effects. Although the CA and adhesion energy between RAC and asphalt was similar to that of serpentine, the porosity of asphalt concrete increases with the increase of RCA. Therefore, when the aggregate contains more RCA, the fatigue performance of the HMA-RCA will decrease.

**Author Contributions:** Conceptualization, Y.H.; Formal Analysis, Y.H. and X.J.; Project Administration, X.J.; Writing—Original draft, X.J. and J.L.; Writing—Review & Editing, X.L.

**Funding:** This study was supported in part by the Natural Science Foundation of Shaanxi Province under Project Nos. 2017JM5034, 2017JQ5030 & 2016KW-044, and the Scientific Research of Central Colleges of China for Chang'an University under Project Nos. 310821172008 & 310821171113.

**Conflicts of Interest:** The authors declare that they have no conflict of interest.

## References

1. Zhang, Y.; Guo, Q.; Li, L.; Jiang, P.; Jiao, Y.; Cheng, Y. Reuse of Boron waste as an additive in road base material. *Materials* **2016**, *9*, 416. [[CrossRef](#)] [[PubMed](#)]
2. Arshad, M.; Ahmed, M.F. Potential use of reclaimed asphalt pavement and recycled concrete aggregate in base/subbase layers of flexible pavements. *Constr. Build. Mater.* **2017**, *151*, 83–97. [[CrossRef](#)]
3. Kim, S.; Ceylan, H.; Gopalakrishnan, K.; White, D.J.; Jahren, C.T.; Phan, T.H. Comparative performance of concrete pavements with recycled concrete aggregate (RCA) and virgin aggregate subbases. In *Transportation and Development Institute Congress 2011: Integrated Transportation and Development for a Better Tomorrow*; American Society of Civil Engineers: Reston, VA, USA, 2011; pp. 710–719.
4. Cho, Y.-H.; Yun, T.; Kim, I.T.; Choi, N.R. The application of Recycled Concrete Aggregate (RCA) for Hot Mix Asphalt (HMA) base layer aggregate. *KSCE J. Civ. Eng.* **2011**, *15*, 473–478. [[CrossRef](#)]

5. Pasandín, A.R.; Pérez, I. Overview of bituminous mixtures made with recycled concrete aggregates. *Constr. Build. Mater.* **2015**, *74*, 151–161. [CrossRef]
6. Pasandín, A.R.; Pérez, I. Mechanical properties of hot-mix asphalt made with recycled concrete aggregates coated with bitumen emulsion. *Constr. Build. Mater.* **2014**, *55*, 350–358. [CrossRef]
7. Wang, F.; Wang, Z.; Li, C.; Xiao, Y.; Wu, S.; Pan, P. The rejuvenating effect in hot asphalt recycling by mortar transfer ratio and image analysis. *Materials* **2017**, *10*, 574. [CrossRef] [PubMed]
8. Andrzejuk, W.; Barnat-Hunek, D.; Siddique, R.; Zegardlo, B.; Lagod, G. Application of recycled ceramic aggregates for the production of mineral-asphalt mixtures. *Materials* **2018**, *11*, 658. [CrossRef]
9. Hou, Y.; Ji, X.; Su, X.; Zhang, W.; Liu, L. Laboratory investigations of activated recycled concrete aggregate for asphalt treated base. *Constr. Build. Mater.* **2014**, *65*, 535–542. [CrossRef]
10. Wong, Y.D.; Sun, D.D.; Lai, D. Value-added utilisation of recycled concrete in hot-mix asphalt. *Waste Manag.* **2007**, *27*, 294–301. [CrossRef]
11. De Farias, M.M.; Sinisterra, F.Q. Influence of asphalt rubber on the crushing of recycled aggregates used in dense HMA. Available online: [http://www.ra-foundation.org/wp-content/uploads/2013/02/044-PAP\\_049.pdf](http://www.ra-foundation.org/wp-content/uploads/2013/02/044-PAP_049.pdf) (accessed on 14 November 2018).
12. Pasandín, A.R.; Pérez, I. Laboratory evaluation of hot-mix asphalt containing construction and demolition waste. *Constr. Build. Mater.* **2013**, *43*, 497–505. [CrossRef]
13. Mills-Beale, J.; You, Z. The mechanical properties of asphalt mixtures with Recycled Concrete Aggregates. *Constr. Build. Mater.* **2010**, *24*, 230–235. [CrossRef]
14. Tahmoorian, F.; Samali, B.; Yeaman, J.; Crabb, R. The use of glass to optimize bitumen absorption of hot mix asphalt containing recycled construction aggregates. *Materials* **2018**, *11*, 1053. [CrossRef] [PubMed]
15. Bhusal, S.; Li, X.; Wen, H. Evaluation of effects of recycled concrete aggregate on volumetrics of HMA. *Transp. Res. Rec.* **2011**, *2205*, 36–39.
16. Juan, M.S.D.; Gutiérrez, P.A. Study on the influence of attached mortar content on the properties of recycled concrete aggregate. *Constr. Build. Mater.* **2009**, *23*, 872–877. [CrossRef]
17. Shen, D.H.; Du, J.C. Application of gray relational analysis to evaluate HMA with reclaimed building materials. *J. Mater. Civ. Eng.* **2005**, *17*, 400–406. [CrossRef]
18. Rafi, M.M.; Qadir, A.; Siddiqui, S.H. Experimental testing of hot mix asphalt mixture made of recycled aggregates. *Waste Manag. Res.* **2011**, *29*, 1316–1326. [CrossRef]
19. Paranavithana, S.; Mohajerani, A. Effects of recycled concrete aggregates on properties of asphalt concrete. *Resour. Conserv. Recycl.* **2006**, *48*, 1–12. [CrossRef]
20. Pérez, I.; Toledano, M.; Gallego, J.; Taibo, J. Mechanical properties of hot mix asphalt made with recycled aggregates from reclaimed construction and demolition debris. *Mater. De Constr.* **2007**, *57*, 17–29.
21. Pérez, I.; Pasandín, A.R.; Gallego, J. Stripping in hot mix asphalt produced by aggregates from construction and demolition waste. *Waste Manag. Res.* **2012**, *30*, 3–11. [CrossRef]
22. Pérez, I.; Pasandín, A.R.; Medina, L. Hot mix asphalt using C&D waste as coarse aggregates. *Mater. Des.* **2012**, *36*, 840–846.
23. Wu, S.; Zhong, J.; Zhu, J.; Wang, D. Influence of demolition waste used as recycled aggregate on performance of asphalt mixture. *Road Mater. Pavement Des.* **2013**, *14*, 679–688. [CrossRef]
24. Zhu, J.; Wu, S.; Zhong, J.; Wang, D. Investigation of asphalt mixture containing demolition waste obtained from earthquake-damaged buildings. *Constr. Build. Mater.* **2012**, *29*, 466–475. [CrossRef]
25. Taibo, J.; Pérez, I.; Gallego, J.; Toledano, M. Asphalt mixtures with construction and demolition debris. *Transport* **2010**, *163*, 165–174.
26. Pérez, I.P.; Pasandín, A.R.; Gallego, J. Impact of Construction and Demolition Waste Aggregates on Stripping in Hot Mix Asphalt. Available online: [https://www.researchgate.net/profile/Ignacio\\_Perez\\_Perez/publication/317345265\\_Impact\\_of\\_Construction\\_and\\_Demolition\\_Waste\\_Aggregates\\_on\\_Stripping\\_in\\_Hot\\_Mix\\_Aspphalt/links/59351a7445851553b6eea4b4/Impact-of-Construction-and-Demolition-Waste-Aggregates-on-Stripping-in-Hot-Mix-Asphalt.pdf](https://www.researchgate.net/profile/Ignacio_Perez_Perez/publication/317345265_Impact_of_Construction_and_Demolition_Waste_Aggregates_on_Stripping_in_Hot_Mix_Aspphalt/links/59351a7445851553b6eea4b4/Impact-of-Construction-and-Demolition-Waste-Aggregates-on-Stripping-in-Hot-Mix-Asphalt.pdf) (accessed on 14 November 2018).
27. Chen, M.; Lin, J.; Wu, S. Potential of recycled fine aggregates powder as filler in asphalt mixture. *Constr. Build. Mater.* **2011**, *25*, 3909–3914. [CrossRef]
28. Gul, W.A.; Guler, M. Rutting susceptibility of asphalt concrete with recycled concrete aggregate using revised Marshall procedure. *Constr. Build. Mater.* **2014**, *55*, 341–349. [CrossRef]

29. Zulkati, A.; Wong, Y.D.; Sun, D.D. Mechanistic performance of asphalt-concrete mixture incorporating coarse recycled concrete aggregate. *J. Mater. Civ. Eng.* **2013**, *25*, 1299–1305. [[CrossRef](#)]
30. Pourtahmasb, M.S.; Karim, M.R.; Shamsirband, S. Resilient modulus prediction of asphalt mixtures containing Recycled Concrete Aggregate using an adaptive neuro-fuzzy methodology. *Constr. Build. Mater.* **2015**, *82*, 257–263. [[CrossRef](#)]
31. Ministry of Transport. *Standard Test Methods of Bitumen and Bituminous Mixtures for Highway Engineering: JTG E20-2000*; China Communications Press: Beijing, China, 2000.
32. Ministry of Transport. *Standard Test Methods of Aggregate for Highway Engineering: JTG E42-2005*; China Communications Press: Beijing, China, 2005.
33. Ministry of Transport. *Technical Specification for Construction of Highway Asphalt Pavements: JTG F40-2004*; China Communications Press: Beijing, China, 2004.
34. Tan, Y.; Guo, M. Using surface free energy method to study the cohesion and adhesion of asphalt mastic. *Constr. Build. Mater.* **2013**, *47*, 254–260. [[CrossRef](#)]
35. Ministry of Transport. *Standard Test Methods of Bitumen and Bituminous Mixtures for Highway Engineering: JTG E20-2011*; China Communications Press: Beijing, China, 2011.



© 2018 by the authors. Licensee MDPI, Basel, Switzerland. This article is an open access article distributed under the terms and conditions of the Creative Commons Attribution (CC BY) license (<http://creativecommons.org/licenses/by/4.0/>).

Article

# Effects of Cement and Emulsified Asphalt on Properties of Mastics and 100% Cold Recycled Asphalt Mixtures

Yanan Li <sup>1</sup>, Yuchao Lyv <sup>1</sup>, Liang Fan <sup>2</sup>  and Yuzhen Zhang <sup>1,\*</sup>

<sup>1</sup> College of Chemical Engineering, China University of Petroleum, Qingdao 266580, Shandong Province, China; liyanan@s.upc.edu.cn (Y.L.); B15030098@s.upc.edu.cn (Y.L.)

<sup>2</sup> Road Engineering Laboratory, Shandong Transportation Research Institute, Jinan 250000, Shandong Province, China; fanliang@sdjtky.cn

\* Correspondence: zhangyuzhen1959@163.com; Tel.: +86-13801017308

Received: 26 January 2019; Accepted: 28 February 2019; Published: 5 March 2019

**Abstract:** Cold recycled asphalt mixtures (CRAM) are a cost-effective and environmentally-friendly way to reuse reclaimed asphalt pavement (RAP). This paper evaluates the rheological properties and microstructure of mineral filler-asphalt mastic, mineral filler-residue mastic, and cement-residue mastic. Then, based on the premise of using 100% RAP with a gradation that was determined experimentally, the effects of emulsified asphalt and cement on the porosity, indirect tensile strength, tensile strength ratio, dynamic stability, and mechanical properties of CRAM were evaluated. It was found that the rheological properties and cohesive coefficient of the cement-residue mastic varied differently to those of the first two types of mastic and the results show that the addition of cement can greatly improve the interfacial bonding between binders and fillers in the mastic, thereby improving the water damage resistance and high-temperature stability of CRAM. The relationships between cement content and the dynamic modulus and phase angle of CRAM are different to that for emulsified asphalt obviously. In addition, under certain conditions, the properties of CRAM can meet the requirements of relevant technical specifications for its application to subsurface layer of pavement. Hence, the use of 100% RAP in CRAM may be feasible.

**Keywords:** cold recycled asphalt mixture; reclaimed asphalt pavement; mastic; rheological properties; emulsified asphalt; cement

## 1. Introduction

Asphalt pavement is subject to aging, and many pavements require servicing after 10–20 years. In order to ensure the performance and safety of roads, many pavements need to be rebuilt, resulting in the production of tens of thousands of tons of reclaimed asphalt pavement (RAP) each year. Therefore, discovering ways of making better use of RAP is important [1,2].

Reclaimed materials have been used in pavement construction for years. Nowadays, RAP's use is increasing rapidly with the advancement of material processing equipment and mix design technologies [3]. Much research has focused on the use of RAP in hot recycled asphalt mixture (HRAM) [4–6]. It has been proven that HRAM with RAP contents of 10% to 30% perform similarly to virgin hot-mix asphalt mixture (HMA) [7,8]. However, due to its higher mixing temperature, it has a shorter period in which it can be used for construction during the year. Additionally, it has high fuel consumption and produces many toxic fumes during the paving process, which are not conducive to energy conservation, emission reduction, and environmental protection. Unlike HRAM, cold recycled asphalt mixture (CRAM) can further solve the above problems to a large extent [9]. With the increasing

concerns of energy conservation and environmental protection, CRAM has been increasingly applied for pavement rehabilitation.

CRAM is regarded as a semi-flexible material, which is different from cement concrete and HMA. CRAM has lower fatigue life as compared with ordinary HMA, especially at high strain mode and high stress model [10]. Cement, lime, and fly ash are increasingly used as additives to improve the properties of CRAM [11–14]. More and more research has focused on the design and performance evaluation of CRAM [15–18]. Despite this, there are few studies on the properties of CRAM when their aggregate gradation uses 100% RAP and no new aggregate is added. Therefore, this paper investigated the influences of emulsified asphalt and cement contents on the properties of CRAM, such as porosity, indirect tensile strength (ITS), freeze–thaw splitting strength ratio, and dynamic modulus, with gradations using 100% RAP.

Asphalt pavement material can be seen as a multi-level distributed system with a spatial network structure. This multi-level dispersion system consists of three levels: a micro-dispersion system (mastic) in which the fillers are dispersed in the asphalt binder, a fine-dispersion system (mortar) in which the fine aggregates are dispersed in the mastic, and a coarse-dispersion system in which the coarse aggregates are dispersed in the mortar. As the first level of micro-dispersion system in the complex composition of pavement materials, the mastic's microstructure and characteristics have important impacts on pavement performance. Therefore, this paper first evaluated and studied the microstructure and characteristics of three types of mastic before evaluating the various properties of CRAM.

## 2. Materials and Methods

### 2.1. Materials

#### 2.1.1. Emulsified Asphalt

Cationic slow-setting emulsified asphalt was prepared by colloidal mill with matrix asphalt binder (SsangYong Brand, South Korean) and cationic emulsifier in laboratory. The specified cationic emulsifier for cold recycled pavement was obtained from Paini Chemical Co., Ltd., Binzhou, China. The properties of the matrix asphalt and emulsified asphalt are presented in Tables 1 and 2, respectively.

**Table 1.** Properties of matrix asphalt.

Parameter	Requirements	Results
Penetration (25 °C; 0.1 mm)	60–80	66
Softening point (°C)	≤46	47.0
Dynamic viscosity (60 °C; Pa·s)	≤180	258
Ductility (10 °C; cm)	≤20	76
Ductility (15 °C; cm)	≤100	>100
Wax content (%)	≥2.2	1.7
Flashing point (°C)	≤260	320
Solubility (%)	≤99.5	99.9
Density (15 °C; g/cm <sup>3</sup> )	Report	1.035
Mass change (%)	±0.8	−0.022
Thin film oven test	Residual penetration ratio (%)	≤61
	Residual ductility (10 °C; cm)	≤6
		71
		19

**Table 2.** Properties of emulsified asphalt.

Parameter	Requirements [19]	Results
Residue content by evaporation (%)	≤62	63
Sieve residue (1.18 mm; %)	≥0.1	0
Storage stability (5 d, 25 °C; %)	≥5	4
Storage stability (1 d, 25 °C; %)	≥1	0.9
Residual asphalt	Penetration (25 °C; 0.1 mm)	50–300
	Ductility (15 °C; cm)	≤40
		75
		>100



## 2.1.2. RAP

The characteristics of RAP have very important impacts on the performance of the mixture. In this study, RAP was collected from the overhaul milling materials of the Qingdao Jiaozhou Bay Highway. The RAP was sieved according to JTG E42-2005 (Test Methods of Aggregate for Highway Engineering) [20] in order to understand its particle size distribution. The results are listed in Table 3. The maximum and minimum values refer to the range of medium-size gradation for CRAM in JTG F41-2008 (Technical Specifications for Highway Asphalt Pavement Recycling) [19].

Table 3. Results of sieving for RAP

Sieve Size (mm)	0.075	0.15	0.3	0.6	1.18	2.36	4.75	9.5	13.2	16	19	26.5
Passing percent	0.87	1.29	1.86	3.09	4.35	6.95	14.9	44.1	64.3	79.4	91.7	100
PP-AE	6.11	7.60	10.1	13.6	21.2	31.9	61.7	74.6	79.1	89.1	98.2	100
Maximum	8	—	21	—	—	50	65	80	—	—	100	100
Minimum	2	—	3	—	—	20	35	60	—	—	90	100
Experimental gradation	3	4	6	9	15	27	50	74	85	92	97	100

As shown in Table 3, the mineral filler and fine aggregate contents were very low. The RAP was then subject to an extraction test and rescreened. The results are presented in Table 3, where PP-AE represents the passing percent after extraction. Compared to the initial RAP gradation, the gradation of RAP after extraction testing was lower, and the mineral filler and fine aggregate contents apparently increased. Furthermore, the microstructure of RAP was investigated by fluorescence microscopy (FM), as shown in Figure 1.

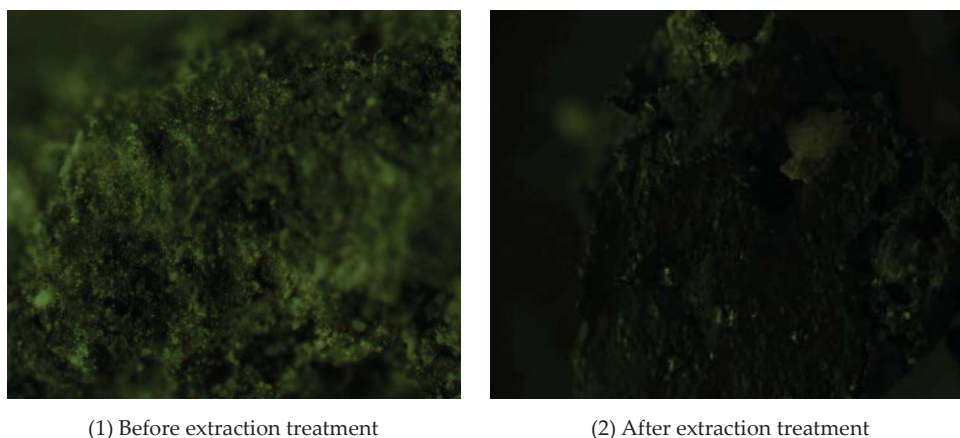


Figure 1. Fluorescence microscopic images of RAP.

It can be seen that a large amount of mineral filler and fine aggregate was wrapped around the asphalt in the RAP before extraction treatment. After the extraction, the above-mentioned mineral filler and fine aggregates all peeled off from the surface of the RAP. This may explain the lack of fine aggregates in the gradation before the extraction experiment.

The experimental gradation was determined by considering the distribution of particle size in RAP and the specification of the medium-size gradation for CRAM in JTG F41-2008. It should be emphasized that the experimental gradation selected in this article used 100% RAP without any new aggregates being added, as shown in Table 3.

To minimize the influences of gradation differences on the experimental results, the RAP was firstly sieved to 12 grades by a sieve shaker, from 0.075 mm to 26.5 mm. The RAP samples were stored separately by size and later combined into an experimental aggregate of the desired gradation according to the percentage passing each sieve.

### 2.1.3. Recycled Asphalt from RAP

The recycled asphalt was extracted from RAP, and its properties are listed in Table 4. It can be seen that the penetration of recycled asphalt was 20 and the ductility was only 34.5 cm, which indicates that the asphalt was seriously aged. Despite this, it still has an important impact on the diffusion process of newly added asphalt binder [21].

**Table 4.** Properties of recycled asphalt

Parameter	Results
Penetration (25 °C; 0.1 mm)	20
Softening point (°C)	65
Ductility (25 °C; cm)	34.5
Dynamic viscosity (60 °C; Pa·s)	544

### 2.1.4. Cement

For CRAM, cement is commonly used to promote demulsification of emulsified asphalt and to increase the initial strength [22]. Ordinary Portland cement (PO. 32.5; Shanshui Brand, Sunnsy Group, Jinan, , China) was used in this study. Only the part of cement that can pass at the 0.075 mm sieve were used to make cement-residue mastic.

### 2.1.5. Mineral Filler

In this study, limestone mineral fillers from five different areas (Pingyin, Longqing, Rilan, Changle, and Dongqing) were used, and labeled 1#, 2#, 3#, 4#, and 5#, respectively. Density, hydrophilicity coefficient (H-C), and methylene blue value (MBV) tests were carried out on the five kinds of mineral filler. The results are shown in Table 5.

**Table 5.** Properties of the mineral fillers

Parameter	1#	2#	3#	4#	5#
Density (g·cm <sup>-3</sup> )	2.673	2.657	2.618	2.711	2.683
H-C	0.671	0.685	0.652	0.752	0.69
MBV (g/kg)	1	2.25	2.75	2.5	0.75

It can be seen that the density and H-C of the five limestone mineral fillers are not much different, but their MBVs have obvious differences. The MBVs of 2#, 3#, and 4# are significantly larger than those of 1# and 5#, indicating that the first three fillers contain more expansive clay mineral components relatively.

## 2.2. Preparation of Three Types of Mastic

Only the part of mineral fillers that can pass at the 0.075 mm sieve were used to make mineral filler-asphalt mastic and mineral filler-residue mastic.

### 2.2.1. Mineral Filler-Asphalt Mastic

Five kinds of mineral filler-asphalt mastics were prepared according to filler–binder mass ratios (FBRs) of 0.6, 0.8, 1.0, 1.2, and 1.4, and labeled 1-H, 2-H, 3-H, 4-H, and 5-H, respectively. The FBR refers to the weight ratio of limestone mineral filler to matrix asphalt binder.

### 2.2.2. Mineral Filler-Residue Mastic

Five kinds of mineral filler-residue mastics were prepared according to FBRs of 0.6, 0.8, 1.0, 1.2, and 1.4, and labeled 1-EH, 2-EH, 3-EH, 4-EH, and 5-EH, respectively. Here, FBR refers to the weight ratio of mineral filler to emulsified asphalt evaporation residue (EAR).

### 2.2.3. Cement-Residue Mastic

After cement is added to the CRAM, it will hydrate with some of the water in the mixture and form hydration products. In order to simulate the process of cement hydration in the laboratory, a certain proportion of cement was first added to the emulsified asphalt and stirred for 15 min. Then, the mixture stood at room temperature for one day. Finally, the water in the mixture was evaporated by an electric heating sleeve to obtain cement-residue mastic, labeled C-EH.

Referring to the conventional dosages used in actual pavement works, the amounts of emulsified asphalt selected were 3.5, 4.5, 5.5, and 6.5 wt %, respectively, while the cement dosages were 1, 2, 3, and 4 wt %, respectively. The above mass percentages are all relative to the aggregate weights in the mixtures. Combined with the solid content of the emulsified asphalt and the amount of cement, the FBR of the cement-residue mastic was calculated (Table 6). It should be noted that the FBR here is the mass ratio of cement to EAR.

**Table 6.** Production parameters of cement-residue mastics

Mastic Type	Asphalt Emulsion (%)	Cement (%)	FBR
E-CH3.5%	3.5	0.5	0.23
	3.5	1	0.46
	3.5	1.5	0.69
	3.5	2	0.92
E-CH4.5%	4.5	0.5	0.18
	4.5	1	0.36
	4.5	1.5	0.54
	4.5	2	0.72
E-CH5.5%	5.5	0.5	0.15
	5.5	1	0.29
	5.5	1.5	0.44
	5.5	2	0.59
E-CH6.5%	6.5	0.5	0.12
	6.5	1	0.25
	6.5	1.5	0.37
	6.5	2	0.5

### 2.3. Preparation of CRAM Specimens

The CRAM specimens were fabricated with RAP, cement, emulsified asphalt, and water at certain proportions using a laboratory mixer. CRAM using 100% RAP was designed by modified Marshall Method in China according to JTG F41-2008 and the method including three processes. Firstly, the optimum water content (OWC) of CRAM was determined by the density of samples prepared by heavy hammer while the emulsified asphalt content was determined as 4.0%. Then, the optimum asphalt emulsion content (OEC) was determined by Marshall stability of samples prepared by Marshall test under the OWC. Lastly, the performance of CRAM was examined by indirect tensile strength and moisture damage resistance. During the mix design process, the OEC and OWC were determined as 4.0% and 5.8% by weight of aggregates, respectively. The CRAM specimens were then placed in the ventilated oven with the temperature of 60 °C for 21 days to fully complete the curing process.

For indirect tensile tests and freeze–thaw splitting tests, the loose mixture was compacted into samples with dimensions of 101.6 mm × 63.5 mm using a Marshall compactor. For rutting tests, the loose mixtures were compacted into specimens with dimensions of 300 mm × 300 mm × 50 mm

using a wheel-rolling compactor. For dynamic modulus tests, the loose mixture was compacted using a superpave gyratory compactor with 55 cycles to produce cylindrical specimens with dimensions of 150 mm × 170 mm. After the curing period, specimens for the dynamic modulus tests were cored from the centers of the compacted specimens and sawed at each end to dimensions of 100 mm × 150 mm.

## 2.4. Experimental Method

### 2.4.1. Dynamic Shear Rheological

Dynamic shear rheology tests can simulate traffic conditions well and can be used to study the high-temperature rheological properties of asphalt and mastics. Prior to carrying out viscoelastic tests, strain sweep tests (0.01–20%) were performed using the dynamic shear rheometer (DSR) to determine the linear viscoelastic (LVE) limit for all mastics at 60 °C and 10 rad/s in this study. The LVE strain range was regarded as the strain within 10% reduced value of the maximum complex modulus with increases in the shear strain [23,24]. Then the test was conducted by the DSR with the 25 mm (1 mm gap) parallel plate set-up in the strain-controlled mode.

### 2.4.2. Indirect Tensile Tests

Indirect tensile tests are used to determine the mechanical properties of an asphalt mixture at a specified temperature and loading rate. They also can be used to evaluate the low-temperature crack resistance of an asphalt mixture. In this study, the experimental temperature was 15 °C, the loading rate was 50 mm/min, and the specimens were immersed in a constant-temperature water tank that was recycled under reflux for not less than 1.5 h before testing.

### 2.4.3. Freeze–Thaw Splitting Tests

The splitting strength ratios of the specimens before and after water damage were determined to evaluate the water stability of the asphalt mixtures. The specimens were divided into two groups for the tests. The first set of samples was used to measure the splitting strength  $R_{T1}$  without freezing and thawing cycles, and the second set was used to determine the splitting strength  $R_{T2}$  of the freeze–thaw cycle. The treatment of freeze–thaw cycles was carried out in accordance with the requirements of AASHTO T283 and JTG E20-2011 (Standard Test Methods of Bitumen and Bituminous Mixture for Highway Engineering) [25]. The tensile strength ratio (TSR) can be calculated by Equation (1).

$$\text{TSR} = \frac{R_{T2}}{R_{T1}} \times 100 \quad (1)$$

### 2.4.4. Rutting Tests

Asphalt mixtures have flow and deformation abilities at high temperature due to their viscoelastic performance [26]. Therefore, the repeated loadings of channel traffic and heavy vehicles can cause permanent and irreversible deformation of the pavement [27]. Dynamical stability at 60 °C was adopted to characterize the high-temperature stability of CRAM in this paper. Studies have shown that curing conditions have an important impact on the performance of asphalt mixtures [28]. The tests were carried out according to the requirements of AASHTO T324 and JTG E20-2011. Before the tests, the specimens were initially cured at room temperature for 12 h and then put into the device with the controlled temperature at 60 °C for 48 h. The testing temperature was 60 °C and the wheel pressure was 0.7 MPa.

### 2.4.5. Dynamic Modulus Tests

In the dynamic modulus tests, a sinusoidal axial compressive stress was applied to CRAM specimens at a given temperature and loading frequency. Figure 2 shows the loading mode of the dynamic modulus tests.

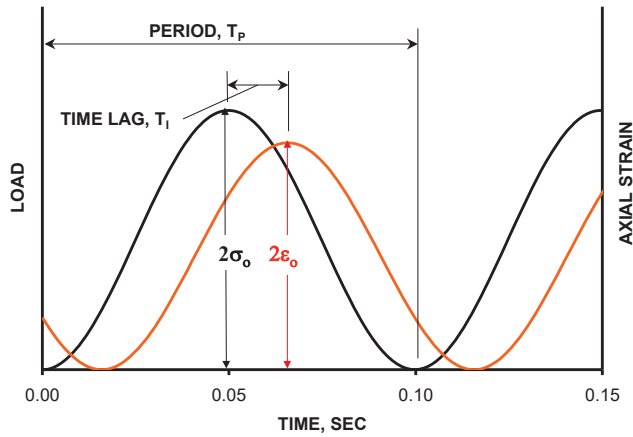


Figure 2. Loading mode of dynamic modulus test.

According to the AASHTO TP62 testing standard, the testing temperature was set to 20 °C and the dynamic modulus and phase angle were measured at nine different loading frequencies: 25, 20, 10, 5, 2, 1.0, 0.5, 0.1, and 0.01 Hz. Testing at a given temperature should begin at the highest loading frequency and proceed to the lowest one.

The applied stress and resulting recoverable axial strain response of the specimens were measured and used to calculate the dynamic modulus and phase angle according to Equations (2)–(5).

$$\sigma(t) = \sigma_0 \sin \omega t \tag{2}$$

$$\omega = 2\pi f \tag{3}$$

$$\varphi = \frac{T_i}{T_p} \times 360 \tag{4}$$

$$|E^*| = \frac{\sigma_0}{\epsilon_0} \tag{5}$$

where,  $\omega$  is the loading angular frequency (rad/s),

$f$  is the loading frequency (Hz),

$\varphi$  is the phase angle (°),

$T_i$  is the average lag time between stress-strain cycles (s),

$T_p$  is the average duration of a stress cycle (s),

$\sigma_0$  is the average peak stress (MPa),

$\epsilon_0$  is the average peak strain (mm/mm), and

$E^*$  is the dynamic modulus (MPa).

### 3. Results and Discussion

#### 3.1. Properties of Mastics

##### 3.1.1. Rheological Properties

In order to avoid the influence of differences in the performances of matrix asphalt or EAR on the experimental results, the modulus of three types of mastics (obtained by DSR tests) was divided by the modulus of the matrix asphalt or EAR to obtain a ratio defined as the modulus increase ratio. Figure 3 shows the relationship between the modulus increase ratio and the FBRs of three types of mastics at 60 °C. It should be noted again that the filler–binder mass ratio in Figure 3(1) is the weight ratio of

mineral filler to asphalt binder; while in Figure 3(2) it is the weight ratio of mineral filler to EAR; and in Figure 3(3) it is the weight ratio of cement to EAR.

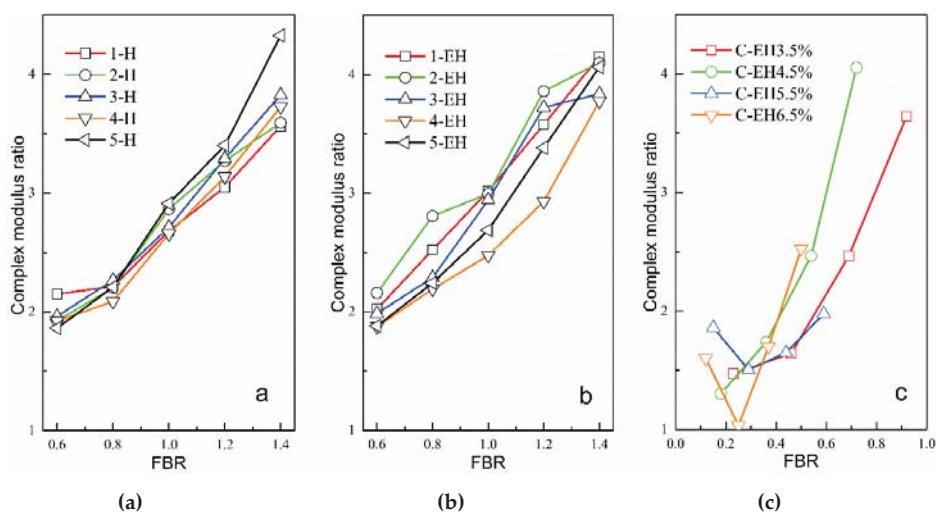


**Figure 3.** Relationship between mastic modulus and FBR. (a) Mineral filler-asphalt mastic (b) Mineral filler-residue mastic (c) Cement-residue mastic. As can be seen in Figure 3, the modulus of the three types of mastics were all higher than those of matrix asphalt or EAR, and the modulus of the mineral filler-asphalt mastic specimen increased linearly with increases in FBR. When the FBR was 0.6, the five kinds of mineral filler doubled the increase, and when the FBR was 1.4, the mineral filler increased the modulus by more than double. The mineral filler-residue mastic exhibited a similar pattern to the mineral filler-asphalt mastic. This result is related to the hardening of inorganic mineral fillers; that is, the addition of mineral filler can increase the elastic recovery modulus of mastics, causing them to exhibit very linear growth relationships, and enhancing the mastics' resistance to deformation [29].

The variation in the cement-residue modulus was more complicated than that of the first two types of mastics. With amounts of emulsified asphalt of 3.5% and 4.5%, the modulus of the mastic increased with increases in FBR. With dosages of 5.5% and 6.5% emulsified asphalt, the modulus of the mastic first decreased and then increased rapidly with increases in FBR, with the lowest value occurring at an FBR of about 0.3. In summary, the modulus-increasing effect of the cement-residue mastic was the most significant. The FBR required to achieve the same modulus increase was smaller than for the first two types of mastics. In other words, when FBR is equal, the modulus of the cement-residue mastic increases more obviously. This is because the cement particles can not only act as a filler, but the formation of hydration products in the mastic greatly promotes the increase of the mastic's modulus.

Figure 4 shows that as FBR increased, the changes in the phase angles of the mineral-asphalt mastic and mineral-residue mastic at 60 °C were not significant, and were stable between 86.5° and 87.5°. That is, under high-temperature conditions, the inorganic mineral filler had little effect on the viscoelastic composition ratio of the base asphalt or EAR but improved the modulus remarkably. The phase angle of the cement-residue mastic was lower than that of the first two types of mastics, which showed that the addition of cement could reduce the strain-to-stress response lag time and increase the elastic solid properties of the mastic as a viscoelastic material.

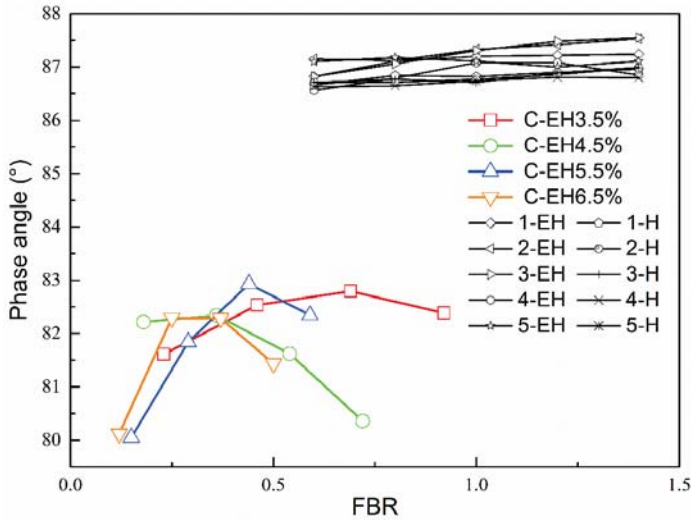


Figure 4. Relationships between mastic phase angles and FBR.

### 3.1.2. Interface Bonding Performance

The indicator K. Ziegel-B was proposed by Ziegel et al. and can be used to evaluate interfacial interactions. It can be calculated by testing the phase angles of asphalt binders and asphalt mastics [30]. The concept is to consider that the interaction between asphalt binder and mineral fillers can make the fillers absorb some asphalt binder fractions, so the effective filler fraction should be based on the real filler fraction. The correction can be achieved by the B value, which is a generalized interaction parameter that can represent complicated physical and chemical interactions. The larger the B value, the stronger the interfacial interaction.

By experimental observation of many composites, the damp of filling system can be calculated as follows,

$$\tan \delta_c = \frac{\tan \delta_m}{1 + \varphi B} \tag{6}$$

So, the B value can be calculated according to Equation (7).

$$B = \frac{\frac{\tan \delta_m}{\tan \delta_c} - 1}{\varphi} \tag{7}$$

where,  $\delta_c$  = phase angle of composite (rad),

$\varphi$  = volume fraction of filler (volume ratio of filler in asphalt mastics),

$\delta_m$  = phase angle of asphalt binder (rad), and

B = the K. Ziegel-B filler-matrix interaction parameter.

In the volume fraction conversion, the density of EAR and asphalt is 1 g/cm<sup>3</sup>, the density of mineral filler (<0.075 mm) is 2.65 g/cm<sup>3</sup>, and the density of cement is 3.14 g/cm<sup>3</sup> [31–33]. The interfacial adhesion coefficients (B) of the three types of mastic were calculated according to Equation (7) and the results are shown in Figure 5.

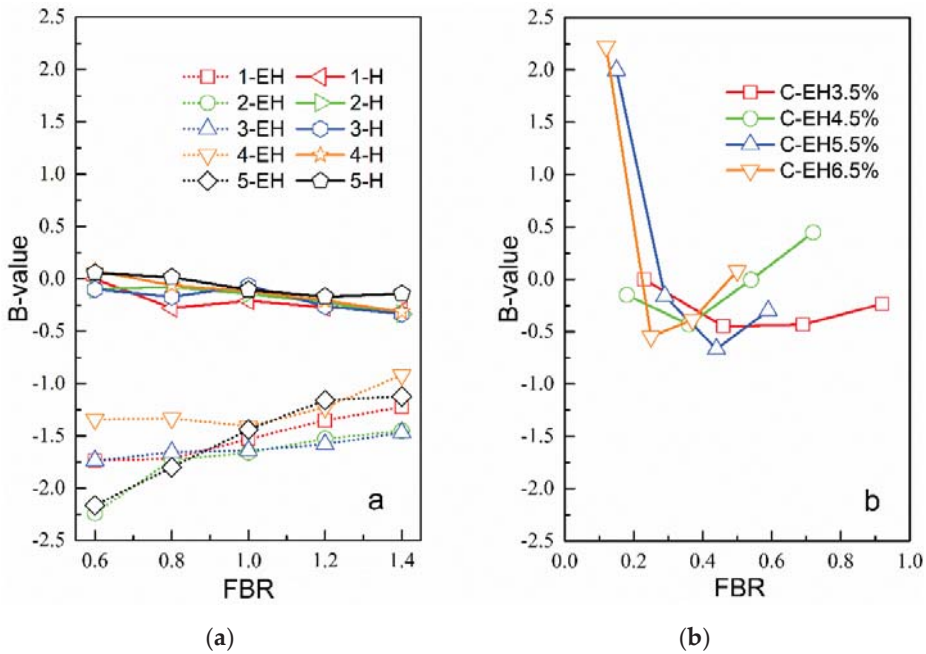


Figure 5. B-values of mastics with (a) mineral filler and (b) cement.

It can be seen that the B-value of the mineral filler-asphalt mastic was higher than that of the mineral filler-residue mastic. The interfacial adhesion coefficient (B-value) of the mineral filler-asphalt mastic decreased with increases in FBR, while for mineral filler-residue mastic it showed a linear increase with FBR.

The interfacial adhesion coefficient of the cement-residue mastic was significantly different from that of the above two kinds of mastics. The B-value of the cement-residue mastic firstly decreased and then increased with increases in FBR. The variations in the samples with the four emulsified asphalt contents were the same. Even when the interface adhesion coefficient was the lowest, it was at the same level as the mineral filler-asphalt mastic. In addition, in most cases, the B-value was higher than that of the above two kinds of mastic. Compared to cement-free mineral filler-residue mastic, the B-value of cement-containing mastic can be several times higher. This shows that the addition of cement can greatly improve the interfacial bonding between binders and fillers in the mastic, thereby improving the water damage resistance and high-temperature stability of CRAM.

### 3.1.3. Microstructure of Mastics

It can be seen from the above experimental results that the properties of cement-residue mastic are very different from those of the other two types of mastic consisting solely of mineral filler. So, the microstructure of mineral filler-asphalt mastic and cement-residue mastic were characterized by FESEM (HitachiS4800, Japan), as shown in Figure 6.



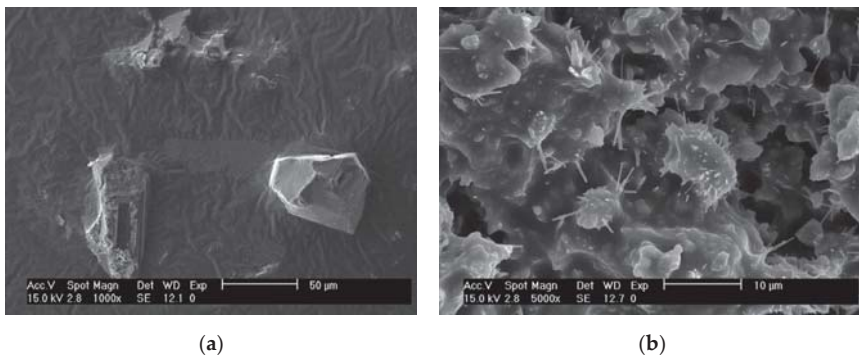
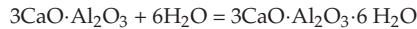


**Figure 6.** SEM images of (a) Mineral filler-asphalt mastic and (b) Cement-residue mastic.

It can be seen that the mineral filler-asphalt mastic exhibited a pure particle filling system, while the cement-residue mastic did not and there were a lot of distinct whisker-like hydration products. This is because the cement can react with the water in the mixture after it is added to the CRAM and the hydration products are very complex. The main components of ordinary Portland cement are tricalcium silicate, dicalcium silicate, tricalcium aluminate, tetracalcium aluminate, and calcium sulfate. The main chemical reactions are



It can be seen from the above chemical reactions that the cement hydration products are mainly alkaline calcium silicate, calcium aluminate, and calcium hydroxide, of which the first two are the main cementing components [34].

When the water-cement ratio changes, the degree of cement hydration will also be different, and a mastic system with a different material composition and microstructure will be formed. Due to the different hydration effects caused by different water-cement ratios, the cement-residue mastic actually consists of complex phases such as unhydrated cement, hydration products, and EAR. The hydration product is in a crystalline state and interwoven with the EAR, and the unhydrated cement particles act as a filler and micro-aggregate in the overall mastic system [35,36]. Therefore, compared with the mineral filler-asphalt mastic and the mineral filler-residue mastic, the modulus and phase angle of the cement-residue mastic changed differently, and the interfacial bonding performance also showed unique characteristics.

As CRAM cannot use a large asphalt content and has a weaker modulus effect caused by fine aggregates and mineral filler, the final strength of CRAM is mainly provided by cement mastic. From this perspective, emulsified asphalt plays an important role in the initial stability of the mixture, while cement hydration has a positive influence on its ultimate strength [37,38].

### 3.2. Effect of Emulsified Asphalt

In combination with the above experimental evaluation of mastic properties and the determined gradation, and using 100% RAP without adding any new aggregate, the influences of emulsified asphalt content on the void ratio, ITS, tensile strength ratio, dynamic stability, and dynamic modulus of

CRAM were investigated. The cement dosage was selected as 2.0 wt % and the overall water content was determined to be 5.8% throughout this section, and the free water usage in different mixtures (with different emulsion content) needed to be adjusted based on the change in the amount of emulsified asphalt.

### 3.2.1. Void Ratio

The void ratio is the main index used to evaluate the compaction of asphalt mixtures. In the process of examining the impact of emulsified asphalt content on the properties of CRAM, the total liquid content should be constant. In this study, the emulsified asphalt contents selected were 2.5, 3.0, 3.5, 4.0, 4.5, 5.0, and 5.5 wt %.

As can be seen from Figure 7, when the emulsified asphalt content increased, the void ratio of CRAM initially decreased to a minimum and then began to increase. The main reason is that the change in viscosity for the total liquid has little effect on the inner friction of the asphalt mixture when the added emulsified asphalt content is lower than 4.0% and the total liquid content is constant. At that time, the residue content of total liquid increases, which will decrease the void ratio. Meanwhile, when the emulsified asphalt content continues to increase above 4.0%, the viscosity of total liquid will increase, and then the inner friction of the asphalt mixture becomes higher, which makes compaction of the mixture difficult. It can be seen that as the amount of emulsified asphalt is further increased, the porosity begins to increase correspondingly.

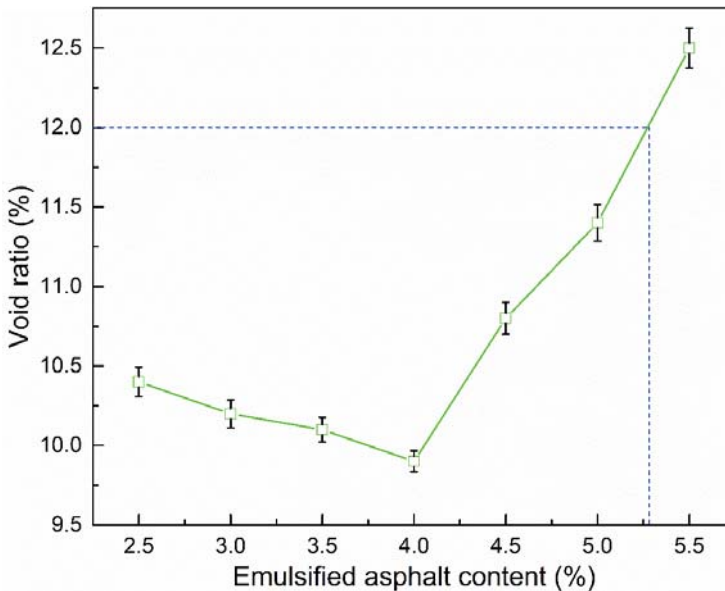


Figure 7. Influence of emulsified asphalt content on void ratio.

### 3.2.2. Indirect Tensile Strength

In this section, the amounts of emulsified asphalt selected were 2.5, 3.0, 3.5, 4.0, 4.5, 5.0, and 5.5 wt %. The influence of emulsified asphalt content on the indirect tensile strength of CRAM are presented in Figure 8.

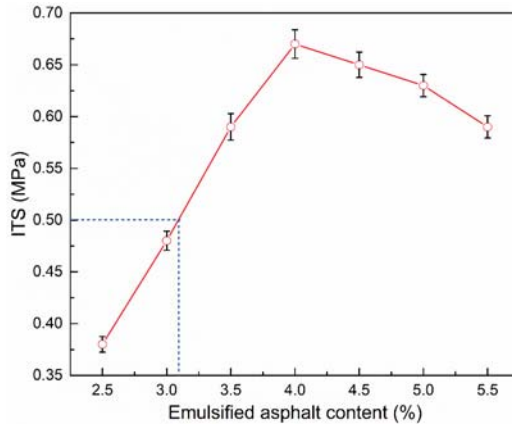


Figure 8. Influence of emulsified asphalt content on ITS.

According to Figure 8, as the amount of emulsified asphalt increases, the ITS of CRAM initially increases to a maximum and then begins to decrease. When the emulsified asphalt content is 4.0%, the ITS is the greatest and the void ratio is the smallest at the same time. This shows that an increase in porosity will hinder the development of ITS.

### 3.2.3. Tensile Strength Ratio

Figure 9 illustrates the influence of emulsified asphalt content on the TSR of CRAM. It can be seen that the TSR increases at first with increases in the amount of emulsified asphalt and then decreases slightly. This suggests that increasing the emulsified asphalt content could improve the moisture resistance stability to a great extent. On the other hand, it can also be seen that the void ratio has a direct impact on TSR and the TSR increases with the decrease of the porosity. The void ratio of CRAM reaches the minimum value when the emulsified asphalt content is 4.0 wt %, while the TSR reaches the maximum value at the same time. This is because the amount of water that can enter the pores of specimen becomes smaller along with the reduction of void ratio, so the inside of the specimen is less susceptible to water damage during the freeze–thaw treatment. Therefore, the water damage resistance of CRAM is enhanced, which is manifested by an increase in TSR. The technical requirements for CRAM design according to JTG F41-2008 are shown in Table 7.

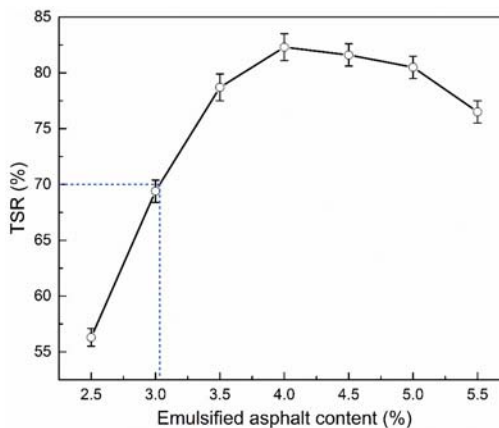


Figure 9. Influence of emulsified asphalt content on TSR.

**Table 7.** Technical requirements for CRAM design

Parameter	Requirements	
	Pavement Base or Subbase	Pavement Subsurface Layer
Void ratio (%)	9–12	9–12
15 °C ITS (MPa)	≥0.40	≥0.50
TSR (%)	≥70	≥70

In addition, it can be seen from Figures 7–9 that when using 100% RAP, 2% cement, and 3.1–5.3% emulsified asphalt, the porosity, ITS, and TSR are all fully compliant with the specifications of the relevant standard.

### 3.2.4. Dynamic Stability

The dynamic stability can be used to evaluate the high-temperature properties of asphalt mixtures. Thus, the dynamic stability at 60 °C and rutting depth of CRAM were evaluated in terms of emulsified asphalt content, as presented in Figure 10.

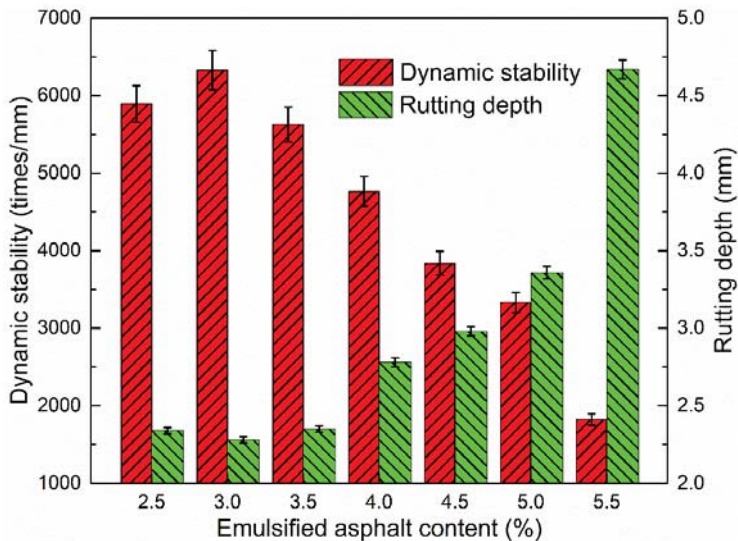


**Figure 10.** Influence of emulsified asphalt content on dynamic stability and rutting depth.

It can be concluded from Figure 10 that as the emulsified asphalt content increases, the dynamic stability of CRAM at 60 °C decreases, which is similar to the variation observed for hot mix asphalt [39]. The above results are caused by the asphalt content in CRAM increasing with increases in emulsified asphalt content, which leads to decreases in CRAM inner friction and shear deformation resistance, so the rutting depth tends to increase.

### 3.2.5. Dynamic Mechanical Analysis

Based on the above investigation of the rheological properties of mastics, the influence of emulsified asphalt content on the rheological properties of CRAM was evaluated. The results are illustrated in Figure 11, where DM and PA represent the dynamic modulus and the phase angle, respectively.

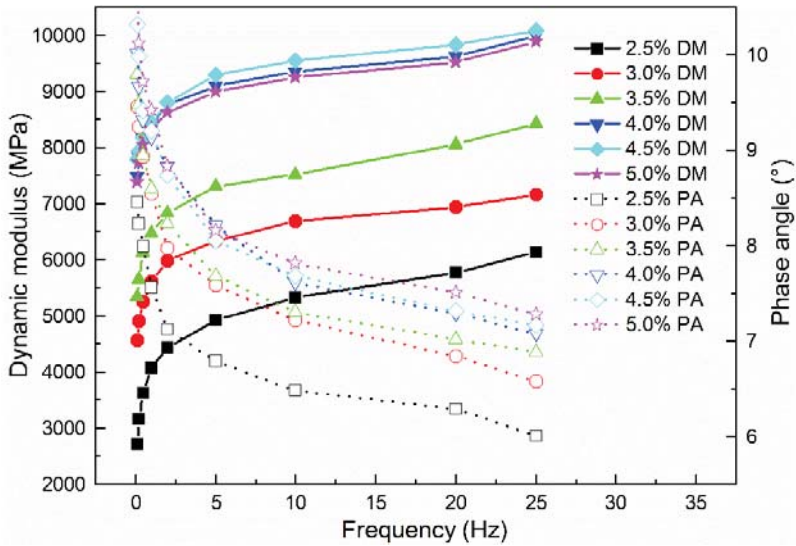


Figure 11. Influence of emulsified asphalt content on mechanical properties of CRAM.

Figure 11 shows that when the amount of emulsified asphalt did not exceed 4.0%, the dynamic modulus of CRAM tended to increase rapidly with increases in emulsified asphalt content. When the amount of emulsified asphalt was more than 4.0%, the dynamic modulus of CRAM tended to be stable and changed little in response to the emulsified asphalt content, while the phase angle still slowly increased.

### 3.3. Effect of Cement

In combination with the above experimental evaluation of the mastics' properties and determined gradation, 100% RAP without adding any new aggregate was used to investigate the influences of cement content on the void ratio, ITS, tensile strength ratio, dynamic stability, and dynamic modulus of CRAM. The asphalt emulsion content was fixed at 4.0 wt % throughout this section and the optimum water content in different mixtures (with different cement content) needed to be adjusted based on the change in the amount of cement. The OWC was determined by the density of samples prepared by heavy hammer according to T0131 of JTG E40-2007 (Test Methods of Soils for Highway Engineering). In this part, the amounts of cement selected were 0, 1.0, 2.0, 3.0, and 4.0 wt %.

#### 3.3.1. Void Ratio

In order to obtain the optimum compaction of CRAM, the optimum water content should be adjusted according to the cement content. The influence of cement content on the void ratio of CRAM was evaluated, and the results are presented in Figure 12.

It can be seen that the optimum liquid content required for CRAM increased as the amount of cement increased. The main reason is that the cement increased the consistency of the slurry in the mixture and, at the same time, the amount of water used for cement hydration also increased, so more water needed to be added to achieve the best compaction effect. The porosity of CRAM gradually decreased as the cement content increased, but the range of variation was small. The interstitial effect of cement and the impairment of the void ratio by hydrated products lead to this result. Therefore, the amount of cement in CRAM should be controlled within a certain range, generally not more than 2.0 wt %.

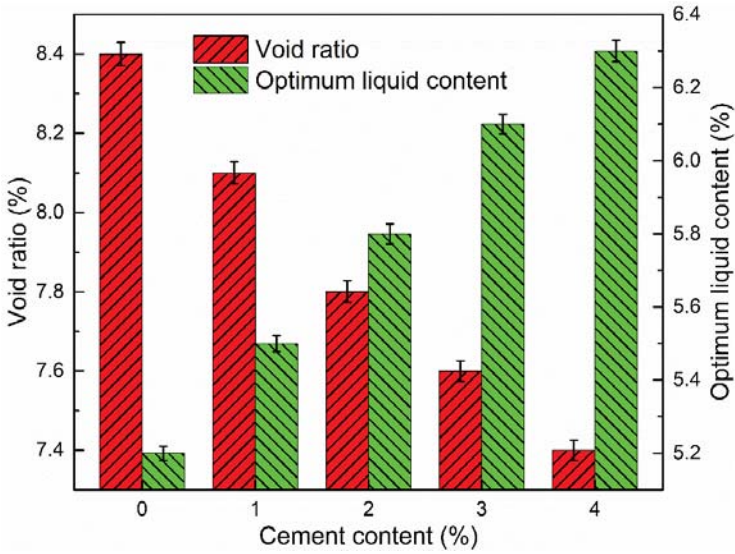


Figure 12. Influence of cement content on void ratio and optimum liquid content.

### 3.3.2. Indirect Tensile Strength

As presented in Figure 13, it can be concluded that the ITS of CRAM apparently increased with cement content. This is basically consistent with the variation observed in the cement-residue mastic bonding coefficient, indicating again that the addition of cement can improve the interfacial bonding of aggregate and binders.

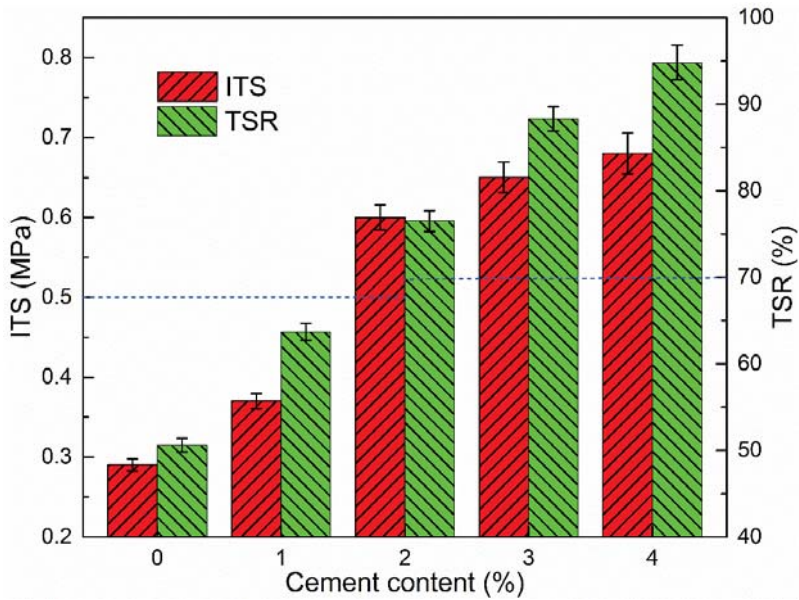


Figure 13. Influence of cement content on ITS and TSR.



### 3.3.3. Tensile Strength Ratio

The results presented in Figure 13 show that the TSR increased with cement content. The reason is that the porosity of CRAM decreases as the amount of cement increases due to the combined action of cement's interstitial effect and the impairment of hydrated products. The porosity reduction thereby enhances the ability of the CRAM to resist water damage and is manifested as an increase in TSR, which is used to characterize the ability of the mixture to resist water damage.

In addition, it can be seen from Figures 12 and 13 that with 100% RAP, 4.0% emulsified asphalt, and 2–4% cement, the porosity, ITS, and TSR are all fully compliant with the specifications of the relevant standard.

### 3.3.4. Dynamic Stability

The results in Figure 14 show that the addition of cement had a great influence on the dynamic stability of CRAM, which varied according to the cement content used. When the cement content was <2.0 wt %, the dynamic stability increased by a large margin, while with >2.0 wt % cement, the increase in dynamic stability with cement content was not as obvious. This relationship is basically consistent with the effect of cement dosage on ITS. It indicates that the addition of cement not only improves the interfacial adhesion of aggregates and binders but also greatly improves the high-temperature stability of CRAM.

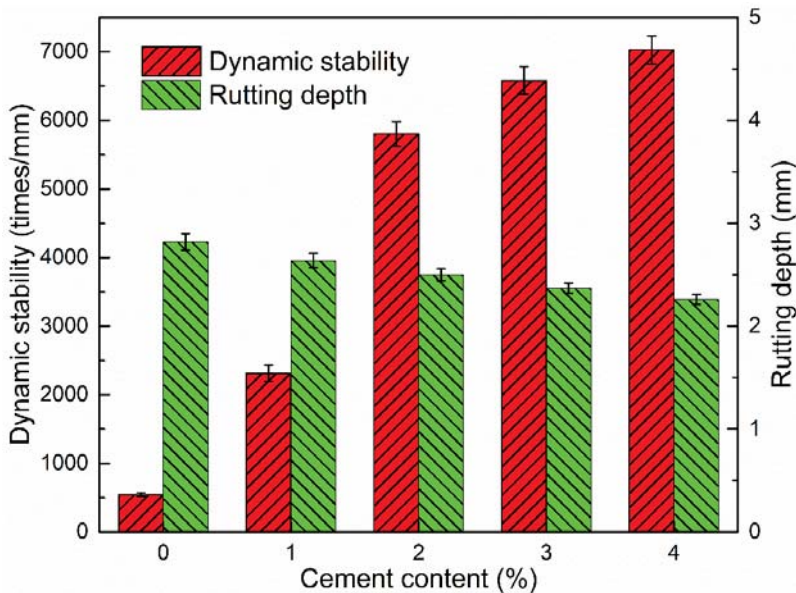


Figure 14. Influence of cement content on dynamic stability and rutting depth.

### 3.3.5. Dynamic Mechanical Analysis

Based on the above investigation of the rheological properties of cement-residue mastic, the influence of cement content on the mechanical properties of CRAM was evaluated. The results are illustrated in Figure 15, where DM and PA represent the dynamic modulus and the phase angle, respectively.

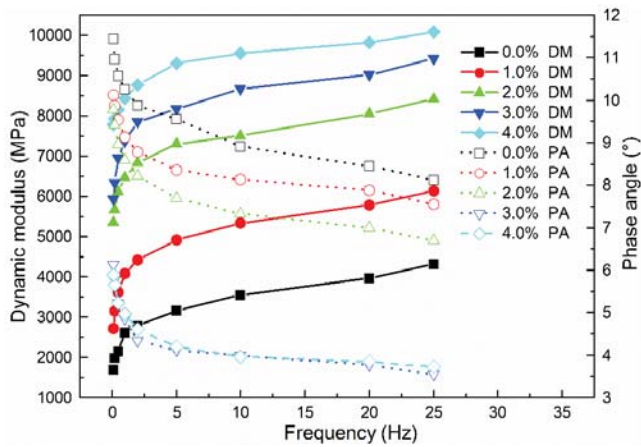


Figure 15. Influence of cement content on mechanical properties of CRAM.

It can be seen that the relationships between cement content and the dynamic modulus and phase angle are different to that for emulsified asphalt. The dynamic modulus increased continuously with increases in cement dosage, with dosages of 1.0–2.0% having the greatest effect. Conversely, the phase angle decreased as the amount of cement increased. When the cement content exceeded 3.0%, the changes in phase angle became very small while the dynamic modulus still increased. Therefore, the addition of cement could reduce the strain-to-stress response lag time and increase the elastic modulus of the CRAM, indicating that the hydration products are beneficial for enhancing the high temperature stability of the CRAM. It is consistent with the previous analysis of the cement-containing mastic's rheological properties.

#### 4. Conclusions

Based on the results described above, the following conclusions can be drawn:

1. Both the modulus of the mineral-filler mastic and mineral-residue mastic increased linearly with the FBR, which is due to the hardening of inorganic mineral filler fillers. The cement-residue mastic's modulus-increasing effect was most pronounced and its phase angle was lower compared to the first two types of mastics. This is due to the hydration of cement helping to increase the elastic solid properties of the cement-residue mastic.
2. Compared to cement-free mastics, the B-values of cement-containing mastics can be several times higher. This shows that the addition of cement can greatly improve the interfacial bonding between binders and fillers in the mastic, thereby improving the water damage resistance and high-temperature stability of CRAM. It is confirmed by the impact of cement content on the ITS, TSR, and dynamic stability of CRAM.
3. The relationships between cement content and the CRAM's phase angle are different to that for emulsified asphalt obviously. The addition of cement reduces the phase angle of the CRAM, and it is consistent with the previous results of cement-residue mastic' rheological properties. This shows the hydration products reduce the strain-to-stress response lag time and increase the elastic modulus of CRAM, and it is beneficial for enhancing the high temperature stability of CRAM.
4. Using 100% RAP, 2.0 wt % cement, and 3.1–5.3 wt % emulsified asphalt, or when using 4.0 wt % emulsified asphalt and 2.0–4.0 wt % cement, the porosity, ITS and TSR of CRAM are all fully compliant with the specifications of JTG F41-2008. Therefore, schemes using CRAM for a subsurface layer of pavement with 100% RAP may be feasible under certain conditions.



**Author Contributions:** Investigation, Y.L. (Yanan Li) and Y.L. (Yuchao Lv); Methodology, Y.L. (Yanan Li) and Y.Z.; Validation, Y.Z.; Writing—original draft, Y.L. (Yanan Li); Writing—review & editing, L.F.

**Funding:** This research was funded by Applied Basic Research Project of the Ministry of Transport (project no. 2013319781140).

**Conflicts of Interest:** The authors declare no conflict of interest.

## References

1. Xiao, F.P.; Amirkhanian, S.N.; Putman, B.J.; Juang, H. Feasibility of Superpave gyratory compaction of rubberized asphalt concrete mixtures containing reclaimed asphalt pavement. *Constr. Build. Mater.* **2012**, *27*, 432–438. [[CrossRef](#)]
2. Zhang, K.; Shen, S.; Lim, J.; Muhunthan, B. Development of dynamic modulus-based mixture blending chart for asphalt mixtures with reclaimed asphalt pavement. *J. Mater. Civ. Eng.* **2019**, *31*, 04018382. [[CrossRef](#)]
3. Hong, F.; Prozzi, J.A. Evaluation of recycled asphalt pavement using economic, environmental, and energy metrics based on long-term pavement performance sections. *Road Mater. Pavement Des.* **2018**, *19*, 1816–1831. [[CrossRef](#)]
4. Xu, J.Z.; Hao, P.W.; Zhang, D.P.; Yuan, G.A. Investigation of reclaimed asphalt pavement blending efficiency based on micro-mechanical properties of layered asphalt binders. *Constr. Build. Mater.* **2018**, *163*, 390–401. [[CrossRef](#)]
5. Sivilevičius, H.; Bražiūnas, J.; Prentkovskis, O. Technologies and principles of hot recycling and investigation of preheated reclaimed asphalt pavement batching process in an asphalt mixing plant. *Appl. Sci.* **2017**, *7*, 1104. [[CrossRef](#)]
6. Frigio, F.; Pasquini, E.; Canestrari, F. Laboratory study to evaluate the influence of reclaimed asphalt content on performance of recycled porous asphalt. *J. Test. Eval.* **2015**, *43*, 1308–1322. [[CrossRef](#)]
7. Yu, X.; Li, Y. Optimal percentage of reclaimed asphalt pavement in central plant hot recycling mixture. *J. Wuhan Univ. Technol. Mater. Sci. Ed.* **2010**, *25*, 659–662. [[CrossRef](#)]
8. Arshad, M.; Ahmed, M.F. Potential use of reclaimed asphalt pavement and recycled concrete aggregate in base/subbase layers of flexible pavements. *Constr. Build. Mater.* **2017**, *151*, 83–97. [[CrossRef](#)]
9. Wang, Y.; Leng, Z.; Li, X.; Hu, C. Cold recycling of reclaimed asphalt pavement towards improved engineering performance. *J. Clean. Prod.* **2018**, *171*, 1031–1038. [[CrossRef](#)]
10. Lin, J.; Hong, J.; Xiao, Y. Dynamic characteristics of 100% cold recycled asphalt mixture using asphalt emulsion and cement. *J. Clean. Prod.* **2017**, *156*, 337–344. [[CrossRef](#)]
11. Alizadeh, A.; Modarres, A. Mechanical and microstructural study of RAP-clay composites containing bitumen emulsion and lime. *J. Mater. Civ. Eng.* **2019**, *31*, 04018383. [[CrossRef](#)]
12. Du, S. Mechanical properties and reaction characteristics of asphalt emulsion mixture with activated ground granulated blast-furnace slag. *Constr. Build. Mater.* **2018**, *187*, 439–447. [[CrossRef](#)]
13. Omrani, M.A.; Modarres, A. Emulsified cold recycled mixtures using cement kiln dust and coal waste ash-mechanical-environmental impacts. *J. Clean. Prod.* **2018**, *199*, 101–111. [[CrossRef](#)]
14. Alsheyab, M.A.T.; Khedaywi, T.S. Effect of electric arc furnace dust (EAFD) on properties of asphalt cement mixture. *Resour. Conserv. Recycl.* **2013**, *70*, 38–43. [[CrossRef](#)]
15. Cheng, H.; Sun, L.; Liu, L.; Li, H. Fatigue characteristics of in-service cold recycling mixture with asphalt emulsion and HMA mixture. *Constr. Build. Mater.* **2018**, *192*, 704–714. [[CrossRef](#)]
16. Dong, W.; Charmot, S. Proposed tests for cold recycling balanced mixture design with measured impact of varying emulsion and cement contents. *J. Mater. Civ. Eng.* **2019**, *31*, 04018387. [[CrossRef](#)]
17. Gu, F.; Ma, W.; West, R.C.; Taylor, A.J.; Zhang, Y. Structural performance and sustainability assessment of cold central-plant and in-place recycled asphalt pavements: A case study. *J. Clean. Prod.* **2019**, *208*, 1513–1523. [[CrossRef](#)]
18. Ling, C.; Bahia, H.U. Development of a volumetric mix design protocol for dense-graded cold mix asphalt. *J. Trans. Eng. Part. B Pavements* **2018**, *144*, 04018039. [[CrossRef](#)]
19. Research Institute of Highway Ministry of Transport, M.O.T. *Technical Specifications for Highway Asphalt Pavement Recycling*; China Communications Press: Beijing, China, 2008.
20. Research Institute of Highway Ministry of Transport, M.O.T. *Test Methods of Aggregate for Highway Engineering*; China Communications Press: Beijing, China, 2005.

21. Karlsson, R.; Isacson, U. Application of FTIR-ATR to characterization of bitumen rejuvenator diffusion. *Mater. Civ. Eng.* **2003**, *15*, 157–165. [[CrossRef](#)]
22. Lin, J.; Huo, L.; Xu, F.; Xiao, Y.; Hong, J. Development of microstructure and early-stage strength for 100% cold recycled asphalt mixture treated with emulsion and cement. *Constr. Build. Mater.* **2018**, *189*, 924–933. [[CrossRef](#)]
23. Diab, A.; You, Z. Small and large strain rheological characterizations of polymer- and crumb rubber-modified asphalt binders. *Constr. Build. Mater.* **2017**, *144*, 168–177. [[CrossRef](#)]
24. Bazzaz, M.; Darabi, M.K.; Little, D.N.; Garg, N. A straightforward procedure to characterize nonlinear viscoelastic response of asphalt concrete at high temperatures. *Trans. Res. Rec.* **2018**, *2672*, 481–492. [[CrossRef](#)]
25. Research Institute of Highway Ministry of Transport, M.O.T. *Standard Test Methods of Bitumen and Bituminous Mixture for Highway Engineering*; China Communications Press: Beijing, China, 2011.
26. Lytton, R.L.; Zhang, Y.; Gu, F.; Luo, X. Characteristics of damaged asphalt mixtures in tension and compression. *Int. J. Pavement Eng.* **2018**, *19*, 292–306. [[CrossRef](#)]
27. Javilla, B.; Fang, H.; Mo, L.; Shu, B.; Wu, S. Test evaluation of rutting performance indicators of asphalt mixtures. *Constr. Build. Mater.* **2017**, *155*, 1215–1223. [[CrossRef](#)]
28. Graziani, A.; Iafelice, C.; Raschia, S.; Perraton, D.; Carter, A. A procedure for characterizing the curing process of cold recycled bitumen emulsion mixtures. *Constr. Build. Mater.* **2018**, *173*, 754–762. [[CrossRef](#)]
29. Fan, L.; Wei, J.; Zhang, Y.; Wang, L. Acting mechanism and performance of asphalt mortars by mineral filler. *J. Build. Mater.* **2014**, *17*, 1096–1101.
30. Ziegel, K.D.; Romanov, A. Modulus reinforcement in elastomer composites. I. Inorganic fillers. *J. Appl. Polym. Sci.* **1973**, *17*, 1119–1131. [[CrossRef](#)]
31. Gómez-Meijide, B.; Pérez, I. A proposed methodology for the global study of the mechanical properties of cold asphalt mixtures. *Mater. Des.* **2014**, *57*, 520–527. [[CrossRef](#)]
32. Tan, Y.; Guo, M. Using surface free energy method to study the cohesion and adhesion of asphalt mastic. *Constr. Build. Mater.* **2013**, *47*, 254–260. [[CrossRef](#)]
33. Tan, Y.; Guo, M. Interfacial thickness and interaction between asphalt and mineral fillers. *Mater. Struct.* **2014**, *47*, 605–614. [[CrossRef](#)]
34. Guo, Y.; Zhang, T.; Tian, W.; Wei, J.; Yu, Q. Physically and chemically bound chlorides in hydrated cement pastes: A comparison study of the effects of silica fume and metakaolin. *J. Mater. Sci.* **2019**, *54*, 2152–2169. [[CrossRef](#)]
35. Aimin, S.H.A.; Zhenjun, W. Microstructure of mastics-aggregate interface in cement emulsified asphalt concrete. *J. Chang'An Univ. Nat. Sci. Ed.* **2008**, *28*, 1–6.
36. Zhen-jun, W.; Ai-min, S.H.A. Microstructure characters of cement emulsified asphalt composite mastics. *J. Chang'An Univ. Nat. Sci. Ed.* **2009**, *29*, 11–14.
37. Wei, T.; Hong, J.; Lin, J. Effect and action mechanism of cement and emulsified asphalt on the strength of cold regeneration. *J. Build. Mater.* **2017**, *20*, 310–315.
38. Godenzoni, C.; Cardone, F.; Graziani, A.; Bocci, M. The effect of curing on the mechanical behavior of cement-bitumen treated materials. In *8th Rilem International Symposium on Testing and Characterization of Sustainable and Innovative Bituminous Materials*; Canestrari, F., Partl, M.N., Eds.; Springer: Dordrecht, The Netherlands, 2016; Volume 11, pp. 879–890.
39. Takaikaw, T.; Tepsriha, P.; Horpibulsuk, S.; Hoy, M.; Kaloush, K.E.; Arulrajah, A. Performance of fiber-reinforced asphalt concretes with various asphalt binders in Thailand. *J. Mater. Civ. Eng.* **2018**, *30*, 04018193. [[CrossRef](#)]



Article

# Enhancement of Dynamic Damping in Eco-Friendly Railway Concrete Sleepers Using Waste-Tyre Crumb Rubber

Sakdirat Kaewunruen <sup>1,2,\*</sup> , Dan Li <sup>2</sup>, Yu Chen <sup>2</sup> and Zhechun Xiang <sup>2</sup>

<sup>1</sup> Birmingham Centre for Railway Research and Education, University of Birmingham, Birmingham B152TT, UK

<sup>2</sup> Department of Civil Engineering, School of Engineering, University of Birmingham, Birmingham B152TT, UK; DXL561@student.bham.ac.uk (D.L.); chenyu304304@outlook.com (Y.C.); 15372291781@163.com (Z.X.)

\* Correspondence: s.kaewunruen@bham.ac.uk; Tel.: +44-(0)-1214-142-670

Received: 20 June 2018; Accepted: 6 July 2018; Published: 9 July 2018

**Abstract:** There is no doubt that the use of waste rubber in concrete applications is a genius alternative because Styrene is the main component of rubber, which has a strong toxicity and is harmful to humans. Therefore, it will significantly reduce impacts on the environment when waste rubber can be recycled for genuine uses. In this paper, the dynamic properties of high-strength rubberised concrete have been investigated by carrying out various experiments to retain the compressive strength, tensile strength, flexural strength, electrical resistivity, and damping characteristics by replacing fine aggregates with micro-scale crumb rubber. Over 20 variations of concrete mixes have been performed. The experimental results confirm that a decrease in the compressive strength can be expected when the rubber content is increased. The new findings demonstrate that the high-strength concrete can be enhanced by optimal rubber particles in order to improve splitting tensile and flexural strengths, damping properties, and electrical resistivity. It is therefore recommended to consider the use of rubberised concrete (up to 10 wt. % crumb rubber) in designing railway sleepers as this will improve the service life of railway track systems and reduce wastes to the environment.

**Keywords:** crumb rubber; high-strength concrete; damping; dynamic moduli; railway application; recycled material

---

## 1. Introduction

At the beginning of the last century, with the development of science and technology, the reduction of forest resources led to the production of steel and concrete railway sleepers rather than wood [1–3]. Since railway sleepers are effective but expensive, reinforced concrete has been used as a reliable and more efficient material for railway sleepers since the 1950s [4]. On the other hand, the rapid development of the automotive industry has led to the rapid development of the rubber tire industry and brought about the dilemma of how to deal with rubber waste that poses a serious threat to the environment.

Recently, many researches have proposed and encouraged the use of waste rubber in concrete to improve its performance [5–7]. More precisely, in the railway sector the rubber concrete sleepers have known a high-demand due to its efficiency in high-intensity pressure vibration environment. In this study, the crumb rubber is replacing the fine aggregates in the concrete sleepers in order to evaluate their ability to absorb the vibration energy. While it is expected to have a material with better performances than conventional concrete, the reason behind this evaluation is to create a rubber concrete that can maintain its strength at an acceptable level, thus enhancing the performance and sustainability of the railway track systems exposed to high-intensity impact loading conditions [8–10].

The purpose of this paper is to highlight the sensitivity of dynamic properties of the high-strength concrete to crumb rubber inclusion as well as its capability in meeting the standards of railway concrete sleepers' manufacturing. Different proportions of crumb rubber with different particle sizes (75, 180, and 400  $\mu\text{m}$ ) have been used in order to analyse their effects on the compressive strength, splitting tensile and flexural strengths, electrical resistivity and damping properties of the rubberised concrete.

## 2. Railway Applications

Conventional rail track structure can be divided into superstructure and substructure (Figure 1). The superstructure includes rails, rail pads, fastening system and rail sleepers. The substructure consists of ballast, sub-ballast and formation. Railway sleeper is one of the most important safety-critical components of the track structure. The main functions of rail sleeper are to transfer vertical loads from rails to foundation and maintain rail gauge. According to Cai [11], the sleepers are laid horizontally under the rail and placed on the track bed, bearing the pressure from the rail and spread it all over the ballast bed.

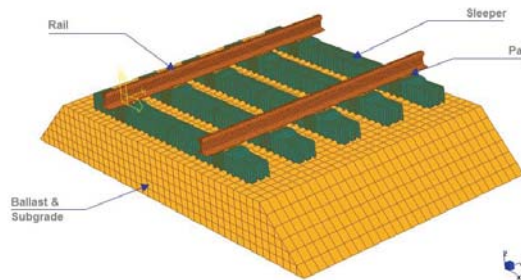


Figure 1. Components of railway tracks.

The sleepers are usually manufactured by timber or concrete composite nowadays. Timber sleepers are often used in North America which have superior elasticity, better mitigation and absorption of vibration, but their life cycle is no more able to meet today's market requirements. Consequently, concrete sleepers have recently become the most widely used due to their low maintenance cost and longer life cycle in comparison with timber sleepers [12].

The railway concrete sleepers are expected to service for 50 years [13,14]. However, in practice the service life of concrete sleepers barely meet the design requirement due to many causes. In order to determine the total energy needed for the failure of railway concrete sleepers under sudden load, their dynamic response was investigated. It has been found that the railway concrete sleepers' impact resistance was more affected under splitting mode as there was a lack of bonding between concrete and steel bars under dynamic circumstances [15]. The most critical problems related to failure of concrete sleepers were surveyed by Stuart. The survey reported that concrete sleepers cracking from dynamic loads were significant [16]. Their durability is reduced as the cracks start to appear which increase the chance of fatigue failure. The cracks in sleepers are initiated when they experience severe loading conditions such as high-magnitude wheel loads created by ruthless wheels or rail abnormalities [17]. It has therefore been observed that the use of crumb rubber in concrete could minimize the damage of cracks in sleepers, as the crumb rubber concrete has shown significant toughness properties and impact resistance. The elastic properties and fatigue resistance will also improve by using crumb rubber in concrete [18]. The previous research conducted by Sallam et al. [19] revealed that resistance of crack under impact loading will be improved in the presence of rubber particle. Hameed and Shashikala [18] indicated that the stiffness of concrete will be increased when containing crumb rubber under cyclic loads. The outcome of this research has indicated the dynamic property of crumb

rubber concrete through various experiments which provide important data for future railway sleeper durability design.

### 3. Methods

#### 3.1. Rubber Wastes and Their Applications

The large amount of abandoned waste tyres (Figure 2) while handled and removed quickly will certainly impact the environment. Common solid waste disposal methods like incinerated and landfilled are not suitable for this kind of waste as they lead to the release of toxic substances which results in serious contaminations of underground water systems. The thousands of hectares of landfills not only occupy sites that can have better usages, but also contribute to bacteria and mosquitoes breeding, causing infectious diseases and blazes [20].



Figure 2. Waste tyres.

As early as 1976, there was a patent for old tyres usage in the United States [21,22]. Nowadays, more granulation methods appeared, such as extraction of steel fibres from waste tyres as reinforcement in concrete is now possible [6]. Some researchers reported that the crumb rubber, when added to ballasted tracks, resulted in better absorption of the vibration impact energy and improved their life cycle [23]. More researches devoted to the possibility of partially replacing aggregates with rubber particles (Figure 3) as an eco-friendly alternative while dealing with rubber waste [24], and also improving the concrete damping characteristics [25].



Figure 3. Crumb rubber concrete.

#### 3.2. Relevant Previous Studies

Most studies have shown that the replacement of the fine aggregates by crumb rubber in concrete will reduce its strength to a certain extent, and the degree of decrease in strength depends on both the particle size and the amount of addition [26]. Still, other studies reported many other benefits of using rubber in concrete. Rubber particles can act as an air-entraining agent and hence providing

concrete with a better freeze-cycle protection [27]. Thermal resistance also presents a challenge for concrete sleepers, and since rubber has good heat insulation it was found that the crumb rubber can increase the thermal resistance of concrete to about 18.52% [28]. Conventional concrete has better fire resistance than crumb rubber concrete as the rubber is a flammable material and its particles on the concrete surfaces can easily be burnt [29]. The dynamic properties are very important in the railway track design process. For concrete sleepers, cracking could be caused by wheel–rail interaction force which can be divided into dynamic load and impact load [30]. Dynamic load is wheel–rail interaction under normal situation, whereas impact load is also wheel–rail interaction caused by defects in wheel or rail. In durability design, sleepers need to withstand dynamic load and impact load. However, the dynamic testing data of crumb rubber concrete is not enough for concrete sleeper design. Therefore, investigation of dynamic properties is necessary for new material concrete sleeper design [31].

#### 4. Materials

The emphasis of this study is placed on the application of recycled crumb rubber to enhance dynamic damping of structural concrete for railway applications. To enable the industry application, specific requirements must be complied (e.g., EN 13230 [32]). The materials for the concrete mix are thus specifically chosen to meet standard requirements.

##### 4.1. Cement

As described in BS EN 197-1 [33], the Portland Cement Type I (CEM I) could be used to mix concrete which has a characteristic strength of 55 MPa.

##### 4.2. Silica Fume

Silica fume is a grey powder that belongs to a broad class of siliceous and aluminous materials called “Pozzolans”, which plays a particular role in filling the pores between the cement. Adding the right amount of silica fume contributes to improving the compressive and flexural strengths, impermeability, corrosion/impact resistances. These improvements are due to the consumption of calcium hydroxides, produced by the hydration of cement, by the silicon dioxide  $\text{SiO}_2$  [34] present in the composition of the silica fume as summarized in Table 1. The use of silica fume in this study is to compensate the loss of strength when crumb rubber is used.

**Table 1.** Chemical and Physical Properties of Undensified Silica Fume [35].

No.	Properties	Value
1	$\text{SiO}_2$	Minimum 90%
2	Loss of Ignition	Maximum 3%
3	Coarse Particles > 45 $\mu\text{m}$	Maximum 1.5% (tested on undensified)
4	Bulk Density (U)	200–350 $\text{kg}/\text{m}^3$
5	Bulk Density (D)	500–700 $\text{kg}/\text{m}^3$

##### 4.3. Coarse Aggregates

Coarse aggregate refers to pebbles and gravel, while fine aggregate refers to natural sand and artificial sand. Aggregates with a particle size greater than 4.75 mm are called coarse aggregates and aggregates with a diameter of 4.75 mm or less are called fine aggregates. Using a vibrating sieve to screen out usable gravels, the gradation table is produced as shown in Table 2. For concrete sleepers, all aggregates should comply with BS EN 12620 [36].

Table 2. Gradation of aggregates.

No.	Sieves (mm)	Weight Retained (g)	% Retained	Cumulative Retained	% Finer
1	20	0	0%	0	100%
2	16	0	0%	0	100%
3	10	835	21%	21%	79%
4	6.7	2710	67.5%	88.5%	11.5%
5	4.75	355	9%	97.5%	2.5%
6	Base	100	2.5%	100%	0%
	Total	4000 g			

#### 4.4. Water

The water used to mix concrete should be clean and easy to obtain on site, in accordance to BS EN 206-1 [37].

#### 4.5. Admixture

Concrete admixtures are substances, once added to the mixture, that improve and adjust the performance of concrete. Typically, according to BS EN 934-2 [33], they cannot be added in excess of 5% of the cement content. The most common such admixtures are water-reducing agents, set retarder, air-entraining admixture, etc.

#### 4.6. Concrete

The general performance of concrete sleepers should conform to BS EN 206-1 [37], which means cylinder samples compressive strength not below 55 MPa, cement content over 300 kg/m<sup>3</sup> and a maximum water–cement ratio of 0.45 cannot be exceeded. After casting, the concrete samples must be covered with plastic sheet for 24 h, and then placed in a water tank for 7 and 28 days prior for testing. The mix design (see Table 3) has been further developed from previous studies to ensure that the concrete could satisfy the minimum requirements [32,33,38]. A pilot test has been conducted to achieve the requirement and reveal an appropriate ratio between water and binder (cement + silica fume). The ration has been retained for all mixes to ensure that the comparison could be rationalised.

Table 3. Concrete mix design.

Ingredients kg/m <sup>3</sup>	Main Components				Silica Fume SF	Mixes A	Mixes B
	Cement	Water	Gravel	Sand		Crumb Rubber CR (180 & 400 µm)	Crumb Rubber CR (75 µm)
SF-0%, CR-0%	530	233	986	630	-	-	-
SF-5%, CR-0%	503	233	986	630	27	-	-
SF-10%, CR-0%	477	233	986	630	53	-	-
SF-5%, CR-5%	503	233	986	598	27	32	32
SF-10%, CR-5%	477	233	986	598	53	32	32
SF-5%, CR-10%	503	233	986	567	27	63	63
SF-10%, CR-10%	477	233	986	567	53	63	63

## 5. Experimental Results and Discussion

Based on the design requirements of the railway concrete sleepers that comply with the British Standards BS EN 206-1 [37], and on the theory described in the “Design of Normal Concrete Mixes” [39], 133 specimens were casted using different materials’ proportions. Silica fume is used as a partial replacement of the cement content and the crumb rubber as an alternative aggregate by replacing different amounts of fine aggregates. One hundred and fourteen specimens were characterized by the use of the crumb rubber, half of them were made using a mix of 180 and 400 micron crumb rubber (Mixes A), and the other half was mixed using 75 micron crumb rubber (Mixes B), as shown in Figure 4 and Table 3.



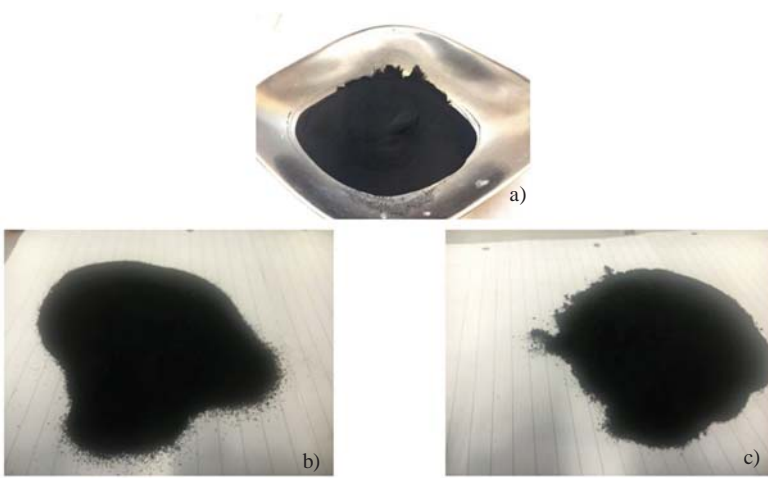


Figure 4. Rubber Powder ((a) 75  $\mu\text{m}$ ; (b) 400  $\mu\text{m}$ ; and (c) 180  $\mu\text{m}$  particle size, respectively).

Serviceability tests were conducted after each mix as shown in Figure 5. Then, they were cured in water (see Figure 6). For each single batch, there were 19 samples manufactured. Once the concrete has been mixed, it was poured directly into different shaped moulds: 100 mm cube,  $\Phi 100 \times L200$  mm cylinder,  $W100 \times H100 \times L500$  mm prism, and  $W45 \times H20 \times L120$  mm prism, each shape corresponding to the compressive strength testing (CS), splitting tensile strength testing (STS), flexural strength testing (FS), and electrical resistivity testing (ER) and vibration testing (VT), respectively as shown in Table 4. In order to provide good curing conditions, the samples are demoulded after 24 h and placed in a tank at appropriate temperature, then removed after 7 and 28 days respectively to carry out tests.



Figure 5. Concrete mixer (left); concrete slump test (right).





Figure 6. Specimen shapes (left); curing tank (right).

Table 4. Types of moulds and corresponding tests.

Mould Type	Number of Samples per Mix	Type of Test
Cube 100 mm	6	Compressive strength
Cylinder $\Phi$ 100 $\times$ L200 mm	3	Splitting Tensile Strength
Prism W100 $\times$ H100 $\times$ L500 mm	6	Flexural Strength
Prism W45 $\times$ H20 $\times$ L120 mm	4	Electrical Resistivity, Vibration, and Damping

### 5.1. Compressive Strength

The compressive strength tests (Figure 7) were carried out according to BS EN 12390-3 [40]. With a total of six cube samples per batch, previously removed from the tank and placed in an oven one day in advance in order to dry, three samples were tested after 7 days and the other half after 28 days. The results of the compressive tests are summarised in Figure 8.



Figure 7. Compressive test setup.

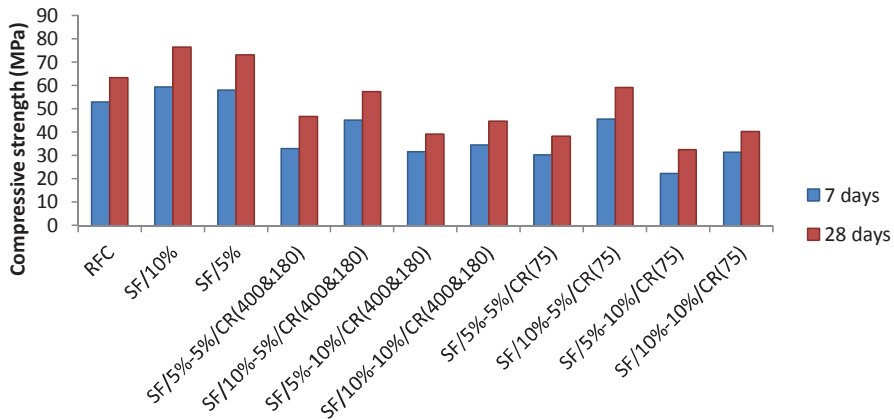


Figure 8. Compressive strength of crumb rubber concrete.

According to Figure 8, the results of compressive strength at 7 days and 28 days of experimental samples is shown. The reference concrete showed a compressive strength of 53.05 MPa at 7 days and 63.33 MPa at 28 days which shows good performance in compressive strength. The highest performance of compressive strength are the samples containing 5% and 10% silica fume, with 73.13 MPa and 76.5 MPa, respectively. Many previous literatures have indicated that the compressive strength would reduce in replacement of fine aggregate with crumb rubber. The results of this research also confirmed this phenomenon. In fact, all the samples with crumb rubber have less performance in compressive strength. There are only 2 samples containing crumb rubber that met the design requirements (55 MPa) according to BS EN 206-1 [37] in which they are 10% silica fume/5% 75 micro-crumb rubber and 10% silica fume/5% 400&180 micro-crumb rubber. The best performance of compressive strength crumb rubber concrete sample is 10% silica fume/5% 75 micro-crumb rubber which has 59.2 MPa compressive strength at 28 days and it is only 6.5% lower than reference concrete.

The 10% silica fume or 5% 400&180 micro-crumb rubber has a similar result which is 57.3 MPa. Obviously, the addition of crumb rubber negatively affected the concrete performance while the silica fume improved it. This has been proved by different authors who establish a proportional relation between the increase of crumb rubber content in the concrete mixture and the reduction in its compressive strength [41–43]. However, the rubber concrete containing a proportion of 10% silica fume and 5% crumb rubber has shown considerable results by reaching 59.20 MPa and 57.30 MPa at 28 days in both cases: 75 micron and the mix of 180 and 400 micron, respectively. The fact that the addition of 75 micron crumb rubber results in higher concrete compressive strength comparing to the mix of 180 and 400 micron by approximately 3.3% is due to the finer rubber particles that have a better ability in filling voids, thus offering a higher compressive strength [44]. Therefore, it has been deducted from the tests' results of this study that the crumb rubber concrete can be considered as a reliable material for railway concrete sleepers, since its compressive strength meet the standard for sleepers manufacturing (55 MPa).

## 5.2. Splitting Tensile and Flexural Strengths

According to BS EN 12390-6 [45], cylindrical specimens are used to test the rubber concrete splitting test after 28 days. In order to stabilize the specimens during the test, a pad is placed between the bearing surface and the press plate of the machine forming a corresponding strip loading between the top and the bottom of the specimens (Figure 9). At the beginning of the test, the loading was carried out continuously and uniformly at a speed ranging from 0.02 to 0.05 MPa/s until it reached 30 N/mm<sup>2</sup>, the loading speed was then increased to range between 0.05 and 0.08 MPa/s until the end

of the test. The test is stopped when the specimen is damaged and the damage load is recorded at an accuracy of 0.01 KN.

On the other hand, in order to measure the flexural strength of the rubberised concrete, several 4-point bending tests (Figure 10) have been carried out on prism specimens at 28 days according to BS EN 12390-5 [46]. The specimens are placed on two roller supports and loaded from an upper roller at a constant rate of 0.05 MPa/s, and the tests' results stop recording once the specimens fail. The results of both tests are presented in each graph of Figure 11.



Figure 9. Splitting tensile test.



Figure 10. 4-point bending test.

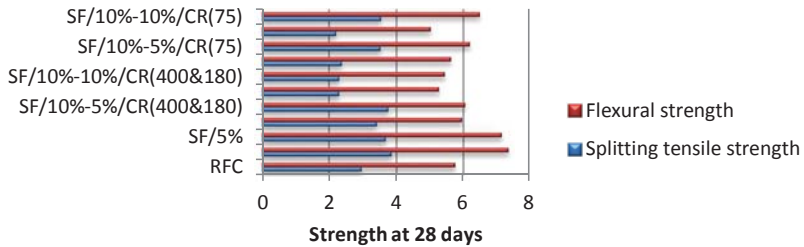


Figure 11. Splitting tensile strength of crumb rubber concrete.

According to BS EN 12390-6 [45], the splitting tensile strength of concrete at 28 days was calculated using the function below:

$$f_{ct} = \frac{2F}{\pi LD} \quad (1)$$

where  $f_{ct}$  is the splitting tensile strength (MPa),  $F$  is the maximum load (N),  $L$  is the length of the line of contact of the specimen (mm), and  $D$  is the designated cross-sectional dimension (mm).

Similarly to the compressive strength results, the increase in silica fume content clearly improved the splitting tensile strength by 30% comparing to conventional concrete, reaching a maximum value of 3.85 MPa at 28 days as shown in Figure 11. Also, as expected from previous studies, the rubber powder replacing fine aggregates has considerably decreased the splitting tensile strength, especially when its amount is increased to 10% and mixed with 5% silica fume, leading to a minimum value lower than the one obtained from the conventional concrete by 35% in the case of 75 micro rubber, and 30% in the case of mixing 180 and 400 micro rubber. Though, the proportions that seemed to show better performance than normal concrete are the ones containing 10% silica fume: mixed with 5% crumb rubber in the case of 180 and 400 micro rubber, and 10% in the case of 75 micro rubber (3.75 MPa and 3.54 MPa respectively).

Likewise, the flexural strength has been calculated following the British standard BS EN 12390-5 [46]:

$$f_{cf} = \frac{FI}{d_1 d_2^2} \quad (2)$$

where  $f_{cf}$  is the flexural strength (MPa),  $F$  is the maximum load (N),  $I$  is the length between roller supports (mm), and  $d_1$  and  $d_2$  are the cross-sectional dimensions of specimen (mm).

As shown in Figure 11, similar trend was observed between the splitting tensile and the flexural strengths. The maximum value recorded is 7.34 MPa and the minimum is 5.02 MPa, both correspond to SF10%/CR0% and SF5%/CR10%, respectively. Same observations have been deducted in the flexural test, which are the improvement of concrete strength by increasing the silica fume content and decreasing the crumb rubber proportion, and its deterioration in the opposite way. Many previous studies have come to similar conclusions regarding both, splitting tensile and flexural strengths of rubberised concrete, when replacing normal coarse aggregates with recycled rubber crumb [21,47,48]. Yet, the specimens containing a combination of 10% silica fume and whether 5% of the 180&400 micro rubber or 10% of 75 micro rubber have shown acceptable flexural strengths superior to plain concrete by 8% and 13%: 6.19 MPa and 6.49 MPa, respectively.

The tensile and flexural ratio can be calculated by:

$$\text{tensile ratio} = \frac{f'_t}{f'_c} * 100\% \quad (3)$$

$$\text{tensile ratio} = \frac{f'_f}{f'_c} * 100\% \quad (4)$$

The tensile ratio and flexural ratio have been calculated by Formulas (3) and (4) shown in Figure 12. Both the tensile and flexural ratio follow the same trend as flexural/splitting tensile strength. From the graph, all the flexural ratio of crumb rubber concrete are more than 10%. The highest tensile/flexural ratio is 10% silica fume/10% 75 micro rubber, which are 8.78% and 16.10%, respectively. Non-crumb rubber samples show very low tensile ratio, they are: 4.69% for reference concrete, 5.03% for 5% silica fume concrete and 5.03% for 10% silica fume; 10% silica fume/10% 400 & 180 micro-crumb rubber has similar tensile ratio with non-crumb rubber sample, which is 5.11%.

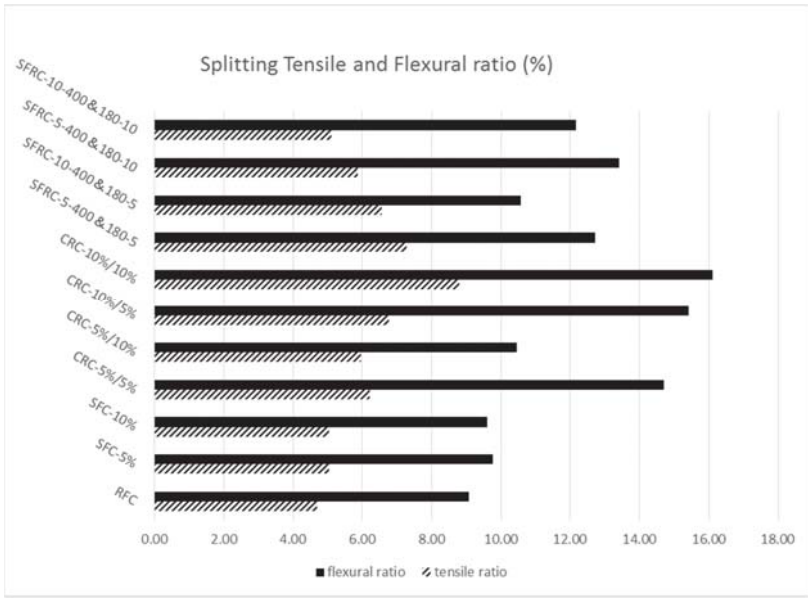


Figure 12. Splitting tensile and flexural ratio of crumb rubber concrete.

### 5.3. Electrical Resistivity

Generally, there are two main methods to measure the electrical resistance of cementitious materials: two-electrode method and four-electrode method [49]. In this study, the two-electrode method has been considered to test prism specimens at 28 days, after having been removed from the tank for natural drying prior for testing. Victor VC60B+, an insulation tester, has been used to determine the electrical resistance (ohm) of the specimens, by connecting leads to both their ends and setting the voltage at a constant value of 1000 Volts as shown in Figure 13. The results of the experiments, shown in Figure 12, are recorded 60 s later.



Figure 13. Electrical resistivity test.

After 28 days, the electrical resistance was measured then calculated using the resistance equation [22]:

$$\rho = k * R; k = \frac{A}{L} \tag{5}$$

where  $R$  is the resistance of concrete,  $k$  is a geometrical factor which depends on the size and shape of the specimen,  $A$  is the cross-sectional area perpendicular to the current,  $L$  is the height of the specimen.

As it can be seen from Figure 14, the plain concrete specimen has the lowest electrical resistivity among all others: 255 kΩ. The concrete’s electrical resistivity increased once the silica fume has been added, which proved what has been found by other researchers [23,50,51]. Obviously, as the rubber is considered as a good insulator, the concrete samples containing crumb rubber have shown the best results in terms of electrical resistivity: 374.25 kΩ and 371 kΩ for SF10%/CR10% (180 & 400) and SF10%/CR5% (75) respectively. Therefore, the addition of crumb rubber is capable of enhancing the electrical resistivity of plain concrete by 47%, and by 17% if it contained 10% of silica fume. In fact, both insulator materials (silica fume and rubber) have shown good performance as expected, due to their ability to prevent the two electrodes to transmit current in concrete [52].

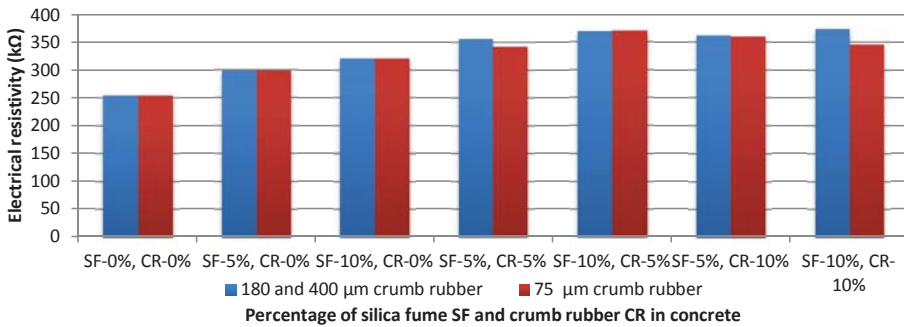


Figure 14. Electrical resistivity of rubber concrete with different particles size.

#### 5.4. Vibration Damping

The vibration tests have been conducted in the civil engineering laboratory to avoid vibration from surrounding environment. Prism specimens were used to carry out these experiments using the following equipment: computer with PROSIG hammer system, DATS modal analysis software, and an accelerometer. The specimens’ surfaces have been cleaned to eliminate bias in tests results [52,53], and a stable support (Figure 15) was used to fix the samples as a cantilever beam since placing the stationary platform on the concrete floor makes the resonant frequency relatively high. The vibration of samples was excited by a PCB hammer (Figure 16) at a frequency range of 0 to 1600 Hz [54,55], and as shown in Figure 16, a 5-order average vibration response of each sample is presented by the frequency response function (FRF). The graph of time series is illustrated in Figure 17.

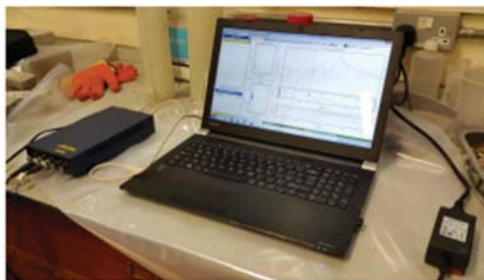


Figure 15. DATS modal analysis suite.



Figure 16. Damping test.

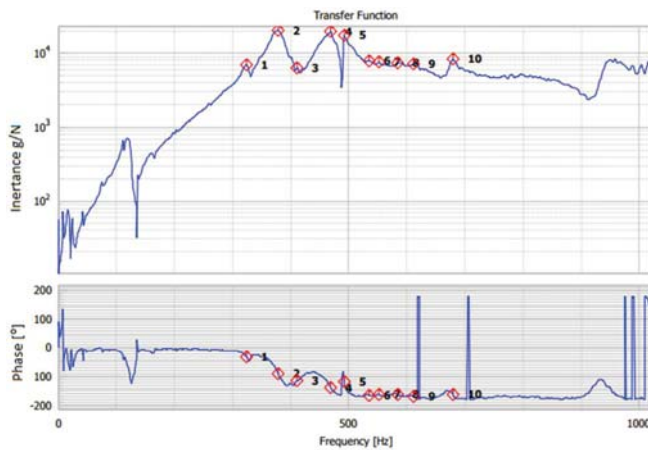


Figure 17. Frequency response function.

Generally, there are two methods to analyse the damping ratio and both have been considered in this study. The first method is called exponential curve fitting method (ECFM); this method is based on calculating the damping ratio directly using the natural frequency and the vibration response of the concrete samples from the FRF graph, as can be seen from Figure 17. The specimen containing 10% silica fume has a natural frequency of 469 Hz, and the one containing the same proportion of silica fume in addition to 5% of crumb rubber (75 micron) has 500 Hz of natural frequency. All the natural frequencies recorded during the tests are presented in Table 5, although, factors such as the high stiffness of concrete and thickness of the metal gasket can affect the range of the natural frequencies [52,56].



Table 5. Types of moulds and corresponding tests.

No.	Mixes	Natural Frequency (Hz)				S.D.
		Sample 1	Sample 2	Sample 3	Average	
1	RFC	478	451	486	471.67	±18.34
2	SF/10%	469	427	433	443	±22.716
3	SF/5%	457	437	462	452	±13.23
4	SF/5%-5%/CR (400&180)	476	452	463	463.67	±12.01
5	SF/10%-5%/CR (400&180)	456	439	454	449.67	±9.29
6	SF/5%-10%/CR (400&180)	479	493	474	482	±9.85
7	SF/10%-10%/CR (400&180)	441	446	435	440.67	±5.51
8	SF/5%-5%/CR (75)	443	462	431	445	±15.63
9	SF/10%-5%/CR (75)	477	500	459	477	±20.55
10	SF/5%-10%/CR (75)	453	456	472	460	±10.21
11	SF/10%-10%/CR (75)	488	493	512	498	±12.66

The acceleration-time graph is then plotted and the exponential line is fitted with the peak amplitude according to the decreasing trend of the vibration response, while the equation of the exponential line is generated from the Microsoft Excel program as illustrated in Figure 18.

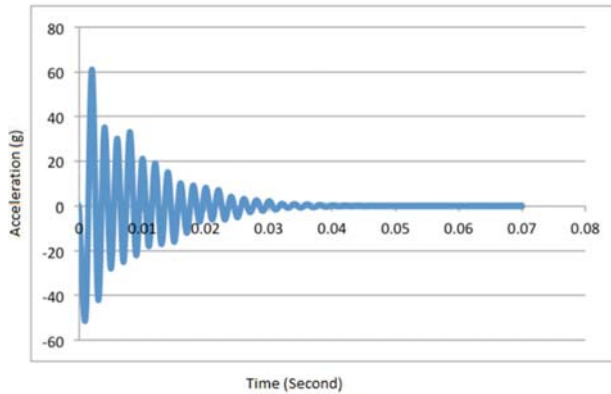


Figure 18. Vibration response of the concrete.

Finally, the equation obtained from the vibration graph (Figure 19) is compared with the reduced general mathematical equation representing the amplitude (Equation (4)), and the damping ratio is obtained as follows:

$$A_t = A_0 \cdot e^{-\zeta \cdot \omega_n \cdot t} \tag{6}$$

where  $A_t$  is the amplitude,  $A_0$  is the peak amplitude,  $\zeta$  is the damping ratio,  $\omega_n$  is the natural frequency (rad/s) equal to  $2\pi f_n$  where  $f_n$  is the natural frequency in Hz, and  $t$  is the time in seconds. The calculation of the damping ratio of the SF5%–CR10% sample presented by the graph of Figure 19 has led to 0.0324, which is 3.24% of critical damping ratio.

The second method is used to verify the value obtained from the ECFM and in order to make sure that the tests' results are more reliable. It is called the logarithmic decrement method (LDM), and the damping ratio in this case is calculated using the logarithmic decrement formulas (Equations (5) and (6)):

$$\delta = \frac{1}{n} \ln \frac{A_0}{A_n} \text{ if } n = 1, 2, 3 \dots \tag{7}$$

$$\zeta = \frac{1}{\sqrt{1 + \left(\frac{2\pi}{\delta}\right)^2}} \approx \frac{\delta}{2\pi} \tag{8}$$



where  $\delta$  is the damping index,  $A_0$  is the peak amplitude,  $A_n$  is the amplitude after  $n$  number of cycles, and  $\zeta$  is the damping ratio.

The damping ratio estimated from the LDM for the same sample tested before using the ECFM is 0.0323 (3.23%), which presents a small error of 0.31%. The results regarding all the samples are plotted in the graph of Figure 20. The graph shows that the two methods have similar trend. The reference concrete has the lowest damping ratio with 0.02239 and 0.02098 respectively according to the ECFM and LDM methods. The addition of 10% silica fume improved slightly the concrete’s damping ratio to reach 0.02822 using ECFM and 0.2791 using LDM, and a little more improvement of 19 and 21% respectively when 10% of 75 micron rubber has been added. This improvement is due to the large interface area between the cement matrix and silica fume particles which offer better vibration energy dissipation [57,58]. Finally, the 180&400 micron rubber have proved to have the best effect on the damping ratio of concrete, by reaching the maximum values obtained in this test: 0.04499 using ECFM and 0.04451 using LDM, which present an improvement of 100 and 112% respectively comparing to the conventional concrete. These results confirm the theory stating that the damping ratio of concrete improves with the increase in the size and the amount of rubber content as declared by Zheng at al. [52]. A damping ratio of 3% could easily reduce up to 20–30% of dynamic actions (bending, shear, and force); however, in order to suppress large-amplitude vibrations the damping coefficient should be around 4–5% [57]. Consequently, since the static and dynamic properties of the rubberised concrete (180&400 micron) meet the design standards, it should highly be recommended for concrete railway sleepers’ manufacturing [53,57].

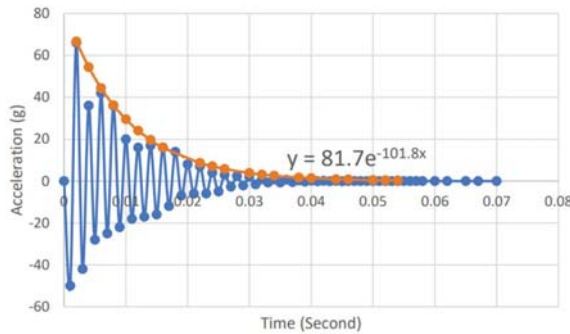


Figure 19. Curve fitting of vibration response of the concrete (75 µm crumb rubber).

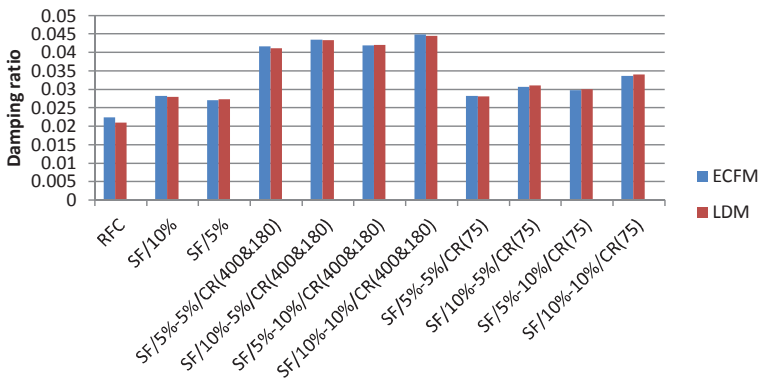


Figure 20. Dynamic damping of crumb rubber concrete at 28 days.

5.5. Dynamic Flexural Moduli

According to Kaewunruen et al., the dynamic flexural modulus of elasticity demonstrates the elastic behaviour of material under flexural loading. The dynamic flexural modulus can be estimated from Equation (9) [49,59–61]. Figure 21 reveals that the early age dynamic moduli at 7 days of the rubberized concrete are decreased compared to the reference concrete (from 7% to 28%, depending on the mixes). This implies that the release of prestressing force on concrete sleepers should be gentle to minimise the effect on initial deformations (i.e., pre-camber and elastic shortening). Figure 22 shows the dynamic moduli of the concrete at 28 days. It can be observed that the use of silica fume can increase the dynamic moduli at 28 days. The deviation of dynamic moduli of the rubberized concrete is from 5% to 26% compared to the reference concrete. Comparatively, it is found that, at 28 days, the dynamic flexural behavior could be expected to be similar to traditional high-strength concrete (reference). This implies that the difference in creep and shrinkage would be minimal to normal concrete sleepers. These requirements are critical for concrete sleepers in ballasted railway tracks. However, the application of this rubberised concrete can be applied to concrete slabs in ballastless tracks of which its requirement is slightly less stringent [59–63].

$$E_d = 0.021\rho^{1.5}\sqrt{f_c} \tag{9}$$

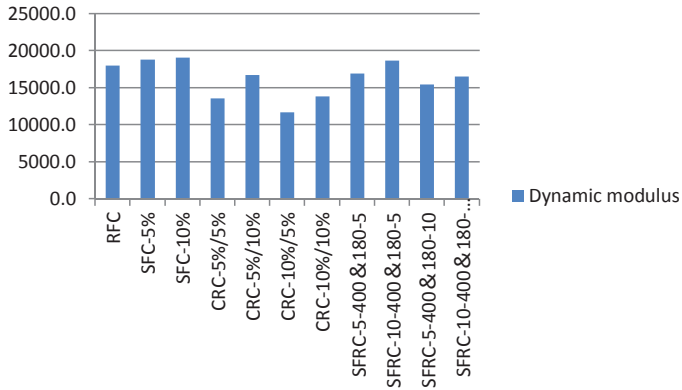


Figure 21. Early-age dynamic moduli of crumb rubber concrete at 7 days (MPa).

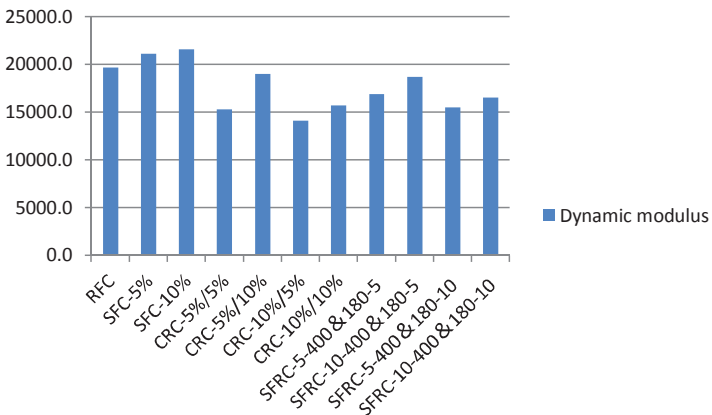


Figure 22. Dynamic moduli of crumb rubber concrete at 28 days (MPa).

## 6. Conclusions

Railway traffic environment is aggressive and the railway infrastructure has to experience heavy-haul or high-speed rail operation. Therefore, material for railway infrastructure needs to be strong, durable, resilient and tough to withstand various unexpected damage. Waste tyre is a global environmental problem which is non-biodegradability, flammability and chemical composition. Waste tyre cannot be solved as a normal method like disposal. This research study aimed to develop an environmentally friendly concrete using crumb rubber, recycled form waste rubber tyres (75 micron and 180 micro mixed with 400 micron), as micro-filler to make concrete sleepers that meet with the railway requirements. Although the emphasis is placed on concrete sleepers in ballasted railway tracks, the application of this recycled concrete can also be applied to concrete slabs in ballastless tracks. Based on diverse proportions of crumb rubber and silica fume, eleven different types of concrete were casted according to British standard. The first experiments carried out on the concrete specimens tested their compressive strength at 7 and 28 days, as it presents the most important property of this material. Similar to previous studies' findings, it has been deduced that the increase in the rubber content results in a drop in compressive strength. However, the rubber concrete containing a proportion of 10% silica fume and 5% crumb rubber has shown considerable results by reaching 57.30 MPa and 59.20 MPa at 28 days in both rubber particle cases 75 micro and the mix of 180 and 400 micro respectively, thus meeting the standard for railway sleepers manufacturing (55 MPa). Likewise, it has been observed a significant deterioration in both splitting tensile and flexural strengths when increasing the crumb rubber proportion in concrete. Still, the proportions that seemed to show better splitting tensile performance than plain concrete are the ones containing 10% silica fume: mixed with 5% crumb rubber in the case of 180 and 400 micro rubber, and 10% in the case of 75 micro rubber (3.75 MPa and 3.54 MPa respectively).

On the other hand, the specimens containing a combination of 10% silica fume and whether 5% of the 180&400 micro rubber or 10% 75 micro rubbers have shown acceptable flexural strengths superior to plain concrete by 8 and 13%: 6.19 MPa and 6.49 MPa, respectively. In terms of electrical resistivity, the concrete samples containing crumb rubber have shown the best results: 374.25 k $\Omega$  and 371 k $\Omega$  for SF10%/CR10% (180&400) and SF10%/CR5% (75) respectively. Therefore, the addition of crumb rubber is capable of enhancing the electrical resistivity of conventional concrete up to 47%. Finally, by conducting vibration tests on rubberised concrete and using both the exponential curve fitting method (ECFM) and the logarithmic decrement method (LDM), it has been concluded that the crumb rubber has clearly improved the concrete's damping ratio, especially when using the 180&400 micro which resulted in an improvement of 100% comparing to normal concrete. It is therefore recommended from the results of this study to use crumb rubber in concrete as micro-filler, and more precisely the SF/10%–CR/5% (400&180) as it showed the best performance in all tests and meets the requirements of railway concrete sleepers. From the environmental perspective, the use of crumb rubber in concrete presents one of the best alternatives while dealing with rubber waste, as it will help both the environment protection and also the reduction in railway sleepers cost.

**Author Contributions:** Conceptualization, S.K., Y.C. and Z.X.; Methodology, S.K., Y.C. and Z.X.; Validation, D.L., Y.C. and Z.X.; Formal Analysis, D.L.; Investigation, Y.C. and Z.X.; Resources, S.K.; Writing-Original Draft Preparation, D.L., Y.C., Z.X.; Writing-Review & Editing, S.K.; Visualization, D.L.; Supervision, S.K.; Funding Acquisition, S.K.

**Funding:** This research was funded by the Japan Society for Promotion of Science (JSPS) grant number L15701 and the APC was funded by the European Commission for H2020-MSCA-RISE Project No. 691135 “RISEN: Rail Infrastructure Systems Engineering Network”.

**Acknowledgments:** The first author wishes to gratefully acknowledge the Japan Society for Promotion of Science (JSPS) for his JSPS Invitation Research Fellowship (Long-term), Grant No. L15701, at Track Dynamics Laboratory, Railway Technical Research Institute and at Concrete Laboratory, the University of Tokyo, Tokyo, Japan. The JSPS financially supports this work as part of the research project entitled “Smart and reliable railway infrastructure”. The authors are very grateful to the European Commission for H2020-MSCA-RISE Project No. 691135 “RISEN: Rail Infrastructure Systems Engineering Network” ([www.risen2rail.eu](http://www.risen2rail.eu)) [64]. In addition, the sponsorships and

assistance from CEMEX, Network Rail, Lehigh Technologies Inc., and RSSB (Rail Safety and Standard Board, UK) are highly appreciated.

**Conflicts of Interest:** The authors declare no conflict of interest.

## References

1. Gourley, J.T.; Johnson, G.B. Developments in geopolymer precast concrete. In Proceedings of the Geopolymer 2005 World Congress, Geopolymer Green Chemistry and Sustainable Development Solutions, Saint-Quentin, France, 29 June–1 July 2005; pp. 139–143.
2. Kaewunruen, S.; You, R.; Ishida, M. Composites for Timber-Replacement Bearers in Railway Switches and Crossings. *Infrastructures* **2017**, *2*, 13. [CrossRef]
3. Kaewunruen, S.; Wu, L.; Goto, K.; Najih, Y.M. Vulnerability of Structural Concrete to Extreme Climate Variations. *Climate* **2018**, *6*, 40. [CrossRef]
4. FIP Commission on Prefabrication, FIP Commission on Prefabrication; Working Group on Concrete Railway Sleepers & Fédération Internationale de la Précontrainte. *Working Group on Concrete Railway Sleepers. Concrete Railway Sleepers*; Thomas Telford Services Ltd.: London, UK, 1987.
5. Gupta, T.; Chaudhary, S.; Sharma, R.K. Mechanical and durability properties of waste rubber fiber concrete with and without silica fume. *J. Clean. Prod.* **2016**, *112*, 702–711. [CrossRef]
6. Aiello, M.; Leuzzi, F. Waste tyre rubberized concrete: Properties at fresh and hardened state. *Waste Manag.* **2010**, *30*, 1696–1704. [CrossRef] [PubMed]
7. Thomas, B.S.; Gupta, R.C. A comprehensive review on the applications of waste tire rubber in cement concrete. *Renew. Sustain. Energy Rev.* **2016**, *54*, 1323–1333. [CrossRef]
8. Remennikov, A.M.; Kaewunruen, S. A review of loading conditions for railway track structures due to train and track vertical interaction. *Struct. Control Health Monit.* **2008**, *15*, 207–234. [CrossRef]
9. Silva, É.A.; Pokropski, D.; You, R.; Kaewunruen, S. Comparison of structural design methods for railway composites and plastic sleepers and bearers. *Aust. J. Struct. Eng.* **2017**, *18*, 160–177. [CrossRef]
10. Kaewunruen, S.; Remennikov, A.M. Progressive failure of prestressed concrete sleepers under multiple high-intensity impact loads. *Eng. Struct.* **2009**, *31*, 2460–2473. [CrossRef]
11. Cai, H.Q. Structure analysis of railway. *J. Hebei Inst. Arch.* **2006**, *29*, 18–20.
12. Kaewunruen, S.; Remennikov, A.M. Influence of voids and pockets on the vibration characteristics of prestressed concrete sleepers. In Proceedings of the Society of Experimental Mechanics (SEM) Annual Conference and Exhibition, Orlando, FL, USA, 19–22 February 2007; pp. 3–6.
13. Esveld, C. *Modern Railway Track*, 2nd ed.; MRT-Productions: Delft, The Netherlands, 2001; ISBN 90-800324-3-3.
14. Indraratna, B.; Rujikiatkamjorn, C.; Salim, W. *Advanced Rail Geotechnology—Ballasted Track*; CRC Press: London, UK, 2011.
15. Remennikov, A.M.; Kaewunruen, S. Resistance of railway concrete sleepers to impact loading. In Proceedings of the 7th International Conference on Shock & Impact Loads on Structures, Beijing, China, 17–19 October 2007; pp. 489–496.
16. You, R.; Li, D.; Ngamkhanong, C.; Janeliukstis, R.; Kaewunruen, S. Fatigue Life Assessment Method for Prestressed Concrete Sleepers. *Front. Built Environ.* **2017**, *3*, 68. [CrossRef]
17. Zhang, X.; Thompson, D.J.; Squicciarini, G. Sound radiation from railway sleepers. *J. Sound Vib.* **2016**, *369*, 178–194. [CrossRef]
18. Hameed, A.S.; Shashikala, A. Suitability of rubber concrete for railway sleepers. *Perspect. Sci.* **2016**, *8*, 32–35. [CrossRef]
19. Salam, H.E.; Sherbini, A.S.; Seleem, M.H.; Balaha, M.M. Impact Resistance of Rubberized Concrete. *Eng. Res. J.* **2008**, *31*, 265–271.
20. Topçu, İ.B.; Demir, A. Durability of Rubberized Mortar and Concrete. *J. Mater. Civ. Eng.* **2007**, *19*, 173–178. [CrossRef]
21. Topçu, İ.B.; Şengel, S. Properties of concretes produced with waste concrete aggregate. *Cem. Concr. Res.* **2004**, *34*, 1307–1312. [CrossRef]
22. Anagennisi Project. Rubberised Concrete. 2017. Available online: <http://anagennisi.org/wordpress/portfolio/rubberised-concrete-optimised-mix> (accessed on 14 February 2018).

23. Sol-Sánchez, M.; Thom, N.; Moreno-Navarro, F.; Rubio-Gámez, M.; Airey, G. A study into the use of crumb rubber in railway ballast. *Constr. Build. Mater.* **2015**, *75*, 19–24. [[CrossRef](#)]
24. Toutanji, H. The use of rubber tire particles in concrete to replace mineral aggregates. *Cem. Concr. Compos.* **1996**, *18*, 135–139. [[CrossRef](#)]
25. Khaloo, A.R.; Dehestani, M.; Rahmatabadi, P. Mechanical properties of concrete containing a high volume of tire-rubber particles. *Waste Manag.* **2008**, *28*, 2472–2482. [[CrossRef](#)] [[PubMed](#)]
26. Ganjian, E.; Khorami, M.; Maghsoudi, A.A. Scrap-tyre-rubber replacement for aggregate and filler in concrete. *Constr. Build. Mater.* **2009**, *23*, 1828–1836. [[CrossRef](#)]
27. Paine, K.A.; Dhir, R.K.; Moroney, R.; Kopasakis, K. Use of Crumb Rubber to Achieve Freeze/Thaw Resisting Concrete. In Proceedings of the International Conference on Concrete for Extreme Conditions, Dundee, UK, 9–11 September 2002; pp. 485–498. [[CrossRef](#)]
28. Hernández-Olivares, F.; Barluenga, G. Fire performance of recycled rubber-filled high-strength concrete. *Cem. Concr. Res.* **2004**, *34*, 109–117. [[CrossRef](#)]
29. Fattuhi, N.; Clark, L. Cement-based materials containing shredded scrap truck tyre rubber. *Constr. Build. Mater.* **1996**, *10*, 229–236. [[CrossRef](#)]
30. Van Dyk, B.J.; Edwards, J.R.; Dersch, M.S.; Ruppert, C.J., Jr.; Barkan, C.P.L. Evaluation of dynamic and impact wheel load factors and their application in design processes. *Proc. Inst. Mech. Eng. Part F* **2017**, *231*, 33–43. [[CrossRef](#)]
31. Kaewunruen, S.; Remennikov, A.M. Sensitivity analysis of free vibration characteristics of an in situ railway concrete sleeper to variations of rail pad parameters. *J. Sound Vib.* **2006**, *298*, 453–461. [[CrossRef](#)]
32. *BS EN 13230 Concrete Sleepers and Bearers*; British Standards Institute: London, UK, 2016.
33. *BS EN 934-2 Admixtures for Concrete, Mortar and Grout*; British Standards Institute: London, UK, 2009.
34. Mazloom, M.; Ramezani-pour, A.; Brooks, J. Effect of silica fume on mechanical properties of high-strength concrete. *Cem. Concr. Compos.* **2004**, *26*, 347–357. [[CrossRef](#)]
35. Elkem-Microsilica Grade 940 for Construction. 2017. Available online: <https://www.elkem.com/silicon-materials/high-performance-concrete/microsilica-concrete-grades/microsilica-grade-940-construction/> (accessed on 14 February 2018).
36. *BS EN 12620 Aggregates for Concrete*; British Standards Institute: London, UK, 2013.
37. *BS EN 206-1 Concrete: Part 1—Specification, Performance, Production and Conformity*; British Standards Institute: London, UK, 2000.
38. Mirza, O.; Kaewunruen, S. Influence of shear bolt connections on modular precast steel-concrete composites for track support structures. *Steel Comp. Struct.* **2018**, *27*, 647–659.
39. *BS EN 13139 Aggregates for Mortar*; British Standards Institute: London, UK, 2013.
40. *BS EN 12390-3 Testing Hardened Concrete: Part 3: Compressive Strength of Test Specimens*; British Standards Institute: London, UK, 2009.
41. Sukontasukkul, P.; Chaikaew, C. Properties of concrete pedestrian block mixed with crumb rubber. *Constr. Build. Mater.* **2006**, *20*, 450–457. [[CrossRef](#)]
42. Atahan, A.O.; Yücel, A.Ö. Crumb rubber in concrete: Static and dynamic evaluation. *Constr. Build. Mater.* **2012**, *36*, 617–622. [[CrossRef](#)]
43. He, L.; Ma, Y.; Liu, Q.; Mu, Y. Surface modification of crumb rubber and its influence on the mechanical properties of rubber-cement concrete. *Constr. Build. Mater.* **2016**, *120*, 403–407. [[CrossRef](#)]
44. Su, H.; Yang, J.; Ling, T.; Ghataora, G.S.; Dirar, S. Properties of concrete prepared with waste tyre rubber particles of uniform and varying sizes. *J. Clean. Prod.* **2015**, *91*, 288–296. [[CrossRef](#)]
45. *BS EN 12390-6 Testing Hardened Concrete: Part 6: Tensile Splitting Strength of Test Specimens*; British Standards Institute: London, UK, 2009.
46. *BS EN 12390-5 Testing Hardened Concrete: Part 5: Flexural Strength of Test Specimens*; British Standards Institute: London, UK, 2009.
47. Xiao, J.; Li, W.; Fan, Y.; Huang, X. An overview of study on recycled aggregate concrete in China (1996–2011). *Constr. Build. Mater.* **2012**, *31*, 364–383. [[CrossRef](#)]
48. Çakır, Ö. Experimental analysis of properties of recycled coarse aggregate (RCA) concrete with mineral additives. *Constr. Build. Mater.* **2014**, *68*, 17–25. [[CrossRef](#)]
49. Kaewunruen, S.; Meesit, R.; Mondal, P. Early age dynamic moduli of crumbed rubber concrete for compliant railway structures. *J. Sustain. Cem.-Based Mater.* **2017**, *6*, 281–292. [[CrossRef](#)]


50. New York State Assembly. NYS Assembly Priority for Waste Tire Cleanups Finally a Reality. 2003. Available online: <http://assembly.state.ny.us/comm/SolidWaste/20030714> (accessed on 14 February 2018).
51. Remennikov, A.M.; Kaewunruen, S. Experimental load rating of aged railway concrete sleepers. *Eng. Struct.* **2014**, *76*, 147–162. [[CrossRef](#)]
52. Zheng, L.; Sharon Huo, X.; Yuan, Y. Experimental investigation on dynamic properties of rubberized concrete. *Constr. Build. Mater.* **2008**, *22*, 939–947. [[CrossRef](#)]
53. Kaewunruen, S.; Akono, A.-T.; Remennikov, A.M. Attenuation effect of material damping on impact vibration responses of railway concrete sleepers. *GeoMEast* **2018**, accepted.
54. Kaewunruen, S.; Meesit, R. Sensitivity of crumb rubber particle sizes on electrical resistance of rubberised concrete. *Cogent Eng.* **2016**, *3*, 1126937. [[CrossRef](#)]
55. Meesit, R.; Kaewunruen, S. Vibration characteristics of micro-engineered crumb rubber concrete for railway sleeper applications. *J. Adv. Concr. Technol.* **2017**, *15*, 55–66. [[CrossRef](#)]
56. Kaewunruen, S.; Remennikov, A.; Aikawa, A. A numerical study to evaluate dynamic responses of voided concrete railway sleepers to impact loading. In Proceedings of the Australian Acoustical Society Conference 2011, Gold Coast, Australia, 2–4 November 2011; Available online: <http://ro.uow.edu.au/engpapers/628/> (accessed on 14 February 2018).
57. Kaewunruen, S.; Rachid, A.; Goto, K. Damping effects on vibrations of railway concrete sleepers. In Proceedings of the 3rd World Multidisciplinary Civil Engineering—Architecture—Urban Planning Symposium, Prigue, Czech, 13–17 June 2016.
58. Xu, Y.; Chung, D. Improving silica fume cement by using silane. *Cem. Concr. Res.* **2000**, *30*, 1305–1311. [[CrossRef](#)]
59. Akono, A.-T.; Chen, J.; Kaewunruen, S. Friction and fracture characteristics of engineered crumb-rubber concrete at microscopic lengthscale. *Constr. Build. Mater.* **2018**, *175*, 735–745. [[CrossRef](#)]
60. Kaewunruen, S.; Remennikov, A.M. Experimental simulation of the railway ballast by resilient materials and its verification by modal testing. *Exp. Tech.* **2008**, *32*, 29–35. [[CrossRef](#)]
61. Kaewunruen, S.; Remennikov, A.M. Nonlinear finite element modeling of railway prestressed concrete sleeper. In Proceedings of the 10th East Asia-Pacific Conference on Structural Engineering and Construction, EASEC 2010, Bangkok, Thailand, 3–5 August 2006; Volume 4, pp. 323–328.
62. Praticò, F.G.; Giunta, M. Proposal of a Key Performance Indicator for Railway Track Based on LCC and RAMS Analyses. *J. Constr. Eng. Manag.* **2018**, *144*, 04017104. [[CrossRef](#)]
63. Zhou, Y.; Wang, K.; Lv, K. Comparison of wheel/rail dynamic responses of the rail weld zones between ballasted track and slab track in high-speed railways. *J. Adv. Veh. Eng.* **2017**, *3*, 177–181.
64. Kaewunruen, S.; Sussman, J.M.; Matsumoto, A. Grand Challenges in Transportation and Transit Systems. *Front. Built Environ.* **2016**, *2*, 4. [[CrossRef](#)]



© 2018 by the authors. Licensee MDPI, Basel, Switzerland. This article is an open access article distributed under the terms and conditions of the Creative Commons Attribution (CC BY) license (<http://creativecommons.org/licenses/by/4.0/>).

Article

# Effect of Modified Polyvinyl Alcohol Fibers on the Mechanical Behavior of Engineered Cementitious Composites

Mian Sun <sup>1,2</sup>, Youzhi Chen <sup>1,2</sup>, Jiaoqun Zhu <sup>1,2</sup>, Tao Sun <sup>1,2,\*</sup>, Zhonghe Shui <sup>1,2</sup>, Gang Ling <sup>1,2</sup>, Haoxuan Zhong <sup>1,2</sup> and Yourui Zheng <sup>1,2</sup>

<sup>1</sup> State Key Laboratory of Silicate Materials for Architectures, Wuhan University of Technology, Wuhan 430070, China; 18202762912@sina.cn (M.S.); cyzly@whut.edu.cn (Y.C.); zhujiaoq@whut.edu.cn (J.Z.); zhshui@whut.edu.cn (Z.S.); linggang0609@163.com (G.L.); 18011134689@163.com (H.Z.); 15150565301@163.com (Y.Z.)

<sup>2</sup> School of Materials Science and Engineering, Wuhan University of Technology, Wuhan 430070, China

\* Correspondence: sunt@whut.edu.cn; Tel.: +86-180-6411-1505

Received: 2 November 2018; Accepted: 19 December 2018; Published: 22 December 2018

**Abstract:** Polyvinyl alcohol (PVA) fiber was proposed to enhance the mechanical performance of engineered cementitious composite in this research. A mixture of engineered cementitious composite with better expected performance was made by adding 2% PVA fiber. Mechanics tests, including pressure resistance, fracture resistance, and ultimate tensile strength, were conducted. They reveal that the engineered cementitious composites not only exhibit good pressure resistance, but they also exhibit excellent fracture resistance and strain capability against tensile stress through mechanics tests, including pressure resistance, fracture resistance, and ultimate tensile resistance. To further improve the engineered composites' ductility, attempts to modify the performance of the PVA fiber surface have been made by using a vinyl acetate (VAE) emulsion, a butadiene–styrene emulsion, and boric anhydride. Results indicated that the VAE emulsion achieved the best performance improvement. Its use in fiber pre-processing enables the formation of a layer of film with weak acidity, which restrains the hydration of adjacent gel materials, and reduces the strength of transitional areas of the fiber/composite interface, which restricts fiber slippage and pulls out as a result of its growth in age, and reduces hydration levels. Research illustrates that the performance-improvement processing that is studied not only improves the strain of the engineered cementitious composites, but can also reduce the attenuation of the strain against tensile stress.

**Keywords:** engineered cementitious composites (ECC); polyvinyl alcohol; fiber modification; mechanical behavior

---

## 1. Introduction

Due to cementitious composites' advantages of convenient construction, fine performance, and cost-saving, they are the most used building materials since their introduction in the 19th century [1]. Nevertheless, the innate disadvantages of inorganic non-metallic materials, including high fragility, low strain, and cracking, have led to multiple issues, and have limited their further development [2]. Specifically, it is the lack of ductility of cementitious composites, and their resultant ultimate loading, that causes fragile cracks and damage due to their lack of durability under normal loading and their lack of sustainability, which have constrained the applications of cementitious composites [3]. Hence, to ensure the harmonious co-existence of artificial facilities and the natural environment, and the reduction of damage to humans due to the collapse of buildings, it is increasingly urgent that concrete possessing high ductility, high extensibility, high durability, and high sustainability is developed for the construction of buildings [4].



At present, the fibers added are all millimeter-grade steel fibers. The steel fiber has a clear reinforcing effect on concrete and can effectively reduce the occurrence of large cracks, but it is not ideal to use the steel fiber to reduce the occurrence of small cracks. Small-scale fibers such as polyhexene fibers and polyvinyl alcohol fibers can restrain the expansion of micro-cracks from some micro-crack sources and prevent the generation of some micro-cracks, so that the crack width becomes smaller, which stops them from being connected [5]. Polymer fibers with a lower modulus of elasticity can reduce the stress concentration of concrete generated due to original defects, which plays a toughening role [6].

Yu K. et al. [7] selected polyethylene fibers and then mixed them into concrete to enhance the tensile load capacity of concrete substrates. High polymer and high-strength polyethylene fibers provide an enough fracture bridging capacity, which significantly improves the tensile toughness of the concrete matrix.

Ezio Cadoni et al. [8] conducted a dynamic tensile test on PVA-FRC (polyvinyl alcohol fiber reinforced concrete) to test fiber-reinforced concrete notched specimens at three different strain rates (50 s, 100 s, and 200 s) using a modified Hopkinson rod device. The experimental result shows that, as the strain rate increases, the tensile strength is significantly improved, and the fracture energy and ultimate deformation are significantly reduced.

M. Haskett et al. [9] studied the compression zone and tension zone of PVA fiber-reinforced concrete and found that PVA fiber in the compression zone effectively inhibited the cracking of concrete and slowed down the damage of the internal structure. Acting as a bridge, the fiber transmits the tensile stress in the tension zone, so PVA fiber reinforced concrete exhibits excellent ductility and a good performance after cracking.

Blanco et al. [10] conducted a comparative experiment to study the effects of different fiber types on the performance of concrete slabs and carried out finite element simulations, which found that different fiber types (steel fibers, plastic fibers) using general design methods led to large differences in the simulation experiment. Therefore, they put forward correction factors for different fiber types in the FRC board design. Therefore, the modification of the interface among PVA and steel fiber and the concrete matrix also requires different modification methods.

Engineered cementitious composites are a type of high-performance fiber-reinforcing composite concrete material that are systematically designed and optimally configured by employing theories in micromechanics, fracture mechanics, and statistics [11]. Through the configuration of the performance and relationship between chopped fibers, cementitious composites, and the transitional area of the interface, dramatic strain and strain-hardening characteristics are derived from the gain of a relatively low volume fraction of fibers [12]. Fabricated engineered cementitious composites should possess the distinctive characteristics of multiple cracks and strain hardening. They should be able to generate only tiny cracks and continuous load bearing when receiving tensile stress and bending stress, and eventually reach above a 3% ultimate strain against tensile stress [13]. The composition of engineered cementitious composites includes fibers, an emulsion, ultrafine sand (generally less than 0.3 mm), water, a highly effective water reducer, and a density-increasing stabilizer. The ratio between water and emulsion is generally less than 0.45 and voluminous auxiliary gel materials such as fly ash are used and the fiber-volume fraction is not greater than 2.5% [14]. Li, V.C. et al. [3] proved that they have radical strain and higher energy-consumption capabilities compared to normal fiber-enforced cementitious composites. Therefore, they will be significantly utilized in improving the ductility of the structure, the energy consumption, and the shock resistance. Cementitious composites have broad developmental potential in the applications of huge transformational structures, anti-shock structures, renovation structures, anti-seismic structures, and road paving structures.

Theoretical research on engineered cementitious composites commenced in 1999 [15]. This is the earliest proposition for adding polyethylene fibers into cementitious composites of high strength and high molecular weight, to achieve the reinforced strength and ductility of cementitious composites. Li and Kanda applied polyvinyl alcohol into cementitious composites, and made PVA-ECC (PVA fiber



reinforced engineered cementitious composite) [16]. Young's modulus and the tensile resistance strength level of PVA fibers are higher than those of general cementitious composites. PVA fibers are able to increase the strength of concrete, and it does not form clusters in the process of stirring. Currently, both domestic and international studies on engineered cementitious composites focus on PVA fibers [17].

The first crack strength of engineered cementitious composites is equal to that of general cementitious composites when receiving tensile stress, but the ultimate tensile strain is approximately 500–1000 times that of the latter, which exhibit the characteristics of strain and ductility at a high magnitude [18]. The significant strain capability against the tensile stress of engineered cementitious composites at the tensile stress–strain curve is extremely similar to that of metallic materials during the process starting from cracking and peak loading to the nullity of the structure as a whole, presenting a pattern of strain hardening. Engineered cementitious composites have changed in fragility compared to traditional cementitious composites and other cementitious composites, and they have overcome an array of disadvantages caused by fragility due to the unique characteristics of multiple cracks, strain-toughness, and superbly powerful ductility [19].

Kanda et al. [20] found that, when the shear span ratio is 1, under the conditions of the non-provision of reinforcing bars, the engineered cementitious composites' shearing resistance loading is exponentially higher than that of the concrete beam. The corresponding distortion capability increases by 225% and exhibits a failure mode with eminent extensibility. Fischer Gregor et al. [21] conducted periodical circulated shearing resistance tests for reinforced concrete and reinforcing bars-engineered cementitious composite compound beam elements. Results suggest that the shearing failure mode of reinforcing bars/engineered cementitious composites is similar to that of the failure mode of extensibility. Numerous tiny slant cracks occur, and anti-shearing ductility remarkably outperforms that of reinforced concrete. In addition, Siad H. [22] found that engineered cementitious composites exhibit moderately high self-healing abilities. Self-healing abilities improve the engineered cementitious composites' working life in a changing environment.

Engineered cementitious composites exhibit good environmental protection performance. More than 600 million tons of fly ash—particles left after the burning of coal—are yielded globally each year [23]. Preventing the ash from flowing into the air, and disposing of the dust particles is a troublesome issue. In the last century, academics have found that the ash can be a partial replacement for cement, to reduce the volume of gel materials in building materials, and to consume the dust particles. In general, normal cementitious composites use 10%–25% fly ash to substitute for cement, whereas engineered cementitious composites use approximately 40%–60% fly ash, whereby superior environmental protection performance is achieved [24].

Normal cementitious composites very often burst under high temperatures [25]. This is mainly due to fire causing the structure's temperature to rise rapidly, which densifies the hydrated products of the cementitious composites in concrete, the structure of which prevents the vapor from escaping. Therefore, substantial vapor pressure is stored in the internal micro-holes of the concrete. When the pressure exceeds the weaker ultimate tensile resistance strength of the cementitious composites, a sudden crash is caused. Organic PVA or PE (polyethylene) fibers in engineered cementitious composites will melt in the high temperature of fire and form paths for vapor and the release of the vapor pressure in elements of engineered cementitious composites, and prevents the cementitious composites as a whole from cracking. As a result, they possess good fire resistance and high temperature resistance capabilities [26].

The paper applies the design principles of engineered cementitious composites as part of the preliminary aims of studying additive agents' impacts on the functional performance of engineered cementitious composites, and optimizes the composition to gain a slurry with good fluidity. Based on this, it aims to make engineered cementitious composites with good performance. This paper discusses the impacts of the processing methods of the fiber surface on the transitional area of the interface, and the ductility of cementitious composites, by which an optimized processing method is sought, to

further improve its ductility, on the basis of making engineered cementitious composites. The impact of processing methods for the fiber surface on the transitional area of the interface, and the ductility of cementitious composites is studied.

## 2. Materials and Methods

### 2.1. Raw Materials

The cement used for this research is PO (ordinary portland cement) 42.5 cement, made by Huaxin Cement Co., Ltd. (Huangshi, China), with a relative density of 3141 kg/m<sup>3</sup> (refer to Tables 1 and 2 for chemical analysis and technical specifications). The fly ash used was first-grade ash made by China Railway Major Bridge Engineering Group Co., Ltd. Ninth Company (Nanjing, China) where d(0.5) is 11.6, d(0.9) is 43.5 (refer to Table 1 for detailed chemical elements, d is diameter). The fine aggregate used was quartz sand, with a fineness of 100 mesh, which means that the diameter per particle was 0.15 mm. A highly effective water reducer called polycarboxylate superplasticizer (made by Wuhan Geruilin Building Materials Technology Co., Ltd., Wuhan, China) was used. The mother liquor is white transparent thick liquid, and the solid content is 40%, which is diluted to 20% for practical use.

**Table 1.** Chemical analysis of cement and fly ash.

Oxide	SiO <sub>2</sub>	Al <sub>2</sub> O <sub>3</sub>	Fe <sub>2</sub> O <sub>3</sub>	CaO	MgO	K <sub>2</sub> O	Na <sub>2</sub> O	SO <sub>3</sub>	Loss
Cement	21.6	5.85	2.84	59.80	2.24	0.67	0.21	2.06	3.70
Fly ash	46.43	38.02	3.11	7.51	0.23	0.89	0.34	0.68	2.78

**Table 2.** Technical specifications of cement.

Stability	Setting Time (min)		Flexural Strength (MPa)		Compressive Strength (MPa)		Specific Surface Area (m <sup>2</sup> /kg)
	Initial	Final	3d	28d	3d	28d	
Qualified	193	273	4.3	6.7	22.6	43.4	342

The polyvinyl alcohol fibers (PVA fibers) used for the study encapsulated two types, and respectively, they are high-strength high elastic modulus PVA fibers (fabricated by Sinopec Chongqing SVW (Sichuan Vinylon Works) Chemical Co., Ltd., Chongqing, China), and REC 15 model PVA fibers (fabricated by Kuraray Co., Ltd., Tokyo, Japan). They were chopped to 12 mm on average (refer to Table 3 for concrete performance specifications).

**Table 3.** Performance indexes of PVA fiber.

Type	Diameter (μm)	Aspect Ratio	Tensile Strength (MPa)	Tensile Elastic Modulus (GPa)	Ultimate Elongation (%)
Domestic PVA	31	387	1400	35	6.5
REC15	40	300	1560	42	7.0

The vinyl acetate emulsion (hereinafter named 'VAE emulsion') that was used for the study is the new model VAE CW40-905 (fabricated by Sinopec Chongqing SVW Chemical Co., Ltd., refer to Table 4 for detailed performance specifications).

**Table 4.** Performance indexes of VAE.

Solid Content (%)	Viscosity (mPa·s)	PH	Ethylene Content (%)	Dilution Stability	MFFT (°C)
54.4	1500–2500	4.0–6.5	≤5.0	≤3.5	≤-3

(MFFT: Minimum film forming temperature).

The hydroxyl propyl methyl cellulose (HPMC) used for the study is HK-type, including 50,000 and 150,000 viscosity (refer to Table 5 for technical specifications). Note that, due to the viscosity of the HPMC being high, and its quantity of use being low, the dried powder does not easily scatter evenly during the process of stirring. Therefore, the HPMC was made into a 1% solution in advance, and the impact of water was omitted in its volume of water content.

**Table 5.** Performance indexes of HPMC.

Nominal Viscosity (mPa·s × 10 <sup>4</sup> )	Methoxyl Content (%)	HydroxyPropyl Content (%)	Water Content (wt%)	Ash Content (wt%)	Density (g/cm <sup>3</sup> )	Fineness (Mesh)
5/15	17.0–24.0	4.0–12.0	≤5.0	≤1.0	1.26–1.31	>80

The boric anhydride used for the study is made by Sinopharm Chemical Reagent Co., Ltd. (Beijing, China). Therein, the purities are as follows: sulfate (SO<sub>4</sub>) ≤0.02%, heavy metal (calculated by Pb) ≤0.005%, silicon and alkali metal content (calculated by SO<sub>4</sub>) ≤0.1%, and purity ≥98.0%. The butylbenzene emulsion was supplied by the Sinopharm Chemical Reagent Co., Ltd. (Beijing, China), model no. JNYS-BS-8825GH.

## 2.2. Specimen Preparation

### 2.2.1. Ratio of the Mixture

The fundamental proportions of the engineered cementitious composites included cement, fly ash, and quartz sand. Per 500 g, the water–binder ratio that was adopted was either 0.3 or 0.35, and a 2% (2% fiber mixing amount can ensure ECC has a tensile strain of 3% to 7%. When the fiber mixing amount exceeds 2%, although the tensile properties of the material increase with the increase of the mixing amount, it cannot guarantee sufficient workability. In addition, it may result in fiber agglomeration and uneven dispersion [27].) The volume fraction of PVA fibers was added as well as a small quantity of HPMC density-increasing stabilizer and a highly effective polycarboxylate superplasticizer. Standard maintenance of the sample was adopted. The HPMC and the fraction of the water reducer were adjusted, accordingly, as in the results and discussion, so that cementitious composites with good fluidity could be obtained.

### 2.2.2. Pre-Processing of the Fibers

The method of pre-processing the fibers was as follows:

- VAE emulsion: Water was added to 50 g VAE emulsion to form a 400 mL volume of diluted solution in a 1 L beaker. The solution was stirred evenly, and an ultra-sonicator (TOSO25-52, Nanjing Toso Ultrasonic Cleaning Machine Co., Ltd, Nanjing, China) was applied to scatter the particles. Pre-calculated and pre-weighed PVA fibers was added and soaked under constant stirring, with the simultaneous application of the ultra-sonicator for 10 min. Afterwards, the fibers were removed and placed on a mesh to be baked at low temperature until it was half-dry. Water was used to wash away the extra emulsion and scattered particles, and the fibers were re-baked for use.
- Cement and boric anhydride: A total of 5 g boric anhydride was made up to a 300 g solution in water, stirred evenly with 100 g cement, and formed into a very thin cement slurry. A pre-calculated and pre-weighed amount of PVA fiber was added and evenly mixed. Then it was removed and placed on a mesh to be baked at a low temperature for use.
- Butyl-benzene emulsion and boric anhydride: A total of 5 g boric anhydride was made up to a 350 g solution with water, and 50 g butyl-benzene emulsion was added with mixing. The subsequent processing method was similar to that of Step a. for processing the VAE emulsion. The derived pre-processed fibers were then ready for use.

### 2.2.3. Mixing Process

The method of the mixing process was as follows:

- A. The preparation of the mortar without fibers. (According to the ASTM C305–14 [28]).
- B. Add the fibers or modification fibers.
- C. Repeat Step A and cast it in two layers.
- D. Strip the mold after 24 to 48 hours and then put them in the standard curing condition.

## 2.3. Experimental Methods

### 2.3.1. Experiment on Rheological Properties

The experiments on rheological properties used the slurry without the fibers added. The study adopted a rotor-type viscosity meter to test the rheological properties of the cementitious composite slurry. An R/S-SST model of a soft-solid rheological property testing instrument (manufactured by Brookfield Co., Ltd., New York, NY, USA) was used, and it was paired with a V 80-40 propeller rotor. The scope of the shearing stress tested was 6–200 Pa, and the shearing velocity could be of an infinitely variable speed within 0–1000 rpm. The time of the shearing velocity was set as:

- a) Under  $200 \text{ s}^{-1}$  constant shearing velocity, with the test conducted on changes in the apparent viscosity at 0 min, 30 min, and 120 min after the slurry was made. The time for each test was 60 s.
- b) Within 180 s, the rotor's shearing velocity was increased constantly from  $0 \text{ s}^{-1}$  to  $200 \text{ s}^{-1}$ , and the test changes of the apparent viscosity, along with the shearing velocity of different slurries at 1 min, 31 min, and 121 min, and the yield viscosity of the slurry, were calculated according to the Rheo V2.8 program (version 2.8, Brookfield Co., Ltd., New York, NY, USA).
- c) Within 180 s, the rotor's shearing velocity was increased constantly from  $0 \text{ s}^{-1}$  to  $200 \text{ s}^{-1}$ . Afterwards, in the same period of time, the rotor's shearing velocity was evenly decreased from  $200 \text{ s}^{-1}$  to  $0 \text{ s}^{-1}$ .

The relationship of the shearing stress, along with the shearing velocities of different slurries at 1 min, 31 min, and 121 min, and the thixotropies of different groups of slurries, were judged as per the area outlined by the curve [29].

### 2.3.2. Test on the Strength of Pressure Resistance and Fracture Resistance

According to the Testing Methods of Strength of Cement Mortar (ISO Methods) [30], an electrical hydraulic universal testing machine (model: WDW 10, supplied by Wuxi Jianyi experiment instrument Co., Ltd., Wuxi, China) was applied to make a sample of mortar and test the strengths of pressure resistance and fracture resistance.

### 2.3.3. Test on Tensile Performance

The equipment used for the tensile performance test was an Instron 5882 electrical universal material testing machine (Instron, Boston, MA, USA). The test was implemented in an environment of  $25 \text{ }^\circ\text{C}$  at 75% humidity using self-made tensile clamps (Figure 1) as per the design and construction recommendations for HPRCC materials, set out by JSCE (Japan Society of Civil Engineers) [31]. The tensile loading device is shown in Figure 2, with a pair of clamps at the top and the bottom. After the sample for tensile testing was ready, aluminum LVDT (linear variable differential transformer) clamps were configured and fixed securely at the tensile area of the sample. The test loaded the tensile test sample through the shift control method, and adopted a  $0.4 \text{ mm/min}$  loading velocity. Shift sensors (model: SCAH series, Abek Sensors Co., Ltd., Beijing, China) were located at the two sides of the sample test data of tensile stress, and transmitted information to the Keithley 2700 data collection apparatus (Keithley 2700, Keithley Instruments, Beaverton, OR, USA). The data for tensile stress and

stress were collected per second. When processing the data, the average value was used for the data, as derived from the shift sensors at two channels.

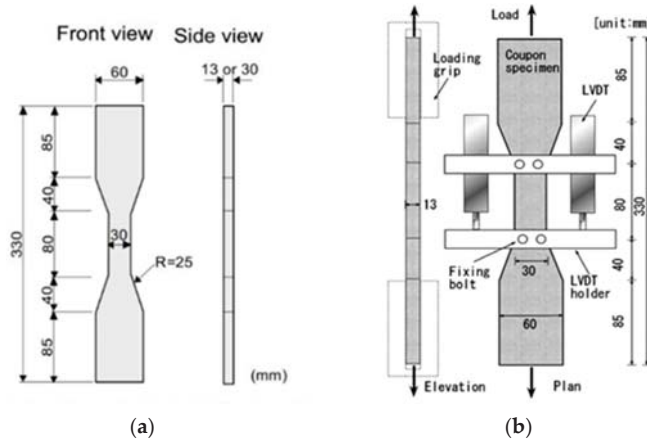


**Figure 1.** The specimen and device of the tensile test. (a) Tensile specimen; (b) Diagram of the tensile loading device

### 2.3.4. Test on Micro-Performance

A field emission scanning electron microscope (Quanta 450 FEG, manufactured by FEI, Hillsboro, OR, USA) was used for the observation and analysis of the scanning electron microscopy (SEM) shape and its appearance in the study. Resolution capability:  $\leq 3$  nm@1 kV, largest pixel:  $6144 \times 4096$ , range of magnification: 10–10,000,000 times. SEM was used for viewing the shape and appearance of the hydrated products of the cementitious composites, the shape and appearance of the transitional area at the interface of the cementitious composites and the fibers, and the shape and appearance of sections after the fibers were pulled [32].

## 3. Results and Discussion

### 3.1. Study on the Rheological Properties of the Slurry

The slurry has outstanding rheology and stability properties, and it ensures that the engineered cementitious composites gain good functional performance and stability, including fluidity, anti-segregation, thixotropy, and thixotropy loss, and more [33–35].

Based on the extensibility test in Table 6, L2, L4, and L5 exhibited good fluid extensibilities. The detailed rheological properties of each group are illustrated and discussed, according to the subsequent rheological instruments.

**Table 6.** The result of the slurry spread.

No.	Water Reducer (%)	HPMC		Slurry Spread (mm)
		Dosage (%)	Viscosity (mPa·s $\times 10^4$ )	
L1	0.9	5	5	295
L2	1.8	5	5	325
L3	0.9	10	5	245
L4	1.8	10	5	310
L5	1.8	5	15	315

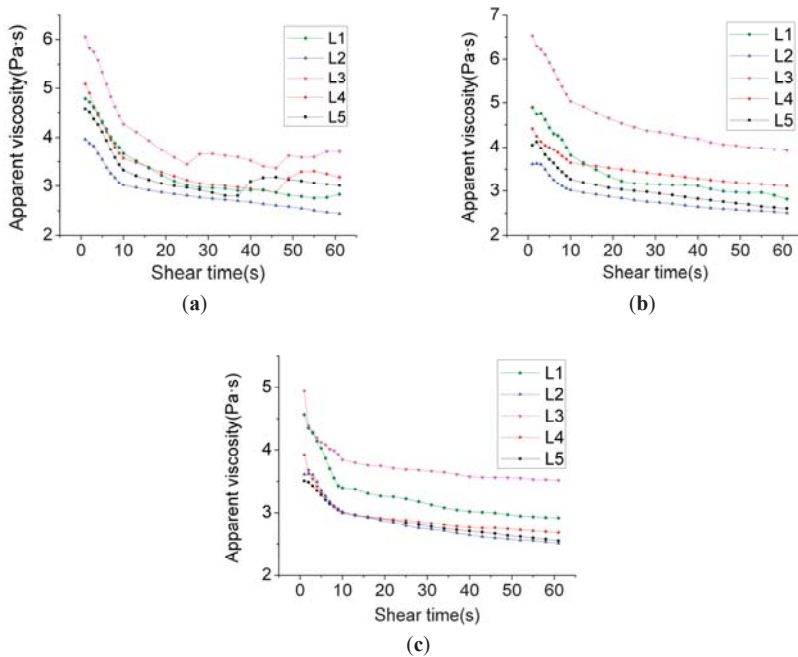


**Figure 2.** Relationship between the slurry shear rate and the apparent viscosity at a constant shear rate. (a) Constant shearing velocity test (hydration for 0 min); (b) Constant shearing velocity test (hydration for 30 min); (c) Constant shearing velocity test (hydration for 120 min).

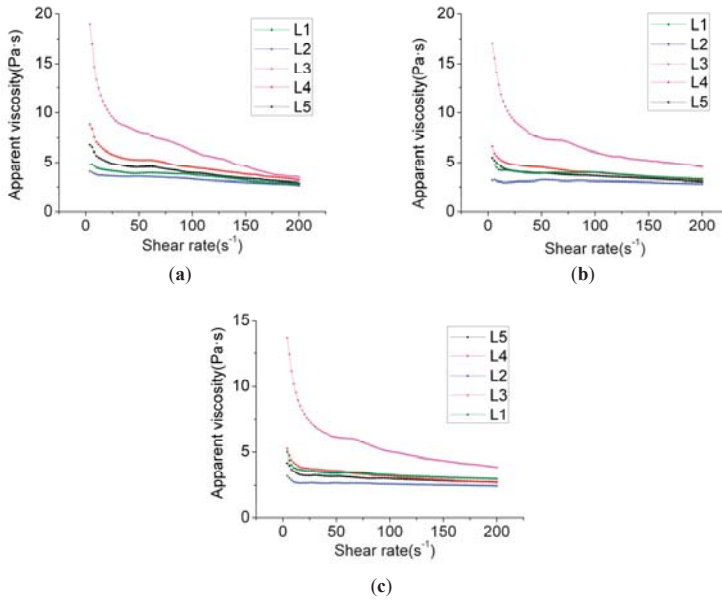
The apparent viscosity of slurry is influenced by the scope of the shearing stress effects, and the temperature and composition of the materials, along with the trend of change of the shearing stress. The apparent viscosity reflects various points of information, including the yield stress and the degree of the hydration of cement [36,37]. Figure 2 exhibits the slurry's laws of change for the apparent viscosity–shearing time curve, along with the time, at different hydrating times. It can be observed from Figure 2a that compared with L1, where only 0.9% water reducer was added, the apparent viscosity of group L2 by mixing 1.8% water reducer was relatively lower, and it was located underneath the L1 curve.

By mixing 10% HPMC of 50,000 viscosity in group L3, the viscosity of the slurry further increased. This was due to the varying molecular weights of HPMC of different viscosities, and also the differing lengths of the molecular chains. For the addition of long-chain molecular HPMC, its branches' composite clusters will absorb water molecules, which further influence the superplasticizer and cement particles. The overlap and intersection of HPMC molecules change the types of clustering of particles on a small scale in the former slurry, and causes the viscosity of the slurry to dramatically increase. In the meantime, it can be observed that an HPMC of 150,000 viscosity produced greater density-increasing effects than HPMC of 50,000 viscosity, but the effects were not significant. From Figure 2, it was found that the relative distribution position of the curve was similar to that of Figure 2b. In the process of the constant shearing velocity test, the types, quantities, and volumes of the water reducer for HPMC generated an impact on the apparent viscosity–shearing velocity relationship, and the effects weakened in sequence. When the hydrating time reached 120 min, L2, L4, and L5's viscosity curves primarily overlapped. Nevertheless, at a later stage, a difference among the three emerged. The regularities of distribution corresponded to the quantities and types of HPMC. The viscosity of L2 using 5% HPMC at 50,000 viscosity was the lowest while the viscosities

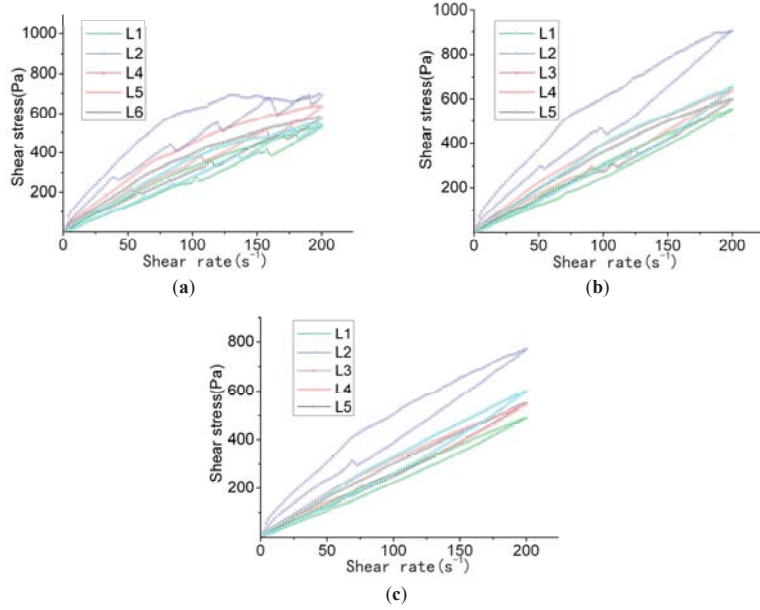
of L4 using 10% HPMC at 50,000 viscosity, and of L5 using 5% HPMC of 150,000 viscosity, were relatively higher.

Figure 3 shows that group L3's apparent viscosity was very low when the shearing velocity was moderately low. However, when the shearing velocity was relatively high, the apparent viscosity rapidly decreased. This suggests that stability of the slurry was poor. Other groups exhibited good stabilities, and the trend of the shearing viscosity decreasing along with the increase of the shearing velocity was moderately mild. This was associated with the equilibrium of effects between the HPMC and the water reducer. Once the long-chain molecule HPMC is added, on the one hand, the composite clusters on the chain that are in proximity to water molecules absorb the water molecules and prevent them from floating upwards. On the other hand, through the absorption of cement particles and the flocculent hydrated product, the clustered cement particles sink and fall, and the proportion of hydrated gel is reduced. Collisions between the particles are reduced. The slurry's stability thus significantly improves. Nonetheless, when excessive HPMC slurry is added, due to the large quantity of long chain-shaped substances, the viscosity of the slurry is excessively great. However, when the shearing frequency is moderately high, due to the HPMC, long chains disaggregate into irregular coil structures. The viscosity of the slurry thereby rapidly falls. Similarly, L4's change of viscosity was the outcome of long-chain disaggregation. Nevertheless, under the conditions of increase in the volume of the water reducer, the viscosity at a low shearing velocity was low. By analyzing L1 and L2's laws of change, it was observed that HPMC significantly influences the viscosity at an early stage while, along with the HPMC's disaggregation at a later stage, the difference of viscosity that is brought about by different types of HPMC slowly decreases. In contrast, different quantities of HPMC influence the viscosity at high levels of shearing stress. Such a difference is closely related to the volume of water reducer. In other words, the effects of shearing stress on the disaggregation of HPMC are rather limited, and when the quantity of use significantly increases while the volume of water reducer remains unchanged, the viscosity at different shearing stress levels increases.

By comparing Figures 2 and 3, and by analyzing the apparent viscosity–shearing time curve at different hydration times in the same group, it can be found that the apparent viscosity reduces along with the extension of hydration time, rather than increasing along with the extension of hydration time. This is possibly due to the chosen polycarboxylate superplasticizer taking effect upon the slow release, and its water-reducing effect gradually becoming distinctive over a period of time after its addition. Therefore, the outcome of apparent viscosity reduction, along with the extension of the hydration time, occurs. Based on the thixotropy test analysis chart and test results (Figure 4), it can be revealed that the thixotropy index generally decreases along with the extension of hydration time, which indicates that the stability of the slurry gradually increases. Moreover, at the stage of the gradual fall of shearing velocity, the fluctuation of the curve gradually decreases. This is congruent with the thixotropy test results. To some extent, thixotropy is able to reflect the changes in the internal structure of the slurry. The greater the thixotropy, the more severe the damage to the flocculation structure that is formed in the slurry.



**Figure 3.** Apparent viscosity changes over time and changes with the shear rate. (a) Accelerated shear test (hydration for 1 min); (b) Accelerated shear test (hydration for 31 min); (c) Accelerated shear test (hydration for 121 min).



**Figure 4.** Testing of thixotropy. (a) Thixotropy test (hydration for 1 min); (b) Thixotropy test (hydration for 31 min); (c) Thixotropy test (hydration for 121 min).

Test results shown in Table 7 also revealed that the thixotropy index of group L2 was moderately low at all points in time. It was, respectively, 9910.953 Pa·s<sup>-1</sup> at 1 min, 7673.119 Pa·s<sup>-1</sup> at 31 min, and



5063.676 Pa·s<sup>-1</sup> at 121 min, with the change of thixotropy being small. After 30 min, the thixotropy index dropped to 2237.834 Pa·s<sup>-1</sup>. After 120 min, the thixotropy index dropped to 4847.277 Pa·s<sup>-1</sup>. Regularities of change were also evident. Therefore, in follow-up experiments, group L2's composition was applied as the benchmark to be implemented in subsequent experiments.

**Table 7.** Thixotropy of the slurry.

No.	Testing Time (min)	Thixotropy (Pa·s <sup>-1</sup> )
L1	1	11,260.893
	31	13,936.090
	121	9248.396
L2	1	9910.953
	31	7673.119
	121	5063.676
L3	1	17,469.007
	31	21,300.803
	121	14,922.739
L4	1	15,206.990
	31	11,401.008
	121	7677.211
L5	1	12,476.844
	31	10,988.725
	121	6695.922

### 3.2. Mechanics Performance

The strength level of the engineered cementitious composites made for the study was 40 MPa (refer to Table 8 for parameters). As such, group C0 was the base group without mixtures of the fibers. Group C1 mixed a 2% volume fraction of REC-15 PVA fibers. Group C2 mixed 2% PVA fibers pre-processed by VAE emulsion. Group C3 mixed boric acid and PVA fibers processed by cement.

**Table 8.** Compressive and flexural strength of 28d mortar.

No.	PVA(%)	Others	Compressive Strength (MPa)	Deviation (%)	Flexural Strength (MPa)	Deviation (%)
C0	0	None	44.4	-	5.7	-
C1	2	None	40.6	100.0	18.2	100.0
C2	2	VAE	42.6	105.0	19.1	105.0
C3	2	Boric anhydride + cement	34.2	84.3	12.5	68.7

The water-binder ratio for each group of cementitious composites was 0.35, with a 28 d strength-of-pressure resistance near 40 MPa, a strength-of-fracture resistance near 15 MPa, and a strength-of-fracture resistance for groups mixed with fibers, which was higher by more than 1 over the C0 base group without mixing in fibers. Nevertheless, the strength-of-pressure resistance of the C0 base group without mixing in fibers was the highest among all of the groups. The strength-of-pressure resistance of group C1 mixing 2% PVA fibers only achieved 40.6 MPa with a decrease of approximately 4 MPa, whereas its strength-of-fracture resistance achieved 18.2 MPa, which was far greater than group C0's 5.7 MPa. The changes of the two strengths may have been caused by the mixture with the fibers. On the one hand, the PVA of high strength and a high elasticity modulus was able to robustly increase the moderately low tensile resistance and bending resistance of the cementitious composites. On the other hand, a 2% volume fraction of PVA fibers would be significantly influential on the dense structures of cementitious composites since numerous tiny air holes would be brought in during the process of stirring, and these are difficult to remove in the process of vibration. Thus, this led to the

evident increase of the strength-of-fracture resistance and the decrease of the strength-of-pressure resistance over a small scale.

Compared to group C1 without pre-processing, the strength-of-pressure resistance and the fracture resistance of group C2 using PVA fibers pre-processed by VAE emulsion increased over a small scale. This may be due to a layer of VAE emulsion film covering the surfaces of the PVA fibers. Through the weak-acid organic film, the hydration of the cementitious composites at the surface area of the fibers would be affected. As a consequence, the fiber strength and adhesive strength would drop slightly, which would mitigate the possibility of the fibers being pulled to be broken by cementitious composites during earlier loading. As a result, the fibers' slippage friction and reinforcing effects are fully utilized.

The strength of group C3, which used PVA fibers processed by boric anhydride and cement slurry, exhibited an evident decrease. Compared with group C1, which used unprocessed PVA fibers, its strength of pressure resistance was only 34.2 MPa, and the strength-of-fracture resistance was only 12.5 MPa. The introduction of boric anhydride creates a moderately significant impact on the strength of the engineered cementitious composites. In contrast, if viewed from a percentage strength attenuation, its impact on the strength-of-pressure resistance was rather small, and its impact on the strength-of-fracture resistance was greater. When the fibers are processed by boric anhydride and cement, the adhesion between the particles on its surface and on the fibers is not firm, and some of the boric anhydride and cement particles will fall off in the process of stirring, and mix with the cementitious composites. Boric anhydride has serious effects on the hydration of cement. Thus, the overall strength-of-pressure resistance of the cementitious composites dropped by 25.7%. Moreover, due to the boric anhydride content being the greatest on the surfaces of the fibers, the effect on the cementitious composites near the interface is the most significant. Excessively low strength and insufficient friction between the fibers and the composites lowers the ductility of the system. Hence, the attenuation of the strength-of-fracture resistance of group C3 reached only 12.5 MPa.

When boric anhydride and a cement slurry are used to process the fibers, due to the adhesion of the slurry, and due to the fibers not being firm, particles will fall off in the process of stirring, and this will cause the overall alkalinity of the cementitious composites to be insufficient and affect hydration. This leads to a decrease in strength and results in poor effects. The acidity of the VAE emulsion is rather weak, and it has a moderately low impact on the alkalinity of the fiber/composite interface. Due to the VAE emulsion not mixing with the boric anhydride, this will cause the VAE emulsion to solidify. Therefore, a follow-up attempt has been made by mixing a butadiene–styrene emulsion into boric anhydride to process the fibers. In addition, an attempt has been made by adjusting the water–binder ratio of the cementitious composites to improve their strength. Refer to Table 9 for important influential factors in the composition and for the test results of strength.

**Table 9.** Compressive and flexural strength of 7d mortar.

Number	Water-Binder Ratio	Others
S1	0.30	None
S2	0.35	VAE
S3	0.35	Boric anhydride + butylbenzene emulsion
S4	0.35	None

It was found from the test results (Figure 5) of the sample with 7 d maintenance, that the strength-of-pressure resistance of group S1 with 0.3 water–binder ratio was higher than that of any of the other groups with 0.35 water–binder ratio, which reached 33.0 MPa. Nonetheless, differences in the strength-of-fracture resistance at an early stage in the groups were insignificant. For groups with 0.35 water–binder ratio, the strength-of-pressure resistance and the fracture resistance of group S2 using VAE emulsion processing was higher than the two groups without fiber processing or that used boric anhydride and butadiene–styrene emulsion processing. This indicates that the fibers with VAE

emulsion processing take effect upon reinforcement. The strength-of-pressure resistance of group S3, which used a butadiene–styrene emulsion and boric anhydride processing, created a certain degree of attenuation, and the impact on the strength-of-fracture resistance was small. This may be caused by the release of boric anhydride onto the surfaces of the fibers.

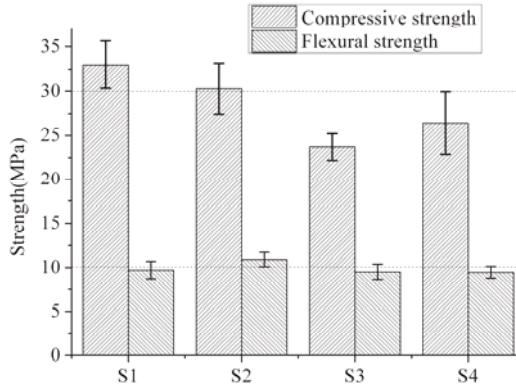


Figure 5. Compressive and flexural strength of 7d ECC.

Table 10 and Figure 6 show the compositions of the tensile samples, and the important influential factors of each group. The test results of the samples in groups G1, G2, and group S were differences in 7 d tensile strength and strain rate.

Table 10. Mixture ratio of tensile testing.

No.	Water-Binder Ratio	Others	First Crack Strength (MPa)	Ultimate Tensile Strength (MPa)	Ultimate Tensile Strain (%)
G1	0.35	Domestic PVA	2.22	2.86	0.46
G2	0.35	Domestic PVA + VAE	2.26	2.79	0.97
S1	0.3	-	2.67	3.52	3.79
S2	0.35	VAE	2.67	3.33	4.05
S3	0.35	Boric anhydride + butylbenzene emulsion	2.5	2.83	2.02
S4	0.35	-	2.63	3.3	3.21

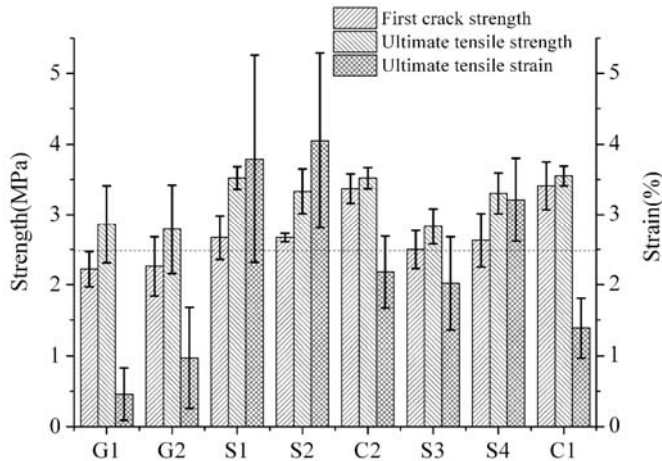


Figure 6. Tensile strength and strain of ECC.

Groups G1 and G2 used domestic PVA fibers (manufactured by Sinopec Chongqing SVW Chemical Co., Ltd., Chongqing, China), and the water–binder ratio was 0.3. The PVA in group G2 was soaked in boric anhydride–butadiene–styrene emulsion diluent for 10 min prior to use, and it was removed and baked at low temperature until it was half-dry. Afterwards, extra emulsion was washed away by water, and the PVA was re-baked for use. A polymer film with acidity will form after processing of the surfaces of the fibers. Due to the domestic fibers' surfaces not being processed, –C–OH composite clusters on the surfaces of the PVA fibers can form firmly combined hydrogen bridges with –OH in the cementitious composites [38]. In addition, the diameter and the strength-of-tensile resistance of a single thread of domestic fiber are weaker than that of the imported fibers. All of these factors increase the probability of the occurrence of fractures at the early stage of cracking in the cementitious composites, and increase their inability to transmit stress and or to utilize better strain capabilities. Regarding the pre-processing of fibers with acid polymer films, on the one hand, the films on the surfaces of the fibers effectively reduce the firm adhesion of the composite clusters that are in proximity to water and the cementitious composites. On the other hand, the acidity of the film will reduce the strength of the transitional area at the fiber–cement interface. Thus, the fibers are able to achieve better slippage-pulling results. It makes more significant use of the fibers' deformation and further improves the ductility of the engineered cementitious composites.

It is revealed by comparing the test results (Figure 7) of group G1 and group G2 that a layer of acid polymer film that is attached to the surfaces of the fibers comes into significant effect for the ultimate tensile strain of the engineered cementitious composites: with the same compositional proportions and with different types of fibers, the tensile strain increased from 0.46% in group G1 to 0.97%, which is an increase of approximately 110.8%.

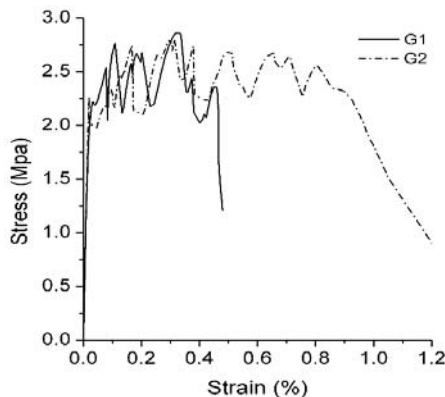


Figure 7. Stress-strain curve of G1 and G2.

Group S1's water–binder ratio was 0.3, and it was mixed with a 2% volume fraction of PVA fibers imported from Japan. After maintenance for 7 d, the strength of the first crack was 2.67 MPa. The ultimate tensile strength was 3.52 MPa and the strain achieved was 3.79%. Group S4's water–binder ratio was 0.35. After maintenance for 7d, the strength of the first crack was 2.63 MPa, the ultimate tensile strength was 3.3 MPa, and the ultimate tensile strain was 3.21%. Both of the two groups exhibited certain strain-hardening abilities (Figure 8). This indicates that group S1, with a lower water–binder ratio, exhibits a moderately higher tensile strength and a greater strain capability. Nevertheless, due to a great gap in fluidity, this study chose a composite proportion of 0.35 water–binder ratio with superior functional performance. As a matter of fact, in accordance with V. C. Li's research findings, it is not necessarily true that the lower the water–binder ratio for engineered cementitious composites is, the better. Under the premise that the strength level requirement is satisfied, a greater water–binder ratio can be adopted to achieve a higher strain capability.

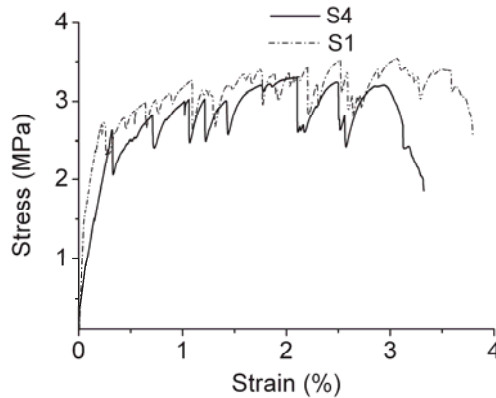


Figure 8. Stress-strain curve of S1 and S4.

Figure 9 exhibits group S2, which adopted the VAE emulsion for modification, and its water–binder ratio was 0.35. After maintenance for 7 d, the first crack strength tested was 2.67 MPa, the ultimate tensile strength was 3.33 MPa, and the ultimate tensile strain was 4.05%. Compared with group S4 with the same composition and using unprocessed REC-15 fibers, their strengths were fundamentally the same, but the ultimate tensile strain increased by 26.2%. The test results clearly suggested that, by applying the VAE emulsion, a film with weak acidity formed on the surfaces of the fibers, and the strength of the composites near the interface decreased while the overall strength of cementitious composites was not affected. The fibers are not easily pulled to be broken in the process of stretching, and the ductility of the engineered cementitious composites improved.

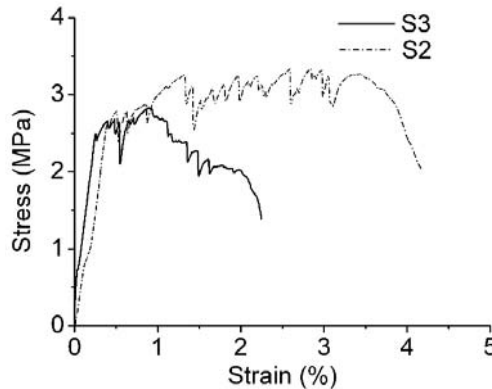


Figure 9. Stress-strain curve of S2 and S3.

The fibers used in group S3 were processed by a diluent of boric anhydride and butadiene–styrene emulsion. Its first crack strength was 2.5 MPa, the ultimate tensile strength was 2.83 MPa, and the ultimate tensile strain was 2.02% (Figure 9). Compared with other groups, its first crack strength and ultimate tensile strength were slightly lower while its strain capability dropped more significantly. As shown in Table 11, compared with base group S4, group S3 dropped by 37.1%. Compared with group S2 with VAE emulsion processing, it only had half the strain value. Furthermore, based on the stress–strain curve, group S3 exhibited strain softening during testing.

Table 11. Tensile properties of S4 and S2.

No.	First Crack Strength (MPa)	Ultimate Tensile Strength (MPa)	Ultimate Tensile Strain (%)
S2-7d	2.67	3.33	4.05
S2-28d	3.4	3.4	2.18
S4-7d	2.63	3.3	3.21
S4-28d	3.2	3.3	1.39

Compared with group S4, which used REC-15 PVA fibers, and group S2, which used modified PVA fibers (Figure 10), it can be found that group S3's first crack strength gained relatively significant increases in 7 d, 28 d strengths (28 d strength is the test result for both group C1 and group C2), which increased from approximately 2.6 MPa at 7 d to approximately 3.4 MPa at 28 d (the first peak value was abnormal, and the second peak value was used in the average). When the first crack occurs in the material, the strain is extremely small, and the stress is borne by cementitious composites. Therefore, the first crack strength can be taken as the tensile resistance strength of the cementitious composites. It mainly reflects the hydration process and the nature of the cementitious composite materials. After the occurrence of the first crack, the fibers at the cracks come into play. They transmit force to the composites that are not cracked, which are characterized by multiple cracks and strain hardening, and derive the peak value of tensile stress. Thus, the ultimate tensile stress of engineered cementitious composites mainly relates to the fibers used, and after maintenance for 28 d, the gains in ultimate tensile strength only increase over a small scale.

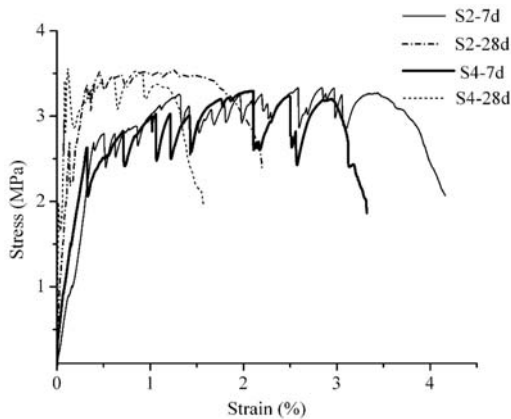


Figure 10. Stress-strain curve of S4 and S2.

The dramatic change in the figure is the ultimate tensile strain. After maintenance for 28 d, the ultimate strain of the general group decreased from 3.21% to 1.39%, and that of the modification group decreased from 4.05% to 2.18%. The attenuations were, respectively, 56.7% and 46.2%. Along with the growth of age and the development of hydration in the cement, not only did the strengths of the composites increase, but the transitional areas of the fiber/composite interfaces became closer. Hence, the tensile slippage of the fibers in the composites is more greatly constrained, and they are more easily broken when pulled. Therefore, the strain capability attenuates radically. Other academics' findings also suggest that, for engineered cementitious composites, the peak value of the tensile strain capability occurs at an age of approximately 10 d.

This study implemented modifications through the pre-processing of the surfaces of the fibers. A layer of acid film was attached onto the surfaces of the PVA fibers that were in proximity to water. Thereby, the firm adhesion between clusters that are in proximity to the water molecules and the

cementitious composites is mitigated. Moreover, the acidity of the film influences the hydration of the gel materials near the fibers/composites, which reduces the strength of the transitional area of the fiber–cement interface, so that the fibers are able to achieve better slippage–pulling out results. The fibers’ deformation is, thus, utilized more significantly and the ductility of the engineered cementitious composites is further enhanced. Hence, the 7 d tensile strain of the modification group was 126.2% that of the general group. The 28 d tensile strain was 156.8% that of the general group. Under the conditions of long age and full hydration, the attenuation rate for the tensile strain of the modification group was 10.5% lower when compared to the general group without modifications on the fibers.

### 3.3. Microstructure

It was found, based on the micro-appearance from SEM, that some gel materials were attached to the surfaces of the fibers in group S4 (Figure 11a), and there were instances of slight ‘neck-shrinking’ phenomena at the breaking points. This suggests that cracking occurs when the fibers in the cementitious composites slip slightly. Small quantities of gel materials are attached onto the surfaces of the fibers in group S2 (Figure 11b). When there is evident slippage on the surface, the friction with the cementitious composites generates axial damage. This indicates that emulsion processing improves the effects of slippage through which strain capability is enhanced.

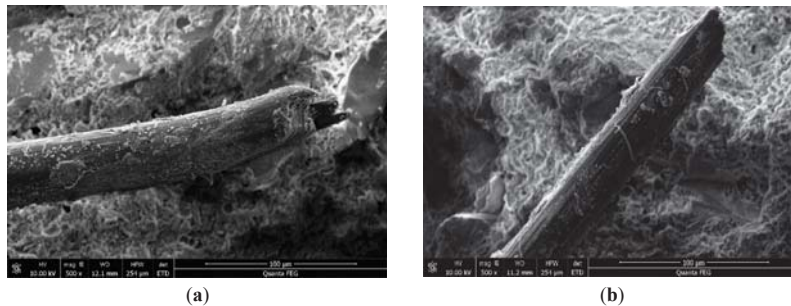


**Figure 11.** Microstructure of S4 and S2. (a) Untreated PVA fiber of S4; (b) Pretreated fiber of S2

Group S3 exhibited strain softening during testing. It was found via analysis of its SEM micro-appearance (Figure 12), that the PVA fibers processed by a diluent of boric anhydride emulsion have a weak binding ability with the cementitious composites, and only a small amount of large fragments was found. It was also found from the scanning results that the pulled fibers were moderately long and complete. This explains why pulling the fibers out from the cementitious composites was rather easy since this may have been due to the weak strength of the cementitious composites near the surfaces of the fibers, which was caused by the acidity of the boric anhydride. The above-mentioned impacts leading to the strain capability of the fibers were not utilized, and the strain capability of group S3 was poor.

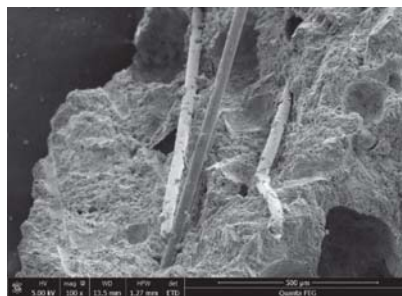


**Figure 12.** Microstructure of S3.



#### 4. Conclusions

This paper investigates the impact of additive agents on the functional performance of engineered cementitious composites, so that a slurry with good fluidity is optimized to form engineered cementitious composites with good performance. The main content of the discussion are concerned with the impact of the processing methods of the fiber surface on the transitional area of the interface and the ductility of the cementitious composites, and the impact of the processing methods of the fiber surface on the transitional area of the interface and the ductility of the cementitious composites. The major results of the research are summarized as follows.

(1) By using HPMC and a polycarboxylate superplasticizer to collectively configure the slurry, a slurry with good performance can be made. By mixing gel materials, including 1.8% water reducer and 0.05% HPMC, the viscosity and the thixotropy of the slurry reach a minimum, and the rheology of the slurry achieves a fine state.

(2) Under the condition that the water reducer is unchanged, using an HPMC of higher viscosity or adding HPMC volume will remarkably increase its initial viscosity. Nevertheless, by accounting for the effects of shearing, its viscosity rapidly decreases and eventually comes to the state of being close.

(3) PVA fibers with modification by a VAE emulsion enable the formation of a film with weak acidity, by which a better pulling–slippage outcome is achieved. Engineered cementitious composites that are made using processed fibers primarily do not affect the strength of the composites. However, an ultimate tensile strain of 4.05% is achieved at 7 d, which is 126.2% that of the PVA fiber groups without processing. This implies that the ductility of the engineered cementitious composites can be further effectively improved.

(4) A film with weak acidity that is added onto the fibers by pre-processing with a VAE emulsion is able to restrain the hydration of the gel materials near the fibers, and reduce the strength of the transitional area at the fiber/composite interface. Furthermore, the restriction of fiber slippage is caused by greater age, and is deepened by the hydrating process. During the time period of 7 d and 28 d, the tensile strain of the engineered cementitious composites with non-modified PVA fibers drops from 3.21% to 1.39%, and that of the modification groups drops from 4.05% to 2.18%, which attenuates by 56.7% and 46.2%. Furthermore, the attenuation rate decreases by 10.5%. This suggests that modification processing not only improves the strain capability, but it also reduces the impact of the tensile strain.

(5) Using a diluent of boric anhydride and butadiene–styrene emulsion also enables the formation of an acid film. Nonetheless, due to boric anhydride having a moderately high impact on the hydration of the gel materials, and its partial release during the process of stirring, the outcomes of the strength of the cementitious composites decreases, the adhesion between the fibers and the cementitious composites is too loose, and the fibers can be easily pulled out. The fibers' deformation ability cannot be utilized. This causes a decrease in the ultimate tensile stress and strain. However, it also implies that its effects on the configuring interface are eminent. The impact of the volume of boric anhydride on cementitious composites needs further study.

**Author Contributions:** Conceptualization, M.S., Y.C., J.Z., T.S. and Y.Z.; Methodology, M.S.; Formal Analysis, M.S., G.L., H.Z. and Y.Z.; Investigation, M.S. and G.L.; Data Curation, M.S., G.L., H.Z. and Y.Z.; Writing-Original Draft Preparation, M.S.; Writing-Review & Editing, M.S., Y.C., J.Z., T.S., Z.S. and Y.Z.; Funding Acquisition, T.S.

**Funding:** This research was funded by the National “Twelfth Five-Year” Plan for Science & Technology Support Development Program of China (grant number: 2014BAB15B01), the National Natural Science Foundation Project of China (grant number: 51204128), YangFan Innovative & Entrepreneurial Research Team Project (grant number: 201312C12), and the Fundamental Research Funds for the Central Universities (grant number: WUT: 2017II51GX).

**Conflicts of Interest:** The authors declare no conflict of interest. The funders had no role in the design of the study; in the collection, analyses, or interpretation of data; in the writing of the manuscript, and in the decision to publish the results.



## References

- Valvona, F.; Toti, J.; Gattulli, V.; Potenza, F. Effective seismic strengthening and monitoring of a masonry vault by using Glass Fiber Reinforced Cementitious Matrix with embedded Fiber Bragg Grating sensors. *Compos. Part B-Eng.* **2017**, *113*, 355–370. [[CrossRef](#)]
- Huang, B.; Li, Q.; Xu, S.; Zhou, B. Tensile fatigue behavior of fiber-reinforced cementitious material with high ductility: Experimental study and novel P-S-N model. *Constr. Build. Mater.* **2018**, *178*, 349–359. [[CrossRef](#)]
- Li, V. Progress and Application of Engineered Cementitious Composites. *J. Chin. Silic. Soc.* **2007**, *35*, 531–536.
- Mo, K.-H.; Loh, Z.-P.; Tan, C.-G.; Alengaram, U.-J.; Yap, S.-P. Behaviour of fibre-reinforced cementitious composite containing high-volume fly ash at elevated temperatures. *Sadhana-Acad. Proc. Eng. Sci.* **2018**, *43*. [[CrossRef](#)]
- Kasagani, H.; Rao, C.-B.-K. Effect of graded fibers on stress strain behaviour of Glass Fiber Reinforced Concrete in tension. *Constr. Build. Mater.* **2018**, *183*, 592–604. [[CrossRef](#)]
- Irshidat, M.-R.; Al-Shannaq, A. Using textile reinforced mortar modified with carbon nano tubes to improve flexural performance of RC beams. *Compos. Struct.* **2018**, *200*, 127–134. [[CrossRef](#)]
- Yu, K.; Wang, Y.; Yu, J.; Xu, S. A strain-hardening cementitious composites with the tensile capacity up to 8%. *Constr. Build. Mater.* **2017**, *137*, 410–419. [[CrossRef](#)]
- Cadoni, E.; Meda, A.; Plizzari, G.-A. Tensile behaviour of FRC under high strain-rate. *Mater. Struct.* **2009**, *42*, 1283–1294. [[CrossRef](#)]
- Haskett, M.; Mohamed Sadakkathulla, M.; Oehlers, D.; Guest, G.; Pritchard, T.; Sedav, V.; Stapleton, B. Adelaide Research and Scholarship: Deflection of GFRP and PVA fibre reinforced concrete beams. In Proceedings of the 6th International Conference on FRP Composites in Civil Engineering (CICE2012), Rome, Italy, 13–15 June 2012.
- Blanco, A.; Pujadas, P.; De la Fuente, A.; Cavalaro, S.H.P.; Aguado, A. Influence of the type of fiber on the structural response and design of FRC slabs. *J. Struct. Eng.* **2016**, *142*, 04016054. [[CrossRef](#)]
- Nezerka, V.; Hrbek, V.; Prosek, Z.; Somr, M.; Tesarek, P.; Fladr, J. Micromechanical characterization and modeling of cement pastes containing waste marble powder. *J. Clean. Prod.* **2018**, *195*, 1081–1090. [[CrossRef](#)]
- Bicer, K.; Yalciner, H.; Balks, A.-P.; Kumbasaroglu, A. Effect of corrosion on flexural strength of reinforced concrete beams with polypropylene fibers. *Constr. Build. Mater.* **2018**, *185*, 574–588. [[CrossRef](#)]
- Yu, J.; Li, H.; Leung, C.-K.-Y.; Lin, X.; Lam, J.-Y.-K.; Sham, I.-M.-L.; Shih, K. Matrix design for waterproof Engineered Cementitious Composites (ECCs). *Constr. Build. Mater.* **2017**, *139*, 438–446. [[CrossRef](#)]
- Khan, M.-Z.-N.; Hao, Y.; Hao, H.; Shaikh, F.-U.-A.; Liu, K. Mechanical properties of ambient cured high-strength plain and hybrid fiber reinforced geopolymer composites from triaxial compressive tests. *Constr. Build. Mater.* **2018**, *185*, 338–353. [[CrossRef](#)]
- Harrison, P.-T.; Levy, L.-S.; Patrick, G.; Pigott, G.-H.; Smith, L.-L. Comparative hazards of chrysotile asbestos and its substitutes: A European perspective. *Environ. Health Perspect.* **1999**, *107*, 607–611. [[CrossRef](#)]
- Kanda, T.; Li, V.-C. Practical Design Criteria for Saturated Pseudo Strain Hardening Behavior in ECC. *J. Adv. Concr. Technol.* **2006**, *4*, 59–78. [[CrossRef](#)]
- Huang, B.; Li, Q.; Xu, S.; Liu, W.; Wang, H. Fatigue deformation behavior and fiber failure mechanism of ultra-high toughness cementitious composites in compression. *Mater. Des.* **2018**, *157*, 457–468. [[CrossRef](#)]
- Ding, Y.; Yu, K.; Yu, J.; Xu, S. Structural behaviors of ultra-high performance engineered cementitious composites (UHP-ECC) beams subjected to bending-experimental study. *Constr. Build. Mater.* **2018**, *177*, 102–115. [[CrossRef](#)]
- Altwair, N.-M.; Johari, M.-A.-M.; Hashim, S.-F.-S. Flexural performance of green engineered cementitious composites containing high volume of palm oil fuel ash. *Constr. Build. Mater.* **2012**, *37*, 518–525. [[CrossRef](#)]
- Kanda, T.; Lin, Z.; Li, V.-C. Tensile stress-strain modeling of pseudostrain hardening cementitious composites. *J. Mater. Civ. Eng.* **2000**, *12*, 147–156. [[CrossRef](#)]
- Fischer, G.; Li, V.-C. Effect of matrix ductility on deformation behavior of steel-reinforced ECC flexural members under reversed cyclic loading conditions. *ACI Struct. J.* **2002**, *99*, 781–790.
- Siad, H.; Lachemi, M.; Sahmaran, M.; Mesbah, H.-A.; Hossain, K.-A. Advanced engineered cementitious composites with combined self-sensing and self-healing functionalities. *Constr. Build. Mater.* **2018**, *176*, 313–322. [[CrossRef](#)]

23. Hussein, A.-A.-E.; Shafiq, N.; Nuruddin, M.-F. Compressive Strength and Interfacial Transition Zone of Sugar Cane Bagasse Ash Concrete: A Comparison to the Established Pozzolans. In *AIP Conference Proceedings*; Ramli, M.F., Junoh, A.K., Roslan, N., Masnan, M.J., Kharuddin, M.H., Eds.; AIP Publishing: Melville, NY, USA, 2015.
24. Kapoor, K.-M.-E.; Singh, S.-P.; Singh, B. Durability of self-compacting concrete made with Recycled Concrete Aggregates and mineral admixtures. *Constr. Build. Mater.* **2016**, *128*, 67–76. [[CrossRef](#)]
25. Chousidis, N.; Ioannou, I.; Rakanta, E.; Koutsodontis, C.; Batis, G. Effect of fly ash chemical composition on the reinforcement corrosion, thermal diffusion and strength of blended cement concretes. *Constr. Build. Mater.* **2016**, *126*, 86–97. [[CrossRef](#)]
26. Li, Q.; Gao, X.; Xu, S.; Peng, Y.; Fu, Y. Microstructure and Mechanical Properties of High-Toughness Fiber-Reinforced Cementitious Composites after Exposure to Elevated Temperatures. *J. Mater. Civ. Eng.* **2016**, *28*, 04016132. [[CrossRef](#)]
27. Li, V. Conditions for Pseudo Strain-Hardening in Fiber Reinforced Brittle Matrix Composites. *Appl. Mech. Rev.* **1992**, *45*, 390–398. [[CrossRef](#)]
28. *Standard Practice for Mechanical Mixing of Hydraulic Cement Pastes and Mortars of Plastic Consistency*; ASTM C305-14; ASTM International: West Conshohocken, PA, USA, 2014.
29. Lu, H.; Xie, C.; Gao, Y.; Li, L.; Zhu, H. Cement Slurries with Rheological Properties Unaffected by Temperature. *SPE Drill. Complet.* **2015**, *30*, 316–321. [[CrossRef](#)]
30. *Cement Test Methods Determination of Strength*; ISO 679:2009(E); ISO: Geneva, Switzerland, 2009.
31. Pellegrino, C.; D'Antino, T. Experimental behaviour of existing precast prestressed reinforced concrete elements strengthened with cementitious composites. *Compos. Part B-Eng.* **2013**, *55*, 31–40. [[CrossRef](#)]
32. Shaikh, F.-U.-A. Deflection hardening behaviour of short fibre reinforced fly ash based geopolymer composites. *Mater. Des.* **2013**, *50*, 674–682. [[CrossRef](#)]
33. Atlasov, R.-A.; Nikolaeva, M.-V.; Popov, B.-I. Analysis of results of casings cementing in the presence of absorption bands on the example of Mastakhskiye gas-condensate field and Nedzhelinskaya area. *Neftyanoe Khozyaistvo* **2017**, *2017*, 42–45. [[CrossRef](#)]
34. Demirci, E.; Wojtanowicz, A.-K. Pilot size process visualization: Gravity fluid displacement method to stop annular gas migration. *J. Nat. Gas Sci. Eng.* **2016**, *29*, 223–231. [[CrossRef](#)]
35. Gu, J.; Ren, C.; Zong, X.; Chen, C.; Winnubst, L. Preparation of alumina membranes comprising a thin separation layer and a support with straight open pores for water desalination. *Ceram. Int.* **2016**, *42*, 12427–12434. [[CrossRef](#)]
36. Roustaei, A.; Gosselin, A.; Frigaard, I.-A. Residual drilling mud during conditioning of uneven boreholes in primary cementing. Part 1: Rheology and geometry effects in non-inertial flows. *J. Non-Newton. Fluid* **2015**, *220*, 87–98. [[CrossRef](#)]
37. Yan, K.; Guan, Z.; Chen, H.; Zhao, X.; Zhang, H. A new calculation method of casing external squeezing loads in complex formation. *Eng. Comput.* **2016**, *33*, 1378–1387. [[CrossRef](#)]
38. Gao, S.; Xu, S. Experimental research on tension property of polyvinyl alcohol fiber reinforced cementitious composites. *J. Dalian Univ. Technol.* **2007**, *47*, 233–239.



© 2018 by the authors. Licensee MDPI, Basel, Switzerland. This article is an open access article distributed under the terms and conditions of the Creative Commons Attribution (CC BY) license (<http://creativecommons.org/licenses/by/4.0/>).

Article

# Rheological Behavior and Microstructure Characteristics of SCC Incorporating Metakaolin and Silica Fume

Gang Ling<sup>1</sup>, Zhonghe Shui<sup>2</sup>, Tao Sun<sup>2,\*</sup> , Xu Gao<sup>3</sup>, Yunyao Wang<sup>1</sup>, Yu Sun<sup>1</sup>, Guiming Wang<sup>2</sup> and Zhiwei Li<sup>1</sup>

<sup>1</sup> School of Materials Science and Engineering, Wuhan University of Technology, Wuhan 430070, China; linggang0609@163.com (G.L.); yywang@whut.edu.cn (Y.W.); yuyuyuxiaomogu@aliyun.com (Y.S.); chunchun2222017@outlook.com (Z.L.)

<sup>2</sup> State Key Laboratory of Silicate Materials for Architectures, Wuhan University of Technology, Wuhan 430070, China; zhshui@whut.edu.cn (Z.S.); guimingw@hotmail.com (G.W.)

<sup>3</sup> School of Civil Engineering and Architecture, Wuhan University of Technology, Wuhan 430070, China; 17702768017@163.com

\* Correspondence: sunt@whut.edu.cn

Received: 20 November 2018; Accepted: 10 December 2018; Published: 18 December 2018

**Abstract:** This study explores the effects of metakaolin (MK) and silica fume (SF) on rheological behaviors and microstructure of self-compacting concrete (SCC). The rheology, slump flow, V-funnel, segregation degree (SA), and compressive strength of SCC are investigated. Microstructure characteristics, including hydration product and pore structure, are also studied. The results show that adding MK and SF instead of 4%, 6% and 8% fly ash (FA) reduces flowability of SCC; this is due to the fact that the specific surface area of MK and SF is larger than FA, and the total water demand increases as a result. However, the flowability increases when replacement ratio is 2%, as the small MK and SF particles will fill in the interstitial space of mixture and more free water is released. The fluidity, slump flow, and SA decrease linearly with the increase of yield stress. The total amount of SF and MK should be no more than 6% to meet the requirement of self-compacting. Adding MK or SF to SCC results in more hydration products, less  $\text{Ca}(\text{OH})_2$  and refinement of pore structure, leading to obvious strength and durability improvements. When the total dosage of MK and SF admixture is 6%, these beneficial effects on workability, mechanical performance, and microstructure are more significant when SF and MK are applied together.

**Keywords:** self-compacting concrete (SCC); rheology; workability; pozzolanic reaction; microstructure

## 1. Introduction

Self-compacting concrete (SCC) is usually characterized as a high-performance concrete that can pass through the gaps between steel bars and fill the formwork completely, only relying on its own gravity during pouring process [1–3]. It is distinguished by excellent workability; thus, no vibration is required during casting, which can significantly reduce the cost, simplify the protocol, shorten the construction time, and guarantee the homogeneity of concrete, especially when applied to the complex cross-section structures [4,5]. Owing to those advantages, increasing attention has been paid to SCC since it was first prepared in 1988 [6]. The workability of self-compacting concrete is assessed by both fluidity and homogeneity. However, a high fluidity is usually accompanied with poor homogeneity, and SCC is sensitive to its manufacturing parameters. Therefore, balancing the fluidity and homogeneity is crucial in the design of SCC [7,8].

The rheological properties of paste have significant influence on the workability of SCC [9–13]. Many studies have been carried out to study the rheological properties of SCC on levels of concrete,

mortar, and paste. It is generally accepted that the rheology of SCC conforms to the Bingham model, and governed by two fundamental parameters: the yield stress and viscosity [14–16]. Yield stress is the minimum force to initiate the flow of SCC, a series of experiments on the relationship between slump and yield stress were conducted, and the results showed that there was an inverse proportional function between yield stress and fluidity [17,18]. A previous study on the influence of mortar rheology on homogeneity showed that yield stress is the key factor to prevent the segregation of aggregate, and the yield stress should be higher than the lowest critical value to ensure the suspension stability [19]. It was also reported that the flow rate of paste is determined by viscosity. The workability of SCC can be partly predicted by analyzing the rheological properties of paste and mortar [20]. For instance, the Krieger–Dougherty (K–D) formula is proven to be able to simulate the correlation of viscosity and yield stress between the mortar and paste [21], the relationship between rheological properties of SCC and paste was established based on the K–D formula and mortar layer model, and a new method for design of SCC based on net paste rheology is provided [22]. Therefore, studying the rheology is of great significance during the design of SCC.

On the other hand, supplementary cementitious material (SCM) has become an important component in the design of modern SCC [23]. Fly ash (FA) is one of the most widely used SCMs in SCC for its beneficial effect on workability. It is found that SCCs that contain 30%–60% FA have good mechanical properties and durability [24]. Moreover, the addition of fly ash to recycled aggregates concrete will improve its workability, compressive/tensile strengths, and resistance to chloride [25,26]. Nevertheless, high-volume FA content also increases the risk of segregation and reduces early strength [27]. Silica fume (SF) is commonly used in concrete to improve the stability and mechanical properties [28,29]. Adding 20% silica fume to SCC was reported to increase the compressive strength by 27% at 28 days [30]. Meanwhile, metakaolin (MK) is a binding material with similar particle size and pozzolanic activity to SF, and has been widely used in concrete [31–35]. Performances, such as mechanical properties and durability, can be remarkably improved after MK is included [36,37]. SF and MK addition in SCC will increase the stability on the one hand, but negatively affect the fluidity on the other hand; the water demand of concrete is significantly increased with SF and MK addition. The poor fluidity will inhibit the discharging of bubbles and damage the filling performance during construction, which is harmful to the general performance of SCC [38,39]. Based on the problems above, it indicates that the use of appropriate compounded MK and SF is a novel approach to develop ultra-high-performance concrete (UHPC) with advanced properties, and the optimum dosage is 3% MK + 5% SF. The reason is that the utilized MK is more active than SF, but an excess amount of MK can increase the viscosity and shrinkage, leading to trapped bubbles and microcracks [40]. Hence, it is logical to study the feasibility of producing SCC by composite use of MK and SF.

The preparation of high-performance SCC usually requires the addition of SF and MK admixtures, but the negative influence on the workability is also a deterrent. Hence, it is of great significance to propose a design criterion of high-performance SCC with consideration of SF and MK. In this study, the effect of SF and MK on the rheology and workability of high-performance SCC is investigated, and importance of the rheology on the workability of SCC is discussed. Then, the enhanced mechanical properties and microstructure of high-performance SCC containing SF and MK admixtures are evaluated.

## 2. Materials and Methods

### 2.1. Materials

In this study, P-II 42.5 cement is used as binding material; fly ash (FA), silica fume (SF), and metakaolin (MK) are used as SCMs, their particle size distributions and chemical constituents are measured by laser particle size analyzer and X-ray fluorescence spectrometer, respectively, as shown in Figure 1 and Table 1, respectively. Natural river sand with fineness modulus of 2.9 is

used as fine aggregate. Continuous graded gravels with a size of 5–20 mm are used as coarse aggregate. A polycarboxylate superplasticizer (SP) with a solid content of 20% is employed to adjust the flowability of SCC.

**Table 1.** Chemical composition of powders in this study (wt %).

Compositions	SiO <sub>2</sub>	Al <sub>2</sub> O <sub>3</sub>	Fe <sub>2</sub> O <sub>3</sub>	CaO	MgO	K <sub>2</sub> O	Na <sub>2</sub> O	SO <sub>3</sub>	LOI	Specific Surface Area (m <sup>2</sup> /kg)
Cement	21.86	4.45	2.35	63.51	1.67	0.55	0.26	2.91	1.89	353
Fly Ash	46.43	38.02	3.11	7.51	0.23	0.89	0.34	0.68	2.78	372
Metakaolin	52.27	44.58	0.70	0.02	0.13	0.34	0.53	0.22	1.02	14,600
Silica Fume	94.65	0.15	0.25	0.33	0.49	0.85	0.16	0.66	2.21	46,100

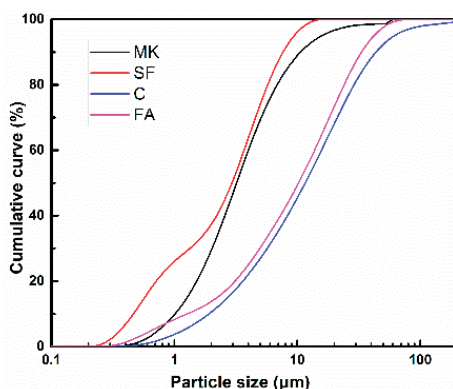


**Figure 1.** Particle size distribution curve of raw materials.

2.2. Mix Design

The mix composition of paste and concrete mixtures are shown in Tables 2 and 3, respectively. Cement accounts for 55% of the total cementitious material and the rest are SCMs. FA is partially replaced by SF and MK to improve the performance of SCC. The water/binder (w/b) ratio is fixed at 0.33 for all mixes. Paste specimens are prepared according to ASTM C 305-2006 and concrete specimens are prepared in accordance with ASTM C192 [41]. Cubic specimens of 100 × 100 × 100 mm<sup>3</sup> are prepared, and demoulded after 24 h, then they are cured under standard conditions (25 ± 2 °C and relative humidity of 98%) until testing.

**Table 2.** Mix design of paste (kg/m<sup>3</sup>).

NO.	Water	Cement	Fly Ash	Metakaolin	Silica Fume	Superplasticizer
P0	552	920	753	0	0	10
PMK2	552	920	720	33	0	10
PMK4	552	920	687	66	0	10
PMK6	552	920	654	99	0	10
PMK8	552	920	621	132	0	10
PSF2	552	920	720	0	33	10
PSF4	552	920	687	0	66	10
PSF6	552	920	654	0	99	10
PSF8	552	920	621	0	132	10
PMK2SF4	552	920	654	66	33	10
PMK4SF2	552	920	654	33	66	10

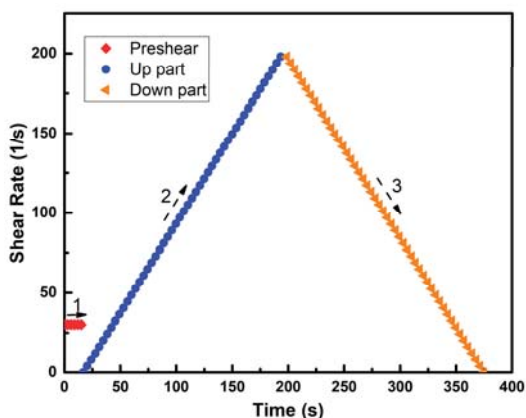
**Table 3.** Mix design of self-compacting concrete (SCC) (kg/m<sup>3</sup>).

NO.	Water	Cement	Fly Ash	Metakaolin	Silica Fume	Sand	Gravel	Superplasticizer
C0	165	275	255	0	0	859	762	5
CMK2	165	275	215	10	0	859	762	5
CMK4	165	275	205	20	0	859	762	5
CMK6	165	275	195	30	0	859	762	5
CMK8	165	275	185	40	0	859	762	5
CSF2	165	275	215	0	10	859	762	5
CSF4	165	275	205	0	20	859	762 <td 5	
CSF6	165	275	195	0	30	859	762	5
CSF8	165	275	185	0	40	859	762	5
CMK2SF4	165	275	195	10	20	859	762	5
CMK4SF2	165	275	195	20	10	859	762	5

### 2.3. Testing Methods

#### 2.3.1. Rheology Behavior

The rheological property of paste is measured by a rotor viscometer. The testing instrument is R/S-SST soft-solid rheometer produced by Brookfield Company (Toronto, Canada). The range of shear stress is 6–200 Pa and the shear rate is 0–1000 rpm. The data obtained by the rheometer can be transmitted to the master computer in real time and analyzed by Rheo V2.8 software. The rheological test procedure of rheometer is shown in Figure 2.

**Figure 2.** Rheological test procedure of rheometer.

#### 2.3.2. Workability

In order to evaluate the workability of SCC, slump flow test and V-funnel test were carried out. Segregation degree of coarse aggregate (SA) was also measured to evaluate the homogeneity of SCC. The tests process was referred to BS EN 12350:2010 [42]. SA was defined as the difference of coarse aggregate weight in different layers: Firstly, the three-layer segregation barrel containing SCC is placed on the jumping table, then the jumping table is started and vibrated 25 times. The concretes in each layer are put into the 5 mm sieves. After washing and drying, the quality of aggregates in different layers is weighed. The SA can be calculated as shown in Equation (1).

$$SA = \frac{m_1 - m_2}{m_0}, \quad (1)$$

where  $m_0$  is the average weight of dried aggregate in concrete, and  $m_1$  and  $m_2$  are the weight of dried aggregates in the bottom and top layer of the segregation barrel, respectively.

### 2.3.3. Compressive Strength

A 3000 kN capacity machine was employed to measure the compressive strength of cube specimens according to ASTM C39 [43]. The test was conducted at the ages of 3 days and 28 days. Three specimens for each batch were measured and the average value was employed to evaluate the compressive strength.

### 2.3.4. Hydration Products

The samples of paste were crushed into small grains after curing for 28 days, and soaked in alcohol to stop hydration. Then, the samples were dried at 60 °C for 24 h in an oven. Afterwards, the samples were grounded into powder and examined by XRD and thermal analysis.

XRD analysis is carried out by D/max-RB type X-ray diffractometer (Japanese RIGAKU, Tokyo, Japan) with scanning step of 0.02, the speed of 10 °/min, the current of 30 mA, and the voltage of 35 kV. Thermal analysis is carried out by Simultaneous Thermal Analyzer (Netzsch STA449F3, Shanghai, China) under nitrogen atmosphere with gas flow of 30 mL/min, heating rate of 10 °C/min, and temperature range of 0–1000 °C.

### 2.3.5. Pore Size Distribution

The small grains with several micrometers in diameter, crushed from 28-day concrete samples, were dried in an oven at 60 °C for 24 h before pore structure examination. The Micromeritics AutoPore-9500 (Micromeritics, Norcross, GA, USA) was used for mercury intrusion porosimetry test (MIP) test, with the generating pressures of mercury intrusion porosimeter ranging from 3 Pa to 379 MPa.

## 3. Results and Discussions

### 3.1. Rheology Behavior

The effect of MK and SF on the fluidity of pastes is shown in Table 4, and it can be seen that fluidity of the paste decreases gradually with the increase of metakaolin and silica fume content. This is due to that the specific surface area of MK and SF is obviously larger than that of fly ash (as shown in Table 1); and the total water demand increases as a result. The free water content in paste is reduced, and the fluidity declined. Compared with P0, the fluidity of paste decreases by 30.9% for 8% MK addition, and 40% for 8% SF addition, respectively, which indicates that SF has greater influence than MK on fluidity. This is because the particle size of SF is smaller as shown in Figure 1, therefore, more water is adsorbed by the powder itself.

**Table 4.** Effect of Silica Fume (SF) and Metakaolin (MK) on the rheology of paste.

No.	Metakaolin (%)	Silica Fume (%)	Slump (mm)	Bingham Equation	Viscosity (Pa·s)	Yield Stress (Pa)
P0	0	0	275	$\tau = 1.140\gamma + 2.804$	1.140	2.804
PMK2	2	0	280	$\tau = 0.704\gamma + 0.385$	0.704	0.385
PMK4	4	0	250	$\tau = 1.341\gamma + 2.858$	1.341	2.858
PMK6	6	0	200	$\tau = 1.387\gamma + 13.913$	1.387	13.913
PMK8	8	0	190	$\tau = 1.582\gamma + 18.266$	1.582	18.266
PSF2	0	2	275	$\tau = 1.130\gamma + 0.823$	1.130	0.823
PSF4	0	4	260	$\tau = 1.416\gamma + 3.061$	1.416	3.061
PSF6	0	6	210	$\tau = 1.611\gamma + 17.939$	1.611	17.939
PSF8	0	8	165	$\tau = 1.988\gamma + 28.711$	1.988	28.711
PMK4SF2	4	2	220	$\tau = 1.379\gamma + 5.568$	1.379	5.568
PMK2SF4	2	4	225	$\tau = 1.318\gamma + 13.411$	1.318	13.411



Figure 3 shows the rheological curve of PMK6. It can be seen that the rheological curve is mainly divided into two parts, corresponding to the second and third parts of the rheological program (as shown in Figure 2). The curve of the up part is irregular, and this phenomenon can be attributed to the reason that the paste is solid-like, and contains the local “weak” regions at the beginning of shearing [44], and pre-shearing will liquefy the paste, but not completely. The down part shows a regular linear relationship, indicating that the paste has been completely liquefied, which is mainly due to the thixotropy of the paste. The analysis of rheological test is mainly focused on the down part, as shown in Figure 3. The Origin Pro 2015 is employed to perform the procedure of linear fitting. The fitting curve of PMK6 is  $y = 1.387x + 13.913$ ,  $R^2$  is 0.99939. It shows that the mathematic relationships between shear stress ( $\tau$ ) with shear rate ( $\dot{\gamma}$ ) of pastes can be determined from being fitted by Bingham model ( $\tau = \tau_0 + \eta \cdot \dot{\gamma}$ ), where slope of the curve,  $\eta$ , represents the viscosity and the vertical intercept;  $\tau_0$ , represents the yield stress of the paste [45].

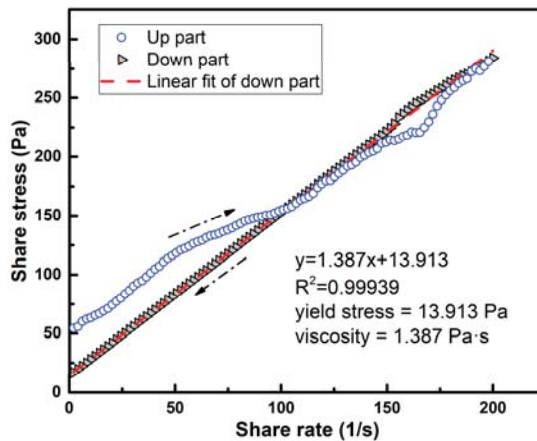
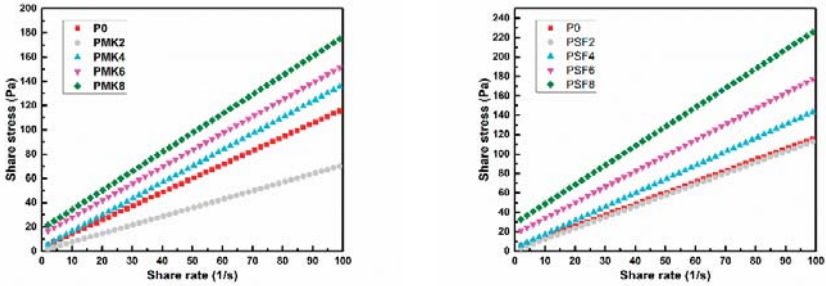


Figure 3. Rheological test results of PMK6.

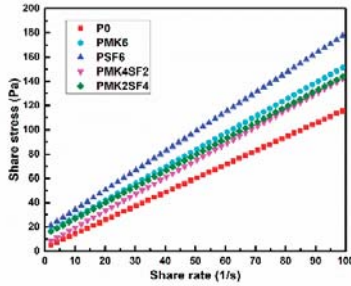
The viscosity and yield stress of different pastes are shown in Table 4 and Figure 4. It can be seen from the Table 4 and Figure 4 that the plastic viscosity and yield stress of the paste increase gradually with increasing contents of MK and SF, which can explain the decrease of paste fluidity. When the content of MK and SF is 2%, the viscosity and yield stress of PMK2 is 38.2% and 86.3% lower than P0, respectively. The reduction of viscosity and yield stress is 8.7% and 70.6% for PSF2, respectively. This is due to the small particle size of MK and SF, which can be filled in the interstitial space between the particles of paste, thus, more free water is released. Comparing PMK8 with P0, it can be found that the viscosity of the paste is increased by 38.4% and the yield stress is increased by 5.5 times when 8% MK is added. This indicates that MK addition can be more significantly affected by the yield stress rather than viscosity. The same observation can be found when SF is added. The phenomenon could be attributed to the following reasons: on the one hand, the particle size of MK and SF are smaller than FA, and the addition of MK and SF will reduce the content of free water in the mixture; on the other hand, MK and SF are more active and will promote the hydration process, and the flocculated hydration products will wrap in the surface of the particles and prevent the relative movement of the particles, resulting in a significant increase of yield stress [46]. When the content of MK and SF is 8%, the yield stress and viscosity of PSF8 are 57.2% and 25.6% higher than that of PMK8, respectively. This indicates that SF has a larger effect on rheological properties than MK, and it is in keeping with the result of fluidity test. When the total content of MK and SF is 6%, the viscosity and yield stress of PMK2SF4 and PMK4SF2 are slightly lower than that of PMK6 and PSF6, indicating that the negative effect of MK or SF on the fluidity can be minimized by the binary use of MK and SF. This is because SF



is finer than MK, when they are used in combination, and the accumulation of the powder becomes more compact and more free water is released, resulting in increased fluidity of paste.



(a) Rheological curves of pastes containing MK (b) Rheological curves of pastes containing SF



(c) Rheological curves of pastes containing MK + SF

Figure 4. Rheological curves of pastes containing metakaolin (MK) and silica fume (SF).

Overall, it can be found that there is an obvious linear relationship between fluidity and yield stress, as shown in the Figure 5, and the fitting curve is  $y = 272 - 4.02x$ , and the square difference,  $R^2$ , is 0.913. This demonstrates that the fluidity of paste is mainly affected by yield stress, which is consist with [17]. Hence, the yield stress of paste needs to be controlled within the appropriate range to obtain excellent fluidity.

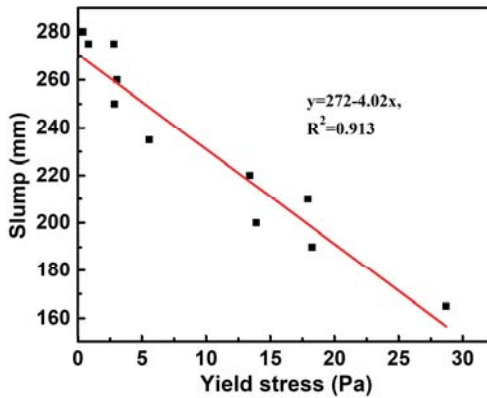


Figure 5. Relationship between fluidity and yield stress of paste.

3.2. Workability

The slump flow, V-flow, and SA values of SCC are shown in Figure 6. It can be seen that the slump flow and SA of SCC decrease with the increase of MK and SF content (Shown as the red arrows in Figure 6). The slump flow and SA of C0 (without MK and SF) are 650 mm and 23.4%, respectively, while the slump flow of SCC with 2% MK (CMK2) and 2% SF (CSF2) is 720 mm and 700 mm, respectively. Similarly, the SA of SCC with 2% MK (CMK2) and 2% SF (CSF2) is 25.1% and 24.1%, respectively. Hence, both MK and SF will increase the fluidity and segregation of SCC when their content is 2%. The slump flow and SA of SCC that contain SF are lower than MK, showing that SF has greater impact on the workability of SCC than MK, which follows a similar tendency as the rheological results, and it is indicated that the rheology of paste is very important to the performance of SCC. When the total dosage of SF and MK admixture is 6%, the slump flow of CMK6 (6% MK) and CSF6 (6% SF) is 630 mm and 620 mm, separately. While the slump flow of CMK2SF4 (2% MK + 4% SF) and CMK4SF2 (4% MK + 2% SF) is 635 mm and 680 mm, separately. It can be seen that the compound use of MK and SF can obtain higher fluidity with the same dosage. This is attributed to difference of particle sizes between MK and SF, then the grain composition and accumulation of powders is optimized by the combination of MK and SF. As a consequence, more free water is released, and the fluidity increased. V-flow is the result of the combined effect of fluidity and stability. Low fluidity will lead to slow flow rate, and the V-flow value will increase. However, excessive fluidity leads to the segregation of aggregate, and the aggregate will concentrate at the outlet, resulting in increased V-flow value. With the incorporation of SF and MK over 6%, the slump flow and V-flow of CMK8 (8% MK) is 580 mm and 20.2 s, and it is 520 mm and 32.2 s for CSF8 (8% SF). The results show that the workability of CMK8 and CSF8 does not meet the requirements of self-compacting concrete (slump flow 600~700 mm, V-flow 5~15 s), therefore, it is suggested that the mixture of SF and MK be controlled to within 6% without increasing the SP dosage in this study.

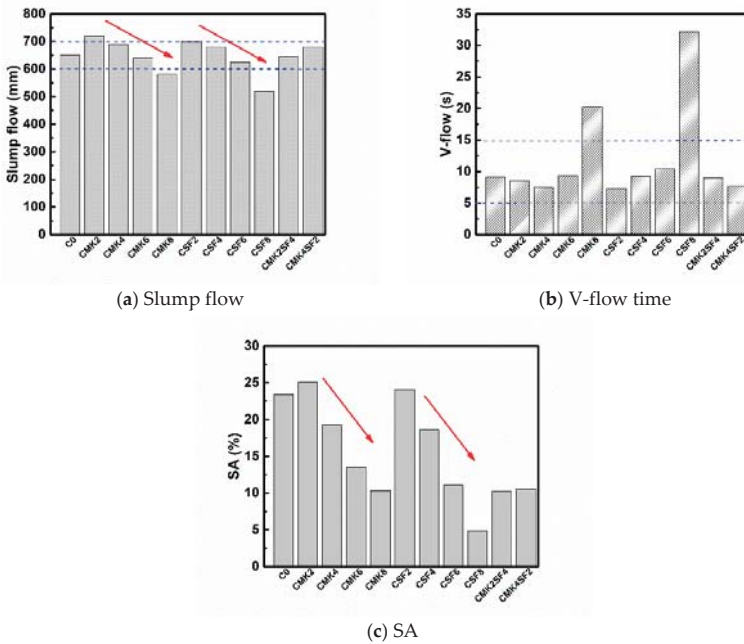


Figure 6. Effect of MK and SF on the workability of self-compacting concrete (SCC) (The red arrows indicate the change of SCC performance with the increase of MK and SF contents).

Figure 7 shows the effect of yield stress of paste on the slump flow of SCC. The fitting curve of yield stress and slump flow is  $y = 711 - 6.18x$ , the square difference  $R^2$  is 0.948, and it shows a significant linear relationship between yield stress and slump flow, and the slump flow decreases with the increase of yield stress. This phenomenon illustrates that the yield stress of paste is the key factor to determining the slump of SCC. The reason is that when the driving force is greater than the yield stress of SCC, the flow continues; conversely, it stops [22].

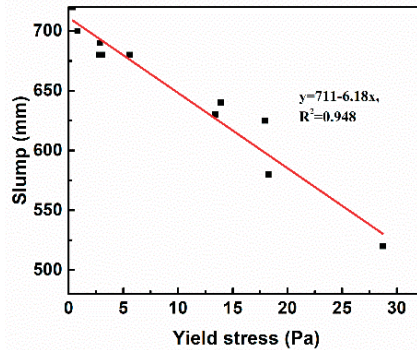


Figure 7. Relationship between yield stress and slump flow of SCC.

Figure 8 shows the relationship between yield stress and SA of SCC. The fitting curve is  $y = 20.09 - 0.581x$ , and  $R^2 = 0.864$ . A linear relationship can also be seen between yield stress and SA of SCC. The fitting curve indicates that the SA decreases with the increase of yield stress, and the segregation of aggregate will not occur ( $SA = 0$ ) when the yield stress is greater than 34.6 Pa. This phenomenon is attributed to by the fact that yield stress is the precondition for the stability of aggregate in concrete, and segregation of aggregate happens only when the difference between gravity and buoyancy of the aggregate is greater than the yield stress [47]. Nevertheless, there is some fluctuation for linear relationship between the yield stress and SA of SCC, and it indicates that SA is also affected by viscosity of concrete. During the SA test, the segregation bucket containing concrete should be placed on the jumping table and vibrated 25 times, and the yield stress will be significantly reduced under these vibration conditions and, as a result, the aggregate will fail to remain suspended and sink [19]. At this point, the sedimentation rate of aggregate is affected by the viscosity based on the Stokes formula. In summary, the rheology of paste is an important factor affecting the workability of SCC, and the performance of SCC can be predicted, to a certain extent, by evaluating the rheology property of the paste [48].

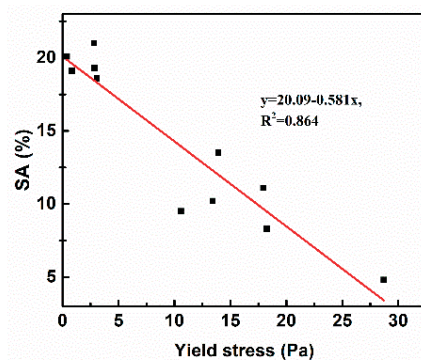


Figure 8. Relationship between yield stress and SA of SCC.

### 3.3. Compressive Strength

The compressive strength of 3 and 28 days of SCC that contain different amounts of MK and SF are shown in the Figure 9. In general, it can be seen that the addition of MK and SF can increase the compressive strength of SCC. For example, comparing with C0, the addition of 6% MK (CMK6) increases the strength of SCC by 22.3% and 15.1% at 3 and 28 days, respectively, and it is 16.0% and 17.0% for CSF6. Moreover, when the dosage of MK and SF in SCC are relatively close (e.g., CMK2SF4 and CMK4SF2), the compressive strengths are higher than that of CMK6 and CSF6. The compressive strength is 64.3MPa for CMK4SF2 at 28 days, which is the highest value in all specimens. This phenomenon can be explained by the following reasons: On the one hand, the particle size of MK and SF are smaller than FA (as shown in Figure 1) and can fill the voids between powers and, moreover, the activity of MK and SF are higher than FA. Thus, more free water in the interspace is released, and the hydration reaction is further facilitated. On the other hand, MK and SF are more active, more hydration products are generated by pozzolanic reaction and fill the voids in hardened concrete. All of these effects will lead to a denser structure and a higher strength [40]. In addition, SF is finer than SF and, when MK and SF are composited, the small MK particle can be the kernel of the early pozzolanic reaction and the formation of C-S-H (calcium silicate hydrate) gels, which can further accelerate the cement hydration and fill the pores. It should be noticed that the differences of the compressive strengths for the samples with same content of MK and SF are relatively small. The enhancement effect is more increased when MK and SF are binary applied. As the addition of MK and SF is 8% (e.g., CMK8 and CSF8), the compressive strength is lower than that of CMK6 and CSF6. It is shown in Figure 6 that the fluidity of CMK8 and CSF8 is too low, and the bubbles in the concrete are difficult to release. Thus, the compactness of hardened concrete structure will be reduced. This illustrates the importance of workability on the mechanical properties of SCC. In order to clearly clarify expound the effect of MK and SF on the mechanical properties of SCC, their microstructures are explored in the sections below.

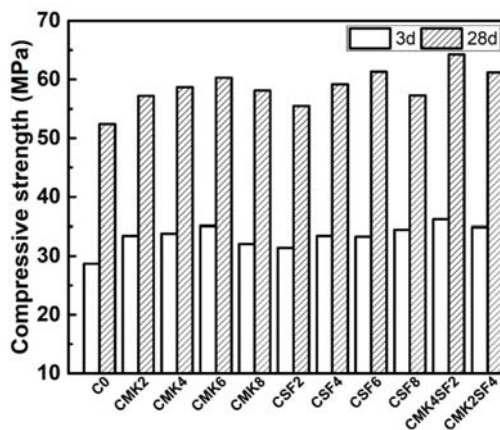


Figure 9. Effect of MK and SF on the compressive strength of SCC.

### 3.4. Hydration Products

The XRD patterns of different mixtures after curing for 28 days are presented in Figure 10. It can be seen that the main hydration products are AFt (ettringite),  $\text{Ca}(\text{OH})_2$  (marked as CH), and  $\text{CaCO}_3$  (marked as C). The diffraction peak of AFt in PSF6 is lower than P0, which indicates that the employment of SF decreases the formation of AFt. This should be attributed to reduction in active aluminum phases and more significant absorption of aluminum by C-S-H gels in SF system. This is in accordance with a previous study [49]. It can be clearly observed that the diffraction peak of  $\text{Ca}(\text{OH})_2$

in PMK6 and PSF6 is inferior to P0, that is, the employment of MK and SF will reduce the content of  $\text{Ca}(\text{OH})_2$ . This is because MK and SF are more active than FA, and doping MK and SF can increase the content of high activity  $\text{SiO}_2$  and  $\text{Al}_2\text{O}_3$  in SCC. Thus, more  $\text{Ca}(\text{OH})_2$  produced by cement hydration is consumed by pozzolanic reaction and better performances, such as with mechanical properties, can result (as shown in Figure 9) [50–52].

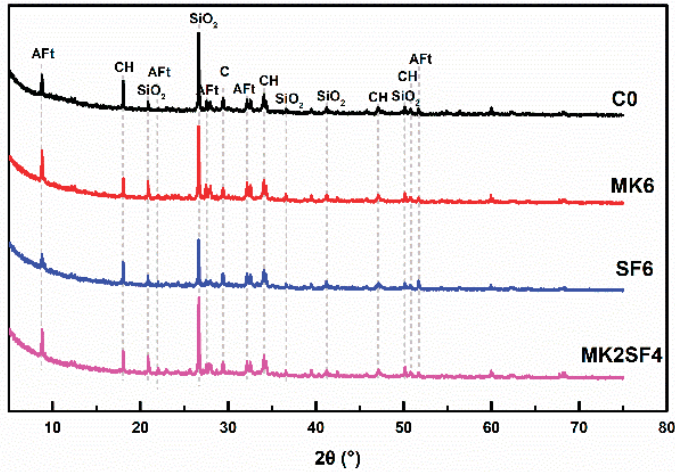


Figure 10. XRD patterns of specimens after curing for 28 days.

DTG (derivative thermogravimetry) curves of specimens after curing for 28 days are presented in Figure 11. As TG-DSC test is conducted on samples after completely dried at  $40^\circ\text{C}$ , and the state that adsorbed water is completely removed, while bound water is not separated has been achieved [53]. Therefore, the weight loss caused by water under this condition is induced by bound water.

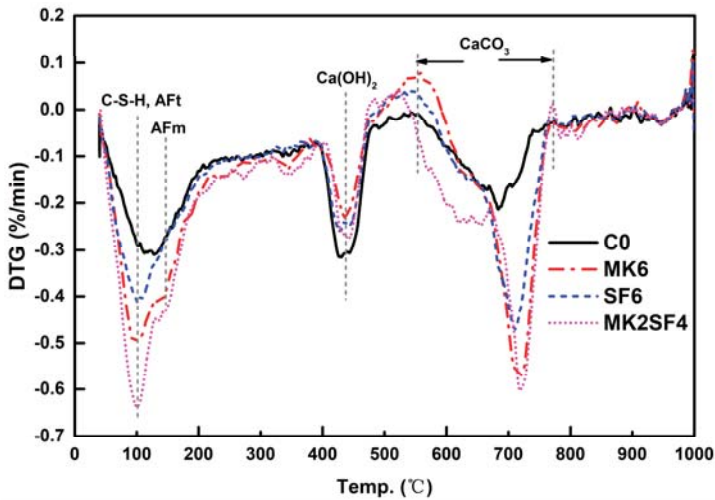


Figure 11. DTG (derivative thermogravimetry) curves of specimens after curing for 28 days.

It can be clearly found from Figure 11 that the curve peak of hydration products (including C-S-H gels, Aft, and  $\text{CaCO}_3$ ) in PMK6 and PSF6 is more remarkable than P0, which means that the addition of MK and

SF induces much more abundant hydration products [54,55]. This is attributed to the accelerated hydration process caused by MK and SF incorporation [56]. The addition of MK and SF reduced the mass loss peak of  $\text{Ca}(\text{OH})_2$ , indicating that the content of  $\text{Ca}(\text{OH})_2$  in hydration products decreases, and is accordant with the XRD results (as shown in Figure 10). The mass loss peak of AFm (hydrated calcium aluminate sulfate) can be expressly discovered for the samples of PMK6 and PMK2SF4 in Figure 11. This is deduced from formation and transformation of  $\text{SO}_4$ -AFm. According to formation of AFt, gypsum dissolves completely in the cement-based system after 2 days. The excess aluminum phases will react with AFt to generate AFm [57]. The content of aluminum phase in MK is relatively high, so the incorporation of MK will lead to more aluminum phases. More remarkable formation of AFm means additional of aluminum phases. As a result, it can be predicted that the mixtures have a better ability to adsorb and solidify chloride, which will lead to preferable durability in chloride-eroded environments (e.g., marine environment).

3.5. Pore Structure

The pore structure of concrete specimens after curing for 28 days is presented in Figure 12 and Table 5. In general, the employment of MK and SF optimizes the pores structures of SCC by reducing the total porosity and the volume of coarse pores [35]. For instance, the pore distribution of C0 is mainly in the range of 10–70 nm, but it is 10–50 nm for CMK6 and CSF6. In addition, incorporating 6% MK and SF can reduce the content of coarse pores (>50 nm) by 18.2% and 13.6%, respectively. Furthermore, both the average diameter and most probate pore diameter are reduced. Hence, the addition of MK and SF is beneficial for refining the pore structure of SCC. Due to the fact that MK and SF are finer and more active, the small MK and SF particles will fill the gaps in the powders, they can also promote the cement hydration and fill the pores, resulting in denser microstructure.

Table 5. Pore structure of SCC after curing for 28 days.

Sample Code	C0	MK6	SF6	MK2SF4
Coarse pores (mL/g)	0.022	0.018	0.019	0.010
Capillary pores (mL/g)	0.044	0.038	0.038	0.044
Total porosity (%)	11.66	10.49	10.58	9.92
Average diameter (nm)	24.4	18.0	20.0	15.4
Most probate pore diameter (nm)	40.3	32.4	32.4	26.3

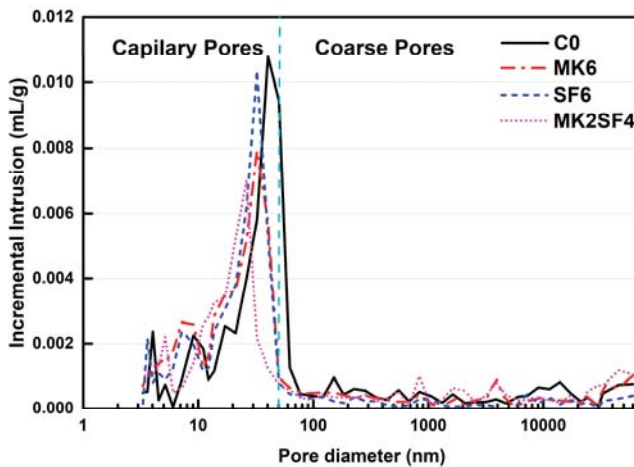


Figure 12. Pore structure analysis of SCC after curing for 28 days.



Compared with CSF6, samples that contain 6% MK (CMK6) have a relatively lower coarse pore volume and smaller average diameter, which means that MK has better capacity to refine pores, and a similar phenomenon has been observed in previous research [35]. However, it is worth noting that the mixture of CMK2SF4 has smaller pore volume than CMK6 and CSF6. Meanwhile, the mixture with compounded MK and SF (CMK2SF4) reduces the coarse pores by 50%. In addition, its average diameter and most probate pore diameter are 15.4 nm and 26.3 nm, respectively, which are the lowest value of the all samples. This means that the pore structure is further optimized when MK and SF are used together. Consequently, applying a SF–MK mixture with proper ratios and contents can be a better method to develop high-performance SCC. These results are consistent with analysis of compressive strength tests [58–60].

#### 4. Conclusions

High performance SCC with MK and SF addition are designed and characterized. The effect of MK and SF on the rheology, workability, compressive strength, and microstructure is investigated. The following conclusions can be drawn based on the results:

The employment of MK and SF, instead of FA, increases the yield stress and viscosity of SCC, resulting in the reduction of fluidity, slump flow, and SA of SCC, which is due to that the utilized MK and SF in this study are finer and more active than FA, so more water is adsorbed by the powder itself and more flocculating products are produced. When the dosage of MK and SF is 2%, the small particles will fill in the interstitial space of mixtures, and more free water is released, leading to an increase of fluidity. The total amount of SF and MK should be no more than 6% to meet the requirement of self-compacting.

The fluidity, slump flow and SA decreases linearly with the increase of yield stress, based on rheology and workability results. This is owing to that yield stress is the key factor determining flow and aggregate settlement of concrete.

The addition of 6% MK and 6% SF instead of FA increases the compressive strength of SCC by 15.1% and 17.0% at 28 days, respectively. On the one hand, the particle size of MK and SF are smaller than FA and can fill the voids between powers. On the other hand, MK and SF are more active, and more hydration products are generated by pozzolanic reaction and fill the voids in the hardened concrete. All of these effects will lead to an optimized pore structure and higher strength. The compressive strength decreases when the contents exceed 8%, and this is due to the excessive yield stress and viscosity, which make it difficult to discharge bubbles and form a compact structure.

The property of SCC, including workability, mechanical performance, and microstructure, could be further improved when SF and MK are applied together. As the particle size of SF is smaller than MK, the accumulation of the powder becomes more compact by compounding MK and SF and, as a result, more free water is released and fluidity is increased. Moreover, the small MK particle can be the kernel of the early pozzolanic reaction and the formation of C–S–H gels, which can further accelerate the cement hydration and fill the pores. Hence, the mechanical performance and microstructure of SCC are improved.

**Author Contributions:** Conceptualization, G.L., Z.S., T.S., X.G., Y.W., Y.S., G.W. and Z.L.; Methodology, G.L., Z.S., T.S., X.G. and Y.S.; Software, G.L., Z.S., T.S., X.G., Y.W.; Validation, G.L., Z.S., T.S.; Formal Analysis, G.L., X.G., Y.W.; Investigation, G.L., Z.S., T.S., X.G. and Z.L.; Resources, G.L., Z.S., T.S. and X.G.; Data Curation, G.L., Z.S., T.S., X.G. and Y.W.; Writing—Original Draft Preparation, G.L., T.S., X.G.; Writing—Review & Editing, G.L., Z.S., T.S., X.G., Y.W., Y.S., G.W. and Z.L.; Visualization, G.L., Z.S., T.S.; Supervision, G.L., Z.S., T.S., X.G.; Project Administration, G.L., Z.S., X.G.; Funding Acquisition, Z.S.

**Funding:** This research was funded by the National Key Research and Development Program of China (NO. 2016YFC0305101), Yang Fan Innovation & Entrepreneurial Research Team Project (NO. 201312C12), the Fundamental Research Funds for the Central Universities (WUT:2017II51GX), and State Key Laboratory of Silicate Materials for Architectures (Wuhan University of Technology).

**Conflicts of Interest:** The authors declare no conflict of interest. The founding sponsors had no role in the design of the study; in the collection, analyses, or interpretation of data; in the writing of the manuscript, and in the decision to publish the results.



## References

1. Hunger, M.; Entrop, A.G.; Mandilaras, I.; Brouwers, H.J.H.; Founti, M. The behavior of self-compacting concrete containing micro-encapsulated phase change materials. *Cem. Concr. Comp.* **2009**, *31*, 731–743. [[CrossRef](#)]
2. Zhu, W.; Bartos, P.J.M. Permeation properties of self-compacting concrete. *Cem. Concr. Res.* **2003**, *33*, 921–926. [[CrossRef](#)]
3. Burak, F.; Selçuk, T.; Bülent, B. Effect of water/cement ratio on the fresh and hardened properties of self-compacting concrete. *Build. Environ.* **2007**, *42*, 1795–1802.
4. Persson, B. A comparison between mechanical properties of self-compacting concrete and the corresponding properties of normal concrete. *Cem. Concr. Res.* **2001**, *31*, 193–198. [[CrossRef](#)]
5. Ouch, M.; SAKAI, E.; Sugiyama, T.; Mitsui, K.; Shindo, T.; Maekawa, K.; Noguchi, T. Self-Compacting Concrete in Japan. In Proceedings of the 8th International Symposium on Utilization of High-Strength and High-Performance Concrete, Tokyo, Japan, 27–29 October 2008; pp. 72–91.
6. Saak, A.W.; Jennings, H.M.; Shah, S.P. New methodology for designing self-compacting concrete. *ACI Mater. J.* **2001**, *98*, 429–439.
7. Loukili, A. Self-compacting concrete. *Adv. Concr. Technol.* **2003**, *1*, 1–23.
8. Brouwers, H.J.H.; Radix, H.J. Self-compacting concrete: Theoretical and experimental study. *Cem. Concr. Res.* **2005**, *35*, 2116–2136. [[CrossRef](#)]
9. Zerbino, R.; Barragán, B.; Garcia, T.; Agulló, L.; Gettu, R. Workability tests and rheological parameters in self-compacting concrete. *Mater. Struct.* **2009**, *42*, 947–960. [[CrossRef](#)]
10. Roussel, N. A theoretical frame to study stability of fresh concrete. *Mater. Struct.* **2006**, *39*, 81–91. [[CrossRef](#)]
11. Bui, V.K.; Akkaya, Y.; Shah, S.P. Rheological model for self-consolidating concrete. *ACI Mater. J.* **2002**, *99*, 549–559.
12. Chidiac, S.E.; Mahmoodzadeh, F. Plastic viscosity of fresh concrete—A critical review of predictions methods. *Cem. Concr. Compos.* **2009**, *31*, 535–544. [[CrossRef](#)]
13. Hu, C.; Larrard, D.F. The rheology of fresh high-performance concrete. *Cem. Concr. Res.* **1996**, *26*, 283–294. [[CrossRef](#)]
14. Golaszewski, J. Influence of cement properties on new generation superplasticizers performance. *Constr. Build. Mater.* **2012**, *35*, 586–596. [[CrossRef](#)]
15. Papo, A.; Piani, L. Effect of various superplasticizers on the rheological properties of Portland cement pastes. *Cem. Concr. Res.* **2004**, *34*, 2097–2101. [[CrossRef](#)]
16. Xie, H.; Liu, F.; Fan, Y.R.; Yang, H.; Chen, J.; Zhang, J.; Zuo, C. Workability and proportion design of pumping concrete based on rheological parameters. *Constr. Build. Mater.* **2013**, *44*, 267–275. [[CrossRef](#)]
17. Flatt, R.J.; Larosa, D.; Roussel, N. Linking yield stress measurements: Spread test versus Viskomat. *Cem. Concr. Res.* **2006**, *36*, 99–109. [[CrossRef](#)]
18. Lootens, D.; Jousset, P.; Martinie, L.; Roussel, N.; Flatt, R.J. Yield stress during setting of cement pastes from penetration tests. *Cem. Concr. Res.* **2009**, *39*, 401–408. [[CrossRef](#)]
19. Wan, B.; Gadalamaria, F.; Petrou, M.F. Influence of mortar rheology on aggregate settlement. *ACI Mater. J.* **2000**, *97*, 479–485.
20. Tregger, N.A.; Pakula, M.E.; Shah, S.P. Influence of clays on the rheology of cement pastes. *Cem. Concr. Res.* **2010**, *40*, 384–391. [[CrossRef](#)]
21. Toutou, Z.; Roussel, N. Multi scale experimental study of concrete rheology: From water scale to gravel scale. *Mater. Struct.* **2006**, *39*, 189–199. [[CrossRef](#)]
22. Wu, Q.; An, X. Development of a mix design method for SCC based on the rheological characteristics of paste. *Constr. Build. Mater.* **2014**, *53*, 642–651. [[CrossRef](#)]
23. Dehwah, H.A.F. Mechanical properties of self-compacting concrete incorporating quarry dust powder, silica fume or fly ash. *Constr. Build. Mater.* **2012**, *26*, 547–551. [[CrossRef](#)]
24. Yazici, H. The effect of silica fume and high-volume Class C fly ash on mechanical properties, chloride penetration and freeze-thaw resistance of self-compacting concrete. *Constr. Build. Mater.* **2008**, *22*, 456–462. [[CrossRef](#)]
25. Faella, C.; Lima, C.; Martinelli, E.; Pepe, M.; Realfonzo, R. Mechanical and durability performance of sustainable structural concretes: An experimental study. *Cem. Concr. Comp.* **2016**, *71*, 85–96. [[CrossRef](#)]

26. Lima, C.; Caggiano, A.; Faella, C.; Martinelli, E.; Pepe, M.; Realfonzo, R. Physical properties and mechanical behaviour of concrete made with recycled aggregates and fly ash. *Constr. Build. Mater.* **2013**, *47*, 547–559. [[CrossRef](#)]
27. Sonebi, M. Medium strength self-compacting concrete containing fly ash: Modelling using factorial experimental plans. *Cem. Concr. Res.* **2004**, *34*, 1199–1208. [[CrossRef](#)]
28. Behforooz, B.; Eftekhari, M.R.; Amin, E.; Ghias, A. Effects of using silica fume (SF) in improving permeability properties of Self-compacting concrete (SCC). In Proceedings of the 9th International Congress on Civil Engineering, Isfahan, Iran, 8 May 2012.
29. Dousti, A.; Beaudoin, J.J.; Shekarchi, M. Chloride binding in hydrated MK, SF and natural zeolite-lime mixtures. *Constr. Build. Mater.* **2017**, *154*, 1035–1047. [[CrossRef](#)]
30. Majid, G.; Ali, K. An investigation on the fresh and hardened properties of self-compacting concrete incorporating magnetic water with various pozzolanic materials. *Constr. Build. Mater.* **2018**, *15*, 173–180.
31. Poon, C.S.; Kou, S.C.; Lam, L. Compressive strength, chloride diffusivity and pore structure of high performance metakaolin and silica fume concrete. *Constr. Build. Mater.* **2006**, *20*, 858–865. [[CrossRef](#)]
32. Zibara, H.; Hooton, R.D.; Thomas, M.D.A.; Stanish, K. Influence of the C/S and C/A ratios of hydration products on the chloride ion binding capacity of lime-SF and lime-MK mixtures. *Cem. Concr. Res.* **2008**, *38*, 422–426. [[CrossRef](#)]
33. Dadsetan, S.; Bai, J.P. Mechanical and microstructural properties of self-compacting concrete blended with metakaolin, ground granulated blast furnace slag and fly ash. *Constr. Build. Mater.* **2017**, *146*, 658–667. [[CrossRef](#)]
34. Madandoust, R.; Mousavi, S.Y. Fresh and hardened properties of self-compacting concrete containing metakaolin. *Constr. Build. Mater.* **2012**, *35*, 752–760. [[CrossRef](#)]
35. Duan, P.; Shui, Z.H.; Chen, W.; Shen, C. Effects of metakaolin, silica fume and slag on pore structure, interfacial transition zone and compressive strength of concrete. *Constr. Build. Mater.* **2013**, *44*, 1–6. [[CrossRef](#)]
36. Hassan, A.A.A.; Mayo, J.R. Influence of mixture composition on the properties of SCC incorporating metakaolin. *Mag. Concr. Res.* **2014**, *66*, 1–15. [[CrossRef](#)]
37. Sfikas, I.P.; Badogiannis, E.G.; Trezos, K.G. Rheology and mechanical characteristics of self-compacting concrete mixtures containing metakaolin. *Constr. Build. Mater.* **2014**, *64*, 121–129. [[CrossRef](#)]
38. Quercia, G.G.; Spiesz, P.P.; Hüsken, G.G.; Brouwers, H.J.H. Effects of amorphous nano-silica additions on mechanical and durability performance of SCC mixtures. In *Durability of Reinforced Concrete from Composition to Protectio*; Andrade, C., Gulikers, J., Polder, R., Eds.; Springer Publishing: New York, NY, USA, 2013; pp. 125–143.
39. Łażniewska-Piekarczyk, B. The influence of admixtures type on the air-voids parameters of non-air-entrained and air-entrained high-performance SCC. *Constr. Build. Mater.* **2013**, *41*, 109–124. [[CrossRef](#)]
40. Song, Q.; Yu, R.; Wang, X.; Rao, S.; Shui, Z. A novel self-compacting ultra-high performance fibre reinforced concrete (SCUHPFRC) derived from compounded high-active powders. *Constr. Build. Mater.* **2018**, *158*, 883–893. [[CrossRef](#)]
41. ASTM C192. *Standard Practice for Making and Curing Concrete Test Specimens in the Laboratory*; ASTM International: West Conshohocken, PA, USA, 2007.
42. BS EN 12350. *Testing fresh concrete, self-compacting concrete*; Technical committee, British Standards Institution: London, UK, 2010.
43. ASTM C39. *Standard Test Method for Compressive Strength of Cylindrical Concrete Specimens*; ASTM International: West Conshohocken, PA, USA, 2011.
44. Ye, Q.; Shiho, K. Distinguishing dynamic and static yield stress of fresh cement mortars through thixotropy. *Cem. Concr. Compos.* **2018**, *86*, 288–296.
45. Ferraris, C.F.; Obla, K.H.; Hill, R. The influence of mineral admixtures on the rheology of cement paste and concrete. *Cem. Concr. Res.* **2001**, *31*, 245–255. [[CrossRef](#)]
46. Janotka, I.; Puertas, F.; Palacios, M.; Kuliffayová, M.; Varga, C. Metakaolin sand-blended-cement pastes: Rheology, hydration process and mechanical properties. *Constr. Build. Mater.* **2010**, *24*, 791–802. [[CrossRef](#)]
47. Schowalter, W.R.; Christensen, G. Toward a rationalization of the slump test for fresh concrete: Comparisons of calculations and experiments. *J. Rheol.* **1998**, *42*, 865–870. [[CrossRef](#)]

48. Ng, I.Y.T.; Ng, P.L.; Kwan, A.K.H. Rheology of mortar and its influences on performance of self-consolidating concrete. *Key Eng. Mater.* **2008**, *400–402*, 421–426. [[CrossRef](#)]
49. Lothenbach, B.; Rentsch, D.; Wieland, E. Hydration of a silica fume blended low-alkali shotcrete cement. *Phys. Chem. Earth* **2014**, *70–71*, 3–16. [[CrossRef](#)]
50. Szeląg, M. Development of cracking patterns in modified cement matrix with microsilica. *Materials* **2018**, *11*, 1928. [[CrossRef](#)] [[PubMed](#)]
51. Roy, D.M.; Arjunan, P.; Silsbee, M.R. Effect of silica fume, metakaolin, and low-calcium fly ash on chemical resistance of concrete. *Cem. Concr. Res.* **2001**, *31*, 1809–1813. [[CrossRef](#)]
52. Nili, M.; Ehsani, A. Investigating the effect of the cement paste and transition zone on strength development of concrete containing nanosilica and silica fume. *Mater. Des.* **2015**, *75*, 174–183. [[CrossRef](#)]
53. Karen, S.; Ruben, S.; Barbara, L. *A Practical Guide to Microstructural Analysis of Cementitious Materials*; CRC Press: Boca Raton, FL, USA, 2016.
54. Zhou, Q.; Glasser, F.P. Thermal stability and decomposition mechanisms of ettringite at <120 °C. *Cem. Concr. Res.* **2001**, *31*, 1333–1339.
55. Nonnet, E.; Lequeux, N.; Boch, P. Elastic properties of high alumina cement castables from room temperature to 1600 °C. *J. Eur. Ceram. Soc.* **1999**, *19*, 1575–1583. [[CrossRef](#)]
56. Siddique, R.; Klaus, J. Influence of metakaolin on the properties of mortar and concrete: A review. *Appl. Clay Sci.* **2009**, *43*, 392–400. [[CrossRef](#)]
57. Lothenbach, B.; Bary, B.; Bescop, P.L.; Schmidt, T.; Leterrier, N. Sulfate ingress in Portland cement. *Cem. Concr. Res.* **2010**, *40*, 1211–1225. [[CrossRef](#)]
58. Wang, Y.; Shui, Z.; Sun, T.; Huang, Y.; Wang, G. Effect of fly ash, sinking beads and metakaolin on the workability, strength, free shrinkage and chloride resistance of concretes: A comparative Study. *Arab. J. Sci. Eng.* **2018**, *43*, 5243–5254. [[CrossRef](#)]
59. Wild, S.; Khatib, J.M. Portlandite consumption in metakaolin cement pastes and mortars. *Cem. Concr. Res.* **1997**, *27*, 137–146. [[CrossRef](#)]
60. Wang, Y.; Shui, Z.; Sun, T.; Duan, P. Properties of coral waste-based mortar incorporating metakaolin: Part II. Chloride migration and binding behaviors. *Constr. Build. Mater.* **2018**, *174*, 433–442. [[CrossRef](#)]



© 2018 by the authors. Licensee MDPI, Basel, Switzerland. This article is an open access article distributed under the terms and conditions of the Creative Commons Attribution (CC BY) license (<http://creativecommons.org/licenses/by/4.0/>).

Article

# Effects of Pumice-Based Porous Material on Hydration Characteristics and Persistent Shrinkage of Ultra-High Performance Concrete (UHPC)

Kaizhi Liu <sup>1,2</sup>, Rui Yu <sup>1,3,\*</sup>, Zhonghe Shui <sup>1,3</sup>, Xiaosheng Li <sup>1,2</sup>, Xuan Ling <sup>1,2</sup>, Wenhao He <sup>2</sup>, Shuangqin Yi <sup>2</sup> and Shuo Wu <sup>1</sup>

<sup>1</sup> State Key Laboratory of Silicate Materials for Architectures, Wuhan University of Technology, Wuhan 430070, China; liu03303116@126.com (K.L.); zhshui@whut.edu.cn (Z.S.);

li-xiaosheng@whut.edu.cn (X.L.); lingxuan@whut.edu.cn (X.L.); wushuo.phyche@hotmail.com (S.W.)

<sup>2</sup> School of Materials Science and Engineering, Wuhan University of Technology, Wuhan 430070, China; 15730325018@163.com (W.H.); x3463973524@163.com (S.Y.)

<sup>3</sup> Wuhan University of Technology Advanced Engineering Technology Research Institute of Zhongshan, Zhongshan 528437, China

\* Correspondence: r.yu@whut.edu.cn; Tel.: +86-134-7609-5912

Received: 26 November 2018; Accepted: 17 December 2018; Published: 20 December 2018

**Abstract:** In this paper, two kinds of pumice particles with different diameters and water absorption rates are employed to substitute the corresponding size of river sands by volume fraction, and their effects on the hydration characteristics and persistent shrinkage of Ultra-High Performance Concrete (UHPC) are investigated. The obtained experimental results show that adopting a low dosage of 0.6–1.25 mm saturated pumice as the internal curing agent in UHPC can effectively retract the persistent shrinkage deformation of concrete without a decrease of strength. Heat flow calorimetry results demonstrate that the additional water has a retarding effect and promotes the hydration process. X-ray Diffraction (XRD) and Differential Thermal Gravimetry (DTG) are utilized to quantify the Ca(OH)<sub>2</sub> content in the hardened paste, which can confirm that the external moisture could accelerate the early cement hydration and secondary hydration of active mineral admixtures. The Ca/Si ratio of C–S–H calculated by the Energy Dispersive Spectrometer (EDS) reveals that the incorporation of wet pumice can transform the composition and structure of hydration products in its effective area.

**Keywords:** Ultra-High Performance Concrete (UHPC); long-term drying shrinkage; hydration characteristic; porous pumice; optimization

## 1. Introduction

UHPC (Ultra-high performance concrete), as a new type of cement-based material, is designed based on the principle of the closest packing between particles of each component with a very low water-to-binder ratio ( $w/b < 0.2$ ) and a certain amount of reinforcing fibers [1–4]. Therefore, UHPC cement-based materials show great potential in applications which satisfy the requirements of structural engineering at a higher height, larger span, and heavier load [5–11]. Along with its excellent mechanical properties and durability, a strong continuous shrinkage deformation of the UHPC matrix can negatively affect its stability and reliability during the practical service life. This can be attributed to a rapid decrease in the relative humidity within the pores inside the UHPC system during the hydration process of cement at a relatively low  $w/b$  [12–14]. Therefore, how to effectively settle the problem of the large volume contraction of UHPC has become a hot topic in current research.

The accepted means to minimize the shrinkage of UHPC by employing internal curing carrier materials [15–19], expansive agents [20,21], shrinkage reducing agents [18,22,23], and other

methods [24–26], can restrict the constriction development, especially its early self-shrinkage. However, the reduction of shrinkage by using an expansive agent alone is not recommendable due to its challenge in controlling the amount of swelling and occurrence time. A shrinkage reducing agent is often accompanied by the inhibition of early strength development and further deterioration of mechanical properties, if it has poor compatibility with chemical admixtures [27]. In contrast, an internal curing (IC) mechanism is considered to be a reasonable solution to fundamentally and effectively control UHPC contraction. Nowadays, most IC agents utilized in UHPC are super absorbent polymers and various types of lightweight aggregates (LWAs). It has been revealed that super absorbent polymers can significantly baste the growth of autogenous shrinkage of UHPC, and even fully compensate for the early contraction of concrete [15,28,29]. Nevertheless, the introduction of super absorbent polymers will negatively influence the compactness of UHPC and increase the porosity, resulting in degradation of the mechanical properties and durability of concrete, which are both important indicators of UHPC. Pre-wetting LWA is a kind of potential IC carrier material that can also delay the self-desiccation of UHPC through the slow-release effect of water, which has excellent volume stability during water absorption and release. Hence, the pre-wetting LWA can be potentially treated as an effective material to minimize the UHPC shrinkage based on experimental and practical points of view.

The commonly applied LWAs in concrete as IC agents include expanded clay, perlite, shale, other types of ceramsite, tuff, and pumice, etc. Philleo's experiment found that the pre-wetted porous ceramic pellets could effectively reduce the self-shrinkage deformation of concrete, and explicitly put forward the concept of IC for the first time [30]. Bentz et al. [31–33] confirmed that the moisture introduced by LWA could not only restrain the contraction and cracking of concrete, but also improve the hydration degree of the surrounding mortar and intensify the strength. Besides, they proposed the formula for calculating the minimum amount of LWA for IC. Bentur et al. [34] showed that there was a significant correlation between the evolution of shrinkage performance and water content of pre-wetting ceramsite in high strength concrete. They found that the saturated ceramsite replacing ordinary aggregates by a volume fraction of 25% would completely offset the shrinkage and even swell. Akcay et al. and Henskensiefken et al. [35–37] demonstrated that the size of the aqueous LWA particles has an obvious influence on the effective range and efficiency of IC, and smaller granules were preferred. Henskensiefken et al. and Lura et al. [38,39] suggested increasing the substitution rate of soaked LWA, which could improve the relative humidity inside the paste and postpone the self-desiccation. Zhutovsky et al. [40–42] scientifically described the effect of exploiting pumice as the IC agent in high strength concrete. They showed that there was an optimal size distribution range of pumice particles in high strength concrete, and oversized or undersized particles would weaken the IC effect. The influence of incorporating saturated pumice on the evolution of total contraction deformation of high strength concrete within 100 days was related to the w/b of the system, while lowering w/b was beneficial to the dry shrinkage. Moreover, when adding wet pumice, the extent of hydration and total porosity of concrete increased, which might lead to impairing the characteristics of the densification matrix. Other scholars [43–47] also expressed concern about the potential negative effects of the introduction of water-absorbing LWAs on the strength, durability, and contraction distortion of concrete in a drying environment. In particular, RILEM TC 196-ICC [48] emphasized that adequate attention should be paid to the continuous shrinkage of IC concrete under dry conditions.

At present, there are few studies on LWAs as the IC carrier materials of UHPC. Suzuki et al. [49] claimed that using a porous ceramic-coarse aggregate as the IC agent of UHPC (w/b = 0.15) could slightly improve the compressive strength of concrete and depress autogenous shrinkage strain, and the effect on drying shrinkage was negligible. Van et al. [17] expounded that the moisture provided by the humid rice husk ash could not only delay the start-up time of the relative humidity drop inside UHPC, but also promote the continuous hydration of the cementitious system, thereby improving the mechanical properties and volume stability of concrete. The results of Wang et al. [50] showed that the incorporation of wet coral sand would clearly condense the self-shrinkage of UHPC, and the total contraction within seven days decreased by 53.9%. Meanwhile, there was a negative correlation

between the development of concrete strength and the level of substitution. Meng and Khayat. [19] superseded river sand by volume fraction with 25% pre-saturated expanded shale, which could reduce the autogenous shrinkage deformation of UHPC by 25.4% and increase the compressive strength by 21.5% in 28 days. Nevertheless, the current concerns on the IC effect of LWAs on UHPC shrinkage are more focused on the early age (first 7 d or most up to 28 d), and the possible adverse effects from extraneous water brought in by the LWAs on the long-term persistent shrinkage deformation behavior under drying condition are usually ignored. In addition, the investigations regarding the effect of the gradation of LWA particles and content of extra water on the hydration process and hydration products in UHPC are limited.

Consequently, in this study, a typical LWA (pumice) is included in the production of UHPC, and the effects of extra water (from pre-wetting LWA) on the macro behaviors, including contraction continuous evolution under low humidity surroundings and the hydration of the composites cementitious system in UHPC, are investigated. The working performance, mechanical properties, and dry shrinkage of the developed UHPC are measured by standardized test methods, while microscopic analysis as hydration heat, XRD, DTG, and EDS are used to clarify some hydration characteristics.

## 2. Materials and Methods

### 2.1. Materials

OPC 52.5 cement (Huaxin Cement Co., Ltd., Huangshi, China), first grade fly ash (FA) (Huaneng Yangluo Power Plant, Wuhan, China), and silica fume (SF) (Southeast Star Technology Development Co., Ltd., Chengdu, China) are used as the active powders in this work and the XRF analysis results are shown in Table 1. Continuously graded river sand (Wuhan, China) and pumice particles (Changbai Mountain, China) (0–0.6 mm and 0.6–1.25 mm) are added as fine aggregates. A highly effective polycarboxylate super plasticizer (SP) (Sobute New Materials Co., Ltd., Nanjing, China), which has a solid content of 20% and a water reduction rate of 40%, is also added.

**Table 1.** Chemical compositions of the employed cementitious materials (%).

Compositions	Na <sub>2</sub> O	MgO	Al <sub>2</sub> O <sub>3</sub>	SiO <sub>2</sub>	P <sub>2</sub> O <sub>5</sub>	SO <sub>3</sub>	K <sub>2</sub> O	CaO	Fe <sub>2</sub> O <sub>3</sub>	LOI
Cement	0.09	1.61	4.18	19.20	0.09	3.35	0.78	64.93	3.32	2.49
SF	0.13	0.47	0.25	94.65	0.17	0.69	0.84	0.36	0.15	2.29
FA	0.33	0.23	38.01	46.44	0.06	0.69	0.88	7.50	3.12	2.79

Pumice stone is well-known as a natural porous mineral material with a well-developed pore structure and an environment scanning electron microscope (ESEM) (FEI, Hillsboro, OR, USA) photomicrograph of it is shown in Figure 1. Pumice has a high porosity (more than 50%) and its pore framework is dominated by micron-sized slender tubular channels, and almost all of them are interconnected [35,51–54]. This typical conformation determines that it can be exploited as an efficient IC vector. The mineral phases are analyzed by XRD (Bruker, Karlsruhe, Germany) and the results are presented in Figure 2, which reveals that the main structure of pumice is Na<sup>+</sup>, K<sup>+</sup> type amorphous phase feldspar with a brilliant stability (A: PDF (ICDD) 10-0393, S: PDF (ICDD) 10-0357, Q: PDF (ICDD) 46-1045). The main chemical components of pumice are SiO<sub>2</sub> 70.55%, Al<sub>2</sub>O<sub>3</sub> 11.21%, Na<sub>2</sub>O 4.79%, Fe<sub>2</sub>O<sub>3</sub> 4.57%, K<sub>2</sub>O 3.76%, and CaO 0.81%, which are provided by XRF. Meanwhile, the apparent densities of 0–0.6 mm and 0.6–1.25 mm pumice are 1.08 g/cm<sup>3</sup> and 0.59 g/cm<sup>3</sup>, respectively, and the corresponding saturated water absorption rates of them are 77.9% and 66.6%, as determined by the tissue wiping method [55,56].



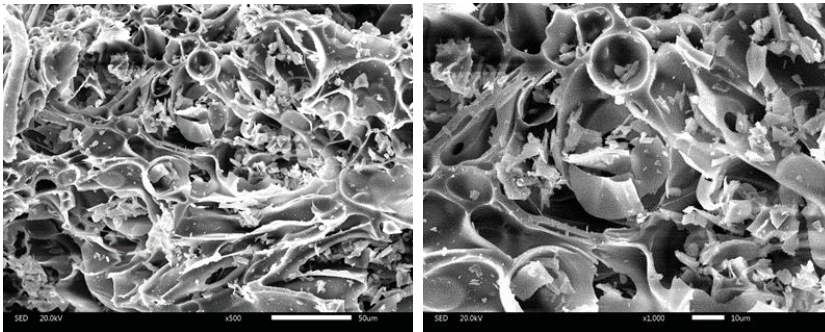


Figure 1. ESEM photomicrographs of the employed pumice stone.

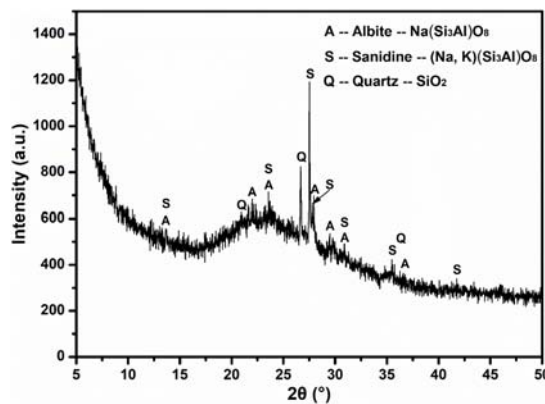


Figure 2. XRD pattern of natural pumice stone.

## 2.2. Experimental Methodology

### 2.2.1. Design Method

The revised Andreasen-Andersen (A&A) model is widely applied in the optimization design of the UHPC mix ratio. Studies confirmed that the optimal range of the distribution coefficient ( $q$ ) is 0.22–0.25 [50,57,58], and the value of  $q$  is selected as 0.23 in this paper.

In order to retain the accumulation state of the UHPC system, the pumice replaces the same-grain river sand with a certain volume ratio. According to the measured particle size distribution of the active powders and the two fine aggregates, the method of least squares (Equation (1)) is used to evaluate the close packing state of granules in UHPC, and the reasonable mixture ratio design scheme of the matrix is exhibited in Table 2, where C0 represents the control group; U and S indicate the water absorption state of the pumice, where U represents unsaturation and S represents saturation; and P<sub>1</sub> and P<sub>2</sub> represent the 0–0.6 mm and 0.6–1.25 mm pumice particle substitution system, respectively.

$$RSS = \frac{\sum_{i=1}^n \left( P_{mix} \left( D_i^{i+1} \right) - P_{tar} \left( D_i^{i+1} \right) \right)^2}{n} \quad (1)$$

where  $D_i^{i+1}$ ,  $n$ ,  $P_{mix}$ , and  $P_{tar}$  denote some gradation of particle size ( $\mu\text{m}$ ), the number of chosen particle sizes, the designed mix, and the target curve, respectively. RSS is sum of the squares of the residuals, which represents the proximity of the designed mix and target curve.



**Table 2.** Recipe of the designed UHPC combined with damp pumice particles (kg/m<sup>3</sup>).

Group	Cement	FA	SF	River Sand		Damp Pumice		Water	SP
				0–0.6	0.6–1.25	0–0.6	0.6–1.25		
C0	750	200	144	770	220	0	0	175	31
UP <sub>1</sub> C10	750	200	144	693	220	37.08	0	175	31
UP <sub>1</sub> C20	750	200	144	616	220	74.16	0	175	31
UP <sub>1</sub> C30	750	200	144	539	220	111.24	0	175	31
UP <sub>2</sub> C10	750	200	144	770	198	0	6.00	175	31
UP <sub>2</sub> C20	750	200	144	770	176	0	12.00	175	31
UP <sub>2</sub> C30	750	200	144	770	154	0	18.00	175	31
SP <sub>1</sub> C10	750	200	144	693	220	55.43	0	175	31
SP <sub>1</sub> C20	750	200	144	616	220	110.86	0	175	31
SP <sub>1</sub> C30	750	200	144	539	220	166.29	0	175	31
SP <sub>2</sub> C10	750	200	144	770	198	0	8.38	175	31
SP <sub>2</sub> C20	750	200	144	770	176	0	16.76	175	31
SP <sub>2</sub> C30	750	200	144	770	154	0	25.14	175	31

The closest stacking curves of the raw materials emerged in Figure 3. It is shown that although the gradation of pumice particles in the same size range is different from that of river sands, no obvious deterioration of the accumulation state between the particles can be observed, whose form are still in a tight status.

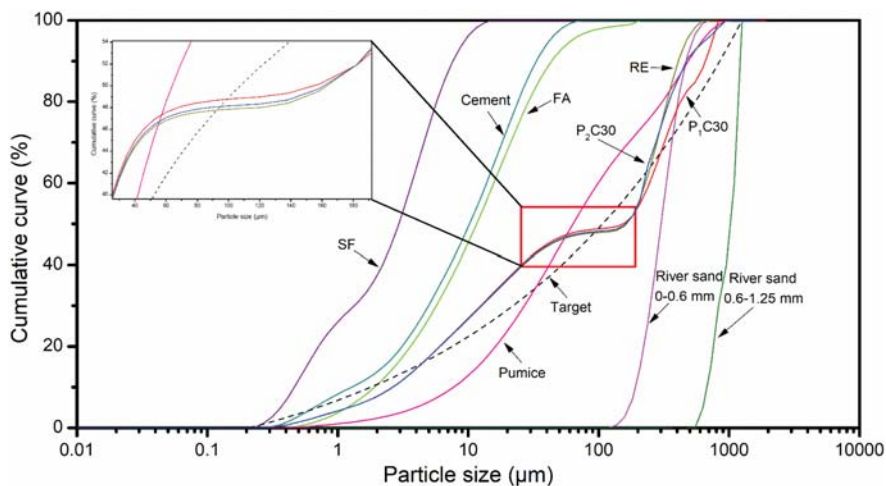


**Figure 3.** Particle size distributions (PSDs) of the crude materials, the target, and optimized grading curves of the composites on account of optimized pre-wetting pumice substances.

### 2.2.2. Flowability

The fluidity of the fresh UHPC paste is evaluated by GB/T 2419-2005 [59]. The test die includes a truncated cone mold and a pattern sleeve, wherein the mould size is as follows: the inner diameters of the upper and lower ports are 70 mm and 100 mm, respectively; and the outer diameter of the lower mouth and height are 120 mm and 60 mm, respectively.

### 2.2.3. Mechanical Properties

UHPC compressive and flexural strength is tested according to GB/T 17671-1999 [60]. The sample size is 40 mm × 40 mm × 160 mm, and the samples are kept in water at a temperature of 20 ± 2 °C. In the experiment, six specimens per mix-age are tested.

#### 2.2.4. Drying Shrinkage

The measurement of UHPC drying shrinkage is based on JC/T 603-2004 [61]. Each group is formed of three samples of 25 mm × 25 mm × 280 mm, and the test blocks is kept in  $20 \pm 2$  °C water for seven days after demolding. After maintenance, the initial length of the specimens is recorded as  $L_0$ , and the pieces are transferred into the dry shrinkage curing box with a condition of temperature of  $20 \pm 2$  °C and humidity of  $60 \pm 2\%$  as the “time zero”, and the length  $L_x$  is measured at the corresponding time.

#### 2.2.5. Hydration Process

To evaluate the effect of extra water introduced by the pre-wetting pumice on the cement hydration kinetic in the UHPC composite system, a heat flow calorimetry modeled TAM AIR is employed. The paste is strictly designed according to the recipes; simultaneously, the rate of heat liberation and total heat within 72 h are monitored.

#### 2.2.6. XRD

The hydration products of UHPC are characterized by a D8 Advance diffractometer with Cu K $\alpha$  radiation, a step size of 0.019 °2 $\theta$ /step, a measuring time of 141.804 s/step, a start position of 5°(2 $\theta$ ), and an end position of 50°(2 $\theta$ ).

#### 2.2.7. DTG

The standard ground sample powders are subjected to thermogravimetric analysis using a NETZSCH STA 2500 synchronous thermal analyzer at a heating rate of 10 °C/min up to 1000 °C.

#### 2.2.8. ESEM-EDS

The micro-domain morphology and structure of the samples' surface are observed by a QUANTA FEG 450 field emission ESEM. At the same time, the EDS analysis can interpret the micro-area components, and the intelligent quantitative results provided by eZAF help to effectively evaluate the atomic ratio of the skin layer elements.

### 3. Results and Discussion

#### 3.1. Fresh Behaviors

The relationship between the fluidity of the fresh paste and the amount of extra water introduced under different mixing ratios is shown in Table 3. The given results indicate that under the same substitution ratio, there is a good positive correlation between the liquidity and the content of water imported; that is, the more water that is introduced, the greater the flowability of the paste. This is attributed to the increase of internal moisture in UHPC, which means that more water participates in the lubrication of the particles, resulting in the increase of the fluidity of the newly poured mortar. Compared with the behavior of the control group, the liquidity of the UHPC compound system is determined by the role of wet pumice particles (whether continuously injected water into the paste or siphon free moisture from the paste during the mixing process). As the water absorption of the pumice particles does not reach saturation, the mortar fluidity will only increase when the volume substitution fraction reaches 30%, whose liquidity exceeds 200 mm ( $C_0 = 183$  mm). When the replacement grade is less than 20%, the flowability drops to a minor extent, with a minimum of 165 mm. When the pumice pellets reach a water saturated state, the paste fluidity is controlled by the amount of water introduced. If the content of extra water exceeds 10 g, the mobility of the paste will improve, and the greater the amount of water introduced, the greater the fluidity of the new mixture. When the external water content reaches 72.9 g, the flow value reaches the maximum value of 374 mm, attaining 204.4% of the control group.

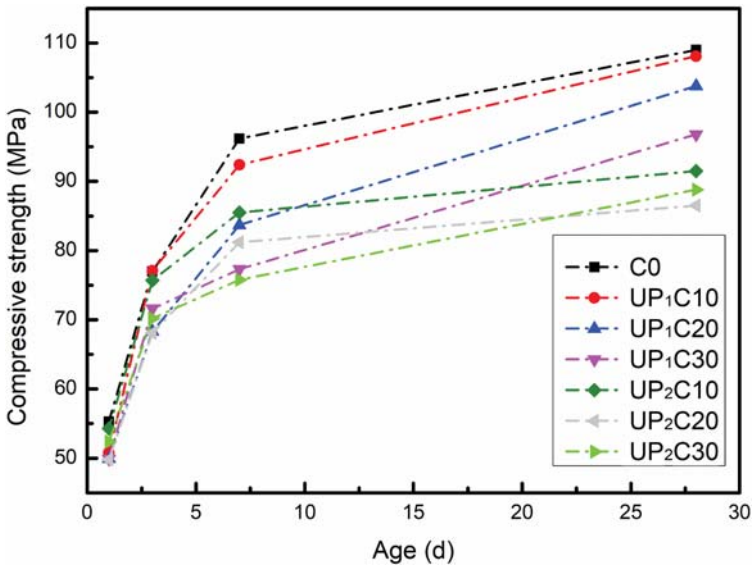
**Table 3.** Fluidity of the designed UHPC with different amounts of extra water introduced by wet pumice.

Group	Extra Water	w/b		Fluidity (mm)
		Free	Total	
C0	0		0.1826	183
UP <sub>1</sub> C10	5.9		0.1880	167
UP <sub>1</sub> C20	11.8		0.1934	173
UP <sub>1</sub> C30	17.7		0.1988	214
UP <sub>2</sub> C10	0.96		0.1835	165
UP <sub>2</sub> C20	1.92		0.1844	180
UP <sub>2</sub> C30	2.88	0.1826	0.1853	201
SP <sub>1</sub> C10	24.3		0.2048	269
SP <sub>1</sub> C20	48.6		0.2271	345
SP <sub>1</sub> C30	72.9		0.2493	374
SP <sub>2</sub> C10	3.35		0.1857	147
SP <sub>2</sub> C20	6.7		0.1888	181
SP <sub>2</sub> C30	10.05		0.1918	186

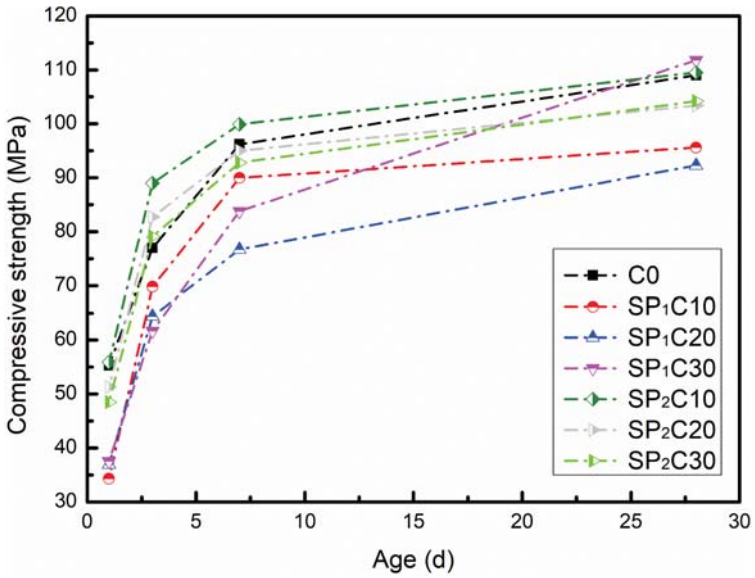
### 3.2. Mechanical Properties

The compressive and flexural strengths of the designed UHPC with different formulas are shown in Figures 4 and 5, respectively. The compressive strength results show that the addition of soaked pumice reduces the compressive strength of UHPC after 28 d curing as a whole, and the average strength of each group is 91.2% of C0, while the maximum compressive strength loss rate (UP<sub>2</sub>C20) is 20.6%. Among them, the strength development of UP<sub>1</sub> and UP<sub>2</sub> substitution systems has a similar law; that is, the strength decreases as the content of extra water increases. The distinction is that the average 28 d compressive strength of UP<sub>1</sub> groups is 5.6% lower than that of C0, while that of UP<sub>2</sub> is 18.4%. For the groups of 0–0.6 mm pumice particles to replace the homologous river sands, as the content of introduced water is in the range of 17.7–48.6 g (UP<sub>1</sub>C30, SP<sub>1</sub>C10, and SP<sub>1</sub>C20), the compressive strength of each age has obvious loss. Meanwhile, the amount of extra water is less than 11.8 g (UP<sub>1</sub>C10, UP<sub>1</sub>C20) or up to 72.9 g (SP<sub>1</sub>C30), the compressive strength loss at 28 d is kept at a low level, and even a slight improvement can be observed. For that 0.6–1.25 mm pumice substitution system, the key factor determining the compressive strength of UHPC is the water absorption state of pumice. If the pumice granules do not reach the saturated water absorption, the strength is significantly depressed. The strength can be held at a similar gradation as the control group while the pumice particles are full of water.

The flexural strength results show that the flexural strengths of the SP<sub>1</sub>C20 and SP<sub>1</sub>C30 groups with a water content exceeding 48.6 g express a downward trend compared with the control group. In addition to the above both groups, the bending strength performance of other recipes embodies the same regular pattern, which is that the bending strength decreases with increasing extra water intake within a uniform substitution system, which remains notably higher than that of C0. The details can be inducted as follows: the flexural strength of the group blended with damp pumice after 1 d is significantly lower than that of C0, with an average value of 80.8%. It grows rapidly within 1–3 d and almost completely exceeds that of C0 at 3 d, with an average of 113.5%. By 28 d, the average bending strength of each group reaches 129.6% compared with C0, and the highest value achieves 157.7% (UP<sub>1</sub>C10).

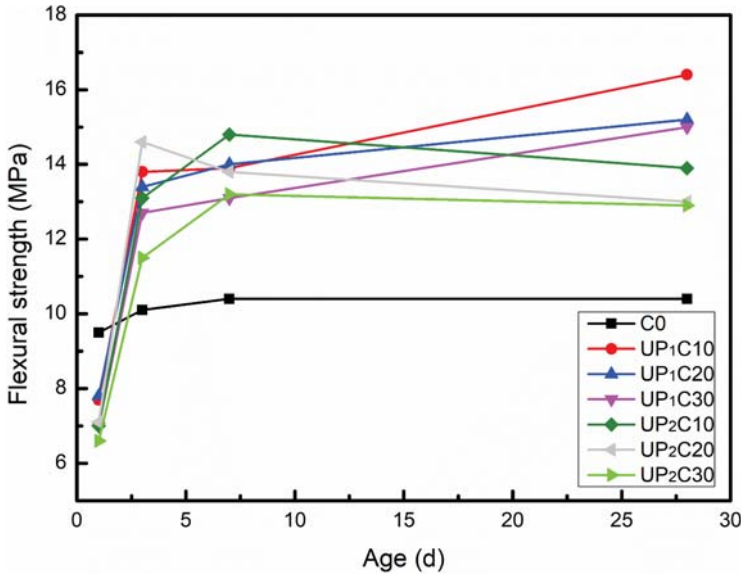


(a)

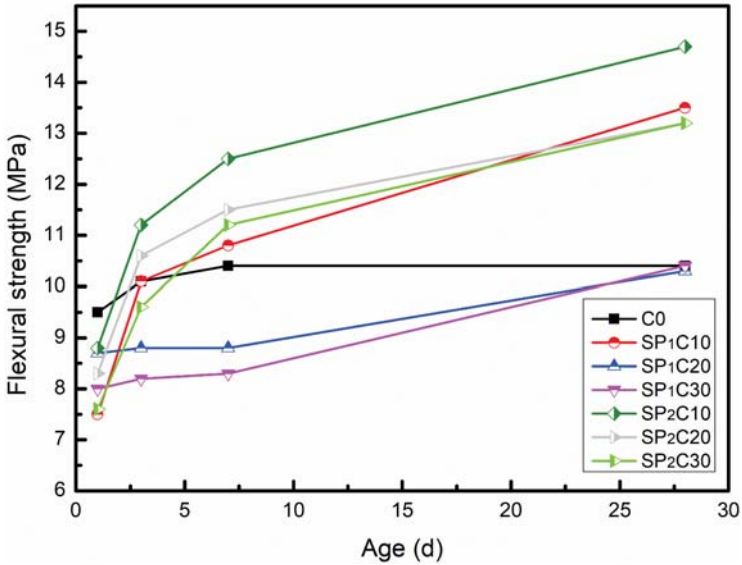


(b)

Figure 4. Compressive strength development of UHPC combined with water absorption pumice: (a) unsaturated pumice substitution; (b) saturated pumice substitution.



(a)



(b)

**Figure 5.** Flexural strength variation of UHPC combined with water absorption pumice: (a) unsaturated pumice substitution; (b) saturated pumice substitution.

The incorporation of pre-moistened pumice has both positive and negative effects on the development of UHPC mechanical properties. Among them, the positive effect is that the sustained release of moisture by the wet pumice will continuously promote the hydration of the unhydrated

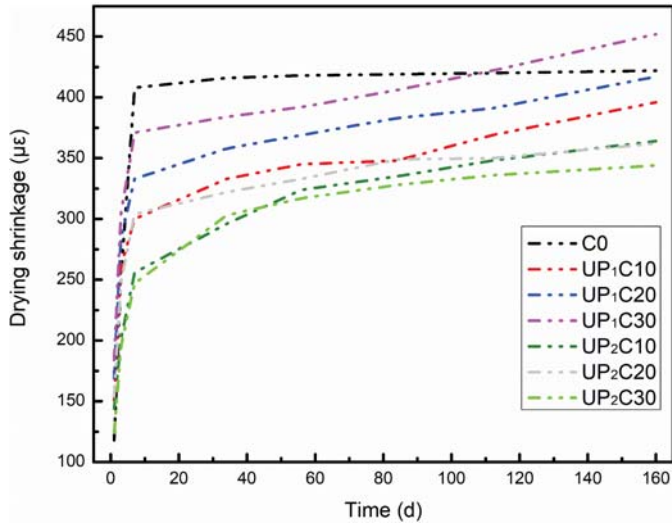
cement particles and secondary hydration of reactive powders (SF and FA) in the cementitious system and then enhance the gelling ability, whose contribution to the development of strength mainly affects the later stage. The negative effect comes from two aspects: primarily, the water released from the pumice pellets will cause the early actual  $w/b$  of the system to rise, thereby affecting the porosity and types of hydration products, which brings a reduction of strength [62]. Secondly, the elastic modulus and crushing value of the pumice particles are clearly lower than those of natural river sand, and the fine mineral aggregates are destroyed under the action of external pressure or impact force, which leads to failure of the specimen [52,54,63]. In a word, the characteristic development of mechanical properties of pumice-based UHPC is a reflection of which effect dominates.

### 3.3. Persistent Shrinkage Deformation

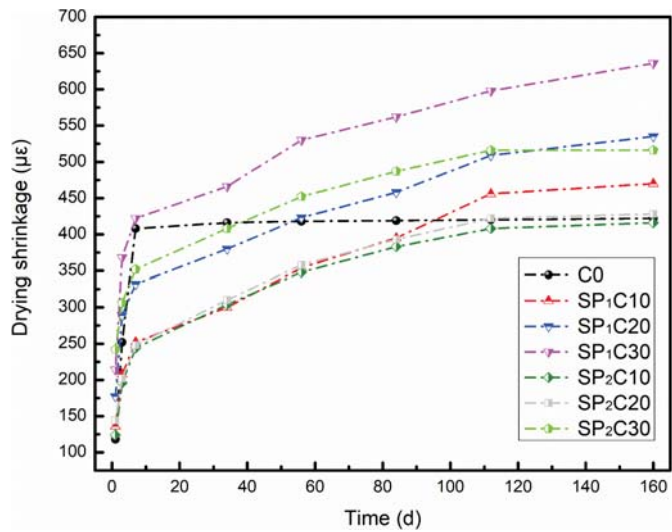
The drying shrinkage curves of UHPC designed with different mix ratios are presented in Figure 6. Actually, the trend of drying shrinkage development is the collective result of the combined action of autogenous shrinkage after seven days and continuous dry shrinkage deformation in the later low humidity environment of concrete. Thus, the curves reflect the sight of the total shrinkage. The given information is that the drying shrinkage evolution characteristics of the UHPC system compounding damp pumice are significantly different from those of the control group. The dry shrinkage develops with a uniform growth in C0 within seven days, and the contraction behavior basically disappears and reaches a volume stable state after that. The first seven days of shrinkage development of UHPC with damp pumice is also swift, but the rate then gradually decreases, and the test piece continues to contract within 7 d~160 d. The constriction development of concrete is related to the moisture migration and pore structure of concrete [64,65]. The  $w/b$  in UHPC is extremely low, and the moisture is quickly consumed in the early stage of hydration, resulting in a rapid decline in the relative humidity inside the system. Therefore, regardless of whether the concrete introduces an IC agent, its early (within 7 d) shrinkage will increase quickly. UHPC has a low porosity and dense architecture, which makes it difficult to exchange moisture with the outside surroundings. Consequently, the C0 group can maintain a relatively stable evolution state after rapid development in the early stage. After being mixed with the humid pumice, the water slow-release effect of the pumice “tank” can effectively delay the decline of the internal relative humidity. Besides, the pumice pore structure has the function of retaining moisture, and restrains the diffusion of water to the outside. The effects of both mentioned above are superimposed, and the rate of contraction development in the UHPC within 7 d of adding the wet pumice is reduced. The release of water from the pumice in the concrete is a continuous process, and the moisture will increase the actual  $w/b$  of the cementitious system, resulting in a raise in the total water capacity and porosity, which will elevate the permeability of UHPC [42]. At the same time, the pore structure of the porous pumice itself may also broaden the channels communicating with the external world. Thus, the drying shrinkage distortion of the UHPC combining the water-absorbing pumice will last for a long time.

The drying shrinkage of C0 after 1 d, 7 d, 34 d, and 160 d is 118  $\mu\epsilon$ , 408  $\mu\epsilon$ , 416  $\mu\epsilon$ , and 422  $\mu\epsilon$ , respectively. Compared with the control group, the contraction value of the designed UHPC with pre-wetted pumice at 1 d is increased, and the promotion of each compounding system is 28.0%, 43.2%, and 55.9% with UP<sub>1</sub>C10~UP<sub>1</sub>C30; UP<sub>2</sub>C10~UP<sub>2</sub>C30 is 22.0%, 30.5%, and 5.1%; SP<sub>1</sub>C10~SP<sub>1</sub>C30 is 15.3%, 50.0%, and 81.4%; and SP<sub>2</sub>C10~SP<sub>2</sub>C30 is 5.1%, 22.0%, and 105.1%, respectively. The analysis results indicate that the development of the shrinkage of the complex UHPC within 1 d is not directly related to the quantity of extra water, and the soaked pumice particles of 0.6–1.25 mm are more sensitive to drying shrinkage than those of 0–0.6 mm. The content of foreign water by SP<sub>1</sub>C10 is 24.3 g, and the constriction is increased by 15.3% compared with C0. Oppositely, the amount of water introduced by SP<sub>2</sub>C20 is 6.7 g, but the corresponding shrinkage value is increased by 22.0%. The extent to which the contraction characteristics of the concrete are affected is determined by the actual water participation in hydration that can effectively promote a reaction in the very early period. In fact, this process is related to the water release behavior of water-absorbing pumice grains in the interior of

UHPC. The smaller the particle size of pumice after crushing, the lower the proportion of coarse holes and the connectivity in the pore structure [41]. It is generally believed that the water release behavior of the pore structure has a higher priority for the one with a larger diameter, which means that the larger beads have a faster water release rate and higher efficiency [66–68]. Under the same conditions, the size of 0.6–1.25 mm pumice granules can supply more water for the IC. In addition, the greater scale of the “miniature reservoir” that affects the effective area of hydration is more expansive [63,69,70].



(a)



(b)

**Figure 6.** Influence of humid pumice on the persistent shrinkage deformation evolvement of the designed UHPC: (a) unsaturated pumice substitution; (b) saturated pumice substitution.

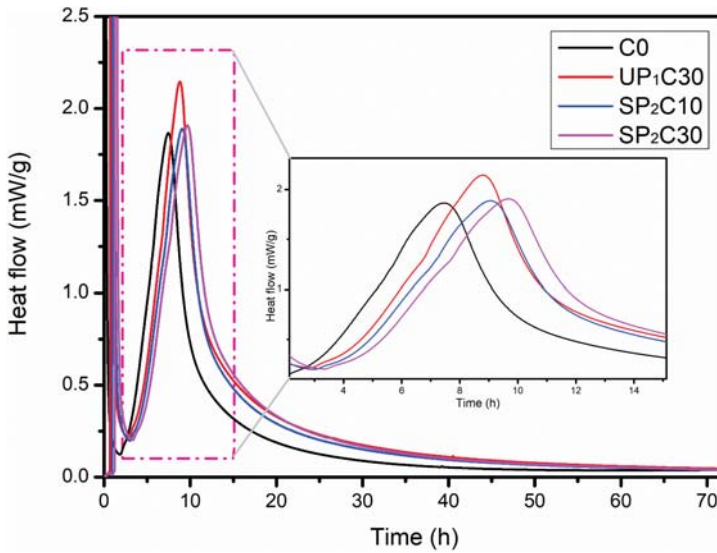


In the 1–7 d age range, the shrinkage growth of the UHPC appending the humid pumice is still relatively fast, but its development rate begins to gradually slow down, and the total value of contraction within 7 d is lower than the control group. Compared with C0, the details of the total dry shrinkage rate during 7 d are that UP<sub>1</sub>C10~UP<sub>1</sub>C30 shrinks by 26.5%, 18.4%, and 9.1%; UP<sub>2</sub>C10~UP<sub>2</sub>C30 retracts by 37.3%, 25.5%, and 39.5%; SP<sub>1</sub>C10~SP<sub>1</sub>C30 shrinks by 38.2%, 18.6%, and −3.4%; and SP<sub>2</sub>C10~SP<sub>2</sub>C30 retracts by 40.2%, 39.2%, and 13.7%, respectively. It reveals that the intake of moisture at this stage remains the postponed effect of self-desiccation inside the matrix. The shrinkage of SP<sub>1</sub>C30 after 7 d has exceeded the value of C0, and it continues to grow in the later period at a high-speed. This can be attributed to the fact that the content of external water in the SP<sub>1</sub>C30 group is too large, the total w/b of the mortar has reached 0.25 (beyond the scope of UHPC), which is disadvantageous to the microstructure development, and the porosity of concrete is then broadened, resulting in the deformation due to continuous moisture loss increases.

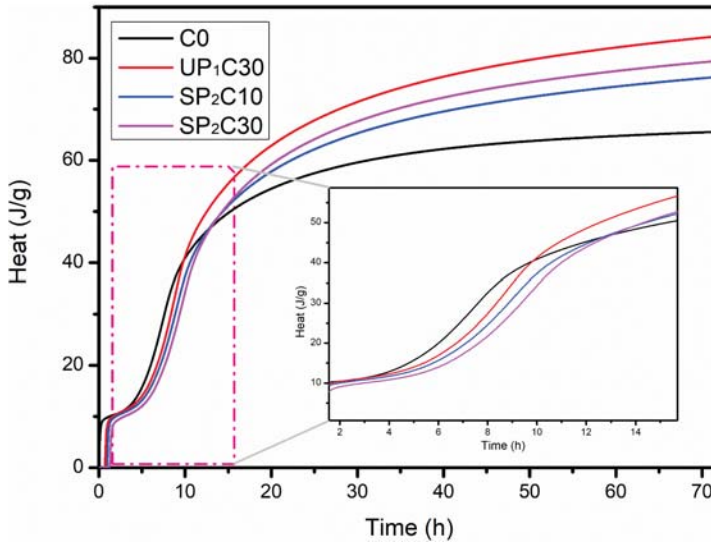
After seven days of hydration, the drying shrinkage of UHPC with dank pumice adjunction continues to develop. The total drying shrinkage of each group at a 160 d age (C0 = 422  $\mu\epsilon$ ) is 396  $\mu\epsilon$ , 417  $\mu\epsilon$ , and 452  $\mu\epsilon$  for UP<sub>1</sub>C10~UP<sub>1</sub>C30; 364  $\mu\epsilon$ , 362  $\mu\epsilon$ , and 344  $\mu\epsilon$  for UP<sub>2</sub>C10~UP<sub>2</sub>C30; 470  $\mu\epsilon$ , 535  $\mu\epsilon$ , and 636  $\mu\epsilon$  for SP<sub>1</sub>C10~SP<sub>1</sub>C30; and 416  $\mu\epsilon$ , 428  $\mu\epsilon$ , and 516  $\mu\epsilon$  for SP<sub>2</sub>C10~SP<sub>2</sub>C30, respectively. Among them, in the 0–0.6 mm wet pumice particles replacement system, the extra water content more than 17.7 g will lead to an increase in the final shrinkage of UHPC. In that substitution group of the 0.6–1.25 mm pumice, the amount of water introduced will only need to be greater than 6.7 g, and the total contraction will rise. The regularity that can be summarized is that the long-term shrinkage of UHPC combined with wet pumice is positively correlated with the amount of water introduced, and the larger particles contribute more to the final contraction deformation. This phenomenon can also be due to the higher water release efficiency of the larger size of pumice particles.

### 3.4. Hydration Process Analysis

The influence of extra water on the heat flow and total heat in the UHPC system within 72 h under several typical mix design conditions is collected in Figure 7. The results indicate that the external moisture introduced by cellular mineral will not change the basic law of cement hydration, but merely has an impact on the hydration course, including exothermic peak location and total heat output. Moreover, it mainly affects the very early hydration, and has a limited influence on the stabilization period. The heat flow curves indicate that C0, UP<sub>1</sub>C30, SP<sub>2</sub>C10, and SP<sub>2</sub>C30 all have a distinct hydration exothermic peak, and the distribution range is 2–20 h after mixing, with good consistency. Despite the same tendency being presented, there are divergences between the exothermic peak values and time schedules in the violent stage, possessing the similar rules. In the period of acceleration, the exothermic peak of C0, UP<sub>1</sub>C30, SP<sub>2</sub>C10, and SP<sub>2</sub>C30 is 1.87 mW/g, 2.15 mW/g, 1.89 mW/g, and 1.91 mW/g, respectively, and the corresponding occurrence time is 7.5 h, 8.8 h, 9.1 h, and 9.7 h. The height of the exothermic peak is positively correlated with the amount of extra water, which can persistently promote the progress during the hydration step [71]. The emergence time of that peak is related to the abundance of moisture in the vicinity of cement particles. Compared with the 0–0.6 mm pumice bead, the water-releasing rate of 0.6–1.25 mm is faster, which manifolds the gross of hydration products on the surface of cement granules within the effective range. The formation of the hydrated products film gravely inhibits the chemical reaction, leading to a modest lag in the time table for that crest [72]. The retarding effect of introducing water is an important reason for the significant decrease in the mechanical properties of UHPC mixed with wet pumice in one day.



(a)



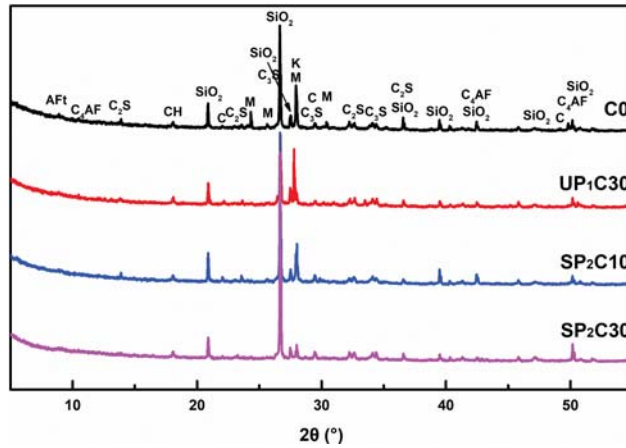
(b)

**Figure 7.** Heat evolution of UHPC system consisting of hydrated pumice within 72 h under several typical mix design conditions: (a) heat flow; (b) total heat.

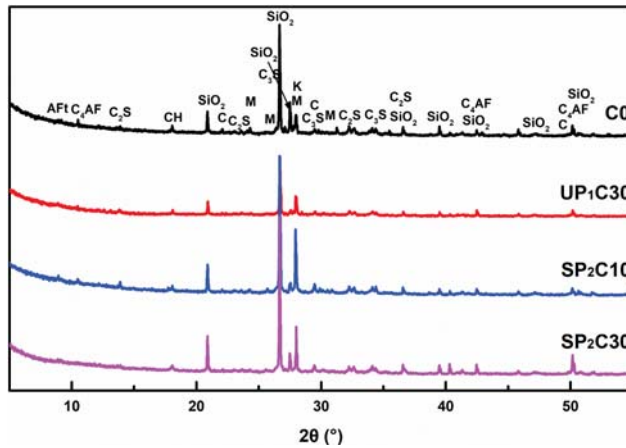
The profiles of total heat reveal that the quantity of heat of C0, UP<sub>1</sub>C30, SP<sub>2</sub>C10, and SP<sub>2</sub>C30 within 72 h is 65.6 J/g, 84.3 J/g, 76.3 J/g, and 79.5 J/g, respectively. As can be gathered, the more added water there is, the higher heat the UHPC system produces. There is an environment with an extreme water shortage inside UHPC, and extra moisture will eventually participate in the reaction at different stages of hydration, improving the degree of hydration and the development of compensation strength.

3.5. XRD

The XRD patterns of several representative UHPC samples at 7 d and 28 d are given in Figure 8. The characterizations of hydration products elaborate that the main phases of different ages in UHPC are  $\text{Ca(OH)}_2$ , Aft, and  $\text{CaCO}_3$ , and the introduction of water-absorbing pumice does not produce byproducts. Besides, there are obvious  $\text{C}_2\text{S}$ ,  $\text{C}_3\text{S}$ , and  $\text{C}_4\text{AF}$  characteristic peaks in each group due to unhydrated cement particles in the UHPC hardened paste.



(a)



(b)

- CH:  $\text{Ca(OH)}_2$ , (PDF (ICDD) 04-0733)
- M: Margarite, (PDF (ICDD) 18-0276)
- K:  $\text{Al}_2\text{SiO}_5$ , (PDF (ICDD) 11-0046)
- C: Calcite, (PDF (ICDD) 51-1524)

**Figure 8.** XRD pattern of UHPC hardened paste formed with pre-humid pumice at 7 d and 28 d age: (a) 7 d age; (b) 28 d age.



### 3.6. DTG

Thermogravimetric analysis is also performed on the samples mentioned above, and the DTG curves for the tested specimen at 7 d and 28 d are exhibited in Figure 10; incidentally, the yield of  $\text{Ca}(\text{OH})_2$  based on calculation is presented in Table 4. According to Figure 10a, the hydration of the cementitious system at 7 d is accelerated by incorporating wet pumice. The weight loss curve of each group at different stages is comparatively analyzed, and sums up that the UHPC designed with the IC mechanism compared to the control group has the following details: (1) The mass loss of C–S–H and AFt in the composite mortar within the range of 100–200 °C while the influence of adsorbed water has been excluded becomes larger, indicating that the content of hydration products in the gelling system increases; (2) although the total amount of  $\text{CaCO}_3$  formed by carbonation of  $\text{Ca}(\text{OH})_2$  is significantly increased, the remaining quality of  $\text{Ca}(\text{OH})_2$  is still large, testifying that the production of  $\text{Ca}(\text{OH})_2$  is also palpably raised, which is sensitive for the large beads; (3) the location of the main decomposition peak of  $\text{CaCO}_3$  manifests some right shifts, which means that the carbonation time is prolonged, and the incipient gelation framework develops slowly. This phenomenon has been corroborated and supported by the widespread suppression of its 1 d strength development.

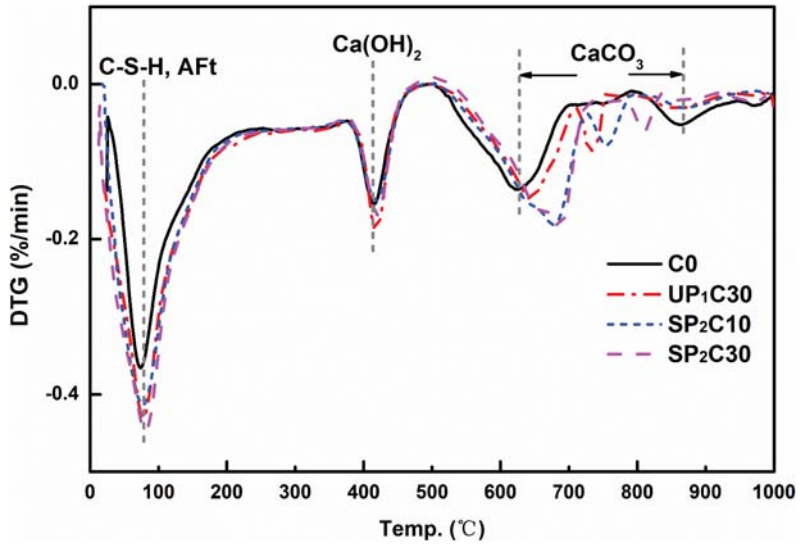
**Table 4.** Generation of  $\text{Ca}(\text{OH})_2$  for corresponding representative groups based on calculation by DTG curves (%).

Group	C0	UP <sub>1</sub> C30	SP <sub>2</sub> C10	SP <sub>2</sub> C30
7 d	0.387	0.517	0.506	0.550
28 d	0.420	0.348	0.385	0.423

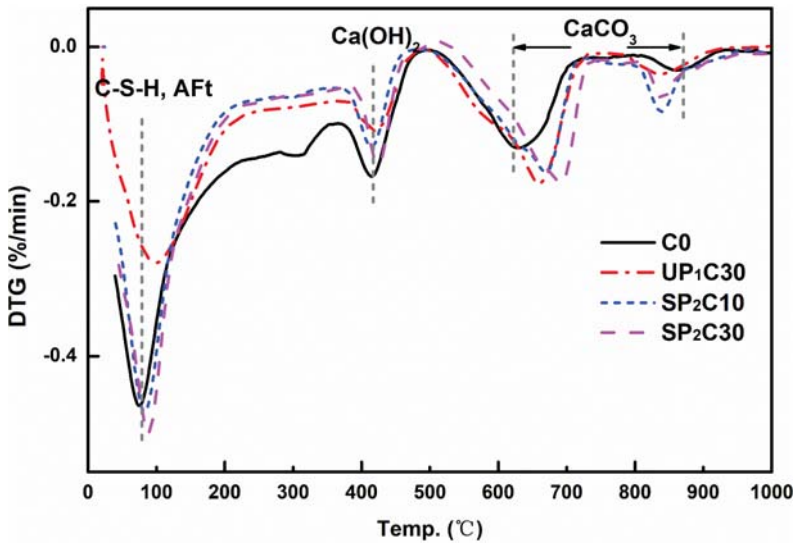
The results shown in Figure 10a,b have a good overall consistency, demonstrating that the effect of pumice containing water on the promotion of hydration of the UHPC system is a continuous process, and the reasoning agrees with the deduction of XRD analysis. After the introduction of the IC pumice, the content of  $\text{Ca}(\text{OH})_2$  is notably lowered at a 28 d age compared to the 7 d age samples; contrarily, that of  $\text{Ca}(\text{OH})_2$  is increased in the control group of UHPC. This is additional evidence that the extra water will promote the secondary hydration of SF and FA in the composite system, which consumes part of  $\text{Ca}(\text{OH})_2$ .

### 3.7. ESEM-EDS

C–S–H gel is the most important hydration product and cementing component in concrete. It is generally accepted that the C–S–H in the hydration products of cement-based materials is divided into two types: C–S–H (I) and C–S–H (II). Among them, Ca/Si of C–S–H (I) is 0.6–1.5, and Ca/Si of C–S–H (II) is about 2.0 [73,74]. The Ca/Si of C–S–H in the hydration products of the 28-day-old UHPC specimen pieces is evaluated by ESEM-EDS, as exhibited in Figure 11. The results reveal that the introduction of humid fine aggregates will lead to a sharp drop in the average Ca/Si of C–S–H in the neighboring mortar. This means that the IC moisture can not only promote the hydration process of the UHPC gelling system, but also make it easier for the reaction to form C–S–H (I), which bears a lower degree of polymerization and crystallinity. The mechanism that causes this phenomenon comes from two aspects: firstly, water introduced by wet pumice will increase the actual w/b of the mortar within its effective range, resulting in a change in the regional hydration products, especially the C–S–H structure [75,76]. Secondly, the Ca/Si in C–S–H is proportional to the content of  $\text{Ca}(\text{OH})_2$  in hardened paste [77], as mentioned in the previous section, and the IC moisture can activate the pozzolanic reaction of active admixtures more and consume  $\text{Ca}(\text{OH})_2$ , resulting in a Ca/Si decrease in C–S–H. The mutation of the C–S–H structure has a non-negligible influence on the UHPC strength development and the extremely late drying shrinkage deformation using the IC mechanism, while C–S–H loses interlayer water and C–S–H gel particles produce irreversible permanent rearrangement [78,79].

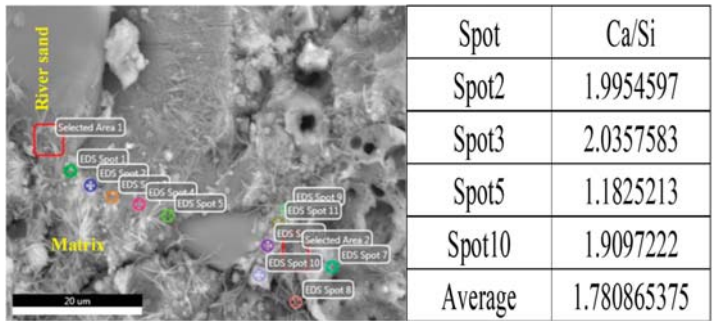


(a)

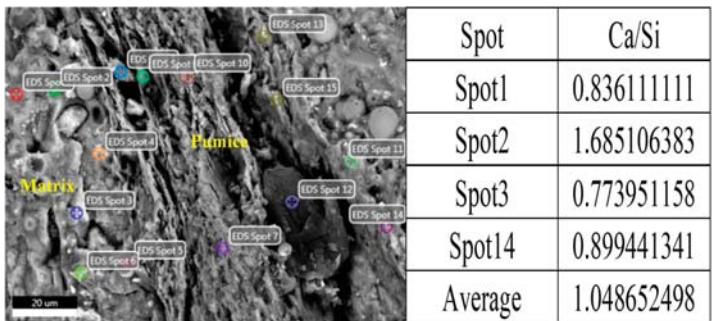


(b)

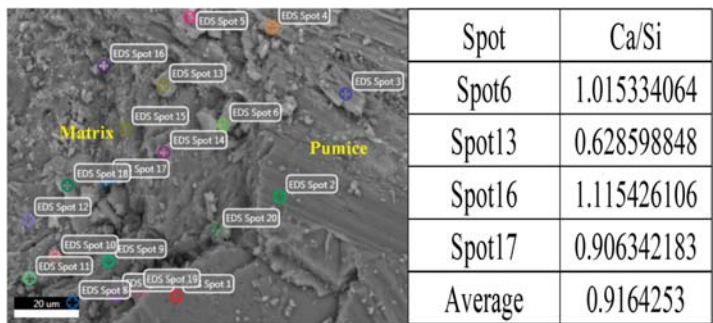
Figure 10. Effect of wet pumice on the thermal decomposition characteristics of several typical UHPC recipes after 7 d and 28 d: (a) 7 d; (b) 28 d.



(a) C0



(b) SP<sub>2</sub>C10



(c) SP<sub>2</sub>C30

**Figure 11.** EDS elemental content analysis of the matrix nearby river sand and wet pumice in C0, SP<sub>2</sub>C10, and SP<sub>2</sub>C30 samples mentioned above after 28 d curing: (a) C0; (b) SP<sub>2</sub>C10; (c) SP<sub>2</sub>C30.

#### 4. Conclusions

In this paper, the effects of water-absorbing pumice on the persistent drying shrinkage and hydration characteristics of UHPC are investigated. Combined with comprehensive characterization analysis, the conclusions are summarized as follows:

(1) The flowability of UHPC fresh paste is related to the water absorption and release behavior of wet pumice during mixing. For the 0–0.6 mm humid pumice substitution system, the injection action



plays a dominant role when the water content exceeds 17.7 g. For that of the 0.6–1.25 mm replacement system, the volume quantities need more than 20% to ensure that the injection action has priority.

(2) The introduction of IC water will result in an average decrease of 8.8% in the compressive strength of UHPC after 28 d curing; meanwhile, the flexural strength will be increased.

(3) Incorporation of impregnated pumice will inhibit the early drying shrinkage deformation behavior of UHPC, but the specimen will continue to contract during the later stage. There is a satisfied rule that the final total shrinkage is proportional to the content of extra water for the unified displacement system, while the larger size of LWA IC granules has greater potential adverse effects on the persistent dry contraction of concrete.

(4) The optimum recipe is 0.6–1.25 mm pumice particles in a saturated water absorption state replacing 10% river sands with the same particle size by volume fraction (SP<sub>2</sub>C10). Its compressive strength increases slightly and the flexural strength increases by 41.3% at 28 d. Meanwhile, the total shrinkage is effectively reduced within 160 d.

(5) The additional water has a retarding effect on mortar, which will delay the peak of the hydration exotherm, but raise the rate of heat release during the accelerated period of hydration and the total exothermic energy of the system.

(6) The introduction of water into pumice will promote the hydration process of the UHPC cementitious system. This effect is a continuous proceeding, including early cement hydration and secondary hydration of the reactive powders.

(7) The wet pumice will make the hydration reaction of the paste nearby more likely to generate C–S–H (I) with poor crystallinity, resulting in changes in the composition and structure of hydration products in its effective area.

**Author Contributions:** Conceptualization, R.Y. and Z.S.; Methodology, K.L. and R.Y.; Formal Analysis, K.L. and X.L. (Xiaosheng Li); Investigation, K.L., W.H. and S.Y.; Writing-Original Draft Preparation, K.L. and X.L. (Xuan Ling); Writing-Review & Editing, K.L. and R.Y.; Visualization, R.Y. and S.W.; Funding Acquisition, R.Y. and Z.S.

**Funding:** This research was funded by the National Nature Science Foundation Project of China (51608409 and 51679179); Major science and technology project in Zhongshan city, Guangdong province (2017A1021); Yang Fan plan of Guangdong Province (201312C12); Science and Technology Program of Guangdong Province in 2016 (2016A090924002); Science and Technology Program of Guangdong Province in 2017 (2017B090907009); Late-model Research Institute Development Program of Zhongshan in 2016: Subsidy for Major Research Platform Construction (2016F2FC0008); and open research project of Advanced Engineering Technology Research Institute of Wuhan University of technology in Zhongshan city (WUT201802).

**Conflicts of Interest:** The authors declare no conflict of interest.

## References

1. Richard, P.; Cheyrezy, M. Composition of reactive powder concretes. *Cem. Concr. Res.* **1995**, *25*, 1501–1511. [[CrossRef](#)]
2. Habel, K.; Viviani, M.; Denarié, E.; Brühwiler, E. Development of the mechanical properties of an Ultra-High Performance Fiber Reinforced Concrete (UHPRFC). *Cem. Concr. Res.* **2006**, *36*, 1362–1370. [[CrossRef](#)]
3. Shi, C.; Wu, Z.; Xiao, J.; Wang, D.; Huang, Z.; Fang, Z. A review on ultra high performance concrete: Part I. Raw materials and mixture design. *Constr. Build. Mater.* **2015**, *101*, 741–751. [[CrossRef](#)]
4. Wang, D.; Shi, C.; Wu, Z.; Xiao, J.; Huang, Z.; Fang, Z. A review on ultra high performance concrete: Part II. Hydration, microstructure and properties. *Constr. Build. Mater.* **2015**, *96*, 368–377. [[CrossRef](#)]
5. Rahman, S.; Molyneaux, T.; Patnaikuni, I. Ultra high performance concrete: Recent applications and research. *Aust. J. Civ. Eng.* **2005**, *2*, 13–20. [[CrossRef](#)]
6. Yu, R. Development of Sustainable Protective Ultra-High Performance Fibre Reinforced Concrete (UHPRFC): Design, assessment and modeling. Ph.D. Thesis, Eindhoven University of Technology, Eindhoven, The Netherlands, 2015.
7. Bärboš, G.-A. Long-term Behavior of Ultra-High Performance Concrete (UHPC) Bended Beams. *Procedia Technol.* **2016**, *22*, 203–210.
8. Yoo, D.Y.; Yoon, Y.S. A Review on Structural Behavior, Design, and Application of Ultra-High-Performance Fiber-Reinforced Concrete. *Int. J. Concr. Struct. Mater.* **2016**, *10*, 125–142. [[CrossRef](#)]

9. Zhou, M.; Lu, W.; Song, J.W.; Lee, G.C. Application of Ultra-High Performance Concrete in bridge engineering. *Constr. Build. Mater.* **2018**, *186*, 1256–1267. [[CrossRef](#)]
10. Ren, L.; Fang, Z.; Wang, K. Design and behavior of super-long span cable-stayed bridge with CFRP cables and UHPC members. *Compos. Part B Eng.* **2018**. [[CrossRef](#)]
11. Azmee, N.M.; Shafiq, N. Ultra-high performance concrete: From fundamental to applications. *Case Stud. Constr. Mater.* **2018**. [[CrossRef](#)]
12. Lura, P.; Jensen, O.M.; van Breugel, K. Autogenous shrinkage in high-performance cement paste: An evaluation of basic mechanisms. *Cem. Concr. Res.* **2003**, *33*, 223–232. [[CrossRef](#)]
13. Garas, V.Y.; Kahn, L.F.; Kurtis, K.E. Short-term tensile creep and shrinkage of ultra-high performance concrete. *Cem. Compos.* **2009**, *31*, 147–152. [[CrossRef](#)]
14. Xie, T.; Fang, C.; Ali, M.S.M.; Visintin, P. Characterizations of autogenous and drying shrinkage of ultra-high performance concrete (UHPC): An experimental study. *Cem. Concr. Compos.* **2018**, *91*, 156–173. [[CrossRef](#)]
15. Justs, J.; Wyrzykowski, M.; Bajare, D.; Lura, P. Internal curing by superabsorbent polymers in ultra-high performance concrete. *Cem. Concr. Res.* **2015**, *76*, 82–90. [[CrossRef](#)]
16. Sensale, G.R.D.; Goncalves, A.F. Effects of Fine LWA and SAP as Internal Water Curing Agents. *Int. J. Concr. Struct. Mater.* **2014**, *8*, 229–238. [[CrossRef](#)]
17. Van, V.T.A.; Rößler, C.; Bui, D.D.; Ludwig, H.-M. Rice husk ash as both pozzolanic admixture and internal curing agent in ultra-high performance concrete. *Cem. Concr. Compos.* **2014**, *53*, 270–278. [[CrossRef](#)]
18. Liu, J.; Ou, Z.; Mo, J.; Chen, Y.; Guo, T.; Deng, W. Effectiveness of Saturated Coral Aggregate and Shrinkage Reducing Admixture on the Autogenous Shrinkage of Ultrahigh Performance Concrete. *Adv. Mater. Sci. Eng.* **2017**, *2017*, 1–11. [[CrossRef](#)]
19. Meng, W.; Khayat, K. Effects of saturated lightweight sand content on key characteristics of ultra-high-performance concrete. *Cem. Concr. Res.* **2017**, *101*, 46–54. [[CrossRef](#)]
20. Sun, W.; Chen, H.; Luo, X.; Qian, H. The effect of hybrid fibers and expansive agent on the shrinkage and permeability of high-performance concrete. *Cem. Concr. Res.* **2001**, *31*, 595–601. [[CrossRef](#)]
21. Corinaldesi, V.; Nardinocchi, A.; Donnini, J. The influence of expansive agent on the performance of fibre reinforced cement-based composites. *Constr. Build. Mater.* **2015**, *91*, 171–179. [[CrossRef](#)]
22. Soliman, A.M.; Nehdi, M.L. Effects of shrinkage reducing admixture and wollastonite microfiber on early-age behavior of ultra-high performance concrete. *Cem. Concr. Compos.* **2014**, *46*, 81–89. [[CrossRef](#)]
23. Yoo, D.Y.; Banthia, N.; Yoon, Y.S. Effectiveness of shrinkage-reducing admixture in reducing autogenous shrinkage stress of ultra-high-performance fiber-reinforced concrete. *Cem. Concr. Compos.* **2015**, *64*, 27–36. [[CrossRef](#)]
24. Ghafari, E.; Ghahari, S.A.; Costa, H.; Júlio, E.; Portugal, A.; Durães, L. Effect of supplementary cementitious materials on autogenous shrinkage of ultra-high performance concrete. *Constr. Build. Mater.* **2016**, *127*, 43–48. [[CrossRef](#)]
25. Li, W.; Huang, Z.; Hu, G.; Duan, W.; Shah, S.P. Early-age shrinkage development of ultra-high-performance concrete under heat curing treatment. *Constr. Build. Mater.* **2017**, *131*, 767–774. [[CrossRef](#)]
26. Shen, P.; Lu, L.; He, Y.; Rao, M.; Fu, Z.; Wang, F.; Hu, S. Experimental investigation on the autogenous shrinkage of steam cured ultra-high performance concrete. *Constr. Build. Mater.* **2018**, *162*, 512–522. [[CrossRef](#)]
27. Rajabipour, F.; Sant, G.; Weiss, J. Interactions between shrinkage reducing admixtures (SRA) and cement paste's pore solution. *Cem. Concr. Res.* **2008**, *38*, 606–615. [[CrossRef](#)]
28. Soliman, A.M.; Nehdi, M.L. Effect of partially hydrated cementitious materials and superabsorbent polymer on early-age shrinkage of UHPC. *Constr. Build. Mater.* **2013**, *41*, 270–275. [[CrossRef](#)]
29. Kang, S.H.; Hong, S.G.; Moon, J. Shrinkage characteristics of heat-treated ultra-high performance concrete and its mitigation using superabsorbent polymer based internal curing method. *Cem. Concr. Compos.* **2018**, *89*, 130–138. [[CrossRef](#)]
30. Philleo, R. Concrete Science and Reality. In *Materials Science of Concrete II*; American Ceramic Society: Westerville, OH, USA, 1991; pp. 1–8.
31. Bentz, D.P.; Snyder, K.A. Protected paste volume in concrete: Extension to internal curing using saturated lightweight fine aggregate. *Cem. Concr. Res.* **1999**, *29*, 1863–1867. [[CrossRef](#)]
32. Bentz, D.P.; Lura, P.; Roberts, J.W. Mixture Proportioning for Internal Curing. *Concr. Int.* **2005**, *27*, 35–40.

33. Bentz, D.P. A review of early-age properties of cement-based materials. *Cem. Concr. Res.* **2008**, *38*, 196–204. [[CrossRef](#)]
34. Bentur, A.; Igarashi, S.I.; Kovler, K. Prevention of autogenous shrinkage in high-strength concrete by internal curing using wet lightweight aggregates. *Cem. Concr. Res.* **2001**, *31*, 1587–1591. [[CrossRef](#)]
35. Akcay, B.; Tasdemir, M.A. Optimisation of using lightweight aggregates in mitigating autogenous deformation of concrete. *Constr. Build. Mater.* **2009**, *23*, 353–363. [[CrossRef](#)]
36. Akcay, B.; Tasdemir, M.A. Effects of distribution of lightweight aggregates on internal curing of concrete. *Cem. Conc. Compos.* **2010**, *32*, 611–616. [[CrossRef](#)]
37. Henkensiefken, R.; Nantung, T.; Weiss, J. Internal Curing-From the Laboratory to Implementation. In Proceedings of the International Bridge Conference on Lightweight Aggregate Concrete Bridges Workshop, Pittsburgh, PA, USA, 14–17 June 2009.
38. Henkensiefken, R.; Bentz, D.; Nantung, T.; Weiss, J. Volume change and cracking in internally cured mixtures made with saturated lightweight aggregate under sealed and unsealed conditions. *Cem. Concr. Compos.* **2009**, *31*, 427–437. [[CrossRef](#)]
39. Lura, P.; Wyrzykowski, M.; Tang, C.; Lehmann, E. Internal curing with lightweight aggregate produced from biomass-derived waste. *Cem. Concr. Res.* **2014**, *59*, 24–33. [[CrossRef](#)]
40. Zhutovsky, S.; Kovler, K.; Bentur, A. Efficiency of lightweight aggregates for internal curing of high strength concrete to eliminate autogenous shrinkage. *Mater. Struct.* **2002**, *35*, 97–101. [[CrossRef](#)]
41. Zhutovsky, S.; Kovler, K.; Bentur, A. Influence of cement paste matrix properties on the autogenous curing of high-performance concrete. *Cem. Concr. Compos.* **2004**, *26*, 499–507. [[CrossRef](#)]
42. Zhutovsky, S.; Kovler, K. Effect of internal curing on durability-related properties of high performance concrete. *Cem. Concr. Res.* **2012**, *42*, 20–26. [[CrossRef](#)]
43. Jensen, O.M.; Hansen, P.F. Water-entrained cement-based materials—I. Principles and theoretical background. *Cem. Concr. Res.* **2001**, *31*, 647–654. [[CrossRef](#)]
44. Craeye, B.; Schutter, G.D. Experimental evaluation of mitigation of autogenous shrinkage by means of a vertical dilatometer for concrete. In Proceedings of the Conference on Volume Changes of Hardening Concrete: Testing and Mitigation, Lyngby, Denmark, 20–23 August 2006; RILEM Publications SARL: UGent, Belgium, 2006; pp. 21–30.
45. Cusson, D.; Hoogeveen, T. Internal curing of high-performance concrete with pre-soaked fine lightweight aggregate for prevention of autogenous shrinkage cracking. *Cem. Concr. Res.* **2008**, *38*, 757–765. [[CrossRef](#)]
46. Paul, A.; Lopez, M. Assessing Lightweight Aggregate Efficiency for Maximizing Internal Curing Performance. *ACI Mater. J.* **2011**, *108*, 385–393.
47. Castro, J.; Keiser, L.; Goliás, M.; Weiss, J. Absorption and desorption properties of fine lightweight aggregate for application to internally cured concrete mixtures. *Cem. Concr. Compos.* **2011**, *33*, 1001–1008. [[CrossRef](#)]
48. *Internal Curing of Concrete, State-of-the-Art Report of RILEM Technical Committee 196-ICC (RILEM TC 196-ICC)*; RILEM Publications S.A.R.L.: Bagneux, France, 2007.
49. Suzuki, M.; Meddah, M.S.; Sato, R.; Kawabata, T. Long-term shrinkage and stress in ultra high strength concrete using porous ceramic waste for internal curing. In Proceedings of the International RILEM Conference on Use of Superabsorbent Polymers and Other New Additives in Concrete, Technical University of Denmark, Lyngby, Denmark, 15–18 August 2010.
50. Wang, X.P.; Yu, R.; Shui, Z.; Songa, Q.; Zhang, Z. Mix design and characteristics evaluation of an eco-friendly Ultra-High Performance Concrete incorporating recycled coral based materials. *J. Clean. Prod.* **2017**, *165*, 70–80. [[CrossRef](#)]
51. Klug, C.; Cashman, K.; Bacon, C. Structure and physical characteristics of pumice from the climactic eruption of Mount Mazama (Crater Lake), Oregon. *Bull. Volcanol.* **2002**, *64*, 486–501.
52. Hossain, A.; Khandaker, M. Properties of volcanic pumice based cement and lightweight concrete. *Cem. Concr. Res.* **2004**, *34*, 283–291. [[CrossRef](#)]
53. Binici, H. Effect of crushed ceramic and basaltic pumice as fine aggregates on concrete mortars properties. *Constr. Build. Mater.* **2007**, *21*, 1191–1197. [[CrossRef](#)]
54. Hossain, K.M.A.; Ahmed, S.; Lachemi, M. Lightweight concrete incorporating pumice based blended cement and aggregate: Mechanical and durability characteristics. *Constr. Build. Mater.* **2011**, *25*, 1186–1195. [[CrossRef](#)]

55. Castro, J.; Weiss, J.; Henkensiefken, R.; Nantung, T.; Bentz, D.P. LWA Absorption and Desorption: The Influence on the Microstructure and Transport Properties of Internally Cured Mortars. In Proceedings of the International Conference on Concrete Under Severe Conditions: Environment & Loading, Merida, Mexico, 7–9 June 2010; Taylor & Francis Group: London, UK, 2010; pp. 1543–1550.
56. ASTM C09, C1761: *Standard Specification for Lightweight Aggregate for Internal Curing of Concrete*; ASTM: West Conshohocken, PA, USA, 2013.
57. Hüsken, G. A Multifunctional Design Approach for Sustainable Concrete with Application to Concrete Mass Products. Ph.D. Thesis, Eindhoven University of Technology, Eindhoven, The Netherlands, 2010.
58. Yu, R.; Spiesz, P.; Brouwers, H.J.H. Mix design and properties assessment of Ultra- High Performance Fibre Reinforced Concrete (UHPRFC). *Cem. Concr. Res.* **2014**, *56*, 29–39. [[CrossRef](#)]
59. GB/T 2419-2005. *PRC National Standard: Test Method for Fluidity of Cement Mortar*; Standards Press of China: Beijing, China, 2005. (In Chinese)
60. GB/T 17671-1999. *PRC National Standard: Method of Testing Cements-Determination of Strength*; Standards Press of China: Beijing, China, 1999. (In Chinese)
61. JC/T 603-2004. *PRC Building Materials Industry Standard: Standard Test Method for Drying Shrinkage of Mortar*; Standards Press of China: Beijing, China, 2004. (In Chinese)
62. Aitcin, P.C. *High Performance Concrete*; CRC Press: Boca Raton, FL, USA, 2011.
63. Lura. Autogenous Deformation and Internal Curing of Concrete. Ph.D. Thesis, Delft University of Technology, Delft, The Netherlands, 2003.
64. Tazawa, E.I.; Miyazawa, S. Experimental study on mechanism of autogenous shrinkage of concrete. *Cem. Concr. Res.* **1995**, *25*, 1633–1638. [[CrossRef](#)]
65. Loukili, A.; Khelidj, A.; Richard, P. Hydration kinetics, change of relative humidity, and autogenous shrinkage of ultra-high-strength concrete. *Cem. Concr. Res.* **1999**, *29*, 577–584. [[CrossRef](#)]
66. Yiotis, A.G.; Stubos, A.K.; Boudouvis, A.G.; Tsimpanogiannis, I.N.; Yortsos, Y.C. Pore-Network Modeling of Isothermal Drying in Porous Media. *Transp. Porous Med.* **2005**, *58*, 63–86. [[CrossRef](#)]
67. Ghourchian, S.; Wyrzykowski, M.; Lura, P.; Shekarchi, M.; Ahmadi, B. An investigation on the use of zeolite aggregates for internal curing of concrete. *Constr. Build. Mater.* **2013**, *40*, 135–144. [[CrossRef](#)]
68. Zou, D.; Li, K.; Li, W.; Cao, T. Effects of pore structure and water absorption on internal curing efficiency of porous aggregates. *Constr. Build. Mater.* **2018**, *163*, 949–959. [[CrossRef](#)]
69. Lura, P.; Bentz, D.P.; Lange, D.A.; Kkovler, o.; Bentur, A.; van Breugel, K. Measurement of water transport from saturated pumice aggregates to hardening cement paste. *Mater. Struct.* **2006**, *39*, 861–868. [[CrossRef](#)]
70. Henkensiefken, R.; Nantung, T.; Weiss, J. Saturated lightweight aggregate for internal curing in low w/c mixtures: Monitoring water movement using x-ray absorption. *Strain* **2011**, *47*, 432–441. [[CrossRef](#)]
71. Bullard, J.W.; Jennings, H.M.; Livingston, R.A.; Nonat, A.; Scherer, G.W.; Schweitzer, J.S.; Scrivener, K.L.; Thomas, J.J. Mechanisms of cement hydration. *Cem. Concr. Res.* **2011**, *41*, 1208–1223. [[CrossRef](#)]
72. Havlica, J.; Roztocká, D.; Sahu, S. Hydration kinetics of calciumaluminat phases in the presence of various ratios of Ca<sup>2+</sup> and SO<sub>4</sub><sup>2-</sup> ions in liquid phase. *Cem. Concr. Res.* **1993**, *23*, 294–300. [[CrossRef](#)]
73. Richardson, I.G. The calcium silicate hydrates. *Cem. Concr. Res.* **2008**, *38*, 137–158. [[CrossRef](#)]
74. Richardson, I.G. Model structures for C–(A)–S–H(I). *Acta Crystallogr. B* **2014**, *70*, 903–923. [[CrossRef](#)]
75. Richardson, I.G. The nature of C–S–H in hardened cements. *Cem. Concr. Res.* **1999**, *29*, 1131–1147. [[CrossRef](#)]
76. Chang, J.; Fang, Y. Quantitative analysis of accelerated carbonation products of the synthetic calcium silicate hydrate(C–S–H) by QXRD and TG/MS. *J. Therm. Anal. Calorim.* **2015**, *119*, 57–62. [[CrossRef](#)]
77. Richardson, I.G.; Groves, G.W. Microstructure and microanalysis of hardened cement pastes involving ground granulated blast-furnace slag. *J. Mater. Sci.* **1992**, *27*, 6204–6212. [[CrossRef](#)]
78. Breugel, K.V. Numerical modelling of volume changes at early ages-Potential, pitfalls and challenges. *Mater. Struct.* **2001**, *34*, 293–301.
79. Juenger, M.C.G.; Jennings, H.M. Examining the relationship between the microstructure of calcium silicate hydrate and drying shrinkage of cement pastes. *Cem. Concr. Res.* **2002**, *32*, 289–296. [[CrossRef](#)]



Article

# Effect of Polyacrylic Acid on Rheology of Cement Paste Plasticized by Polycarboxylate Superplasticizer

Baoguo Ma, Yi Peng, Hongbo Tan \* , Zhenghang Lv and Xiufeng Deng

State Key Laboratory of Silicate Materials for Architectures, Wuhan University of Technology, Wuhan 430070, China; mbgjob@163.com (B.M.); pengyi@whut.edu.cn (Y.P.); lvzhenghang@whut.edu.cn (Z.L.); dxf@whut.edu.cn (X.D.)

\* Correspondence: thbwhut@whut.edu.cn

Received: 18 May 2018; Accepted: 21 June 2018; Published: 25 June 2018

**Abstract:** Viscosity-enhancing agents (VEA) have been widely employed in high flowability cement-based materials, so as to ensure that no bleeding and segregation would occur. However, in most cases, interaction between VEA and superplasticizer would be unavoidable. In this study, the effect of polyacrylic acid (PAA), known as one of the most commonly used VEAs, on rheology performance of cement paste containing polycarboxylate superplasticizer (PCE), was studied. The initial fluidity was assessed with mini slump, and rheological behavior of cement paste was evaluated with rotor rheometer. Adsorption amount was examined with total organic carbon (TOC) analyzer, and the zeta potential was also tested. The interaction between PAA and PCE in the presence of calcium ion ( $\text{Ca}^{2+}$ ) was analyzed with conductivity, X-ray photoelectron spectroscope (XPS), and dynamic light scattering (DLS). The results illustrate that PAA can adsorb onto the surface of cement particles to plasticize cement paste, being similar to PCE. In the presence of  $\text{Ca}^{2+}$ , PAA can be curled and crosslinked, as a result of the combination between carboxyl groups ( $\text{COO}^-$ ) and  $\text{Ca}^{2+}$ , thereby affecting the adsorption performance and conformation behavior. It is interesting that negative impact of PAA on dispersion efficiency of PCE can be demonstrated; one reason is the reduced adsorption amount of PCE by PAA competitively adsorbing onto the cement surface, and another possible reason is the invalidated PCE by adsorption of PAA. Additionally, molecular weight of PAA should be considered if being used as VEA in PCE system.

**Keywords:** polyacrylic acid; fluidity; rheology; adsorption; combination

## 1. Introduction

No bleeding and segregation is mandatory in high fluidity cement-based materials, such as self-compacting concrete, self-leveling floor, and grout materials. Generally, this can be obtained with addition of viscosity-enhancing agent (VEA) and superplasticizer [1–3]. Polyacrylic acid (PAA) is one of the most commonly used viscosity-enhancing agents with an excellent effect on resisting bleeding and segregation [4,5]. The primary mechanism behind includes two aspects: one is that it can increase viscosity of liquid phase by means of the formation of intermolecular network structure, and the other is that PAA molecule with great molecular weight can connect these cement particles through adsorbing on the surface of cement particles [6,7].

Polycarboxylate superplasticizer (PCE), regarded as a kind of high-efficiency water-reducing agent, are used to efficiently plasticize cement paste for achieving high fluidity of cement-based materials by using less mass of water [8–10]. The dispersion efficiency of PCE is closely related to the activity of long side chain (PEO, polyethylene oxide, which offers the steric hindrance as the main dispersion force) and the effective adsorption of PCE is the precondition for the effect of long side chain PEO [11]. Generally, greater adsorption amount and higher activity of PEO would lead to stronger

dispersion efficiency [12]. However, adsorption of PCE can be perturbed with addition of additives. Retarders in PCE system, such as sodium tripolyphosphate (STPP), sodium gluconate (SG), borax and sulfate, have an obvious impact on the dispersion capacity of PCE [13–16]. For example, competitive adsorption between SG and PCE would inevitably occur, which could decline the adsorption amount of PCE, thereby weakening the dispersion efficiency of the mixed system. Furthermore, the activity of long side chain PEO could be weakened, in some cases. Many studies had revealed that the insertion of PEO into the interlayer of montmorillonite would notably weaken the effective activity of PEO, leading to the decline in dispersion efficiency. Moreover, some chemicals can also accelerate the inactivation of PEO in PCE [17–19]. For example, the intercalation of PCE can be enhanced by STPP to further inactivate the PEO, and in this case, the dispersion efficiency of PCE would be declined immediately [15].

Despite that the addition of PAA can obviously increase the viscosity to solve the problems of segregation and bleeding, the negative impact of PAA on dispersion capacity of PCE cannot be ignored. On account of the adsorption of PAA onto the surface of cement particles, the interaction between PAA and PCE must be considered. In order to verify these, the effect of PAA on fluidity and rheology of cement paste in the presence of PCE was investigated in this paper, and the molecular weight of PAA was taken into account. Competitive adsorption between PAA and PCE was analyzed, and the conformation behavior of PAA and PCE was discussed. Finally, a dispersion mechanism was systematically analyzed. These conclusions would be expected to offer useful experience for the use of viscosity-enhancing agent in concrete engineering.

## 2. Materials and Test Methods

### 2.1. Materials

#### 2.1.1. Cement

Cement used in this research is an ordinary portland cement (42.5 Wuhan Yadong Cement Co., Ltd., Wuhan, China), and the fundamental performance of cement is shown in Table 1.

**Table 1.** Fundamental performance of cement.

Flexural Strength (MPa)		Compressive Strength (MPa)		Setting Time (min)	
3 d	28 d	3 d	28 d	Initial setting	Final setting
4.6	7.6	25.6	45.5	238	291

#### 2.1.2. Additives

A commercially available polycarboxylate superplasticizer (PCE, made by Wuhan Huaxuan Co., Ltd., Wuhan, China) was used in this study. The molecular structure and fundamental performance, obtained from the company, are shown in Figure 1 and Table 2. Polyacrylic acid (PAA, made by Shanghai Macklin Biochemical Co., Ltd., Shanghai, China) was employed in this research, and the added dosage was recorded as solid content. The molecular structure and fundamental performance, obtained from the company, are shown in Figure 2 and Table 3. Furthermore, the polymers were dried in a vacuum drying oven at about 65 °C, and then were characterized by Fourier-transform infrared spectroscopy (FTIR, Nexus, made by Thermo Nicolet, Madison, WI, USA). The presence of fundamental chemical groups in PAA could be found from the FTIR spectroscopy. As shown in Figure 3,  $-\text{CH}_2-$ ,  $\text{C}=\text{O}$ ,  $-\text{OH}$ , and  $\text{C}-\text{O}-\text{C}$  groups can be obviously found. This result demonstrates the presence of  $\text{COO}^-$  group in PAA.

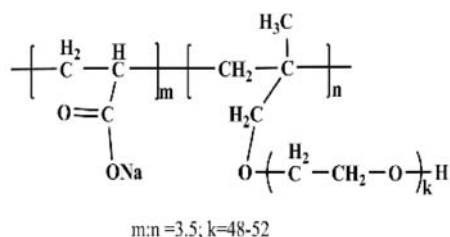


Figure 1. Molecular structure of PCE.

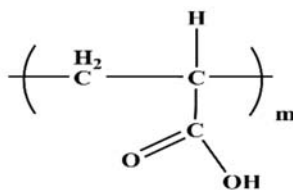


Figure 2. Molecular structure of PAA.

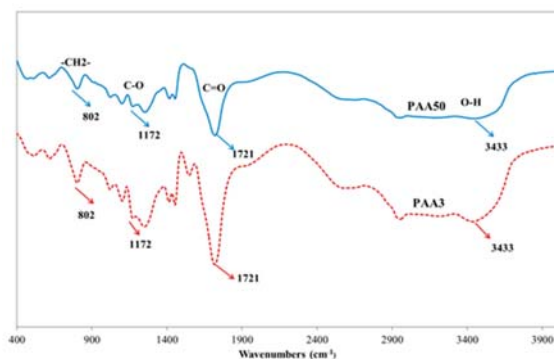


Figure 3. FTIR spectra of PAA.

Table 2. Fundamental performance of PCE.

Cl <sup>-</sup> (%)	Alkali Content (%)	Water reducing Ratio (%)	pH Value	Solid Content (%)	M <sub>w</sub> (g/mol)
0.03	3.75	30.1	7.2	40.0	67,500

Table 3. The fundamental performance of PAA.

	Solid Content (%)	pH Value	M <sub>w</sub> (g/mol)
PAA3	30	3.0–3.5	3000
PAA50	50	2.5–3.0	50,000

## 2.2. Test Methods

### 2.2.1. Fluidity Performance

Chemicals were mixed with water in advance. Cement paste with PAA (0.00%, 0.04%, 0.08%, 0.12%, 0.16%, 0.20% of cement) were prepared with water and cement ratio (W/C) of 0.5. Cement



paste with PAA (0.00%, 0.02%, 0.04%, 0.08%, 0.12%, 0.16%, 0.20% of cement) and PCE (0.1% of cement) were prepared with W/C of 0.29. The initial fluidity (within 5 min) was measured with a truncated cone mold (height: 60 mm; top diameter: 36 mm; bottom diameter: 60 mm) in accordance with the Chinese standard of GB/T 8077-2012. The truncated cone was firstly put on a smooth glass plate, and then it was filled with the cement paste; the cone was slowly lifted vertically, and the maximum diameter of the spread sample and the maximum width perpendicular to that diameter were measured after 30 s. The average of these two values was defined as the initial fluidity value (mm).

### 2.2.2. Rheology Performance

Cement paste with PAA, and cement paste with PAA and PCE, were prepared with the same process and parameters as above, except that the dosage of PCE in cement with PAA and PCE system is 0.07% of cement, rather than 0.1%. The purpose of reducing the dosage of PCE is to control the yield stress to above zero. These cement pastes were stirred for 5 min, and then, the rotor rheometer (R/S-SST, rotor: CC45, made by Brookfield, New York, NY, USA) was used to test the rheology performance of paste. The process of measurement was divided into four steps. In order to bring the cement paste to a reference structural state, it was firstly pre-sheared at a shear rate equal to  $100\text{ s}^{-1}$  for 30 s, and then paused for 10 s. An increasing shear rate was directly applied from  $0\text{--}120\text{ s}^{-1}$  within 100 s. After that, a decreasing shear rate was applied from  $120\text{--}0\text{ s}^{-1}$  within 100 s. The Bingham fluid mode was adopted to analyze the data obtained from rheology software (2000 V2.8, Brookfield, NY, USA). Based on this, yield stress and plastic viscosity can be calculated.

### 2.2.3. Adsorption Amount

Total organic carbon (TOC) meter (Elementar, Langensfeld, Germany) was used to measure the adsorption amount of these organics on the surface of cement particles. The carbon content of these organics with various concentrations ( $0\text{--}2.0\text{ g/L}$ ) was tested, and the results are shown in Figure 4. This figure indicates the relationship between concentration and carbon content of the polymer, and based on this, the concentration of these polymers can be calculated from the TOC value.

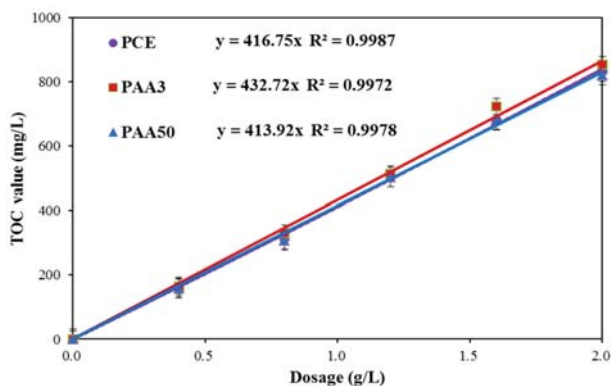


Figure 4. Relation between concentration and total organic carbon (TOC) value.

One gram of cement was added into these organics solution with various concentrations ( $0, 0.4\text{ g/L}, 0.8\text{ g/L}, 1.2\text{ g/L}, 1.6\text{ g/L}, 2.0\text{ g/L}, 20\text{ mL}$ ). Afterwards, these samples were mixed for 5 min, and then centrifuged with high speed centrifugal treatment (HDL-4, Hongke instrument Ltd., Changzhou, China) at  $4000\text{ r/min}$  for 5 min. The carbon content in supernatant of these samples was measured. According to Figure 4, the concentration of PCE and PAA in upper supernatant

(i.e., residual concentration) was obtained. Adsorption amount of PCE and PAA (mg/g-cement) was calculated as follows:

$$\text{Adsorption amount} = V(C_0 - C)/m$$

where  $C_0$  is the initial concentration (g/L) of PCE and PAA before adsorption;  $C$  is the residual concentration (g/L) after adsorption;  $V$  is the volume of the solution (mL); and  $m$  is the mass of the cement (g).

One gram of cement was also added into the mixed solutions at various concentrations (0.0–8.0 g/L PAA; 1.2 g/L PCE; 20 mL), respectively, the same measuring process as mentioned above was executed. The carbon content of supernatant in PCE–PAA binary system, directly tested by TOC, was defined as the measured results. The summation of the carbon content of supernatant in single system of PAA and PCE after adsorption, which was obtained in the single system, was defined as the expected results. If the expected results were smaller than the measured results, competitive adsorption between PAA and PCE would occur; otherwise, the competitive adsorption would not take place [13].

#### 2.2.4. Zeta Potential

One gram of cement was added into the solutions of PAA at various concentrations (0, 1.0 g/L, 2.0 g/L, 3.0 g/L, 4.0 g/L, 5.0 g/L; 20 mL), respectively, and stirred for 5 min. The cement suspension (1.0 g) was diluted with deionized water (49 g). The Malvern Nano-ZetaSizer instrument (Malvern Instrument Ltd., Malvern, UK) was used to test the zeta potential of the suspension.

#### 2.2.5. Conductivity

Solutions of calcium hydroxide (CH, 1.0 g/L), PAA (4.0 g/L), and PCE (4.0 g/L) were prepared in advance. The electrical conductivity analyzer (Seven Compact S230, Mettler Toledo, Greifensee, Switzerland) was used to measure the conductivity value of these solutions (100 g) or the reference (i.e., deionized water, 100 g) with continuous and even drop of CH solution (300 g), and the data was recorded automatically by the instrument.

#### 2.2.6. Binding Energy of $\text{Ca}^{2+}$

Organics solutions (PAA and PCE, 10.0 g/L) were mixed with CH (1.0 g/L), respectively. These samples were dried in a vacuum drying oven, and the temperature was controlled at about 65 °C. Afterwards, these solids were examined with the X-ray photoelectron spectroscopy (XPS, Escalab 250Xi, Thermo Fisher Scientific, Waltham, MA, USA). For the instrument, aluminum is used as an anode target ( $h\nu = 1486.6$  eV); energy resolution was 0.100 eV. The tested data was processed with XPS Peak Fitting Program (Version 4.0, The Chinese University of Hong Kong, Hong Kong, China), and extra peaks, except the peak belonging to CH, were added to fit the observed curve.

#### 2.2.7. Conformation Behavior of PAA and PCE

Solutions of PAA (2.0 g/L), PCE (2.0 g/L), and PAA-PCE (2.0 g/L PAA, 2.0 g/L PCE) were obtained in advance, and these samples (10.0 g) were added into CH solution (1.0 g/L, 10.0 g) or deionized water (10.0 g), respectively. Afterwards, the dynamic light scattering (DLS, Zetasizer Nano, Malvern instrument Ltd., Malvern, UK) was applied to measure the particle size distribution of the samples.

### 3. Results and Discussion

#### 3.1. Fluidity

Fluidity of cement paste with PAA was measured. As presented in Figure 5a, the fluidity is increased with increasing dosage of PAA, which illustrates that PAA can plasticize the cement paste.

By contrast, PAA50 can exert sharper increasing tendency than that of PAA3. This result indicates the stronger plasticizing effect of PAA50 than PAA3.

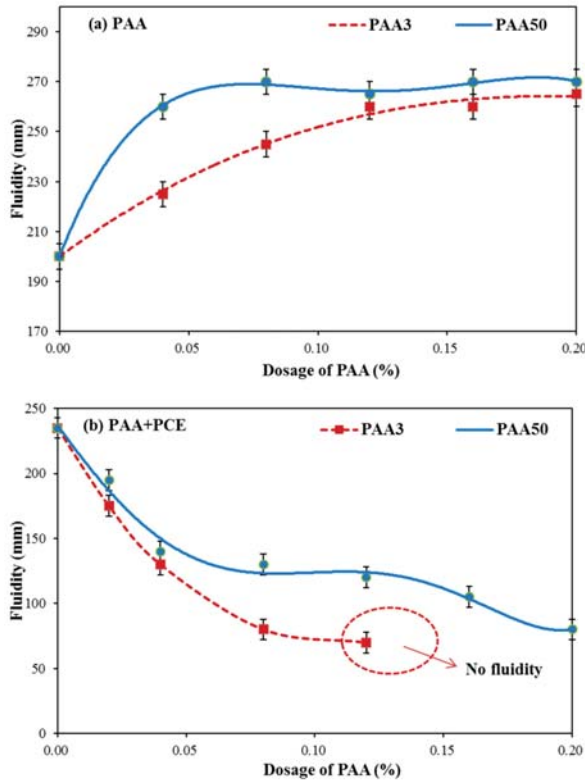


Figure 5. Effect of polymers on fluidity performance of cement paste (a: PAA; b: PAA–PCE).

The fluidity of cement paste in the presence of PAA and PCE (0.10%) was measured. As presented in Figure 5b, the fluidity of cement paste declined with the increasing dosage of PAA3 and PAA50. This result indicates that PAA can decline dispersion capacity of PCE. That is to say, a negative impact of PAA on fluidity of cement paste plasticized by PCE can be observed, which is contrary to the result as presented in Figure 5a. Furthermore, PAA3–PCE system has sharper declining tendency than PAA50–PCE system, indicating that PAA3 has stronger negative impact than that of PAA50.

On the basis of the analysis above, the plasticizing effect of PAA can be found obviously, and possibly, this is associated with the adsorption performance of PAA. Furthermore, PAA has obviously negative impact on flowability of cement paste in the presence of PCE, and negative impact of PAA3 seems stronger than that of PAA50. Probably, the reason is related to the activity of PEO, adsorption amount of PCE, and molecular weight of PAA, as well [3,15].

### 3.2. Rheology Performance

In order to further illustrate the negative impact of PAA on the dispersion capacity of PCE, the rheology performance of cement paste with PAA was firstly discussed. As presented in Figure 6a,b, with the increasing dosage of PAA, an obvious declining tendency for the yield stress and plastic viscosity can be seen, which also indicates that PAA can plasticize the cement paste, in agreement with the results as shown in Figure 5a. Furthermore, PAA50 can lead to a sharper declining tendency of the

yield stress and plastic viscosity than that of PAA3. That is to say, when the same dosage of PAA was added, the yield stress and plastic viscosity of cement paste with PAA50 is smaller than that of PAA3. These results further demonstrate that PAA50 has stronger plasticizing effect on cement paste than that of PAA3.

The rheology of cement paste with addition of PAA and PCE (0.07%) was discussed. As presented in Figure 7a,b, with the increasing dosage of PAA, yield stress and plastic viscosity are obviously increased. These results also demonstrate that the addition of PAA can lead to an obvious impact on rheology performance of paste in the presence of PCE. A significant reason can be explained in that PAA has a negative impact on dispersion efficiency of PCE.

Based on discussion above, by contrast, PAA3 can make sharper increasing tendency of yield stress and plastic viscosity than that of PAA50, which can be explained by that PAA3 has a smaller plasticizing effect on cement paste than that of PAA50. A stronger negative impact of PAA3 on dispersion capacity of PCE than that of PAA50 can be found, which can be further demonstrated later.

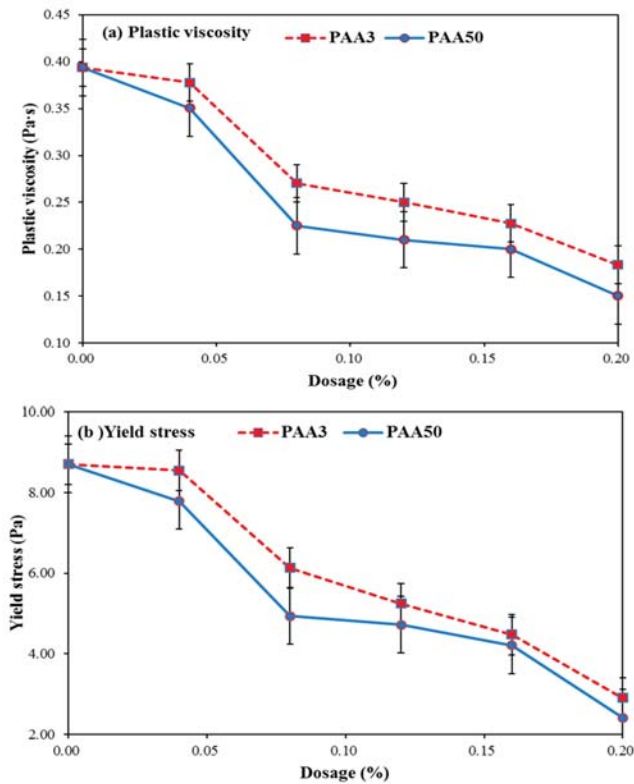


Figure 6. Effect of PAA on rheology performance of cement paste (a: plastic viscosity; b: yield stress).

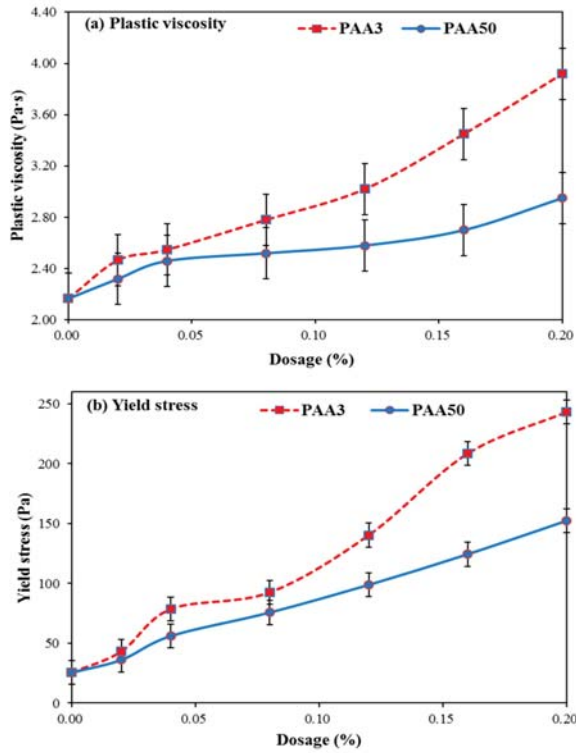


Figure 7. Effect of PAA on rheology of cement paste in the presence of PCE (a: plastic viscosity; b: yield stress).

### 3.3. Adsorption Amount

#### (1) Adsorption Behavior of PAA and PCE

Adsorption amount of these organics was presented in Figure 8. An obvious phenomenon can be seen that surface-active points of cement particles can be adsorbed by both PAA and PCE. Whereas, with the identical dosage, the adsorption amount of PAA3 is greater than PAA50, and adsorption amount of PCE is the lowest.

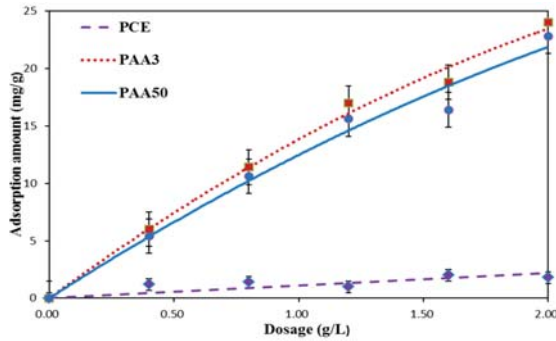


Figure 8. Adsorption amount of PAA and PCE.

It has been revealed that adsorption of PCE onto the surface of cement particles is the precondition for exerting high dispersion efficiency of PCE [3,20]. Carboxyl groups exist in the side chain of PAA, and these active groups can adsorb on the surface of cement particles by means of chemical combination and electrostatic force [21–23]. In this case, mutual influence on adsorption of PAA and PCE, namely competitive adsorption, may take place. This means that many effective adsorption points occupied by PAA cannot be available for PCE.

(2) Competitive Adsorption between PAA and PCE

To further prove this result, the expected results and the measured results were compared as follows: the expected results are defined as the summation of remainder carbon content in supernatant of single system of PCE and PAA after adsorption with the same dosage, and the measured results, obtained directly from the instrument, are the carbon contents in the supernatant of the PAA–PCE system after adsorption. If there is no obvious difference between these two results, no competitive adsorption would occur; if the expected result were smaller than the measured result, competitive adsorption would happen, indicating that the adsorption of PCE would be perturbed by PAA [12]. As presented in Figure 9, the gap between these two can be observed, which demonstrates the competitive adsorption between PCE and PAA. Accordingly, the addition of PAA would inevitably hinder the adsorption of PCE, thereby resulting in descend on dispersion ability of PCE.

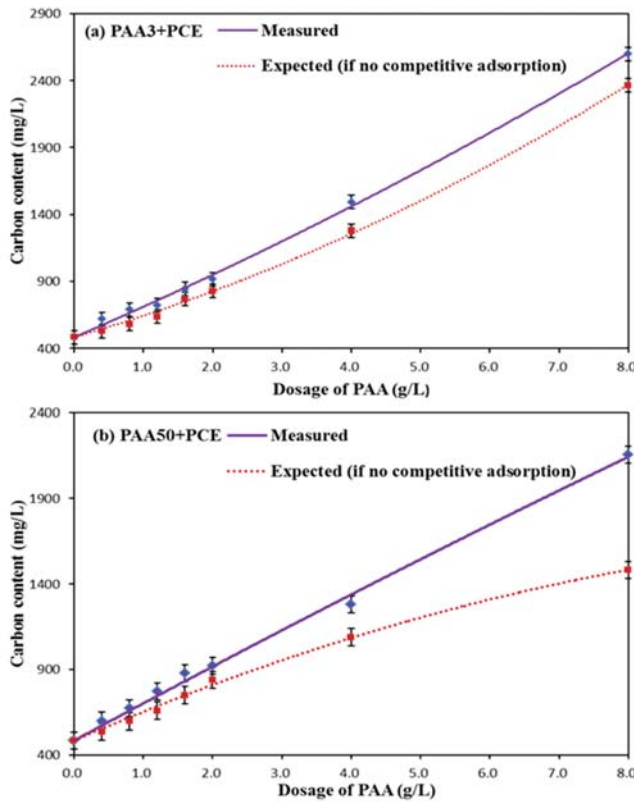


Figure 9. Competitive adsorption between PAA and PCE (1.2 g/L) (a: PAA3–PCE; b: PAA50–PCE).

Additionally, the adsorption ability of PAA3 is stronger than PAA50, which means that the competitive adsorption ability of PAA3 is stronger than PAA50. Accordingly, PAA3 can exert stronger negative impact on the fluidity plasticized by PCE, following that the yield stress in PAA3–PCE has sharper increasing tendency than PAA50–PCE. The possible reason for this phenomenon is due to the difference of molecular weight.

### 3.4. Zeta Potential

The relative value of zeta potential depends on the adsorption amount of chemicals in some extent [24–26]. The zeta potential of cement suspension with PAA was tested. As presented in Figure 10, the zeta potential is increased with the increasing concentration of PAA. Generally, the change of zeta potential is commonly associated with the adsorption behavior of PAA. By contrast, PAA50 would exert stronger increasing tendency than that of PAA3, as presented in Figure 10, and this could be one of main reasons why PAA50 exerts stronger plasticizing effect than PAA3 (as presented in Figure 5a). However, PAA3 with more adsorption amount should exert more, rather than less zeta potential, and this contradictory result may be related to the difference in adsorption and conformation behavior of PAA, caused by the difference in molecular weight. Especially, PAA causes cement particles to carry a negative charge, and this would interfere with the adsorption of PCE on the surface of cement via electrostatic forces.

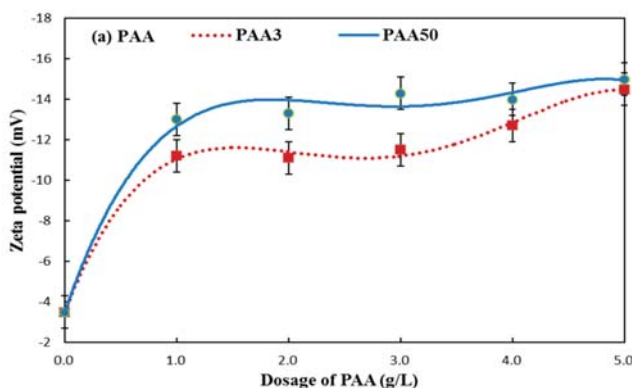


Figure 10. Zeta potential of cement suspension in the presence of PAA.

### 3.5. Combination of Carboxyl Groups with $\text{Ca}^{2+}$

Chemical combination with calcium ion ( $\text{Ca}^{2+}$ ) as one of the forces, makes polymers adsorb on the surface of cement particle, because these  $\text{Ca}^{2+}$  molecules are easy to react with carboxyl groups [27,28]. The interaction among these organics and  $\text{Ca}^{2+}$  would be unavoidable, and this can be illustrated from the conductivity. As presented in Figure 11, with addition of CH (1.0 g/L), the conductivity value of reference has a rapid increase. However, the conductivity value of these polymer solutions is firstly decreased and then increased. This result means that the ions (i.e.,  $\text{Ca}^{2+}$ ) can be consumed in a range of dosage. When the dosage of CH (0.5 g/L) is increased continuously, the curve of PCE appears a visible turning point, as presented in Figure 11a; and as presented in Figure 11b, other curves of PAA3 or PAA50 also present the same tendency in the presence of CH (1.0 g/L), and these results demonstrate that the combination of  $\text{Ca}^{2+}$  with these polymers happens before the turning point. That is to say, it can be inferred that at the turning point, almost all available combining chemical groups (i.e.,  $\text{COO}^-$ ) have been consumed. Moreover, the consumption amount of CH solution for PAA3 is 252 g, which indicates that 1.0 g PAA3 would consume 0.63 g CH. Furthermore, for PAA50 it is approximately 180 g, which also indicates that 1.0 g PAA50 would consume 0.43 g CH. This means that PAA3 has a greater



combination ability with  $\text{Ca}^{2+}$  than that of PAA50, which demonstrates the greater adsorption ability of PAA3 than PAA50, in agreement with the adsorption results.

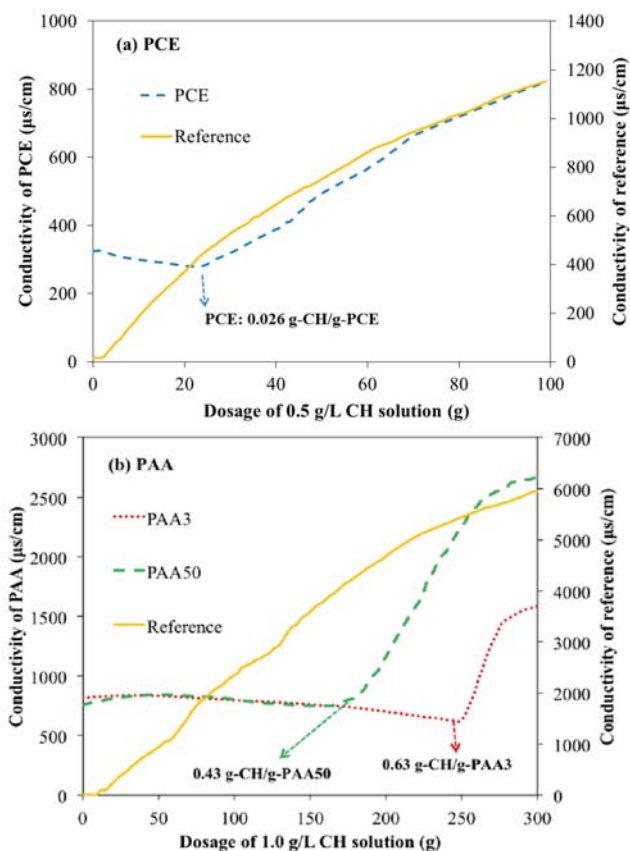


Figure 11. Conductivity of polymers with addition of CH solution (a: PCE; b: PAA).

In order to clarify the reaction of carboxyl groups with  $\text{Ca}^{2+}$ , the binding energy of  $\text{Ca}^{2+}$  with polymers was characterized with XPS. As presented in Figure 12a, in CH system, the peaks of curve for  $\text{Ca}2p_{3/2}$  and  $\text{Ca}2p_{1/2}$  are 346.37 eV and 349.75 eV. Nevertheless, for PCE-CH system, two new peaks can be found, including 347.28 eV for  $\text{Ca}2p_{3/2}$  and 350.68 eV for  $\text{Ca}2p_{1/2}$ , as presented in Figure 12b. This result indicates that combination of  $\text{Ca}^{2+}$  with carboxyl groups can occur, and the combination of PCE-Ca in PCE-CH system can be confirmed. It is noticed that the same results have happened in Figure 12c,d. Therefore, these results further illustrate that a kind of new calcium bond, such as PAA3-Ca or PAA50-Ca, has been produced. Additionally, the ratio of these calcium bonds can be calculated from the ratio of each divided peak area. The relative ratio for calcium in PAA-Ca and CH can be obtained according to peak area. As presented in Figure 12c,d, the relative ratio of PAA50-Ca in PAA50-CH is 31.00%, which is much smaller than that of PAA3-Ca in PAA3-CH (63.60%), indicating that PAA3 has stronger combination ability with  $\text{Ca}^{2+}$  than that of PAA50.

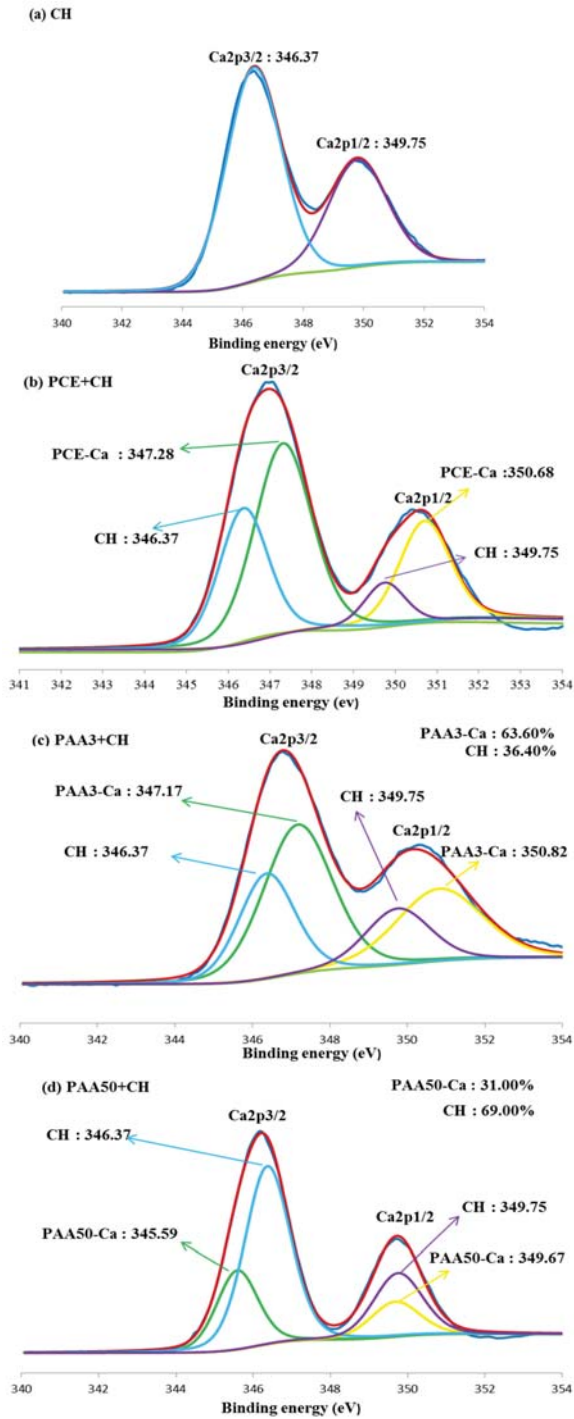


Figure 12. Binding energy of  $\text{Ca}^{2+}$  (a: CH; b: PCE-Ca; c: PAA3-Ca; d: PAA50-Ca).

In summary, one crucial conclusion can be drawn that PAA3 has stronger combination capacity with  $\text{Ca}^{2+}$  than that of PAA50, which is as one of the main reasons for the stronger adsorption ability of PAA3 than PAA50.

3.6. Aggregation Behavior of PAA and PCE

Many studies demonstrated that the conformation of polymers could be altered in the presence of some salts [29,30]. Once cement particles contacted with water, the cement particles would rapidly release CH solution into pore solution [31], the conformation of these polymers could be obviously affected by  $\text{Ca}^{2+}$  [32]. The size distribution of these polymers was obtained with DLS so as to reveal the conformation behavior of PCE and PAA in the presence and absence of CH. As presented in Figure 13, the size distribution of PAA3 is 164–255 nm, while for PAA50 it is 164–341 nm. With the addition of CH into polymer solutions, the size distribution of polymers for PAA3 and PAA50 is about 161–396 nm and 191–458 nm. In the presence of  $\text{Ca}^{2+}$ , PAA molecule might be curled because of the combination of  $\text{Ca}^{2+}$  and the formation of hydrogen bond; it could be deduced that several carboxyl groups ( $\text{COO}^-$ ) from different PAA molecules could be connected with one  $\text{Ca}^{2+}$ , and several carboxyl groups ( $\text{COO}^-$ ) in one PAA molecule could also be connected with one  $\text{Ca}^{2+}$  [4,5]. In this case, the conformation behavior of PAA would be altered in cement suspension. This result indicates that  $\text{Ca}^{2+}$  can result in agglomeration of the PAA. Accordingly, PAA can be connected via  $\text{Ca}^{2+}$ , which means that these  $\text{Ca}^{2+}$  can connect several PAA molecules together.

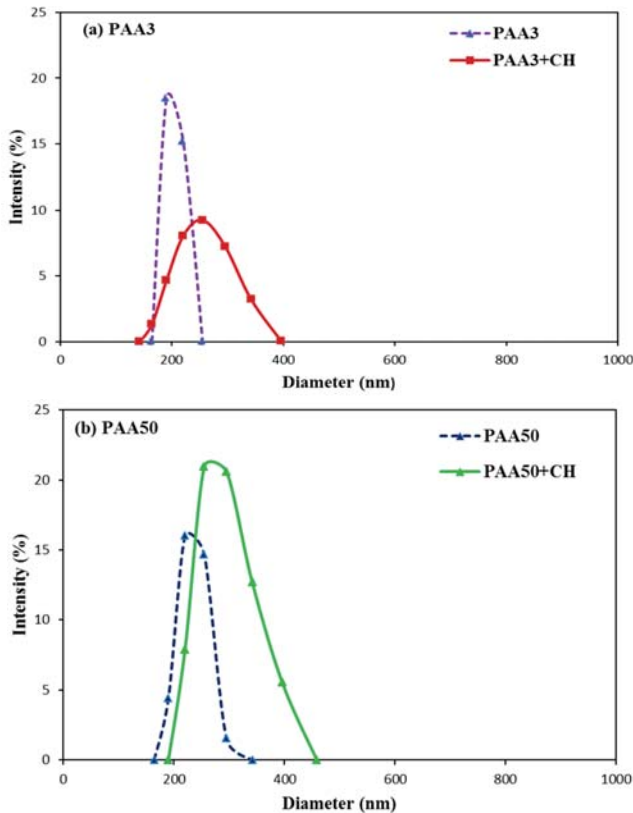
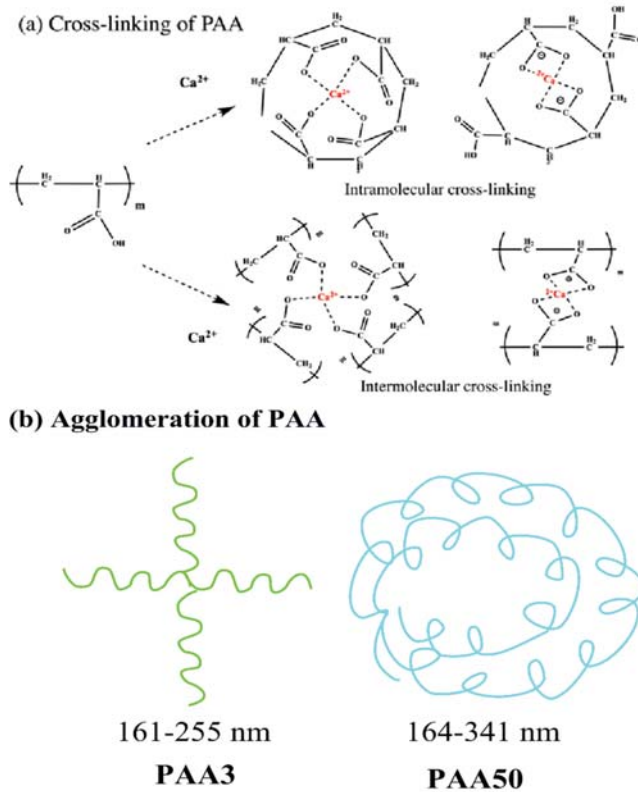


Figure 13. Size distribution of PAA in deionized water and CH solution (a: PAA3; b: PAA50).

As presented in Figure 14a, the aggregation of PAA3 is probably due to the intermolecular crosslinking, and that for PAA50 is the intramolecular crosslinking. Accordingly, even if there is a much greater molecular weight of PAA50 than that of PAA3, the diameter of PAA50 is only slightly larger than that of PAA3, due to the different curled structures, as presented in Figure 14b.



**Figure 14.** Conformation behavior of PAA in calcium solution (a: Cross-linking structures; b: agglomeration).

The size distribution of PCE and PAA system in the presence of CH solution (1.0 g/L) was also measured by DLS. As presented in Figure 15a, in the presence of CH, the size distribution of PCE, PAA3, and PCE–PAA3 is 531–1281 nm, 141–396 nm, and 220–712 nm. If there is no combination between PAA3 and PCE via  $\text{Ca}^{2+}$ , the size of PAA3–PCE would range from 141–1281 nm, or divided into two parts, such as 141–396 nm and 531–1281 nm. However, one obvious phenomenon can be found in the size of PCE–PAA3–CH (i.e., 220–712 nm), which is in the middle of PCE–CH and PAA3–CH. Obviously, greater particles, which should be formed by PCE and CH, disappear. The PAA50–PCE system also shows the same phenomenon, as presented in Figure 15b. This can be probably accounted for by the fact that the addition of PAA into PCE–CH solution can detach the structure of PCE–Ca–PCE, thereby forming a new structure with smaller size (PCE–Ca–PAA). These results indicate the interaction among these polymers via  $\text{Ca}^{2+}$ , which would provide further evidence to prove the combination between PAA and PCE via bridging  $\text{Ca}^{2+}$ .

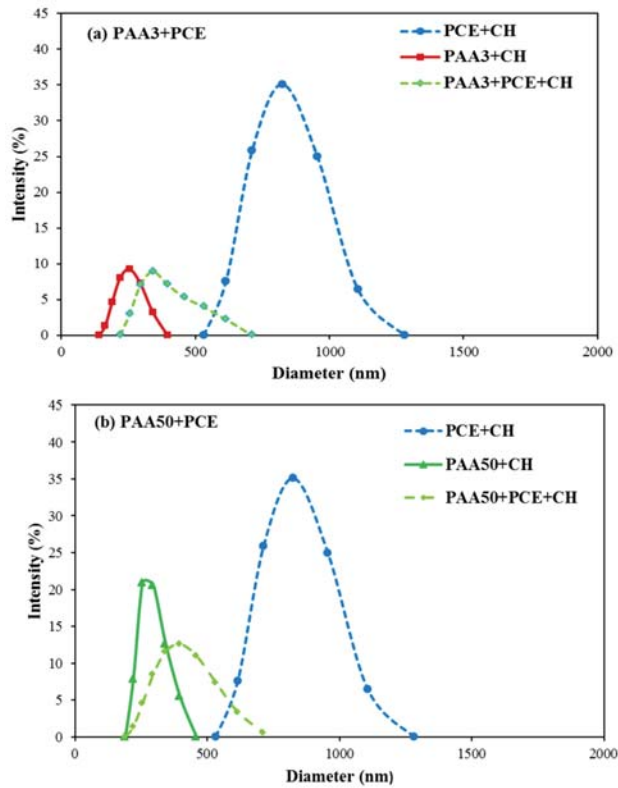


Figure 15. Size distribution of PAA and PCE in CH solution (a: PAA3–PCE; b: PAA50–PCE).

In this situation, PCE may adsorb on the surface of crosslinking structure of PAA, rather than on the surface of cement particles by combination of  $Ca^{2+}$ , thereby leading to more amount of ineffective adsorption of PCE [3].

3.7. Mechanism

(1) Effect of PAA on fluidity performance of cement paste

It has been demonstrated that the conformation of PAA can be altered in CH solution, resulting from intramolecular crosslinking and intermolecular crosslinking, as presented in Figure 15. In cement suspension, as presented in Figure 16, PAA molecule can adsorb onto the surface of cement particles to form water film via hydrogen-bond effect of hydrophilic group, thereby lubricating cement particles to improve the fluidity. Furthermore, PAA also can increase the zeta potential of cement particles to offer dispersion force, thereby increasing the fluidity of cement paste. Due to the plasticizing effect of PAA, the yield stress and plastic viscosity of the paste can decline with the addition of PAA.

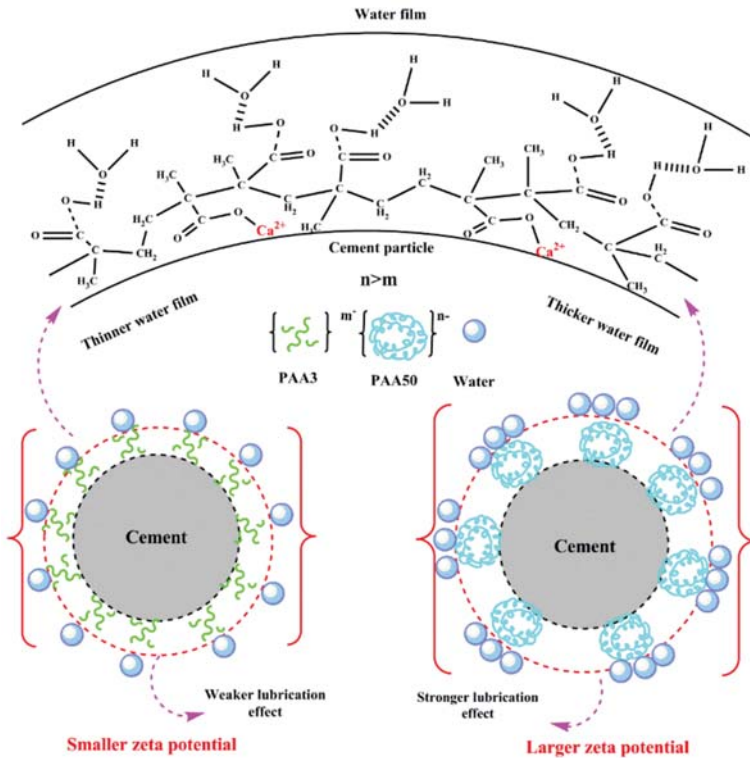


Figure 16. Mechanism model of cement suspension without PCE.

The main reason for stronger plasticizing effect of PAA50 than that of PAA3 can be illustrated as follows: on the one hand, because the molecular weight of PAA50 is much greater than that of PAA3, and the curled degree of PAA50 in  $\text{Ca}^{2+}$  ions solution is much stronger than that of PAA3, probably forming the spherical structure with nano particles. These spherical structures can adsorb onto the surface of cement particles and exert stronger lubricating effect to plasticize the cement paste. On the other hand, the aggregation of PAA50 can wrap lots of carboxyl groups into the inside of the spherical structure, resulting in larger negative charge than that of PAA3. In this case, PAA50 adsorbed on the surface of cement particles can bring out stronger zeta potential to plasticize the cement paste.

(2) Effect of PAA on performance of PCE

Addition of PAA into PCE can significantly reduce the dispersion capacity of the system, and the main reason includes three aspects, as follows:

First of all, on account of the competitive adsorption among these organics, adsorption points would be consumed by PAA molecule, and these occupied active points cannot be available for PCE [16,33]. The adsorption of PAA would perturb adsorption of PCE, and the effective adsorption of PCE would be decreased, thereby weakening the dispersion efficiency of PCE.

Moreover, as presented in Figure 17, similar to PAA, PCE can also adsorb onto the surface of these crosslinking structures, or be fixed inside the structure via combining  $\text{Ca}^{2+}$ . Therefore, the adsorption amount of PCE on the surface of cement particles can decline, thereby weakening the dispersion ability of PCE. Moreover, PCE adsorbed on the surface of cement particles would be covered by the crosslinking structure of PAA, which can weaken the activity of PEO and decrease the dispersion efficiency of PCE [34–36].

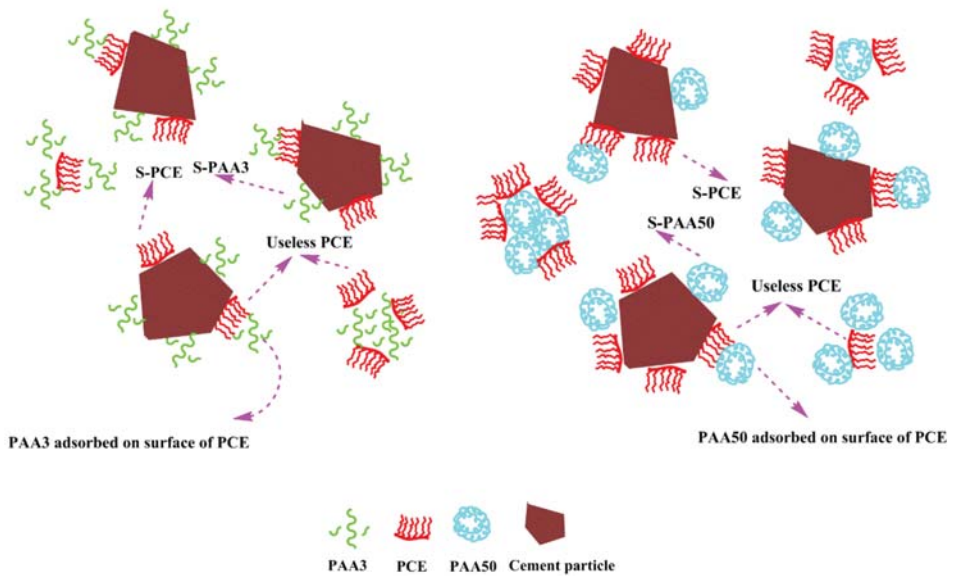


Figure 17. Mechanism model of cement suspension with PCE.

However, the negative impact of PAA3 and PAA50 can be distinguished clearly, as shown in the following:

Since PAA3 has stronger adsorption capacity than that of PAA50, the competitive adsorption ability of PAA3 is stronger than that of PAA50, which means that PAA3 would exert larger obstruction to the adsorption of PCE. This result indicates that PAA3 would result in a stronger ability to decline the dispersion of the system. Furthermore, zeta potential caused by PAA50 is stronger than that of PAA3, and the lubricating effect of PAA50 is also stronger; this implies that PAA50 has a stronger ability to contribute to the fluidity. These aspects can be related to the reason why the fluidity of cement paste containing PCE-PAA50 is greater than that of PCE-PAA3. It can be deduced that the competitive adsorption effect between PCE and PAA3 should have a predominant role in causing sharper decline in fluidity and quicker increase in plastic viscosity and yield stress (as presented in Figure 7b).

In view of these points, mentioned above, the negative impact of PAA on dispersion ability of PCE should be taken into account when PAA is used as additive. In addition, the molecular weight of PAA, as one vital factor, should be considered so as to mitigate the negative impact as much as possible. It is suggested that PAA with greater molecular weight would be more suitable to solve the problems of bleeding and segregation in concrete engineering, with less negative impact on the plasticizing effect of superplasticizer.

#### 4. Conclusions

- (1) PAA can adsorb onto the surface of cement particles, and smaller molecular weight of PAA has stronger adsorption ability. In the presence of  $\text{Ca}^{2+}$ , PAA can be curled, as a result of the combination between carboxyl groups and  $\text{Ca}^{2+}$ . PAA with greater molecular weight may be curled more obviously, and form a spherical structure in the presence of  $\text{Ca}^{2+}$ .
- (2) PAA can plasticize cement paste, because of the lubricating effect and the increased zeta potential; greater molecular weight results in stronger plasticizing ability.
- (3) PAA has a negative effect on dispersion of PCE, and smaller molecular weight results in stronger negative effect. The main reason for this is due to the competitive adsorption effect.



**Author Contributions:** Conceptualization, B.M. and Y.P.; Methodology, H.T. and Y.P.; Software, Z.L. and X.D.; Validation, B.M. and H.T.; Formal Analysis, Y.P. and X.D.; Investigation, Y.P.; Resources, B.M.; Data Curation, Y.P. and Z.L.; Writing-Original Draft Preparation, B.M. and Y.P.; Writing-Review & Editing, H.T.; Visualization, B.M.; Supervision, H.T.; Project Administration, B.M.; Funding Acquisition, H.T.

**Funding:** Financial support from National Natural Science Foundation of China (51772227) is gratefully acknowledged.

**Acknowledgments:** Technical support and material donations provided by Wuhan Huaxuan Co., Ltd.

**Conflicts of Interest:** The authors declare no conflict of interest.

## References

1. Schmidt, W.; Brouwers, H.J.H.; Kühne, H.-C.; Meng, B. Influences of superplasticizer modification and mixture composition on the performance of self-compacting concrete at varied ambient temperatures. *Cem. Concr. Compos.* **2014**, *49*, 111–126. [[CrossRef](#)]
2. Ma, C.; Tan, Y.; Li, E.; Dai, Y.; Yang, M. High-Performance Grouting Mortar Based on Mineral Admixtures. *Adv. Mater. Sci. Eng.* **2015**, *2015*, 425456. [[CrossRef](#)]
3. Ma, B.; Peng, Y.; Tan, H.; Jian, S.; Zhi, Z.; Guo, Y.; Qi, H.; Zhang, T.; He, X. Effect of hydroxypropyl-methyl cellulose ether on rheology of cement paste plasticized by polycarboxylate superplasticizer. *Constr. Build. Mater.* **2018**, *160*, 341–350. [[CrossRef](#)]
4. Wang, M.; Wang, R.; Zheng, S.; Farhan, S.; Yao, H.; Jiang, H. Research on the chemical mechanism in the polyacrylate latex modified cement system. *Cem. Concr. Res.* **2015**, *76*, 62–69. [[CrossRef](#)]
5. Guo, Y.; Ma, B.; Zhi, Z.; Tan, H.; Liu, M.; Jian, S.; Guo, Y. Effect of polyacrylic acid emulsion on fluidity of cement paste. *Colloids Surf. A Physicochem. Eng. Asp.* **2017**, *535*, 139–148. [[CrossRef](#)]
6. Bey, H.B.; Hot, J.; Baumann, R.; Roussel, N. Consequences of competitive adsorption between polymers on the rheological behaviour of cement pastes. *Cem. Concr. Compos.* **2014**, *54*, 17–20. [[CrossRef](#)]
7. Wiśniewska, M.; Nosal-Wiercińska, A.; Dąbrowska, I.; Szewczuk-Karpisz, K. Effect of the solid pore size on the structure of polymer film at the metal oxide/polyacrylic acid solution interface—Temperature impact. *Microporous Mesoporous Mater.* **2013**, *175*, 92–98. [[CrossRef](#)]
8. Zhang, Y.-R.; Kong, X.-M.; Lu, Z.-B.; Lu, Z.-C.; Hou, S.-S. Effects of the charge characteristics of polycarboxylate superplasticizers on the adsorption and the retardation in cement pastes. *Cem. Concr. Res.* **2015**, *67*, 184–196. [[CrossRef](#)]
9. Dalas, F.; Pourchet, S.; Nonat, A.; Rinaldi, D.; Sabio, S.; Mosquet, M. Fluidizing efficiency of comb-like superplasticizers: The effect of the anionic function, the side chain length and the grafting degree. *Cem. Concr. Res.* **2015**, *75*, 115–123. [[CrossRef](#)]
10. Kong, F.-R.; Pan, L.-S.; Wang, C.-M.; Zhang, D.-L.; Xu, N. Effects of polycarboxylate superplasticizers with different molecular structure on the hydration behavior of cement paste. *Constr. Build. Mater.* **2016**, *105*, 545–553. [[CrossRef](#)]
11. Tan, H.; Guo, Y.; Ma, B.; Li, X.; Gu, B. Adsorbing Behavior of Polycarboxylate Superplasticizer in the Presence of Ester Group in Side Chain. *J. Dispers. Sci. Technol.* **2017**, *38*, 743–749. [[CrossRef](#)]
12. Zou, F.; Tan, H.; Guo, Y.; Ma, B.; He, X.; Zhou, Y. Effect of sodium gluconate on dispersion of polycarboxylate superplasticizer with different grafting density in side chain. *J. Ind. Eng. Chem.* **2017**, *55*, 91–100. [[CrossRef](#)]
13. Tan, H.; Zou, F.; Ma, B.; Guo, Y.; Li, X.; Mei, J. Effect of competitive adsorption between sodium gluconate and polycarboxylate superplasticizer on rheology of cement paste. *Constr. Build. Mater.* **2017**, *144*, 338–346. [[CrossRef](#)]
14. Tan, H.; Guo, Y.; Zou, F.; Jian, S.; Ma, B.; Zhi, Z. Effect of borax on rheology of calcium sulphoaluminate cement paste in the presence of polycarboxylate superplasticizer. *Constr. Build. Mater.* **2017**, *139*, 277–285. [[CrossRef](#)]
15. Tan, H.; Zou, F.; Ma, B.; Liu, M.; Li, X.; Jian, S. Effect of sodium tripolyphosphate on adsorbing behavior of polycarboxylate superplasticizer. *Constr. Build. Mater.* **2016**, *136*, 617–623. [[CrossRef](#)]
16. Li, G.; He, T.; Hu, D.; Shi, C. Effects of two retarders on the fluidity of pastes plasticized with aminosulfonic acid-based superplasticizers. *Constr. Build. Mater.* **2012**, *26*, 72–78. [[CrossRef](#)]
17. Tan, H.; Gu, B.; Guo, Y.; Ma, B.; Huang, J.; Ren, J.; Zou, F.; Guo, Y. Improvement in compatibility of polycarboxylate superplasticizer with poor-quality aggregate containing montmorillonite by incorporating polymeric ferric sulfate. *Constr. Build. Mater.* **2018**, *162*, 566–575. [[CrossRef](#)]

18. Tan, H.; Gu, B.; Ma, B.; Li, X.; Lin, C.; Li, X. Mechanism of intercalation of polycarboxylate superplasticizer into montmorillonite. *Appl. Clay Sci.* **2016**, *139*, 40–46. [[CrossRef](#)]
19. Ait-Akbour, R.; Boustingorry, P.; Leroux, F.; Leising, F.; Taviot-Gueho, C. Adsorption of PolyCarboxylate Poly(ethylene glycol) (PCP) esters on Montmorillonite (Mmt): Effect of exchangeable cations ( $\text{Na}^+$ ,  $\text{Mg}^{2+}$  and  $\text{Ca}^{2+}$ ) and PCP molecular structure. *J. Colloids Interface Sci.* **2015**, *437*, 227–234. [[CrossRef](#)] [[PubMed](#)]
20. Yu, B.; Zeng, Z.; Ren, Q.; Chen, Y.; Liang, M.; Zou, H. Study on the performance of polycarboxylate-based superplasticizers synthesized by reversible addition–fragmentation chain transfer (RAFT) polymerization. *J. Mol. Struct.* **2016**, *1120*, 171–179. [[CrossRef](#)]
21. Bessaies-Bey, H.; Baumann, R.; Schmitz, M.; Radler, M.; Roussel, N. Organic admixtures and cement particles: Competitive adsorption and its macroscopic rheological consequences. *Cem. Concr. Res.* **2016**, *80*, 1–9. [[CrossRef](#)]
22. Gupta, C.; Nadelman, E.; Washburn, N.R.; Kurtis, K.E. Lignopolymer Superplasticizers for Low- $\text{CO}_2$  Cements. *ACS Sustain. Chem. Eng.* **2017**, *5*, 4041–4049. [[CrossRef](#)]
23. Lu, Z.; Kong, X.; Zhang, C.; Xing, F.; Cai, Y.; Jiang, L.; Zhang, Y.; Dong, B. Effect of surface modification of colloidal particles in polymer latexes on cement hydration. *Constr. Build. Mater.* **2017**, *155*, 1147–1157. [[CrossRef](#)]
24. Plank, J.; Hirsch, C. Impact of zeta potential of early cement hydration phases on superplasticizer adsorption. *Cem. Concr. Res.* **2007**, *37*, 537–542. [[CrossRef](#)]
25. Zingg, A.; Winnefeld, F.; Holzer, L.; Pakusch, J.; Becker, S.; Gauckler, L. Adsorption of polyelectrolytes and its influence on the rheology, zeta potential, and microstructure of various cement and hydrate phases. *J. Colloids Interface Sci.* **2008**, *323*, 301–312. [[CrossRef](#)] [[PubMed](#)]
26. Srinivasan, S.; Barbhuiya, S.A.; Charan, D.; Pandey, S.P. Characterising cement–superplasticiser interaction using zeta potential measurements. *Constr. Build. Mater.* **2010**, *24*, 2517–2521. [[CrossRef](#)]
27. Bonapasta, A.A.; Buda, F.; Colombet, P. Interaction between Ca ions and poly (acrylic acid) chains in macro-defect-free cements: A theoretical study. *Chem. Mater.* **2001**, *13*, 64–70. [[CrossRef](#)]
28. Ma, H.; Tian, Y.; Li, Z. Interactions between organic and inorganic paste in PA and PA/PU modified cement based materials. *J. Mater. Civ. Eng.* **2011**, *23*, 1412–1421. [[CrossRef](#)]
29. Şakar-Deliormanli, A. Flow behavior of hydroxypropyl methyl cellulose/polyacrylic acid interpolymer complexes in aqueous media. *Polym. Int.* **2012**, *61*, 1751–1757. [[CrossRef](#)]
30. Li, Q.; Yuan, R.; Ying, L. Study on the molecular behavior of hydrophobically modified poly (acrylic acid) in aqueous solution and its emulsion-stabilizing capacity. *J. Appl. Polym. Sci.* **2013**, *128*, 206–215. [[CrossRef](#)]
31. Azarijafari, H.; Kazemian, A.; Ahmadi, B.; Berenjian, J.; Shekarchi, M. Studying effects of chemical admixtures on the workability retention of zeolitic Portland cement mortar. *Constr. Build. Mater.* **2014**, *72*, 262–269. [[CrossRef](#)]
32. Wang, Z.; Wu, J.; Zhao, P.; Dai, N.; Zhai, Z.; Ai, T. Improving cracking resistance of cement mortar by thermo-sensitive poly N-isopropyl acrylamide (PNIPAM) gels. *J. Clean. Prod.* **2018**, *176*, 1292–1303. [[CrossRef](#)]
33. Zhang, G.; Li, G.; Li, Y. Effects of superplasticizers and retarders on the fluidity and strength of sulphoaluminate cement. *Constr. Build. Mater.* **2016**, *126*, 44–54. [[CrossRef](#)]
34. Plank, J.; Winter, C. Competitive adsorption between superplasticizer and retarder molecules on mineral binder surface. *Cem. Concr. Res.* **2008**, *38*, 599–605. [[CrossRef](#)]
35. Lesage, K.; Cizer, Ö.; Desmet, B.; Vantomme, J.; De Schutter, G.; Vandewalle, L. Plasticising mechanism of sodium gluconate combined with PCE. *Adv. Cem. Res.* **2015**, *27*, 163–174. [[CrossRef](#)]
36. Wu, Y.; He, T.; Song, X.; Liang, G. Effect of sodium gluconate on polynaphthalene sulfonate adsorption. *Adv. Cem. Res.* **2011**, *23*, 249–254. [[CrossRef](#)]





Article

# Comparative Study of Water-Leaching and Acid-Leaching Pretreatment on the Thermal Stability and Reactivity of Biomass Silica for Viability as a Pozzolanic Additive in Cement

Weiting Xu <sup>1,\*</sup>, Jiangxiong Wei <sup>1,\*</sup>, Jiajian Chen <sup>2</sup>, Bin Zhang <sup>1</sup>, Peng Xu <sup>3</sup>, Jie Ren <sup>4</sup> and Qijun Yu <sup>1</sup>

<sup>1</sup> School of Materials Science and Engineering, South China University of Technology, Guangzhou 510641, China; mszhangbin@mail.scut.edu.cn (B.Z.); concyuq@scut.edu.cn (Q.Y.)

<sup>2</sup> Department of Civil Engineering, Foshan University, Foshan 528000, China; chenjiajian@fosu.edu.cn

<sup>3</sup> Department of Mechanics and Civil Engineering, Jinan University, Guangzhou 510632, China; t60at3@gmail.com

<sup>4</sup> Department of Infrastructure Engineering, The University of Melbourne, Melbourne, VIC 3010, Australia; renjie630@gmail.com

\* Correspondence: xuweiting@scut.edu.cn (W.X.); jxwei@scut.edu.cn (J.W.);  
Tel.: +86-20-87110629 (W.X. & J.W.)

Received: 2 August 2018; Accepted: 10 September 2018; Published: 12 September 2018

**Abstract:** The present work aims to introduce a novel and eco-friendly method, i.e., a water-leaching pretreatment for extracting highly reactive biomass silica from rice husk (RH), for viability as a pozzolanic additive in cement. For comparison, the traditional acid pretreatment method was also employed throughout the experimental study. The silica from RH was extracted using boiled deionized water and acid solution as leaching agents to remove the alkali metal impurities, and then dried and submitted to pyrolysis treatment. The results indicated that potassium was found to be the major contaminant metal inducing the formation of undesirable black carbon particles and the decrease in crystallization temperature of amorphous RHA silica. The boiling-water-leaching pretreatment and acid-leaching pretreatment on RHs significantly removed the metallic impurities and reduced the crystallization sensitivity of RHA silica to calcination temperature. A highly reactive amorphous silica with purity of 96% was obtained from RH via 1 N hydrochloric acid leaching followed by controlled calcination at 600 °C for 2 h. The acid treatments increased the crystallization temperature of silica to 1200 °C and retained the amorphous state of silica for 2.5 h. In the case of water-leaching pretreatment, leaching duration for 2.5 h could yield an amorphous silica with purity of 94% and render the silica amorphous at 900 °C for 7 h. The RHA silica yielded by water-leaching pretreatment presented a comparable enhancing effect to that of acid leaching on hydration and improved the strength of cement. Furthermore, compared with the acid-leaching method, the water-leaching pretreatment method is more environmentally friendly and easier to operate, and hence more widely available.

**Keywords:** amorphous silica; crystallization sensitivity; water-leaching pretreatment; rice husk ash; cement

## 1. Introduction

Rice husk (RH) is the outer shell of the rice grain, which is a by-product of the rice milling process. It is an agricultural waste in all rice-producing countries. Most of the RH usually ends up either being

dumped or burned in open spaces, which not only occupies a large land area but also represents a major source of contamination [1–3].

The major components of RH are organic materials such as hemicellulose, cellulose, and lignin, totaling about 85%, and the remaining ash content is 15–20% [4]. Of all the residues of edible plants, the ash obtained from the calcined RH has the highest silica content [5]. The orthosilicic acid was ingested from soil and groundwater by the rice crop and further polymerized in the tissue structure of the plant, contributing to the formation of amorphous silica in the husk. After burning, RH becomes rice husk ash (RHA), which normally contains 85–95% of silica ( $\text{SiO}_2$ ), 5–8% of alkali metal oxides, and some carbonaceous materials by mass [6].

Amorphous silica has a wide range of industrial applications, such as raw materials for ceramics synthesis, refractories, plastics, silica gels, silica chip, activated carbon and silica, catalysts, zeolites, ingredients for lithium-ion batteries, graphene, energy storage/capacitor, carbon capture, and drug delivery vehicles [7–17]. Compared with other industrial fields, the use of amorphous RHA silica in the production of concrete can realize large-scale consumption and reuse of waste, and hence eventually reduces the environmental impact due to improper disposal and land occupation. RHA is economical, widely available and highly reactive as a supplementary cementing material, due to its excellent physically filling and chemically pozzolanic effects [18–22]. It is also a promising substitute for replacing silica fume (SF) in high-performance concrete production.

Under a controlled calcination procedure and temperature, the calcination of RH removes hydrocarbon compounds and yields amorphous silica-rich powders with a large surface area. A highly reactive RHA silica is produced by burning RH at a temperature of 500 °C or lower for a comparatively protracted time under oxidizing environment or for a shorter time at a temperature of up to 700 °C [23]. The calcination of RH beyond this temperature may lead to the conversion of amorphous silica to crystalline silica polymorphs (quartz, cristobalite, and tridymite) [24]. Moreover, these crystals tend to predominate in unacceptable quantities and particle agglomeration may occur as the temperature increases, thereby reducing the chemical reactivity of RHA silica [25].

The temperature-sensitive nature of RHA silica leads to a rigid requirement for combustion instrument and pyrolysis technology, consequently capping the large-scale industrial production. To achieve amorphous silica ash of a desirable quality, a controlled combustion temperature and time are compulsory. Moreover, even if the RH is burned under controlled calcination conditions, the internal heat of the RH heap is difficult to release, and the temperature will rapidly exceed the crystallization point of the RHA silica. Thus, reducing the crystallization sensitivity of RHA silica to calcination temperature is the most critical issue for achieving large-scale production of biomass silica.

Studies indicate that the phase transformation temperature of RHA silica is markedly influenced by the inorganic chemical impurities [26]. Alkali metals, such as potassium, sodium, and calcium salts in RH, preferably react with silica to form eutectic mixtures with low melting points. At a high concentration of potassium or sodium, the melting point of eutectic mixtures is as low as 600–700 °C, significantly reducing the normal crystalline temperature of RHA silica [27].

The acid-leaching pretreatment on RH has been proved to be effective to remove the metallic contamination. The amorphous silica obtained from the acid pretreatment contains very high purity silica (above 95%) [28,29]. However, the use of acid as a leaching agent usually causes corrosion in pipes and instruments, and increases the operational difficulty and production costs. Hence, it is of great importance to find a novel eco-friendly pretreatment method to remove metallic impurities from RHA silica.

In addition, the kinetics of the thermal stability of amorphous RHA silica under various leaching-pyrolysis treatments have not been clearly established. Moreover, major metallic contamination, which induces the amorphous silica in biomass RH compounds to crystallize at a relatively low calcination temperature, has not been verified.

In view of the fact that the biomass metallic salts are mostly soluble, this study explores using boiling water as a leaching agent for rinsing off alkali metal impurities in RHA silica and

consequently obtaining a purified and highly reactive RHA silica. The present work aims to reveal the influence of water-leaching pretreatments on the crystallization behavior and chemical reactivity of RHA silica, consequently extending our knowledge for the industrialized mass manufacture and application of biomass silica. For comparison, the traditional acid pretreatment method is also assessed throughout the study. In this study, the effects of boiling-water-leaching pretreatment and acid-leaching pretreatment on crystallization sensitivity of RHA silica to pyrolysis conditions (calcination time and duration) were investigated and compared. The influences of metallic impurity and content on the thermal stability of RHA silica were identified by testing the crystallization behavior of the mixtures of purified RH and alkali salt. To examine the pozzolanic reactivity of the as-prepared RHA silica samples for their viability as a pozzolanic additive for the production of high-strength cement and concrete, the compressive strength, chemically bound water, and hydration product mineralogy of cement pastes with 10% cement replaced by RHA samples were examined.

## 2. Materials and Methods

### 2.1. Materials

Rice husk (RH) collected from a local rice processing plant (Academy of Agricultural Sciences Institute, Guangzhou, China) during the process of rice manufacturing was used as the starting material in this study. Commercially available chemical reagents, such as hydrochloric acid (HCl), sulfuric acid (H<sub>2</sub>SO<sub>4</sub>), and nitric acid (HNO<sub>3</sub>), were of analytical grades and used as the acid-leaching agents for RH. Deionized water was used for the boiling-water-leaching pretreatment test as well as the residue rinsing of RH throughout the experiments.

### 2.2. Leaching-Pyrolysis Treatment of RH

RH samples were examined in this study by employing the leaching-pyrolysis steps. Two leaching pretreatment regimes, i.e., the boiling-water-leaching and acid-leaching pretreatment on RH, were applied in this study to remove alkali metal impurities from RH.

In the case of boiling-water-leaching pretreatment, the RHs were weighed into three consignments of 10 g each. Each consignment was soaked in boiling water of 100 °C for 2.5, 5, or 10 h, and then filtered and air-dried.

As for the acid pretreatment, RHs were weighed separately in three batches of 10 g each, and each batch was subjected to immersion in the acid solution (hydrochloric acid, sulfuric acid, or nitric acid) at a concentration of 1, 2, or 3 N acid solution for 1 or 2.5 h with constant stirring at ambient temperature. After the acidic solution was drained off, RH was rinsed with deionized water until the pH rose to 7, then filtered and air-dried.

After the leaching pretreatments, the as-pretreated RH samples were collected and dried in a drying oven at 50 °C for 24 h, and then separately subjected to pyrolysis in an electronic furnace for burning out at the desired temperature (600–1200 °C) until the appointed time (0.25–2 h). After the furnace hearth naturally cooled down to room temperature, the ash obtained was collected and subjected to grinding for 10 min in a laboratory mill. The ground ashes were kept separately in a desiccator for future material characterization tests.

The original RH was represented by RH. In the case of acid-leached RH, the HCl-, H<sub>2</sub>SO<sub>4</sub>-, and HNO<sub>3</sub>-pretreated RH samples were marked as Cl-RH, S-RH, and N-RH, respectively. The boiling-water-leaching-pretreated RH samples were labeled W-RH. Accordingly, each RHA sample is named for clarification, e.g., 1Cl-RHA600-2h, which implies RHA with HCl leaching pretreatment for 1 h and then burning out at 600 °C for 2 h.

### 2.3. Testing of RH

Scanning electron microscopy (SEM) analyses were conducted to study the structure of acid-leaching- and water-leaching-pretreated RH samples at the micro level. The dried RH samples

were coated with gold in a sputter coater. The SEM experiment was performed on a PHILIPS ESEM XL-30 (FEI, Hillsboro, OR, USA) operating at 20 kV with a 15 mm working distance.

The functional groups in the RH samples were determined using an FTIR equipment BRUKER EQUINOX 55 (Bruker, Karlsruhe, Germany). The spectra were recorded with 32 scans at a resolution of  $4\text{ cm}^{-1}$  in the range of  $4000\text{--}400\text{ cm}^{-1}$ .

## 2.4. Testing of RHA

### 2.4.1. Characterization of RHA

Quantitative chemical analyses of RHA were accomplished by X-ray fluorescence. The particle size was determined by the laser diffraction analyzer Easysize 20 (OMEC, Zhuhai, China). The surface area and pore volume of RHA were measured by Brunauer-Emmett-Teller (BET) and Barrett-Joyner-Halenda (BJH) methods, respectively, according to ASTM D3663-03 using Micromeritics Tristar 3000 Surface Area (Micromeritics, Norcross, GA, USA) and Porosity Analyzer (Micromeritics, Norcross, GA, USA).

The functional groups in the RHA samples were detected by the FTIR technique.

The pozzolanic reactivity of RHA silica was examined by the electrical conductivity change test, i.e., the reaction between RHA and a saturated calcium hydroxide solution. Each test utilized 200 mL of solution, which contained approximately 0.4 g of  $\text{Ca}(\text{OH})_2$ . Solutions were placed in a plastic Erlenmeyer flask and stirred at a constant temperature of  $80\text{ }^\circ\text{C}$ . Initial conductivity values were registered by a conductivity meter. Then, 5 g of RHA was added.  $\text{SiO}_2$  reacting with  $\text{Ca}^{2+}$  ions led to the formation of C-S-H, a non-conductive compound, and hence decreased the solution conductivity over time. The conductivity change value was recorded as an indication of the chemical reactivity of amorphous silica.

X-ray diffraction (XRD, Bruker, Karlsruhe, Germany) patterns were obtained using a Bruker MSAL XD2 X-ray Diffractometer using  $\text{CuK}\alpha$  operated at 36 kV and 24 mA. The scanning two theta is between  $10^\circ$  and  $60^\circ$ . EVA™ Software (Bruker, Karlsruhe, Germany) was used to record and analyze the structural pattern of the sample.

### 2.4.2. Identification Tests for Metallic Contamination in RHA

To identify the metallic trace element that leads to the decrease in crystallization temperature of RHA silica composites, the potential contaminant elements (the constituent trace elements of RH) in terms of chlorine salts were separately incorporated into the HCl-purified RH. The trace element was incorporated into RH powder at a dosage of 2% by weight of the binder. The RH powder and chlorine salt were mixed for 1 min to obtain a homogenous powder mix. Then the mix was subjected to calcination at  $600\text{ }^\circ\text{C}$  for 2 h to yield an ash sample (silica composite).

To reveal the effect of potassium content on the crystalline behavior of silica in RHA, potassium in the form of KCl was incorporated into the acid-pretreated RH powder at five dosage levels of 0%, 0.5%, 1%, 5%, and 10% by weight of the binder. The binder of KCl and purified RH was mixed for 1 min to obtain a homogenous powder mix. Then the mix was subjected to calcination at 500 and  $700\text{ }^\circ\text{C}$  for 2 h.

All the ash samples obtained were labeled and sealed separately in plastic bags for XRD characterization tests.

## 2.5. Compressive Strength of RHA Incorporated Cement Paste

The compressive strength of 20 mm mortar cube after three, seven, and 28 days of moist curing was determined in accordance with the ASTM C 311-07 standard. This test was carried out to examine the pozzolanic activity of the ash samples with various leaching pretreatments. One control mix (P0) and five pastes ((PR, P2.5WR, P5WR, P10WR and PCIR)) incorporating RHA obtained by calcining unpretreated RH or leaching-pretreated RH at  $600\text{ }^\circ\text{C}$  for 2 h were prepared. PR is the paste incorporating RHA yielded by calcining unpretreated RH at  $600\text{ }^\circ\text{C}$  for 2 h. P2.5WR, P5WR and



P10WR represent the paste incorporating RHA obtained by 2.5, 5, and 10 h boiling-water-leaching pretreatment and calcining at 600 °C for 2 h, respectively; PCIR denotes the paste incorporating RHA obtained by 1 h HCl leaching pretreatment and calcining at 600 °C for 2 h. All the pastes were blended with 10% RHA by mass of cement and had a water binder ratio of 0.4. The test yielded paste indicates the pozzolanic reactivity degree of RHA silica.

### 2.6. Chemically Bound Water Content of RHA Incorporated Cement Paste

To investigate the effect of the RHA silica on the hydration of cement matrix, a chemically bound water content test was conducted. After the compressive strength test, the broken paste fragments were selected and immediately immersed in anhydrous ethanol to stop cement hydration at the predetermined age. Then the fragments were baked in an electronic furnace at 105 °C for 16 h to a constant weight, and then naturally cooled down to the ambient temperature and weighed. After that the fragments were subjected to heating at 1000 °C for 20 min, and then cooled down and weighed. Each test was repeated three times to ensure accuracy. The data recorded were subsequently used to calculate the chemically bound water content in the paste samples.

### 2.7. XRD Analysis of Hydration Products of RHA Incorporated Cement Paste

To investigate the effect of RHA on the hydration products of cement, the XRD analysis of cement pastes without and with water-leaching and acid-leaching-pretreated RHA were determined at the age of 7 days. The XRD scanning were performed at two theta between 10° to 60°.

## 3. Results and Discussion

### 3.1. Chemical Compositions and Physical Properties of RHA

Chemical compositions and physical properties of RHAs without and with pretreatment are summarized in Tables 1 and 2, respectively. It is seen that silica oxide forms the main component (89–96%) of RHAs with trace elements in the form of composite oxides K<sub>2</sub>O, Na<sub>2</sub>O, CaO, MgO, Fe<sub>2</sub>O<sub>3</sub>, and Al<sub>2</sub>O<sub>3</sub>. In the case of unpretreated RHA, 89.6% of silica was produced by calcining RH at 600 °C for 2 h. Potassium (K) was detected to account for the highest concentration (2.53%) among the metallic trace elements. With the increase in calcination temperature and duration, silica content and undesirable carbon residue (represented by LOI) were slightly increased. The specific surface area tends to decrease with the increase of calcination temperature and duration, contributing to the particle agglomeration. It is apparent that the capacity of controlled calcination condition for improving the silica purity and chemical reactivity of silica is rather limited.

The leaching pretreatment process results in significant changes in trace element concentrations in RHA. In the case of acid-leaching pretreatment, HCl exerts superior performance in removing metallic impurities to the other leaching agents. The RHA yielded by 1 N HCl leaching pretreatment and calcination at 600 °C for 2 h possesses the highest silica content (96.41%) and surface area (248.21 m<sup>2</sup>/g). The trace elements are reduced to a very low level, especially in the case of potassium, which is reduced to 0.06%. HNO<sub>3</sub> and H<sub>2</sub>SO<sub>4</sub> as leaching agents also have excellent performance in washing off alkali metals and improving the surface area, as well as reducing the carbon residue content of RHA.

In the case of boiling-water-leaching pretreatment, the RH pretreated by boiling water leaching for 2.5 h and burning out at 600 °C for 2 h yields RHA with a silica content of 94.03% and a surface area of 130.82 m<sup>2</sup>/g. However, extending the water-leaching duration to 10 h does not seem like a responsible way to increase the concentration and surface area of silica. Thus, a water-leaching duration of 2.5 h is sufficient for pretreating RH to extract pure silica. It is worth noting that, although the boiling water-leaching pretreatment is inferior in extracting a high content of silica and rinsing off metallic impurities in RH during the acid-leaching pretreatment, the boiling water-leaching pretreatment method is more eco-friendly and economical.



The weight loss data obtained from thermogravimetric studies are presented in Table 1. It is clearly seen that the residual organics or undesirable carbon of RHA are gotten rid of with greater ease from the acid-leaching- or water-leaching-pretreated RH upon heating in comparison to that of the unpretreated RHA.

**Table 1.** Chemical composition of RHAs.

RHA Samples	SiO <sub>2</sub> (%)	K <sub>2</sub> O (%)	Na <sub>2</sub> O (%)	CaO (%)	MgO (%)	Al <sub>2</sub> O <sub>3</sub> (%)	Fe <sub>2</sub> O <sub>3</sub> (%)	LOI (%)
RHA600-2	89.61	2.53	0.16	1.52	0.56	0.36	0.90	3.53
RHA600-8	90.42	2.48	0.14	1.57	0.59	0.39	0.88	3.74
RHA900-2	91.76	2.13	0.11	1.33	0.62	0.33	0.79	4.61
RHA1200-0.5	92.23	1.92	0.09	1.21	0.71	0.28	0.37	4.92
1Cl-RHA600-2	96.41	0.06	0.05	0.07	0.24	0.19	0.28	1.80
1S-RHA600-2	95.52	0.07	0.07	0.64	0.22	0.21	0.32	2.24
1N-RHA600-2	95.81	0.06	0.06	0.59	0.22	0.18	0.29	2.11
2.5W-RHA600-2	94.03	0.26	0.12	0.95	0.32	0.23	0.33	3.32
2.5W-RHA900-2	94.42	0.24	0.09	0.99	0.41	0.22	0.31	2.04
5W-RHA900-2	94.80	0.22	0.10	0.95	0.29	0.21	0.29	2.96
10W-RHA900-2	94.92	0.21	0.11	0.92	0.29	0.19	0.28	2.90

Note: LOI represents the loss of ignition.

The average particle size, BET surface area, pore volume, and pore diameter of RHA samples are given in Table 2. It is seen that leaching pretreatment significantly affects the surface area as well as the pore volume of RHA silica. The average pore diameter of acid-leached RHA, water-leached RHA, and unpretreated RHA is around 6, 6 and 32 nm, respectively, indicating that the RHAs produced are mainly mesoporous. The pore volume of the acid-leached RHA and the water-leached RHA are higher than that of the unpretreated one. It is noteworthy that either the acid-leaching pretreatment or the water-leaching pretreatment can markedly increase the surface area and the pore volume, as well as reduce the pore diameter of RHA. This is mainly attributed to the hydrolysis of lignin and cellulose into smaller compounds and the dissolution of alkali metals after leaching pretreatment, which promote the volatilization of fixed carbon in RHA with greater ease during combustion. Moreover, the removal of the organic carbohydrates causes the inside pores in RHA to open and hence leads to a more loose and highly porous structure of RHA.

**Table 2.** Particle size, BET surface area, and conductivity of RHAs.

RHA Samples	Average Particle Size (μm)	BET Surface Area (m <sup>2</sup> /g)	Total Pore Volume (cm <sup>3</sup> /g)	Average Pore Diameter (nm)	Conductivity Change (ms/cm)
RHA600-2	5.47	74.88	0.082997	32.78	0.38
RHA600-8	6.21	68.83	0.072315	33.19	0.42
RHA900-2	6.47	10.59	0.053497	35.14	0.11
RHA1200-0.5	6.96	10.02	0.042749	38.17	0.00
1Cl-RHA600-2	5.02	248.21	0.368958	5.15	6.09
1Cl-RHA900-2	5.63	250.32	0.312846	6.07	6.11
1Cl-RHA1200-0.5	6.21	200.02	0.287963	7.70	0.22
1S-RHA600-2	5.20	232.97	0.324875	5.38	5.73
1N-RHA600-2	5.14	241.76	0.357947	5.23	5.91
2.5W-RHA600-2	5.34	130.82	0.257617	6.45	4.42
2.5W-RHA900-2	6.02	120.85	0.184237	7.02	4.64
5W-RHA900-2	5.88	133.78	0.274633	6.88	4.75
10W-RHA900-2	5.42	137.96	0.302141	6.64	4.87

The N<sub>2</sub> adsorption-desorption isotherms and pore size distribution curves of the RHA samples are shown in Figure 1, respectively. It is seen that the adsorption is not limited to high values of P/P<sub>0</sub> above 0.95. In addition, the isotherms present a vertical asymptotic profile at high values of P/P<sub>0</sub>, which is characteristic of a mesoporous structure with non-uniform sized particles.

It is seen from Figure 1a that the untreated RHA presented the type I hysteresis loop [30] according to de Boer's classification of hysteresis loops, suggesting an intergranular pore structure formed by the spherical granules compactly accumulating together. As shown in Figure 1b,c, both the boiling water-pretreated RHA and the acid-pretreated RHA present type III hysteresis loops, indicating a bottle-shaped pore structure. The absorption and desorption of type III isotherms are more steep, suggesting that the porosity of the pretreated RHA is higher than that of the untreated one.

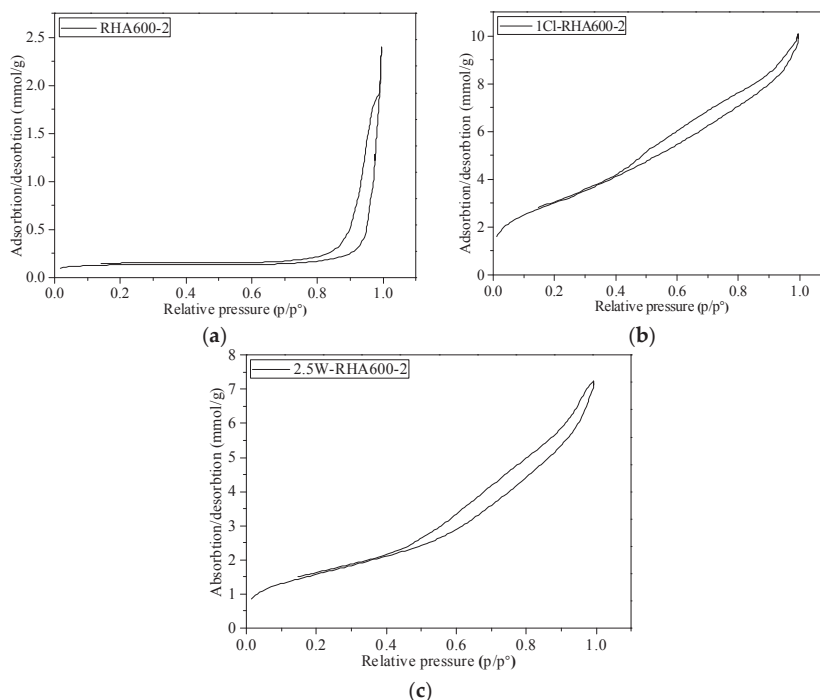


**Figure 1.** Nitrogen adsorption-desorption isotherm for (a) untreated RHA; (b) acid-treated RHA and (c) water-treated RHA.

Figure 2 gives the information on the BJH pore volume and diameter of RHAs. It is seen from Figure 2a that the untreated RHA has a mean pore diameter of 32.7804 nm, indicating that it is between mesoporous and macroporous. Its pore volume is  $0.082997 \text{ cm}^3/\text{g}$ , suggesting a low quantity of pores. In contrast, the acid-leaching and water-leaching pretreatment lead to a reduction of RHA pore diameter to 6.4479 and 5.1521 nm, and an increase of pore volume to  $0.257617$  and  $0.368958 \text{ cm}^3/\text{g}$ , respectively. It is evident that leaching pretreatment improves the internal porosity of RHA.

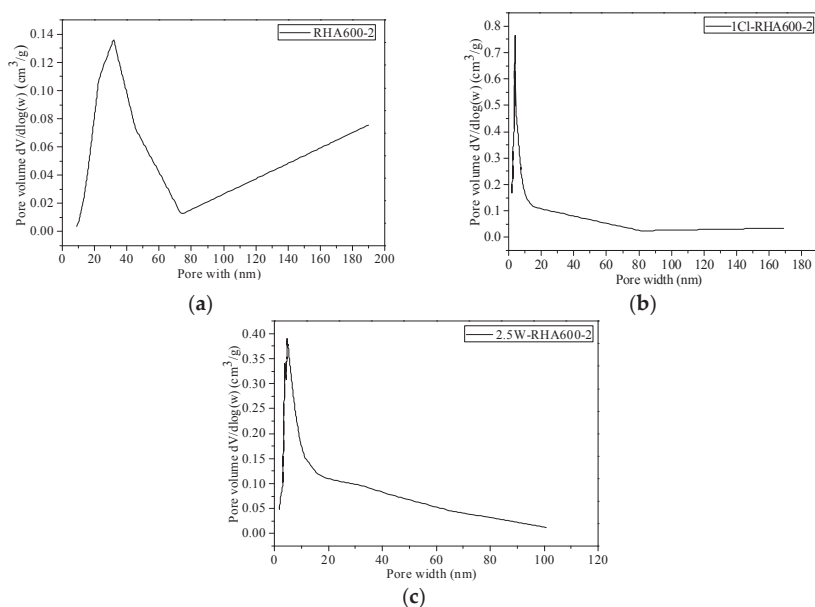


**Figure 2.** Pore size distribution calculated via BJH algorithm of (a) untreated RHA; (b) acid-treated RHA and (c) water-treated RHA.

### 3.2. Conductivity Change Test of RHA

The conductivity change testing results are listed in Table 2. The conductivity change value is an indication of the pozzolanic reactivity of the testing powder. The greater the change value in conductivity of the testing solution, the higher the chemical reactivity of RHA silica. The conductivity change value of RHA silica shows both leaching pretreatment- and pyrolysis condition- (temperature and duration) dependent behavior. In the case of unpretreated ash RHA600-2, the conductivity change value is 0.38. In the case of acid-leaching-pretreated RHA samples, the conductivity change value of 1Cl-RHA600-2, 1N-RHA600-2 and 1S-RHA600-2 is 6.09, 5.91, and 5.73, which is 1502.6%, 1407.9%, and 1243.2% higher, respectively, than that of the unpretreated ash RHA600-2. In the case of water-leaching-pretreated RHA samples, the conductivity change value of 2.5W-RHA600-2 and 2.5W-RHA900-2 is 4.42 and 4.64, which is 1063.2% and 1121.1% higher, respectively, than that of RHA600-2. It is apparent that with the assistance of an acid- or water-leaching process, the metallic concentration in RH is significantly reduced, while the chemical reactivity of the yielded RHA is distinctly increased as compared to the unpretreated one. In addition, it is noteworthy that prolonging the duration of water leaching does not lead to an obvious improvement in the conductivity change value of the testing solution. In other words, excessive water-leaching pretreatment time is not related to a significant increase in the pozzolanic reactivity of RHA. Thus, a duration of 2.5 h for boiling water leaching is reasonable and economical.

### 3.3. FTIR Analysis of RH and RHA

The FTIR spectra of the unpretreated, HCl-leaching-pretreated, and water-leaching-pretreated RHs are shown in Figure 3. The broad band observed around 3420 cm<sup>-1</sup> is attributed to the stretching vibration of C-H and OH groups, indicating the cellulose structure and water absorption (hydroxyl groups bound to the cellulose structure) in RH [31,32]. The band at 2929 cm<sup>-1</sup> represents the stretching and/or vibration of the C-H group, attributed to the aliphatic-saturated compounds in the cellulose [33]. A slight shoulder at 1740 cm<sup>-1</sup> is referent to the stretching vibration of the C=O bond in hemicellulose

or carboxylic acid groups in the ferulic and *p*-coumaric components of the lignin [31,34]. These organic groups suggest that the cellulose and lignin are not rinsed off from RH by the acid-leaching or water-leaching pretreatment. The characteristic absorption peaks of SiO<sub>2</sub> appear at 480 cm<sup>-1</sup> (bending vibration of O-Si-O), 800–820 cm<sup>-1</sup> (stretching vibration of Si-O-Si or Si-C), and 1110–1130 cm<sup>-1</sup> (asymmetric stretching vibration of Si-O-Si) [35,36].

In general, the FTIR spectra of RHs without and with pretreatment showed similar trend curves, suggesting that the leaching pretreatment does not change the functional group structure of SiO<sub>2</sub> and the main organic matter (cellulose and lignin) in RH. However, the characteristic peaks of SiO<sub>2</sub> (480 cm<sup>-1</sup>, 800–820 cm<sup>-1</sup>, and 1110–1130 cm<sup>-1</sup>), C=O group (1740 cm<sup>-1</sup>), and C-H group (2929 cm<sup>-1</sup>) of RH samples by water- or acid-leaching pretreatment are more obvious than those of the unpretreated one. This is due to the fact that leaching pretreatment removes most of the metallic impurities, so that the concentration of SiO<sub>2</sub> and carbon-containing compounds become more apparent, and the enhancing effect is more pronounced in the case of the acid-pretreated RH.

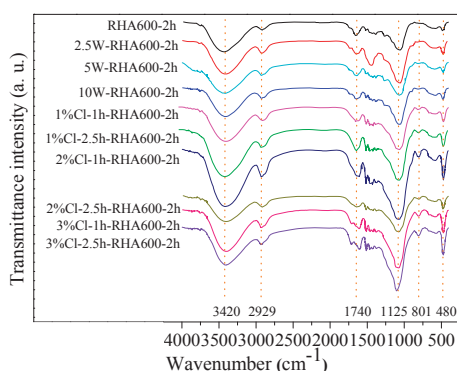


Figure 3. FTIR spectra of RH with and without various pretreatments.

The FTIR spectra of RHAs are illustrated in Figure 4. It is seen that, after pyrolysis, the C-H bond (2929 cm<sup>-1</sup>) and the C=O bond (1740 cm<sup>-1</sup>) refer to the functional groups of cellulose and lignin disappear for all the ash samples, suggesting that most of the organic compounds are burnt out. The intensity of SiO<sub>2</sub> characteristic peaks at 480, 800–820, and 1110–1130 cm<sup>-1</sup> of RHAs follows the ascending order of the untreated RHA, the water-leaching-pretreated RHA, and the acid-leaching-pretreated RHA, suggesting that the reactivity of the leaching-pretreated RHA is higher than that of the unpretreated one.

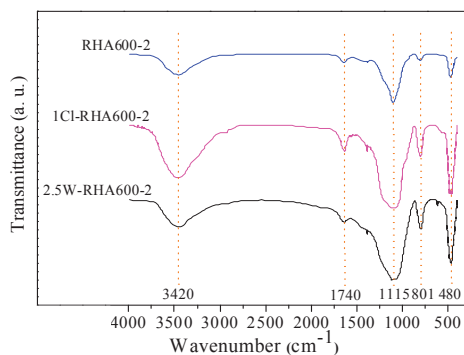
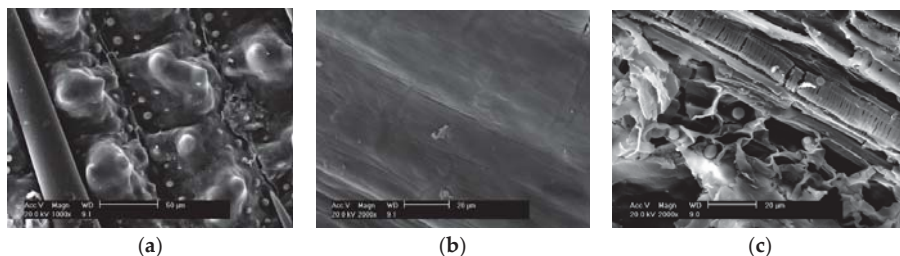


Figure 4. FTIR spectra of RHA with and without various pretreatments.

### 3.4. SEM Morphology of RHs

The SEM morphologies of the outer surface, inside surface, and interlayer of the water-leaching-pretreated RH are presented in Figure 5. Figure 5a presents the outer surface of the water-pretreated RH. The outer surface is uneven and highly roughened. Many bulges are neatly arranged with a crochet sprout between. From Figure 5b, it is seen that the inner surface of the RH is smooth and dense. Figure 5c is a cross-sectional view of the RH interlayer. It is seen that the porous inside layer is a plate-like structure constituted of a multilayer mesoporous structure. It is apparent that the water-leaching pretreatment does not significantly change the surface morphology or inner skeleton structure of RH.



**Figure 5.** SEM morphologies of (a) outside surface; (b) inside surface and (c) interlayer of the water-leached RH.

The morphologies of the outer surface, inside surface, and cross section morphology of the HCl leaching pretreated RH are presented in Figure 6a–c respectively. It is seen that, after acid leaching, the outer surfaces, smooth inside surface, and porous interlayer of RH were significantly corroded as compared to the corresponding part of the water-leaching-pretreated one shown in Figure 5. These morphological changes are presumably due to the hydrolysis of some organic components by acid.

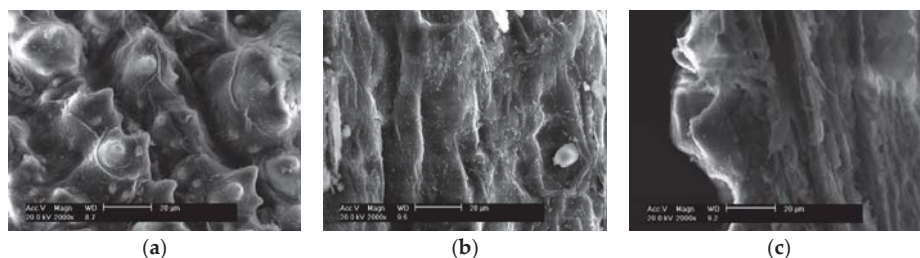


**Figure 6.** SEM morphologies of (a) outside surface, (b) inside surface, and (c) interlayer of the acid-leached RH.

### 3.5. XRD Analysis of RHA

XRD spectra of the unpretreated RHA, the water-leaching-pretreated RHA, and the acid-leaching-pretreated RHA with various calcination temperatures and durations are shown in Figure 7. The XRD patterns of unpretreated RHA obtained by calcining at various temperatures are shown in Figure 7a. It is seen that broad diffused peaks with maximum intensity at  $2\theta = 22.5^\circ$  are observed at RHA600-2, indicating the amorphous nature of silica. At  $700^\circ\text{C}$  the presence of quartz ( $2\theta = 26.7^\circ$ ) is observed. As the temperature increased to  $900^\circ\text{C}$ , cristobalite ( $2\theta = 22.5^\circ$ ) and tridymite ( $2\theta = 26^\circ$ ) were also detected, as reflected by the peak intensities. These phenomena demonstrate the thermal instability of amorphous silica of unpretreated RH, which has been extensively shown in previous research works [5,37]. The phase transformation of RHA silica from amorphous to crystalline

is very sensitive to pyrolysis temperatures above 700 °C. Hence, the crystallization sensitivity nature of RHA silica challenges the mass production of highly reactive silica based on existing industrial calcination equipment and techniques.

It has been reported elsewhere [38] that the presence of alkali metal salts results in a marked decrease in the crystallization temperature of the eutectic silica in RH. The calcination-temperature-dependent nature of silica is remarkably weakened by leaching treatment, as confirmed in Figure 7b. It is evident that acid-leaching-pretreated RHA silica shows completely amorphous structures upon combustion at 900 °C for 6 h. In addition, water-leaching-pretreated RHA silica presents similar mineralogical features at this thermal station. This is because of the removal of alkali metals, which preferably react with RHA silica to form eutectic composite with a low crystalline temperature. However, as the calcination duration extends to 7 h, the incipient cristobalite formation becomes apparent in the XRD patterns of the water-leaching-pretreated RHA silica powders. When pyrolysis takes place at 1200 °C for 0.5 h, the crystalline impurities cristobalite and quartz predominate. In the case of acid-leaching-pretreated RHA silica at this pyrolysis stage, tenuous peaks of cristobalite and tridymite gradually began to be visible, suggesting that crystalline silica formation starts to occur. It is seen that the ceiling capability for water-leaching pretreatment is to keep silica amorphous at 900 °C for 7 h. At 1200 °C, as shown in Figure 7d, small elevations corresponding to patterns of cristobalite and quartz arise in the acid-leached silica samples, i.e., acid-leaching pretreatment raises the crystalline transformation temperature of silica up to 1200 °C. In the case of water-leaching-pretreated RHA, cristobalite and quartz are formed to a large extent, along with the tenuous appearance of tridymite. It is apparent that the acid-leaching pretreatment has superior performance to the water-leaching pretreatment in reducing the crystallization sensitivity of RHA silica. However, the water-leaching treatment can use industrial cooling water as the leaching agent, hence reducing the investment in process technology and sophisticated equipment in comparison to acid-leaching treatment.

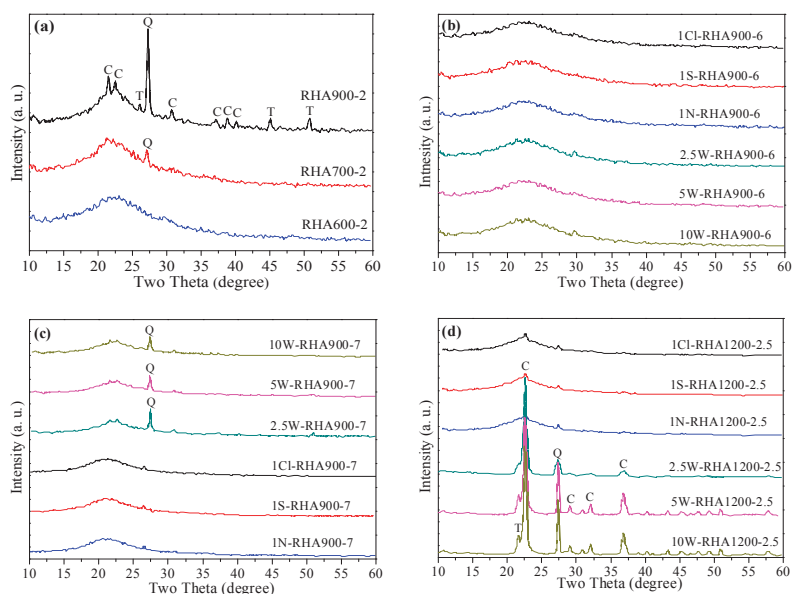


**Figure 7.** XRD spectra of RHAs obtained from: (a) unpretreated RHAs burnt out at 600, 700, and 900 °C for 2 h; (b) various leaching-pretreated RHAs burnt out at 900 °C for 6 h; (c) various leaching-pretreated RHAs burnt out at 900 °C for 7 h; (d) various leaching-pretreated RHAs burnt out at 1200 °C for 2.5 h. (C = cristobalite; Q = quartz; T = tridymite).

### 3.6. Influence of Alkali Metals on Crystallization in RHA Silica

To identify the influences of metallic impurity and content on thermal stability of RHA silica, mixtures of 1 N HCl-purified RH incorporated 2 wt % various alkali metallic trace elements in the form of chlorine salts are subjected to burning out at 600 °C for 2 h. The XRD spectra of the ash mixtures are plotted in Figure 8a. It is seen that a sharp intensity peak at  $2\theta = 22.5^\circ$  corresponding to cristobalite is noticed in the XRD pattern. Similarly, the incorporation of  $\text{NaCl}_2$ ,  $\text{MgCl}_2$ , and  $\text{CaCl}_2$  into silica promotes formation of the crystals cristobalite and quartz in the resulting blends. In the case of  $\text{NaCl}_2$  & 1Cl-RH ash blends, an incipient peak referent to the tridymite at  $2\theta = 23^\circ$  is observed, suggesting that Mg promotes tridymite formation. However, silica blend with the incorporation of  $\text{AlCl}_3$  and  $\text{FeCl}_2$  shows no obvious  $\text{SiO}_2$  crystallization, indicating that the trace elements Al and Fe rarely contribute to promoting the crystallization of RHA silica.

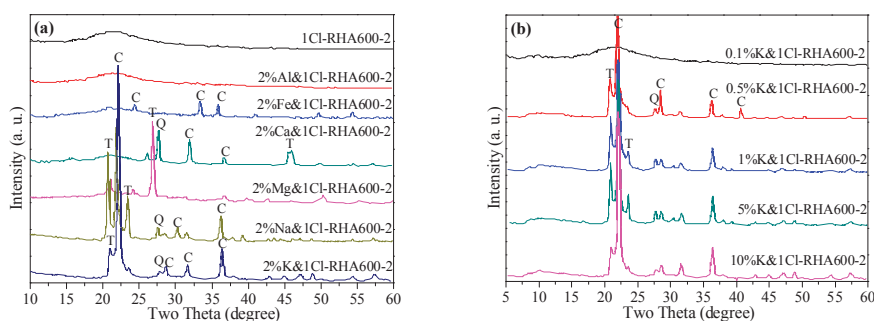


**Figure 8.** XRD spectra of (a) the mixture of HCl-pretreated RH and chlorine salts after burning out at 600 °C for 2 h; (b) the mixture of HCl-pretreated RHA silica various dosage of KCl after burning out at 600 °C for 2 h. (C = cristobalite; Q = quartz; T = tridymite).

Combined with the XRF chemical composition results, K is detected as the most abundant trace element in RHA, and hence it is the major contributor leading to the reduction of the crystallization temperature of the eutectic silica system. This finding is in line with the report of Krishnarao et al. [28]. It is also interesting to note the effect of K content on the crystallization behavior of RHA silica. The XRD spectra of the 1 N HCl-purified RH-incorporated mixtures with various addition ratios of K are given in Figure 8b. It is seen that a 0.1% addition of K has no impact on the crystallization of the silica blend. With the incorporation ratio of K increasing to 0.5% and above, the detracted crystalline peak corresponding to cristobalite becomes intensive and sharp. Thus, it is inferred that K exerts its function in accelerating the crystallization of RHA silica when its concentration in RHA is beyond 0.5%.

### 3.7. Compressive Strength of RHA Incorporated Cement Paste

To investigate the pozzolanic reactivity of the RHA silica, a compressive strength test of the blended cement paste was carried out. The compressive strength results of paste specimens at the age of three, seven, and 28 days are shown in Figure 9. P0 is the control paste. PR represents the paste with 10% cement replaced by the RHA obtained by burning RH at 600 °C for 2 h. P2.5WR, P5WR, and P10WR denote pastes with 10% cement replaced by the RHA obtained from water-leaching pretreatment on RH for 2.5, 5, and 10 h, respectively, and then burning out at 600 °C for 2 h. PCIR stands for the paste with 10% cement replaced by the RHA obtained from 1 N hydrochloric on RH for 1 h and then burning out at 600 °C for 2 h.

It is seen that the compressive strength of paste undergoes a significant improvement when 10% of RHA is incorporated. The compressive strength of paste with unpretreated RHA is 20.2% higher than that of the control paste. The enhancing effect of RHA is improved by leaching pretreatment on



RH prior to calcination. This can be attributed to the high silica content and high specific surface area of the leaching-pretreated RHA silica. The highest compressive strength appears in the paste with incorporation of acid-leaching-pretreated RHA (67.4 MPa), and the value is 48.1% higher than that of the control paste. In the case of the water-leaching-pretreated, RHA-incorporated cement paste, the RH with water-leaching pretreatment for 2.5 h yields the resulting RHA-blended paste having a compressive strength of 64.8 MPa, and this value is 42.4% higher than that of the control paste. Prolonging the water-leaching duration to 10 h, the strength value of the resulting ash-incorporated cement paste is increased to 65.6 Mpa. It is apparent that extending the water-leaching duration does not lead to obvious improvement in the pozzolanic reactivity of RHA. Thus, 2.5 h is an acceptable duration for water-leaching pretreatment on RH to yield a highly reactive pozzolana. It is worth noting that the water-leaching-pretreated RHA has better performance at improving the compressive strength of cement paste as compared to undispersed silica fume, as reported by Ji et al. [39], and presents comparable pozzolanic reactivity to dispersed silica fume and metakaolin, as per [40]. The enhancing effect of RHA on the compactness of the cement body is attributed to the silicate tetrahedron of RHA participating in the composition of hydrated calcium silicate (C-S-H) to prolong the chains of C-S-H, and soluble silicate-oxide chains of RHA also react with the free Ca(OH)<sub>2</sub> released from the cement hydration to form more C-S-H phase in the cement matrix [41].

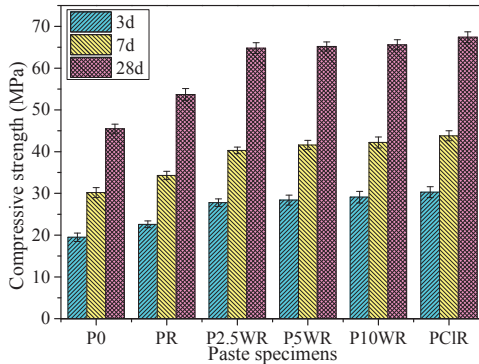


Figure 9. Compressive strength as a function of age for RHA cement paste.

### 3.8. Chemically Bound Water Content of RHA Incorporated Cement Paste

To investigate the effect of the RHA silica on the hydration degree of cement matrix, the chemically bound water of the paste fragments of the above compressive strength test was calculated.

The water in the hardened cement paste is divided into evaporated water (free water) and non-evaporated water (chemically bound water). A study [42] has revealed that the volume of evaporating water can be used as a measure of the pore volume in the cement paste, while the amount of non-evaporating water refers to the amount of hydration products. Therefore, the amount of chemically bound water measured at different ages can be used as a representative value of the degree of hydration of cement paste. The unit mass of chemical combined water was calculated as in the following equation:

$$X1 = (M1 - M2)/M2 - Xad.c/(1 - Xad.c), \tag{1}$$

where X1 is the chemical combined water content per unit mass of cementitious material, M1 is the quality of the paste sample after drying at 105 °C, and M2 is the quality of the sample after drying at 1000 °C. Xad.c refers to Equation (2):

$$Xad.c = XadXad.1 + XcXc.1, \tag{2}$$

where  $X_{ad}$  and  $X_c$  are the mass fraction of the admixture and cement, respectively;  $X_{ad.1}$  and  $X_{c.1}$  are the loss on ignition of the admixture and cement, respectively.

The amount of chemically bound water of the cement paste at the early age is expressed in terms of unit mass of cement and denoted as  $X_2$ , as per Equation (3):

$$X_2 = X_1 / (1 - X_{ad}). \quad (3)$$

To quantitatively characterize the effect of admixture on cement hydration, a hydration influence factor  $F$  of the admixture is introduced and calculated as  $F = \text{equivalent bound water } (X_2) / \text{combined water of the pure cement at the same age}$ . If  $F$  is more than 1, the admixture promotes the hydration of the cement. The larger the value, the more obvious the promotion effect; if  $F$  is less than 1, the admixture delays the hydration of the cement. The larger the value, the more obvious the delay effect.

The chemically bound water results of RHA incorporated cement paste specimens are shown in Table 3. It is seen that the chemically bound water in control paste was only 11.3% and 19.7% at the age of 7 and 28 days, while addition of the RHA results in a remarkable increase in the content of chemically bound water in the resulting paste at each age. In the case of the paste with incorporation of the water-leaching-pretreated RHA, the chemically bound water of 28 days is improved to 29.3 to 30.2% depending on the leaching duration, and the variation is not very noticeable. The paste with hydrochloric acid pretreated RHA shows the chemically bound water content is 30.3%, which is the highest value. These calculation results are in line with the conductivity and compressive strength results. It is also worth noting that the boiling-water-pretreated RHA silica has a comparable performance at improving the cement hydration with the acid-pretreated one.

**Table 3.** Chemical combined water and factors of RHA pastes.

Paste Samples	7 Days		28 Days	
	$X_1$	$F$	$X_1$	$F$
Control	11.3%	1	19.7%	1
PR	11.8%	1.16	21.6%	1.22
P2.5WR	18.0%	1.77	29.3%	1.65
P5WR	18.5%	1.82	29.5%	1.66
P10WR	18.7%	1.84	30.2%	1.70
PCIR	18.7%	1.86	30.3%	1.72

### 3.9. XRD Analysis of Hydration Products of RHA Incorporated Cement Paste

To investigate the effect of RHA silica on the hydration products of cement, the XRD analysis of paste samples P0, PR, P2.5W, P10W and PCI were determined at the age of 7 days. The results are plotted in Figure 10. It is seen that the intensity of  $\text{Ca(OH)}_2$  diffraction peak in the control cement paste P0 is very sharp. The addition of RHA weakens the X-ray diffraction peak intensity of  $\text{Ca(OH)}_2$ . The phenomenon is attributed to the fact that silica in RHA can react with the free  $\text{Ca(OH)}_2$  to form crystalline or semi-crystalline hydrated calcium silicate (CSH), improving the compactness of the hardened cement body. In addition, the intensity of  $\text{Ca(OH)}_2$  diffraction peak is in the ascending order of the paste PCI, P10W, P2.5W, PR, and P0, indicating the pozzolanic reactivity of RHA following the descending order of 1Cl-RHA600-2, 10W-RHA900-2, 2.5W-RHA900-2, and RHA600-2. These results are in line with the compressive strength test and chemically bound water content test results.

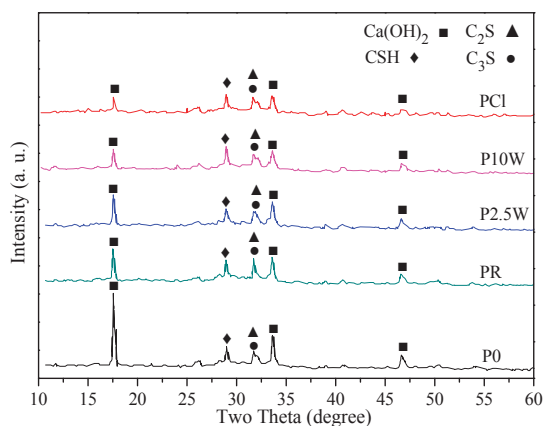


Figure 10. XRD patterns of RHA cement paste at the age of seven days.

#### 4. Conclusions

After burning, RHs become RHA that normally contained 90% silica ( $\text{SiO}_2$ ), 5–8% of alkali metal oxides, and some carbonaceous materials by mass. The reactive amorphous silica is extracted from RH via burning out of organic cellulose and lignin under controlled calcination at  $600\text{ }^\circ\text{C}$  for 2 h. Raising the calcination temperature or extending the calcination duration can increase the silica concentration but lead to accelerated formation of crystalline compounds (mainly in the form of quartz and cristobalite) in the ashes. Potassium was proven to cause surface melting of a eutectic potassium-silica compound, restraining carbon emissions from burning RH and hence leading to the formation of fixed black carbonaceous matter and accelerating the crystallization of amorphous silica to form cristobalite.

Acid-leaching pretreatment can effectively remove the concentration of alkali metal impurities in RH. An amorphous silica with purity above 96% is yielded from RH by 1 N hydrochloric acid leaching followed by calcination at  $600\text{ }^\circ\text{C}$  for 2 h. Sulfuric acid and nitric acid have comparable rinsing performance to hydrochloric acid. The acid treatment increases the crystallization temperature of RHA silica to  $1200\text{ }^\circ\text{C}$  and retains the amorphous state for 2.5 h.

Water-leaching pretreatment also exerted sound performance in rinsing off the alkali metal impurities. A reactive amorphous silica with a concentration of 94% is yielded via water-leaching pretreatment for 2.5 h and pyrolysis of  $600\text{ }^\circ\text{C}$  for 2 h. Moreover, water-leaching pretreatment on RH for 2.5 h could maintain the amorphous state of silica at  $900\text{ }^\circ\text{C}$  for 7 h.

The compressive strength of the acid-leaching-pretreated, RHA-incorporated paste is 48.1% higher than that of the control paste. The RH with boiling-water-leaching pretreatment for 2.5 h yields ash-blended paste having a compressive strength of 64.8 MPa, which was 42.4% higher than that of the control paste. Expanding the water-leaching duration did not obviously improve the pozzolanic reactivity of RHA. Thus, 2.5 h was an acceptable duration for boiling-water-leaching treatment on RH to achieve a highly reactive pozzolana. In addition, the boiling-water-leaching-pretreated RHA silica has a comparable pozzolanic performance at improving the cement hydration to the acid-pretreated one, as reflected by the calculation results of chemically bound water content.

In summary, the boiling-water-leaching pretreatment is slightly inferior to the hydrochloric-acid-leaching pretreatment at improving the thermal stability and removing the metal impurities of RHA silica. However, the boiling-water-leaching treatment is superior to the acid-leaching pretreatment in using an industrial cooling water system and hence reducing the investment in process technology and sophisticated equipment. Furthermore, the amorphous silica obtained under the water-leaching-pyrolysis treatment achieves a biomass amorphous silica with high purity and large surface area, and hence can be produced at a large scale as a highly reactive

pozzolana for applying in the production of high-strength cement and concrete. Thus, this study is of great significance for the extension of RHA in the practical application of cement engineering.

**Author Contributions:** W.X. designed the experiments and wrote the paper. J.W., J.C., B.Z., P.X. and J.R. performed the experiments and analyzed the data. Q.Y. supervised the project.

**Funding:** This research was funded by the National Natural Science Foundation of China (Grant No. 51408363), the China Postdoctoral Science Foundation (Grant Nos. 2017M610526 and 2018T110869) and the Fundamental Research Funds for the Central Universities (Grant No. 2018MS08).

**Acknowledgments:** The authors thank the reviewers for their valuable comments and suggestions concerning our manuscript.

**Conflicts of Interest:** The authors declare no conflict of interest.

## References

1. Pode, R. Potential applications of rice husk ash waste from rice husk biomass power plant. *Renew. Sustain. Energy Rev.* **2016**, *53*, 1468–1485. [[CrossRef](#)]
2. Prasara-A, J.; Gheewala, S.H. Sustainable utilization of rice husk ash from power plants: A review. *J. Clean. Prod.* **2017**, *167*, 1020–1028. [[CrossRef](#)]
3. Sun, L.; Gong, K. Silica-Based Materials from Rice Husks and Their Applications. *Ind. Eng. Chem. Res.* **2001**, *40*, 5861–5877. [[CrossRef](#)]
4. Roselló, J.; Soriano, L.; Santamarina, M.P.; Akasaki, J.L.; Monzó, J.; Payá, J. Rice straw ash: A potential pozzolanic supplementary material for cementing systems. *Ind. Crops Prod.* **2017**, *103*, 39–50. [[CrossRef](#)]
5. Xu, W.; Lo, T.Y.; Memon, S.A. Microstructure and reactivity of rich husk ash. *Constr. Build. Mater.* **2012**, *29*, 541–547. [[CrossRef](#)]
6. Fapohunda, C.; Akinbile, B.; Shittu, A. Structure and properties of mortar and concrete with rice husk ash as partial replacement of ordinary Portland cement-A review. *Int. J. Sustain. Built Environ.* **2017**, *6*, 675–692. [[CrossRef](#)]
7. Sutas, J.; Mana, A.; Pitak, L. Effect of Rice Husk and Rice Husk Ash to Properties of Bricks. *Procedia Eng.* **2012**, *32*, 1061–1067. [[CrossRef](#)]
8. Pongdong, W.; Kummerlöwe, C.; Vennemann, N.; Thitithammawong, A.; Nakason, C. Property correlations for dynamically cured rice husk ash filled epoxidized natural rubber/thermoplastic polyurethane blends: Influences of RHA loading. *Polym. Test.* **2016**, *53*, 245–256. [[CrossRef](#)]
9. Chiang, K.Y.; Chou, P.H.; Hua, C.R.; Chien, K.L.; Cheeseman, C. Lightweight bricks manufactured from water treatment sludge and rice husks. *J. Hazard. Mater.* **2009**, *171*, 76–82. [[CrossRef](#)] [[PubMed](#)]
10. Feng, Q.; Chen, K.; Ma, D.; Lin, H.; Liu, Z.; Qin, S.; Luo, Y. Synthesis of high specific surface area silica aerogel from rice husk ash via ambient pressure drying. *Colloid Surf. A* **2018**, *539*, 399–406. [[CrossRef](#)]
11. Soltani, N.; Bahrami, A.; Pech-Canul, M.I.; González, L.A. Review on the physicochemical treatments of rice husk for production of advanced materials. *Chem. Eng. J.* **2015**, *264*, 899–935. [[CrossRef](#)]
12. Menya, E.; Olupot, P.W.; Storz, H.; Lubwama, M.; Kiros, Y. Production and performance of activated carbon from rice husks for removal of natural organic matter from water: A review. *Chem. Eng. Res. Des.* **2018**, *129*, 271–296. [[CrossRef](#)]
13. Yu, K.; Li, J.; Qi, H.; Liang, C. High-capacity activated carbon anode material for lithium-ion batteries prepared from rice husk by a facile method. *Diam. Relat. Mater.* **2018**, *86*, 139–145. [[CrossRef](#)]
14. Zhang, S.; Zhu, S.; Zhang, H.; Chen, T.; Xiong, Y. Catalytic fast pyrolysis of rice husk: Effect of coupling leaching with torrefaction pretreatment. *J. Anal. Appl. Pyrolysis* **2018**, *133*, 91–96. [[CrossRef](#)]
15. Wang, Q.; Zhu, X.; Liu, Y.; Fang, Y.; Zhou, X.; Bao, J. Rice husk-derived hard carbons as high-performance anode materials for sodium-ion batteries. *Carbon* **2018**, *127*, 658–666. [[CrossRef](#)]
16. Chen, S.Y.; Chou, P.F.; Chan, W.K.; Lin, H.M. Preparation and characterization of mesoporous bioactive glass from agricultural waste rice husk for targeted anticancer drug delivery. *Ceram. Int.* **2017**, *43*, 2239–2245. [[CrossRef](#)]
17. Shen, Y.; Fu, Y. KOH-activated rice husk char via CO<sub>2</sub> pyrolysis for phenol adsorption. *Mater. Today* **2018**, *9*, 397–405. [[CrossRef](#)]

18. Wei, J.; Meyer, C. Utilization of rice husk ash in green natural fiber-reinforced cement composites: Mitigating degradation of sisal fiber. *Cem. Concr. Res.* **2016**, *81*, 94–111. [[CrossRef](#)]
19. Allahbakhsh, A.; Noei Khodabadi, F.; Hosseini, F.S.; Haghghi, A.H. 3-Aminopropyl-triethoxysilane-functionalized rice husk and rice husk ash reinforced polyamide 6/graphene oxide sustainable nanocomposites. *Eur. Polym. J.* **2017**, *94*, 417–430. [[CrossRef](#)]
20. Rhee, I.; Lee, J.S.; Kim, J.H.; Kim, Y.A. Thermal performance, freeze-and-thaw resistance, and bond strength of cement mortar using rice husk-derived graphene. *Constr. Build. Mater.* **2017**, *146*, 350–359. [[CrossRef](#)]
21. Ziegler, D.; Formia, A.; Tulliani, J.M.; Palmero, P. Environmentally-friendly dense and porous geopolymers using fly ash and rice husk ash as raw materials. *Materials* **2016**, *9*, 466. [[CrossRef](#)] [[PubMed](#)]
22. Karim, R.M.; Hossain, M.M.; Khan, N.M.; Zain, F.M.; Jamil, M.; Lai, C.F. On the Utilization of Pozzolanic Wastes as an Alternative Resource of Cement. *Materials* **2014**, *7*, 7809–7827. [[CrossRef](#)] [[PubMed](#)]
23. Saad, S.A.; Nuruddin, M.F.; Shafiq, N.; Ali, M. The Effect of Incineration Temperature to the Chemical and Physical Properties of Ultrafine Treated Rice Husk Ash (UFTRHA) as Supplementary Cementing Material (SCM). *Procedia Eng.* **2016**, *148*, 163–167. [[CrossRef](#)]
24. Bakar, R.A.; Yahya, R.; Gan, S.N. Production of High Purity Amorphous Silica from Rice Husk. *Procedia Chem.* **2016**, *19*, 189–195. [[CrossRef](#)]
25. Hu, S.; Xiang, J.; Sun, L.; Xu, M.; Qiu, J.; Fu, P. Characterization of char from rapid pyrolysis of rice husk. *Fuel Process. Technol.* **2008**, *89*, 1096–1105. [[CrossRef](#)]
26. Della, V.P.; Kühn, I.; Hotza, D. Rice husk ash as an alternate source for active silica production. *Mater. Lett.* **2002**, *57*, 818–821. [[CrossRef](#)]
27. Danewalia, S.S.; Sharma, G.; Thakur, S.; Singh, K. Agricultural wastes as a resource of raw materials for developing low-dielectric glass-ceramics. *Sci. Rep.* **2016**, *6*, 24617. [[CrossRef](#)] [[PubMed](#)]
28. Krishnarao, R.V.; Subrahmanyam, J.; Jagadish, K.T. Studies on the formation of black particles in rice husk silica ash. *J. Eur. Ceram. Soc.* **2001**, *21*, 99–104. [[CrossRef](#)]
29. Shen, J.; Liu, X.; Zhu, S.; Zhang, H.; Tan, J. Effects of calcination parameters on the silica phase of original and leached rice husk ash. *Mater. Lett.* **2011**, *65*, 1179–1183. [[CrossRef](#)]
30. Gregg, S.J.; Sing, K.S.W. *Adsorption, Surface Area and Porosity*; Wiley: New York, NY, USA, 1982.
31. Johar, N.; Ahmad, I.; Dufresne, A. Extraction, preparation and characterization of cellulose fibres and nanocrystals from rice husk. *Ind. Crops Prod.* **2012**, *37*, 93–99. [[CrossRef](#)]
32. Yeh, S.K.; Hsieh, C.C.; Chang, H.C.; Yen, C.C.C.; Chang, Y.C. Synergistic effect of coupling agents and fiber treatments on mechanical properties and moisture absorption of polypropylene–rice husk composites and their foam. *Compos. Appl. Sci. Manuf.* **2015**, *68*, 313–322. [[CrossRef](#)]
33. Tran, T.P.T.; Bénézet, J.C.; Bergeret, A. Rice and Einkorn wheat husks reinforced poly(lactic acid) (PLA) biocomposites: Effects of alkaline and silane surface treatments of husks. *Ind. Crops Prod.* **2014**, *58*, 111–124. [[CrossRef](#)]
34. Das, A.M.; Ali, A.A.; Hazarika, M.P. Synthesis and characterization of cellulose acetate from rice husk: Eco-friendly condition. *Carbohydr. Polym.* **2014**, *112*, 342–349. [[CrossRef](#)] [[PubMed](#)]
35. Costa, J.A.S.; Garcia, A.C.F.S.; Santos, D.O.; Sarmento, V.H.V.; De Mesquita, M.E.; Romão, L.P.C. Applications of inorganic–organic mesoporous materials constructed by self-assembly processes for removal of benzo[k]fluoranthene and benzo[b]fluoranthene. *J. Sol-Gel Sci. Technol.* **2015**, *75*, 495–507. [[CrossRef](#)]
36. Santos, D.O.; De Lourdes Nascimento Santos, M.; Costa, J.A.S.; De Jesus, R.A.; Navickiene, S.; Sussuchi, E.M.; De Mesquita, M.E. Investigating the potential of functionalized MCM-41 on adsorption of Remazol Red dye. *Environ. Sci. Pollut. Res.* **2013**, *20*, 5028–5035. [[CrossRef](#)] [[PubMed](#)]
37. Xu, W.; Lo, T.Y.; Wang, W.; Ouyang, D.; Wang, P.; Xing, F. Pozzolanic Reactivity of Silica Fume and Ground Rice Husk Ash as Reactive Silica in a Cementitious System: A Comparative Study. *Materials* **2016**, *9*, 146. [[CrossRef](#)] [[PubMed](#)]
38. Santana Costa, J.A.; Paranhos, C.M. Systematic evaluation of amorphous silica production from rice husk ashes. *J. Clean. Prod.* **2018**, *192*, 688–697. [[CrossRef](#)]
39. Ji, Y.; Jong, H.C. Effects of densified silica fume on microstructure and compressive strength of blended cement pastes. *Cem. Concr. Res.* **2003**, *33*, 1543–1548. [[CrossRef](#)]
40. Sinthaworn, S.; Nimityongskul, P. Quick monitoring of pozzolanic reactivity of waste ashes. *Waste Manag.* **2009**, *29*, 1526–1531. [[CrossRef](#)] [[PubMed](#)]

41. Garg, N.; Skibsted, J. Pozzolanic reactivity of a calcined interstratified illite/smectite (70/30) clay. *Cem. Concr. Res.* **2016**, *79*, 101–111. [[CrossRef](#)]
42. Shen, D.S.; Qiu, Q.Y. Systematization of physical order parameters of fly ash. *J. Chin. Ceram. Soc.* **1992**, *20*, 302–308. [[CrossRef](#)]



© 2018 by the authors. Licensee MDPI, Basel, Switzerland. This article is an open access article distributed under the terms and conditions of the Creative Commons Attribution (CC BY) license (<http://creativecommons.org/licenses/by/4.0/>).

Article

# Preparation and Thermal Properties of Molecular-Bridged Expanded Graphite/Polyethylene Glycol Composite Phase Change Materials for Building Energy Conservation

Dong Zhang, Meizhu Chen <sup>\*</sup>, Quantao Liu, Jiuming Wan <sup>id</sup> and Jinxuan Hu

State Key Laboratory of Silicate Materials for Architectures, Wuhan University of Technology, Wuhan 430070, China; pytmac@whut.edu.cn (D.Z.); liuqt@whut.edu.cn (Q.L.); wanjm@whut.edu.cn (J.W.); hujinxuan221@whut.edu.cn (J.H.)

<sup>\*</sup> Correspondence: chenmzh@whut.edu.cn; Tel.: +86-27-8716-2595

Received: 20 April 2018; Accepted: 12 May 2018; Published: 16 May 2018

**Abstract:** Using phase change materials (PCMs) in building envelopes became a reliable method to improve indoor comfort and reduce buildings' energy consumption. This research developed molecular-bridged expanded graphite (EG)/polyethylene glycol (PEG) composite PCMs (m-EPs) to conserve energy in buildings. The m-EPs were prepared through a vacuum absorption technique, and a titanate coupling agent was used to build a molecular bridge between EG and PEG. SEM, mercury intrusion porosimetry (MIP), the leakage test, microcalorimetry, X-ray photoelectron spectroscopy (XPS), and Fourier transform infrared spectroscopy (FT-IR) were conducted to characterize the morphology, pore structure, absorbability, and modifying effects of the m-EPs. The phase change temperature, latent heat, thermal stability, and thermal conductivity of the m-EPs were determined by a differential scanning calorimeter (DSC), TGA, and a thermal constants analyzer. Results showed that the maximum mass ratio of PEG to EG without leakage was 1:7, and a stable connection was established in the m-EPs after modification. Compared with the unmodified EPs, the supercooling degree of the m-EPs reduced by about 3 °C, but the latent heats and initial decomposition temperatures increased by approximately 10% and 20 °C, respectively, which indicated an improvement in the thermal energy storage efficiency. The thermal conductivities of the m-EPs were 10 times higher than those of the pristine PEGs, which ensured a rapid responding to building temperature fluctuations.

**Keywords:** expanded graphite; polyethylene glycol; phase change materials; titanate coupling agent; molecular bridge; building envelopes; thermal property; building energy conservation

## 1. Introduction

The rapid development of human civilization has led to a rising demand for energy. Statistics show that the global energy consumption reached  $6.607 \times 10^{14}$  MJ so far, and more than three-quarters of them are conventional fossil fuels (such as coal, petroleum oil, and natural gas) [1,2]. The extensive use of non-renewable energy leads to severe resource scarcity and environmental pollution problems [3]. On the other hand, the residential and commercial buildings consume almost 40% of the world's total energy usage for heating, ventilating, and air conditioning, which make it the leading energy consuming sector [4]. Therefore, exploiting green and energy-efficient buildings would be of benefit to the solution of energy and environment challenges facing the world. Applying phase change materials (PCMs) in building envelopes (such as wallboard [5], concrete [6], and insulation materials [7]) is a promising approach to decrease the energy consumption in buildings. The PCMs in building



envelopes can spontaneously absorb thermal energy during hot daytime, and release thermal energy when the surrounding temperature dropped at nighttime. The phase transition of PCMs is a spontaneous process, and the phase transition temperature is constant. Therefore, using PCM-enhanced building envelopes to regulate temperature is an ideal way of improving the indoor comfort and conserving building energy.

Based on the phase transition modes, PCMs can be classified into different types such as solid–solid, solid–liquid, solid–gas, and liquid–gas [8]. Up to now, the solid–liquid type PCMs with the merits of volume stability, proper phase change temperatures, and lower cost have become the most widespread PCMs in building thermal management [9]. The solid–liquid PCMs can be categorized into inorganic, organic, and eutectic mixture according to their chemical compositions. The inorganic PCMs refer to various salt hydrates that have high thermal energy storage density, high thermal conductivity, and low cost. However, these materials are subject to many constraints such as corrosion, supercooling, and segregation during their service [8]. Comparatively, the organic PCMs, such as paraffins, carbohydrates, and derived lipids exhibit broader prospects due to their favorable chemical stability, heat of fusion, and resistances to supercooling and phase separation. Despite the flaws of low-thermal conductivity and liquid leakage, the organic PCMs are still the most widely used [10]. As for the eutectic mixture, it refers to a combination of two or more either organic or inorganic compounds, or a mixture of both [11]. The melting point of eutectics can be tailored to any desired temperature. However, the advantage of custom-tailoring also results in the high cost of eutectics, which is commonly two or three times greater than the organic or inorganic compounds.

As the most favorable PCMs in building envelopes, a host of attempts have been proposed to overcome the shortcomings of organic PCMs. Finned tubes [12], heat-conducting fillers [13], and a metal/graphite matrix [14] have been applied to enhance the thermal conductivity of organic PCMs. Meanwhile, the encapsulation approaches such as the in situ polymerization method [15], complex coacervation method [16], sol–gel method [17,18], and solvent extraction/evaporation method [19] were developed to fabricate form-stable PCMs (FSPCM). Among all of these performance-enhancing methods of organic PCMs, using expanded graphite (EG) as a matrix to absorb solid–liquid PCMs is an ideal way to enhance the heat transfer rate as well as prevent leakage. EG is a porous carbonaceous material with favorable absorbability, thermal conductivity, and chemical stability, and its applications on the encapsulation of PCMs has become a research focus in recent years. Scholars have conducted constructive studies on the fabrication and application of EG-based FSPCMs. Zhang et al. [20] and Sari et al. [21] verified the feasibility of applying EG as a heat transfer enhancer and shape stabilizer for paraffin PCMs. Xia et al. [22], Zeng et al. [23], Wang et al. [24], and Ling et al. [25] have separately applied various organic PCMs as functional components, and performed a series of tests on the morphologies, absorptive capacities, thermal conductivities, phase change temperatures, and enthalpies of the EG-based FSPCMs. Zhang et al. [26], Li et al. [27], and He et al. [28] incorporated different EG-based FSPCMs into cement mortars and evaluated their thermal energy storage performances. The results indicated that EG-based FSPCMs could reduce the indoor temperature variation and energy consumption of buildings.

Although the EG-based FSPCMs have been successfully applied in building envelopes, the liquid leakage and performance degradation are still inevitable to a certain extent, because the PCMs are bonded with the EG matrix only through weak physical connections (capillarity and van der Waals force). Meanwhile, few attempts have been made to enhance the interaction between EG and PCMs. Therefore, the objective of this research was to fabricate a novel EG-based FSPCM with strong chemical bonding. EG matrices with different particle sizes and pore structures were used to absorb polyethylene glycol (PEG). The optimal EG matrix for PEG absorption was determined by detecting the absorbability and weight loss of EG/PEG composite PCMs (EPs) under a high temperature. A titanate coupling agent KR-385 was employed to build a molecular bridge between an EG matrix and PEG. The modified EG matrix (m-EG) was prepared and mixed with five different PEGs to fabricate molecular-bridged EPs (m-EPs). Thermal properties, including the phase change temperature, supercooling degree, latent

heat, heat transfer rate, and thermal reliability of m-EPs were characterized to demonstrate their performance improvement in this research.

## 2. Materials and Methods

### 2.1. Materials

Polyethylene glycols (PEGs, 98%, chemical pure) with different relative molecular mass (800, 1000, 1500, 2000, and 3000, named as PEG<sub>800</sub>, PEG<sub>1000</sub>, PEG<sub>1500</sub>, PEG<sub>2000</sub>, and PEG<sub>3000</sub>, respectively) were supplied by Sinopharm Chemical Reagent Co., Ltd. (Wuhan, China). An isopropyl tri-(dioctylpyrophosphate) titanate coupling agent (C<sub>51</sub>H<sub>112</sub>O<sub>22</sub>P<sub>6</sub>Ti, KR-38S) was obtained from Kenrich Petrochemicals Inc. (New York, NY, USA). Expanded graphite (EG) with different particle sizes (45 μm, 75 μm, 125 μm, 180 μm, and 300 μm, named as EG<sub>45</sub>, EG<sub>75</sub>, EG<sub>125</sub>, EG<sub>180</sub>, and EG<sub>300</sub>, respectively) were purchased from Qingdao Graphite Co., Ltd. (Qingdao, China). All of the materials were used as received without any further purification. The basic properties of PEGs and EGs were tested and demonstrated in Tables 1 and 2, respectively.

**Table 1.** Basic properties of the polyethylene glycols (PEGs) used in this research.

Categories	<i>Mr</i>	<i>T</i> <sub>onset-m</sub> (°C)	<i>T</i> <sub>onset-c</sub> (°C)	Δ <i>T</i> (°C)	Δ <i>H</i> <sub>m</sub> (J/g)	Δ <i>H</i> <sub>c</sub> (J/g)	λ (W/m·K)
PEG <sub>800</sub>	800	21.79	23.56	−1.77	143.51	126.63	0.2606
PEG <sub>1000</sub>	1000	27.92	30.74	−2.82	163.10	152.08	0.2790
PEG <sub>1500</sub>	1500	43.36	31.04	12.32	170.34	159.24	0.3038
PEG <sub>2000</sub>	2000	50.38	40.76	9.62	187.24	171.87	0.3151
PEG <sub>3000</sub>	3000	55.15	43.24	11.91	186.50	160.86	0.3281

Note: *Mr*: relative molecular mass; *T*<sub>onset-m</sub>: onset melting temperature; *T*<sub>onset-c</sub>: onset crystallization temperature; Δ*T*: supercooling degree, equals the temperature difference between *T*<sub>onset-m</sub> and *T*<sub>onset-c</sub>; Δ*H*<sub>m</sub>: melting enthalpy; Δ*H*<sub>c</sub>: crystallization enthalpy; λ: thermal conductivity.

**Table 2.** Basic properties of expanded graphites (EGs) used in this research.

Categories	Average Particle Size (μm)	Specific Surface Area (m <sup>2</sup> /g)	Pore Volume (cm <sup>3</sup> /g)	Average Pore Radius (μm)
EG <sub>45</sub>	45	52.1099	1.4110	0.2101
EG <sub>75</sub>	75	45.7174	3.2946	0.2584
EG <sub>125</sub>	125	41.5314	7.1265	0.3152
EG <sub>180</sub>	180	40.1269	7.7437	0.3273
EG <sub>300</sub>	300	32.9647	9.2215	0.3439

### 2.2. Selection of EG Matrix for PEG Absorption

Exploratory experiments were conducted to investigate the influence of PEGs molecular mass on the absorption capacity of EG. Results showed that no connection existed between the two. Therefore, PEG<sub>2000</sub> was selected as a PCM in this section to explore the optimal EG particle size for PEG absorption and the maximum absorbability. The EG/PEG composite PCMs (EPs) were fabricated in the following steps. First, the EG matrix was desiccated in a vacuum oven at 90 °C in order to weigh it accurately. Afterwards, the weighted EG matrix was mixed with PEG<sub>2000</sub> isopropanol solution proportionally by an ultrasonic oscillation at 70 °C for 15 min; the oscillating frequency was 40 kHz. Finally, the mixtures were treated in a vacuum pump at 80 °C for 4 h, in order to vaporize the isopropanol solvents and absorb the melted PEG<sub>2000</sub>. The schematic for the preparation of EPs was shown in Figure 1.

The optimal particle size of EG for the absorption of PCMs was determined by a series of experiments. First, liquid leakage tests were conducted by spreading the EP samples on filter papers uniformly and heating them in a vacuum oven at 85 °C for 1 h. The weight loss and mass ratio of each sample were considered as the indicators to select an optimal EG matrix with favorable thermal stability and absorptivity. Subsequently, mercury intrusion porosimetry (MIP, AutoPore IV 9510, Micromeritics

Instrument Corp., Norcross, GA, USA) and a scanning electron microscope (SEM, Quanta 450 FEG, FEI, Hillsboro, OR, USA) were employed to characterize the pore structure and morphology of each EG matrix and the corresponding EP. Finally, the optimal EG matrix was determined based on the aforementioned tests results.

### 2.3. Preparation of Modified EG (m-EG) and Molecular-Bridged EP (m-EP)

The absorption and compatibility between an EG matrix and PCMs depend mainly on the functional groups on the EG surface, and it was critical to modify the EG according to the PCM category and working condition of the FSPCM. KR-38S is a titanate coupling agent with high coupling efficiency on polymers and inorganic fillers. The modification principle of KR-38S on the EG matrix in this research can be described as follows: the alkoxy groups of KR-38S react with the hydroxyl groups of the EG matrix to produce a monomolecular layer on the EG surface. When the PEG was mixed with the modified EG (m-EG), a transesterification reaction between KR-38S and the terminal hydroxyl groups of PEG (which have similar properties as alcoholic hydroxyls) could occur on the surface of m-EG; consequently, a strong combination between m-EG and PEG was established by using KR-38S as the molecular bridge.

The schematic of EG matrix modification was also shown in Figure 1. The EG matrix was dried in a vacuum oven at 90 °C for 16 h to remove moisture. Then, the isopropanol solutions with different KR-38S dosages (1 wt %, 2 wt %, 3 wt %, and 4 wt % of EG) were prepared and mixed with the EG matrix. The mixing process was performed by ultrasonic oscillation at three different temperatures (50 °C, 60 °C, and 70 °C) to simulate different modifying conditions. The time and frequency of modifications were 15 min and 40 kHz, respectively. When the ultrasonic treatment was complete, the isopropanol solvents were vaporized in a vacuum pump at 80 °C for 4 h, and the modified EG matrix (m-EG) was fabricated. Microcalorimetry (C80, Setaram, Caluire, France) and X-ray photoelectron spectroscopy (XPS, ESCALAB 250Xi, Thermo Fisher Scientific, Waltham, MA, USA) were used to detect the isothermal calorimetric curve of each reaction and chemical state of the m-EGs, in order to determine the optimal modifying condition.

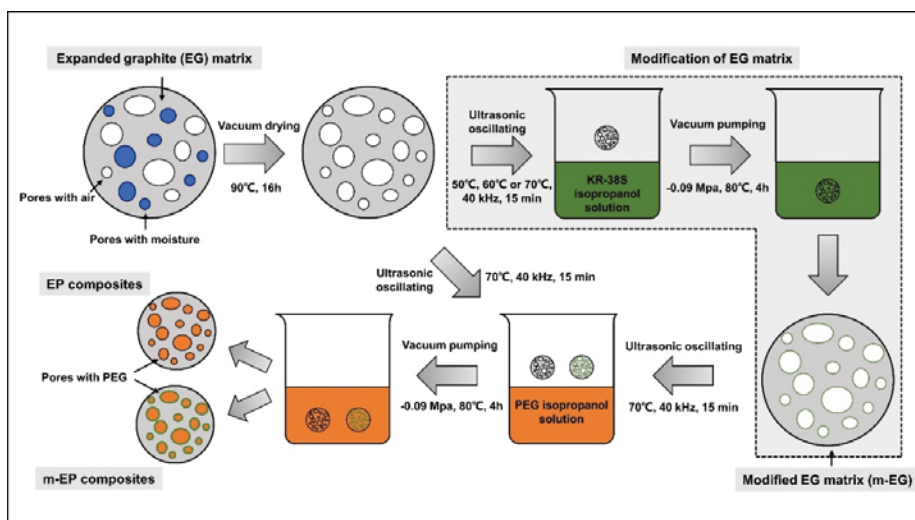


**Figure 1.** Schematic for the preparation of molecular-bridged EG/PEG composite phase change materials (m-EPs).

## 2.4. Characterization of m-EPs

The properties of EPs and m-EPs were characterized in this section. The phase change temperatures and latent heats were investigated by a differential scanning calorimeter (DSC, Pyris1DSC, Perkin Elmer, Waltham, MA, USA). Indium was selected as a reference for instrument calibration. The heating rate was 1 °C/min, and the testing temperature range was 0–70 °C. Fourier transform infrared spectroscopy (FT-IR, Nicolet™ 6700, Thermo Fisher Scientific, Waltham, MA, USA) was employed to manifest the chemical composition of EPs and m-EPs. The scanning range was from 4000 cm<sup>-1</sup> to 400 cm<sup>-1</sup> with a 4 cm<sup>-1</sup> resolution. A thermogravimetric analyzer (TGA, STA449F3 Jupiter, NETZSCH, Bavaria, Germany) was used to compare the thermal stabilities of EPs and m-EPs. The measurements were conducted from the ambient temperature to 700 °C at a heating rate of 10 °C/min, the experimental atmosphere was N<sub>2</sub>, and the flow rate was 100 mL/min. Thermal conductivities were measured by using a thermal constants analyzer (TPS 2500S, Hot Disk, Goteborg, Sweden). Samples were prepared by a dry-pressing process with a cylindrical mold of 45 mm in diameter and 15 mm in height. The packing density of all of the samples was 1.13 ± 0.02 g/cm<sup>3</sup>, which was consistent with that of the pristine PEGs, in order to avoid the influence of packing density on thermal conductivity.

## 3. Results and Discussion

### 3.1. Preparation of m-EPs

#### 3.1.1. Selection of EG Matrix

Latent heat is critical for the application of PCMs; typically, a higher latent heat is beneficial for an efficient and economical utilization of building envelopes. Therefore, it is vital to incorporate more PEGs in the limited pore volumes of EG without degrading its performance. Five kinds of EG matrices were selected as the supporting materials to absorb PEG<sub>2000</sub>, and the mass ratios of EG and PEG<sub>2000</sub> were 1:1, 1:2, 1:3, 1:4, 1:5, 1:6, 1:7, 1:8, 1:9, and 1:10, respectively. The leakage tests were performed to determine the optimal supporting material and the maximum absorbability. As presented in Figure 2, the weight loss percentages of five kinds EG matrices exhibited a similar trend that decreased initially and then increased, which indicated that each EG matrix had a certain absorbability. Specifically, the EG<sub>300</sub> matrix exhibited the minimum weight loss percentage (5.66 wt % of EP) when the EG/PEG mass ratio was 1:8, while both the minimum weight loss percentages of EG<sub>180</sub> and EG<sub>125</sub> (3.94 wt % and 2.15 wt % of the corresponding EPs, respectively) were achieved when the EG/PEG mass ratio was 1:7. This phenomenon might be because EG<sub>300</sub> possessed abundant pore volume compared with EG<sub>180</sub> and EG<sub>125</sub> (as seen in Table 2). Meanwhile, the macropores and mesopores in EG<sub>300</sub> were more suitable for the adsorption of large molecules. Despite a higher absorbability, the weight losses of EG<sub>300</sub> in each mass ratio were also higher in comparison with EG<sub>180</sub> and EG<sub>125</sub>. Therefore, the packaging stability of the EG<sub>300</sub> matrix was considered inferior to that of EG<sub>180</sub> and EG<sub>125</sub>. Similarly, EG<sub>125</sub> was a better supporting material than EG<sub>180</sub> in this research. As for EG<sub>75</sub> and EG<sub>45</sub>, their maximum EG/PEG mass ratios were both 1:4, and the weight losses increased dramatically when the mass ratios exceeded this threshold. This phenomenon can be explained by the limited amount of absorptive macropores and mesopores in EG<sub>75</sub> and EG<sub>45</sub> hindering the absorption of PEG. Hence, the EG<sub>125</sub> matrix, which had the maximum EG/PEG mass ratio of 1:7, was considered as the optimal supporting material for PEG in this research.

The pore structure parameters and micromorphology of various EGs and the corresponding EPs with the maximum PEG absorption capacities are shown in Tables 3 and 4, respectively. As presented in Table 2, the specific surface areas of the EG matrices decreased as their particle sizes increased; however, the pore volumes and average pore radii exhibited the opposite tendencies. This could be because the higher expansion ratio of the large-sized EG particles resulted in an increase of macropores and mesopores for absorption, as well as a reduction in the amount of micropores that have large

specific surface areas. When the maximum absorption capacities were achieved, the specific surface area, pore volume, and average pore radius of various EGs showed significant reductions, as illustrated in Table 3. These phenomena proved that the PEG was absorbed in the framework of the EG matrix. Furthermore, the leakage tests demonstrated that the maximum PEG absorption capacities increased from 1:4 to 1:8 as the EG particle size increased, and this trend was ascribed to the quantity variance of macropores.

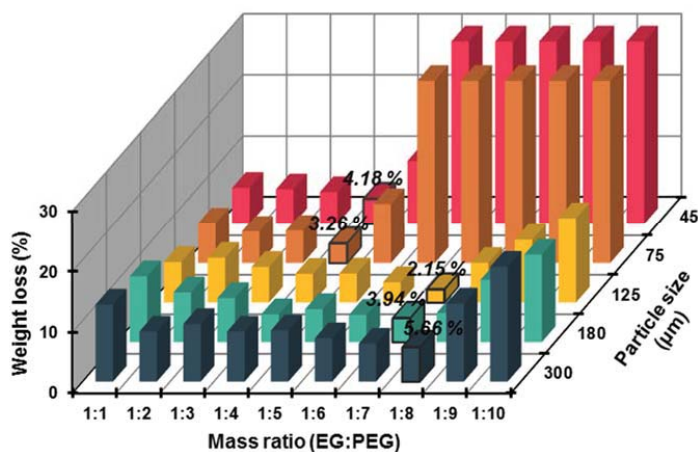


Figure 2. Weight loss of different EG/PEG composite phase change materials (EPs) after heat treatment.

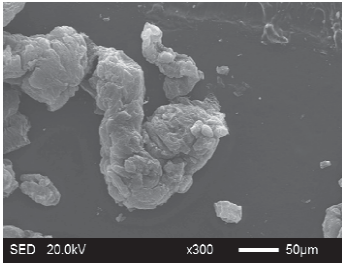
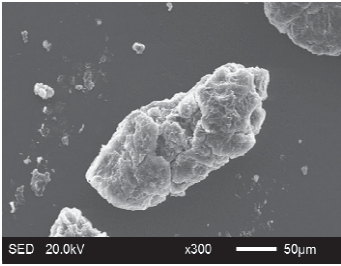
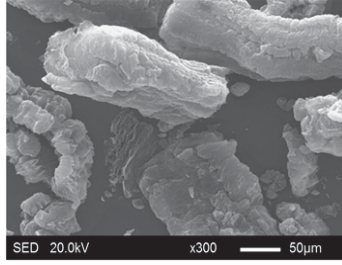
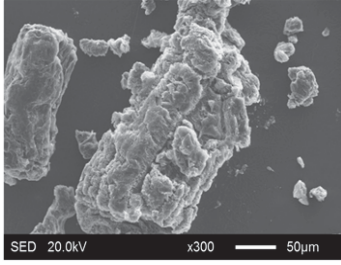
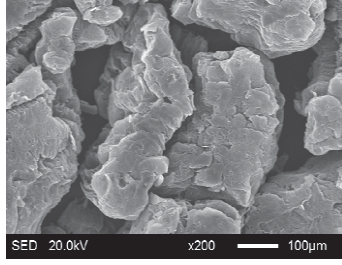
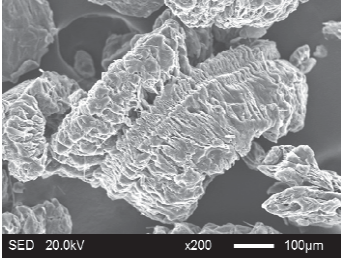
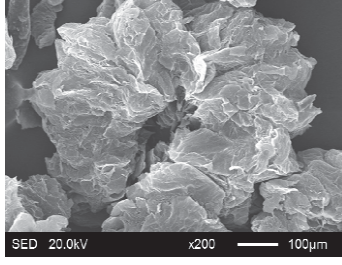
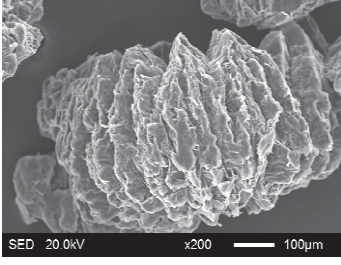
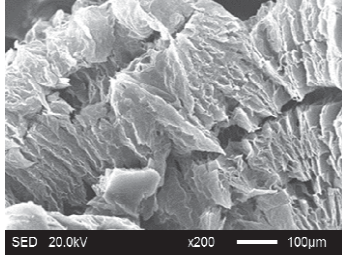
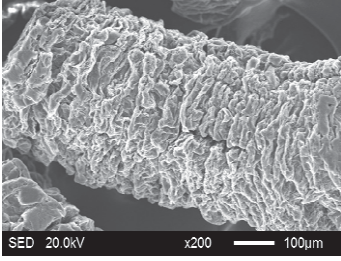
The SEM images showed that all of the EG matrices had the worm-like structures, which were favorable to expanding the surface areas and enhancing the absorption capacities. It also can be noted that with the increase in EG particle size, the folding-type macropores, which ensured the great surface tension and capillary force of the EG matrix, were increased. These results were consistent with the outcomes of the pore structure analyses. As for the EPs, different features were exhibited in their morphologies. The surfaces of EG<sub>45</sub> and EG<sub>75</sub> were coated with massive PEG crystal when the mass ratios of EG/PEG were 1:4. On the other hand, when the absorption capacities of EG<sub>125</sub>, EG<sub>180</sub>, and EG<sub>300</sub> were achieved, the frameworks of these EGs were still distinct, except for a slight amount of PEG crystal on the surface. Considering the variance in maximum absorption capacity, it can be concluded that the absorption of the EG<sub>45</sub> and EG<sub>75</sub> matrices to PEG was mainly depended on their extensive surface areas, while the massive macropore structures were responsible for the absorption of EG<sub>125</sub>, EG<sub>180</sub>, and EG<sub>300</sub>. It is also noteworthy that the worm-like structures of EG<sub>180</sub> and EG<sub>300</sub> were slightly damaged, owing to their high expansion ratios. These structural defects might be detrimental to the further processing of EPs. Therefore, based on the analyses of pore structures and morphologies, the EG<sub>125</sub> matrix, which had the maximum PEG absorption capacity of 1:7, was determined to be the optimal supporting material in this research.

Table 3. Pore structure parameters of EGs with the maximum absorptive capacities.

Categories	Specific Surface Area (m <sup>2</sup> /g)	Pore Volume (cm <sup>3</sup> /g)	Average Pore Radius (μm)	Maximum Mass Ratio of EG to PEG
EG <sub>45</sub>	21.5468	0.0954	0.0109	1:4
EG <sub>75</sub>	24.3368	0.1089	0.0142	1:4
EG <sub>125</sub>	17.6056	0.1354	0.0379	1:7
EG <sub>180</sub>	15.3005	0.2025	0.0326	1:7
EG <sub>300</sub>	14.5487	0.2944	0.0335	1:8

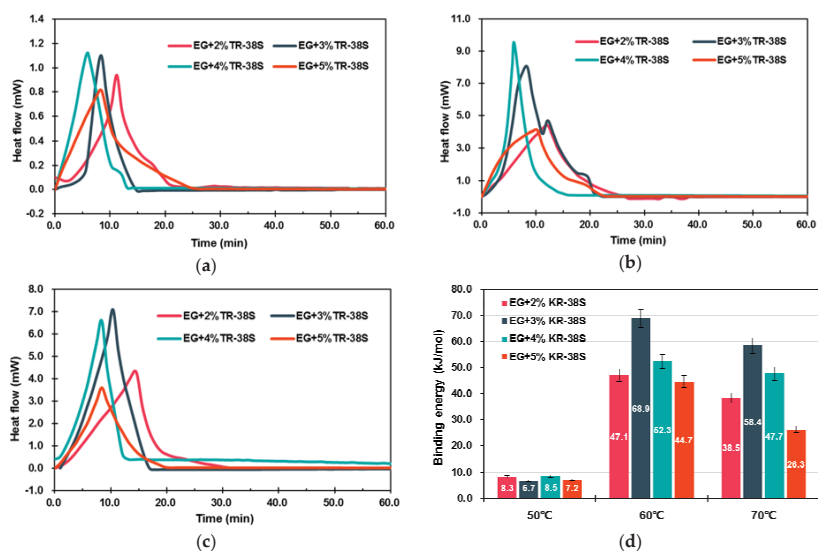


Table 4. Micromorphologies of EGs before and after PEG absorption.

Categories	Before Absorption	After Absorption
EG <sub>45</sub>	 SED 20.0kV x300 50μm	 SED 20.0kV x300 50μm
EG <sub>75</sub>	 SED 20.0kV x300 50μm	 SED 20.0kV x300 50μm
EG <sub>125</sub>	 SED 20.0kV x200 100μm	 SED 20.0kV x200 100μm
EG <sub>180</sub>	 SED 20.0kV x200 100μm	 SED 20.0kV x200 100μm
EG <sub>300</sub>	 SED 20.0kV x200 100μm	 SED 20.0kV x200 100μm

## 3.1.2. Modification of EG Matrix

The occurrence of chemical and physical reactions is always accompanied by the release or absorption of heat. Analyzing the heats would be helpful for determining the category and characteristic of the reactions. Figure 3 illustrated the isothermal calorimetric curves and binding energy values of EG-modifying reactions. As shown in the calorimetric curves of Figure 3, the reactions between EG and KR-38S were exothermic, and the shapes as well as the positions of the peaks varied with the KR-38S dosage and reaction temperature. These results indicated that the modifier was absorbed on the surface of the EG, and the absorption efficiencies were dependent on the modification conditions. To be specific, the binding energy values of the modifications at 50 °C were less than 10 kJ/mol, indicating that the coupling agent molecules were unactivated, and the physisorption (less than 40 kJ/mol of binding energy) that was caused by the van der Waals force was dominant [29]. When the temperature increased to 60 °C, the binding energy of each sample exhibited a significant increase. It can be inferred that a chemisorption between the EG surface and the coupling agent molecules might have occurred. Furthermore, the binding energy at 60 °C initially increased, and decreased subsequently as the KR-38S dosage increased. This phenomenon can be explained by the modification being optimized when a monomolecular layer was created on the surface of the EG. Adding an excessive coupling agent that hampered the chemical reaction between KR-38S and EG consequently resulted in the reduction of binding energy. As for the modifications at 70 °C, the binding energy values demonstrated the same tendencies, but lower values in comparison with those at 60 °C. The reason was that the modification temperature had exceeded the optimal activation temperature of KR-38S, and the chemisorptions were hindered. Therefore, it could be concluded from this section that the chemisorption could occur between the coupling agent and the EG matrix, and the optimal modifying condition was obtained by adding 3 wt % of KR-38S at 60 °C. The chemisorptions enhanced the connection between the EG and PEGs, which was beneficial for improving the thermal stability and energy storage density of the m-EPs, as well as the energy conservation efficiency of the building envelopes.



**Figure 3.** Calorimetric curves and binding energy values for the preparation of modified EGs (m-EGs). (a) calorimetric curves at 50 °C; (b) calorimetric curves at 60 °C; (c) calorimetric curves at 70 °C; (d) binding energy of reactions.



The XPS spectra of EG and m-EG are demonstrated in Figure 4. It was noticeable that two characteristic spectral peaks of O1s and C1s were illustrated in the spectrum of the EG matrix. The O1s was the oxidant residual during EG fabrication and adventitious carbon contamination in the atmosphere. Comparing with the EG matrix, the intensity of the O1s peak was obviously higher in the spectrum of the m-EG, and a new characteristic peak at 462.2 eV, corresponding to Ti2p, emerged. The peak table indicated that the oxygen element content in the EG matrix increased from 3.17 at % to 11.21 at % with the modification of KR-38S, and the titanium element was increased from 0.19 at % to 2.71 at %. This indicated that the coupling agent was attached on the surface of the EG matrix. In order to better investigate the modification mechanism, the C1s spectra of the EG and m-EG was deconvoluted by using the Gauss–Lorentz function, and at the same time, the chemical state of the C1s electron was characterized [30]. It was obvious that two dominant peaks with bonding energies of 284.6 eV and 285.5 eV, corresponding to C-C and C-OH, respectively, were shown in the C1s spectrum of the EG. The appearance of a C-OH peak indicated the existence of hydroxyl groups on the EG surface. Compared with EG, the C1s spectrum of m-EG exhibited another two peaks at 287.5 eV and 288.9 eV corresponding to C=O and O=C-OH, respectively. These new peaks were ascribed to the reactions between KR-38S and the EG matrix. The XPS results indicated that a satisfying modification effectiveness on the EG matrix was achieved, which was consistent with the conclusion of the microcalorimetry tests.

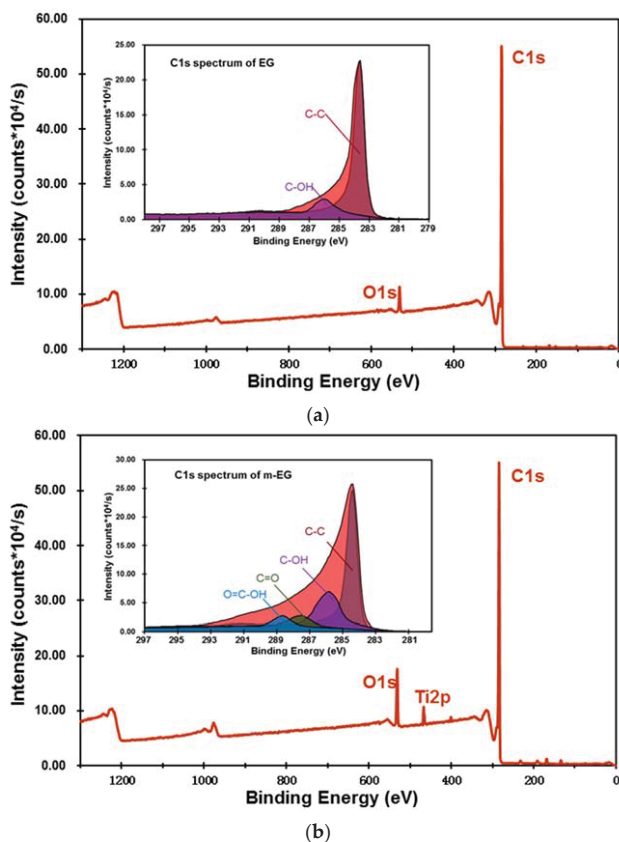
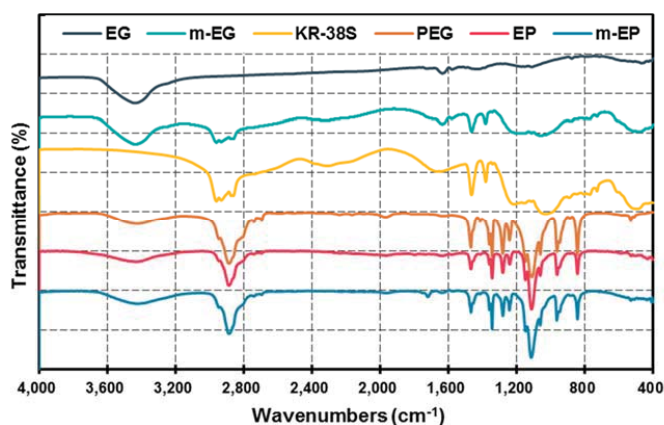


Figure 4. X-ray photoelectron spectroscopy (XPS) spectra of the EG matrix (a) and the m-EG matrix (b).

### 3.1.3. Preparation and Chemical Composition of m-EP

The FT-IR spectra of the EG, m-EG, KR-38S, PEG, EP, and m-EP at the wavenumbers between  $4000\text{ cm}^{-1}$  and  $400\text{ cm}^{-1}$  were shown in Figure 5. From the spectrum of EG, three peaks at the wavenumbers of  $1641\text{ cm}^{-1}$ ,  $1580\text{ cm}^{-1}$ , and  $1432\text{ cm}^{-1}$ , which were caused by the stretching vibration of C=C, the stretching vibration of C=O, and the in-plane bending vibration of -OH, respectively, could be noticed. As for the coupling agent KR-38S, the chief characteristic peaks that can be observed in the spectrum were the symmetrical and asymmetrical stretching vibrations of -CH<sub>3</sub> at  $2958\text{ cm}^{-1}$  and  $2875\text{ cm}^{-1}$ , respectively. Moreover, the symmetrical and asymmetrical deformation vibrations of -CH<sub>3</sub> at  $1464\text{ cm}^{-1}$  and  $1386\text{ cm}^{-1}$  could also be detected. Furthermore, the characteristic peaks at  $1036\text{ cm}^{-1}$  and  $609\text{ cm}^{-1}$ , corresponding to the vibrations of P-O and Ti-O, respectively, were critical for determining the type of coupling agent. When the modification of the EG matrix was performed, the four mentioned characteristic peaks belonging to the stretching and deformation vibrations of KR-38S appeared in the spectrum of m-EG matrix, but the in-plane bending vibration of -OH at  $1432\text{ cm}^{-1}$  disappeared. This phenomenon could be because the peak position of the -OH in-plane bending vibration overlapped with the position of the symmetrical and asymmetrical deformation vibrations of -CH<sub>3</sub>.

Comparing the spectra of PEG and EP, it was notable that most of the characteristic peaks appeared in both spectra, except for some slight shifts. To be specific, the characteristic peaks at  $845\text{ cm}^{-1}$  and  $961\text{ cm}^{-1}$  corresponded to the bending vibrations of the -CH<sub>2</sub>CH<sub>2</sub>O- and -C-O-C- functional groups, respectively. The peaks at  $1103\text{ cm}^{-1}$  and  $1149\text{ cm}^{-1}$  were the stretching vibration of C-O. The peaks at the wavenumbers of  $1242\text{ cm}^{-1}$  and  $1281\text{ cm}^{-1}$  were the results of -OH symmetrical and asymmetrical stretching vibrations, respectively. The peaks at  $1342\text{ cm}^{-1}$  and  $1469\text{ cm}^{-1}$  represented the bending vibrations of the functional groups of -CH<sub>2</sub> and -OH, respectively. The similar FT-IR spectrum features between the EP and PEG indicated that the reaction between PEG and EG mainly depended on the capillary force and hydrogen bonding, rather than the chemical bonding. As for the m-EP, the characteristic peak at wavenumber of  $1802\text{ cm}^{-1}$ , representing the symmetrical stretching vibration of anhydride C=O, disappeared. However, a new peak belonging to the stretching vibration of ester C=O appeared at  $1781\text{ cm}^{-1}$ . These results indicated that a transesterification between KR-38S and PEG might have occurred, and a chemical combination was established in m-EP.



**Figure 5.** Fourier transform infrared (FT-IR) spectra of EG, the modified EG matrix (m-EG), KR-38S, PEG, EP, and m-EP.

3.2. Thermal Properties of m-EPs

3.2.1. Latent Heat and Phase Change Temperature

Figure 6 demonstrated the DSC curves of the EPs and m-EPs. Their corresponding thermal properties are summarized in Table 5. As seen in Figure 6, the melting and crystallization temperatures of the EPs and m-EPs increased with the increase in the molecular mass of PEG. This feature was consistent with the trend of pristine PEG, indicating the successful incorporation of PEGs into the EG matrix. Meanwhile, the DSC curves of the m-EPs were smoother, and the endothermic/exothermic peaks were narrower in comparison to those of the EPs. This result indicated that applying a m-EG was beneficial for the stabilization of the FSPCM phase change process in the building envelopes. Specifically, the EPs exhibited lower  $T_{onset-m}$  and  $T_{onset-c}$  values compared with those of the PEGs, because the crystallization-promoting effects of the EG surface accelerated the crystallization of PEGs [31]. Furthermore, the  $T_{onset-m}$  and  $T_{onset-c}$  of the m-EPs approached or even exceeded the pristine PEGs. The reason could be interpreted in two aspects: for the elevation of  $T_{onset-m}$ , the molecular bridge of the coupling agent enhanced the bonding between the PEGs and the EG matrix; hence, more energy was required to transform the PEG crystal to liquid. As for the crystallization process, the KR-38S molecule improved the compatibility between the PEGs and the EG surface, and consequently hindered the heterogeneous nucleation of the PEGs. The reduction of  $\Delta T$  also supported this conclusion. Therefore, it can be concluded that the modification of the EG matrix improved the  $T_{onset-m}$ ,  $T_{onset-c}$ , and  $\Delta T$  of the m-EPs.

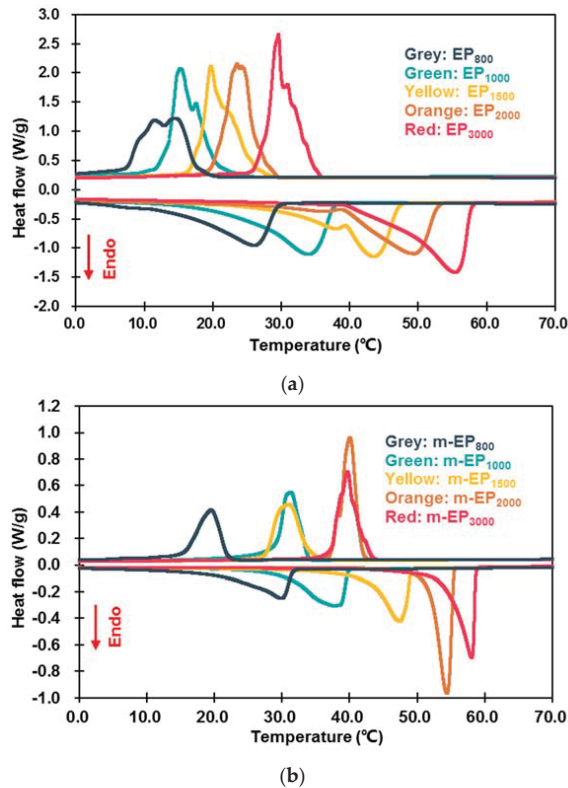


Figure 6. Differential scanning calorimeter (DSC) curves of EPs (a) and m-EPs (b).

**Table 5.** Thermal properties of EPs and m-EPs.

Categories	$T_{onset-m}$ (°C)	$T_{onset-c}$ (°C)	$\Delta T$ (°C)	$\Delta H_m$ (J/g)	$\Delta H_c$ (J/g)	$\eta_m$ (%)	$\eta_c$ (%)
EP <sub>800</sub>	14.30	17.53	−3.23	89.50	80.61	71.27	72.75
EP <sub>1000</sub>	23.96	18.49	5.47	108.22	101.92	75.83	76.59
EP <sub>1500</sub>	37.67	22.36	15.31	104.13	104.56	69.86	75.04
EP <sub>2000</sub>	39.29	26.36	12.93	110.40	107.01	67.38	71.16
EP <sub>3000</sub>	45.98	30.63	15.35	120.50	113.56	73.84	80.68
m-EP <sub>800</sub>	22.64	21.90	0.74	97.66	92.91	77.77	83.85
m-EP <sub>1000</sub>	30.18	33.64	−3.46	121.89	116.80	85.41	87.77
m-EP <sub>1500</sub>	42.67	33.93	8.74	122.94	114.88	82.48	82.45
m-EP <sub>2000</sub>	51.95	41.66	10.29	143.79	137.53	87.77	91.45
m-EP <sub>3000</sub>	54.63	41.27	13.36	141.60	124.12	86.77	88.18

Note:  $\eta_m$ : melting enthalpy efficiency,  $\eta_m = \frac{\Delta H_m \text{ of EP or m-EP}}{(\Delta H_m \text{ of PEG}) \times (\text{PEG \% in EP or m-EP})} \times 100\%$ ;  $\eta_c$ : crystallization enthalpy efficiency,  $\eta_c = \frac{\Delta H_c \text{ of EP or m-EP}}{(\Delta H_c \text{ of PEG}) \times (\text{PEG \% in EP or m-EP})} \times 100\%$ .

As for the latent heats during phase change, the  $\Delta H_m$  and  $\Delta H_c$  of the EPs and m-EPs were lower than that of their corresponding PEGs. This was because the supporting materials in the composites couldn't store thermal energy. Meanwhile, the  $\Delta H_m$  and  $\Delta H_c$  of the m-EPs were higher than that of the EPs. This could be attributed to the additional amount of PEGs that anchored on the m-EG matrix due to the strong chemical bonding. Furthermore, the  $\eta_m$  and  $\eta_c$  of the EPs were 67.38–75.83% and 71.16–80.68%, respectively, and the corresponding values for the m-EPs were 77.77–87.77% and 82.45–91.45%. It could be noted that all of the melting and crystallization enthalpies of the EPs and m-EPs were lower than the theoretical latent heat values. This was because the PEGs couldn't be incorporated into the pore structure of the matrix, and the residual PEGs on the surface would vanish during phase transition. It was also noted that the  $\eta_m$  values were lower than  $\eta_c$  for both the EPs and the m-EPs, which could be ascribed to the inherent supercooling in the PEGs, as shown in the DSC curves. In conclusion, applying m-EGs as the supporting material could increase both the melting and crystallization enthalpies of the m-EPs by approximately 10%, and the enhancement on thermal storage capacity would reduce the cost of m-EPs in buildings.

### 3.2.2. Thermal Stability

The thermal stability of EPs and m-EPs was evaluated by determining the mass loss. As the TGA curves illustrated in Figure 7 indicate, the EPs and m-EPs exhibited similar thermal stability characteristics. No decomposition occurred until the heating temperatures exceeded 300 °C, and the decomposition completed at the temperatures of 420 °C. Based on the TGA curves of EPs and m-EPs, it could be inferred that the thermal stabilities of EG-based FSPCMs were satisfied at the intermediate low temperature. By comparing the initial decomposition temperatures (defined in this research as the temperature at which 10% of the weight was lost) of EPs and m-EPs, it could be noticed that the initial decomposition temperatures of the m-EPs were approximately 20 °C higher than those of the EPs. This indicated that the modification endowed the m-EPs with better thermal stability, and these kinds of composite PCMs were able to embed in building materials under high temperatures. Furthermore, it is also worth noting that the residue of the EPs and m-EPs after TGA was about 13 wt %, which was equivalent to the mass ratio of the supporting materials.

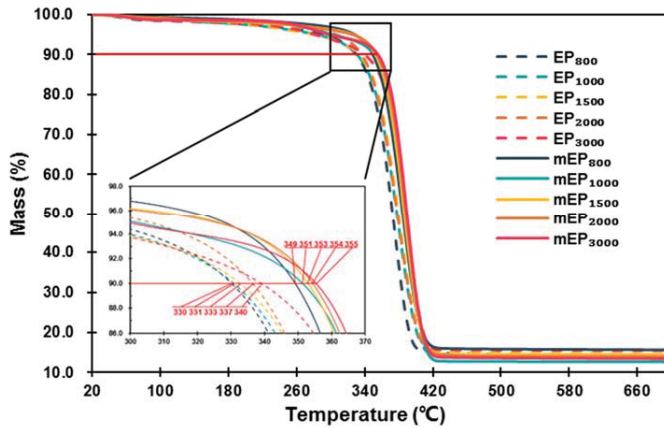


Figure 7. Thermogravimetric analyzer (TGA) curves of EPs and m-EPs.

### 3.2.3. Thermal Conductivity

The thermal conductivities of PEGs, EPs, and m-EPs were shown in Figure 8. Packing density affects the thermal transfer rates of EG-based PCMs significantly due to the high porosity and thermal conductivity of the EG matrix. Therefore, the EPs and m-EPs were pressed to tablet samples, and their packing densities were consistent with the pristine PEGs. As illustrated in Figure 8, the measured thermal conductivities of pristine PEGs were as low as approximately 0.3 W/m·K, which was detrimental to the thermal energy storage efficiency in the building envelopes. When the EG matrix was applied, the thermal conductivities of EPs were increased significantly to about 3.5 W/m·K. This proved the enhancement of the EG matrix on the thermal transfer rate of the latent heat thermal energy storage system. Meanwhile, the thermal conductivity of the pristine PEGs increased with the increase in their molecular mass, and a similar tendency could be detected in the thermal conductivities of the EPs and m-EPs. This result indicated that both the properties of the supporting and functional components determined the thermal performance of the FSPCMs. Furthermore, the thermal conductivity values of the m-EPs were slightly lower in comparison with those of the EPs. This might be because the modification of the organic coupling agent decreased the thermal transfer rate of the EG matrix to some extent. Even so, the thermal conductivities of the m-EPs were still 10 times higher than those of the pristine PEGs, which ensured a rapid response to the temperature fluctuations in the buildings.

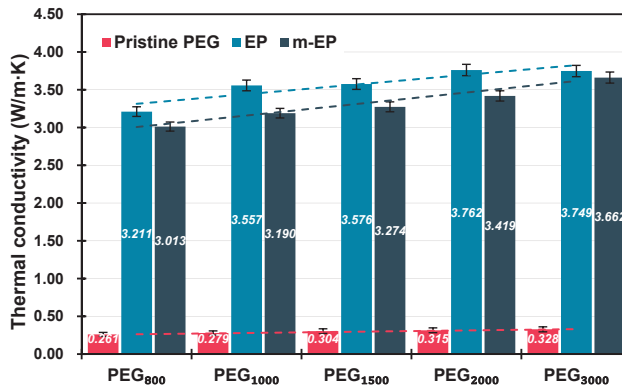


Figure 8. Thermal conductivity of PEGs, EGs, and m-EGs at the same packing density.

#### 4. Conclusions

An expanded graphite (EG)/polyethylene glycol (PEG) composite phase change material (PCM) was prepared for the purpose of bridging the gap between energy supply and demand in buildings. A titanate coupling agent KR-38S was used to build a molecular bridge between EG and PEG, and various thermal properties of the composite PCM were investigated in this paper. The following conclusions were drawn:

The EG matrix with macropores and mesopores was beneficial to the absorption of PEG. The optimal EG particle size for PEG absorption was determined as 125  $\mu\text{m}$ , and the maximum mass ratio of PEG to EG was 1:7 in this research. The modification of KR-38S increased the quantity of the oxygen functional groups on the EG matrix, and a stable molecular bridge was established between the EG matrix and PEG. The optimal modification condition was obtained by adding 3 wt % of KR-38S at 60  $^{\circ}\text{C}$ . Compared with the EPs, the melting and crystallization temperatures of the m-EPs showed little variation, but the phase change temperature ranges and supercooling degree decreased significantly, indicating that the phase transition abilities of the EPs were enhanced after modification. The melting and crystallization enthalpies of the m-EPs increased by approximately 10%, and the initial decomposition temperatures rose by about 20  $^{\circ}\text{C}$  in comparison with the EPs. These results indicated the improvements to the thermal energy storage efficiency and stability of the m-EPs, which are beneficial for the application of m-EPs in building envelopes. The thermal conductivities of the m-EPs were 10 times higher than those of the pristine PEGs. This result indicated that using m-EPs in building envelopes could enhance the heat transfer rate as well as ensure a rapid response to temperature fluctuations.

In summary, using titanate coupling agent could build a molecular bridge in m-EPs, and improve the phase change temperature range, supercooling, heat storage density, thermal stability, and thermal conductivity of m-EPs. This research can benefit the application of PCMs in building energy conservation.

**Author Contributions:** M.C. and D.Z. conceived and designed the experiments; D.Z., J.H. and J.W. performed the experiments; M.C. and D.Z. analyzed the data; Q.L. contributed reagents/materials/analysis tools; D.Z. wrote the paper.

**Funding:** This research was funded by the National Natural Science Foundation of China (No. 51778515). The authors gratefully acknowledge their financial support.

**Conflicts of Interest:** There are no conflicts of interest regarding the publication of this paper.

#### References

1. EIA. *International Energy Outlook 2017*; U.S. Energy Information Administration: Washington, DC, USA, 2017.
2. BP. *BP Energy Outlook 2017 Edition*; BP PLC: London, UK, 2017.
3. Grimaud, A.; Rougé, L. Polluting non-renewable resources, innovation and growth: Welfare and environmental policy. *Resour. Energy Econ.* **2005**, *27*, 109–129. [[CrossRef](#)]
4. Qin, M.; Walton, G.; Belarbi, R.; Allard, F. Simulation of whole building coupled hygrothermal-airflow transfer in different climates. *Energy Convers. Manag.* **2011**, *52*, 1470–1478. [[CrossRef](#)]
5. Wang, E.; Kong, X.; Rong, X.; Yao, C.; Yang, H.; Qi, C. A study on a novel phase change material panel based on tetradecanol/lauric acid/expanded perlite/aluminium powder for building heat storage. *Materials* **2016**, *9*, 896. [[CrossRef](#)] [[PubMed](#)]
6. Šavija, B.; Zhang, H.; Schlangen, E. Influence of microencapsulated phase change material (PCM) addition on (Micro) mechanical properties of cement paste. *Materials* **2017**, *10*, e863. [[CrossRef](#)] [[PubMed](#)]
7. Ismail, K.A.R.; Castro, J.N.C. PCM thermal insulation in buildings. *Int. J. Energy Res.* **2015**, *21*, 1281–1296. [[CrossRef](#)]
8. Sharma, A.; Tyagi, V.V.; Chen, C.R.; Buddhi, D. Review on thermal energy storage with phase change materials and applications. *Renew. Sustain. Energy Rev.* **2009**, *13*, 318–345. [[CrossRef](#)]
9. Kuznik, F.; David, D.; Johannes, K.; Roux, J.J. A review on phase change materials integrated in building walls. *Renew. Sustain. Energy Rev.* **2011**, *15*, 379–391. [[CrossRef](#)]

10. Akeiber, H.; Nejat, P.; Majid, M.Z.A.; Wahid, M.A.; Jomehzadeh, F.; Famileh, I.Z.; Calautit, J.K.; Hughes, B.R.; Zaki, S.A. A review on phase change material (PCM) for sustainable passive cooling in building envelopes. *Renew. Sustain. Energy Rev.* **2016**, *60*, 1470–1497. [[CrossRef](#)]
11. Raj, V.A.A.; Velraj, R. Review on free cooling of buildings using phase change materials. *Renew. Sustain. Energy Rev.* **2010**, *14*, 2819–2829. [[CrossRef](#)]
12. Shon, J.; Kim, H.; Lee, K. Improved heat storage rate for an automobile coolant waste heat recovery system using phase-change material in a fin–tube heat exchanger. *Appl. Energy* **2014**, *113*, 680–689. [[CrossRef](#)]
13. Li, M. A nano-graphite/paraffin phase change material with high thermal conductivity. *Appl. Energy* **2013**, *106*, 25–30. [[CrossRef](#)]
14. Mesalhy, O.; Lafdi, K.; Elgafy, A.; Bowman, K. Numerical study for enhancing the thermal conductivity of phase change material (PCM) storage using high thermal conductivity porous matrix. *Energy Convers. Manag.* **2005**, *46*, 847–867. [[CrossRef](#)]
15. Kuznik, F.; Virgone, J.; Johannes, K. In-situ study of thermal comfort enhancement in a renovated building equipped with phase change material wallboard. *Renew. Energy* **2011**, *36*, 1458–1462. [[CrossRef](#)]
16. Onder, E.; Sarier, N.; Cimen, E. Encapsulation of phase change materials by complex coacervation to improve thermal performances of woven fabrics. *Thermochim. Acta* **2008**, *467*, 63–72. [[CrossRef](#)]
17. Zhang, H.; Wang, X.; Wu, D. Silica encapsulation of n-octadecane via sol–gel process: A novel microencapsulated phase-change material with enhanced thermal conductivity and performance. *J. Colloid Interface Sci.* **2010**, *343*, 246–255. [[CrossRef](#)] [[PubMed](#)]
18. Ma, B.; Zhou, X.; Liu, J.; You, Z.; Wei, K.; Huang, X. Determination of specific heat capacity on composite shape-stabilized phase change materials and asphalt mixtures by heat exchange system. *Materials* **2016**, *9*, 389. [[CrossRef](#)] [[PubMed](#)]
19. Yu, J.X.; Liu, T.Q. Preparation and characterization of microencapsulated phase change coating. *Appl. Mech. Mater.* **2013**, *204–208*, 4173–4176. [[CrossRef](#)]
20. Zhang, Z.; Fang, X. Study on paraffin/expanded graphite composite phase change thermal energy storage material. *Energy Convers. Manag.* **2006**, *47*, 303–310. [[CrossRef](#)]
21. Sari, A.; Karaipekli, A. Thermal conductivity and latent heat thermal energy storage characteristics of paraffin/expanded graphite composite as phase change material. *Appl. Therm. Eng.* **2007**, *27*, 1271–1277. [[CrossRef](#)]
22. Xia, L.; Zhang, P.; Wang, R.Z. Preparation and thermal characterization of expanded graphite/paraffin composite phase change material. *Carbon* **2010**, *48*, 2538–2548. [[CrossRef](#)]
23. Zeng, J.L.; Gan, J.; Zhu, F.R.; Yu, S.B.; Xiao, Z.L.; Yan, W.P.; Zhu, L.; Liu, Z.Q.; Sun, L.X.; Cao, Z. Tetradecanol/expanded graphite composite form-stable phase change material for thermal energy storage. *Sol. Energy Mater. Sol. Cells* **2014**, *127*, 122–128. [[CrossRef](#)]
24. Wang, S.; Qin, P.; Fang, X.; Zhang, Z.; Wang, S.; Liu, X. A novel sebacic acid/expanded graphite composite phase change material for solar thermal medium-temperature applications. *Sol. Energy* **2014**, *99*, 283–290. [[CrossRef](#)]
25. Ling, Z.; Chen, J.; Xu, T.; Fang, X.; Gao, X.; Zhang, Z. Thermal conductivity of an organic phase change material/expanded graphite composite across the phase change temperature range and a novel thermal conductivity model. *Energy Convers. Manag.* **2015**, *102*, 202–208. [[CrossRef](#)]
26. Zhang, Z.; Shi, G.; Wang, S.; Fang, X.; Liu, X. Thermal energy storage cement mortar containing n-octadecane/expanded graphite composite phase change material. *Renew. Energy* **2013**, *50*, 670–675. [[CrossRef](#)]
27. Li, M.; Wu, Z.; Tan, J. Heat storage properties of the cement mortar incorporated with composite phase change material. *Appl. Energy* **2013**, *103*, 393–399. [[CrossRef](#)]
28. He, Y.; Zhang, X.; Zhang, Y.; Song, Q.; Liao, X. Utilization of lauric acid-myristic acid/expanded graphite phase change materials to improve thermal properties of cement mortar. *Energy Build.* **2016**, *133*, 547–558. [[CrossRef](#)]
29. Lüth, H. *Surfaces and Interfaces of Solids*; Springer: Berlin, Germany, 1995.



30. Shirley, D.A. High-resolution x-ray photoemission spectrum of the valence bands of gold. *Phys. Rev. B* **1972**, *5*, 4709–4714. [[CrossRef](#)]
31. Xia, L.; Zhang, P. Thermal property measurement and heat transfer analysis of acetamide and acetamide/expanded graphite composite phase change material for solar heat storage. *Sol. Energy Mater. Sol. Cells* **2011**, *95*, 2246–2254. [[CrossRef](#)]



© 2018 by the authors. Licensee MDPI, Basel, Switzerland. This article is an open access article distributed under the terms and conditions of the Creative Commons Attribution (CC BY) license (<http://creativecommons.org/licenses/by/4.0/>).

Article

# Graphene-Modulated Removal Performance of Nitrogen and Phosphorus Pollutants in a Sequencing Batch *Chlorella* Reactor

Gonghan Xia <sup>1</sup>, Wenlai Xu <sup>1,2,3,\*</sup>, Qinglin Fang <sup>1</sup>, Zishen Mou <sup>1,\*</sup> and Zhicheng Pan <sup>2</sup>

<sup>1</sup> State Key Laboratory of Geohazard Prevention and Geoenvironment Protection, Chengdu University of Technology, Chengdu 610059, China; txgsfy@163.com (G.X.); nstxdy@163.com (Q.F.)

<sup>2</sup> Haitian Water Grp. Co. Ltd., Chengdu 610059, China; pan12487616@126.com

<sup>3</sup> Department of Chemical Engineering, Tokyo University of Agriculture & Technology, Tokyo 1848588, Japan

\* Correspondence: xwl@my.swjtu.edu.cn (W.X.); mouzishenchengdu@163.com (Z.M.); Tel.: +86-135-510-29646 (W.X.)

Received: 31 July 2018; Accepted: 29 October 2018; Published: 4 November 2018

**Abstract:** In this work, the influence of graphene on nitrogen and phosphorus in a batch *Chlorella* reactor was studied. The impact of graphene on the removal performance of *Chlorella* was investigated in a home-built sewage treatment system with seven identical sequencing batch *Chlorella* reactors with graphene contents of 0 mg/L (T1), 0.05 mg/L (T2), 0.1 mg/L (T3), 0.2 mg/L (T4), 0.4 mg/L (T5), 0.8 mg/L (T6) and 10 mg/L (T7). The influence of graphene concentration and reaction time on the pollutant removal performance was studied. The malondialdehyde (MDA) and total superoxide dismutase (SOD) concentrations in each reactor were measured, and optical microscopy and scanning electron microscopy (SEM) characterizations were performed to determine the related mechanism. The results show that after 168 h, the total nitrogen (TN), ammonia nitrogen (AN) and total phosphorus (TP) removal rates of reactors T1–T7 become stable, and the TN, AN and TP removal rates were gradually reduced with increasing graphene concentration. At 96 h, the concentrations of both MDA and SOD in T1–T7 gradually increased as the graphene concentration increased. In optical microscopy and SEM measurements, it was found that graphene was adsorbed on the surface of *Chlorella*, and entered *Chlorella* cells, deforming and reducing *Chlorella*. Through the blood plate count method, we estimated an average *Chlorella* reduction of 16%. According to the water quality and microscopic experiments, it can be concluded that the addition of graphene causes oxidative damage to microalgae and destruction of the *Chlorella* cell wall and cell membrane, inhibiting the nitrogen and phosphorus removal in *Chlorella* reactors. This study provides theoretical and practical support for the safe use of graphene.

**Keywords:** graphene; nitrogen and phosphorus removal; MDA; SOD; sequencing batch *Chlorella* reactor; SEM

## 1. Introduction

Since Geim et al. used graphite to prepare graphene in 2004, scientists in various fields have extensively studied the physical, chemical, electrical, optical and mechanical properties of graphene [1]. Thanks to its special structure, high thermal conductivity, excellent electrical conductivity, high mechanical strength and unique optical properties, graphene can be widely used in the fields of composite materials, energy, catalysis, electronic devices, optical detection and environmental protection.

In the process of production, transportation, application, treatment and recovery, graphene will inevitably enter the environment. As a nanomaterial, microscale graphene can cause certain toxic

effects on plants, animals and microorganisms [2]. If the functional microorganisms in the wastewater treatment process suffer from the toxic effect, the sewage treatment efficiency can be directly affected.

Using algae to treat wastewater is a hot topic in the environmental field. Chen Guang et al. used two cascade high-efficiency algal pond systems to treat rural sewage in Taihu, and showed that when the hydraulic retention time (HRT) was 8 days, the average removal rates of COD (chemical oxygen demand), TN and TP were 69.4%, 41.7% and 45.6%, respectively [3]. Huang et al. studied a high-efficiency algal pond system for treating rural sewage in Taihu. At HRT of 1.6 days, the effluent TN and TP can be kept at 5 mg/L and below 1 mg/L, respectively, which complies with the GB189182-2002 first level B emission standard of China [4]. Li et al. applied algal-immobilized methods to realize nitrogen and phosphorus removal in domestic sewage [5].

The influence of nanoparticles on algae has also been studied [6–9]. Li et al. studied the cell coercion of nano nickel oxide to *Chlorella vulgaris*, and found that the cell apoptosis phenomenon occurred when the cells were exposed to nano NiO [10]. Zhu et al. studied the toxic effects of fullerene (C<sub>60</sub>), single-walled carbon nanotubes (SWCNTs) and multiwalled carbon nanotubes on *Scenedesmus obliquus*. The results showed that the minimum inhibitory concentrations of the three materials for *Scenedesmus obliquus* were 5, 10 and 0.5 mg/L, respectively [11]. Xiao et al. carried out experiments on the effect of nano ZnO on phosphorus removal by *Chlorella*, and concluded that the addition of nano ZnO could inhibit the growth of *Chlorella*. The phosphorus removal efficiency of *Chlorella vulgaris* decreased from 76.2% to 27.4% in the first 7 h [12]. At present, the toxicity of nanoscale graphene to algae is mostly manifested in harmful effects on algae quantity, morphology and enzyme activity in vivo. The effect of graphene nanoparticles on nitrogen and phosphorus in activated sludge treatment systems has been widely studied. Nevertheless, there is almost no report on the effect on algae wastewater treatment systems. Therefore, the purpose of this paper is to reflect the effect of graphene nanoparticles on the removal of nitrogen and phosphorus from algae wastewater treatment systems, as well as to analyze the toxicity of graphene to algae from a novel point of view of wastewater treatment. Overall, in this work, the effect of graphene on a sequencing batch *Chlorella* reactor was studied.

*Chlorella pyrenoidosa* exhibits great efficiency in water treatment. In the experiments by Wang et al., the removal rates of nitrogen and COD in living sewage by *Chlorella* were 69% and 80.9%, respectively [13]. According to the study by Lu Furong and Huang Kui [14,15], the removal efficiency of nitrogen and phosphorus by *Chlorella* spp. could reach 70% and 60%, respectively, in the first 12 h under autotrophic conditions, and the organic compounds in a water body could be enriched and absorbed as assimilated carbon sources, nitrogen sources and sulfur sources during the growth and reproduction of *Chlorella* spp. Therefore, the timely addition of organic carbon will promote the absorption of nitrogen and phosphorus by *Chlorella*. By comparing the six species of algae, Cai et al. concluded that *Chlorella vulgaris* was suitable for nitrogen and phosphorus removal, and the removal rates of TP, TN and AN were 87.88%, 87.27% and 89.25%, respectively [16]. Through the test of five species of algae, Huang et al. concluded that *Chlorella* is the most suitable organism for sewage treatment. The removal rate of nitrogen and phosphorus in water can reach over 80% [17]. In this study, a home-built sequencing batch *Chlorella* reactor was employed, and *Chlorella vulgaris* was selected as the algae species. Graphene was added into the reactor. The effect of graphene concentration and reaction time on the wastewater treatment efficiency was studied, and the toxicity of graphene to the sequencing batch *Chlorella* reactor system was explored.

## 2. Materials and Methods

### 2.1. Experimental Materials

#### 2.1.1. Source of Graphene

Graphene was acquired from the xGnp Grade M graphene powder (American XGS Company, New York, NY, USA), which was stacked together by 6–10 layers of graphene sheets. The average

thickness of the sheet is about 6–8 nm, and the specific surface area is 120–150 m<sup>2</sup>/g. The average diameter of the sheet is 5 μm.

### 2.1.2. Source of *Chlorella*

The algae species were provided by the aquatic organisms of the Chinese Academy of Sciences (Beijing, China), which were cultured in a light incubator at 4000 lux, 23 °C, light/dark ratio of 12 h:12 h, and oscillating two times a day (8:00–9:00; 18:00–19:00). The BG (Blue-Green) 11 medium (Beijing Land Bridge Technology CO, LTD, Beijing, China) was used in the culture medium. The references of BG medium can be found in [18].

### 2.1.3. Simulated Domestic Wastewater

In this experiment, artificial domestic sewage was prepared, and the water composition and its distribution were as the following (mg/L): C<sub>6</sub>H<sub>12</sub>O<sub>6</sub> 150; peptone 150; CH<sub>3</sub>COONa 80; NH<sub>4</sub>Cl 80; KH<sub>2</sub>PO<sub>4</sub> 26; MgSO<sub>4</sub>·7H<sub>2</sub>O 180; CaCl<sub>2</sub> 10.6; NaHCO<sub>3</sub> 80; EDTA 3; FeCl<sub>3</sub>·6H<sub>2</sub>O 0.45; MnCl<sub>2</sub>·6H<sub>2</sub>O 0.036; H<sub>3</sub>BO<sub>3</sub> 0.045; ZnSO<sub>4</sub>·7H<sub>2</sub>O 0.036; CuSO<sub>4</sub>·5H<sub>2</sub>O 0.054; KI 0.054. The pH of the wastewater was adjusted to 8 [19].

### 2.2. Measurement Methods

According to the national standard method of China, TN was determined by alkaline potassium persulfate method, AN was determined by Nessler's reagent photometry, and TP was obtained by ammonium molybdate spectrophotometric method. MDA and SOD indicators were purchased from Nanjing Jian Technology Co, Ltd (Nanjing, China).

### 2.3. Experimental Methods

Seven identical sequencing batch *Chlorella* reactors T1, T2, T3, T4, T5, T6 and T7 were employed in the experiment. The volume of the reactors was 500 mL, as shown in Figure 1. Each reactor contained 250 mL artificial wastewater (high-temperature sterilization was used to avoid the influence of functional microorganisms in water). The number of initial *Chlorella* was 1.75 × 10<sup>6</sup>. The TN content was 46.9 mg/L ± 0.1%, AN was 42.9 mg/L ± 0.2%, and TP was 2.1 mg/L ± 0.1%.

Graphene was added to each reactor, and the graphene concentration in each reactor is shown in Table 1.

**Table 1.** Graphene concentration in each reactor.

	T1	T2	T3	T4	T5	T6	T7
Graphene (mg/L)	0	0.5	1	2	4	8	10

According to the optimum growth conditions of *Chlorella vulgaris* [14], the reactor was placed in the light incubator at 4000 lux and 23 °C. 60 mL reaction liquid was taken every 12 h using a filter membrane suction method. Next, 60 mL artificial wastewater (high-temperature sterilization) with the same initial concentration was added to the reactor, and the TN, AN and TP were measured for each discharging water. The effect of graphene on removal efficiency of nitrogen and phosphorus pollutant in the sequencing batch *Chlorella* reactor was investigated.

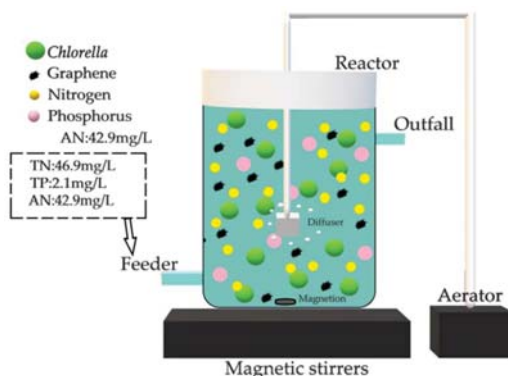


Figure 1. Schematic diagram of the reactor.

#### 2.4. Oxidative Stress Experiment

Based on the water quality experiment, the concentration of MDA and the activity of SOD in each reactor were determined.

MDA is an important indicator of cell oxidative damage. It mainly reflects the concentration of oxygen free radicals produced by the interaction among phospholipids, enzymes and fatty acids in membrane receptors. Higher MDA concentration leads to greater lipid peroxidation in plant cells, which indirectly reflects the degree of damage to the organism. The vitality of SOD reflects the ability of the organism to scavenge oxygen free radicals, and increasing SOD activity indicates the increase of oxygen free radicals in plant cells. Therefore, SOD indicators often match the MDA index with the oxidative damage of reactive cells.

The MDA kit is developed by Nanjing Jian Cheng Technology Co, Ltd (Nanjing, China). The test method is as follows:

The reagent and the sample were added to the test kit. The test tubes include blank tube ( $OD_0$ ), standard tube ( $OD_s$ ), measuring tube ( $OD_m$ ) and the care ( $OD_c$ ). The vortex mixer of each sample was mixed, and the tube mouth was tightened with fresh-keeping film. A small hole was opened with needle, and the water bath was set to 95 °C for 40 min. After being taken out of the water, the sample was cooled, followed by centrifugation for ten minutes at 3500–4000 turns/points. The absorbance of the supernatant for each tube was measured at 523 nm and 1 cm light path. Double water was used to calibrate zero point.

The formula for calculating MDA content in plant tissues is as below (1):

$$MDA = \frac{OD_m - OD_c}{OD_s - OD_0} \times 10 \text{ nmol/mL} \div C(\text{protein}) \quad (1)$$

The SOD kit is developed by Nanjing Technology Co, Ltd (Nanjing, China). The test method is as follows:

According to the reagent box operation and samples, the test tube ( $OD_m$ ) and the sample ( $OD_c$ ) were used. The vortex mixer of each sample was mixed and placed at 37 °C for 40 min in water bath with constant temperature. Next, the chromogenic agent was added to the mix, and placed at room temperature for ten minutes. The absorbance of the supernatant of each tube was measured at 550 nm and 1 cm light path with double water to adjust zero.

The formula for calculating the total SOD vitality is shown in Equation (2):

$$SOD = \frac{OD_c - OD_m}{OD_c} \div 50\% \times \frac{V_{\text{total}}}{V_{\text{sampling}}} \div C(\text{protein}) \quad (2)$$

### 3. Results and Discussions

#### 3.1. Graphene Characterization

Graphene characterization is shown in Figure 2.

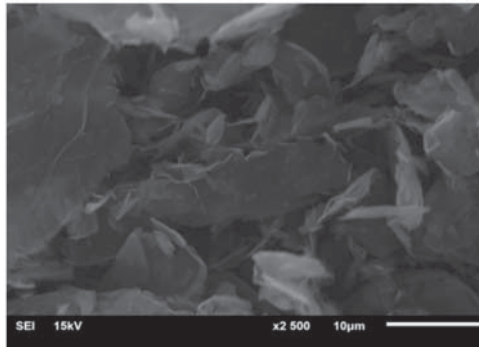


Figure 2. SEM characterization of graphene sheets.

#### 3.2. Effect of Graphene Content and Reaction Time on Removal Efficiency of Pollutants in Reactor

##### 3.2.1. Treatment Effect of TN in Reactors T1–T7

From Figure 3, it can be seen that the removal efficiency of TN in T1 (the concentration of graphene is 0 mg/L) increases gradually at 0–96 h. After 96 h, the removal rate of TN tends to be stable at  $51.7\% \pm 0.3\%$ .

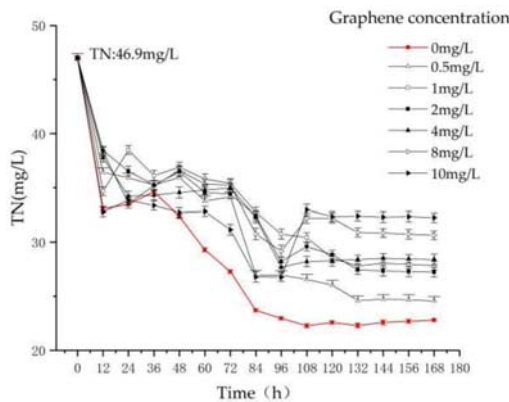


Figure 3. The variation of TN as a function of reaction time and graphene concentration.

At 0–96 h, the removal rate of TN increases with different graphene concentrations in T2–T7. At 12 h, the removal efficiency of T7 (the concentration of graphene is 10 mg/L) is greater than T1, indicating that graphene has adsorption on TN. After 96 h, the TN concentrations of reactors T4, T5, T6 and T7 increase, and the TN concentrations in reactors T2 and T3 become stable, which indicates that the capacity of the reactor to remove TN decreases with increasing graphene concentration. Finally, the TN removal rates of T2–T7 are stable at  $47.7\% \pm 0.1\%$ ,  $42.9\% \pm 0.3\%$ ,  $41.5\% \pm 0.4\%$ ,  $39.6\% \pm 0.2\%$ ,  $34.9\% \pm 0.1\%$ , and  $30.8\% \pm 0.3\%$ , respectively. In this experiment, the removal efficiency of TN in the sequencing batch *Chlorella* reactor decreases as the concentration of graphene increases.

### 3.2.2. Treatment Effect of AN in Reactors T1–T7

From Figure 4, the AN removal in each reactor is similar to TN, indicating that the removal of nitrogen in the sequencing batch *Chlorella* reactor is mainly due to the removal of AN. In T1, the removal rate of AN tends to be stable at  $73.2\% \pm 0.4\%$ .

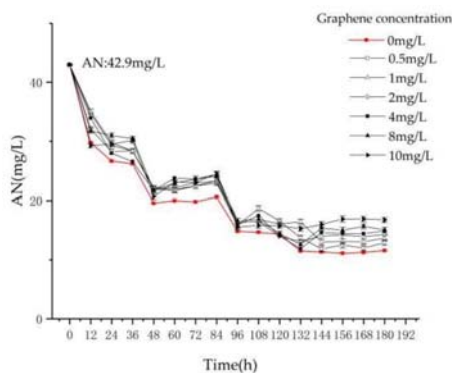


Figure 4. The variation of AN with reaction time and graphene concentration.

In T2–T7, the removal rate of AN by T7 in the first 12 h is greater than T1, which proves that graphene has adsorption effect on AN in water. However, with increasing time, the adsorption of graphene in reactor T7 becomes gradually stable, and the removal of AN mainly depends on the assimilation of *Chlorella* to AN and the volatilization of AN itself [20–22]. At 0–121 h, the concentrations of AN in reactors T1–T7 are decreasing due to volatilization and *Chlorella* assimilation. After 121 h, the gradual increase of graphene concentration in T2–T7 increases the destruction of *Chlorella*. Finally, the removal efficiencies of AN in T2–T7 are stable at  $70\% \pm 0.5\%$ ,  $68.3\% \pm 0.2\%$ ,  $66.9\% \pm 0.2\%$ ,  $65.4\% \pm 0.1\%$ ,  $65.1\% \pm 0.4\%$ , and  $61.2\% \pm 0.3\%$ , respectively. In this experiment, the removal efficiency of AN in the sequencing batch *Chlorella* reactor decreases as the concentration of graphene increases.

### 3.2.3. Treatment Effect of TP in Reactors T1–T7

From Figure 5, graphene shows great influence on TP in the reactor. In T1, the removal efficiency of TP is stable at  $80.6\% \pm 0.8\%$ .

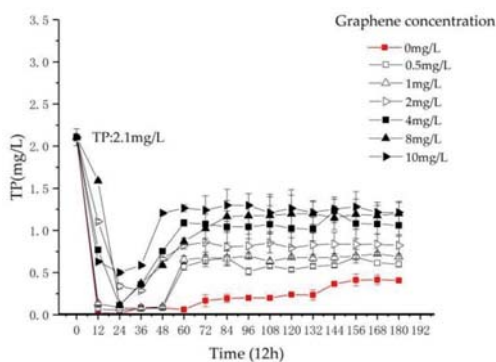


Figure 5. The variation of TP with reaction time and graphene concentration.

At 0–36 h, the TP concentration in T2–T7 decreases continuously. After 36 h, the TP concentration in T2–T7 increases continuously. The TP concentrations in T2–T7 after 168 h are rising gradually.



The removal efficiencies of TP in T2–T7 are stable at  $71.4\% \pm 0.3\%$ ,  $67.3\% \pm 0.2\%$ ,  $61\% \pm 0.1\%$ ,  $49.6\% \pm 0.1\%$ ,  $43\% \pm 0.3\%$  and  $42.3\% \pm 0.3\%$ , respectively.

In previous studies, the destruction of the algal cell wall and cell membrane by nanoparticles was observed. The increase of TP in the reactor containing graphene is due to the damage by graphene to the cell wall and cell membrane of *Chlorella*. The reduction of *Chlorella* quantity reduced the phosphorus removal efficiency, and the decomposition of *Chlorella vulgaris* itself increases the phosphorus content in the process. This result is consistent with the research by Xiao et al. on phosphorus removal in a nano-ZnO-treated *Chlorella* treatment system [12].

To sum up, in the determination of TN, AN and TP in the reactor, the addition of graphene inhibited the removal of nitrogen and phosphorus pollutants in the reactor. On one hand, the photosynthesis of *Chlorella vulgaris* may be affected by the shielding effect of graphene. On the other hand, there may be a toxic effect by graphene as a nanoparticle on *Chlorella*, leading to *Chlorella* damage, decreasing its quantity and self-decomposition. Therefore, the nitrogen and phosphorus in water cannot be effectively removed.

### 3.3. Oxidative Stress Experiment

In the experiment of water quality test for T1–T7, we can conclude that the increase of graphene concentration decreases the efficiency of *Chlorella* in nitrogen and phosphorus removal. In order to further verify the effect of graphene on the damage and reduction of *Chlorella*, the MDA content and SOD activity in the reactor were measured, and the *Chlorella* was observed by high-magnification optical microscopy and SEM.

#### 3.3.1. Result of MDA Measurements

Cells can produce oxygen free radicals by enzyme systems and nonenzyme systems. Oxygen free radicals can cause cell damage by peroxidation of polyunsaturated fatty acids in biofilm, triggering lipid peroxidation and forming lipid peroxides. MDA is a product of lipid peroxidation. MDA can be determined by lipid peroxidation. It reflects the degree of lipid peroxidation and indirectly reflects the extent of cell damage.

Combined with the above pollutant removal experiments, the water samples from each reactor were used to determine the concentration of MDA at 96 h [14].

From Figure 6, at 0–96 h, with the increase of graphene concentration in reactors T1–T7, the concentrations of MDA increase. Compared to T1, the increase of MDA in T2 is not obvious. This indicates that the oxidation damage of *Chlorella* is not obvious at low graphene concentration. Nevertheless, after increasing the concentration of graphene, the increase of MDA becomes significant. In T7, the MDA concentration of 27.54 nmol/mL is 6.16-times that of T1, which proves that graphene can cause heavy damage to *Chlorella* cells.

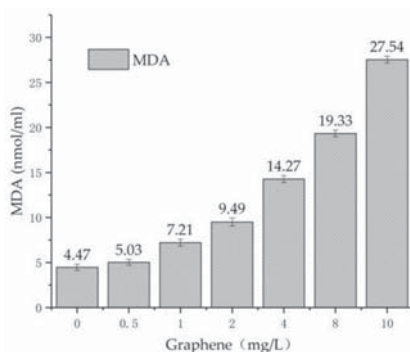


Figure 6. The variation of MDA with graphene concentration.

### 3.3.2. Results of SOD Determination

SOD plays an important role in the oxidation and antioxidant balance of the body. SOD can clear the superoxide anion radical, and protect the cell from damage. High SOD activity indicates high free-radical content and high degree of cell damage.

Combined with the above pollutant removal experiments, 96 h was used as the time to determine the SOD concentration [10]. From Figure 7, in T1–T7, the concentration of SOD increases with the increase of graphene concentration, from the initial 1.15  $\mu$ /mg prot to 19.25  $\mu$ /mg prot. The addition of graphene induces the increase of SOD activity in *Chlorella*, which is also related to the increase of MDA. The corresponding relationship between SOD and MDA proves that graphene produces oxidative stress on *Chlorella*. The research [22] by Zhao shows that the nanoparticles can combine with the algae chloroplast to cause lipid peroxidation of the algae cell membrane. The result is consistent with our study.

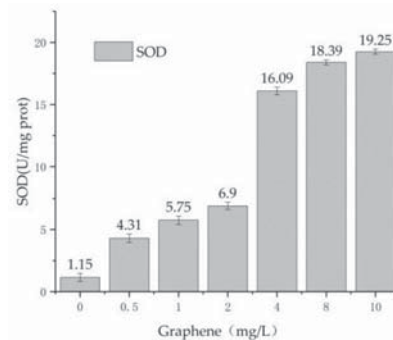


Figure 7. The variation of SOD with graphene concentration.

### 3.3.3. Observation by Optical Microscope

Through the test of MDA concentration and SOD activity, the damage effect of graphene to the algal cells in reactor T4 is apparent. Therefore, the *Chlorella* from T1 and T4 were examined under a 40 $\times$  optical microscope. It can be seen from Figure 8 that the morphology and internal structure of *Chlorella vulgaris* under normal conditions (T1) and with added graphene (T4) demonstrate significant change under microscope. Figure 8a shows that the *Chlorella* in T1 is striped or spherical with the basic structure of microorganisms inside the cell, such as chloroplasts. Figure 8b shows that there are some black materials in the microalgal algae. From the image, we can see that graphene enters the *Chlorella* cell, and affects the chloroplast inside the *Chlorella*. Combining with previous experiments on the coexistence of *Chlorella* and graphene, the experiments show that graphene exerts a harmful effect on the growth of *Chlorella*. The result [23] is consistent with our study.

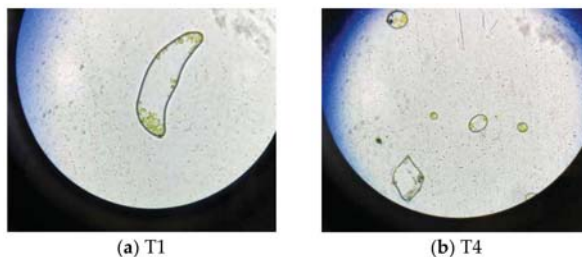
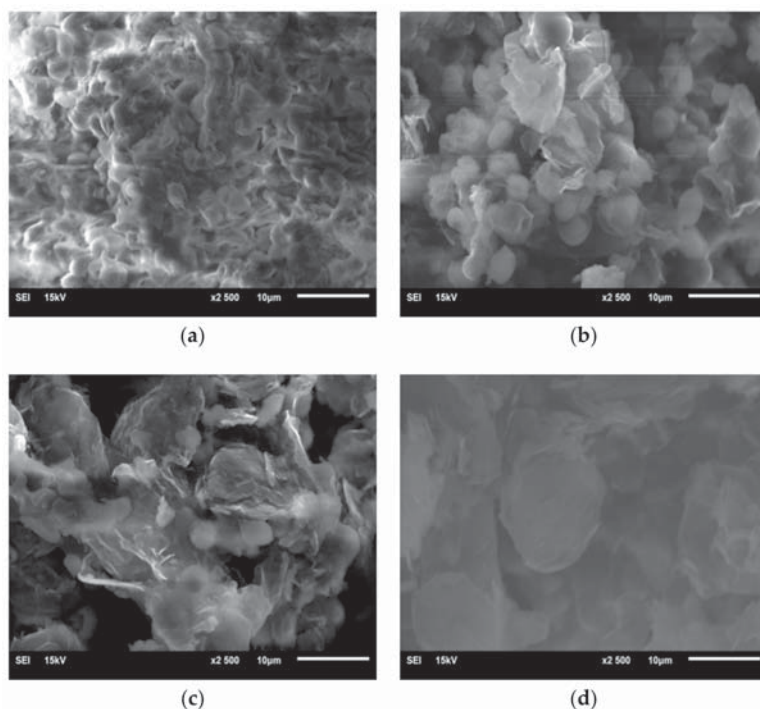


Figure 8. (a) *Chlorella vulgaris* under normal conditions; (b) *Chlorella* in reactor T4 with graphene addition.

### 3.3.4. SEM Measurements

In order to further obtain morphological changes of *Chlorella* with increasing graphene concentration, *Chlorella vulgaris* in T1, T3, T5 and T6 reactors was observed under SEM. From Figure 9, *Chlorella* in T1 has a smooth surface with regular morphological algal bloom (Figure 9a). When graphene is introduced in T3, it forms flocs around the *Chlorella*. It is speculated that the addition of graphene causes self-protection of *Chlorella*, resulting in increased extracellular polymeric substances on the surface of *Chlorella* (Figure 9b). The increase of graphene and decrease in the number of *Chlorella* can be seen in T5 (Figure 9c). The morphology of *Chlorella* in reactor T5 is irregular. The white flocculus surface of *Chlorella* is surrounded by *Chlorella*, and *Chlorella* demonstrates an irregular smog-ball shape (Figure 9c). From the *Chlorella* in T6 (Figure 9d), complete *Chlorella* almost disappears, and the surface of *Chlorella* is covered by graphene. The full contact between graphene and *Chlorella* causes the morphology of *Chlorella* to become extremely irregular, and the white floc on the surface of *Chlorella* disappears. Instead of white floc, flaky graphene, attached to the surface of *Chlorella*, damages the *Chlorella*.



**Figure 9.** (a) SEM image of *Chlorella* in normal state; (b) SEM image of *Chlorella* in reactor T3 with graphene concentration of 1 mg/L; (c) SEM image of *Chlorella* in reactor T5 with graphene concentration of 4 mg/L; (d) SEM image of *Chlorella* in reactor T6 with graphene concentration 8 mg/L.

Using the blood plate count method, we obtained *Chlorella* with an average reduction of 16%.

## 4. Conclusions

- (1) In the experiment of pollutant removal, the removal rates of TN and AN of reactors T1–T7 decrease with the increase of graphene concentration, and the removal efficiency of TN in reactor T2–T7 is lower than T1 by 4%, 8.8%, 10.2%, 12.1%, 16.8% and 20.9%, respectively. The removal rate of AN is lower by 10.2%, 16.5%, 20.2%, 21.2%, 24% and 28.4%, respectively. The removal rate of TP is lower by 9.2%, 13.3%, 19.6%, 31%, 37.6% and 38.3%, respectively.

- (2) In order to verify the damage of *Chlorella* by graphene, the concentration of MDA and the activity of SOD in the algal cells were measured. The results show that in reactors T1–T7, the concentration of MDA increases from 4.47 nmol/mL to 27.54 nmol/mL, and the activity of SOD increases from 1.15  $\mu$ /mg prot to 19.25  $\mu$ /mg prot. As the concentration of graphene increases, MDA and SOD increase regularly during the same period. Thus, it is concluded that the addition of graphene can cause oxidative damage to *Chlorella vulgaris*.
- (3) Using optical microscopy and SEM, it is found that graphene is adsorbed on the surface of *Chlorella*, and enters the interior of *Chlorella*. It is shown that graphene causes microscopic damage on *Chlorella*. Through the blood plate count method, we estimated an average *Chlorella* reduction of 16%. Nevertheless, it is necessary to further explore whether graphene destroys or modifies the internal structure and material of chloroplasts inside *Chlorella*.
- (4) The damage of *Chlorella* by graphene can inhibit *Chlorella* from removing pollutants in sewage, and decrease the removal efficiency of nitrogen and phosphorus pollutants in the sequencing batch *Chlorella* reactor. This study provides theoretical and practical support for the safe use of graphene.

**Author Contributions:** W.X. conceived and designed the experiments and wrote the paper; Q.F. and Z.P. performed the experiments and contributed reagents and analysis tools; G.X. and Z.M. analyzed the data.

**Funding:** This research is funded by Chinese National Natural Science Foundations (41502333), Sichuan science and technology support project (2017JY0141, 2018GZ0416), China Postdoctoral Science Foundation (2017M610598, 2018T110963), Chengdu University of Technology extracurricular science and technology project (2018KJY0231) and the State Key Laboratory of Geohazard Prevention and Geoenvironment Protection Foundation (SKLGP2016Z019). We received above funds for covering the costs to publish in open access.

**Acknowledgments:** The authors gratefully acknowledge the technical support of Peng, J.F. in Southwest Jiaotong University.

**Conflicts of Interest:** The authors declare no conflict of interest.

## References

1. Ren, W.J.; Teng, Y. Environmental behavior of graphene and its effect on the transport and fate of pollutants in environment. *J. App. Ecol.* **2014**, *25*, 2723–2732.
2. Cornelis, G.; Hund-Rinke, K.; Kuhlbusch, T. Fate and bioavailability of engineered nanoparticles in soils: A review. *Crit. Rev. Environ. Sci. Technol.* **2014**, *44*, 2720–2764. [[CrossRef](#)]
3. Chen, G.; Huang, X.F.; An, L.; He, S.L.; Li, X.D.; Yang, D.H. Pilot-scale research on high rate algal pond for rural domestic sewage treatment at area around Taihu Lake. *Water Wastewater Eng.* **2006**, *32*, 37–40.
4. Huang, X.F.; He, S.L.; Chen, G.; Li, X.D.; Yang, D.H.; Zhou, Q. Enhancement of nutrient removal from domestic wastewater with HRAP in rural areas. *Environ. Eng.* **2008**, *1*, 7–10.
5. Li, M.; Jin, J.R.; Liu, D.Q. Research on immobilized algae cell flow bed for treatment living sewage. *J. Suzhou Inst. Silk Text. Technol.* **2013**, *6*, 6–9.
6. Clément, L.; Hurel, C.; Marmier, N. Toxicity of TiO<sub>2</sub> nanoparticles to cladocerans, algae, rotifers and plants-effects of size and crystalline structure. *Chemosphere* **2013**, *90*, 1083–1090. [[CrossRef](#)] [[PubMed](#)]
7. Jiang, G.X.; Shen, Z.Y.; Niu, J.F.; Zhuang, L.P.; He, T.D. Nanotoxicity of engineered nanomaterials in the environment. *Prog. Chem.* **2011**, *23*, 1769–1781.
8. Chen, A.W.; Zeng, G.M.; Chen, G.Q.; Yi, B.; Guo, Z. Advance in research on toxicity of metal nanomaterials. *Environ. Chem.* **2014**, *33*, 568–575.
9. Li, X.K.; Hu, X.G.; Zhou, Q.X. Research progress in phytotoxicity of carbon nanoparticles and its mechanisms. *J. Agro-Environ. Sci.* **2015**, *11*, 2041–2047.
10. Li, Y.X.; Feng, W.; Gong, N.; Sun, Y.Q.; Xiong, D.Q. Study of inhabitation of NiO nanoparticles to *Chlorella* sp. *Mari. Environ. Sci.* **2009**, *28*, 151–153.
11. Zhu, X.S. Study on the Ecotoxicology of Several Artificial Nanomaterials. Master's Thesis, University of Nankai, Tianjin, China, 2007. (In Chinese)
12. Xiao, H.X. Dissolution Behavior of Nano ZnO and Its Effect on Phosphorus Removal Efficiency of *Chlorella Vulgaris*. Master's Thesis, University of Xiangtan, Xiangtan, China, 2007. (In Chinese)

13. Wang, X.J.; Li, Z.S.; Xing, G.L.; Li, Z.N.; Yuan, H.L.; Yang, J.S. Optimization of *Chlorella pyrenoidosa*-15 photoheterotrophic culture and its use in wastewater treatment. *Environ. Sci.* **2012**, *33*, 2735–2740.
14. Huang, K.; Liu, L.; Dong, H.L. Study on *Chlorella* in sewage treatment. *Jiangxi Chem. Ind.* **2007**, *1*, 25–26. (In Chinese)
15. Lv, F.R.; Yang, H.B.; Li, Y.M.; Zhang, X.H.; Yu, Y.; Liu, Y. Study on the N,P purification ability of *Chlorella* under autotrophic condition. *Biotechnology* **2003**, *13*, 46–47.
16. Cai, Y.F.; Wei, Q.; Guo, L.N.; Sun, H.Y.; Zhou, J.; Zhang, J.L. Nitrogen and phosphorus removing from wastewater by six species of algal biofilm. *J. Guangxi Univ. (Nat. Sci. Ed.)* **2013**, *3*, 668–672. (In Chinese)
17. Huang, K. Study on the Removal of Nitrogen and Phosphorus from Sewage by Algae and Its Mechanism. Master's Thesis, University of Nanchang, Nanchang, China, 2007. (In Chinese)
18. Zhang, Y.L.; Zhu, H.Q.; Zhou, X.F.; Su, G.X. *The Principle and Technology of Wastewater Microalgae Resource Treatment*, 1st ed.; Science Press: Beijing, China, 2015; pp. 89–98. (In Chinese)
19. Gonçalves, A.L.; Pires, J.C.M.; Simões, M. A review on the use of microalgal consortia for wastewater treatment. *Algal Res.* **2017**, *24*, 403–415. [CrossRef]
20. Li, M.L.; Jiang, Y.L. Behaviors of engineered nanoparticles in aquatic environments and impacts on marine phytoplankton. *Environ. Sci.* **2015**, *36*, 365–372.
21. Zhang, N.; Jin, X.L.; Li, X.; Yue, J.J.; Wei, D.F. Progress of toxic effects of artificial nano materials on alga. *J. Anhui Agric. Sci.* **2011**, *39*, 6000–6003.
22. Zhao, W. Toxic Effects of Nanoscale TiO<sub>2</sub> on Typical Red Tide Algae. Master's Thesis, Ocean University of China, Qingdao, China, 2007. (In Chinese)
23. Yang, X.P.; Zhao, F.J. A review of uptake translocation and phytotoxicity of engineered nanoparticles in plants. *Environ. Sci.* **2013**, *34*, 4495–4502.



© 2018 by the authors. Licensee MDPI, Basel, Switzerland. This article is an open access article distributed under the terms and conditions of the Creative Commons Attribution (CC BY) license (<http://creativecommons.org/licenses/by/4.0/>).



MDPI  
St. Alban-Anlage 66  
4052 Basel  
Switzerland  
Tel. +41 61 683 77 34  
Fax +41 61 302 89 18  
[www.mdpi.com](http://www.mdpi.com)

*Materials* Editorial Office  
E-mail: [materials@mdpi.com](mailto:materials@mdpi.com)  
[www.mdpi.com/journal/materials](http://www.mdpi.com/journal/materials)







MDPI  
St. Alban-Anlage 66  
4052 Basel  
Switzerland

Tel: +41 61 683 77 34  
Fax: +41 61 302 89 18

[www.mdpi.com](http://www.mdpi.com)



ISBN 978-3-03921-017-6